T.F.
Cy. 1
APR 2 2 1983
MAY 0 6 1983
AGARD-CP-335
1984

AGARD-CP-335

AGARD

ADVISORY GROUP FOR AEROSPACE RESEARCH & DEVELOPMENT

7 RUE ANCELLE 92200 NEUILLY SUR SEINE FRANCE

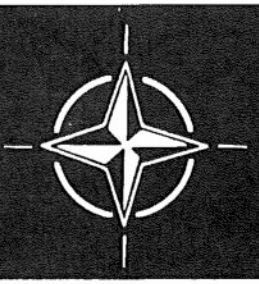
Property of U. S. Air Force
AEDC LIBRARY
F40600-81-C-0004

AGARD CONFERENCE PROCEEDINGS No. 335

Wall Interference in Wind Tunnels

TECHNICAL REPORTS
FILE COPY

NORTH ATLANTIC TREATY ORGANIZATION



DISTRIBUTION AND AVAILABILITY
ON BACK COVER

AGARD-CP-335

NORTH ATLANTIC TREATY ORGANIZATION

ADVISORY GROUP FOR AEROSPACE RESEARCH AND DEVELOPMENT

(ORGANISATION DU TRAITE DE L'ATLANTIQUE NORD)

AGARD Conference Proceedings No.335

WALL INTERFERENCE IN WIND TUNNELS

Papers presented and discussion held at the Fluid Dynamics Panel Specialists' Meeting held at Church House, London SW1, United Kingdom, 19–20 May 1982.

THE MISSION OF AGARD

The mission of AGARD is to bring together the leading personalities of the NATO nations in the fields of science and technology relating to aerospace for the following purposes:

- Exchanging of scientific and technical information;
- Continuously stimulating advances in the aerospace sciences relevant to strengthening the common defence posture;
- Improving the co-operation among member nations in aerospace research and development;
- Providing scientific and technical advice and assistance to the North Atlantic Military Committee in the field of aerospace research and development;
- Rendering scientific and technical assistance, as requested, to other NATO bodies and to member nations in connection with research and development problems in the aerospace field;
- Providing assistance to member nations for the purpose of increasing their scientific and technical potential;
- Recommending effective ways for the member nations to use their research and development capabilities for the common benefit of the NATO community.

The highest authority within AGARD is the National Delegates Board consisting of officially appointed senior representatives from each member nation. The mission of AGARD is carried out through the Panels which are composed of experts appointed by the National Delegates, the Consultant and Exchange Programme and the Aerospace Applications Studies Programme. The results of AGARD work are reported to the member nations and the NATO Authorities through the AGARD series of publications of which this is one.

Participation in AGARD activities is by invitation only and is normally limited to citizens of the NATO nations.

The content of this publication has been reproduced
directly from material supplied by AGARD or the authors.

Published September 1982

Copyright © AGARD 1982
All Rights Reserved

ISBN 92-835-0321-X



Printed by Technical Editing and Reproduction Ltd
5–11 Mortimer Street, London, W1N 7RH

PREFACE

The successful development of aircraft has depended heavily on the use of the wind tunnel since the beginning of powered flight. The experimental aerodynamicist has many problems to consider in using the wind tunnel in order to acquire useful aerodynamic data. These problems include Reynold's number corrections, wall and support interference, flow quality, and aeroelasticity. The purpose of this specialists' meeting was to bring those experimental aerodynamicists together to review and discuss current usage and basic developments for wind tunnel wall corrections. This specialists' meeting concentrated upon subsonic and transonic flow wall corrections. The meeting was organized into sessions of solid wall, ventilated wall, and adaptive wall wind tunnels and a summarizing round table discussion. No attempt will be made here to summarize in detail results of this meeting. This is very adequately covered in the round table discussion by the session chairmen; Professor A.D.Young, Mr L.H.Ohman, and Professor W.R.Sears.

The specialists' meeting has revealed encouraging progress in the area of wind tunnel wall correction. Not only are correction procedures improving but a great deal of research progress is evident with adaptive walls to reduce or eliminate wall interference. Most approaches for wall corrections seem now to rely upon measuring boundary conditions at or near the tunnel walls. For solid wall tunnels one independent flow variable, usually static pressure, is needed if the flow is assumed to be parallel (or corrected for boundary layer growth) to the walls. For ventilated wall tunnels, two independent flow variables are needed and are usually selected from static pressure, lateral pressure gradient, or velocity and its vector. The older concept of modeling the ventilated wall boundary conditions is not nearly so popular now as it was a decade ago.

In the adaptive wall research we see the Europeans heavily pursuing research with solid wall tunnels whereas in the United States there is more effort with ventilated adaptive wall tunnels and somewhat less with solid wall tunnels. The advantage of the solid wall approach is the requirement to measure only one independent flow variable, whereas the ventilated wall tunnel requires two. On the other hand a ventilated wall tunnel may be easier to control at transonic Mach numbers and offer a higher Mach number capability. This and many other practical questions will need answers before the tunnel designer can settle upon an approach for application in full scale production wind tunnels. The practicality of the adaptive wall tunnel has been greatly enhanced by advances in computer hardware and software and mathematical algorithms. With rapid advances in this area it does not appear that computational time will be a major constraint in using adaptive walls on a practical basis.

DR M.L.LASTER
Programme Chairman

AGARD FLUID DYNAMICS PANEL

M. l'Ing en Chef B.Monnerie (Chairman)
Chef de la Division d'Aérodynamique Appliquée
ONERA
29, Avenue de la Division Leclerc
B.P. 72
92322 Châtillon – France

Dr L.Roberts (Deputy Chairman)
Joint Institute for Aeronautics and Astronautics
Department of Aeronautics and Astronautics
Stanford University
Stanford, California 94305-2186 – USA

PROGRAM COMMITTEE MEMBERS

Dr M.L.Laster (Chairman)
Director of Technology (DOT)
Hqs. Arnold Engineering Development Center
Arnold Air Force Station
Tennessee 37389 – USA

Prof. Dr Ing. B.Laschka
Institut für Stromungsmechanik
der Tech. Univers.
Bienroder Weg 3
D-3300 Braunschweig – Germany

Prof. E.Mattioli
Director Istituto Mecchanica Applicata
Universita di Ancona
Via Delia Montagnola 30
60100 Ancona – Italy

Ir. J.P.Hartzuiker
Chief, Compressible Aerodynamics Dept.
National Aerospace Laboratory NLR
Anthony Fokkerweg 2
1059 CM Amsterdam – Netherlands

Mr L.H.Ohman
Head, High Speed Aerodynamics Lab.
National Aeronautical Establishment
National Research Council – Montreal Rd.
Ottawa, Ontario K1A OR6 – Canada

Prof. A.D.Young
Queen Mary College
Aeronautics Dept.
Mile End Road
London E1 4N6 – UK

M. l'Ing C.Dujarric
STPA
4, Avenue de la Porte d'Issy
75996 Paris Armées – France

PANEL EXECUTIVE

Mr R.H.Rollins II
Executive, Fluid Dynamics Panel
AGARD
7, rue Ancelle
92200 Neuilly sur Seine – France

CONTENTS

	Page
PREFACE	iii
PANEL AND PROGRAM OFFICERS	iv
	Reference
SESSION I – SOLID WALL WIND TUNNELS	
A METHOD FOR DETERMINING WALL-INTERFERENCE CORRECTIONS IN SOLID-WALL TUNNELS FROM MEASUREMENTS OF STATIC PRESSURE AT THE WALLS by P.R.Ashill and D.J.Weeks	1
THE USE OF PANEL METHODS FOR THE EVALUATION OF SUBSONIC WALL INTERFERENCE by D.R.Holt and B.Hunt	2
SIMILARITY RULES FOR EFFECTS OF SIDEWALL BOUNDARY LAYER IN TWO-DIMENSIONAL WIND TUNNELS by R.W.Barnwell and W.G.Sewall	3
REYNOLDS NUMBER EFFECTS ON TRANSONIC SHOCK LOCATION by F.Aulehla and A.Eberle	4
A REPORT OF A GARTEUR ACTION GROUP ON "TWO-DIMENSIONAL TRANSONIC TESTING METHODS" by A.Elsenaar and E.Stanewsky	5
SESSION II – VENTILATED WALL WIND TUNNELS	
FLOW PROPERTIES OF SLOTTED-WALL TEST SECTIONS by S.B.Berndt	6
WALL BOUNDARY-LAYER EFFECTS IN TRANSONIC WIND TUNNELS by Y.Y.Chan	7
THREE DIMENSIONAL WALL CORRECTIONS FOR VENTILATED WIND TUNNELS by H.Holst	8
MEASURED BOUNDARY CONDITIONS METHODS FOR 2D FLOW by J.Smith	9
SUBSONIC WALL INTERFERENCE CORRECTIONS FOR FINITE-LENGTH TEST SECTIONS USING BOUNDARY PRESSURE MEASUREMENTS by M.Mokry	10
AMELIORATIONS DES CALCULS DES EFFETS DE PAROIS DANS LES SOUFFLERIES INDUSTRIELLES DE L'ONERA par X.Vaucheret	11
EXPERIMENTAL STUDY AND THEORETICAL VERIFICATION OF WALL INTERFERENCE WITH A "CALIBRATION MODEL" IN HIGH SPEED WIND TUNNELS OF DIFFERENT SIZES* by B.Schulze	12
SESSION III – ADAPTIVE WALL WIND TUNNELS	
ON THE USE OF ADAPTIVE WALLS FOR TRANSONIC WIND TUNNEL by U.Ganzer	13

* Paper presented but no manuscript available.

	Reference
UTILISATION DE PAROIS ADAPTABLES POUR LES ESSAIS EN COURANT PLAN par J.P.Archambaud et J.P.Chevallier	14
THE STATUS OF TWO- AND THREE-DIMENSIONAL TESTING IN THE UNIVERSITY OF SOUTHAMPTON TRANSONIC SELF-STREAMLINING WIND TUNNEL by S.W.D.Wolf, I.D.Cook and M.J.Goodyer	15
ADAPTIVE-WALL TUNNEL-RESEARCH AT AMES RESEARCH CENTER by E.T.Schairer and J.P.Mendoza	16
DEVELOPMENT OF A THREE-DIMENSIONAL ADAPTIVE WALL TEST SECTION WITH PERFORATED WALLS by R.L.Parker, Jr. and J.C.Erickson, Jr.	17
ROUND TABLE DISCUSSION	RTD

A METHOD FOR DETERMINING WALL-INTERFERENCE CORRECTIONS IN SOLID-WALL TUNNELS FROM MEASUREMENTS OF STATIC PRESSURE AT THE WALLS

by

P. R. Ashill and D. J. Weeks
Aerodynamics Department, Royal Aircraft Establishment,
Bedford MK41 6AE, England

SUMMARY

A method is described for calculating wall interference in solid-wall tunnels from measurements of pressures at the walls. The method has the advantage over similar techniques of not requiring a description of the flow in the region of the model. Calculations of wall interference for aerofoil tests at high subsonic speeds are presented, and the wall corrections obtained are compared with results from other methods. Generally good agreement is obtained. A theoretical evaluation of the method suggests that it is suitable for calculating wall corrections for three-dimensional configurations that are not amenable to correction by classical methods.

SYMBOLS

b	tunnel breadth
c	aerofoil chord
C_D	drag coefficient, referred to $\frac{1}{2}\rho_e U_e^2 c$
C_m	coefficient of pitching moment about leading edge, nose up positive, referred to $\frac{1}{2}\rho_e U_e^2 c^2$
C_N	normal-force coefficient, referred to $\frac{1}{2}\rho_e U_e^2 c$
C_p	static-pressure coefficient referred to conditions far upstream of model
dS'	element of area on surface Σ
f and r	upstream and downstream extremities of surface Σ
h	tunnel height
M	Mach number
m', n'	integers defining numbers of steps in numerical integration of velocities induced by vortex distribution
N	normal to S_2, inward to Λ in transformed space
n	normal to S_2, inward to Λ in physical space
o( )	at most of order
p,P,q,Q	integers defining numbers of streamwise rows of wall static holes
R	see equation (5)
R_c	Reynolds number based on aerofoil chord
S_1	surface surrounding areas of transonic flow and shear layers associated with model (Fig 1)
S_2	cylindrical outer part of surface Σ (Fig 1)
U	stream speed
u,v,w	x, y, z components of perturbation velocity
x,y,z	rectangular Cartesian coordinate system, x positive in streamwise direction and z positive upwards
(X,Y,Z)	$= (x, \beta y, \beta z)$
α	incidence
α_G	geometric or uncorrected incidence
β	$= (1 - M_e^2)^{\frac{1}{2}}$
Δ	prefix denoting increment due to wall constraint
δ^*	wall boundary-layer displacement thickness
Λ	region between tunnel walls and model where flow is of small perturbation type
ρ	density of undisturbed stream
Σ	surface bounding region Λ (Fig 1)
Φ	velocity potential
ϕ	perturbation velocity potential
ν	region bounded by surface S_1 (Fig 1)

Suffixes

c	quantity referred or corrected to empty-tunnel conditions
e	effective free-stream or corrected conditions
f,r	upstream and downstream extremities of surface Σ
∞	far upstream

Primes refer to source point in integrals defining wall effect

* refers to local sonic conditions

1. INTRODUCTION

The continuing need to refine wind-tunnel test techniques has stimulated work in recent years on the use of flow measurements to determine tunnel-wall corrections. For some time, it has been realised that classical wall-correction methods are unsatisfactory in a number of respects. For tunnels with slotted walls, the 'classical' wall boundary

condition is known to be unrepresentative[1], while, in the case of perforated-wall tunnels, the assumptions made in deriving wall porosity are questionable. In the case of tunnels with solid walls, the wall boundary conditions are reasonably well defined but, generally, the corrections are numerically larger than those for tunnels with slotted or perforated walls. Consequently, greater emphasis has to be placed on representing the model flow field. In the classical methods, the assumption is made that the flow is uniformly of the small-perturbation type[2], and consequently they fail to simulate conditions close to the model in a number of important cases (eg transonic flows, high-lift models).

In order to overcome these problems, several methods have been developed that are based on measurements of static pressure at or close to the tunnel walls. Possibly the earliest example is the method proposed by Göthert[3] for calculating blockage corrections associated with tests at high subsonic speeds in solid-wall tunnels. This method relies on measurements of static pressure at the walls to redefine the strengths of the sources simulating the volume effect of the model. More recently, Hackett, Wilsden and Stevens[4] have employed a similar approach in connection with low-speed tests on models at high angles of incidence. The method of Smith[5] and the related technique of Capelier, Chevallier and Bouniol[6] are examples of methods in which the measurements of static pressure at or near the tunnel walls are used to provide alternative boundary conditions.

The method to be described in this paper has the advantage over these methods of not requiring a simulation of the flow in the region of the model. This feature is of particular benefit in cases where the flows are complex and hence are not easily modelled, for example, those with shocks and/or separations. On the other hand, unlike the methods of Smith and Capelier *et al*, it presumes a knowledge of flow angle as well as of static pressure close to the tunnel walls. However, in the case of tunnels with solid walls, the boundary flow angle is essentially defined by the condition of no flow through the tunnel walls, and so only static pressures need be measured.

The method is formulated in general terms in Section 2, after which the paper is concerned exclusively with solid-wall tunnels. In Section 3, the method is used to obtain wall corrections for aerofoil tests at high subsonic speeds in the 8 ft x 8 ft Tunnel (RAE) and in the Adaptive Wall Tunnel T2 (ONERA). Where possible, comparisons are made with other wall-correction methods, and, in the case of T2, the method is used to determine wall corrections for nominally interference-free conditions. Finally, in Section 4, a feasibility study is described into the application of the method to tests on three-dimensional models.

2. FORMULATION OF METHOD

It is supposed that there exists a region Λ between the tunnel walls and the model where the flow can be adequately described by the small-perturbation form of the potential equation

$$\beta^2\phi_{xx} + \phi_{yy} + \phi_{zz} = 0 \ .$$

This region (Fig 1) excludes shear layers and areas of transonic flow, and is bounded by the surface S_1 surrounding the model and an outer surface S_2 which is taken to be cylindrical.

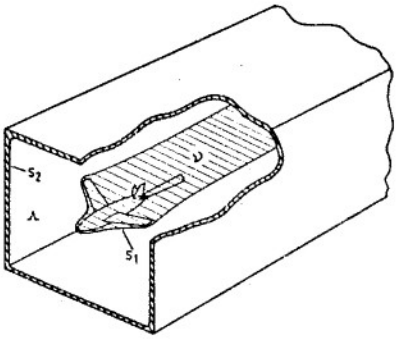


FIG.1 REGION AND BOUNDING SURFACES FOR APPLICATION OF GREEN'S THEOREM

In the classical way[7], the small-perturbation equation is reduced to the Laplace equation

$$\phi_{XX} + \phi_{YY} + \phi_{ZZ} = 0 \qquad (1)$$

by using the transformation

$$(X, Y, Z) = (x, \beta y, \beta z) \ .$$

Here we have followed Evans[8] in writing the β factor in terms of the corrected Mach number, M_e.

The perturbation potential is defined by

$$\phi = \Phi - U_\infty x \ , \qquad (2)$$

where Φ is velocity potential and U_∞ is stream speed far upstream.

Using Green's theorem[9] we are able to write the formal solution to equation (1) for the flow in Λ as

$$\phi(X,Y,Z) = -\frac{1}{4\pi}\iint_{\Sigma}\{\frac{\partial\phi}{\partial N}\frac{1}{R} - \phi\frac{\partial}{\partial N}(\frac{1}{R})\}dS' \ , \qquad (3)$$

where

$$\Sigma = S_1 + S_2 + f + r \ ,$$

and f and r are the upstream and downstream extremities of the surface Σ surrounding the region Λ. For convenience, f and r are taken to be planar and perpendicular to the X direction so that

$$\partial/\partial N \equiv \pm\, \partial/\partial X \qquad (4)$$

at f and r, respectively. The directional derivatives are defined positive inward to the region and

$$R = \{(X - X')^2 + (Y - Y')^2 + (Z - Z')^2\}^{\frac{1}{2}} , \qquad (5)$$

where (X', Y', Z') are the coordinates of the element dS' of the surface Σ.

Because ϕ is the perturbation potential

$$\partial\phi/\partial X \to 0, \text{ and } \phi \to 0 \text{ as } X \to -\infty , \qquad (6)$$

and hence, using equations (3), (4), (5) and (6), we find that the contribution to ϕ of the surface integral over f tends to zero as the distance of the surface f upstream of the model is increased.

It is assumed that the flow in A far downstream of the model is irrotational and hence may be described by potential singularities simulating the model and the associated images beyond the tunnel walls. Consideration of flows of such singularities indicates that, in general,

$$\left.\begin{aligned} \phi(X,Y,Z) &\sim k_1 X + k_2 \ln X + k_3 g(Y,Z) + o(1/X) \\ \partial\phi(X,Y,Z)/\partial X &\sim k_1 + k_2/X + o(1/X^2) \end{aligned}\right\} , \qquad (7)$$

where k_1, k_2 and k_3 are coefficients which depend on factors such as the model and the tunnel-wall configuration, and o( ) denotes 'at most of order'. The function g(Y,Z) is bounded within the confines of the tunnel.

Combining equations (3), (4), (5) and (7), we find that, in the region of the model, the contribution to ϕ from the integral over r is $o(\ln X_r / X_r^2)$. Therefore the contributions of the surfaces f and r may be ignored provided that they are placed sufficiently far from the model. Consequently the integration may be supposed to be restricted to the surfaces S_1 and S_2 provided that S_2 is understood to extend far upstream and downstream.

Next, consider a free-air flow that is equivalent to the wind-tunnel flow and which has the free-stream speed U_e. In this case, the perturbation potential is given by

$$\phi_e = \Phi_e - U_e x - U_e \Delta\alpha z . \qquad (8)$$

The last term arises because the free stream is inclined upwards relative to the wind tunnel flow far upstream by the angle

$$\Delta\alpha = \alpha_e - \alpha_G ,$$

where α_G is the uncorrected incidence of the model in the tunnel.

The surface bounding A is taken to be S_1, as before, together with the internal surface of a sphere centred on a point within the model. As the radius of the sphere increases towards infinity, its contribution to ϕ_e vanishes[9] leaving

$$\phi_e(X,Y,Z) = -\frac{1}{4\pi}\iint_{S_1}\left\{\frac{\partial\phi_e}{\partial N}\frac{1}{R} - \phi_e\frac{\partial}{\partial N}\left(\frac{1}{R}\right)\right\}dS' . \qquad (9)$$

Subtracting equation (9) from equation (3) and recalling that the suffix Σ is replaced by $S_1 + S_2$ in the latter equation, we obtain for the difference in perturbation potential between the two flows

$$\phi - \phi_e = \Delta\phi - \frac{1}{4\pi}\iint_{S_1}\left\{\frac{\partial(\phi - \phi_e)}{\partial N}\frac{1}{R} - (\phi - \phi_e)\frac{\partial}{\partial N}\left(\frac{1}{R}\right)\right\}dS' , \qquad (10)$$

where

$$\Delta\phi = -\frac{1}{4\pi}\iint_{S_2}\left\{\frac{\partial\phi}{\partial N}\frac{1}{R} - \phi\frac{\partial}{\partial N}\left(\frac{1}{R}\right)\right\}dS' \qquad (11)$$

is the increment in perturbation potential due to wall constraint.

Strict equivalence between the two flows is achieved provided that $\phi = \phi_e$ everywhere in the near flow field of the model. It follows from equations (2) and (8) that, in this region,

$$\phi - \phi_e = (U_e - U_\infty)x + U_e\Delta\alpha z . \qquad (12)$$

Consequently, $\phi - \phi_e$ satisfies Laplace's equation (1) within the region ν (shown hatched in Fig 1) enclosing the model and its associated regions of transonic flow and shear layers, and hence from the divergence theorem[9] the integral in equation (10) vanishes identically. Therefore, referring to equations (10) and (12), we have

$$\phi - \phi_e = \Delta\phi = (U_e - U_\infty)x + U_e\Delta\alpha z ,$$

This implies that the wall-induced increments in streamwise velocity

$$\Delta u = \partial\Delta\phi/\partial x = U_e - U_\infty$$

and upwash

$$\Delta w = \partial\Delta\phi/\partial z = U_e\Delta\alpha$$

do not vary in the region of the model. Such flows are generally called 'correctable'. It follows that, for flows that are not 'correctable', strict equivalence cannot be achieved. Limited equivalence can, however, be accomplished by adjusting the shape of the model so that, for example, the pressure distributions on the model are the same in the two cases. In practice, this is not easily done except for small-perturbation flows. In Section 3.2, the small perturbation method is used to determine the change in camber required in

free-air flows to allow for the effect on model pressure distribution of the chordwise variation of wall-induced upwash in tunnel tests on an aerofoil at high subsonic speeds.

The first part of the integral of equation (11) is the contribution of a distribution of sources and the second represents a distribution of doublets with axes perpendicular to S_2. It may be shown[10] that the doublet distribution is directly equivalent to a distribution of elementary horseshoe vortices of strength, $u = \partial\phi/\partial x$. Hence the interference potential is completely defined by two components of perturbation velocity at the surface S_2.

For a tunnel with a cylindrical working section and an infinitesimally thick boundary layer, S_2 may be chosen to coincide with the tunnel walls. If, in addition, the walls are solid, the normal velocity at S_2, $\partial\phi/\partial n$, is zero. Hence the source strength

$$\partial\phi/\partial N = (1/\beta)\partial\phi/\partial n = 0.$$

In this case, therefore, the source term of equation (11) vanishes, and the wall interference may be calculated once the streamwise component of perturbation velocity at the walls is determined. This is most conveniently achieved by measuring the static pressures at the walls and by using the linearised version of Bernoulli's equation

$$C_p = -2u/U_\infty \ , \qquad (13)$$

where the static-pressure coefficient C_p is referred to conditions far upstream.

In practice, the displacement surface representing the tunnel walls and their boundary layers, is not truly cylindrical. Partial allowance is generally made for this by referring measurements of wall static pressures to empty-tunnel conditions (ie conditions in the empty tunnel with the flow far upstream the same as those with the model in the tunnel). However, this correction is complete only if the normal velocity at S_2 does not change between the empty-tunnel state and the condition with the model in the working section. Clearly, this is not the case if the tunnel walls are either porous or solid and adaptive. For such tunnels, the present method requires the change in normal velocity (or flow angle) at S_2 to be determined either by measurement or some other means. In this paper, we confine our attention to solid-wall tunnels. Allowance for the change in shape of the walls of adaptive-wall tunnels is made by invoking the condition of no flow through the tunnel walls. To the order of accuracy of the small perturbation theory this implies that at S_2

$$\partial\phi/\partial N = (1/\beta)U_\infty[\partial n_c/\partial x]_{WALL} \ . \qquad (14)$$

Similar allowance is made for the change in displacement effect of the wall boundary layer due to the presence of the model and wall adaptation, δ_c^*, the appropriate source strength being

$$\partial\phi/\partial N = (1/\beta)U_\infty \ \partial(\delta_c^*)/\partial x \ . \qquad (15)$$

For two-dimensional flows around aerofoils mounted between the sidewalls of wind tunnels with rectangular working sections, the singularities on the sidewalls are ignored, and those on the roof and the floor are replaced by two-dimensional sources and vortices[11]. In practice, such flows are not strictly two dimensional because of the interaction between the sidewall boundary layers and the aerofoil. However, although this effect can be significant, it is doubtful if the calculation of it justifies the complication of measuring the boundary conditions on the sidewalls. A number of attempts[12,13,14,15] have been made to treat this problem theoretically but not with complete success. Perhaps the most promising of these is the method proposed by Barnwell[14] and recently extended by Sewall[15] to transonic flows. However, in its present form, the method is limited to cases of small $\beta b/c$, where b is model span (or tunnel breadth) and c is aerofoil chord.

Before passing to applications of the method we note that the wall-induced velocities may be obtained by vector differentiation of equation (11). Because the integrand of this expression is smooth and continuous, the differentiation may be taken under the integral sign.

3. APPLICATION OF METHOD TO TESTS ON AEROFOILS

3.1 Numerical approximation

Measurements of static pressure increments and wall displacements on the centre line of the roof and the floor of the working section are interpolated by using the Cubic-Spline method. Extrapolation of the static-pressure increments to infinity upstream and downstream is achieved by making use of the exponential character of the wall-velocity increments in the classical theory of solid-wall interference. Furthermore, it is assumed that, far downstream, the static-pressure coefficient[2]

$$C_{p_c} = -\frac{c}{h}\frac{(1 + 0.4M_e^2)}{\beta^2} \ C_D \ .$$

Here h is working-section height and C_D is the section drag coefficient. The wall displacements are extrapolated by assuming that, upstream and downstream of the region where they are measured, the streamwise slope of the wall displacement is zero.

The integrals in the expressions for the wall-velocity increments are evaluated by using Simpson's rule with a step length $\Delta x = 0.025\beta h$ over the interval $-2\beta h \leqslant x \leqslant 2\beta h$, where x is measured from the leading edge of the aerofoil. On the basis of a number of trial calculations, the contributions of the integrals over the interval $-\infty \leqslant x < -2\beta h$ are

ignored, and, in the interval $2\beta h < x \leqslant \infty$, the static-pressure increments are assumed to be equal to their values at $x = 2\beta h$. This allows the integration of the vortex distribution to be performed analytically in the interval $2\beta h < x \leqslant \infty$.

3.2 Tests in RAE 8 ft x 8 ft Wind Tunnel

A series of aerofoil sections has been tested in the 8 ft x 8 ft Wind Tunnel with the aim of providing a better understanding of the boundary layers on 'advanced' aerofoil sections. These sections share the same shape ahead of 65% chord, differing in the degree of rear camber or trailing-edge thickness. The size of the model (c/h = 0.260, thickness/chord ratio 0.14) is decided primarily by the need to make detailed measurements of the boundary-layer flows over a wide range of Reynolds number (up to 20 x 10^6). Transition is fixed at 5% chord on both surfaces of the aerofoils by means of the air-injection method, in which air is injected into the boundary layer through a large number of holes drilled normal to the surface. Details of the construction of the system can be found in Ref 11. The method has the advantage of allowing the disturbance required to fix transition to be minimised for any given conditions during the test.

As is normal for subsonic tests in the 8 ft x 8 ft Tunnel, the flexible (roof and floor) liners were maintained in an essentially straight configuration[16]. As a consequence of this and of the relatively large size of the model, some of the flows examined are not 'correctable' in the strict sense. This point is illustrated in Fig 2 which shows the variation along the model chord of the wall interference for two typical cases. The chordwise variation of the streamwise (or blockage) increment in Mach number is small, suggesting that, as regards blockage, the flow is 'correctable'. On the other hand, for cases of interest (M_e = 0.73, 0.3 < C_N < 0.7), the chordwise variation of wall-induced upwash is significant and cannot reasonably be ignored.

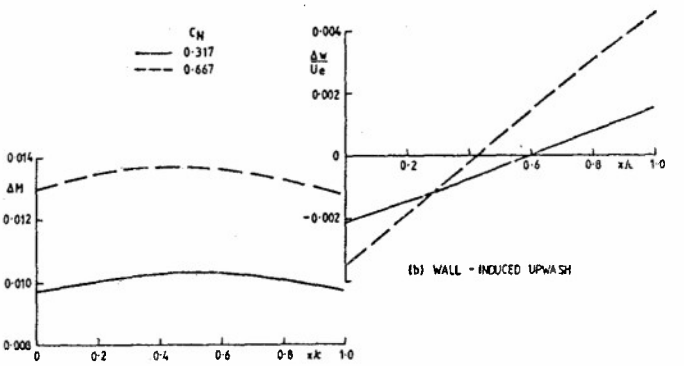


FIG.2 VARIATION ALONG THE CHORD LINE OF THE MODEL OF WALL - INTERFERENCE ; M_e = 0·73

Measurements have been made of static pressures on the aerofoils as well as on the roof and the floor (Fig 3). In addition, drag has been determined from measurements of total and static pressures made with a wake rake situated approximately two chords downstream of the aerofoil. Typical results for the static-pressure coefficient C_{p_c} are shown in Fig 4. From this it will be inferred that the assumptions of the present method are not invalidated near the wall, even for cases with significant regions of supercritical flow close to the aerofoil.

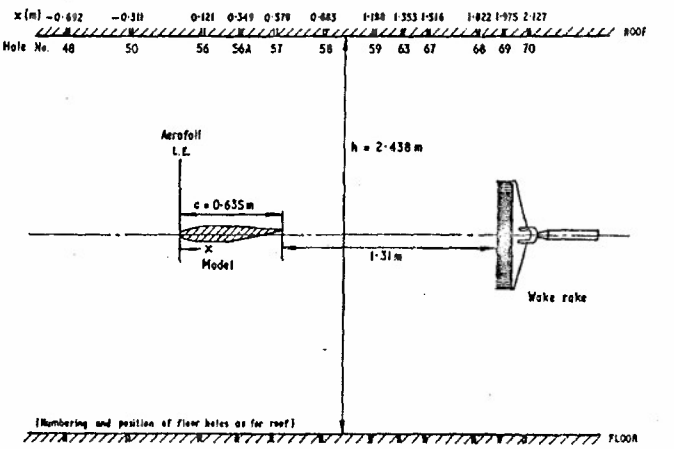


FIG.3 NUMBERING AND POSITIONS OF WALL STATIC PRESSURE HOLES FOR ROOF AND FLOOR OF WORKING SECTION

The following discussion is concerned with results for wall interference calculated for tests at a Reynolds number of 20 x 10^6 on one of the aerofoil sections, RAE 5225. This aerofoil section is designed to have a high degree of rear loading and an essentially shock-free flow on the upper surface for C_N = 0.6, M_∞ = 0.734 and a chordal Reynolds number R_c = 20 x 10^6. No allowance is made for the interaction between the flow field of the model and the wall boundary layers. Calculations have been made of the effect of the roof and floor boundary layers by using the Lag Entrainment method[17] in conjunction with measured pressure distributions. Results obtained for the increments in Mach number and upwash[10,11] indicate that the effect is negligible.

As has already been noted, methods currently available for calculating the effect of the sidewall boundary layers are not entirely adequate. This matter is currently receiving attention at RAE, and it is hoped to report on the work in the near future. In the present case, however, the displacement thickness of the wall boundary layer is small compared with

the span of the model ($\delta^*/b \simeq 0.005$) and the aspect ratio of the model is relatively large ($b/c \simeq 3.8$). It is anticipated, therefore, that the effect is small.

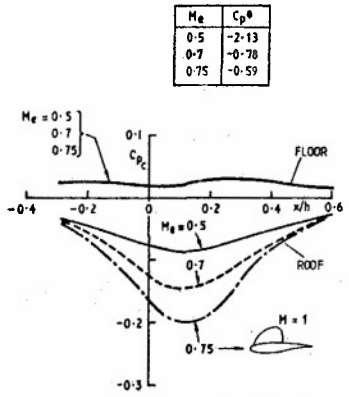


FIG.4 WALL STATIC PRESSURE INCREMENTS $\alpha_g = 1{\cdot}5^\circ$ ($C_N \simeq 0{\cdot}5$)

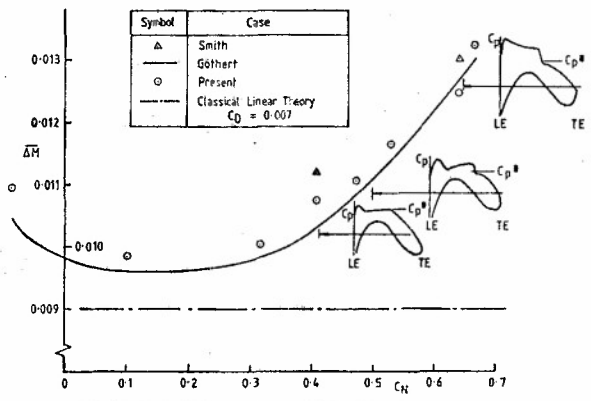


FIG.5 BLOCKAGE INCREMENT IN MACH NUMBER, VARIATION WITH NORMAL-FORCE COEFFICIENT; $M_e \simeq 0{\cdot}73$

Since the streamwise variation of the blockage increment in Mach number is small, it is reasonable to define a mean value along the chord $\overline{\Delta M}$. Various calculations of this increment are shown in Fig 5 plotted against normal-force coefficient for $M_e \simeq 0.73$. As well as those of the present method, results are shown from Smith's method[5], Göthert's technique[3] and classical linear theory[2]. The agreement between the first three methods is reasonable, the variation with normal-force coefficient indicated by the present method being closely matched by that of Göthert's method. By contrast, classical linear theory gives values that are consistently lower than those of the other methods. This is especially evident for $C_N > 0.4$ where non-linear effects associated with compressibility and model lift[2] would be expected to influence the wall static-pressure increments and hence the blockage. The present method and Göthert's technique are found to give blockage increments that are in good agreement over the range of Mach numbers and normal-force coefficients tested.

With the exception of Göthert's method, which is restricted to the calculation of blockage, corresponding variations with normal-force coefficient of the wall-induced upwash and its streamwise gradient, in each case at mid chord, are shown in Figs 6(a) and (b). The agreement between the present method and classical theory (accurate to order $(c/\beta h)^2$) is seen to be particularly good. This might have been expected because

(a) the wall boundary conditions are reasonably well defined for a solid wall tunnel;

(b) for specified values of c/h and free-stream Mach number, classical theory indicates that the wall-induced upwash depends primarily on lift and pitching moment which are known from measurements of static pressure on the model.

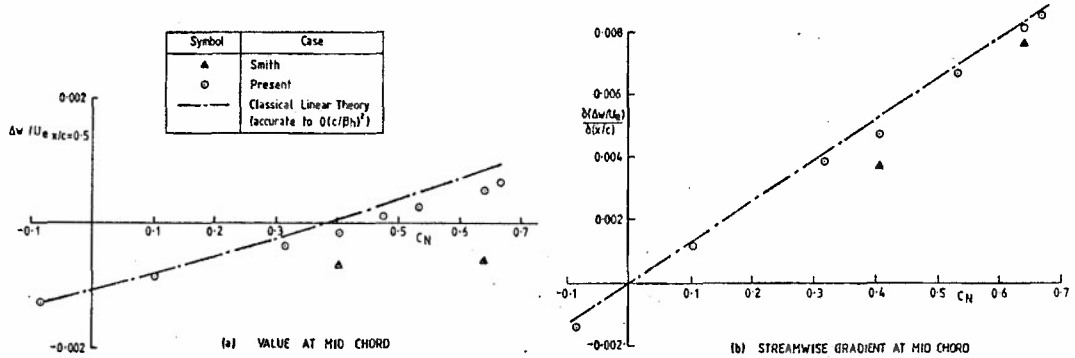


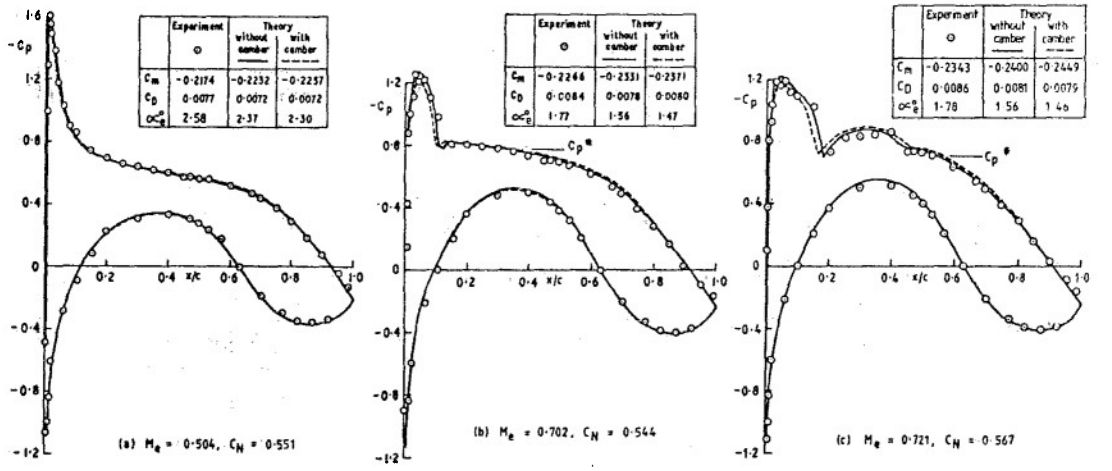
FIG.6 VARIATION WITH NORMAL-FORCE COEFFICIENT OF WALL-INDUCED UPWASH

Although the flows examined are not strictly 'correctable', comparisons have been made between measurement and calculation of the equivalent free-air flows with the object of assessing the accuracy of the wall-interference correction of the present method. The calculations have been made by using the viscous version of the Garabedian and Korn program

(VGK)[18]. Allowance for the chordwise variation of wall-induced upwash is made by adjusting the camber of the aerofoil. The wall-induced upwash used to derive the camber increment is obtained from classical theory which, as noted above, is in good agreement with the present method. The increment in aerofoil camber may be written as

$$\frac{\Delta z}{c}\text{CAMBER} = \frac{C_N}{\beta}\frac{\pi}{48}\left(\frac{c}{h}\right)^2 \frac{x}{c}\left\{1 - \frac{x}{c}\right\} .$$

Because of the speculative nature of this correction, which is strictly justified only for small-perturbation flows, the calculations have been done both with and without the camber adjustment. In all the calculations, the artificial viscosity parameter, ε, is taken to be 0.8, and, on the basis of comparisons made by Lock between results from the Garabedian and Korn program and numerical solutions of Euler's equation, the quasi-conservative difference parameter (λ) is set equal to 0.25.

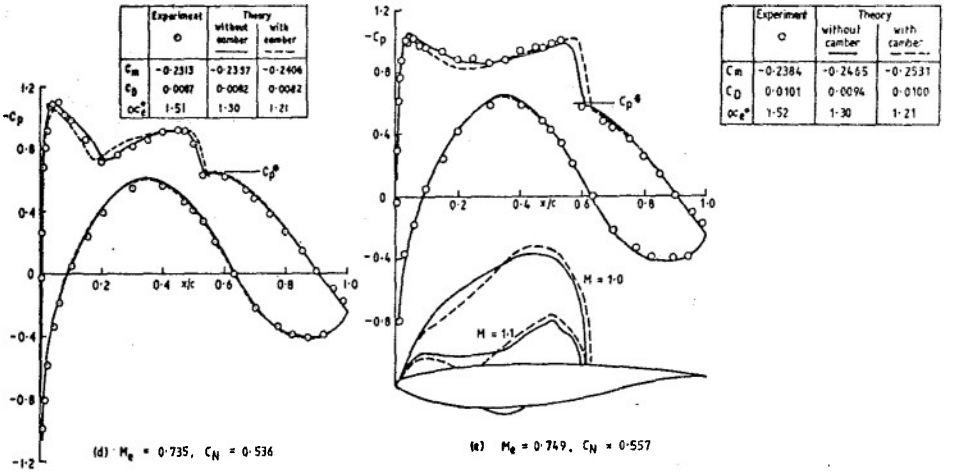


	Experiment ○	Theory without camber	Theory with camber
C_m	-0·2174	-0·2232	-0·2257
C_D	0·0077	0·0072	0·0072
$\alpha_c°$	2·58	2·37	2·30

	Experiment ○	Theory without camber	Theory with camber
C_m	-0·2246	-0·2331	-0·2371
C_D	0·0084	0·0078	0·0080
$\alpha_c°$	1·77	1·56	1·47

	Experiment ○	Theory without camber	Theory with camber
C_m	-0·2343	-0·2400	-0·2449
C_D	0·0086	0·0081	0·0079
$\alpha_c°$	1·78	1·56	1·46

FIG. 7
RAE 5225 PRESSURE DISTRIBUTIONS - COMPARISON BETWEEN VGK THEORY AND MEASUREMENT



	Experiment ○	Theory without camber	Theory with camber
C_m	-0·2313	-0·2357	-0·2404
C_D	0·0087	0·0082	0·0082
$\alpha_c°$	1·51	1·30	1·21

	Experiment ○	Theory without camber	Theory with camber
C_m	-0·2384	-0·2465	-0·2531
C_D	0·0101	0·0094	0·0100
$\alpha_c°$	1·52	1·30	1·21

Comparisons between measured and calculated aerofoil pressure distributions are shown in Figs 7(a) to (e) for $C_N \simeq 0.55$ and for corrected Mach numbers from 0.5 to 0.75. Uncertainties in the angle of incidence arising from, for example, inadequacies in the treatment of the viscous/inviscid interactions in the theory, are accommodated by making the comparisons at a given lift rather than at the same angle of incidence. Generally, the agreement between theory and measurement is good, with little difference between the two sets of calculations. However, at $M_e = 0.75$, the calculation with the camber correction, gives a shock position that is significantly further downstream than that indicated by the measurements. Because of the approximate nature of the camber-correction technique, it is not possible to say if this is a genuine effect. It may be argued, quite reasonably, that the supercritical flow depends primarily on the actual shape and curvature of the aerofoil surface ahead of the shock wave. However, the simple technique does show that wall-induced flow curvature is potentially a serious problem deserving further study, and it suggests that, for routine testing of aerofoils, the effect is best minimised. The relatively good agreement between theory and measurement on the forward part of the lower surface suggests that the correction to Mach number given by the present method is reliable.

3.3 T2 Adaptive-Wall Tunnel

The T2 Tunnel is the subject of a paper to be presented by Archambaud and Chevallier[19] at this Symposium. We will therefore not describe the tunnel but, because it is relevant to wall-correction methods, will briefly consider the method used to adapt the walls.

The working section is equipped with upper and lower walls that can be distorted to minimise or to eliminate wall interference. In order to establish substantially interference-free conditions, an iterative procedure is used; this is based on a comparison between a flow variable (eg static pressure) measured at the walls and the corresponding quantity inferred from the hypothetical unconfined flow. In the calculation procedure, allowance is made for the change in displacement thickness of the roof and floor boundary layers due to the presence of the model and the change in wall shape.

As an independent check on the technique, the present method has been used to calculate the wall interference for a NACA 0012 aerofoil of chord length 150 mm (c/h = 0.390). The cases considered are listed in Table 1.

TABLE 1

Case	M_∞	α°_G	ΔM	$\Delta\alpha^\circ$	Remarks
1	0.73	0	0.023	-0.007	Straight walls
2	0.73	0	0.002	0.005	Adapted walls
3	0.73	2	0.009	0.144	Unadapted walls*
4	0.73	2	0.004	0.017	Adapted walls
5	0.73	3	0.004	-0.001	Adapted walls
6	0.85	0	0.076	0.012	Unadapted walls (M > 1 at wall)
7	0.85	0	0.012	0.027	Adapted walls (M < 1 at wall)

ΔM and $\Delta\alpha$ evaluated at mid-chord (x/h = -0.065)
*Walls adapted for Case 2

WALL-INDUCED INCREMENTS IN MACH NUMBER AND INCIDENCE, NACA 0012 IN T2 TUNNEL

As noted in Section 2, the boundary values used in the present method are referred to those of the empty tunnel, which is unambiguously defined as the tunnel configuration with straight walls and with a mean line that is parallel to the reference velocity vector. A significant amount of random scatter is observed in the wall static pressures for the empty tunnel which is not evident with the model in the tunnel. After averaging the data for various empty-tunnel tests at the same reference conditions it is found that the correction to empty-tunnel conditions is found to be negligible except at a small number of static holes. The static pressures at these holes, which are presumably affected by surface imperfections, have been duly corrected. Typical distributions of the static-pressure coefficient C_{p_c} and the wall deflection are shown in Fig 8.

In order to be consistent with the method used to determine the wall shape[20], the present calculations include the effect of the compliancy of the roof and floor boundary layers. As in the case of the aerofoil tests in the 8 ft x 8 ft Tunnel the change in displacement thickness of the wall boundary layers is calculated by using the Lag Entrainment method[17].

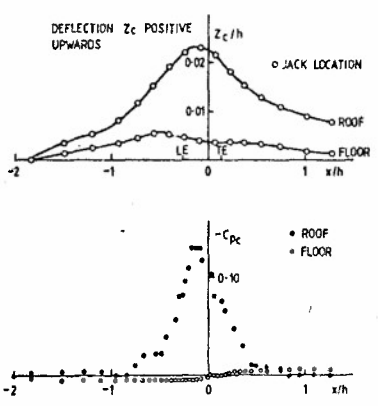


FIG. 8 WALL DEFLECTIONS AND WALL STATIC PRESSURE INCREMENTS; CASE 4

The results obtained for the wall-induced increments in Mach number and incidence at mid chord are shown in Table 1. For all but one of the cases with the walls adapted (ie nominally interference-free flow), the increments are seen to be small although perhaps not negligible. The exception is Case 7 for which the increments are significant. Possible reasons for this are considered later.

Graphs of the streamwise variation of the wall-induced velocities are shown in Fig 9. Four of the cases with M_∞ = 0.73 are shown, two of which are with walls adapted. The effect of adapting the walls is to reduce the variation along the aerofoil chord of the wall-induced velocities considerably. Experience, such as that described in Section 3.2, suggests that the adapted-wall cases shown in Fig 9 can reasonably be called 'correctable', whereas the others probably cannot.

As an illustration of the relative contributions to the wall interference of the vortex and source distributions, Fig 10 shows an analysis of the wall-induced velocities for Case 4. It will be appreciated from this that a delicate balance has to be achieved between the vortex (wall static pressure) and source (wall plus boundary-layer displacement) contributions to achieve interference-free flows. This may be offered as a plausible

explanation for the magnitude of the wall-velocity increments in Case 7. In this case, the free-stream Mach number is closer to unity than for the other examples with adapted walls. As may be inferred from equations (11), (14) and (15), the contribution of the source integral to the wall-velocity increments is increasingly sensitive to errors in wall or boundary-layer displacement as free-stream Mach number approaches unity. Therefore it becomes more difficult to achieve the desired balance between the two terms as free-stream speed approaches the sonic value. However, this is unlikely to prove to be a practical problem if (a) the flow obtained is 'correctable' and (b) the method used to correct the data is reliable.

4 EVALUATION OF THE METHOD FOR TESTS ON THREE-DIMENSIONAL MODELS

In principle, there are no difficulties in applying equation (11) to three-dimensional flows. However, the three-dimensional version of the method requires measurements of static pressure on at least three of the walls. This should not cause great difficulty but, clearly, the method is likely to be more attractive if it can be shown to give reliable values of wall-interference velocities from a modest number of wall static-pressure measurements (say less than about 200).

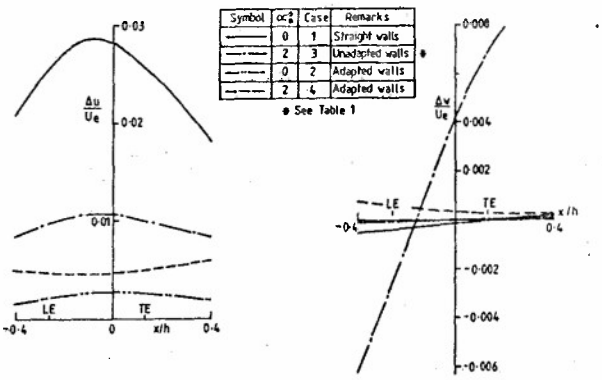


FIG. 9 STREAMWISE VARIATION OF WALL-INDUCED VELOCITIES AT MODEL; M_∞ = 0·73

In this section, the method is assessed for tunnels with cylindrical walls of rectangular cross section. This is done by using the classical method of images to provide static pressures at specified 'wall holes' and to evaluate the accuracy of the wall-induced velocities. Wall boundary-layer effects are not considered. Furthermore, only flows with a vertical plane of symmetry are examined since they are representative of the majority of wind-tunnel tests. This implies that it is only necessary to measure static pressures on one side of the vertical plane of symmetry of the tunnel.

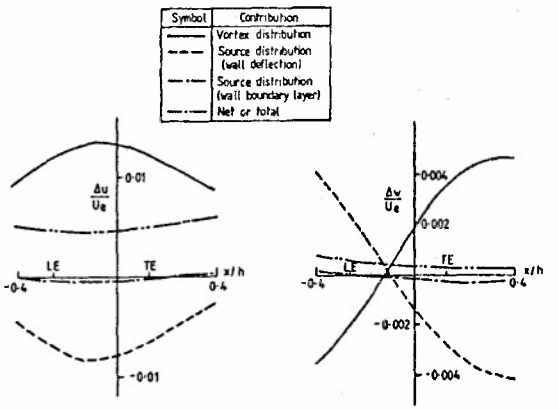


FIG. 10 BREAKDOWN OF CONTRIBUTIONS TO WALL-INDUCED VELOCITIES; CASE 4 TABLE 1

4.1 Interpolation techniques and numerical integration

The accuracy of the numerical approximation to the theory depends to a large extent on the way the wall pressure data are interpolated. Based on our experience of two-dimensional wall interference, we have used the Cubic Spline method for interpolation in both directions on each wall. Interpolation in the streamwise direction is performed first, and the extrapolation to infinity upstream and downstream is carried out in the same way as for the two-dimensional case. The end conditions required at the corners for the interpolations in the directions normal to the stream are defined in terms of the value of C_p and its first derivative with respect to y or z. The value of C_p is assumed to be derived from the streamwise interpolation of a row of static-pressure holes placed at either corner, while the first derivative is found from the condition of irrotationality

$$\partial u/\partial y - \partial v/\partial x = \partial u/\partial z - \partial w/\partial x = 0 \ . \qquad (16)$$

Since v and w, the perturbation velocities in the y and z direction, are both zero at the corners, it follows from equations (13) and (16) that the end conditions for the derivatives are

$$\partial C_p/\partial y = \partial C_p/\partial z = 0 \ .$$

In addition to the static-pressure holes at the corners, it is assumed that there are P streamwise rows of static holes on both the roof and the floor at

$$2y/b = p/P \ , \quad p = 0, 1, 2, \ldots . (P-1)$$

and Q rows on one sidewall at

$$z/h = \pm q/(Q + 1) \ , \quad q = 0, 1, 2, \ldots .(Q - 1)/2 \ .$$

For the sake of simplicity, the streamwise distribution of holes is assumed to be the same for each row, namely

$$x/h = -0.8(0.2)-0.2(0.1)0.2(0.2)0.8 \ ,$$

where x = 0 is a datum close to the position of the model. This distribution has been chosen on the basis of calculations for two-dimensional flows, and, in general, it implies that there are 11 x (2P + Q + 2) static holes in the tunnel walls.

The numerical integration of the velocity increments induced by the distribution of elementary horseshoe vortices on the walls is carried out by approximating the perturbation velocity u with a stepwise distribution as shown in Fig 11. (This is equivalent to assuming that the distribution may be replaced by a finite number of horseshoe vortices of non-zero span[9]). The span of each of the m' elements on both the roof and the floor is b/m', while on either sidewall there are n' elements of span h/n'. Trial calculations have indicated that satisfactory accuracy is achieved with m' = n' = 10.

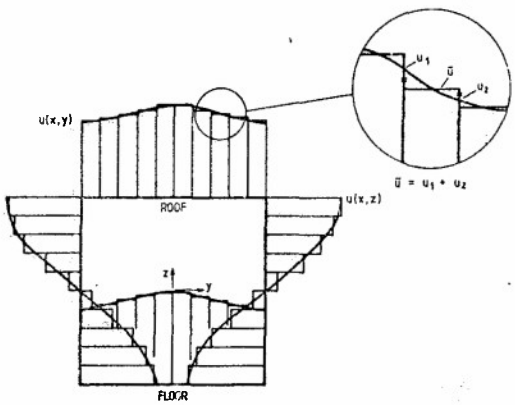


FIG 11 DISCRETIZATION OF TUNNEL-WALL VORTEX DISTRIBUTION

4.2 Evaluation

The examples chosen for the evaluation are as follows:

1 A source-sink pair simulating a closed body with an axis of symmetry on the centre line of the working section (y = z = 0). The distance apart of the two singularities is 0.2h and the centre of volume of the body is at x = 0.

2 A point source at either (0, 0, 0) or (0, 0, 0.1h), with, in each case, a companion sink of equal strength infinitely far downstream. This flow may be considered similar in some respects to that of a wake or a jet, and is the 'building block' of more complicated flows.

3 A horseshoe vortex on the plane z = 0, with its centre line at y = z = 0. The 'bound' part of the vortex is situated at x = 0, and the vortex span is 0.6b.

In all the cases examined, the tunnel is of square cross section (h/b = 1) and the effective freestream Mach number is 0.6.

Comparisons between the wall-induced velocities calculated by the present method and the image method at the tunnel centre line are shown in Figs 12 to 15. In particular, Fig 12 shows the streamwise distribution of the blockage increment in velocity for the first example. It reveals that good agreement is obtained between the two methods for a relatively small number of static holes (P = Q = 1 or 55 holes). A similar situation is found in the second example, as shown in Fig 13. With the point source offset from the tunnel centre line, the walls induce an upwash at the tunnel axis which, as shown in Fig 14, is approximated reasonably well when use is made of between 50 and 100 holes. Finally, Fig 15 shows that for example 3 the method gives a wall induced upwash that is within 5% of the 'exact' value if 55 holes are used and to better than 1% with 99 holes (P = 2, Q = 3). For all practical purposes, an accuracy of between 1% and 5% in the upwash correction is probably adequate.

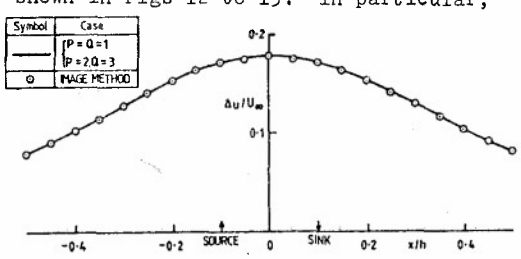


FIG.12 EXAMPLE 1. SOURCE/SINK PAIR, STREAMWISE VELOCITY INDUCED BY TUNNEL WALLS

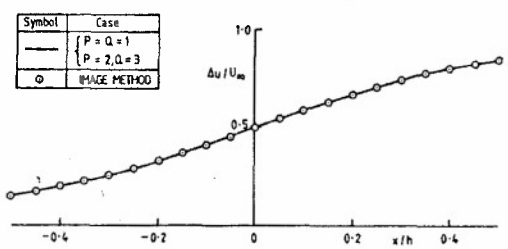


FIG.13 EXAMPLE 2. POINT SOURCE AT ORIGIN; STREAMWISE VELOCITY INDUCED BY TUNNEL WALLS, Z = 0 AND Z = 0·1h (CURVES INDISTINGUISHABLE)

So far, no attempt has been made to optimise the number of wall static holes. Despite this, the results obtained are sufficiently encouraging to suggest that the method may be used to obtain accurate values of wall corrections with a reasonable number of wall holes for flows that are of the small perturbation type in the region of the walls. In incompressible flows this restriction may be relaxed somewhat because the method is exact in the region Λ. However, in some of these cases, equation (13) may no longer be sufficiently accurate for deriving the streamwise velocity component from measured pressures (eg models at high lift). In this

eventuality, it is necessary to determine the streamwise velocity component either by direct measurement or by integrating Euler's equations for the flow at the edges of the wall boundary layers. Of the two methods, the latter is preferable because of the difficulties in measuring flow angle accurately.

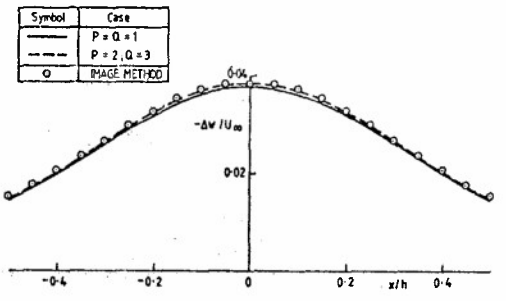


FIG.14 EXAMPLE 2. POINT SOURCE AT ORIGIN; UPWASH INDUCED BY TUNNEL WALLS Z = 0·1h

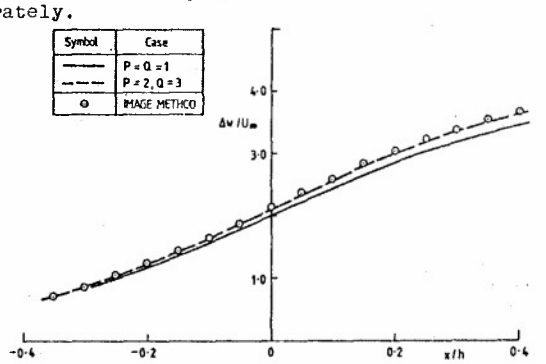


FIG.15 EXAMPLE 3. HORSESHOE VORTEX IN PLANE Z = 0; UPWASH INDUCED BY TUNNEL WALLS

5. CONCLUSIONS

A method has been developed for calculating the wall interference in solid-wall tunnels from measurements of static pressure at the walls. This technique has the advantage over other methods of not requiring a description of the flow in the region of the model. This is an attractive feature for models with flows that are not easily simulated.

To date, the method has mainly been applied to tests on aerofoils. Measurements made in the 8 ft x 8 ft Wind Tunnel at RAE on an aerofoil of advanced design have been used as a basis for assessing the method. Comparisons between calculations of wall interference by the present method and the methods of Göthert[3] and Smith[5] show reasonably good agreement in terms of blockage increment in Mach number, and all three approaches give Mach-number corrections that are significantly higher than those of linear theory. In contrast, linear theory and the present method are in good agreement in their calculations of wall-induced upwash.

Comparisons between pressure distribution obtained from, on the one hand, calculations by VGK of the equivalent free-air flows and, on the other, measurement suggest that the correction to Mach number given by the present method is satisfactory. In these calculations, an allowance has been made for the chordwise variation of wall-induced upwash by adjusting the aerofoil camber. However, it is arguable whether or not the calculated effect on shock position of the camber adjustment is representative of the influence of wall-induced upwash. Further work is needed on this aspect of the problem.

Some calculations have also been made of the wall interference in tests on a NACA 0012 aerofoil in T2 Adaptive-Wall Tunnel (ONERA). These show that, with the walls adapted, the wall-induced increments are generally small, although not negligible, and that the effect of adapting the walls is to reduce considerably the calculated chordwise variation of the wall-induced velocities. An analysis of the wall interference shows that, in order to achieve interference-free conditions, the vortex (static pressure) and source (wall plus boundary-layer displacement) contributions are required to cancel identically. This becomes increasingly difficult as free-stream Mach number approaches unity because of the increased sensitivity of the source term to errors in wall displacement.

An evaluation of a three-dimensional version of the method, indicates that it may be expected to give accurate values of wall-induced velocities for tests at high subsonic speed with a modest number of wall static holes, provided that the flow satisfies the small perturbation equation in the region of the tunnel walls. The method may therefore be used to derive wall corrections in a number of practically-important cases where the classical methods are unreliable because of their failure to represent the conditions close to the model.

REFERENCES

1. S.B. Berndt, H. Sorensen — Flow properties of slotted walls for transonic test sections. AGARD CP 174, Paper 17, 1975.

2. H.C. Garner, E.W.E. Rogers, W.E.A. Acum, E.C. Maskell — Subsonic wind tunnel wall corrections. AGARDograph 109, 1966.

3. B. Göthert — Windkanalkorrekturen bei hohen unterschallgeschwindigkeiten unter besonderer berücksichtigung des geschlossenen kreiskanals. Deutsche Luftfahrtforschung Forschungsbericht 1216, 1940 (translated as NACA Tech Memo 1300).

4. J.E. Hackett, D.J. Wilsden, W.A. Stevens — Pressure signature and other tunnel constraint correction methods for high angle-of-attack tests. Paper presented at Chatanooga meeting of AGARD FDP subcommittee on wind tunnels and testing techniques, 1980.

5. J. Smith — A method for determining 2D wall interference on an aerofoil from measured pressure distributions near the walls and on the model. NLR TR 81016U, 1981.

6. C. Capelier, J.P. Chevallier, F. Bouniol — Nouvelle methode de correction des effets de parois en courant plan. La Recherche Aerospatiale, No 1 (p 1-11), 1978.

7. S. Goldstein, A.D. Young — The linear perturbation theory of compressible flow with applications to wind tunnel interference. ACR R&M 1909, 1943.

8. J.Y.G. Evans — Corrections to velocity for wall constraint in any 10 x 7 rectangular subsonic wind tunnel. ARC R&M 2662, 1949.

9. A. Robinson, J.A. Laurmann — Wing Theory. Cambridge University Press (p 22-23), 1956.

10. P.R. Ashill, D.J. Weeks — A method for determining wall-interference corrections in solid-wall tunnels from measurements of static pressure at the walls. RAE report in preparation.

11. P.R. Ashill, D.J. Weeks — An experimental investigation of the drag of thick supercritical aerofoils - a progress report. RAE TM Aero 1765, 1978.

12. J.H. Preston — The interference on a wing spanning a closed tunnel, arising from the boundary layers on the sidewalls with special reference to the design of two-dimensional tunnels. ARC R&M 1924, 1944.

13. K.G. Winter, J.H.B. Smith — A comment on the origin of endwall interference in wind-tunnel tests of aerofoils. RAE TM Aero 1816, 1979.

14. R.W. Barnwell — Similarity rule for sidewall boundary-layer effect in two-dimensional wind tunnels. AIAA Journal, Vol 18, No 1, 1980.

15. W.G. Sewall — The effects of sidewall boundary layers in two-dimensional subsonic and transonic wind tunnels. AIAA 81-1297, 1981.

16. D. Isaacs — Calibration of the 8 ft x 8 ft Wind Tunnel at subsonic speeds. RAE TR 67038, 1967.

17. J.E. Green, D.J. Weeks, J.W.F. Brooman — Prediction of turbulent boundary layers and wakes in compressible flow by a lag-entrainment method. ARC R&M 3791, 1973.

18. M.R. Collyer, R.C. Lock — Improvements to the Viscous Garabedian and Korn (VGK) method for calculating transonic flow past an aerofoil. RAE TR 78039, 1978.

19. J.P. Archambaud, J.P. Chevallier — Use of adaptive walls in 2-D tests. Paper 14 AGARD Fluid Dynamics Panel Specialists Meeting on 'Wall Interference in Wind Tunnels', May 1982.

20. J.P. Chevallier — Soufflerie transsonique a parois auto - adaptables. Paper 12, AGARD CP 174, 1976.

6 ACKNOWLEDGEMENTS

The authors are grateful to M J P Chevallier of ONERA for permission to make use of the data from T2 Adaptive-Wall Tunnel. Also they wish to acknowledge the help of Mrs I Gaudet in programming the method.

Copyright (c), Controller HMSO, London

THE USE OF PANEL METHODS FOR THE EVALUATION OF SUBSONIC WALL INTERFERENCE

by

D.R. Holt* B. Hunt**

British Aerospace (Aircraft Group)

SUMMARY

The use of panel methods is discussed for the evaluation of subsonic wall interference effecta in both two and three dimensions. The paper concentrates on the techniques that the experimenter must adopt in order to use the methods efficiently and accurately, rather than on once and for all corrections. Particular examples are given to illustrate the general approach together with further uses of panel methods in the general field of support interference.

NOTATION

A	aerofoil cross-sectional area
c	aerofoil chord
C_L	lift coefficient
C_D	drag coefficient
C_m	pitching moment coefficient
C_P	local static pressure coefficient
h	tunnel height
t	aerofoil maximum thickness
x,y	co-ordinates in real plane
z	$= x + iy$
α	aerofoil incidence
β	$= \sqrt{1-M_\infty^2}$
δ	flap deflection
ϵ	aolid blockage factor
ζ	$= \xi + i\eta$
ξ,η	co-ordinates in transformed plane

* Kingston-Brough Division, Brough, N. Humberside, HU15 1EQ

** Warton Division, Preston, Lancashire PR4 1AX

1. INTRODUCTION

The so called panel methods, using surface distributions of singularities, have for some years provided fast, economic, and reliable means of calculating the low-speed flow over complex aircraft shapes. Within the numerical accuracy of the discretisation adopted, these calculations represent solutions of the Laplace equations for the true aircraft geometry including relaxed vortex wakes where appropriate. To the experimenter, this immediately suggests their use to evaluate tunnel wall interference corrections either to validate the present rather simple formulae or to improve upon them. Such improvements might take the form of better formulae produced on a once and for all basis for general use, or the establishment of generalised techniques whereby panel methods can be used to suit particular test requirements. The present paper deals with this latter aspect by providing illustrations of the use of the methods and drawing from these examples some generalised approaches, techniques, or "rules" for their future use as part of the standard armoury of correction techniques for wind tunnel testing.

The first example, in section 2 below, concerns two-dimensional testing under high lift conditions : this is solved in an economic way by making use of a standard transformation. The next example (Section 3) concerns three dimensional effects where one must necessarily panel the tunnel walls directly. Discussion centres on how this is best achieved and the resultant evaluation of the effects of the walls on vortex wakes (and hence sidewash and downwash) leading finally to the complex interactions involved in close-coupled canards.

Based on the assumption that experimenters are using panel methods regularly on the above topics, it is natural to extend their use to other interference effects. Section 4 discusses two of these applications briefly.

2. TWO-DIMENSIONAL EFFECTS

We had long heen concerned about the use of standard tunnel corrections for modern high lift testing. This concern centred on two aspects. Firstly with large-chord flaps at large deflections, a large part of the "aerofoil" was at a significant distance from the tunnel centre-line; secondly, lift coefficients equal to 5 were commonly generated which again seemed to stretch the credibility of the use of the standard corrections.

Our first attempt was simply to panel the roof and floor directly, using linear distributions of vorticity. Both the above effects (streamline curvature and the displacement of the trailing edge towards the floor) produced considerable "leakage" through the wall panels due to the numerical discretisation error. Convergence tests showed that not only had these wall panels to be extremely densely packed but also the panelling had to extend several chord lengths in front of and behind the aerofoil. Thus as many, or more, singularities were needed to represent the walls as the aerofoil and, of course, the wall leakage was never absolutely zero (if the same singularities are used on both aerofoil and walls, then the leakage is comparable on both). Another technique is to panel a few of the infinite number of image aerofoils, reflected in the roof and floor. Again, for converged solutions, considerable computational effort is required. A technique which is computationally efficient and gives an accurate representation of the roof and floor boundary conditions is described in the following sub-section.

2.1 Use of the Panel Method

The technique adopted[2] is to use a standard Schwartz-Christoffel trsnsformation (see for example Ref. 3). The region of the z-plane (Fig.1) between the tunnel walls ($z = \pm h/2$) is mapped onto the upper half of the ($\zeta = \xi + i\eta$) plane, the origin in the latter plane corresponding to $x = -\infty$ in the z-plane. The boundary condition of zero flow across the tunnel walls is satisfied by applying a reflection about the ξ- axis in the transformed plane, surface singularities being placed on the transformed aerofoil using a suitable panel method (e.g. Ref. 4). Once the influence coefficients of the surface singularities (including the effect of their images) have been calculated, the surface velocities can be evaluated and transformed back to the z-plane. Alternatively, the influence coefficients can be transformed back to the real plane before the evaluation of velocities. This latter technique is more attractive when performing iterative calculations which include the effect of viscosity on the aerofoil via surface transpiration.

The next sub-section sets down the standard interference corrections, the final subsection gives comparisons of the interference effects calculated by the two techniques and an illustration of how the panel method is used in practice. Since the standard corrections ignore the effects of viscosity, all the calculations shown here are for potential flow only.

2.2 Standard Corrections

The standard corrections (taken from Ref. 1), against which the present technique is to be compared are as follows.

Interference corrections to incidence (α), lift coefficient (C_L) and pitching moment coefficient (C_m) :-

$$\Delta\alpha = \frac{\pi c^2}{96\, h^2}\cdot (C_L + 4C_m) \qquad (1)$$

$$\Delta C_L = -\frac{\pi^2}{48}\cdot (c/\beta h)^2\, C_L \qquad (2)$$

$$\Delta C_m = \frac{\pi^2}{192}\cdot (c/\beta h)^2\, C_L \qquad (3)$$

where h is the tunnel height, c the aerofoil chord and β the Prandtl Glauert compressibility factor and $\Delta\alpha$ is measured in radians.

The solid blockage correction :-

$$\epsilon(\alpha) = \frac{\pi}{6}\cdot [1+1.2\beta(t/c)]\cdot \frac{A}{\beta^3 h^2}\cdot [1 + 1.1\beta(c/t)\alpha^2]$$

where t is the maximum aerofoil thickness and A the cross-sectional area of the aerofoil section.

Graphical corrections for flapped aerofoils are available from two sources. Preston and Manwell[5] considered thin symmetrical aerofoils and de Jager and van de Vooren[6] considered the non-linear problem for flap angles up to 80 degrees. Both these sources are considered in the comparisons below.

2.3 Examples

All the examplea concern a particular aerofoil of 2 ft. chord length spanning a tunnel of 7 ft. height. The maximum thickness of the aerofoil is approximately 7% and it is equipped with a 10% chord leading-edge flap and a 30% chord trailing-edge flap.

Figure 2 shows lift curves for the clean aerofoil. The solid line represents the results of panel method calculations in the wind tunnel; the dashed line (----) represents these results corrected to free-air conditions by the formulae of sub-section 2-2. Finally the chain-dashed line (-.-) represents panel method calculations in free air. It is clear that these latter two curves are in close agreement over a very wide range of C_L and α; for practical purposes the standard corrections are entirely satisfactory.

The situation when the trailing-edge flap is deflected through 45 degrees is illustrated in Figure 3. Here, any agreement that exists is between the calculations in the tunnel and in free-air, the corrected tunnel results being very different from the true free air calculations. Similarly (Figure 4) when the flaps are deflected through 45 degrees (leading-edge) and 60 degrees (trailing-edge) the standard corrections of equations (1), (2) and (4) are far from adequate.

So far, we have simply compared curves to illustrate the limitations of the standard formulae. The experimenter, with a set of measured data points, must be able to correct each point to an equivalent free-air condition. The technique inherent in the standard corrections, i.e. matched suction peaks, is again used for corrections derived on the basis of panel method calculations. For a flapped aerofoil the flap angle is adjusted (in the free air calculation) until the same suction over the flap knuckle is obtained as in the wind tunnel calculation. The incidence is then adjusted to equalise the leading-edge suction. Of course with a deflected leading-edge flap there is considerable interaction between the changes to incidence and flap angle. These changes to the flap angles could be computed in the panel method by use of the transpiration velocity technique, though in the present work actual rotations of the flap were used. From this exercise, the flap deflection, incidence, lift and moment coefficients, follow for the equivalent free-air condition. If this is repeated for several wind tunnel data points then correlations for the various corrections can be deduced for application to real wind tunnel experiments. However, an incidence scan with fixed flap angles in the tunnel, now produces free-air data with varying flap angles. Free-air data with fixed flap angle can be produced by interpolation of several tunnel runs with differing flap angles.

Figure 5 shows the incidence corrections from equation 1 and from the above technique for the aerofoil with 45 degrees trailing-edge flap deflection in the wind tunnel. The latter exhibit some scatter since, instead of curve-fitting the suction peaks to obtain the true maximum, the highest calculated value at the fixed set of output points was used. Figure 6 shows the pressure distributions for one pair of equivalent points, the two distributions are sufficiently similar to suggest that the values of drag coefficient are also very similar (in fact a viscous version of the program including boundary layer control by tangential blowing allows the drag to be computed). For this particular configuration, correlation of the panel method results yielded the following corrections,

$$\Delta\alpha = -0.0025 - 0.0020\, C_L + 0.0007\, C_L^2 \qquad (5)$$

$$\Delta C_L = -0.0128 + 0.0053\, C_L - 0.0033\, C_L^2 \qquad (6)$$

$$\Delta C_m = 0.0027 - 0.0018\, C_L + 0.0020\, C_L^2 - 0.0004\, C_L^3 \qquad (7)$$

$$\Delta\delta = -0.0038 + 0.0079\, C_L - 0.0019\, C_L^2 \qquad (8)$$

For quite normal ranges of lift coefficient, the higher order terms are clearly of real significance. The lift increments given by equation 6 are compared with standard corrections and those of Refs. 5 and 6 in Figure 7. Standard interference only (i.e. ignoring the blockage correction) is, perhaps fortuitously, closer to the panel method result (which includes interference and blockage) than the full correction but Ref. 6 is the best of the standard methods.

The effects on the pitching moments (here taken about the leading-edge) are shown in Figure 8, where the differences between free-air calculation and correction by the panel method or Ref. 6 are not discernible over the incidence range shown.

Finally, because the corrections are based on matched suction peaks, then if the stall is a sudden one, $C_{L_{MAX}}$ can be corrected with confidence which is not so certain if the separation grows gradually as incidence is increased.

3. THREE-DIMENSIONAL EFFECTS

3.1 Trailing Vortices in a Wind Tunnel

The main feature characterising the flow over a 3-D lifting configuration is the trailing vortex system carrying away the vorticity generated within the surface boundary layer. Such a vortex system is, of course, absent from a 2-D flow.

In the case of a simple 3-D wing, this vortex system induces a perturbation velocity field in the vicinity of the wing which is such that the resultant spanwise distribution of the lift on the wing differs substantially from a uniform or near-uniform 2-D shape and takes on the well-known elliptic or near-elliptic form. The actual form of this distribution (i.e. how far from elliptic it is) bears directly on the "inviscid" vortex-induced component of the drag, as well as on the lift. The effect of wind-tunnel walls clearly modifies the induced velocity field due to the trailing vortex system, and thereby leads to a modification of the lift distribution and drag on the configuration; these effects are additional to the 2-D type effects associated with the "bound" vorticity on the configuration. In the case of a simple wing at low or moderate angle of attack, the approximate effects of this type of wall constraint can be estimated by classical techniques, generally these consist of "corrections" to the nominal angle-of-attack ("downwash") and dynamic head ("blockage").

In the case of more complex configurations, however, and especially those with a canard layout, there is another type of wall effect which is much more difficult to estimate. In such configurations the vortex system from the upstream component passes over (or under) downstream surfaces and modifies (often substantislly) the flow on such surfaces; indeed, in the case of strakes and a number of canard configurations, such an effect is consciously built in as a part of the design process, e.g. to delay or suppress the stall. Clesrly, the magnitude of this effect depends strongly on the vertical distance between the wing surface and the free vortex, and on the spanwise location of the vortex relative to the wing. Since one of the effects of the wall constraints is to modify the trajectory of such a vortex, the induced effect on the main wing inside a wind tunnel will differ from that in an unconstrained flow. (Furthermore the strength of the vortex itself will be different, for "classical" reasons). For such a configuration, therefore, in addition to the standard corrections for incidence and blockage, there should in principle be corrections to the vertical spacing snd the angular setting between a canard and a wing; these corrections themselves will be incidence-dependent. The same arguments apply with respect to other downstream surfaces such as fins. Without such corrections it is clear that under certain circumstances the wind tunnel is likely to give misleading indications not only for the lift and drag of such a configuration, but, perhaps more seriously, for the stability parameters.

The presence of vortex flows of various types - canard wakes, strake and other leading-edge vortices, and forebody vortices - is a very important feature for fighter aircraft designed to manoeuvre st high sngle-of-attack. The effect of Reynolds number on such flows has for a long time raised questions about the credibility of wind-tunnel test results; however, for such flows a number of other sensitive features should be pointed out. These were discussed in some detail in the recent AGARD Lecture Series on High Angle of Attack Aerodynamics (Ref 7). Perhaps the most important features in this respect are asymmetric vortex formation from slender forebodies, and the phenomenon of vortex bursting and its effect on the aerodynamic properties of the configuration. Both these features are sensitive to the presence of the wind-tunnel walls and the inevitable non-uniformity of the wind-tunnel flow.

Asymmetric forebody vortices occur at high angle of attack (the actual angle at which the switch from a symmetric pattern occurs depends, amongst other things, on the nose shape and the local pressure field). Their effect is to produce very large side-forces and yawing moments when nominally zero values may be expected. The dominant contribution to these forces and moments comes from the direct pressures on the forebody itself, but important contributions also arise due to the interaction beteen these asymmetric vortices and other downstream surfaces (wings, fins). As outlined earlier, these latter contributions are modified via the tendency of the wind-tunnel to change the trajectory of the vortices. Additionally, however, the angle at which asymmetry commences will itself be subject to wall-constraint effects; indeed, whether asymmetry occurs at all, for a particular configuration, can in principle depend on these effects. It is perhaps not universally accepted that this applied even when some attempt, e.g. by the use of nose strakes, is made to force the vortex separation lines to be symmetric. The value of strake apex angle below which asymmetry can occur, in the angle-of-attack range of interest, will be modified (most usually to an insignificant extent) by wall constraint effects.

The physical mechanisms behind the vortex bursting phenonenon are not yet fully understood.

The state of the art is discussed in the paper (8) presented by Wedermeyer at the extended version of the above AGARD Lecture Series given at the von Karman Institute in Brussels. The paper (9) in the same Lecture Series by Wendt describes the role of compressibility with respect to the effects which occur when, as the angle of attack increases, the burst point of a vortex moves progressively upstream until it eventually reaches the vicinity of a wing trailing edge. Even when the vortex pattern is nominally symmetric, this will always occur first with one of each part of vortices (whether this is a port or starboard vortex depends on random external fsctors). The burst point of this vortex will then suddenly jump forwards from the wing trailing edge to somewhere about midchord, this jump coinciding with a sudden loss of lift, perhaps as large ss 50%, on the adjacent wing. lf the incidence is now gradually reduced, the burst point moves progressively back downstream, some degree of hysteresis being evident. In a real flow where the aircraft can react dynamically to this large change in force and in all three moments, the interaction between the motion of the aircraft and this vortex-induced flow behaviour can lead to an oscillatory state, e.g. wing rock, which may be stable or unstable and lead to departure. Now the vortex bursting phenomenon is undoubtedly sensitive to the external pressure field, and if the pressure field prevailing in the wind tunnel differs from that in free air, then this type of phenomenon will not be reproduced in realistic fashion, and in fact the indications of wind-tunnel tests may be totally misleading. Such difficulties must be viewed alongside the traditional deficiencies of wind-tunnels (Reynolds number, etc).

At the present time, no adequate model of the vortex-bursting phenomenon is available to assist in the quantification of the above type of problem, but when one does become available its use in conjunction with a panel method must be considered as a means of valididting (or otherwise) the results produced by wind-tunnel tests. In the case of asymmetric vortex formation, some very recent unpublished work at BAe Warton [mentioned briefly in the above AGARD Lecture Series, Ref (10)], and some independent work (11) at RAE Farnborough, have demonstrated the ability to predict asymmetric vortex formation from symmetric separation lines on a symmetric body in unyawed flow. Within the limitations of the simple models developed so far [e.g. the RAE work (11) is based on conical flow theory], it appears possible even to predict the incidence at which asymmetry commences. Further development of this work, within the framework of a three-dimensional panel method [perhaps using the so-called "hybrid" method developed at Warton, as outlined in Refs (10, (12, (13)] could quite possibly lead to the ability to quantify the spurious effects due to wall-constraint effects and to identify valid or invalid test results. At the present time such theoretical possibilities have not yet been fully developed and must remain goals of the future.

The following sections define a number of current possibilities accessible to panel methods calculations, following s discussion of the means whereby the tunnel walls may be modelled by panel-method techniques.

3.2 Modelling of Tunnel Walls

The fundamental mathematical concepts underlying most of the successful panel methods currently available are based on the joint objectives of high numerical accuracy and sound numerical conditioning (i.e. ease of solution of the equation system via iterative numerical techniques). The basic principles are described comprehensively in Refs (12), (14), (15). Most of the methods used are optimised with respect to external aerodynamic problems, i.e. the normal vector points outwards from an essentially convex body, into the fluid. A wind-tunnel does not conform to this norm : here the "body" in question encloses the fluid domain, and some of the desirable mathematical properties which are taken for granted in the case of a convex body, vanish totally in the case of a wind-tunnel.

For example, an attempt could be made to represent a wind tunnel as a box, with solid horizontal floor and ceiling and solid vertical streamwise walls, and with the other vertical faces (i.e. those perpendicular to the flow) carrying, say, uniform distributions of velocity vectored into and out of the box. Unfortunately, there is an infinite number of different source and/or doublet distributions on these six surfaces, able to satisfy the required boundary conditions. In other words, the matrix of influence coefficients inherent in a panel method formulation is "singular" in such a case and a solution would be very difficult to achieve by standard means. This is true, whether or not the total configuration includes a body inside the tunnel. Such problems of uniqueness and existence of solutions are discussed in (12), (14), (15).

This difficulty may be circumvented by modelling the wind tunnel as a long open-ended tube installed in an external flow field and parallel to that flow field. If the upstream tunnel surfaces extend indefinitely far forward, being parallel to the unperturbed flow, they do not perturb this flow at locations far upstream of the working section; they consequently require to carry only vanishingly small source and/or doublet densities in order to satisfy the required boundary conditions; consequently a finite upstream extension of these surfaces is generally adequate. This argument does not apply for downstream extensions of the tunnel walls, however. In the 3-D case, the trailing vortex system extends an indefinite distance downstream, and in order to satisfy the wall boundary conditions a finite density of source and/or doublet on the walls is always required. It can be argued, however, that at some distance the trailing vortex system must adopt some stable location within the tunnel, and the longitudinal variation of wall singularity densities will then correspondingly vanish; in this case a quasi 2-D argument can be adopted for the downstream part of the tunnel.

The questions now relate to how far upstream and downstream the discrete panelling of the tunnel needs to be extended, and what density of panelling is required around the cross-section of the tunnel. The answer to this latter question depends strongly on the form of singularity (source or doublet) used to simulate the walls. Whilst numerous works utilize a vortex-lattice type of model, the preferred practice at BAe Warton is to employ source distributions; the usual piecewise-constant discretisation has been found to be adequate. This choice is based on investigations of the conservation of mass flux down the wind tunnel. The above model generally leads to low levels of "leakage" through the walls (the boundary condition is enforced only at a single point - the centroid - of each source panel, and in principle the fluid is free to "leak" through the surface between these points, thereby producing an apparently varying mass flux down the wind tunnel).

The field produced by these wall source distributions is exactly equivalent to that due to the alternative model employing an infinite array of "images". However, it is computationally much more efficient to panel the walls explicitly with a small but sufficient number of panels, than to attempt to employ an array of images of all the singularities representing the body.

In order to decide upon an adequate arrangement of panels to represent the wind-tunnel surfaces, some knowledge is required of how the source density is expected to vary. In regions where the source density varies slowly, a coarse panelling will be sufficient, whereas a denser concentration of panels should be used in regions where the source gradient is large. (This argument is based on the use of piecewise-constant source distributions; an alternative would be to use higher-order representations, such as piecewise linear sources, in regions of large source gradient). Obviously the objective is to use the smallest number of panels consistent with sufficient accuracy.

It may generally be assumed that a wall panelling arrangement suitable for use in conjunction with a complex aircraft configuration may be chosen on the basis of an arrangement considered suitable for use with a simple wing of corresponding dimensions. This is because the flow field induced by the aircraft, in the vicinity of the walls, is dominated by the primary lifting system and its trailing vortices. A study performed some years ago at BAe Warton [Ref (16)] will serve to illustrate how an adequate wall panelling arrangement can be chosen.

In this calculation a tapered, swept wing with RAE Wing A planform (see Fig.9) and 5% thick symmetric section was installed centrally at the angle of attack of 15 deg inside a rectangular wind tunnel. The root chord of the wing was of unit length, the half-span being equal to 2, whilst the tunnel half-width was 3, its height being 4. Advantage was taken of lateral symmetry by calculating the flow on only the port side of the wing; the tunnel panelling extended slightly across the centreline to allow results to be obtained on the centreline.

Preliminary calculations were performed to ensure that sufficient panels were used on the wing. For the panel method used [Hunt-Semple Mark 1A, Ref (14), employing piecewise-uniform surface sources and piecewise-uniform distributed vorticity on the camber surface] it proved sufficient to employ 180 source panels arranged in 6 strips of panels over the half-wing, with a total of 30 surface source panels around each strip. This arrangement gave a lift prediction (obtained by pressure integration) to within 0.5% of the fully-converged solution (i.e. using the same program with four times the total number of panels). These preliminary calculations were performed with a "rigid wake" approximation wherein the wake extended downstream in the wing plane, the vortex lines being parallel to the wing root chord.

Further calculations were also done with an alternative "rigid wake" model wherein the wake vortex lines initially proceeded as above (i.e. parallel to the local chord line for a distance of 10% of local chord) but then continued along straight lines parallel to the unperturbed onset flow. In the trailing-edge region, where the Kutta conditions are satisfied, this gives a local wake configuration similar to that in the previous case. However, the uniform inclination of the remainder of the semi-infinite vortex lines demands a slight and approximately uniform increase in the vortex strengths in order to maintain the Kutta conditions. The latter model led to an increase in circulation and lift of less than 1%, without perceptibly changing the shape of the spanwise circulation and lift distributions. It may be anticipated that the direct effect on the wing, due to the approximately vertical shift of the rolled-up wake, csused by the presence of the tunnel walls, will be of the same order. If significantly larger effects are observed, then these must be due to the additional influence of the walls themselves (i.e. of the equivalent infinite array of images). The effects on the wing will be discussed later; the present objective is to establish a basis for choosing an adequate wall panelling to ensure that these wall effects are properly simulated.

In order to ensure credible results, an unrepresentatively large number of panels was used for the wind tunnel -larger than that for the wing itself. The distribution is shown in Fig.9. A total of 192 panels was used to represent the tunnel, arranged in 12 strips of 16 panels (5 on the half-roof and half-floor and 6 on the vertical side wall). With the origin of co-ordinates defined at the wing apex (the root chord being of unit length) and x measured positive downstream along the tunnel axis, the tunnel was panelled from approximately 8 root-chords upstream of the apex to approximatey 11 root-chords downstream of the wing-tip trailing edge.

The computed source densities on the tunnel walls are shown in Fig.10 as curves around the tunnel periphery, from the floor centreline towards the vertical wall, up the vertical wall to the roof, and across to the roof centreline. In these calculations the wing wake was "relaxed" and took up a physically realistic-trajectory down the wind tunnel. It can be seen that the wall panels upstream of the apex (negative x) carry very small values of the source density , and with very small peripheral and longitudinal gradients. In this region it would be adequate to use very small numbers of panels - perhaps one strip from say $x = -10$ to $x = -2$ and one strip from $x = -2$ to $x = 0$, with perhaps one panel on each strip on the half-roof and half-floor, and two on the vertical wall.

In the immediate vicinity of the wing, say from $x = 0$ to $x = 2$, the streamwise source gradients are similar in magnitude to the peripheral gradients, so that approximately square panels are appropriate; the panel density used in this case is probably adequate here. Over each of the roof, vertical wall and floor, the peripheral gradient is approximately linear. Now, the self-induced normal velocity at the midpoint on a planar panel depends solely on the source density at that midpoint; it is insensitive to any superimposed source gradient on that panel; only the self-induced tangential velocity depends upon that gradient. Furthermore, at a distance of, say, one panel spacing away from a planar network of square panels carrying piecewise-uniform source density, the induced vector velocity field will be virtually indistinguishable from that due to a network carrying piecewise-linear distributions with the same mean strengths. It thus follows that the present model will accurately represent the required local source density on the walls and will accurately reproduce the required velocity field in the region of intcrest - i.e. at the aircraft location; the errors will be a maximum at the walls themselves, but the calculated results will still be of reasonable accuracy even there. (The same argument does not apply to a simple vortex lattice model, however).

The above argument extends and simplifies for the region of the tunnel walls downstream of the wing. Here the wall source densities rapidly stabilise and have very small streamwise gradient, so that long thin panels should suffice - say one strip of panels from $x = 2$ to $x = 3$ followed by a single strip from $x = 3$ to $x = 10$. In this downstream region the peripheral gradient of the wall source density remains relatively large because of the trailing vortex system of the wing. The peripheral panelling density used here was probably at least enough for the present purposes.

The mass flux down the length of the tunnel (i.e. with the wing installed inside the tunnel) was computed by integration of the velocity calculated at planes of points at various cross-sectional stations down the tunnel. This demonstrated a leakage of less than 1% of the total flux, through the tunnel walls. The velocity V_∞ inside the tunnel, upstream of the wing, was within 0.1% of the external freestream speed. The technique used here, of modelling the wind-tunnel as an open tube installed in an external uniform flow parallel to the tunnel axis, requires this check on inlet flow speed to be carried out in all cases, as the blockage effect of the configuration in question could reduce the effective inlet speed if the upstream continuation of the tunnel walls is not sufficient to ensurc negligible flow perturbation at this upstream end.

Fig.10 also shows (as a dashed line) the source distribution estimated for each tunnel wall in turn, but modelled as an infinite plane in the absence of the other walls. In these calculations the wing and its wake are replaced by a single pair of vortices of infinite length, parallel to the tunnel axis, located symmetrically on its central horizontal plane a distance $\pi/2$ times the wing semispan apart, and with strength equal to the maximum (centreline) circulation calculated for the wing. The required wall source density in this case is exactly equal to twice the normal velocity induced at that wall by the vortex pair. It can be seen that the general trend of the downstream parts in the full calculation is approximately reproduced by this simplified model; the simple model underestimates the source strengths on the floor and overestimates those on the roof because in the full calculation the wake sinks below the tunnel centreline, thereby producing a greater effect on the floor and a smaller effect on the roof. This can be seen also from the results on the vertical wall for the full calculation: the crossover point where the source switches from negative to positive (i.e. the vortex-induced sidewash changes sign) moves nearer the floor with increasing distance downstream. Also, as simple theory would indicate, the wall source strengths near the x-position of the wing ($x = 0.5$, say) are approximately one half of the downstream values. It is thus clear that the wall source densities, and therefore an adequate panelling distribution, can be estimated on the basis of a simple calculation for each wall taken in isolation.

This fact allows a suitable panelling arrangement for the tunnel to be selected in advance by performing simple comparisons between appropriate analytical and panel-program calculations for a vortex pair near an infinite surface. In particular, such a calculation allows the wall panelling to be selected if it is required to use a panel program calculation to establish tunnel corrections for the flow velocity measured external to the body, e.g. if flow measurements are taken below or above an aircraft for use in subsequent trajectory calculations. If some type of estimate is not made to "guarantee" the adequacy of the wall panel density, then the results of the numerical (panel program) calculation, i.e. the estimates of the corrections to be applied to the wind-tunnel measurements, must be held in doubt. The alternative "guarantee", by using a very large number of panels on the tunnel walls, is computationally expensive, especially since wake relaxation calculations are also involved.

3.3 Wake Relaxation

One of the main effects of wind-tunnel walls is to suppress the downward drift of air downstream of a lifting configuration. Consequently the trailing vortex system inside a wind-tunnel must have a different trajectory from the free air case, even when the lift on the configuration is identical. The cross-sectional shape of the vortex system will also be modified. An illuminating investigation of these problems, using a time-dependent two-dimensional analogy, is described in Ref 17. This modification of the vertical position and the vorticity distribution within a trailing vortex system will clearly affect the interaction between that wake and other surfaces in its vicinity. No established techniques exist for correcting wind-tunnel results for this effect in connection with, say, canard configurations. The use of a panel method, for estimating the magnitude of the corrections needed, would appear to be a very attractive possibility.

The simple exercise mentioned in the previous section also demonstrates the feasibility, and indeed the simplicity, of performing calculations of wake trajectories inside a wind tunnel. The wake relaxation algorithm in question is built in as a standard facility in the Hunt-Semple Mark 1A panel program and is outlined in Ref (13). The algorithm represents the wake as a series of discrete line segments which are iteratively positioned to lie along local streamlines. Once relaxed, the field induced by this wake is computed by converting the line segments into equivalent piecewise-constant sheet vorticity panels. In order to stabilise the numerical calculation, the algorithm incorporates a coalescence process whereby each vortex line is allowed to spiral a maximum of 270 deg about the tip vortex "core" before that line is coalesced into the tip vortex. Exactly the same standard program was used to compute the relaxed wake inside the tunnel; no special treatment was required. The incidence of 15 deg was chosen to give adequately large effects, although the calculated flow over the wing would not be expected to be realistic (in reality the flow would be at least partly separated for the simple wing considered here).

The effects of wake relaxation inside and outside a wind tunnel, on the spanwise loading distribution, are shown in Fig.11. It can be seen that, for the swept wing in question, at α = 15 deg, the effect of relaxation in both cases is to reduce the overall calculated lift by about 5% relative to the "rigid wake" approximation most usually employed. Near the wing centreline the loading is little affected, but there is a progressively increasing reduction in the loading as the wing tip is approached. In contrast, the effect of the wind tunnel, both with and without wake relaxation, is to increase the loading over the entire span by about 5%, in a manner analogous to an increase in incidence of about 0.8 deg. (The "classical" tunnel correction formula for this case gives an incidence correction of about 1 deg). The main lesson to be learned here is that if a panel program is to be used to estimate even the simplest ("classical") type of tunnel constraint effect, then it is essential to be consistent in the "in tunnel" and "out of tunnel" calculations with respect to the assumptions used for the wake.

The different wake trajectories in free air and in the wind tunnel are indicated in Fig.12. At a distance of about 2 root chords downstream of the tip trailing edge the vertical (upward) shift in the wake cross-section is approximately 5% of root chord, this increasing to about 20% at 8 root chords. This vertical shift is approximately linear with distance downstream from the wing trailing edge.

Since interaction between this wake and an adjacent surface depends on the vertical distance between the wake and the surface, it is clear that the overall force and moment measurements on a close-coupled (e.g. canard-wing) configuration cannot be corrected by a simple incidence correction. A panel program can certainly play a part in devising a rational basis for corrections of this type.

3.4 Tunnel Effects on Canard Configurations

The configuration in Fig.13, taken from Ref (10), shows the trailing-edge wake from a foreplane relaxing over a cranked wing on a fuselage; the wing trailing edge wake is itself relaxed. This computation was performed during certain parametric studies at BAe Warton (parts of the configuration are suppressed from this figure). Calculations were performed with and without wind-tunnel, the relative dimensions of wing and tunnel being approximately the same as those described earlier for the simple wing configuration.

The figure also shows the computed spanwise loading distributions on the foreplane and the main wing at an incidence of 4 deg, with a foreplane setting of 10 deg relative to the wing chord. One effect of the tunnel constraint is to increase the canard loading by about 10% in a manner analogous to a change of foreplane incidence; this incidence effect is due to the "classical" constraint effect discussed earlier, plus an (approximately uniform) change in upwash at the foreplane due to the changed circulation on the main wing. The effect on the main wing is more complex. In addition to the "classical" incidence effect, there is a modification in the wing loading distribution due to the changed position of the canard wake. The overall effect in this particular case is an approximately uniform increase in the spanwise loading; the overall tunnel effect on wing lift is approximately one quarter of the overall effect of the foreplane on the wing lift (i.e. relative to the foreplane-off case); this "non-classical' effect can by no means be considered negligible, particularly in view of the comments made in section 3.1 regarding vortex bursting.

Figure 13 also shows the effect computed on the wing when a "rigid" wake is assumed from the foreplane. In this case the foreplane wake is fixed, with an arbitary but plausible geometry; no attempt is made to relax the wake and make it force-free. It can be seen that a highly peaky and erroneous loading form is predicted for the wing. The lesson to be learned here is that if a panel program, or indeed any other numerical method such as a finite difference or finite element method, is used to estimate wind-tunnel corrections for this type of configuration, then it is essential to relax the foreplane wake.

Further calculations described in Ref.(10) show that in practice it is quite acceptable to replace the complicated and expensive foreplane wake relaxation process by a much aimpler line vortex relaxation. In this case, a bound vortex, of strength equal to the foreplane centreline circulation given by a "rigid wake" calculation, represents the foreplane, this vortex having a span approximately three-quarters of the foreplane span. The trailing legs of the horseshoe are then relaxed over the wing. For the cases in question it was not necessary to also relax the wake of the main wing, though in more severe cases, and especially those where the vortex comes from a leading-edge extension or strake on the main wing, it is desirable to do so. Once again, if a "rigid" horseshoe vortex with arbitrarily fixed, but plausible, geometry is used to simulate the foreplane and its wake, a totally unrealistic simulation of the wing loading is predicted.

To summarise, it is possible to obtain useful indications of the magnitude of tunnel constraint effects on the main wing of a canard configuration by replacing the foreplane and its wake by a simple horseshoe vortex system. However it is essential to relax the trailing legs of this vortex system. Also, it is difficult to estimate the appropriate strength for the vortex, and if an estimate of the tunnel effects on the foreplane are also required, it may be preferable to perform a full wake relaxation for the foreplane. The same arguments would apply to more complex calculations, not yet feasible, involving modelling of foreplane and wing leading edge vortices.

4. OTHER USES OF PANEL METHODS

The previous sections suggest that many of the subsonic interference effects in wind tunnels can be solved satisfactorily by the use of panel methods. On the premise that experimenters will therefore make regular recourse to panel methods, a brief insight into their further use is described below. In passing, it is worth noting that most panel methods make use of surface transpiration for the representation of viscous effects, in principle this same technique could be used to represent porous wind tunnel walls.

4.1 Sting Interference Effects[18]

Normal sting design practice is to incorporate a parallel section immediately aft of the model base of at least 4 sting-diameters in length. With the advent of highlymanoeuvrable combat aircraft, the extreme normal forces dictate that, for reasons of strength, some of this parallel portion must be sacrificed. Figure 14 shows two typical parallel and non-parallel sting designs and the resultant pressure fields as calculated by a panel method. When applied to the model, buoyancy drag coefficients of -0.000422 (parallel sting) and -0.00059 (tapered sting) were deduced representing a difference of less than 1% in the model zero-lift drag coefficient. Previous sting interference calculations were based on the theory of Ref.(19) together with the empirical data of Ref.(20), Fig.15 compares the sting induced pressure field from this method with the panel method. Since it is the change in C_p over the model length rather than its absolute value which determines the buoyancy effect, the maximum difference yields a very small difference in buoyancy drag.

4.2 Afterbody Rig Design

For the purposes of illustration, an example of an actual application of a panel method at BAe Warton, will now be described for a problem which at first sight would appear to be outside the range of applicability of panel methods; nonetheless the calculations succeeded in meeting the engineering requirements.

The problem was to attempt to modify the design of an existing support rig for use in experimental afterbody development work. The rig was originally designed for supersonic flows, but subsequently it was decided to attempt to achieve a rig design suitable for both superaonic snd high subsonic testing.

Calculations using the Hunt-Semple Mark 1A panel program at a Mach number in excess of 0.9 (normally considered to be outside its range of applicability) indicated that the original supersonic rig produced undesirable flow properties at this subsonic Mach number.

The layout of the original rig is shown in panelled form in Fig.16. The rig not only supports the model, but also carries compressed air lines for the engine simulation system employed in the afterbody evaluation tests. The parallel afterbody shown in the figure was used for interference pressure field evaluation during tests to assess the suitability of the support rig. This parallel afterbody extended from the split-line (i.e. the junction between the pressure-tapped afterbody and the untapped forebody) to a distance well downstream of any likely actual sfterbody. Static pressure tappings were positioned around the periphery of this afterbody, over its whole length.

The objective of the present exercise was to achieve a rig design which induced an acceptably low level of interference pressure field, with small longitudinal gradient. In the absence of the support rig, the pressure gradient on the downstream part of the parallel afterbody would be extremely small.

Fig.17 shows the calculated pressure distribution on the bottom centreline of the parallel afterbody, without an enclosing wind-tunnel but in the presence of the original aupport rig. There is a significant pressure gradient along the afterbody, which reduces somewhat when the supersonic centre support (see Fig.16) is removed from the calculation. Subsequent measurements, also shown on Fig.17, also displayed an undesirably large pressure gradient along the afterbody. The difference between experiment and

calculation is due mainly to blockage effects present in the wind tunnel, and in smaller part to errors in the calculation associated with the high value of Mach number.

A series of modifications to the rig shape, including an increase in wing span, were evaluated by means of the panel program; during the later stages the wind tunnel walls were also included in the calculation. Finally a rig design was achieved which met the objectives. Subsequent wind-tunnel tests on this design confirmed the success of the exercise, even though the absolute level of agreement between theory and experiment was of course substantially less than would normally be expected. It is difficult to see how the design objectives could have been met otherwise than by performing actual wind tunnel tests on a series of different designs. This approach would of course have been much more expensive and time consuming.

This example illustrates an application where the objective was not to obtain an accurate prediction of absolute values, but, by means of a panel method, to gain a good indication of general trends in order to allow an experimental rig to be constructed, the experimental results of which could then be treated with some confidence.

4.3 Miscellaneous Topics

The above specific examples of the use of panel methods are illustrative of a much wider range of applications. A technique which must be mentioned in that known as the "ghost" concept as applied to the flowfield over a wind tunnel model. We have shown how the model and the tunnel walls can be "panelled" so that the confined flow can be calculated and compared with a free-air computation. If the velocities induced by the model singularities are ignored, so that only the velocities induced by the wall singularities (whose values were calculated with the model present) are computed, then the influence of the walls on the flow over the model can be evaluated directly. This isolates the effects of streamline curvature in the absence of blockage for use either in correcting experimental data or as a modified onset flow to a more sophisticated theoretical calculation, such as the Euler equations.

Further uses of panel methods arise in experiments designed to examine particular physical aspects of flows. Here the panel methods can be used to ensure that the particular feature will be achieved and that other, undesirable, features are removed or minimised. An interesting example concerns the provision of uniform spanwise loading on a swept wing between end-plates for the study of sheared-wing flows (Ref.21). Instead of shaping the end-walls, the panel method was used to modify the wing planform close to the walls. Fig.18 shows a constant chord planform together with the tapered wing designed by the panel method. The figure also shows the calculated load distributions for the two wings, demonstrating the success of the exercise.

The experimenter who makes regular use of a panel method will undoubtedly discover more and more uses for it in both the analysis of results and the design of the experiment.

5. FINAL REMARKS

The paper has dealt with the use, by experimenters, of panel methods in both two and three dimensional steady flow. It is the contention of the authors that such methods provide valuable tools in both the planning (design) and analysis phases of experimentation. A few examples have been given to support this view and to give some insight into the much broader uses to which panel methods can be put in the context of wind tunnel testing.

REFERENCES

1. Garner, H.C., Acum, W.E.A., Rogers, E.W.E., Maskell, E.C. — Subsonic wind tunnel wall corrections. AGARDograph 109 (1966)

2. Burton, K.W., Cross, A.G.T. — Wind tunnel corrections under low speed high lift conditions. BAe (Brough) Note No. YAD 3438 (1981)

3. Milne Thomson, L.M. — Theoretical Aerodynamics (p.76) Macmillan (1952)

4. Petrie, J.A.H. — Description of the sub-critical panel method SPARV including first order viscous effects and wake relaxation. BAe (Brough) Note No. YAD 3457 (1982)

5. Preston, J.H., Manwell, A.R. — Calculation of the interference on a thin symmetrical aerofoil with hinged flap spanning a closed wind tunnel. A.R.C. R. & M. 2465, 1941

6. de Jager, E.M., van de Vooren, A.I. — Tunnel wall corrections for a wing-flap system between two parallel walls. N.L.R. Report W.7, 1961.

7. AGARD Lecture Series No.121 on High Angle-of-Attack Aerodynamics, given at NASA Langley 10-11 March 1982, and at DFVLR, Gottingen, 22-23 March 1982 and in extended form at the von Karman Institute, Brussels, March 15-19, 1982.

8. Wedermeyer, E. — Vortex breakdown. Paper given at VKI, in (7).

9. Wendt, J.F. — Compressibility effects on flows around simple components. In (7).

10. Hunt, B. — The role of computational fluid dynamics in high angle-of-attack aerodynamics. In (7).

11. Dyer, D.E.; Fiddes, S.P.; Smith, J.H.B. — Asymmetric vortex formation from cones at incidence - a simple inviscid model. RAE Technical Report 81130, October 1981.

12. Hunt, B. — Recent and anticipated advances in the panel method. The key to generalised field calculations? VKI L.S. 1980-5, Brussels March 24-28, 1980.

13. Jepps, S.A. — The computation of vortex flows by panel methods. VKI L.S. 1978-4, Brussels, March 13-17, 1978.

14. Hunt, B. — The panel method for subsonic aerodynamic flows. A survey of mathematical formulations and numerical models, and an outline of the new British Aerospace scheme. VKI L.S. 1978-4, Brussels, March 13-17, 1978.

15. Hunt, B. — The mathematical basis and numerical principles of the Boundary Integral Method for incompressible potential flow over 3-D aerodynamic configurations. In "Numerical Methods in Applied Fluid Dynamics", (Editor, Hunt) Academic Press, London, N.Y., 1980.

16. Hall, P.F. — Wind tunnel effects in relation to wings and associated wakes. BAe Warton note, MSN 217, Sept. 1976.

17. Mokry, M.; Rainbird, W.J. — Calculation of vortex sheet roll-up in a rectangular wind tunnel. J. Aircraft, 12, No.9, Sept. 1975, pages 750-752.

18. Elliott, M. — Private Communication BAe (Brough) 1981.

19. Tunnell, P.I. — An investigation of sting support interference on base pressure and forebody chord force at Mach numbers from 0.6 to 1.3. N.A.C.A. R.M. A54K 16a (1955).

20. Fellows, Mrs. K.A. — Sting support interference on bluff based bodies. A.R.A. Model Test Note M49/3 (1974).

21. Butter, D.J. — Private communication. BAe (Manchester), 1982.

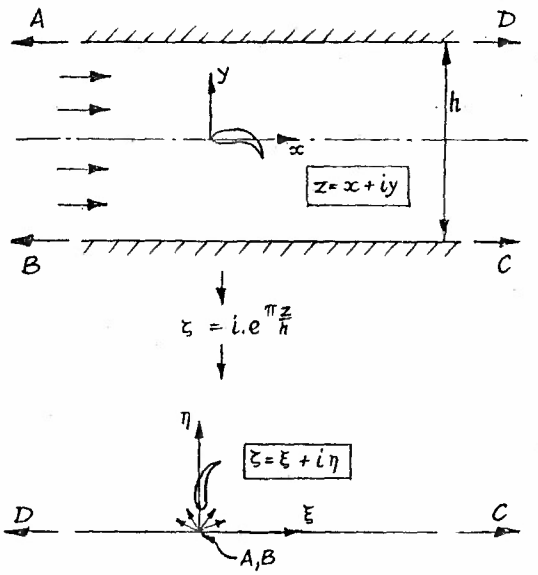


Fig.1 THE TRANSFORMATION

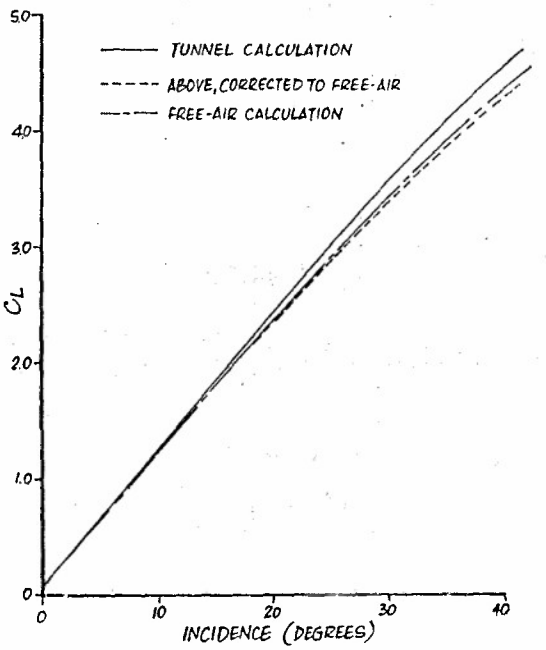


Fig.2 LIFT CURVES FOR CLEAN AEROFOIL

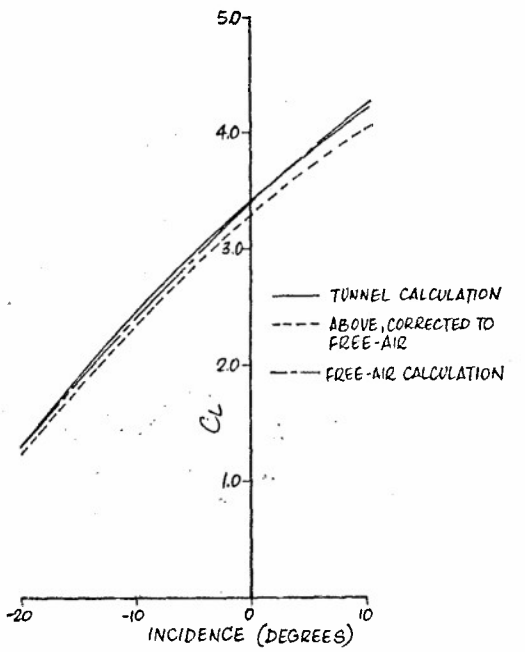


Fig.3 LIFT CURVES, TRAILING-EDGE FLAP DEFLECTED 45 DEGREES

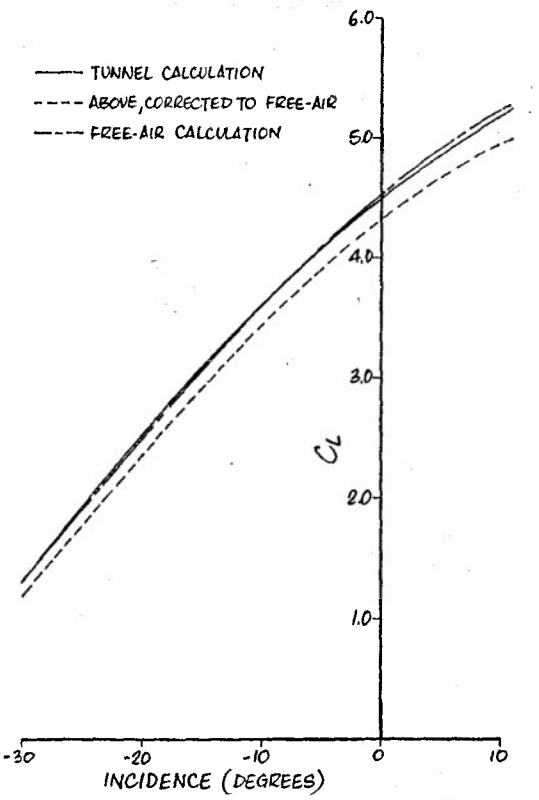


Fig.4 LIFT CURVES, LEADING-EDGE FLAP DEFLECTED 45 DEGREES, TRAILING-EDGE FLAP DEFLECTED 60 DEGREES

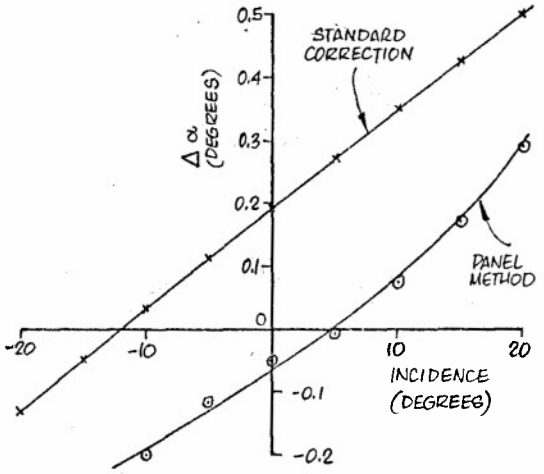


Fig.5 INCIDENCE CORRECTIONS, TRAILING-EDGE FLAP DEFLECTED 45 DEGREES

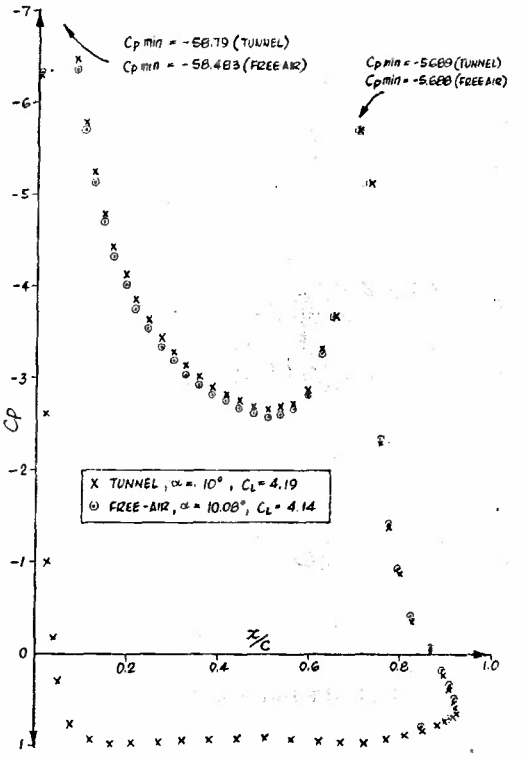


Fig.6 PRESSURE DISTRIBUTIONS AT EQUIVALENT TUNNEL AND FREE AIR CONDITIONS, TRAILING-EDGE FLAP DEFLECTED 45 DEGREES

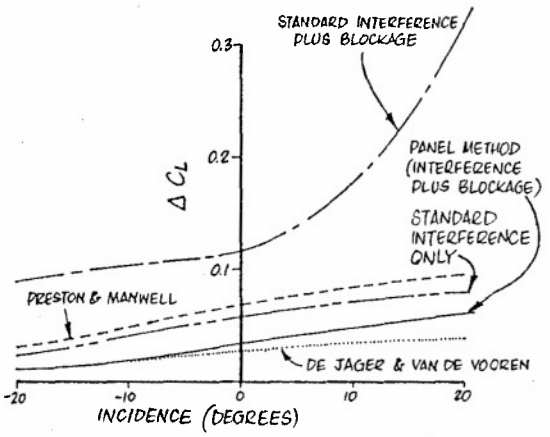


Fig.7 LIFT CORRECTIONS, TRAILING-EDGE FLAP DEFLECTED 45 DEGREES

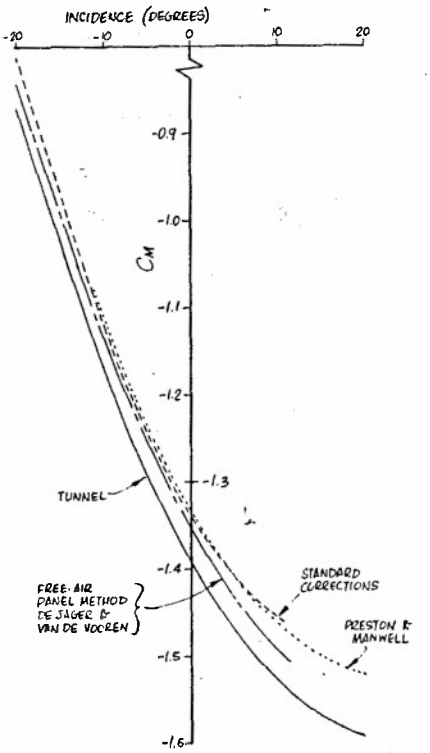


Fig.8 PITCHING MOMENT CURVES, TRAILING-EDGE FLAP DEFLECTED 45 DEGREES

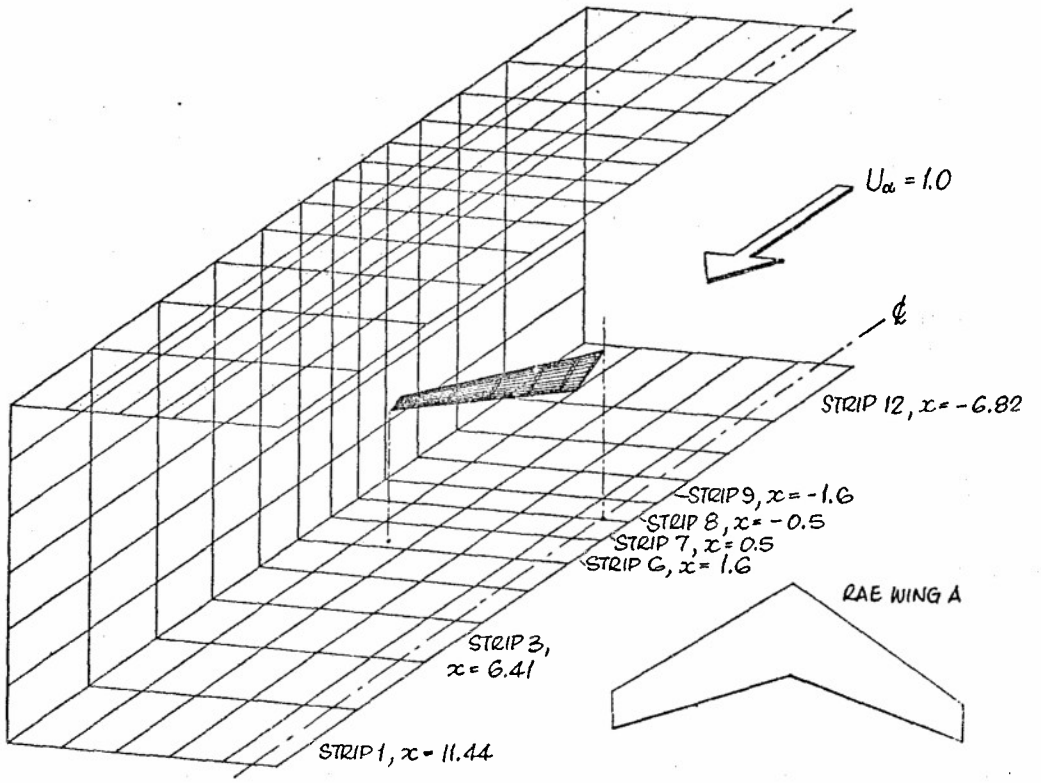


Fig.9 VIEW SHOWING WING IN WIND TUNNEL, AND PANELLING ARRANGEMENT USED

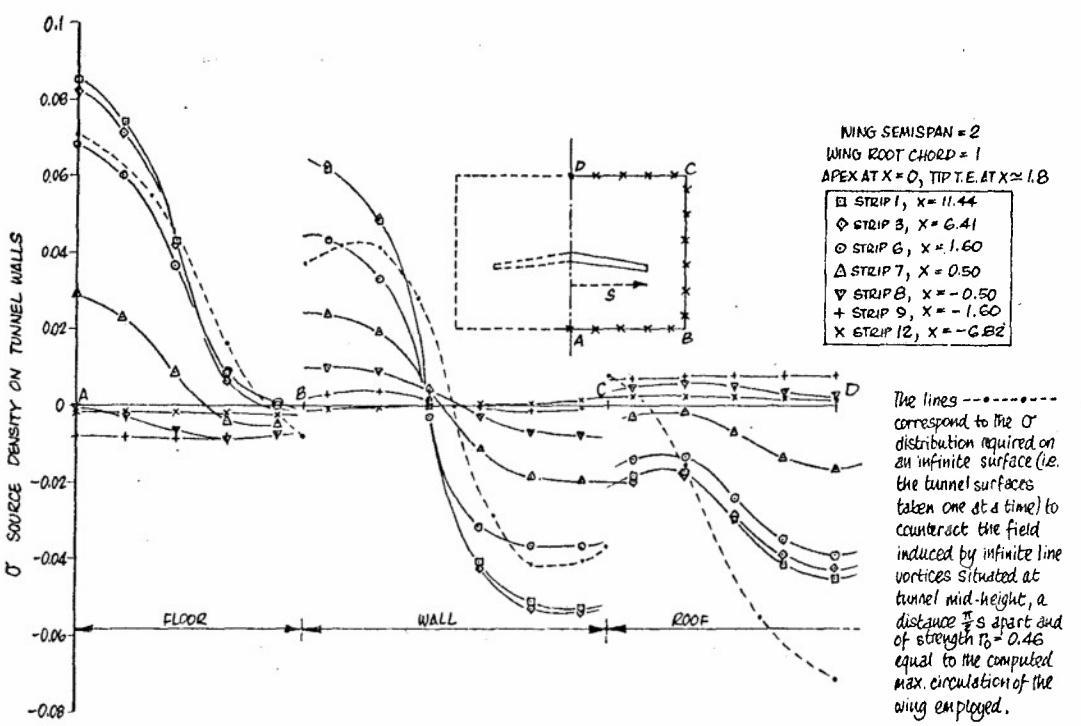


Fig.10 COMPUTED SOURCE DENSITIES ON THE WIND TUNNEL WALLS

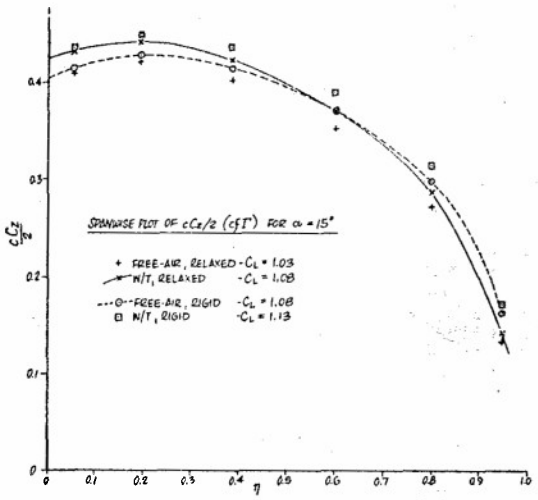
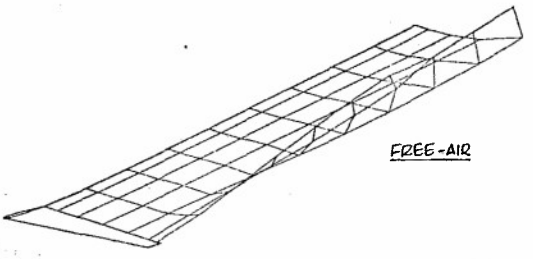


Fig.11 EFFECT OF WAKE RELAXATION AND TUNNEL CONSTRAINT ON SPAN WISE LOADING



VIEW OF RELAXED WAKE GEOMETRY (FREE AIR)

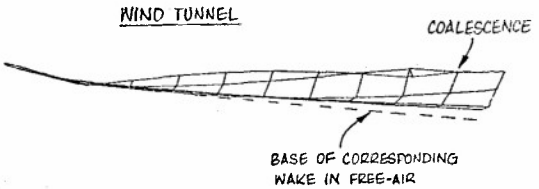
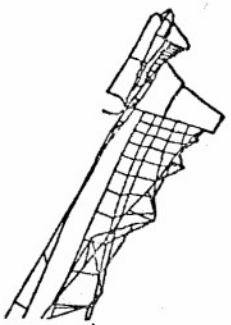


Fig.12 SIDE VIEW OF RELAXED WAKE IN WIND TUNNEL



α = 7°, η_c = 10°

α = 4°, η_c = 10°

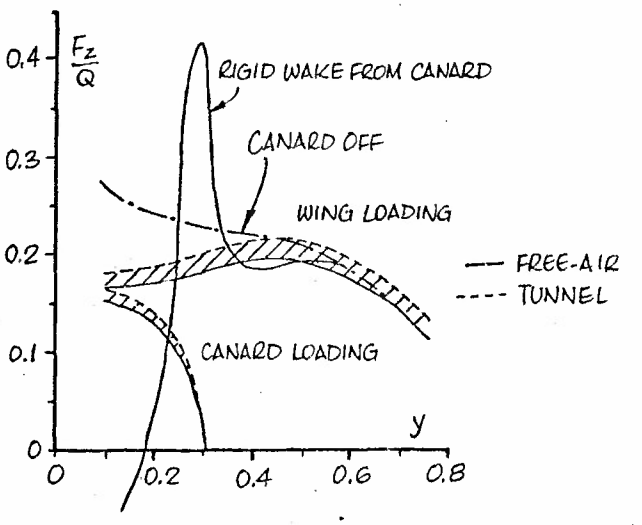


Fig.13 WAKE RELAXATION FOR WING/BODY/CANARD CONFIGURATION

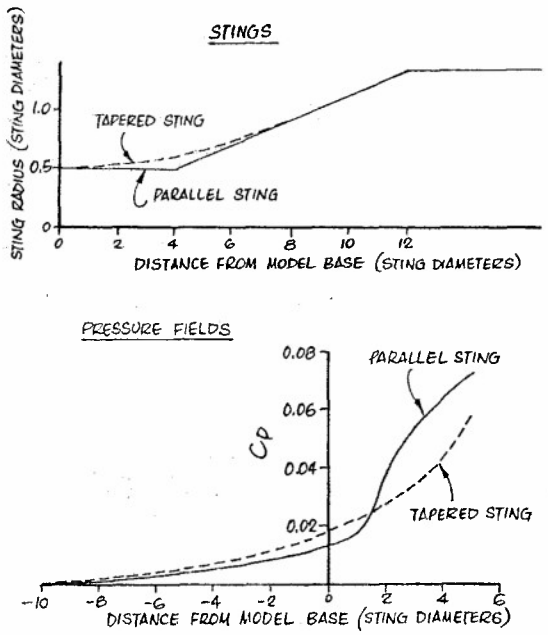


Fig.14 STINGS AND INDUCED PRESSURE FIELDS

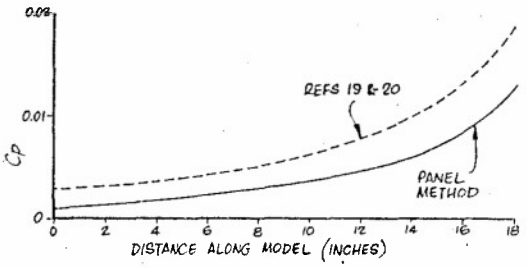


Fig.15 COMPARISON OF PREDICTED BUOYANCY FIELDS

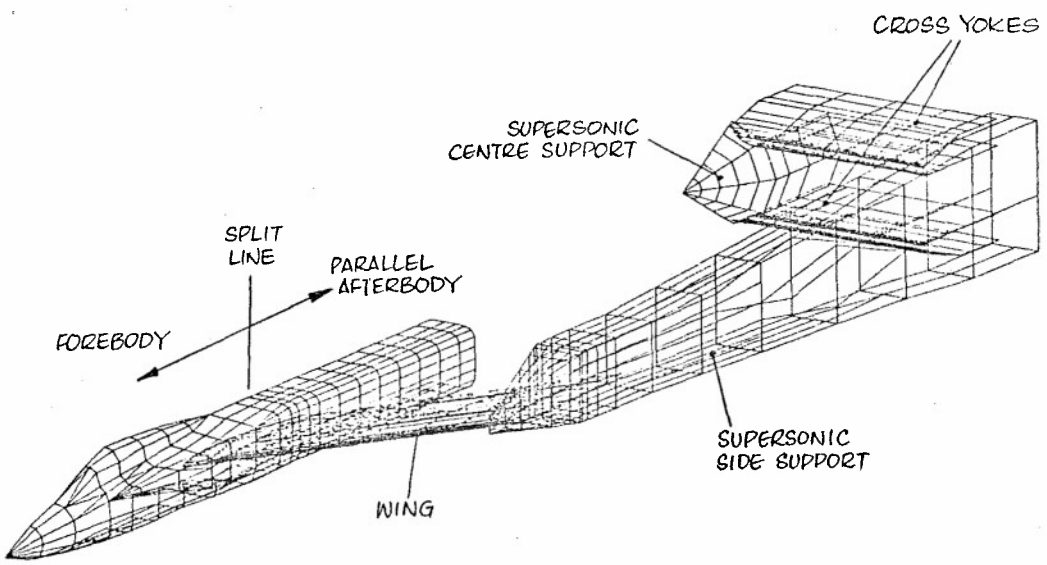


Fig.16 PANELLED GEOMETRY OF ORIGINAL SUPPORT RIG FOR SUPERSONIC AFTERBODY TESTING

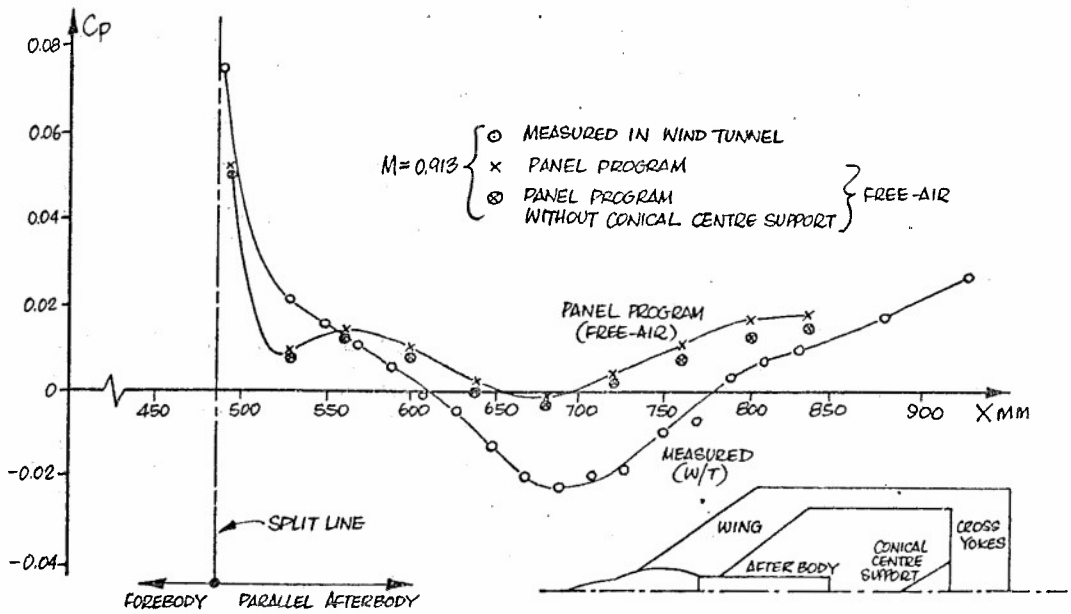


Fig.17 PRESSURES ON PARALLEL AFTERBODY
(BOTTOM CENTRELINE; ORIGINAL SUPERSONIC RIG)

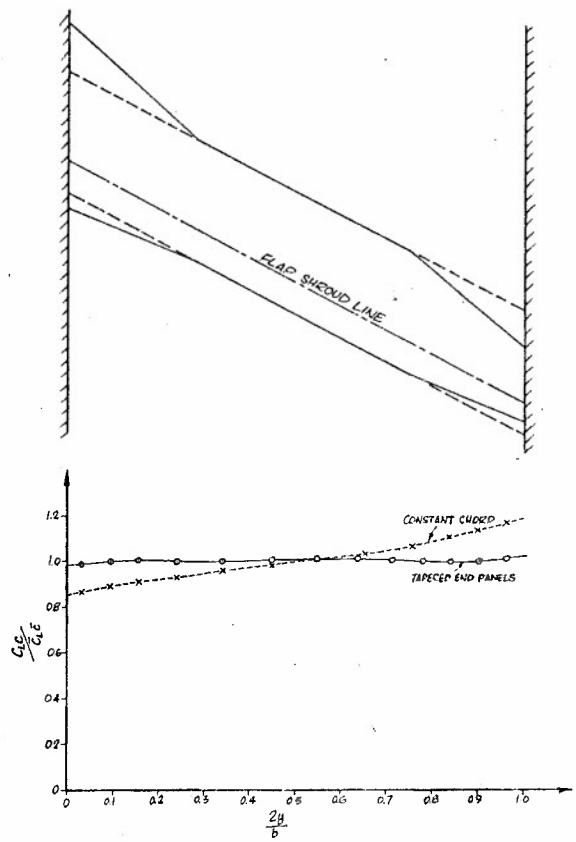


Fig.18 LOAD DISTRIBUTION OF A SHEARED WING IN A WIND TUNNEL

SIMILARITY RULES FOR EFFECTS OF SIDEWALL BOUNDARY LAYER IN TWO-DIMENSIONAL WIND TUNNELS

Richard W. Barnwell
Head, NTF Aerodynamics Branch

William G. Sewall
Aerospace Engineer

NASA Langley Research Center
Hampton, Virginia 23665

SUMMARY

A simple analysis of the interaction of the model pressure field with the boundary layer on an unventilated wind-tunnel wall is presented. It is shown that the effects of this interaction are similar to compressibility effects for sidewall boundary layers in two-dimensional wind tunnels. This similarity is used to derive modified forms of the Prandtl-Glauert rule for subsonic flow and the von Karman rule for transonic flow which are validated by comparison with experimental data. The three-dimensional interaction problem is discussed, and it is shown that model-pressure-field/wall-boundary-layer-interaction effects are not similar to compressibility effects in three-dimensional wind tunnels.

INTRODUCTION

The influence which the walls of a wind tunnel exert on the flow in the tunnel has long been a subject of concern and study for both two- and three-dimensional facilities. This influence, or interference, results from the displacement of the streamlines near the wall away from their free-air locations. Efforts to account for tunnel-wall-interference effects include facility modifications to reduce or eliminate them and the development of analytical methods to predict them. In this paper, an analytical and experimental study of interference in two-dimensional subsonic and transonic wind tunnels caused by the interaction of the model pressure field with the tunnel sidewall boundary layer will be presented, and the analogous situation in three-dimensional wind tunnels will be discussed.

The interference effects caused by the upper and lower walls in two-dimensional wind tunnels can be viewed as primarily inviscid phenomena. The principal modification made to these walls to reduce interference is ventilation with holes (pores) or longitudinal slots to relieve blockage. A number of linear analytical methods have been developed to predict blockage and lift interference effects in subsonic and transonic tunnels with closed, open, and ventilated upper and lower walls. A summary of these methods is given by Pindzola and Lo (ref. 1). Several nonlinear methods, such as those of Kemp (ref. 2) and Murman (ref. 3), have been developed for the problem of upper- and lower-wall interference in two-dimensional transonic wind tunnels. Unlike the methods of reference 1, the nonlinear methods require a detailed description of the model and measured pressure distributions along the upper and lower walls.

The interference effects caused by the sidewalls in two-dimensional wind tunnels occur because of the presence of the sidewall boundary layer and, thus, are substantially different from those effects caused by the upper and lower walls. The two sidewall interference problems which have received the most attention are the growth of the sidewall boundary layer due to the shearing stress at the sidewall and the separation of the sidewall boundary layer due to interaction with large model-induced pressure gradients. The problem of boundary-layer growth due to shearing stress is accounted for in some wind tunnels by a slight outward inclination of the walls, and the problem of sidewall boundary-layer separation can be controlled to some extent with suction or tangential blowing at the sidewall.

The first theoretical treatment of the intermediate problem of the interaction of the attached sidewall boundary layer with the pressure field of an airfoil model is that of Preston (ref. 4), who modeled the vorticity distribution within the boundary layer approximately and calculated the spanwise downwash distribution. This theory was in general agreement with the data of Cowley and McMillen (ref. 5), but overpredicted the later data of Mendelsohn and Polhamus (ref. 6).

Little additional attention was paid to the attached-sidewall-boundary-layer/model-pressure-field interaction problem until Bernald-Guelle (refs. 7 and 8) conducted an experiment in a transonic wind tunnel in which the sidewall boundary-layer thickness could be controlled with suction upstream of the model. The results of this parametric experiment show the effects of sidewall boundary-layer thickness on airfoil lift at both subsonic and transonic conditions. Barnwell (refs. 9 and 10) presented a simple analysis which shows that the sidewall boundary-layer interaction is similar to the compressibility effect for small disturbance flows and thin boundary layers, and that this similarity leads to a modified form of the Prandtl-Glauert rule which correlates the subsonic data of references 7 and 8. Sewall (ref. 11) measured airfoil lift and drag data at subsonic and transonic conditions for several boundary-layer thicknesses and showed that the similarity of compressibility and sidewall boundary-layer effects results in a modified form of the von Karman transonic similarity rule which correlates his data. Kemp and Adcock (ref. 12) have developed a four-wall correction method for airfoil wind tunnels

which combines the upper- and lower-wall analysis of reference 2 with the sidewall analysis of references 10 and 11.

Winter and Smith (ref. 13) have analyzed the data of reference 7 phenomenologically, treating the parts of the wind tunnel above and below the airfoil as channels with different widths due to the influence of the model pressure field on the sidewall boundary layers. This method is more difficult to implement than that of Barnwell and Sewall because it requires the integration of estimated boundary-layer characteristics over the sidewall. It should be noted that only the part of the model pressure field associated with lift is interacted with the sidewall boundary layer in the methods of references 4 and 13; whereas, the entire pressure field is interacted in the method of references 10 and 11.

The interaction of the model pressure field with the wall boundary layer in three-dimensional wind tunnels can be formulated in the same manner used for sidewall boundary layers in two-dimensional wind tunnels. Because compressibility and wall boundary-layer effects are not similar for three-dimensional flow, the two- and three-dimensional solutions are considerably different. It is noted that, the wall boundary-layer interaction problem has been studied by Berndt (ref. 14) and Lofgren (ref. 15) for transonic flow past models in closed three-dimensional wind tunnels. However, the basic formulation used in these references differs from that of the present method.

ANALYSIS

Governing equations and boundary conditions.- Consider steady, isentropic, small-perturbation flow in a rectangular wind tunnel of width b. Let the Cartesian coordinates in freestream, vertical, and horizontal directions be x, y, and z, and the respective velocity components be $U = U_\infty + u$, v, and w, where U_∞ is the freestream speed. Assume that the vertical walls, or sidewalls, are solid and have a displacement thickness δ^* which varies slightly with respect to x and y. The effective tunnel width is $b - 2\delta^*$. This wind tunnel with an airfoil mounted in it is depicted in figure 1.

The flow in this wind tunnel is governed by the irrotational conditions and the small perturbation equations for the conservation of mass and energy. A sufficient form of the conservation of mass equation is

$$(1 - M^2)\frac{\partial u}{\partial x} + \frac{\partial v}{\partial y} + \frac{\partial w}{\partial z} = 0 \tag{1}$$

where M is the Mach number. The boundary condition at the sidewall is

$$w_z = \pm b/2 = \mp U_e \frac{\partial \delta^*}{\partial x} \tag{2}$$

where the subscript e denotes boundary-layer edge values.

Sidewall boundary-layer model.- The dynamics of the sidewall boundary layer are modeled with the von Karman momentum integral, which can be written as

$$\frac{\partial \delta^*}{\partial x} = -\frac{\delta^*}{U_e}(2 + H - M_e^2)\frac{\partial U_e}{\partial x} + \frac{\delta^*}{H}\frac{\partial H}{\partial x} + \frac{\tau_w}{\rho_e U_e^2} \tag{3}$$

where ρ, H, and τ_w are the density and the sidewall shape factor and surface shearing stress. For the present problem, equation (3) can be simplified because the sidewall boundary layer in most wind tunnels can be approximated as a flat-plate boundary layer with a large Reynolds number and an equivalent length of the order of $\delta^*/(\tau_w/\rho_e U_e^2)$. In general, the model chord or length scale c is much smaller than the boundary layer equivalent length so that the inequality

$$\frac{\tau_w}{\rho_e U_e^2} \ll \frac{\delta^*}{c} \tag{4}$$

applies, and, as a result, the last term in equation (3) can be neglected in the first approximation. As shown in reference 15, the shape factor for boundary layers with constant total temperature can be approximated as

$$H = (\bar{H} + 1)\left(1 + \frac{\gamma - 1}{2} M^2\right) - 1 \tag{5}$$

where $\bar{H}$ is the transformed shape factor and γ is the ratio of specific heats. Because $\bar{H}$ approaches one as the Reynolds number becomes large, equation (5) can be written

$$H = 1 + (\gamma - 1) M^2 \tag{6}$$

for the present problem. From equation (6) and the small-perturbation conservation of energy equation, it follows that

$$\frac{\partial H}{\partial x} = \frac{(H - 1)(H + 1)}{U_e} \frac{\partial U_e}{\partial x} \tag{7}$$

With inequality (4) and equation (7), equation (3) can be written as

$$\frac{\partial \delta^*}{\partial x} = - \frac{\delta^*}{U_e}\left(2 + \frac{1}{H} - M_e^2\right) \frac{\partial U_e}{\partial x} \tag{8}$$

Two-dimensional formulation.- Assume that an airfoil model occupies the tunnel, as shown in figure 1, and that tbe boundary conditions for the model and the upper and lower walls are independent of z. Also assume that tbe tunnel is narrow enough for the flow at each sidewall to be strongly influenced by the other sidewall boundary layer. To lowest order, the spanwise velocity component varies linearly with z as

$$w = \frac{2z}{b} \quad w_{z = b/2} = \frac{2z\delta^*}{b}\left(2 + \frac{1}{H} - M^2\right) \frac{\partial U_e}{\partial x} \tag{9}$$

It follows from the assumptions above and equations (1) and (9) that the problem is independent of z. As a result, the subscript e in equation (9) can be dropped and that equation can be used to write equation (1) as

$$\left\{1 - M^2 + \frac{2\delta^*}{b}\left[2 + \frac{1}{H} - M^2\right]\right\}\frac{\partial u}{\partial x} + \frac{\partial v}{\partial y} = 0 \tag{10}$$

Note that tne terms in equation (10) wnich are due to the sidewall boundary layer are similar to the compressibility term.

In this report, it has been assumed tbat the sidewall boundary layers are attached and the flat-plate growth rate of the boundary layer at the model station is small. Therefore, the shape factor H and the displacement thickness δ^* of the sidewall boundary layer near the model can be approximated to lowest order by the values of the model station in the empty tunnel.

Modified Prandtl-Glauert rule.- In tbe subsonic speed regime, equation (10) can be linearized because the local Mach number M can be approximated by the freestream value of M_∞ and because constant approximate values for δ^* and H can be used. As a result, the pressure coefficients and integrals of the pressure coefficients for different subsonic flows can be related with the Prandtl-Glauert rule. For example, the nearly two-dimensional normal force coefficient $\bar{C}_n$ in a wind tunnel with a sidewall boundary layer is related to the two-dimensional normal force coefficient C_n at the same freestream Mach number M_∞ in the same wind tunnel witb no sidewall boundary layer by the equation

$$\bar{\beta}\, \bar{C}_n = \beta\, C_n \tag{11}$$

where

$$\bar{\beta} = \sqrt{1 - M_\infty^2 + \frac{2\delta^*}{b}\left(2 + \frac{1}{H} - M_\infty^2\right)} \tag{12}$$

$$\beta = \sqrt{1 - M_\infty^2} \tag{13}$$

Modified von Karman rule.- With equation (12) and the small-perturbation conservation of mass equation, equation (10) can be rewritten as

$$\bar{\beta}^2 \frac{\partial u}{\partial x} + \frac{\partial v}{\partial y} = (\gamma + 1)\, M_\infty^2 \frac{u}{U_\infty} \frac{\partial u}{\partial x} \tag{14}$$

If constant values of δ^* and H are used, a direct application of the von Karman transonic similarity rule can be made. This rule relates the pressure coefficient of two flow fields, identified with subscripts 1 and 2, as

$$\frac{(\gamma_1 + 1)\, M_{\infty,1}^2}{\bar{\beta}_1^2}\, C_{p,1} = \frac{(\gamma_2 + 1)\, M_{\infty,2}^2}{\bar{\beta}_2^2}\, C_{p,2} \tag{15}$$

subject to the constraint

$$\frac{\bar{\beta}_1^2}{\left[t_1(\gamma_1 + 1)\, M_{\infty,1}^2\right]^{2/3}} = \frac{\bar{\beta}_2^2}{\left[t_2(\gamma_2 + 1)\, M_{\infty,2}^2\right]^{2/3}} \tag{16}$$

where t is the maximum thickness to chord ratio.

Let $\bar{C}_p$ be the pressure coefficient measured in a two-dimensional wind tunnel with sidewall displacement thickness δ^*, and let $\bar{\bar{C}}_p$ and $\bar{\bar{M}}_\infty$ be the adjusted pressure coefficient and Mach number for the same model and test gas $(t_1 = t_2,\ \gamma_1 = \gamma_2)$ in the same wind tunnel with no sidewall boundary layer $(\delta^* = 0)$. Equations (15) and (16) become

$$\bar{\bar{C}}_p = \frac{\beta}{\sqrt{(1 - M_\infty^2)}}\, \bar{C}_p \tag{17}$$

$$\frac{\bar{\bar{M}}_\infty}{(1 - \bar{\bar{M}}_\infty^2)^{3/4}} = \frac{M_\infty}{\bar{\beta}^{3/2}} \tag{18}$$

Equation (17) can be integrated over the airfoil surface to obtain adjusted normal force and drag coefficients, $\bar{\bar{C}}_n$ and $\bar{\bar{C}}_d$, as

$$\frac{\bar{\bar{C}}_n}{\bar{C}_n} = \frac{\bar{\bar{C}}_d}{\bar{C}_d} = \frac{\bar{\beta}}{\sqrt{(1 - \bar{\bar{M}}_\infty^2)}} \tag{19}$$

where $\bar{C}_n$ and $\bar{C}_d$ are measured normal-force and drag coefficients.

Independence from other boundary conditions.- The boundary conditions for the upper and lower tunnel walls and the model boundary condition have not been used in the present derivation. Therefore, the present results for sidewall interference depend upon the details of the upper and lower walls and the model only in the way these quantities affect the variables M, H, and δ^* in equation (10). If approximate constant values are used for these quantities, the sidewall interference predictions are independent of the nature of the upper and lower walls and the details of the model such as its size and shape. The upper and lower wall subsonic interference predictions given in reference 1 are influenced by the sidewall interference to the extent that these predictions are a function of $\bar{\beta}$, given by equation (12), rather than β, given by equation (13).

Three-dimensional formulation.- Assume that a three-dimensional model is located in the center of the tunnel, that the vertical walls, or sidewalls, are solid, and that the nature of the upper and lower walls is arbitrary. With equations (2) and (8), the three-dimensional boundary layer condition for the right sidewall in figure 1 can be written as

$$w - \delta^*\left(2 + \frac{1}{H} - M^2\right)\frac{\partial u}{\partial x} = 0 \tag{20}$$

This condition is like the boundary conditions for slotted and porous walls, which can be written as

$$u + \frac{1}{K}\,\frac{\partial w}{\partial x} = 0 \tag{21}$$

and

$$u + Pw = 0 \tag{22}$$

respectively, where K and P are constants which depend on the wall properties. Solutions to the linear form of equation (1) and boundary conditions (21) and (22) are given in reference 1 for simple representations of three-dimensional models. The same techniques can be used to solve the linear form of equation (1) and boundary condition (20). Also, the nonlinear form of equation (1) can be solved subject to boundary condition (20) with the three-dimensional counterparts of the methods discussed in references 2 and 3.

Boundary condition (20) cannot be used to simplify the governing equation for three-dimensional flow as it was for the two-dimensional flow. Therefore, the effect of interaction of the model pressure field with wall boundary layer for three-dimensional flow is not similar to the compressibility effect as in the two-dimensional case.

COMPARISON WITH EXPERIMENT

The experimental verification of the present theory is accomplished principally with the results of two experiments. The data of Bernard-Guelle (refs. 7 and 8) are used to validate the modified Prandtl-Glauert rule, and the data of Sewall (ref. 11) are used to validate the modified von Karman rule.

Modified Prandtl-Glauert Rule.- The experiment described in references 7 and 8 was performed in the ONERA R1Ch wind tunnel, which is sketched on the left side of figure 2. This is a high-pressure blow-down tunnel with a height and width of 38 cm and 8 cm, respectively, which can be fitted with either solid or porous upper and lower walls. There is a porous plate on the sidewall upstream of the model which is 50 cm long and which ends about 20 cm upstream of the model leading edge. Suction can be applied to this plate to remove mass from the sidewall boundary layer and, hence, control the sidewall boundary layer thickness at the model.

The data of present interest are the measurements of the normal force on models at fixed angles of attack for different sidewall boundary-layer thicknesses. The sidewall boundary layer was measured near the model station in an empty tunnel for various values of the sidewall suction rate. Then the chordwise pressure distributions on the models were measured for the same sidewall suction rates. The normal-force coefficients were obtained from tbese pressure distributions.

A comparison of the experimental and theoretical results for the effect of the sidewall boundary-layer displacement thickness parameter $2\delta^*/b$ on the normal-force coefficient of an NASA 0012 airfoil at an angle of attack of 10° in the R1Ch wind tunnel with solid upper and lower walls is given on the right side of figure 2. The freestream Macb number and Reynolds number based on chord are $M_\infty = 0.325$ and $R = 3.5 \times 10^6$, respectively, and the model cbord is 12 cm. As noted in reference 7, the experimental results for the normal-force coefficient vary linearly with the displacement thickness, and the extrapolated value for tbe normal-force coefficient for zero displacement thickness is about 10 percent greater than the value for no suction. The theoretical results, which are obtained from equation (11), are in excellent agreement witb experiment. For this wind tunnel, which has parallel sidewalls, the ideal two-dimensional normal-force coefficient C_n in equation (11) is the same as the normal-force coefficient for zero displacement thickness.

Test results for models of the LC 100D supercritical airfoil with chords of 6 cm and 11 cm are also presented in reference 7, and additional data for the NACA 0012 airfoil and both models of the LC 100D airfoil are presented in reference 8. In reference 7, the data given for the small LC 100D airfoil were obtained at the conditions $M_\infty = 0.32$, $R = 2.5 \times 10^6$ in the range $\alpha = 2.5^\circ$ to 10°, and the data given for the large model were obtained at the conditions $M_\infty = 0.319$, $R = 3.2 \times 10^6$, $\alpha = 9.5^\circ$, and $R = 6.5 \times 10^6$, $\alpha = 0.8^\circ$ in the range $M_\infty \approx 0.7$ to 0.9. Porous upper and lower walls with an openness ratio of 7 percent were used to obtain the supercritical airfoil data presented in reference 7. The additional data in reference 8 for the small LC 100D model are for two angles of attack and cover the Mach number range from $M_\infty \approx 0.3$ to $M_\infty \approx 0.85$. A few data points are given for the large LC 100D model for one angle of attack in the transonic range. Tbe additional data for the NACA 0012 airfoil are for the angles of attack $\alpha = 2.5^\circ$, 5°, and 7.5° and for Mach numbers extending from $M_\infty = 0.3$ into the transonic range for each angle of attack. The Reynolds numbers at which the additional data in reference 8 were obtained are not given, and the nature of the upper and lower walls is not indicated.

In figure 3, the experimental results for the normal-force coefficient ratio $\bar{C}_n/C_n$ obtained from reference 7 and a representative sample of the results obtained from reference 8 are compared witb theoretical results obtained from equation (11). This comparison indicates that the present theory is in general qualitative agreement with experiment. The subsonic results indicate good quantitative agreement as the incompressible limit is approached. The data for the supercritical airfoil show the same rapid decrease in $\bar{C}_n/C_n$ predicted by the theory as the freestream Mach number M_∞ increases toward one. The tbeoretical results for $\bar{C}_n/C_n$ for Mach numbers near the critical value differ from the experimental solution for both airfoils. This difference probably occurs because the tbeoretical solution for $\bar{C}_n/C_n$ does not account for nonlinear transonic effects.

For values of M_∞ greater than about 0.84, the experimental values for $\bar{C}_n/C_n$ for the supercritical LC 100D airfoil are greater than one. The experimental values for $\bar{C}_n/C_n$ for the NACA 0012 airfoil exceed one for values of M_∞ just larger than the critical value, and, hence, much smaller than the value for the supercritical airfoil. In fact, the effect occurs for the NACA 0012 airfoil before the beginning of the decrease in $\bar{C}_n/C_n$ caused by the singularity at $M_\infty = 1$. None of the experimental values for $\bar{C}_n/C_n$ greater than one are shown in figure 3. This effect may be caused by the interaction of the airfoil shock wave with the sidewall boundary layer, which can produce three-dimensional secondary flows not addressed by the present theory. The magnitude of the interaction is probably dependent on the strength of the airfoil shock

wave. Therefore, the NACA 0012 airfoil, which has a stronger shock wave at a given freestream Mach number and the angles of attack shown than the LC 100D airfoil, should experience the interaction at a lower Mach number.

It is shown in figure 4 that tbe present theory can be used to correlate results for the variation of the normal-force coefficient with angle of attack obtained in wind tunnels with different values of the sidewall boundary-layer parameter. The airfoil which is used is the NACA 0012. The wind tunnels in which the data were obtained are the NASA Low Turbulence Pressure Tunnel (LTPT), which has closed walls, and the ONERA R1Ch tunnel with closed upper and lower walls. The sidewalls of the LTPT are inclined outward slightly to account for flat-plate-type boundary-layer growth rate. The empty-tunnel displacement thickness and the tunnel width at the model station in this tunnel are 0.51cm (0.20 in.) and 91.46 cm (36 in), respectively, and, as a result, the displacement thickness parameter is $2\delta^*/b = 0.011$. Tbe LTPT results are for the Mach numbers $M_\infty = 0.299$ and $M_\infty = 0.359$ and the respective Reynolds numbers $R = 3.87 \times 10^6$ and $R = 3.91 \times 10^6$†. The R1Ch data shown in figure 4 were obtained with no sidewall suction and are for the conditions $M_\infty = 0.325$ and $R = 3.5 \times 10^6$. It can be seen that the traditional function $\beta\bar{C}_n$ does not correlate the data between the two wind tunnels, but that the function $\bar{\beta}\bar{C}_n$ does. The maximum values of the $\bar{\beta}\bar{C}_n$ curve appear to depend on M_∞.

The results presented in figure 4 are not corrected for interference from the closed upper and lower walls because the corrections for the two model-to-tunnel combinations are almost the same. The values of the principal parameter governing solid-wall interference, the model-chord-tunnel-height ratio, for the Low Turbulence Pressure Tunnel and the R1Ch tunnel are $c/h = .267$ and $c/h = .315$, respectively. The analysis of reference 1 shows tbat the difference in the uncorrected normal-force coefficients for the two experiments due to interference from the upper and lower walls is only about 0.6 percent of the coefficient value.

Modified von Karman rule.- To study the effect of the sidewall boundary-layer displacement thickness in a two-dimensional transonic tunnel, the sidewall boundary layer in the Langley 6- by 19-Inch Transonic Tunnel (ref. 16) has been successively thickened for tests on airfoil models at subsonic and transonic flow conditions. This tunnel is relatively narrow, which helps satisfy the approximation on spanwise velocity, w, given by equation (9).

The sidewall boundary layers have been artificially thickened using thin plates each having three rows of pins protruding from the surface (ref. 17). These plates are mounted on the sidewalls of the tunnel contraction region at 121.9 cm upstream of the model station. Three pairs of plates are used in the experiment. One pair of plates has no pins, the second pair has pins 2.54 cm high, and the third pair has pins 3.8 cm high.

The boundary layers generated by tbese thickening devices have been surveyed at several streamwise stations along the test section centerline with total head fixed rake tube probes. These probes have tubes from the surface of the wall to about 5.10 cm away from the wall surface. The static pressure at each probe location is determined from a calibration obtained during the tunnel-empty Mach number calibration. In addition, a static temperature distribution in the boundary layer, obtained from reference 18, is assumed as

$$\frac{T}{T_e} = 1 + .1793\, M_e^2 \left[1 - \left(\frac{U}{U_e}\right)^2\right] \tag{23}$$

where T and T_e are the static temperatures at velocities U and U_e, so that the velocity distribution in the boundary layer can be determined using the local Mach number and static temperature at each tube location. The velocity distributions are then integrated to determine the displacement thickness δ^* and the momentum thickness. For the three sidewall boundary-layer thickening configurations tested, the displacement thickness ranged from 0.20 cm to 0.78 cm and the shape factor H ranged from 1.30 to 1.59. The transformed shape factor $\bar{H}$, which is assumed to be one in the analysis, ranged from 1.18 to 1.26.

The skin friction coefficient is obtained by applying the Preston tube calibration suggested by Allen (ref. 19) to the surface tube of the rake probe. For the present experiment, the values of the nondimensional shearing stress, $\tau_w/\rho_e U_e^2$, which are obtained from the skin-friction measurements, range from 0.0010 to 0.0012, while the values of δ^*/c range between 0.014 to 0.052. It is concluded that inequality (4) is satisfied sufficiently.

Results of tunnel-empty boundary-layer surveys in the unthickened boundary layer and the artificially thickened boundary layers are presented in figures 5 and 6. The model-station velocity profiles shown in figure 5 indicate that the artificially

---

†The data from the LTPT were obtained by Charles L. Ladson

thickened boundary layers have developed sufficiently to have adequate similarity with the unthickened boundary layers for the purpose of this experiment. The variations of δ^* with x/c near the model station, presented in figure 6, are small. Therefore, the pressure gradients generated by the model should be the dominating cause of variations in the effective tunnel width, $b - 2\delta^*$, that modify the continuity equation in the manner indicated by the analysis.

The variations of shock-wave location with both M_∞ and $\bar{M}_\infty$ for all three boundary layers are presented in figure 7. The model is an NACA 0012 airfoil at an angle of attack of zero. A significantly improved correlation is obtained when $\bar{M}_\infty$ rather than M_∞ is used.

Another transonic characteristic of the NACA 0012 airfoil which was used to evaluate the application of the similarity rule was the variation of the section drag coefficient at the zero angle of attack with freestream Mach number. Here, the similarity rule requires the application of equation (19) to alter the measured drag coefficient to the adjusted drag coefficient, $\bar{C}_d$. This adjustment actually applies only to the component of pressure drag in the drag coefficient, and does not account for the skin-friction component. Figure (8) shows the comparison between the measured section drag coefficient, C_d, plotted against M_∞ and the adjusted section drag coefficient, $\bar{C}_d$, plotted against $\bar{M}_\infty$, for the three sidewall boundary layers. In figure (8), the similarity rule provides a substantially improved drag correlation in the region of drag rise, but loses quality below the drag rise. This is probably because the majority of the drag comes from the skin friction below drag rise, whereas the adjusted drag coefficient is derived for the pressure drag. The correlation improves as the pressure drag becomes a larger fraction of the total drag, as seen in the drag-rise region. Figure 8 also indicates more scatter in the drag data measured with the thickest sidewall boundary layer. This boundary layer was approximately 5.2 cm thick at the model station, tunnel empty, so that the two sidewall boundary layers occupied approximately two-thirds of the tunnel width. This large amount of sidewall boundary layer probably adversely influences the drag measurements made with the wake probe.

The final characteristic investigated was the variation of section normal-force coefficient at a fixed angle of attack with freestream Mach number. This investigation was performed with a supercritical airfoil rather than the NACA 0012 airfoil, because the shock wave on a supercritical airfoil is generally much weaker than that on the NACA 0012 airfoil at lifting conditions. The use of this airfoil reduced the three-dimensional interaction between the model shock wave and the sidewall boundary layer.

For the section normal-force coefficient, the similarity rule requires equation (19) to be used to provide an adjusted section normal-force coefficient, $\bar{C}_n$. Figure 9 shows the comparison between C_n plotted against M_∞ and $\bar{C}_n$ plotted against $\bar{M}_\infty$.

Figures 7, 8, and 9 show that an improved correlation is obtained using the similarity rule, particularly for the two thinnest sidewall boundary layers. The correlation quality diminishes for the third sidewall boundary layer, probably because of its large thickness compared to the tunnel width. Therefore, the data for the thickest sidewall boundary layer are presented with open symbols, while the data for the two thinner sidewall boundary layers, where the similarity rule is more applicable, are presented with solid symbols.

CONCLUDING REMARKS

An analysis of the interaction of model pressure fields with attached wind-tunnel wall boundary layers has been presented. It has been shown that the effects of this interaction are similar to compressibility effects for sidewall boundary layers in two-dimensional wind tunnels, and subsonic and transonic rules have been presented. It has been demonstrated that these rules correlate experimental data. The similarity rules apply as long as the sidewall boundary layers do not separate and three-dimensional interactions do not occur.

The analysis includes the development of an interaction-related linear boundary condition for boundary layers in three-dimensional wind tunnels. This boundary condition is like the linear boundary conditions for ventilated wind-tunnel walls and can be solved with the same general techniques. It is shown that the interaction effect is not similar to the compressibility effect for three-dimensional wind tunnels.

REFERENCES

1. Pindzola, M.; and Lo, C. F.: Boundary Interference at Subsonic Speeds in Wind Tunnels with Ventilated Walls. AEDC TR-69, May 1969.

2. Kemp, William B., Jr.: Transonic Assessment of Two-Dimensional Wind-Tunnel Wall Interference Using Measured Wall Pressures. NASA CP-2046, pp. 473-486, March 1978.

3. Murman, E. M.: A Correction Method for Transonic Wind-Tunnel Wall Interference. AIAA Paper No. 79-1533, July 1979.

4. Preston, J. H.: The Interference on a Wing Spanning a Closed Tunnel, Arising from the Boundary Layers on the Sidewalls, with Special Reference to the Design of Two-Dimensional Tunnels. N. P. L., Teddington, Middlesex, England, R & M 1924, March 1944.

5. Cowley, W. L.; and McMillan, G. A.: Pressure Exploration Over an Airfoil That Completely Spans a Wind Tunnel. R & M 1597, 1934.

6. Mendelsohn, R. A.; and Polhamus, Josephine F.: Effect of the Wind-Tunnel Wall Boundary Layer on Test Results of a Wing Protruding from a Tunnel Wall. NACA TN-1244, 1947.

7. Bernard-Guelle, R.: Influence of Wind-Tunnel Wall Boundary Layers on Two-Dimensional Transonic Tests. Paper presented at 12th Applied Aerodynamics Colloquium, ENSMA/CEAT-Poitiers, Nov. 5-7, 1975, ONERA 1976, pp. 1-22. (Available as NASA TT F-17255.)

8. Bernard-Guelle, R.; and Chevalier, Jean-Pierre: Lateral Boundary Layer Effects on Two-Dimensional Tests. Paper presented at 48th Annual Meeting of Supersonic Tunnel Association, Toulouse, Sept. 14-15, 1977.

9. Barnwell, R. W.: A Similarity Rule for Compressibility and Sidewall Boundary Layer Effects in Two-Dimensional Wind Tunnels. AIAA Paper No. 79-0108, 1979.

10. Barnwell, R. W.: Similarity Rule for Sidewall Boundary-Layer Effect in Two-Dimensional Wind Tunnels. AIAA Journal, Vol. 18, No. 9, pp. 1149-1151, Sept. 1980.

11. Sewall, William G.: Effects of Sidewall Boundary Layers in Two-Dimensional Subsonic and Transonic Wind Tunnels. AIAA Paper No. 81-1297, 1981.

12. Kemp, W. B., Jr.; and Adcock, J. B.: Combined Four-Wall Interference Assessment in Two-Dimensional Airfoil Tests. AIAA Paper No. 82-0586, March 1982.

13. Winter, K. G.; and Smith, J. H. B: A Comment on the Origin of End-Wall Interference in Wind-Tunnel Tests of Airfoils. RAE Tech Memo AERO 1816, August 1979.

14. Berndt, Sune B.: On the Influence of Wall Boundary Layers in Closed Transonic Test Sections. FFA Report 71, 1957.

15. Lofgren, Peje: Simplification of the Boundary Condition at a Slotted Wind-Tunnel Wall with a Boundary Layer. FFA Technical Note AV-932, March 1975.

16. Ladson, C. L.: Description and Calibration of the Langley 6- by 19-Inch Transonic Tunnel. NASA TN D-7182, 1973.

17. Johnson, D. F.; and Mitchell, G. A.: Experimental Investigation of Two Methods for Generating an Artificially Thickened Boundary Layer. NASA TM X-2238, 1971.

18. White, F. M.: Viscous Fluid Flow. McGraw Hill Book Co., New York, p. 627, 1974.

19. Allen, J. M.: Evaluation of Compressible-Flow Preston Tube Calibrations. NASA TN D-7190, 1973.

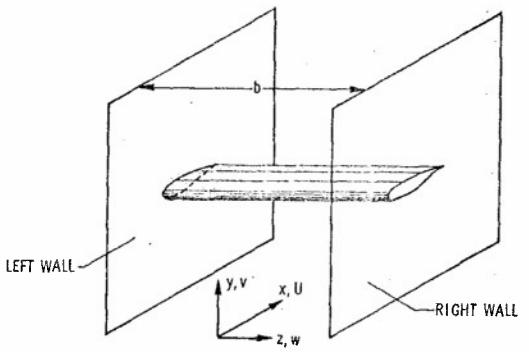


Fig. 1.- Model of two-dimensional wind tunnel

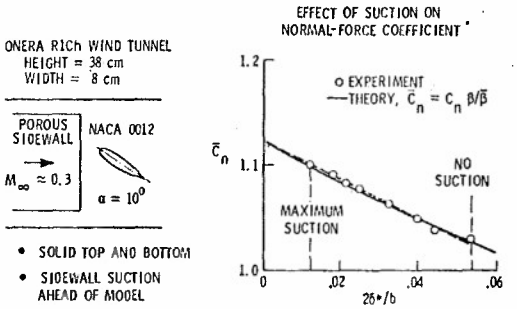


Fig. 2.- Effect of sidewall boundary layer on normal-force coefficient in ONERA R1Ch wind tunnel.

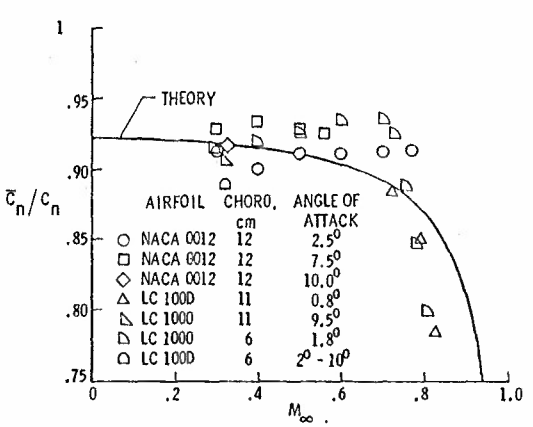


Fig. 3.- Comparison of theory with data obtained in ONERA R1Ch wind tunnel with no sidewall suction upstream of model.

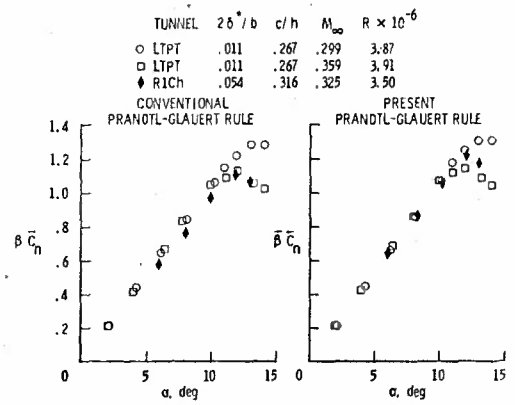


Fig. 4.- Comparison of conventional and present forms of Prandtl-Glauert rule.

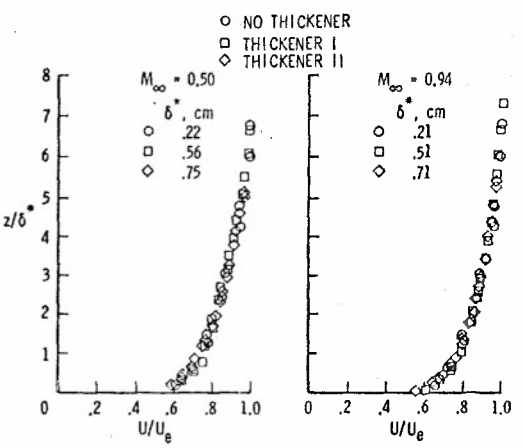


Fig. 5.- Nondimensional velocity distributions in artificially-thickened sidewall boundary layers.

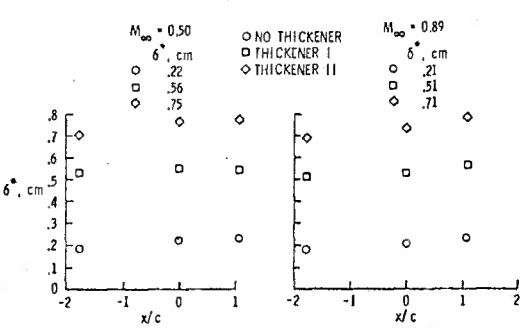
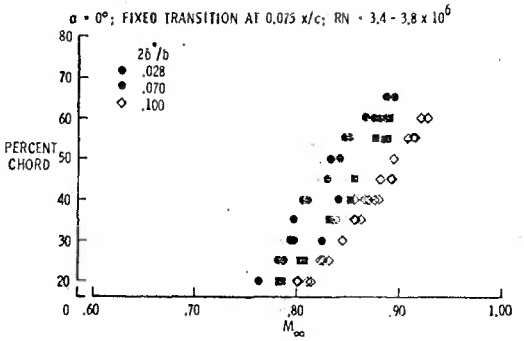
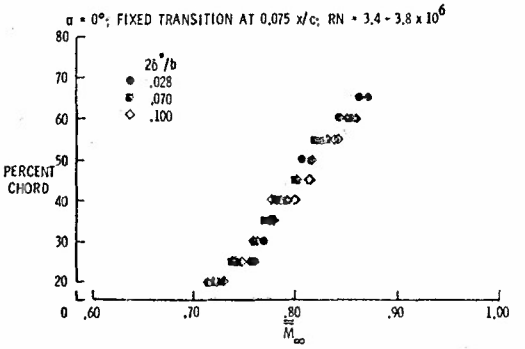


Fig. 6.- The variation of the measured boundary-layer displacement thickness near the model station.

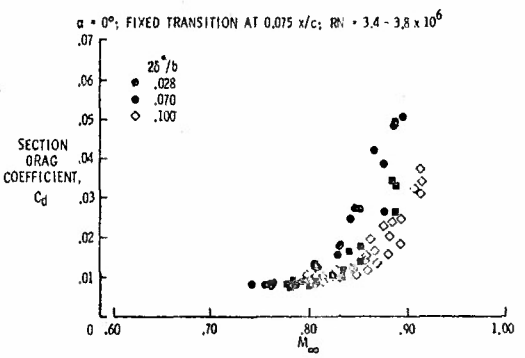


(a) Shock-wave location vs. freestream Mach number

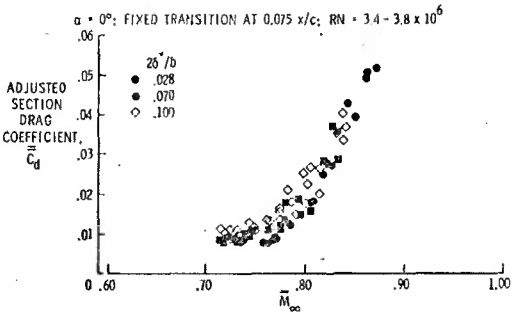


(b) Shock-wave location vs. equivalent freestream Mach number

Fig. 7.- Variation of shock wave location with freestream Mach number of the NACA 0012 airfoil tested with three sidewall boundary-layer displacement thicknesses.

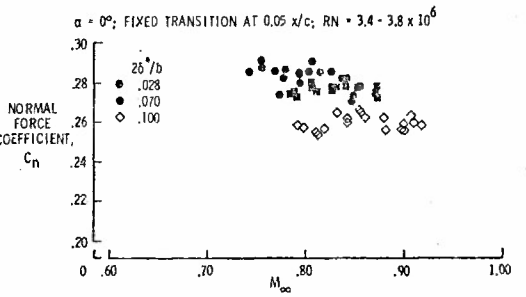


(a) Section drag coefficient vs. freestream Mach number

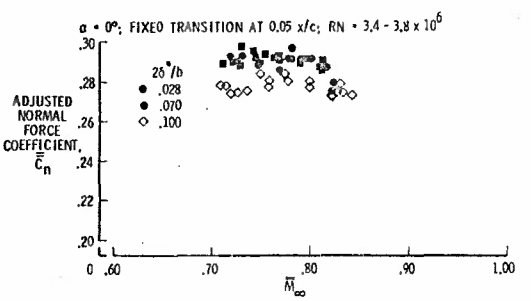


(b) Adjusted section drag coefficient vs. equivalent freestream Mach number

Fig. 8.- Variation of section drag coefficient with freestream Mach number for the NACA 0012 airfoil tested with three sidewall boundary-layer displacement thicknesses.



(a) Section normal-force coefficient vs. freestream Mach number



(b) Adjusted section normal-force coefficient vs. equivalent freestream Mach number

Fig. 9.- Variation of section normal-force coefficient with freestream Mach number for a supercritical airfoil tested with three sidewall boundary-layer displacement thicknesses.

REYNOLDS NUMBER EFFECTS ON TRANSONIC SHOCK LOCATION

by
F. Aulehla and A. Eberle
Messerschmitt-Bölkow-Blohm GmbH
Unternehmensbereich Flugzeuge
Postfach 801160
D 8000 München 80
Federal Republic of Germany

SUMMARY

The example of a variable density transonic wind tunnel shows that the boundary layer displacement at the test section wall is about hundred times bigger than the corresponding effects at the model. Altering Reynolds number by a factor of four causes these displacement areas to change by an amount which again is hundred times larger at the test section wall as compared to that at the model surface.

Computations using these variable boundary conditions at the test section wall show that the shock location on an axisymmetric body is noticeably altered. These computed shifts in shock location agree very well with those measured in the wind tunnel leaving little room for true Reynolds number effects on the model itself. A corresponding exercise is also presented for the two-dimensional case of a Whitcomb-profile.

In both, the axisymmetric and the two-dimensional cases the viscous effects at the model were deliberately neglected so that the computed changes in shock location can be completely attributed to the changed boundary conditions at the test section wall.

Lastly, an opposite and purely theoretical approach is presented, in which the shock location on a Korn profile was computed for the free flight case and for a model boundary layer assumed to be fully turbulent. The results show that for this particular example with fixed transition there is only a negligible change in shock location when Reynolds number is raised from 4 million to 20 000 million.

The conclusion to be drawn from these three different examples is that the true Reynolds number effects on transonic shock location appear to be by orders of magnitudes smaller than generally quoted from variable density wind tunnel measurements. Thus, the considerable discrepancies between shock location trends measured in wind tunnels and free flight, seem to be largely explained.

1. INTRODUCTION

In past aircraft developments large discrepancies were often found between Reynolds number trends obtained from wind tunnel and flight tests. Typical examples thereof are afterbody pressure drag (ref.1) and wing shock location (ref.2). There have been long disputes about how much of these observed Reynolds number effects were true effects and how much should be attributed to systematic measurement errors in the wind tunnel and flight test respectively.

Argument No. 1, the rapid increase of afterbody pressure drag with Reynolds number has been explained in ref.1 and 3 to be a systematic error, which can be eliminated by a proper wind tunnel calibration. In the meanwhile, this explanation has been accepted (ref.4) and proven by experiment (ref. 5 and 6).

Critical reviews of argument No.2, the effect of Reynolds number on the transonic shock location, have been treated in several previous publications, e.g. in ref. 7, 8 and, experimentally, in ref. 9. In ref.15 it was shown by inviscid computations that the measured change in transonic shock location on the axisymmetric MBB body No.3 can almost be completely attributed to the Reynolds number dependent change of the wind tunnel wall conditions. However, as the total shock travel was only about half a percent of the length of the body, critics of this paper argued that an agreement which comprised only half a percent of the body length was simply too small to prove this case, especially as the effects looked for on wings were larger than 10 %. Therefore, in the present paper the same computations with identical Reynolds number dependent wind tunnel wall boundary conditions were undertaken for the two-dimensional case of a Whitcomb-profile representative for today's transonic airfoil technology. For convenience the main results of the axisymmetric case reported in ref.15 are briefly repeated first.

2. VARIABLE BOUNDARY CONDITIONS

2.1 Wind Tunnel Pressure Gradients

In free flight, the stream lines of a flow past a body are free to bulge out, which in conventional wind tunnels with non-adaptive, real walls is prevented to a large extent (wind tunnel wall interference, fig.2). Imaginary walls are defined here as walls located at the place of the real plane walls and do not interfere with the flow.

Along these imaginary walls the pressure varies. These pressure variations can be used to define linearized pressure gradients along these imaginary walls for the interference-free case. These interference-free (linearized) pressure gradients are

compared with those measured by 24 pressure tappings at the centre-line of the upper test section wall in the Göttingen Transonic 1 m x 1 m Wind Tunnel, fig.1: Tunnel total pressure ("Re-number") appears to have a significant effect on the wall pressure gradient and so do the presence of the model and its cross-sectional area distribution. Both models have the same maximum cross-section and produced a tunnel blockage of 1,13 %. In these tests, the test section sidewalls were kept at a constant divergence angle of 0,5 degree relative to the centre-line.

Fig. 3 compares the displacement thickness of the boundary layer at the model with that at the test section wall. For M_o = 0,8 and a tunnel total pressure P_{T_o} = 300 ... ...1200 mm Hg simple flat plate calculations show that the displacement thickness of the boundary layer times perimeter of the test section, is about 90 times bigger than the corresponding value at the maximum cross-section of the model.

Increasing the tunnel total pressure P_{T_o} from 300 to 1200 mm Hg, i.e. raising the Re-number by a factor of four, causes the changes in these displacement areas (D.A.) to be about hundred times greater at the wind tunnel walls than at the model (blockage = 1,13 %, test section = 1 m x 1 m, assumed wetted length = 6 m for the tunnel walls and = 0,4 m for the model).

These flat plate boundary layer relations together with 1-dimensional duct flow calculations were used to obtain the linearized wall pressure gradients plotted in fig.4. Qualitative agreement exists between computed and measured curves. The diagram shows also that the contribution of the model boundary layer itself, i.e. with the model absent, is only about 20% relative to that of the wind tunnel wall boundary layer ($0 < x/L < 1$).

2.2 Wind Tunnel Pressure Level

In addition to the axial pressure gradients mentioned above, variable density wind tunnels will also experience small changes in the pressure level, which need to be taken into account for sensitive measurements by extremely careful tunnel calibrations (ref. 3, 4, 6). In general, however, this has only recently been done. That is, before that time it was assumed that the tunnel calibration conducted only at the nominal total pressure would also hold for different total pressures, i.e. different Reynolds numbers. Fig. 5 shows such a decrease in pressure level in the test section of the Göttingen transonic wind tunnel prior to a Reynolds number calibration. It is expected that this trend is typical for all conventional variable density wind tunnels.

The combination of the changes in pressure level and in axial pressure gradient as used for the subsequent computations of the shock location changes is shown in fig.6 schematically.

3. COMPUTED EFFECT OF PRESSURE GRADIENT AND PRESSURE LEVEL ON SHOCK LOCATION CHANGE

3.1 MBB Body of Revolution No. 3

The geometry of the MBB bodies of revolution is shown in fig.9. They have a thickness ratio of 15 %. The exact definition is given in ref. 1, 3, or 7.

Using the computer code for the Finite Element Method (ref.10, 11, 12) the pressure distribution along the equivalent (1 m^2), non-ventilated axisymmetric test section was computed for body No.3 at zero incidence and M_o = 0,8. (The mesh grid used and the resulting wall pressures are given in ref.15.) This pressure distribution was then modified by superimposing systematic variations of axial pressure gradients and shifts in pressure level to give the new boundary conditions for the subsequent flow field computations.

The resulting new shock locations are plotted in fig. 7. It can be seen that both a more positive pressure gradient and a more negative pressure level act in the same direction, that is, they move the shock rearwards (the shock location is defined to be where the local pressure coefficient corresponds to sonic flow conditions).

Note that the changes of the wall disturbance parameters (pressure level and pressure gradient) used to compute the shock locations in fig.7 are assumed values. If, therefore, the actually measured Reynolds number dependent wall disturbance parameters are taken, then the shock locations of fig.7 can be cross-plotted to give the computed shock locations versus Reynolds number in fig.8. There is a remarkable agreement between the measured and computed shock location changes, except at the higher Reynolds numbers for curve B. This levelling-off is caused by the corresponding trend of the measured wall pressures in fig. 5. However, in ref.15 there was some justification made to use a linear extrapolation of the wall pressures instead, i.e. curve D. The wall pressure gradient used for the cross-plotting is given in ref. 15 but differs only slightly from that shown in fig. 1 for M_o = 0,8.

The good agreement in fig.8 seems to prove that the measured changes in shock location were almost completely caused by deviations in pressure level and by wall pressure gradients rather than by true Re-number effects on the model itself (note that in these computations viscous effects on the model were not taken into account).

Fig.9 shows the measured shock locations for bodies No. 2 to 5. The different slopes of these straight lines suggest that the sensitivity of the shock location towards Reynolds number or rather towards Reynolds number dependent wall disturbances, decreases with increasing body surface curvature. This result has been confirmed by two-dimensional investigations: There are profiles which are particularly sensitive to such superimposed wall disturbances while others are not.

Considering the whole family of curves in fig.9 it is felt that measured shock location changes can be discriminated down to 0,01 % of the body length (L = 800 mm), which some critics of this work denied (0,01 % L $\hat{=}$ $\Delta c_p \approx 6 \cdot 10^{-4}$). The main point of their critique, however, was that the overall shock location change of 0,5 % L was so small relative to the corresponding changes of about 10 %c measured on profiles that no generalization of these Reynolds number effects on shock location should be made. Therefore, a similar investigation was undertaken for the two-dimensional case of a Whitcomb-profile.

3.2 Whitcomb Airfoil

Two methods have been applied for the computation of the flow past this airfoil placed at the centerline of a wind tunnel. The first is based on the Transonic Small Perturbation theory whereas the other solves Euler's equations using a new highly absorbing boundary algorithm.

3.2.1 Calculations with a Fast TSP-Method

From the well-known ADI method first introduced by Ballhaus (ref.16) a fast pseudo-unsteady TSP-method was derived based on the truncated potential equation

$$-\varphi_{xt} + \{1 - M^2 - [3 + (\kappa-1)M^2]\, M^2 \varphi_x\}\, \varphi_{xx} + \varphi_{zz} = 0$$

The transonic switch is formulated in full conservation form. The resulting difference equations are solved implicitly using a two-step algorithm.

$$\text{x-sweep:} \quad -\tilde{\varphi}_{xt} + A\tilde{\varphi}_{xx} = -\tilde{\varphi}_{zz}$$

$$\text{z-sweep:} \quad -\varphi_{xt} + \frac{\varphi_{zz}}{2} = \frac{\tilde{\varphi}_{zz}}{2}$$

The linearized boundary condition is entered only in the z-sweep in the usual way. Key point for obtaining fast convergence is the proper choice of the time step. Essentially Δt should run during the transient through a series of values damping all unsteady wave lengths which may occur. For simplicity, however, an optimum time step can be found by performing some trial runs of the scheme. For a quick check of changes of the pressure distribution past an airfoil due to superimposed small perturbations along wind tunnel walls the present procedure seems to be particularly suited.

As base line geometry a Whitcomb-profile was chosen, parameters and coordinates of which are given in fig.10. The wind tunnel walls were set off the airfoil to give a blockage of 1.6 %. The grid for this configuration is shown in fig. 11. The parametric study comprised the 12 cases listed in fig.12 with the definition of the pressure gradient and pressure level taken from fig.6. All calculations followed the same sequence, see fig. 12:

(1) Calculation with closed walls

(2) Integrate incremental perturbation potential from given Δc_p-wall

(3) Restart calculation using initial guess from (1) this time, however, with potential distribution prescribed along both walls

$$\varphi(3)_{wall} = \varphi(1)_{wall} + \Delta\varphi(2)$$

From the resulting pressure distributions the shock locations were then obtained using the same definition as in section 3.1, i.e. the shock was assumed to be where the local pressure was equivalent to sonic conditions ($c_p = c_p^*$). The results of the 12 computed cases are compiled in fig.13b: The inviscid computations described above show that due to a maximum of Reynolds number dependent changes in wall interference the shock on a low curvature profile (Whitcomb) moves backwards by 14 %c. This maximum change in wall interference was obtained from a rather incomprehensive measurement of wall pressures (24 only, top wall) in the Göttingen Transonic Wind Tunnel for a Reynolds number increase from 4 to 17 million without applying any Reynolds number calibration. However, from the data available at MBB it appears that many other variable density wind tunnels have similar or even larger Reynolds number dependent changes in wall interference. For the Reynolds number increase quoted above for the Göttingen Transonic Wind Tunnel the axial pressure gradient $\partial c_p/\partial(x/L)$ becomes more positive by 0,015 and the pressure level decreases by $\Delta c_p = 0{,}009$. The latter corresponds to an unnoticed increase in free stream Mach number of $\Delta M_o = 0{,}0042$ at $M_o = 0{,}82$. Another important result of fig.13b is that for other wind tunnels in which the two disturbance parameters i.e. the change in pressure level and in axial pressure gradient, do not act in the same direction, any non-monotonous shock travel versus Reynolds number, as shown occasionally in the literature, will result.

3.2 Calculations with an Euler Code

Since the previous TSP-method contains some uncertainties concerning the accuracy of the reference pressure distribution (closed wall conditions) it was felt to repeat at least this case using a method based on the exact equations. For this purpose an Euler code from ref. 17 was rewritten for the wind tunnel mode.

It is based on the pseudo unsteady governing equations with the assumption of constant total enthalpy included.

At interior (non-boundary) points the solution is updated in conservative finite difference form by a modified explicit Mac Cormack scheme for curvilinear grids. Key point of the method is a new absorbing boundary algorithm which becomes particularly important for ducted flow problems since the solid wall boundary conditions often tend to reflect waves with increased amplitude. It is based in brief on linear characteristic combinations of Euler's equations such that the matrix of the difference equations at the boundaries is as dominant as possible.

In addition to the usual approach of using only the normal characteristic equations for this purpose also a "trailing characteristic" system of linear combinations is introduced stabilizing the scheme considerably. Also the choice of boundary conditions to be prescribed at the wind tunnel entrance and exit is important for optimum transport of unsteady perturbation energy out of the numerical flow field. Best results were obtained by prescribing the sum of the static pressure and the momentum multiplied by a constant taken from the isentropic relation. For increasing the convergence speed the local maximum allowable time step is adopted.

Since the free flight airfoil code was successfully examined versus the GAMM-workshop 79 results it is adequate first to compare the result of this code with the established full potential mass flux procedure of ref. 18. The discrepancies in fig.14 may be partly due to the different treatment of the circulation, different number of mesh points (the Euler grid shown is pretty crude) and different formulation of the basic equations. We are well aware that particularly the influence of the mesh spacing requires further examination.

Fig.15 shows the upper surface pressure distributions for some wind tunnel heights obtained by the present method for closed walls. The trend points qualitatively into the correct direction.

The results presented should indicate that Euler codes are no longer exclusively a subject of pure research but may now also become part of the routine work of engineering aerodynamicists.

3.3 Korn-Profile

In contrast to the two preceeding sections where the model boundary layer was deliberately neglected and only the Reynolds number dependent wind tunnel wall disturbances were taken into account, this section presents the calculated shock location changes on a Korn-profile for the free flight case and for a fully turbulent boundary layer (ref.19). Fig.16 compares these two profiles. Unfortunately, the curvature of the upper sides of the two profiles is not the same. Fig.17 shows the computed shock locations on the Korn-profile: for the lower Reynolds numbers there is an onset of numerical instability; for Reynolds numbers lower than shown in the diagram the solution did not converge.

However, the main conclusion to be drawn from these results is that Reynolds number appears to have very little influence on shock location for this profile: for an increase in Reynolds number from 10^7 to 10^9 the shock moves backwards only by 0,7 %c. Even if all data points are considered then the shock location is altered by 3,1 %c for the full Reynolds number change ($4 \cdot 10^6$ ... $2 \cdot 10^{10}$), which still is a very weak sensitivity as compared to measurements in variable density wind tunnels showing shock excursions larger than 10 %c for Reynolds number changes as small as 3 million to 20 million (ref.2). It is planned to recompute this free flight case also for the above Whitcomb-profile. It is felt that if the same result as for the Korn-profile should be obtained, then an almost perfect proof for the predominant influence of the Reynolds number dependent wall interference effects has been furnished.

4. CONCLUSIONS AND RECOMMENDATIONS

4.1 The main goal of this paper was not to assess any differences between tunnel data and free flight, but to correlate the Re-number trends measured in the wind tunnel with the measured boundary conditions at the test section wall by means of computing the flow field in the test section.

4.2 The shock location on the model is strongly influenced by the Re-number effects at the wall (changes of pressure level and gradients). These effects can largely be eliminated by extremely careful tunnel calibrations for all flow conditions, which may require better standards than currently in use.

4.3 Sensitive measurements like afterbody/part body testing and transonic shock location assessment require very accurate determination of free stream static pressure or Mach number. Desirable accuracy is $\Delta M_o \approx 5 \cdot 10^{-4}$ and $\Delta c_p = 10^{-3}$ respectively, which corresponds to 1/9 of the total error in pressure level ($\Delta c_p = 9 \cdot 10^{-3}$) typical for

an uncalibrated Re-No. change from 4 to 17 million. Also, for interpolation and computational correction purposes the inclusion of one or two additional settings of the wall divergence angle may be appropriate in future wind tunnel test programs containing measurements which are sensitive to pressure gradients. This procedure could serve as interim solution until adaptive wall wind tunnels have been fully developed.

4.4 For the calibration of the pressure level in the empty tunnel the measurement of the surface pressures at all 4 walls is considered a simple and very accurate method which should supplement the standard calibration of the complete flow field. The wall pressure calibration method could be used to correct previous results. For future wind tunnel measurements it is recommended to record a sufficiently large number of wall pressures to be used in theoretical correction methods presently being developed.

4.5 It is suggested that other theoreticians do similar computations using the same wall disturbance parameters in order to provide a larger body of results for generalization of the present conclusions on spurious Reynolds number effects.

REFERENCES

[1] Aulehla, F., and G. Besigk
Reynolds Number Effects on Fore- and Aftbody Pressure Drag
AGARD-CP-150, Chapter 12 (1974)

[2] Blackerby, W.T., and J.F. Cahill
High Reynolds Number Tests of a C-141A Aircraft Semispan Model to Investigate Shock-Induced Separation
NASA CR-2604 (1975)

[3] Aulehla, F., and G. Besigk
Fore- and Aftbody Flow Field Interaction with Consideration of Reynolds Number Effects
AGARD AG-208, Chapter II-F (1975)

[4] Jackson, F.M.
Calibration of the AEDC-PWT 16 FT Transonic Tunnel Aerodynamic Test Sections at Various Reynolds Numbers
AEDC TR-78-60, Feb. 1979

[5] Reubush, D.E.
The Effect of Reynolds Number on Boattail Drag
Paper 75-63 presented at 13th AIAA Aerospace Sciences Meeting, Pasadena, Calif., January 20-22, 1975

[6] Fanning, A.E., and E.J. Lucas
Engine/Aircraft Afterbody Interactions: Recommended Testing Techniques Based on YF-17 Experience
J. Aircraft, Vol. 17, No. 11

[7] Aulehla, F.
Drag Measurement in Transonic Wind Tunnels
AGARD-CP-242, Paper 7 (1977)

[8] Aulehla, F.
Grenzen der Widerstandsbestimmung schlanker Körper in transsonischen Windkanälen
Messerschmitt-Bölkow-Blohm GmbH, Report No. UFE 1315 ö, June 1976

[9] Vidal, R.J., J.C. Erickson, Jr., and P.A. Catlin
Experiments with a Self-Correcting Wind Tunnel
AGARD-CP-174, Chapter 11 (1975)

[10] Eberle, A.
Eine Methode finiter Elemente zur Berechnung der transsonischen Potentialströmung um Profile
Messerschmitt-Bölkow-Blohm GmbH, Report No. UFE 1352 (ö), 1977

[11] Eberle, A.
Eine Methode der finiten Volumen zur Berechnung der transsonischen Potentialströmung um Flügel aus dem Druckminimumintegral
Messerschmitt-Bölkow-Blohm GmbH, Report No. UFE 1407 (ö), 1978

[12] Eberle, A.
Transonic Potential Flow Computations by Finite Elements: Airfoil and Wing Analysis, Airfoil Optimisation
Messerschmitt-Bölkow-Blohm GmbH, Report No. UFE 1428 (ö), 1978

[13] Data from Testing five Bodies of Revolution in the Göttingen Transonic Wind Tunnel, 1970/1972/1974 (unpublished)

[14] Stanewsky, E., and B.H. Little, Jr.
Studies of Separation and Reattachment in Transonic Flow
AIAA Atmospheric Flight Mechanics Conf., Tullahoma, Tenn., AIAA Paper 70-541, 1970

[15] Aulehla F., and R. Kleebaur
Reynolds Number Effects on Wind Tunnel Wall Boundary Layer and Influence on Transonic Shock Location
AGARD Meeting on Integration of Computer and Wind Tunnel Testing, Bedford, Beds, UK, 18/19 February 1981

[16] Ballhaus, W.F. and J.L. Steger
Implicit Approximate-Factorization Schemes for the Low-Frequency Transonic Equation
NASA TM X-73082, 1975

[17] Eberle A.
Methods for Solving Euler's Equations for Airfoil and Intake Flow
Proceedings of the Fourth GAMM Conference for Numerical Fluid Mechanics, Paris 81
To appear in: Notes on Numerical Fluid Mechanics, Vol.V, Vieweg Verlag, 1982

[18] Lucchi C.W.
Subdomain Finite Element Method to Compute the Transonic Potential Flow around a Profile or in a Cascade
Messerschmitt-Bölkow-Blohm GmbH, Report No. MBB/FE122/S/R/1508, 1980

[19] Niestroy, H.
Ein Verfahren zur Nachrechnung von Tragflügelprofilen in transsonischer Strömung mit Berücksichtigung der Grenzschicht
Messerschmitt-Bölkow-Blohm GmbH, Report No. MBB/FE122/S/R/1524, 1981

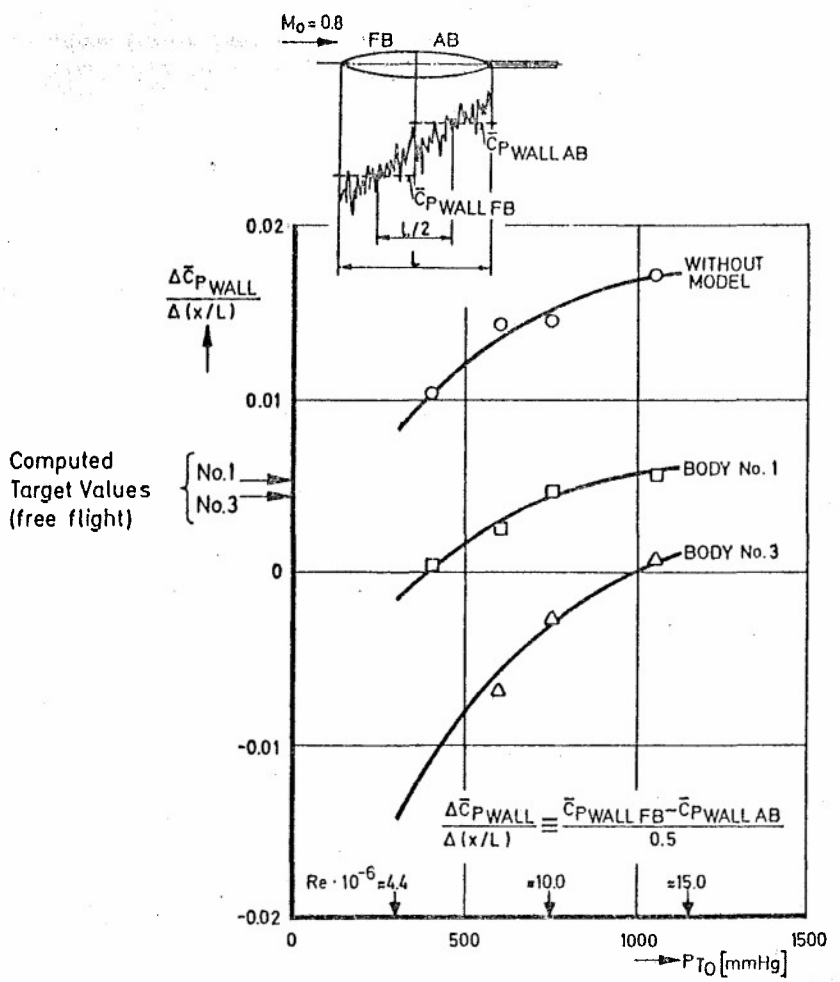


Fig. 1 Effect of tunnel total pressure on measured pressure gradient at upper test section wall

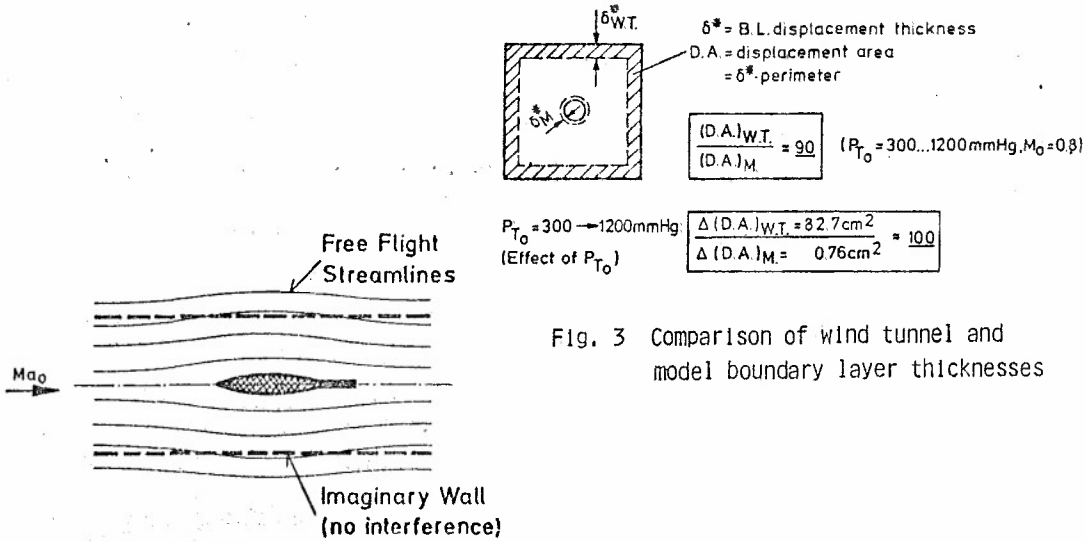


Fig. 2 Definition of imaginary wall

Fig. 3 Comparison of wind tunnel and model boundary layer thicknesses

Note: Re-number is based on body length L

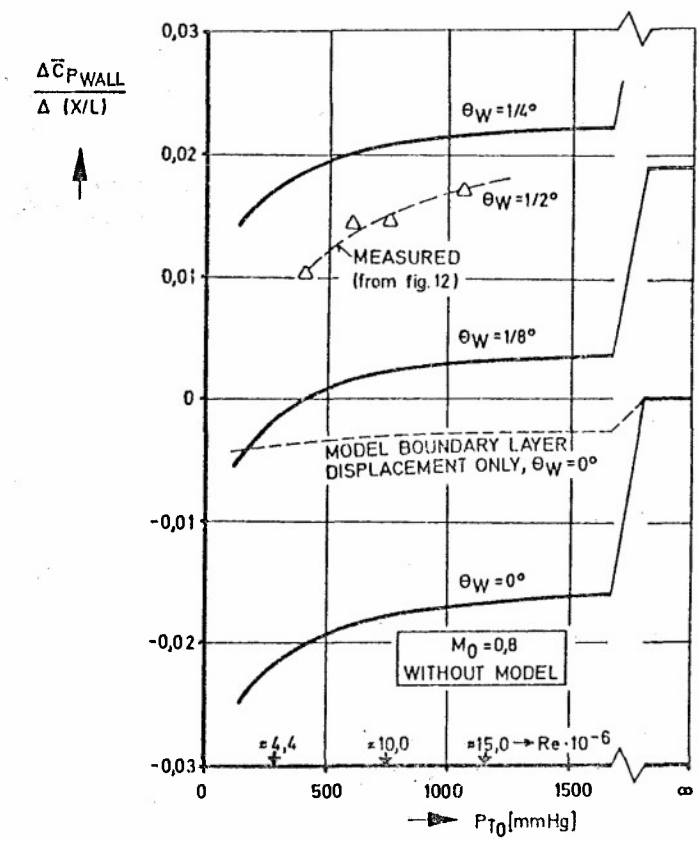


Fig. 4 Computed effect of wall divergence angle Θ_W and boundary layer displacement thickness on wall pressure gradient

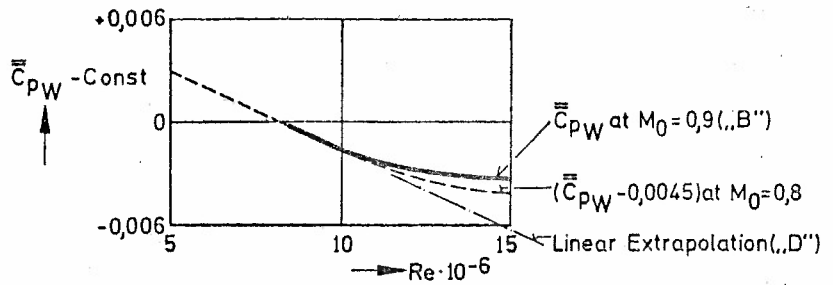


Fig. 5 Mean values of measured wall pressure coefficients at M_0 = 0,8 and 0,9 respectively

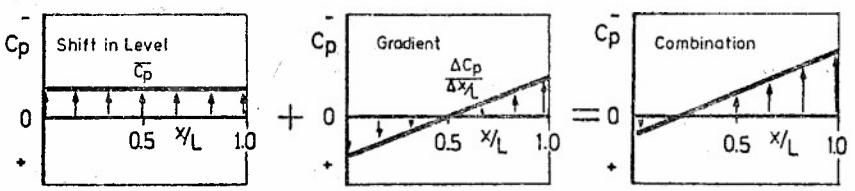


Fig. 6 Combination of pressure level shift and pressure gradient (schematic)

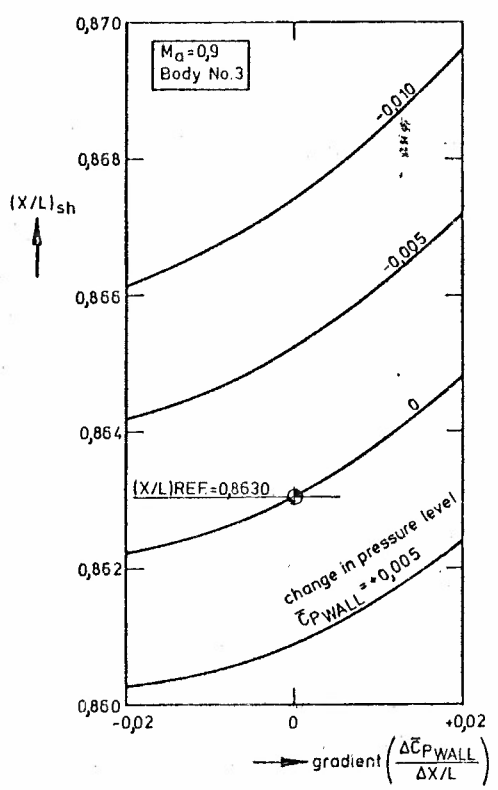


Fig. 7 Computed shock locations for assumed changes in wall pressure gradient and in pressure level

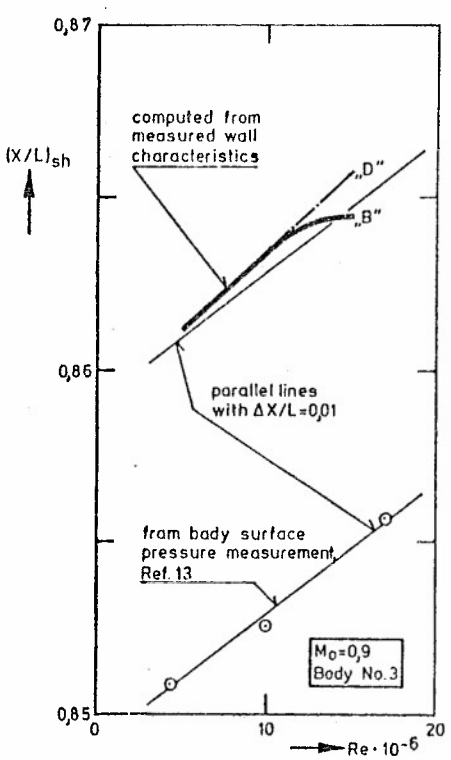


Fig. 8 Comparison of measured and computed shock locations

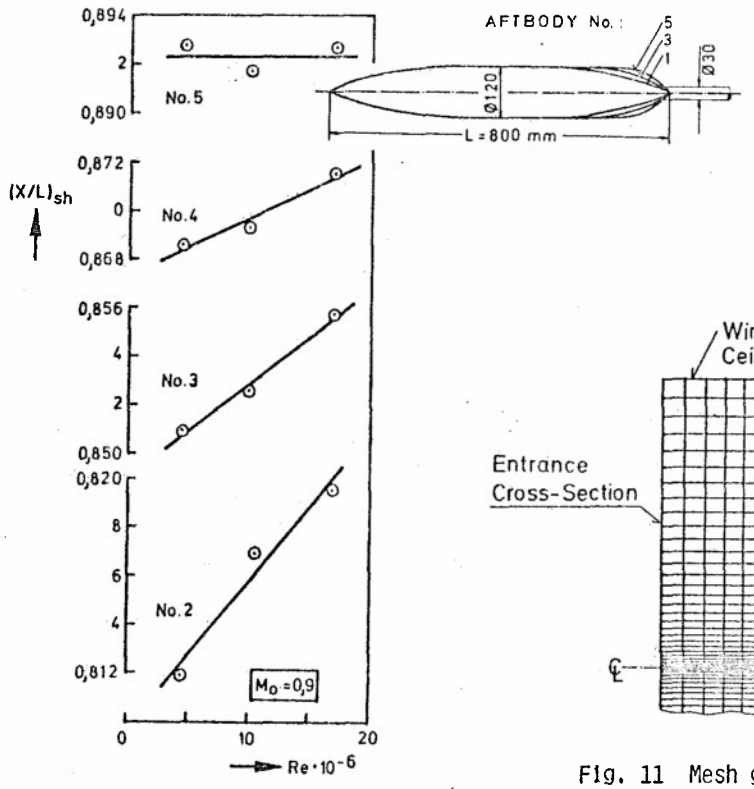


Fig. 9 Shock location versus Reynolds number as measured on bodies No. 2 through 5

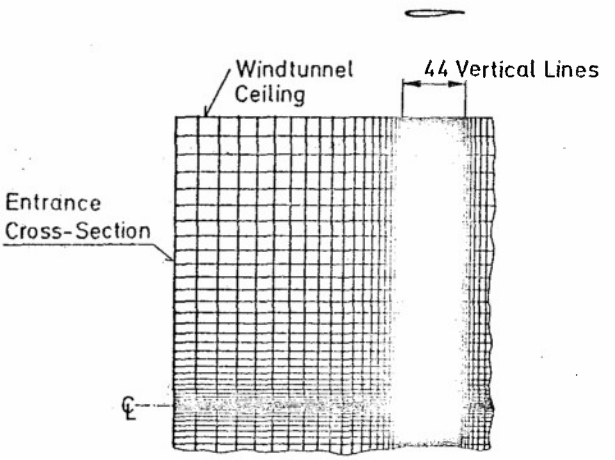
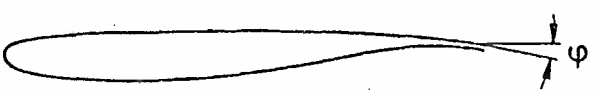


Fig. 11 Mesh grid of Whitcomb-profile in wind tunnel



t/c = 0,098 φ = -10°

X	z_{Lower}	z_{Upper}	X	z_{Lower}	z_{Upper}
0.0	0.0	0.0	0.50000	-0.03924	0.04987
0.01655	-0.02308	0.02200	0.52770	-0.03627	0.04969
0.03416	-0.03049	0.02782	0.55536	-0.03277	0.04943
0.05278	-0.03553	0.03184	0.58290	-0.02863	0.04910
0.07236	-0.03931	0.03498	0.61029	-0.02370	0.04869
0.09284	-0.04224	0.03756	0.63746	-0.01793	0.04818
0.11417	-0.04455	0.03974	0.66437	-0.01223	0.04760
0.13630	-0.04636	0.04158	0.69096	-0.00698	0.04693
0.15917	-0.04774	0.04317	0.71718	-0.00218	0.04615
0.18273	-0.04875	0.04454	0.74297	0.00217	0.04527
0.20693	-0.04944	0.04570	0.76829	0.00606	0.04427
0.23171	-0.04985	0.04669	0.79307	0.00949	0.04313
0.25703	-0.05000	0.04752	0.81727	0.01243	0.04186
0.28282	-0.04991	0.04822	0.84083	0.01487	0.04042
0.30904	-0.04957	0.04879	0.86370	0.01676	0.03880
0.33563	-0.04899	0.04923	0.88583	0.01808	0.03702
0.36254	-0.04814	0.04957	0.90716	0.01880	0.03504
0.38971	-0.04700	0.04980	0.92764	0.01887	0.03288
0.41710	-0.04558	0.04994	0.94722	0.01829	0.03055
0.44464	-0.04383	0.04999	0.96584	0.01704	0.02803
0.47229	-0.04174	0.04997	0.98345	0.01514	0.02538
			1.00000	0.01260	0.02261

Fig. 10 Geometry of Whitcomb-profile

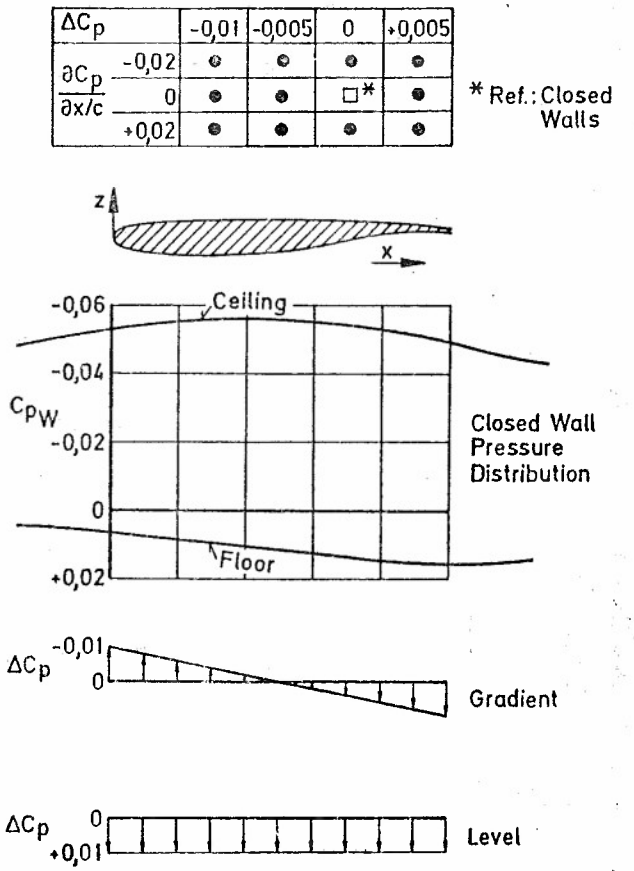


Fig. 12 Basic wall pressure distribution, wall pressure changes and parametric variation (12 cases)

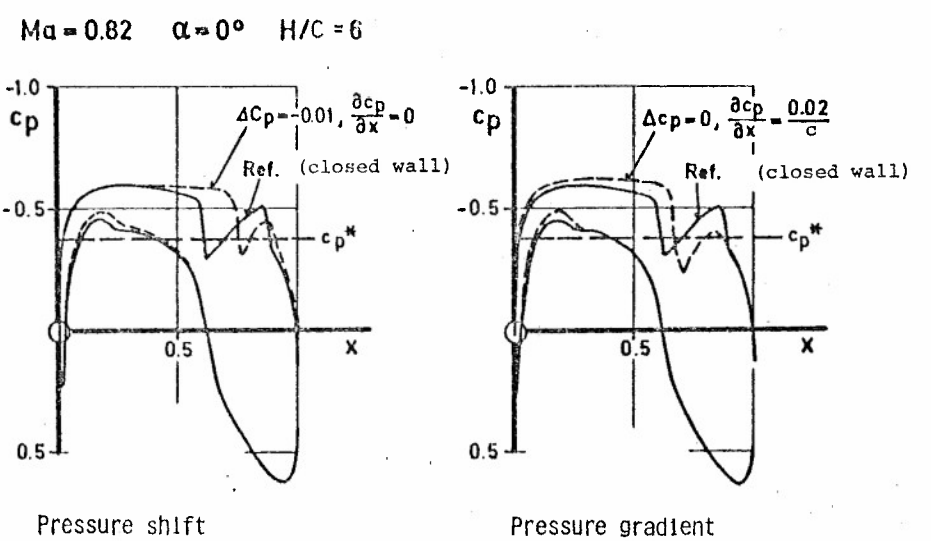


Fig. 13a Effect of pressure shift and axial wall pressure gradient on shock location

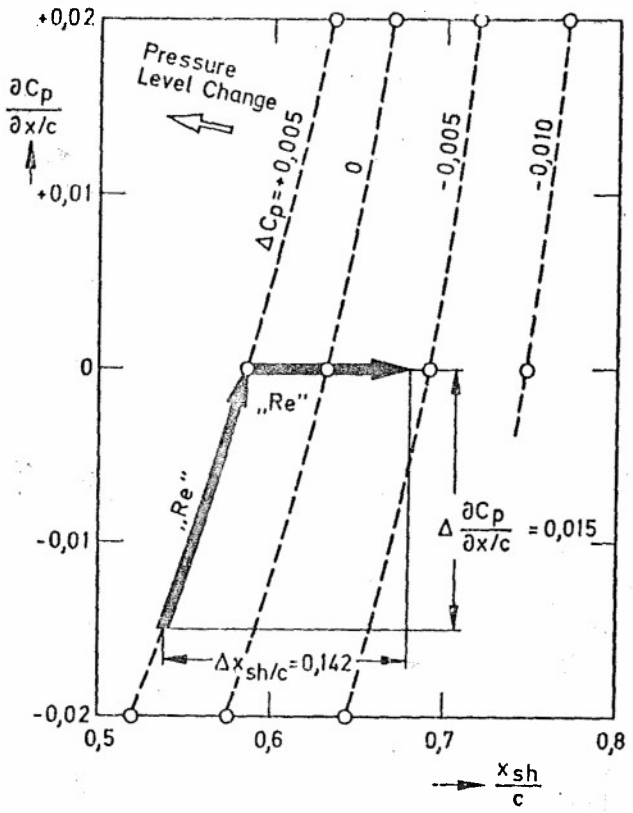
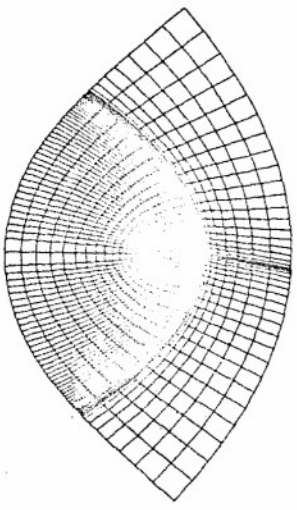


Fig. 13b Shock travel versus Reynolds number dependent changes of wall pressure for the Whitcomb-profile



Meshgrid (Euler)

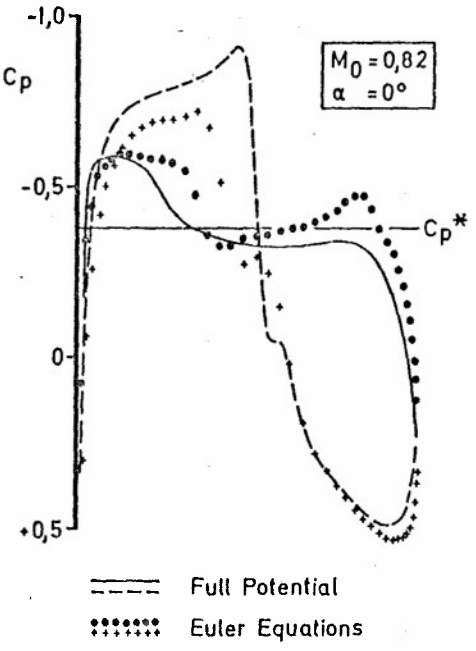


Fig. 14 Comparison of present Euler method with full potential equation

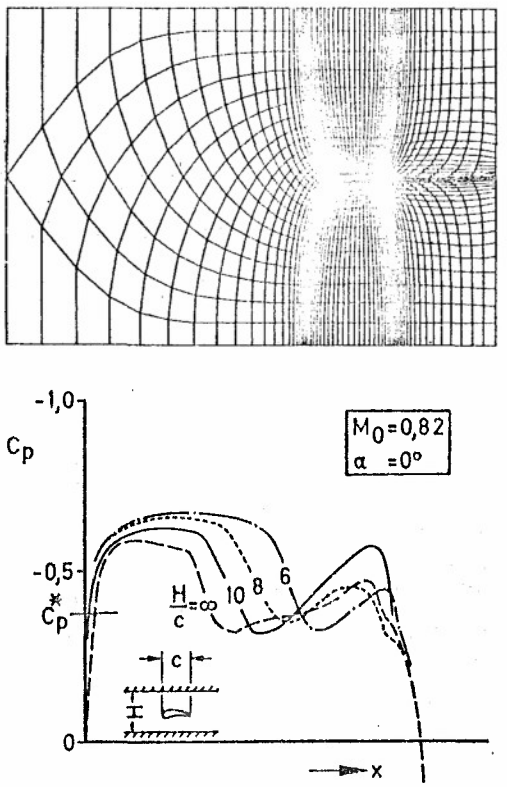


Fig. 15 Influence of wind tunnel height on upper surface pressure of Whitcomb-airfoil (Euler)

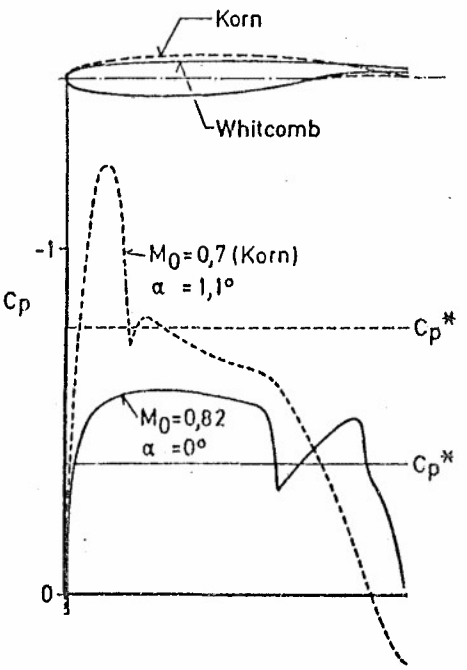


Fig. 16 Comparison of Whitcomb- and Korn-profiles

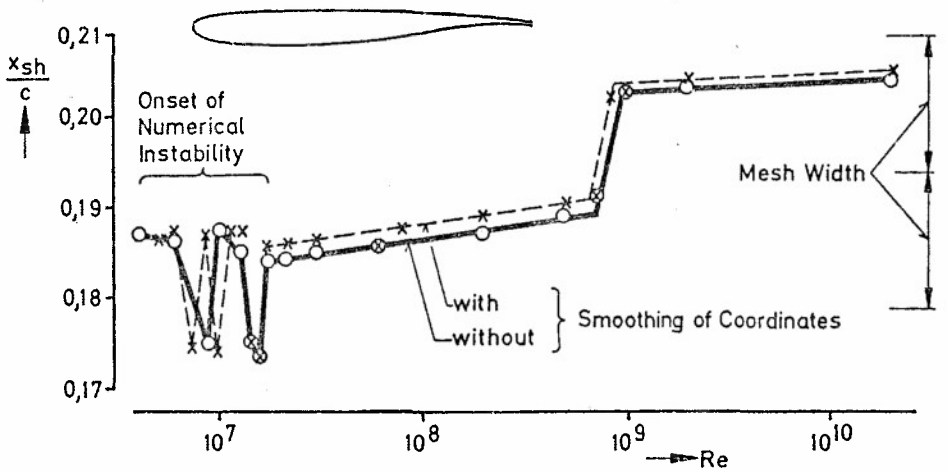


Fig. 17 Computed effect of Reynolds number on shock location for a Korn-profile in free flight

A REPORT OF A GARTEUR ACTION GROUP ON "TWO-DIMENSIONAL TRANSONIC TESTING METHODS"

by

A. Elsenaar (Chairman) and E. Stanewsky (Vice-Chairman)
Anthony Fokkerweg 2, 1059 CM Amsterdam, The Netherlands
Dunsenstrasse 10, 3400 Göttingen, West Germany

SUMMARY

A progress report is presented of a GARTEur Action Group on "Two-dimensional Transonic Testing Methods". As part of the action group activities measurements were made of the CAST-7/DOA1 airfoil in 7 European facilities, involving perforated, slotted and flexible wall wind tunnels.
A comparison was made of the "best data available" for each tunnel, using various wall interference correction methods. Also, a limited comparison of some of the correction methods themselves was carried out.
A large variation in experimental results was found for the uncorrected data. However, different types of correction methods reduce this scatter considerably. From this comparison it can be concluded that measured boundary condition methods and the flexible wall concept appear to be very promising. It is expected that a further analysis of these preliminary results might reduce the experimental uncertainty even more, so establishing a well defined data base for viscous transonic flow computational methods.

1. INTRODUCTION

The interest in two-dimensional testing techniques is directly related to aircraft development. Airfoil sections are still the corner-stones of most wing designs and they are often selected on the basis of their experimentally determined characteristics at design and off-design conditions. An accurate knowledge of the change in flow conditions due to the presence of the tunnel walls is therefore required. In the transonic speed regime testing problems are aggravated considerably since the transonic flow on airfoils is very sensitive to small Mach number and incidence changes. The ability to calculate viscous transonic flow further increased the need for "interference free" windtunnel data for verification. For three dimensional testing the wall interference problem is even worse. Although the interference is likely to be less, the need for accurate drag data imposes a very severe requirement on wall correction methods. At the design condition of a modern transport-type of aircraft an error of $.01^{o}$ in angle of incidence corresponds with one drag count for "on the balance" measured wind tunnel models. The assessment of tunnel wall correction methods in the 2-D case can be regarded as a first step on the road to success for the 3-D problem.

For these reasons the European countries England, France, West-Germany and The Netherlands, co-operating in GARTEur (meaning "Group for Aeronautical Research and Technology in Europe"), established an Action Group on "Two-Dimensional Transonic Testing Methods" (AD/AG-02) in 1980. The action group activities concentrate on wall interference correction methods, three-dimensional effects and a comparison of test results of one airfoil measured in different European wind tunnels. This paper concentrates on the last item. In 1979 the AGARD Working Group 04 recommended the CAST-7/DO A1 airfoil (hereafter referred to as CAST-7) as a prime candidate for such a comparison (ref. 1). Moreover, as part of another GARTEur activity a comparison of theoretical calculations was made for this airfoil (ref. 2). The selection of CAST-7 for this experimental program was therefore a natural choice. Since part of the experimental results has been corrected for wall interference (in fact each tunnel provided its "best possible data") a brief overview of the various correction methods as applied will be given in section 2. Section 3 of this paper elucidates the scope of the experimental program in more detail. Some preliminary results of the final comparison will be presented in section 4.

The action group is expected to finish its activities before the end of 1982. The analysis of the (recently completed) test programmes is still underway and this paper should be considered as a progress report. The action group members that contributed to this exercise are given at the end of this paper.

2. REVIEW OF CORRECTION METHODS

The various wall interference correction methods as applied to the experimental results given in section 4 are in order of increased "sophistication" :

- no corrections applied (TKG, TWB)
- corrections based on "Baldwin-type" homogeneous boundary conditions (ARA)
- corrections based on measured pressures at or near the walls (S-3Ma, NLR)
- the flexible wall concept (T-2, TU-B).

Table I summarizes the wind tunnels involved in the comparison and the type of method to derive the corrections. Figure 1 shows, as an example, the magnitude of the corrections as applied for the various wind tunnels. The illustration has been taken from the CAST-7 comparison for a Mach number of .76. TKG and TWB use wall geometries that have been optimized experimentally for minimum wall interference. However, it is difficult, if not impossible, to approximate interference-free conditions both in Mach and α by adjustment of wall porosity. In the ARA 2-D wind tunnel the slots were optimized for zero-blockage. In this approach lift-dependent blockage is not taken into account. The remaining α-corrections are derived from the classical formula of ref. 8 with empirically determined constants. Correction methods using measured boundary conditions are the most sophisticated in the sense that each test point can be corrected independently by calculation. In the CAST-7 comparison S-3Ma and NLR-PT make use of correction methods of that type. It must be noted here that different versions of the ONERA method exist depending on the velocity component used as a boundary condition. In this paper the one requiring wall pressures only is considered. Finally, the flexible wall concept makes it possible, in principle, to eliminate wall corrections altogether by adjustment of tunnel walls on

the basis of measured wall pressures. Significant progress has been made in recent years with the development of the last two types of methods. The action group has evaluated these methods in more detail. In the context of the present paper only two examples will be shown. One is related to a comparison of wall pressure methods, the other is concerned with the flexible wall.

The three methods using measured boundary conditions as developed at RAE (ref. 9), ONERA (ref. 3) and NLR (ref. 6) differ in the sense that the RAE-method requires the measurement of both velocity components near the wall, whereas the two other methods require the measurement of one component (or c_p) at the wall. However, the price of the simpler boundary condition is that a mathematical representation of the far flow field around the model is required. Therefore, a mutual comparison of the three methods can only be made for solid wall test sections where the normal velocity component at the wall is zero. Figure 2 shows wall-induced velocities as calculated by the three different methods. All methods use the same set of wall data, measured in the solid wall 8x8' wind tunnel of RAE, sufficiently far up- and downstream of the particular model. In this well-defined test case acceptable agreement is found, although it must be noted that differences as large as 0.1 degrees can still be observed. Similar and sometimes even larger differences have been observed for other cases, especially with the ONERA method. The ONERA method uses at present a rather simple model representation and truncates the wall pressures up- and downstream of the model. In reference 10 it is shown that the application of measured boundary condition methods is limited in a practical sense by the test section length and the technique to measure wall pressures or velocities. Also, the accuracy of the model representation, if needed, is of prime importance. The current standard of instrumentation and test section dimensions do not always meet the requirements imposed by the theoretical methods to determine wall interference.

The second example is taken from the T-2 tunnel with flexible walls. In the flexible wall technique, computations of the outer flow field are required to define the necessary wall adjustments. The RAE-method should be viewed as complementary in the sense that the remaining wall interference for the inner flow field can be computed after each iteration step. Figure 3 shows the so-calculated residual corrections at mid-chord position after each iteration step for the CAST-7 airfoil at a condition close to maximum lift. Figure 4 shows the interference variation over the airfoil chord after the first and final iteration for the same test point. A similar variation is shown in figure 5 at the design condition of CAST-7. One can conclude that the flexible wall concept is fairly succesful in these cases, although some variation of the interference flow field still remains over the airfoil chord.

One should also view the experimental results in connection with other imperfections inherent to 2-D testing such as a variation of the interference flow field over the airfoil chord and tunnel side wall effects. Some brief comments will be made here.

It is well known that solid wall test sections introduce large streamwise curvature effects (see also fig. 2). These effects are reduced considerably with slotted or perforated walls but Mach number variations as large as 0.01 over the airfoil chord can still be found (fig. 6). This reflects a basic limitation to the application of theoretical correction methods for fixed tunnel geometries. Also, the acceptable degree of "correctability" is hard to establish.

The information on tunnel side wall effects is limited and conflicting (see ref. 11 for an excellent review). A distinction should be made between subsonic and transonic regimes. In subsonic flow, the disturbances originating from the side walls, will cause a mild spanwise variation of the flow direction (Preston, ref. 12) or velocity (Barnwell, refs. 13, 14). It is likely that correction methods based on measured wall pressures in the mid-section will take the larger part of these effects into account provided the aspect ratio is large enough. In the transonic regime oblique shocks originate at the walls (ref. 11). If they extend far enough into the test section they will affect the local flow field at the centre line and the resulting pressure distribution is most likely "non-correctable". The TU-B data might suffer from this effect as will be shown later, in view of the small aspect ratio.
All these arguments, related to the accuracy of the 2-D correction methods and the additional 3-D effects, should be kept in mind in the assessment of the experimental comparison to be presented in section 4.

3. EXPERIMENTAL PROGRAM

Comparative tests with the airfoil CAST7 were conducted in 7 European wind tunnels. The tunnels were provided with slotted (3), perforated (1) or flexible (2) walls. One tunnel had a mixed perforated/slotted wall arrangement. Eight different models were machined to fit the particular tunnel dimensions. The machining accuracies of the different models are all of the same order, generally between 0.02 and 0.04% of the model chord. They are given in the respective data reports (ref. 19-25). The characteristics of the tunnels, together with the test section/model dimensions relevant to the present exercise are summarized in Table II and figure 7. Most tunnels have tunnel height to chord ratios $H/c \simeq 3$ and aspect ratios $B/c \simeq 1.5$. Extremes are the TKG with $H/c \simeq B/c \simeq 5$ and the adaptive wall tunnel TU-B with $H/c = B/c = 1.5$.

The airfoil CAST7 was designed by Dornier and originally tested in the TKG (ref. 15, 16). The co-ordinates and other characteristics can be found in reference 1. The airfoil (11.8% thick) is designed to be almost shock-free in the theoretical design condition $M = .76$, $C_L = .573$ (ref. 15). It has moderate rear loading with moderate rear adverse pressure gradients on the upper surface. The Reynolds number sensitivity is such that sufficiently accurate corrections can be made for the small Reynolds number differences as encountered in the present comparison.

The test program, including 3 $\alpha$and 2 Mach sweeps, is given in table IV. Two reference conditions were prescribed to facilitate the comparison of pressure distributions at a given lift. The first of these ($C_L = .52$, $M_\infty = .76$) is close to the design lift and represents a case where the pressure distribution is very sensitive to changes in free stream conditions. The other reference condition ($C_L = .73$, $M_\infty = .76$) is close to maximum lift. The complete test program was run in the various tunnels with a few exceptions. In TU-B no drag measurements were made whereas drag data from TKG are not complete at this moment. In the T-2 flexible wall tunnel two series of tests were made. The low Reynolds number data have been taken from the first test period (ref. 23) whereas the larger part of the 6 million data (indicated with a ☆ in the respective figures) have been taken from the only recently completed test program. It has been reported by ONERA that a very small residual correction might still be present.

Unfortunately, it was not possible to test in all participating wind tunnels at the same Reynolds number (see Table III). Thus, two target Reynolds numbers were selected, viz. $Re = 2.5 \times 10^6$ and $Re = 6 \times 10^6$.

In some of the figures to be discussed in section 4, the measured data have been corrected for the remaining difference with the nearest target Reynolds number. This will be pointed out in the text.

Measurements were made with fixed transition at approximately 7% of the chord on upper and lower surface. The effectiveness of the tripping device was ensured by appropriate tests in each tunnel. The relative strip size could be estimated with the relation (see Table III):

$$\left(\frac{Re_1}{Re_2}\right)^{-\frac{2}{4}} = \frac{K_1}{K_2} \cdot \frac{C_2}{C_1}$$

based on the work of reference 17. Suffix 1 refers to the TKG data for a 200 mm chord model at Re = 2.4 x 10^6. In Table III the ratio of the actually applied and estimated strip sizes is presented.

Complete data reports have been written (refs. 19-25) with both uncorrected and corrected data. Most of the comparisons are based on the "best data available" as discussed in section 2, Table I. This means that cases are included without any corrections on the one side and point-to-point corrected results on the other side of the spectrum. It must be stressed here again that some of the data are preliminary, especially with respect to the applied tunnel wall corrections.

4. COMPARISON OF EXPERIMENTAL RESULTS

4.1 Design condition

Although somewhat below the theoretical design condition, the condition C_L = .52, M_∞ = .760 will be denominated hereafter the design condition. The geometric angle of attack range necessary to obtain this lift coefficient, should closely reflect the range of test section wall characteristics of the tunnels involved with respect to lift interference, as well as the Reynolds number sensitivity of the airfoil itself. This angle was, therefore, plotted for the individual tunnels as function of the Reynolds number, (fig. 8). The large spread of data is reduced considerably for the corrected cases. The S-3Ma data seem to be slightly over-corrected. As mentioned already in section 2, the S-3Ma corrections might be slightly erroneous, due to a too simple model representation. The ONERA corrections will be re-calculated in the near future. At present all the corrected cases (S3Ma, NLR, ARA and T-2) are within 0.2°. Of the available theories VGK and Bousquet (ref. 2) give a somewhat lower angle of attack, DFVLR being closer to the mean experimental value. All tunnels show essentially the same Reynolds number dependence, also in accordance with theory, with the exception of S-3Ma which gives a slightly larger dependence. Note that in this and the forthcoming figures on Reynolds number dependence, only the data points obtained with one and the same model have been connected.

The uncorrected pressure distributions at the design condition show generally good agreement, especially for Re = 6 x 10^6 (figs. 9 and 10). Differences such as for instance in shock location, are mainly attributable to differences in the effective freestream Mach number. This is particularly obvious in case of the TKG data: reducing the uncorrected Mach number to M_∞ = .75 moves the shock forward to a position more comparable to the ones determined in the other tunnels. A further analysis is needed to investigate if the observed differences in the pressure distributions are mainly attributable to small Mach and α variations or that other effects, like interference flow field variations over the airfoil chord or side-wall effects are also of importance. Three-dimensional effects have been reported by TU-Berlin. LDA measurements, made on this wind tunnel model, revealed the shock to be curved with a more forward shock position near the side walls. Since the pressure orifices were arranged along an arc off the centre line, a more forward shock position was picked up. Note also the lower Reynolds number in this case.

To round up the comparison at the design condition, the wake drag and pitching moment coefficients are presented as function of Reynolds number in figures 11 and 12. All wind tunnels show, in agreement with theoretical results (ref. 2) essentially the same Reynolds number effect on drag (fig. 11). Especially the NLR, ARA, S3-Ma and TWB (200 mm model) data are close together within a couple of counts. Since the design condition is near drag rise, the higher values for TKG can be explained from increased wave drag as result of a higher effective Mach number (see also figs. 15-17). Also the pitching moment (fig. 12) shows good agreement in Reynolds number dependence. The uncorrected data show a large scatter, partly due to the strong dependence of pitching moment on Mach number as indicated in the figure. Again, the corrected results for ARA, S-3Ma, NLR and T-2 are very close together. Theory predicts a much lower value for the pitching moment.

4.2 Lift development

The C_L-α curves are presented in figures 13 and 14 for a Reynolds number of 2.5 x 10^6 and 6 x 10^6 respectively. To enable a proper comparison at constant Reynolds number, the data points that deviated from these target Reynolds numbers have been shifted in C_L-direction. This shift was obtained from the average trend of C_L versus Reynolds number for all the results, similar to the trend indicated in figure 8. C_L-max values were shifted according to the trend as depicted in figure 19. Since the results are corrected to the nearest target Reynolds number, the shifts are generally very small.

In order to judge the wall correction methods as applied, a datum set of results is needed. It is very tempting to use the T-2 results as such a datum. The independent calculations by RAE as presented in the figures 3, 4 and 5 also support this choice. For the lower Reynolds number the NLR data show good agreement with T-2. The ONERA-method seems to over-correct the measured data for both Reynolds numbers, as was also noted in section 4.1. The semi-empirical ARA corrections give good agreement for the lower Reynolds number, but slightly under-correct at Re = 6 x 10^6. It is obvious that TWB and TKG data require corrections in spite of an optimization of the test section wall geometry by testing different size models of the same airfoil (ref. 27). A comment concerning the results obtained in the adaptive wall tunnel TU-B is needed. First of all, the Reynolds number difference is too large for the simple Reynolds trend shift as applied. Also, it was noted already that the observed 3-D effects in this tunnel might have caused some lift reduction. Some of the theoretical results taken from refs. 2 and 26 are also presented in figure 14. They indicate that theory needs some improvement. Finally some uncorrected (!) results for lift divergence are shown in figure 15 to illustrate the Mach number characteristics for TU-B and TKG. These tunnels could not be included in the drag divergence comparison (see section 4.3) since drag data were not available. Note that,

since the uncorrected results all go through the pre-selected design point C_L = .52 M_∞ = .76, differences in wall interference effects do not show up in this figure. The shift in lift divergence Mach number closely reflects the order of shock positions as shown in figure 9 (the NLR corrections are very small).

4.3 Drag development

A drag comparison at the design condition was already discussed in section 4.1, figure 11. The good agreement could be obtained since the incidence does not enter critically in this comparison and Mach number dependence is weak, provided one is not to close to the drag divergence boundary. This weak Mach number dependence is clearly indicated in the C_D versus M_∞ (corrected !) curves at constant α as shown in the figures 16 and 17. Note that all data exhibit a similar drag creep, except for the TWB results at Re = 3 x 10^6. This cannot be explained at present. Large differences occur for drag rise that can partly be explained from differences in the effective Mach number, since lift coefficients are almost the same. Differences as large as 0.01 in Mach can be observed. The interpretation in this case however is more difficult as for the C_L-α comparison. There is some ambiguity in the determination of the drag divergence Mach number due to the relatively large Mach spacing. Since there is a rather strong dependence of the drag divergence boundary on lift, even small lift changes might have a noticeable effect. This is especially true for the TWB data at Re = 3 x 10^6. Also, when comparing figures 16 and 17, the favourable Reynolds number influence on drag divergence should be taken into account: the ARA data suggest over this range an improvement of 0.004 in M_{DD}. If these assumptions hold, the T-2, S-3Ma, ARA and NLR data are in reasonable agreement with a maximum difference in the order of $\pm$ .003 in Mach. Clearly, more analysis is needed before any definite conclusions can be drawn.

4.4 Maximum lift

Maximum lift, being one of the important off-design boundaries in airfoil design, will be considered finally. To rule out Reynolds number effects, the maximum lift coefficients for the various wind tunnels have been plotted as a function of Reynolds number. At M_∞ = .6 (fig. 18) large differences in C_L-max of the order of 0.1 can be observed even after wall corrections are applied. Trying to correlate these differences with the aspect ratios of the test set-ups failed completely, although 3-D effects may not be excluded. The effectiveness of wall correction methods is not clear in this case: note that the corrections for S-3Ma and NLR have opposite sign, making the data further apart ! Since both methods rely on a model representation, it is doubtful if they can be used at separated flow conditions.

At M_∞ = .76 (figure 19) the differences in maximum lift are somewhat reduced. Also, there is in this case a strong direct influence of Mach number, as opposed to the M_∞ = .6 results. The effect of a shift of 0.01 in Mach number, derived from a more extensive survey made at TKG, has been indicated in figure 19. This helps to explain the lower C_L-max values as measured in TKG and TWB, in line with the previous results (figs. 15, 16 and 17).

Some remarks must be made with respect to the TU-B and TKG results for the 100 mm model. At Mach = .76 maximum lift is higher and at Mach = .6 lower than the average value indicates. A likely explanation can be found in a not-effective transition strip. It is well known (ref. 18) that the strip effectiveness decreases for higher incidences. Also, a laminar shock-wave boundary layer interaction may increase the maximum lift when the pressure plateau is formed (at M_∞ = .76) whereas with a peaky pressure distribution (at M_∞ = .6) the laminar separation near the airfoil leading edge may on the contrary result in a lower C_L-max value.

5. CONCLUSIONS

To assess the value of two-dimensional testing, measurements were made of the CAST-7/DOA1 airfoil in 7 European wind tunnels. A comparison was made of the "best data available" for each tunnel, including both corrected and uncorrected results.

Also, a limited comparison of some of the correction methods themselves was carried out. A large variation in experimental results was found for the non-corrected data. However, different types of correction methods (a semi-empirical method with Baldwin-type boundary conditions, two measured boundary condition methods and the flexible wall) reduce this scatter considerably. The resulting variation for attached flow conditions is estimated to be less then $\pm$ .2° in α and $\pm$ .003 in Mach. If it is assumed that the "true interference-free" results are within this band of data, it can be concluded that :

1. the flexible wall concept appears to be very promising
2. the "measured boundary condition" correction methods do fairly well; however :
   - if these methods require a model representation, this has to be done very carefully; also a proper treatment of the wall boundary conditions is necessary; the latter may require the development of better instrumentation and/or longer test sections;
   - the methods reveal non-uniformities in the wall-induced interference flow field that can only be eliminated with a better optimization of the tunnel wall geometry. It can be further remarked that:
3. Reynolds number trends are generally very similar for different wind tunnels
4. large, as yet unexplained differences in C_L-max (of the order of 0.1) were found at a moderate Mach number; differences in C_L-max appear to be much smaller near the design Mach number, when based on the corrected Mach number
5. the present set of data should be considered quite useful as a datum-set for theoretical calculation methods
6. a careful analysis of the available data and additional cross-checks of the various wall correction methods may result in a further reduction of the experimental uncertainty.

ACKNOWLEDGEMENT

The following action group members contributed in this exercise :
X. Vaucheret, J.P. Chevallier (DNERA), E. Stanewsky(DFVLR), U. Ganzer (TU-Berlin), P.R. Ashill (RAE), T.E.B. Bateman, M.P. Carr (ARA), A. Elsenaar, J. Smith (NLR). Many others participated in wind tunnel tests, computer calculations and writing data reports. The action group is thankful to them.

6. REFERENCES

1. Barche, J. et al — Experimental data base for computer program assessment. Report of FDP Working Group 04, AGARD AR 138, 1979

2. Lock, R.C. — Report on a combined experimental and theoretical investigation of the airfoil CAST-7. RAE TR 79073, 1979

3. Capelier, C., Chevallier, J.P., Bouniol, F. — Nouvelle méthode de correction des effets de parois en courant plan. La Recherche Aerospatiale, No. 1978-1, pp. 1-11

4. Archambaud, J.P., Chevallier, J.P. — Use of adaptive walls in 2-D tests. AGARD FDP Spec. Meeting on Wall Interference in Wind Tunnels, May 1982

5. Ganzer, U. — On the use of compliant walls for transonic wind tunnel testing. AGARD FDP Spec. Meeting on Wall Interference in Wind Tunnels, May 1982

6. Smith, J. — A method for determining 2-D wall interference on an airfoil from measured pressure distributions near the walls and on the model. NLR TR 81016 U, 1981

7. Hammond, B.F.L. — Some notes on model testing in the ARA two-dimensional facility. ARA, Memo no. 170, 1975

8. Garner, H.C. et al — Subsonic wind tunnel wall corrections. AGARDograph 109, 1966

9. Ashill, P.R., Weeks, D.J. — A method for determining wall interference. Corrections in solid-wall tunnels from measurement of static pressures at the walls. AGARD FDP Spec. Meeting on Wall Interference in Wind Tunnels, May 1982

10. Smith, J. — Measured boundary condition methods for 2-D flow. AGARD FDP Spec. Meeting on Wall Interference in Wind Tunnels, May 1982

11. Chevallier, J.P. — Effets tri-dimensionels sur les profils. ONERA TP no. 1981-117, 1981

12. Preston, J.H. — The interference on a wing spanning a closed tunnel arising from the boundary layers on the side walls, with special reference to the design of two-dimensional tunnels. R & M, no. 1924, 1944

13. Barnwell, R.W. — A similarity rule for compressibility and side wall boundary layer effects in two-dimensional wind tunnels. AIAA 79-108, 1979

14. Barnwell, R.W. — Similarity rule for sidewall boundary-layer effect in two-dimensional wind tunnels. AIAA Journal, Sept. 1980

15. Kühl, P., Zimmer, H. — The design of airfoils for transport aircraft with improved high speed characteristics. DORNIER GmbH, Report 74/168, 1974

16. Stanewsky, E., Zimmer, H. — Development and wind tunnel tests of three supercritical airfoils for transport aircraft. Z.Flugwiss. 23, Heft 7/8, 1975

17. Braslow, A.L., Knox, C. — Simplified method for determination of critical height of distributed roughness particles for boundary layer transition at Mach number from 0 to 5. NACA Technical Note 4363, 1958

18. Stanewsky, E. — The effect of roughness height and location on the flow development on the transonic airfoil CAST 10-2/DOA2 (unpublished results)

19. Vaucheret, X. — Data report on the CAST 7/DOA1 profile in the ONERA S3Ma wind tunnel. ONERA Technical Report No. 201/1464 GN, 1982

20. Puffert-Meissner, W. — Data report on the CAST 7/DDA1 airfoil in the transonic wind tunnel Braunschweig. DFVLR Report IB 129-82/2, 1982

21. Bateman, T.E.B.
Results of tests on the CAST 7/DOA1 airfoil in the ARA two-dimensional tunnel
ARA model test note, T28/15, 1981

22. Stanewsky, E.
Heddergott, A.
Results of tests with the CAST 7/DOA1 airfoil in the DFVLR transonic wind tunnel Göttingen
DFVLR Report IB 222-82 A 15, 1982

23. Archambaud, J.P.
Mignosi, A.
Seraudie, A.
Gobert, J.L.
Rapport d'essais de deux profils CAST 7 de 120 à 200 mm de corde en présence de parois auto-adaptable effectués à la soufflerie T2 de l'ONERA/CERT
ONERA/CERT Rapport Technique OA No. 21/3075, 1980

24. Smith, J.
Data report on the CAST 7/DOA1 airfoil in the NLR Pilot tunnel - test nr. 1101
NLR TR 81117 L, 1981

25. Ziemann, J.
Data report on the CAST 7/DOA1 airfoil in the TU-Berlin transonic wind tunnel
Institut für Luft- und Raumfahrt, Technische Universität Berlin, ILR Mitt. 94, 1981

26. Stanewsky, E.
Nandana, M.
Inger, G.R.
The coupling of a shock boundary layer interaction module with viscous-inviscid computation method
Proceedings of the Symposium on Computation of Viscous-Inviscid Interactions, AGARD CP 291, 1981

27. Stanewsky, E.
Puffert, W.
Müller, R
The DFVLR transonic wind tunnel Braunschweig: Calibration results for the modified test section and results for the airfoil CAST 7/DOA1
DFVLR Report IB 151-77/10, 1977

INSTITUTION	FACILITY	CORRECTION METHOD	REF. TO CORR.METH.
ONERA	S-3Ma	MEASURED BOUNDARY CONDITION METHOD WITH MODEL REPRESENTATION	REF. 3
ONERA	T-2	ADAPTIVE WALLS	REF. 4
DFVLR	TKG	OPTIMIZED SLOTS; NO CORRECTIONS APPLIED	-
DFVLR	TWB	OPTIMIZED SLOTS; NO CORRECTIONS APPLIED	REF. 27
TU-Berlin	TU-8	ADAPTIVE WALLS	REF. 5
NLR	NLR-PT	MEASURED BOUNDARY CONDITION METHOD WITH MODEL REPRESENTATION	REF. 6
ARA	ARA-2D	SLOTS OPTIMIZED FOR CORRECT MACH NUMBER; α AND C_L-CORRECTIONS FROM CLASSICAL FORMULA WITH EMPIRICAL CONSTANTS	REFS. 7, 8
RAE	-	MEASURED BOUNDARY CONDITION METHOD WITHOUT MODEL REPRESENTATION	REF. 9

TABLE I: WINDTUNNEL AND CORRECTION METHODS FOR CAST-7 COMARISON

No.	Tunnel	b x H (m^2)	Type	σ(%)	NS[1]	b/c	H/c	δ^*/b	Remarks
1	S3Ma	0.56 x 0.78	Perforated	9.7	-	2.8	3.9	0.010	Straigh holes; solid side walls
2	TWB	0.34 x 0.60	Slotted	2.35	4	2.3 1.7	4.0 3.0	-	Solid side walls
3	ARA	0.20 x 0.46	Slotted	3.2	6	1.6	3.6	0.015	Solid side walls
4	TKG	0.99 x 0.98	Slotted[2]	3.4[3]	4	5	4.9	0.011	Solid side walls
5	T-2	0.40 x 0.38	Solid	-	-	3.3 2.0[4]	3.2 1.9[4]	0.005	Parallel side walls; flexible top and bottom walls
6	NLR	0.42 x 0.55	Slotted	10	7	2.3	3.1	0.007	Solid side walls
7	TU-8	0.15 x 0.15	Solid	-	-	1.5	1.5	-	Parallel side walls; flexible top and bottom walls

1) No. of slots (excluding slots at intersection of vertical and horizontal walls)

2) Aluminium bars of 10 mm thickness mounted on perforated walls

3) Based on slot width only

4) The 200 mm model was positioned 80 mm below the tunnel centre line
- see TABLE III for chord length -

TABLE II: CHARACTERISTICS OF WIND TUNNELS INVOLVED

TUNNEL	CHORD (m)	$Re_{chord} \times 10^{-6}$	K_{actual} [1] (mm)	$\frac{K_{actual}}{K_{estimated}}$
S-3Ma	0.2	3.5	.146 BA	1.67
	0.2	6	.116 BA	1.99
	0.2	10	.09 BA	2.26
TWB[2]	0.15	3	.09 BA	1.22
	0.15	6	.06 BA	1.36
	0.2	11	.06 BA	1.62
ARA	0.125	2.5	.07 BA	1.0
	0.125	6	.04 BA	1.1
TKG[3]	0.1	1.3	.107 BA	1.16
	0.2	2.34	.107 BA	0.90
T-2[4]	0.12	~ 4	.06 K	1.28
	0.2	~ 7&6	.06 K	1.15
NLR	0.18	~ 2.2	.104 K	0.87
TU-B	0.1	1.3	.107 BA	1.16

1) Average diameter or height of roughness in mm; BA ≙ Ballotini, K ≙ Carborundum grit
2) Two models were used to cover the Reynolds number range; when available, data for the smaller model were used
3) The smallest model, used for comparison with TU-B only, was placed between two end-plates
4) Results from both models were used in the comparison. The 6 million Reynolds number results have been obtained at a second entry; these results are indicated in the figures with an ☆

- The tripping devices were located at 7% chord on upper and lower surfaces; they were generally 1% of chord wide -

TABLE III: MODEL DIMENSIONS AND TEST CONDITIONS

A. Angle of attack sweeps

M_∞ \ α	-2	-1	0	1	1.5	2	2.5	3	3.5	4	4.5	5	5.5	6	6.5	7	7.5	8
0.60	●	●	●	●		●		●		●		●	●	●	●	●	●	●
0.70	●	●	●	●		●		●	●	●	●	●	●					
0.76	●	●	●	●	●	●	●	●	●									

B. Mach number sweeps

M_∞	0.60	0.65	0.70	0.72	0.74	0.75	0.76	0.77	0.78	0.79	0.80	0.82

at angles of attack giving at $M_\infty = 0.76$ lift coefficients of $C_L = 0.52$ and $C_L = 0.73$, respectively (for α at $C_L = 0.52$ see Fig. 8)

TABLE IV: TEST PROGRAM

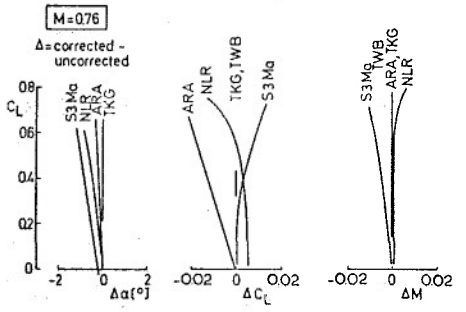


Fig. 1 Examples of tunnel wall corrections applied in CAST-7 tests

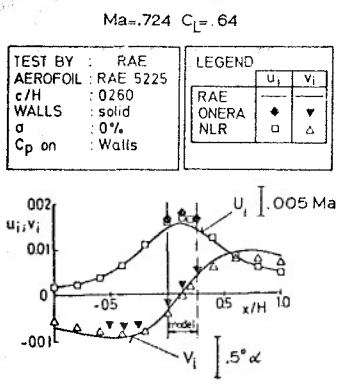


Fig. 2 Calculated wall-induced velocity distributions along test section centre line (RAE-case)

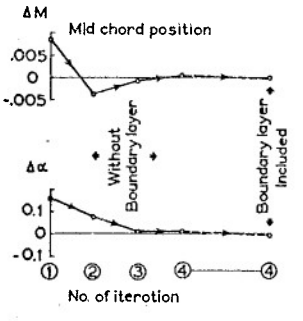


Fig. 3 Convergence in wall interference for T-2 as calculated by RAE (M_∞ =.76, C_L = .73, CAST-7)

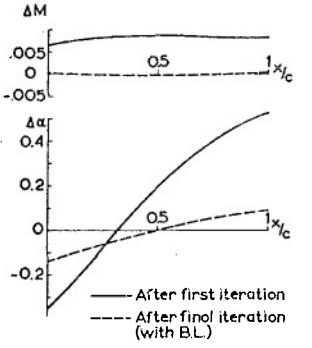


Fig. 4 Chordwise variation of wall interference as calculated by RAE for T-2 (M_∞ =.76, C_L = .73, CAST-7)

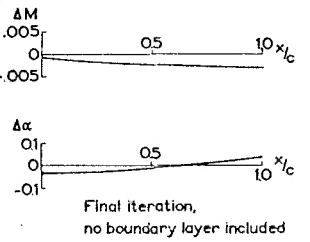


Fig. 5 Chordwise variation of wall interference as calculated by RAE for T-2 (M_∞ =.76, C_L = .52, CAST-7)

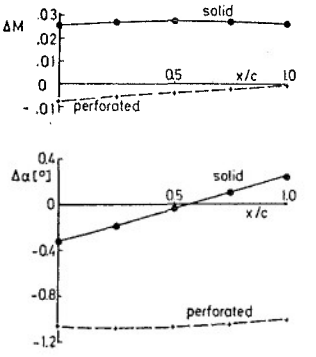


Fig. 6 Example of calculated wall interference along airfoil chord(NLR-method, S-3Ma CAST-7 tests, M_∞ = .76, C_L = .73)

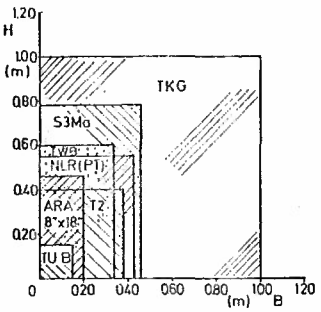


Fig. 7 Wind tunnels involved in CAST-7 tests

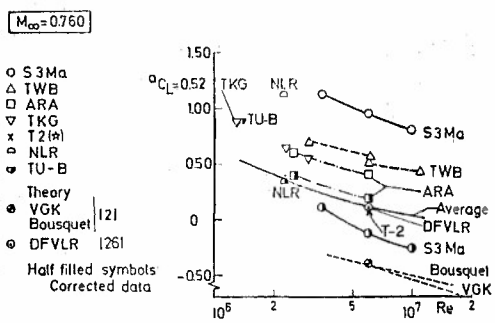


Fig. 8 Corrected and un-corrected angle of incidence at design condition

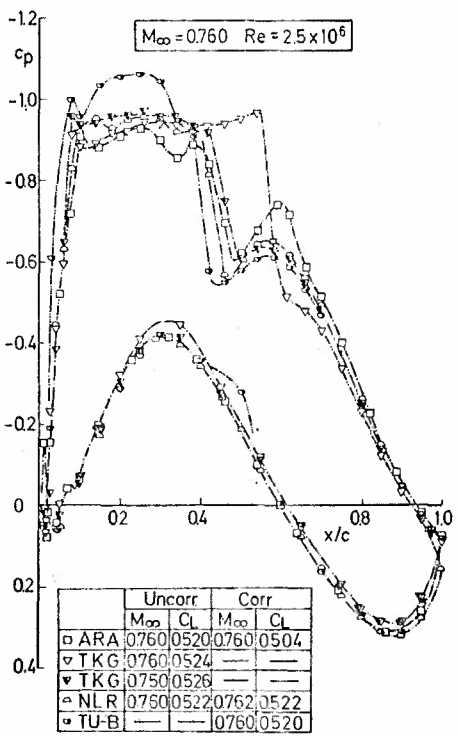


Fig. 9 Comparison of un-corrected pressure distributions at the design condition(Re=2.5x10^6)

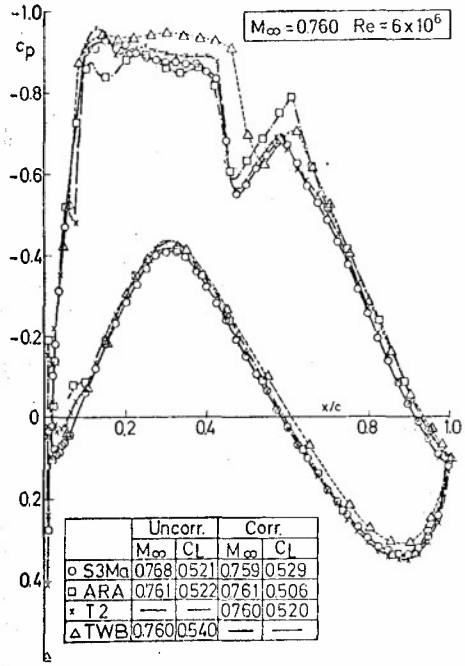


Fig. 10 Comparison of un-corrected pressure distributions at the design condition(Re=6x10^6)

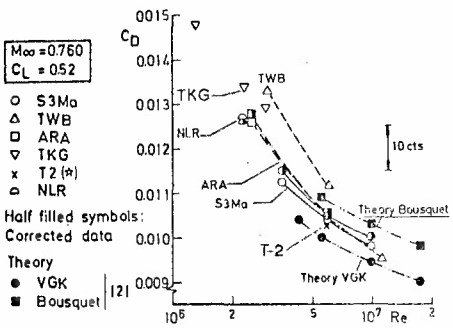


Fig. 11 Comparison of drag at the design condition

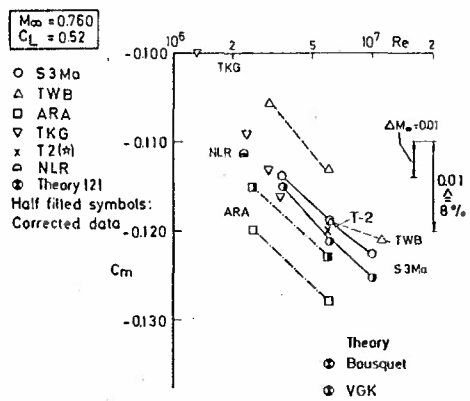


Fig. 12 Comparison of pitching moment at the design condition

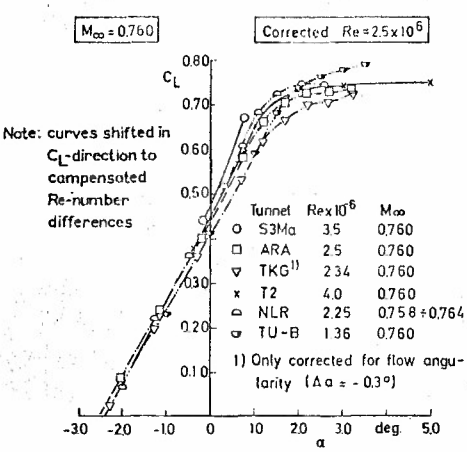


Fig. 13 Lift-curves at M_∞ = .76, Re=2.5x10^6

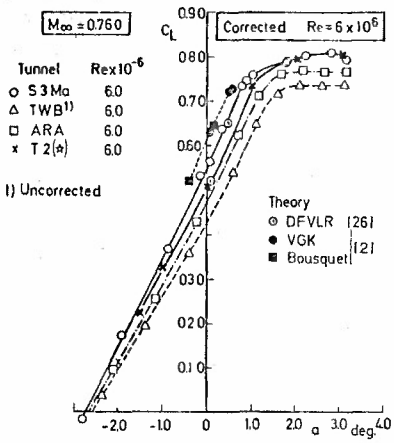


Fig. 14 Lift-curves at M_∞ = .76, Re= 6x10^6

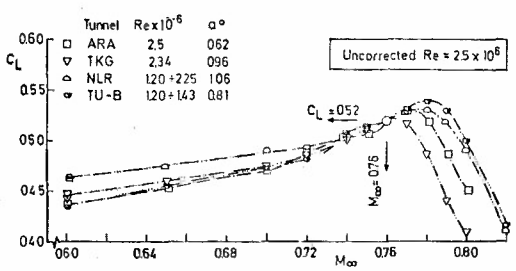


Fig. 15 Lift-development with Mach for α = (C_L = .52, M_∞ = .76) (un-corrected results)

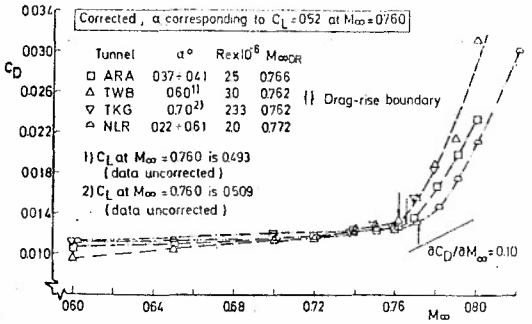


Fig. 16 Drag development with Mach for α = (C_L = .52, M_∞ = .76) corrected results, Re=2.5x10^6

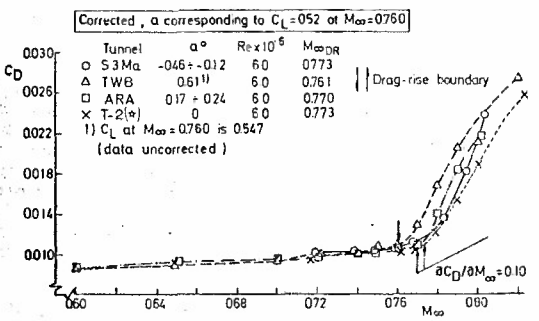


Fig. 17 Drag development with Mach for α = (C_L = .52, M_∞ = .76) corrected results, Re=6x10^6)

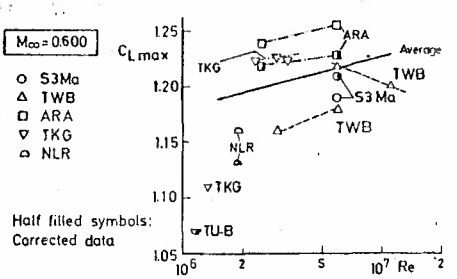


Fig. 18 Maximum lift as function of Reynolds number, M_∞ = .6

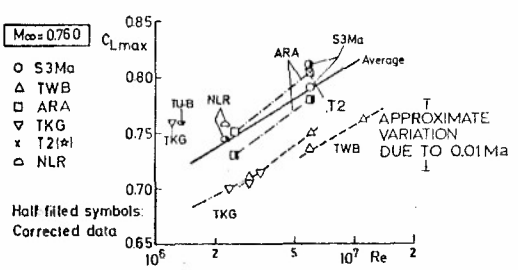


Fig. 19 Maximum lift as function of Reynolds number, M_∞ = .76

ANNEXE

REEVALUATION DES RESULTATS CORRIGES DU PROFIL CAST 7 à S3MA.

psr X. VAUCHERET.
ONERA.

INTRODUCTION -

A la suite de la confrontstion des résultsts corrigés du profil CAST 7 dans la soufflerie S3MA, à l'aide des méthodes de correction utilisées par NLR - ONERA et RAE, des différences ont été constatées, en psrticulier sur les niveaux de corrections d'incidence; ces différences spparaissaient sussi bien en parois pleines qu'en parois perforées. La condition de coïncidence des résultats corrigés dans ces deux cas de parois apparaissait remplie, en utilisant l'une ou l'autre méthode. Cette condition nécessaire n'était donc pas suffisante puisque des écarts apparaisssient, attribuables aux méthodes.

Plus que les méthodes utilisées, il y avait lieu de considérer leur application et en particulier le programme de calcul des corrections, fondé sur la méthode utilisée, mais pouvant être influencé par deux points essentiels :

- la troncature des signatures aux parois.
- la modélisation de la maquette.

La méthode utilisée par l'ONERA [1] est en fait tributsire de ces deux éléments et il s'agissait donc de regarder quels étaient leurs effets sur les résultats corrigés.

1 - UTILISATION DE LA METHODE DE CORRECTION ONERA -

Les corrections effectuées [2] découlaient de la modélisation suivante :

- volume: un seul doublet situé su maître couple du profil (34% de profondeur pour le profil CAST 7) et d'intensité :

$$\sigma = \frac{U_\infty}{\rho} \, ec \left(1 + 1{,}2 \beta \frac{e}{c}\right) 0{,}95$$

- sillage: une seule source située au même emplacement que le doublet et d'intensité

$$m = U_\infty \frac{c}{2} C_{x_w}$$

- portance: un seul tourbillon situé su point neutre et de circulstion Γ :

$$\Gamma = U_\infty \frac{c}{2} C_z$$

En ce qui concerne les pressions mesurées sur les parois de la veine d'essais, il n'était pas tenu compte des résultats obtenus en l'absence du profil. Un nettoyage était effectué pour éliminer (figure 1) :

- les pressions affectées par l'interaction du peigne de sillage.
- les prises situées en amont.
- des défauts de prises.

De ce fait, l'étendue des signatures retenues s'étendait de - 3,2 à + 2,0 cordesde psrt et d'autre du centre du profil.

2 - INFLUENCE DE LA TRONCATURE DES SIGNATURES.-

La première critique énoncée envers lea résultats corrigés par la méthode ONERA relevait d'un défaut d'étendue dea signatures. Spécialement dans le cas de la correction d'incidence, la pondération des écarts de Kp entre les deux parois, de 1 à l'infini amont à 0 à l'infini aval, pouvait donc intervenir selon l'étendue des mesurcs.

Le programme de calcul a été modifié pour tenir compte des mesures des aignatures en l'absence du profil, c'est-à-dire dcs qualités des prises, de la veine et de l'interaction du peigne de sillage. Un exemple des signatures, normécs à celles obtenues sans profil, est donné figure 2 (dans les mêmes conditions de M, α que la figure 1). On voit que les signatures peuvent êtrc utiliséea dans un domaine pratiquement deux fois plus étendu: de - 6,2 à + 3,6 cordesde part et d'autre du centre du profil.

Lea valeurs corrigéea avec cette troncature réduite sont comparées aux anciennes obtenues avec la troncature d'origine aur la figure 3. L'effet de l'étendue des aignatures est faible et n'explique en aucun cas les désaccords d'incidence constatés entre lea résultats obtenus à S3MA et dans la soufflerie à parois adaptables T2 de l'ONERA.

3 - INFLUENCE DE LA MODELISATION DU PROFIL -

L'examen dcs aignatures, normées aux mesures en veine vide, obtenues à portance nulle eat significatif (figure 4). Les signatures sur plafond et plancher sont, certes confondues aux infinis amont et aval, mais décalécs longitudinalement. Les différences entre les deux signatures (figure 4) se aituent sur une courbe antisymétrique montrant bien que la circulation est nulle, ce qui était attendu, mais surtout l'effet de dissymétrie du profil dû à aa courbure.

La modélisation de la portance par un seul tourbillon d'intensité liéc au CZ n'était donc pas compatible avec les signatures mesurées. En fait, la vérification avait été effectuée pour le profil NACA 0012 symétrique et non pour un profil cambré.

Le programme de calcul a été retouché pour inclure deux tourbillons situés à 25 et 100% de profondeur et d'intensités déduites des deux mesures CZ et Cm.

Lea résultats ainsi corrigés aont comparés aux anciens sur la figure 5. Un écart systématique d'environ 0,2 degré apparaît pour toute la gamme de portance. En référence des valeurs non corrigées, le défaut de modélisation des termes de portance se traduisait par une correction excessive de l'incidence.

4 - COMPARAISON DES RESULTATS OBTENUS A S3MA et T2 -

Les résultats corrigés du profil CAST 7 à S3MA, après les améliorations précédemment exposés, sont comparés sur la figure 6 à ceux obtenus dans la aoufflerie à parois adaptables T2 de l'ONERA.

Les écarts d'incidence n'excèdent plus 0,05 degré alors que précédemment ils étaient voisins de 0,2 degré. Cette concordancc, maintenant satisfaisante, est obtenue même dans lc cas de hauteurs de rugosités diversea, dont l'influence reste faible.

CONCLUSION -

La confrontation des corrections obtenues par diverses méthodes et des réaultats d'essais dans diverses souffleries, a permis d'affiner non paa la méthode qui s'avère correcte mais l'utilisation trop rustique qui en était faite.

Les comparaisons des résultats corrigés en veine conventionnelle telle que S3MA avec ceux obtenus dans le nouveau concept de parois adaptables peuvent être considérées comme satisfaisantes d'autant plus que les répartitions de pressions sur le profil sont très voisines.

REFERENCES -

[1] - C. CAPELIER - J.P. CHEVALLIER - F. BOUNIOL.
Nouvelle méthode de correction des effets de parois en courant plan.
La Recherche Aérospatiale n° 1978-1 - p. 1.11.

[2] - X. VAUCHERET.
Data Report on the CAST 7/DOA1 profil in the ONERA S3MA wind tunnel.
ONERA - Technical Report n° 201/1464 GN (1982).

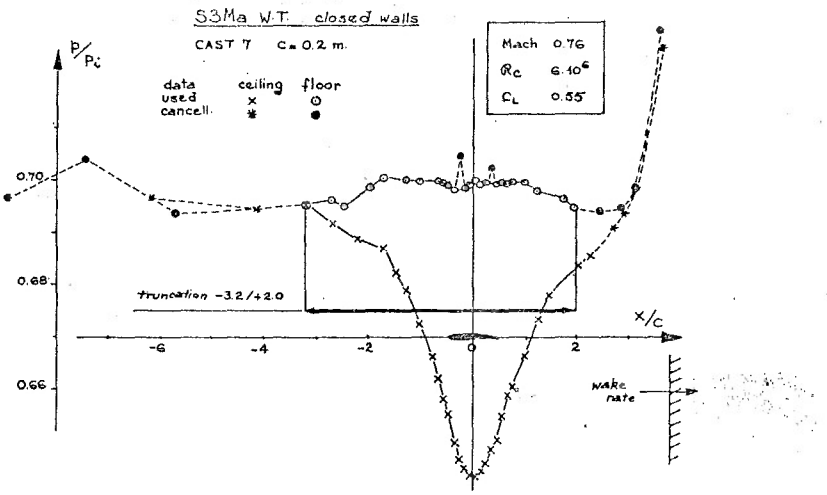


Planche 1

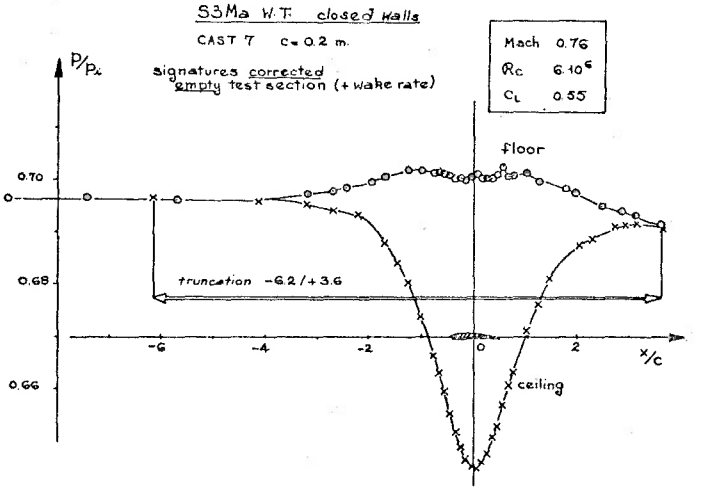


Planche 2

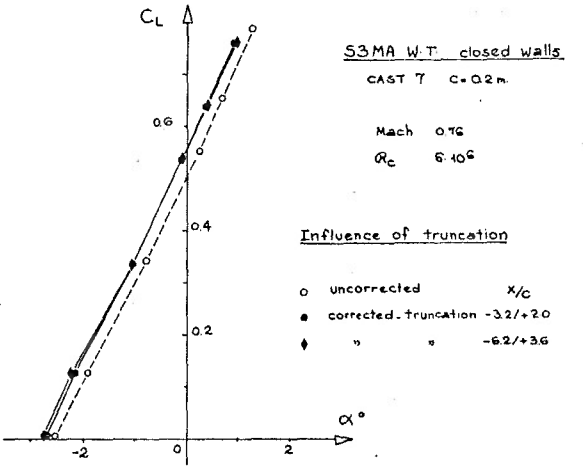


Planche 3

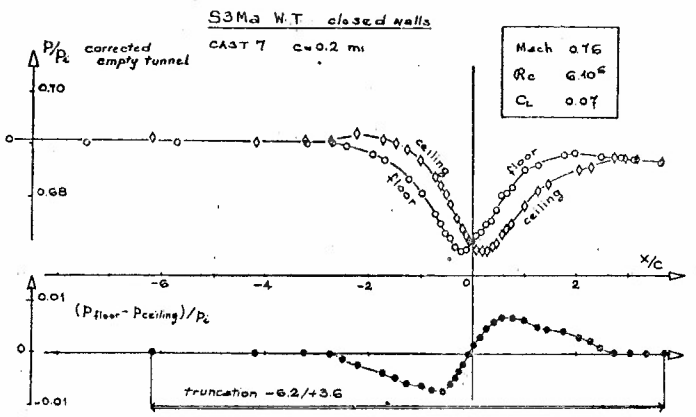


Planche 4

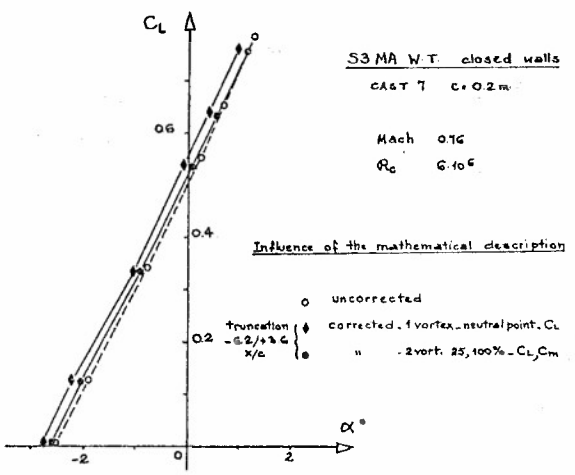


Planche 5

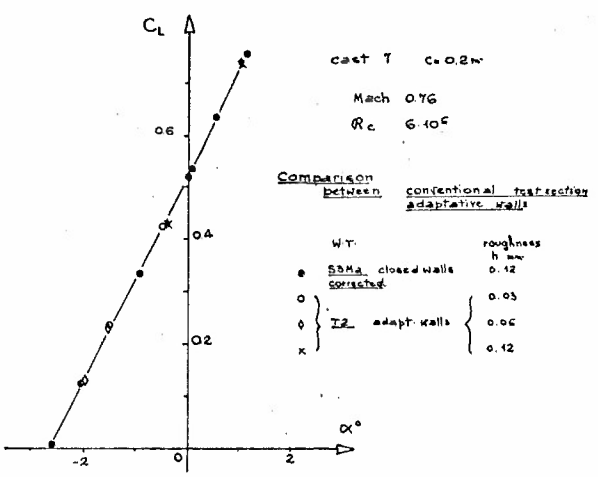


Planche 6

FLOW PROPERTIES OF SLOTTED-WALL TEST SECTIONS

by
Sune B. Berndt
Royal Institute of Technology
S-100 44 Stockholm, Sweden

SUMMARY

This paper gives a brief survey of results and problems relevant to the objective of eliminating wall interference in three-dimensional transonic tests by proper shaping of the slots. The principal features of the flow in a slotted test section are described and then illustrated by experimental results from two FFA wind tunnels. The importance of maintaining free-stream velocity to the full depth of the slots is stressed; the viscous effects evident in the experiments are viewed against this need. The classical inviscid flow model of two-dimensional slotted wall flow is compared with experiments and shown to give fair agreement in its range of validity. A fully three-dimensional and general inviscid flow model is described briefly and interference-free slot shapes for axisymmetric flows computed with this flow model are reviewed. Finally, problems of correcting the theoretical results for viscous effects are touched upon.

INTRODUCTION

Significant progress has been made in recent years in understanding and accounting for the flow properties of slotted walls. The ultimate goal is to be able to eliminate the wall interference - in particular in three-dimensional transonic tests - by shaping the slots properly, possibly in an 'adaptive' mode. Progress towards this goal is the subject of this paper, which, however, is not a comprehensive review of all recent work in the field. Rather it is an attempt to highlight a few features and problems of current interest so as to provide a backdrop for some of the other conference papers. For a historical perspective the reader should refer to relevant sections of Bernhard Goethert's Technical Evaluation Report on the AGARD Symposium in Wind tunnel Design and Testing Techniques held in 1975 [1].

The presentation is largely illustrated by experimental and computational results obtained by Swedish colleagues: Hans Sörensén and others of the FFA, and Yngve C.-J. Sedin and K. Roland Karlsson of the SAAB-SCANIA Company. The author is much indebted to them for helpful discussions and also for permission to use some of their unpublished material.

The paper first describes the principal features of the flow in a slotted test section [2]. Then present practice in the use of slotted test sections is recalled, in particular how one defines a free-stream Mach number. Experimental results from two FFA wind tunnels are next analysed in broad terms in order to verify qualitatively our ideas about slot flow. Special attention is paid to viscous effects in the slots so as to get an idea about the applicability of inviscid theory. Finally computed results [4] based on a general inviscid flow model [3] are reviewed, results which show - in an axisymmetric situation - how to shape the slots so as to eliminate the wall interference.

The presentation is non-mathematical and does not go into details of experimental technique. Only open slots are considered; slots with perforated cover plates or internal baffles belong in the family of perforated walls.

PRINCIPAL FEATURES OF FLOW IN A SLOTTED TEST SECTION

Basic to any description of the flow properties of a slotted wall is an appreciation of the principal features of the flow in a slotted test section: the flow into narrow slots, inside the slots, into the plenum, inside the plenum and, finally, out of the plenum (through the slots or otherwise).

Fig. 1 shows schematically how things might work out with a non-lifting model at high subsonic Mach numbers. The slot flow from the upstream part of the test section penetrates into the plenum as jets of high momentum air and continues to the outlet, undergoing some loss of momentum on the way and inducing a secondary flow in the plenum. To the extent that the slots in the downstream region are filled with low-momentum plenum air rather than high momentum air from the test section, the plenum pressure is free to penetrate into the test section.

The inlet Mach number M_1 is controlled by the down-stream variable throat: M_1 is independent of the size and shape of the model and the slots (disregarding viscous effects) as long as the slots and outlet are open enough for the flow to choke at the downstream throat rather than the model.

The plenum pressure p_p, on the other hand, depends upon these geometrical parameters. This is evident from the fact that the mass flux displaced by the model must go into the plenum in front of the maximum cross section of the model (if the wall interference is to be small). In other words, in each particular situation the plenum pressure automatically adjusts to that value for which mass flux conservation is established in the upstream part of test section. Therefore the plenum pressure will be lower than the inlet pressure p_1 and the pressure difference will increase when the model is made bigger and the slots are made shorter and narrower. It might also be conjectured that the pressure difference will be smaller at low Mach numbers, where the mass flux density can still increase in response to the presence of the model. We shall return to the experimental evidence further on.

THE NOMINAL FREE-STREAM MACH NUMBER

At first, however, let us consider briefly the crucial question of how to determine the free-stream Mach number M_∞ of a corresponding uniform and unbounded flow (if indeed there is such a flow) and also describe other aspects of the experimental arrangements.

The method used "in the trade" for obtaining an M_∞ is to calibrate the Mach number of the empty test section against the plenum pressure (after having adjusted the test section geometry, including one or more trim flaps as indicated in Fig. 1, to arrange for uniform flow). With the model present the free-stream Mach number is then taken to be equal to the Mach number in the empty test section at the same plenum pressure. This value for M_∞ might be called the nominal free-stream Mach number of the test.

As long as the model is not too large, this scheme seems to work well, as is perhaps not surprising since the slot width often has been selected to achieve just that for typical models. There is, of course, no reason to believe that a better result could not be obtained with a more rational method for determining M_∞ and selecting the slot geometry and model size. Indeed, to achieve that, is part of our ultimate objective. In a fully adaptive mode of operation the answer will come out automatically (see e.g. [5]).

TWO FFA WIND TUNNELS

The free-stream Mach numbers in the FFA experiments to be considered were obtained in the way just described. Two tunnels were used, one two-dimensional and one three-dimensional with octagonal cross-section. None of them had slots designed to minimise interferense.

Fig. 2 shows the two-dimensional test section. Note that the slots are of constant width and depth. Their open area ratio is around 5%. The blockage ratio of the model is 2.2%. The slotted part of the test section extends more than two model chords upstream as well as downstream of the model.

The three-dimensional test section (Fig. 3) is similar to that of the classical NACA angley wind tunnels. The slot width varies along the test section. At the position of the model centre the open-area ratio is 9.2% (and lower over the leading part of the model). The slot depth was constant and about half the slot width at the model centre in one case and one and half that slot width in another case. The model used was a slender parabolic-arc body of revolution. It was oversized, with its length roughly equal to the tunnel height and with the blockage ratio 2.2% (the same as in the two-dimensional tests). The model, tested in two different longitudinal positions, protruded, both upstream and downstream, into regions considered outside of the usual test section. The reason for choosing such a large model was simply to get large wall interference effects suitable for testing the theory.

Finally, it should be noted that both test sections have their walls strictly parallel so that even without a model there is a flux through the slots into the plenum, caused by the boundary layer build-up along the walls. The corresponding cross-flow velocity through the slots is generally larger in the two-dimensional test section with its narrower slots on two walls only. This was true also with the models present.

FLOW IN UPSTREAM PART OF TEST SECTION

There is no room for more than a few observations on the experimental results, which are rich and varied. The two-dimensional results have been described earlier [2] and the three-dimensional ones, not yet fully evaluated, will be reported in the near future. For presentation here results have been selected at $M_\infty = 0.90$ in the two-dimensional case and $M_\infty = 0.98$ in the axisymmetric case. The shock wave from the model reaches the wall in the latter case but not quite in the former case.

First we return to our conjectures on the structure of the inlet flow. Accordingly, for a constant inlet Mach number M_1, the plenum pressure (lower than the inlet pressure) is determined basically in an inviscid manner by the slot and model geometries upstream of the 'throat' between the model and the wall. Now the experiments were run at constant nominal Mach number, plenum pressure held constant. We expect therefore that the inlet pressure (higher than the plenum pressure) is determined by the upstream slot and model geometry.

Fig. 4 shows the pressure distribution at $M_\infty = 0.98$ along the centreline of a slat in the three-dimensional tunnel with the axisymmetric model in two different positions. In the region of constant slot width the pressure distribution is seen to move with the body, while farther upstream, where the slot width is small and varies strongly, there is an overpressure, i.e. a reduced inlet Mach number, the effect being stronger with the body in the forward position. This is what we expected and it indicates, of course, that there is strong wall interference present in the upstream part of the flow field. The results in the two-dimensional test section support the same conclusion (Fig. 5).

We will now compare the experiments with interference-free data in order to see more precisely what the interference is. For this purpose we use pressure distributions computed by the transonic small-perturbation approximation [4]. (They are known to be reliable for the present kind of body of revolution.) Fig. 6 shows pressure distributions along a slat as well as at the body surface with the body in its forward position. There is good agreement around the maximum thickness of the body, both at the wall and at the model. This includes the shock location. At the wall we see the expected large deviation in the upstream region. While at the body the interference is there, it is relatively weaker. This leaves little doubt that an appropriate widening of the slots in the forward part of the test section would produce almost interference-free flow at the model.

In view of the large size of the model this is a remarkable result. It gives great hope that it will indeed be possible in the future to use larger models than now (and it also tends to strengthen the position of the empiricism of the classical concept of a slotted test section of course, although the agreement found might apply only to the particular model and Mach number and therefore be fortuitous).

The slot width distribution thus controls the wall interference and might therefore be used as a means for reducing the wall interference. How about the slot depth? In Fig. 7 the pressure distributions at the wall and model for $M_\infty = 0.98$ are shown again, this time completed with results for a deeper slot, 11 cm instead of 4 cm (but with the same slot width distribution). The effect is seen to be quite strong over the model. The deeper slot maintains a larger pressure difference across the wall (as would a more narrow slot) and in this sense is more efficient than the shallow one. It is noteworthy that the effect is restricted to the region across from the model, where the classical streamline curvature term might be expected to come into play and does indeed depend upon slot depth in the manner indicated, while in the upstream region, and in the downstream region where the plenum pressure penetrates into the test section, the slot depth is unimportant.

The pressure difference due to streamline curvature is nothing but the old 'garden hose effect': the longitudinal momentum inside the slot is deflected laterally by the amplified cross flow velocity in the narrow slot. Hence the dependence on the slot depth just noticed: the deeper the slot the more longitudinal momentum it carries.

EXPERIMENTAL OBSERVATIONS OF VISCOUS EFFECTS

Turning now to viscous effects, we expect from what has just been said that a serious reduction in slot effectiveness will arise if the longitudinal velocity within the slot cannot be maintained close to free-stream velocity (while viscous effects on the cross-flow velocity could be controlled by changing the slot width). Let us therefore take a look at experimental values for the flow velocity along the slot centreline on the plenum side of the slot. Fig. 8 shows the longitudinal distribution of this velocity in the octagonal test section for the two differently deep slots, with and without a model. Clearly there is a considerable reduction of the velocity when the test section is empty. With a model present the velocity reduction is also considerable far upstream, where the slot is narrow, and over the rear of the model, where the slot flow is very likely going back into the test section. The reduction is reasonably small only in the intermediate region where the flux through the slot into the plenum is expected to have a maximum. There the difference between the two slots is remarkably small. Note that these considerable viscous effects are present in a situation where the slot in the region of the model is wider than the thickness of the wall boundary layer.

The viscous effects in the two-dimensional test were considerably smaller, as evident from Fig. 9. In that case good agreement with theory was obtained after only minor corrections for viscous effects [2]. In the three-dimensional case studied here these corrections no doubt will have to be substantial.

The remarkable thing about the two-dimensional case is that the wall boundary layer is much thicker than the slot width and still stays out of the slot. Evidently cross-flow velocity, which is larger in the two-dimensional case, is a more important parameter than boundary layer thickness in determining viscous effects in the slot. Perhaps slotted test sections should be designed with convergent walls.

INVISCID FLOW MODELS

We turn now to the computation of wall interference in slotted transonic test sections. The classical approach is to assume inviscid small perturbations of a uniform near-sonic flow and prescribe plenum pressure at the bottom of the slots. An approximate

solution is then obtained locally at the wall, from which is derived an equivalent 'homogeneous' wall boundary condition, an average condition, as it were, over slots and slats. This condition is then used for computing the flow around the model.

In the 'standard' situation of uniformly distributed uniform slots and two-dimensional flow towards the wall, this inviscid flow model gives for the pressure difference between the centreline of a slot and the plenum

$$\tfrac{1}{2}(C_{p_w} - C_{p_p}) = K \cdot \frac{d\theta}{d(x/d)} + \tfrac{1}{2}\left(\frac{d}{a}\cdot\theta\right)^2, \quad d = \text{distance between slots}, \quad a = \text{slot width},$$

where $\theta(x)$ is the average streamline slope at the wall (x = streamwise coordinate) and

$$K = -\frac{1}{\pi}\ell n \sin\frac{\pi a}{2d} + \frac{1}{\pi}\left(1 - \ell n\,\frac{2}{\pi}\right) + \frac{\ell}{a}, \quad \ell = \text{slot depth}$$

The pressure at the wall is seen to be the sum of two effects: the streamline curvature effect and the cross-flow Bernoulli effect. The latter is important in the two-dimensional case with its large cross-flow velocity [2], and less so in the axisymmetric case. Note that there is no term which is linear in the cross-flow velocity, such as one often saw in the early literature [1].

The wall geometry acts by way of the coefficient K as given above. As indicated earlier it contains a term ℓ/a, measuring the contribution of the longitudinal momentum carried inside the slot. To demonstrate how well this formula for K agrees with experiments Fig. 10 has been prepared, showing recent experimental results of Everhart and Barnwell [6] and also our own result [2]. It shows K + leading logarithmic term as a function of ℓ/a. According to theory the points should fall along a straight line of unit slope and intercept 0.46, and that seems to be nearly so. The scatter is considerable, which is not surprising in view of experimental difficulties. Still, a systematic deviation upwards is discernible and can be attributed to viscous effects. Our experimental point, for example, would agree with theory if K were computed with the slot width reduced by 15%. The new experimental results also confirm that no linear cross-flow term is called for.

The inviscid flow model must be generalized in various ways. For two-dimensional tests one would like to be able to account for longitudinal variation of slot geometry, including the depth to which there is high momentum air in the slot. For three-dimensional tests we must, in addition, be able to treat walls in which different slots have different geometry and flow conditions.

Fig. 11 shows a flow model capable of such generality. It is necessarily rather complicated and it will not be described here in any detail. An essential feature is that the high-momentum air going into the slot might split into two streams, one going into the plenum as a jet, and one turning back into the test section, there forming a narrow longitudinal bubble filled with quiescent plenum air. Note the combined surface y_p and y_{p_o}; on this the condition of plenum pressure is prescribed.

Using this flow model the author [3] developed a few years ago a three-dimensional theory which treats each slot individually by a singular perturbation method, yet permits the establishment of a 'homogeneous' wall boundary condition generalizing the classical one. This boundary condition is of course more complicated than the old one but it is still quite manageable when solving the transonic small-perturbation equation numerically for the test section flow.

INVISCID CALCULATIONS

Sedin and Karlsson have carried out a large number of such calculations, most of them concerned with axisymmetric flows. In particular, they have considered the problem of shaping the slots so as to eliminate the wall interference [4]. Fig. 12 shows a typical result. It applies to the same situation as the experiments we considered earlier, a large parabolic-arc body at Mach number 0.98. The slot depth is constant and nearly equal to the larger depth tested. The optimal slot, giving essentially zero wall interference at the model with a very small Mach number correction, is seen to be wider than the FFA slot over the forward part of the model, just as we predicted. The fairly large depth of the slot, together with a reduced slot width, is required over the rear part of the model in order to keep the plenum pressure from penetrating into the test section.

Similar results are shown in Fig. 13. Taken together, these calculations of Sedin and Karlsson give a very clear picture of how the optimum slot-width distribution at zero lift depends upon the shape and size of a slender model and upon free-stream Mach number. There is no need to go into details here.

More recently Sedin and Karlsson have taken up computations with lifting delta wings. A first report will be presented at the 13th ICAS Congress [7]. Corresponding experiments are being planned at the FFA.

VISCOUS CORRECTIONS

It seems probable therefore that we will soon know how to shape the slots in order to eliminate wall interference, in an inviscid approximation that is. We have seen that there is risk for considerable viscous effects, in particular when the cross-flow velocity at the wall is small. These are being emphasised in analysing the FFA experiments.

The next step will be to devise a scheme by which viscous effects can be accounted for in describing the flow properties of a slotted wall. Such a scheme might have to be based on measurements in situ during tests. They might include local measurements at the plenum side of each slot in order to determine the longitudinal momentum flux in the slot and the local plenum pressure (as influenced by entrainment and secondary flow in the plenum chamber). A similar scheme worked well in the two-dimensional case considered at FFA several years ago.

Very likely further and better experimental data will be required before the final answers are to hand. In view of the individual treatment of the slots in the generalized inviscid flow model such experiments can be performed in two-dimensional test sections, for example by the method of Ref. 6 or similar methods [8].

CONCLUDING REMARKS

Provided, then, that we will be able soon to describe with good accuracy the flow properties of slotted walls and thus to shape the slots properly, how can we use that capability in practice? First we must devise methods by which the slot geometry can be changed conveniently before or during tests. Then we must work out a strategy for changing the geometry according to predicted or measured distributions of pressure and streamline slope along the wall. Different solutions are likely to be required for different types of wind tunnel. In any case, the slotted wall would seem to be a viable competitor when it comes to designing an adaptive-wall wind tunnel for three-dimensional testing at high subsonic Mach numbers.

REFERENCES

[1] Goethert, B.H. — Technical Evaluation Report on the AGARD Specialist meeting on wind tunnel design and testing techniques. London, UK, 6-8 October 1975, (1976)

[2] Berndt, S.B., Sörensén, H. — Flow properties of slotted walls for transonic test sections. AGARD Conference Proceedings No. 174, Paper No. 17 (1975).

[3] Berndt, S.B. — Inviscid theory of wall interference in slotted test sections. AIAA Journal, Vol. 15, Sept. 1977, pp. 1278-1287.

[4] Karlsson, K.R., Sedin, Y.C.-J. — Numerical design and analysis of optimal slot shapes for transonic test sections - axisymmetric flows. Journal of Aircraft, Vol. 18, March 1981, pp. 168-175.

[5] Sears, W.R. — On the definition of free-stream conditions in wind tunnel testing. Proc. Symposium on Numerical and Physical Aspects of Aerodynamic Flows, California State Univ., Long Beach CA, Jan. 1981.

[6] Everhart, J.L., Barnwell, R.W. — A parametric experimental study of the slotted-wall boundary condition. NASA CP 2045, Part 2, (1978) pp. 459-471.

[7] Sedin, Y.C.-J. Karlsson, K.R. — Some theoretical wall interference calculations in slotted transonic test sections - three-dimensional flows. Paper ICAS-82-6,3,2, 13th ICAS Congress (1982).

[8] Berndt, S.B. — Measuring the flow properties of slotted test section walls. FFA Report 135 (1982).

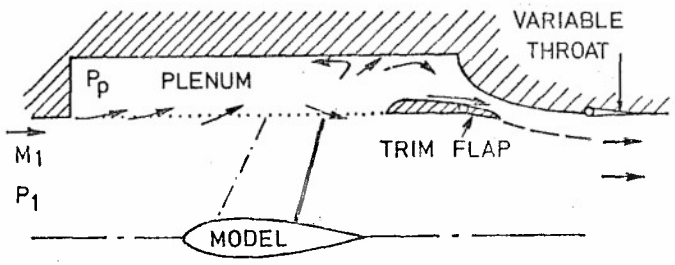


Fig. 1 Principal features of flow in a slotted test section.

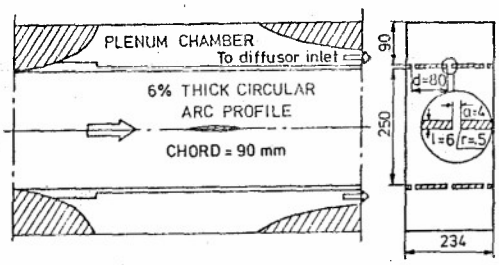


Fig. 2 Two-dimensional test section of transonic FFA wind tunnel [2].

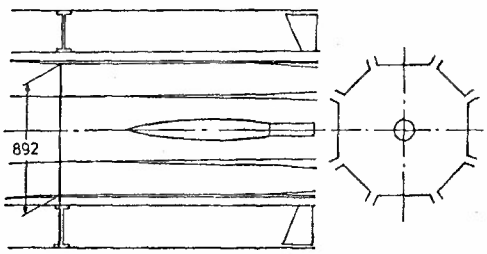


Fig. 3 Three-dimensional test section of transonic FFA wind tunnel.

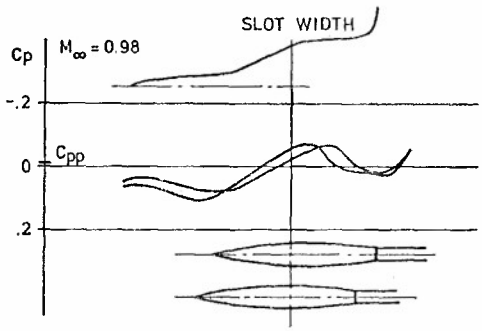


Fig. 4 Pressure distribution along centre line of slat with parabolic-arc axisymmetric body in two longitudinal positions.

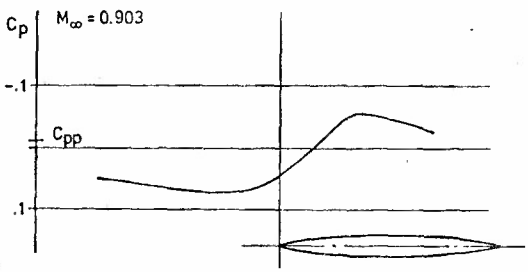


Fig. 5 Pressure distribution along centre line of slat with parabolic-arc wing in two-dimensional test section.

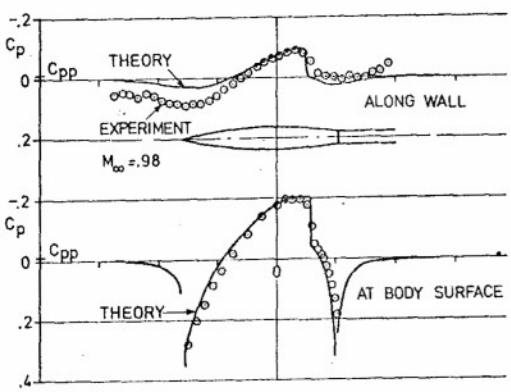


Fig. 6 Pressure distributions along slat and axisymmetric body compared with theoretical distributions in in unbounded flow.

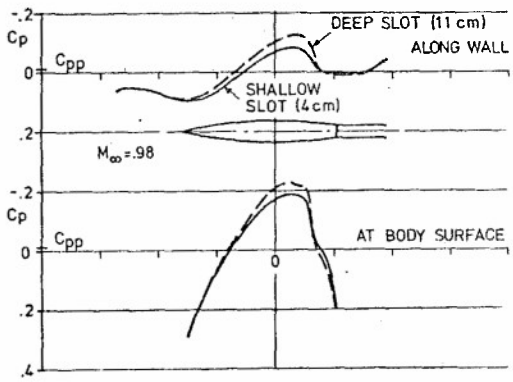


Fig. 7 Pressure distributions with slots of different depth.

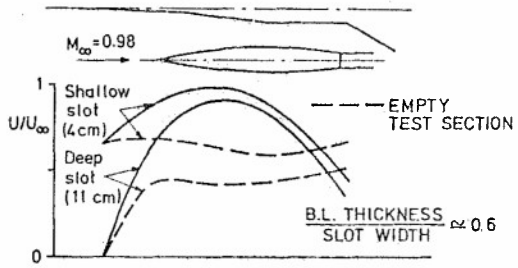


Fig. 8 Flow velocity at slot centre line on plenum side: axisymmetric flow.

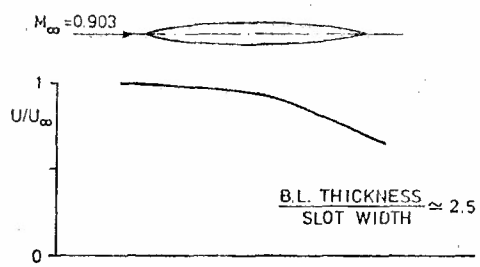


Fig. 9 Flow velocity at slot centre line on plenum side; two-dimensional flow [2].

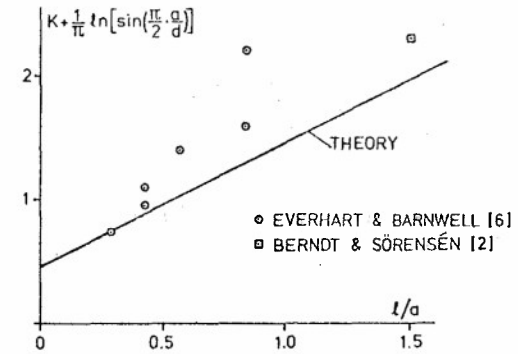


Fig. 10 Variation of slot parameter K with slot depth.

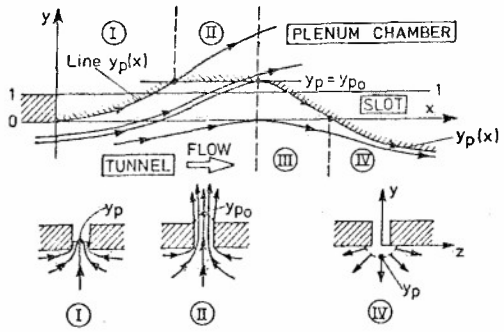


Fig. 11 Generalized slot flow model [2, 3].

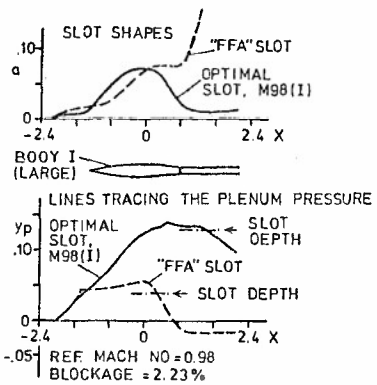


Fig. 12 Calculated slot shapes to eliminate wall interference on long axisymmetric parabolic-arc body at $M_\infty = 0.98$ [4].

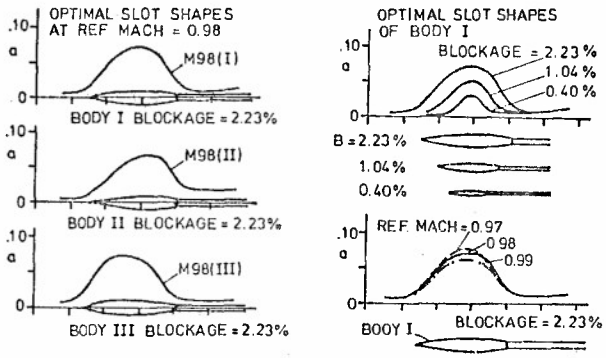


Fig. 13 Calculated slot shapes to eliminate wall interference on other axisymmetric bodies and at other free-stream Mach numbers [4].

WALL BOUNDARY-LAYER EFFECTS IN TRANSONIC WIND TUNNELS

Y.Y. Chan
High Speed Aerodynamics Laboratory
National Aeronautical Establishment
National Researeh Counеil of Canada
Ottawa, Canada

SUMMARY

Boundary-layer developments on the perforated walls and the sidewalls of a transonie two-dimensional wind tunnel have been studied experimentally and computationally. For the upper and lower walls, the wall charaeteristics are strongly modulated by the boundary layer and a correlation depending explicitly on the displacement thickness is obtained. A method of calculating the boundary-layer displacement effect is derived, providing the boundary condition for the calculation of the interference flow in the tunnel. For the sidewalls, the three-dimensional boundary-layer developments at the vieinity of the model mount has been calculated and its displacement effect analyzed. The effectiveness of controlling the adverse effects hy moderate surface suction is demonstrated.

1.0 Introduction

The requirement of accurate prediction of the wind-tunnel wall interferenee for tests at transonic speeds has led to detailed studies of the flow at the walls which provides the boundary condition for the calculation of the tunnel flows. This paper presents some analyses, both experimental and computational, of boundary-layer developments on walls of a transonic wind tunnel. Two topics will be discussed: (1) The boundary-layer developments along the top and the bottom perforated walls of a two-dimensional test section and their effects on the boundary condition of the tunnel flow. (2) The three-dimensional boundary-layer flows on the sidewall induced by the pressure field of a two-dimensional model and the control of their adverse effeets.

2.0 TOP AND BOTTOM WALL BOUNDARY LAYERS

For a solid wall wind tunnel, the boundary-layer growth is closely to that on a flat plate as the pressure gradient is very small along the wall. The displacement effect on the tunnel flow can be simply compensated by opening up the wall slightly downstream. For a ventilated wind tunnel with perforated walls, the boundary-layer development along the wall is much more eomplicated because of the inflow and outflow at the wall induced by the pressure field in the tunnel. The rapid growth of the boundary layer due to inflow at the wall causes a much more severe displacement effect and the wall eharacteristics become nonlinear. Since the eonditions at the wall constitute the boundary condition for the wall interference calculation. Thus a detailed study of the boundary-layer development and its effects is deemed necessary for accurate calculation of the tunnel flow. For many years, the boundary condition at the perforated wall assumes a linear relation for the local flow angle and the pressure difference between the test section and the plenum chamber[1,2,3]. The proportional constant of the linear relation is the porosity factor which depends on the physical configuration of the wall. In the transonic Mach number range, some nonlinear characteristic was readily observed and attributed to the boundary-layer development[4,5,6]. These early experiments were performed in empty tunnels and the averaged mass flows over the tunnel wall were measured. In real model testing condition, however, the pressure field generated by the model induces a variation of crossflow along the wall and inturn leads to a complicate development of the boundary-layer flow. The wall characteristics in such a condition were investigated by Jacocks[7]. His measurements indicate that the pressure-crossflow relation at the wall is far from linear and is correlated to the displacement thickness along the wall. The data presented by Jacocks, however, were averaged over the tunnel wall and the variations of the flow parameters along the wall were lost.

To determine the mutual interaction of the wall characteristics and the boundary layer, detailed studies of the flow development along the wall are required. A scheme for a thorough investigation has been proposed by Freestone and Henington[8]. An experimental study with the same intention has been carried out in the NAE transonic wind tunnel recently[9]. In this study, the boundary layer along the perforated wall was measured in transonic testing eonditions with the pressure field generated by a model. In between the measuring station, a computation code was employed to fill in the boundary-layer flow, giving finer details for the evaluation of the displacement effect and the wall characteristics. The results show that the pressure-normal velocity relation is highly nonlinear. The wall characteristics are strongly modulated by the boundary layer and a correlatiou depending explicitly on the displacement thickness is derived. Since the boundary-layer development is mainly controlled by the inflow or outflow at the wall, a similarity eorrelation for the normal velocity at the edge of the houndary layer and the mass transfer at the wall is also obtained. With these correlations, the boundary-layer development can be calculated if the wall pressure distrihution is known. The normal velocity just outside the boundary layer can then be determined and provides the required boundary condition for the calculation of the interference flow in the tunnel.

2.1 NAE Experiments

The NAE two-dimensional test faeility has a working section of 38 X 150 cm (15 X 60 in.). The top and bottom walls are perforated with 1.27 cm (0.5 in.) diameter normal holes at 2.59 cm (1.04 in.) centers in staggered rows, giving a porosity of 20.5%. The thickness of the perforated wall is 1.27 cm (0.5 in.). The test model has a BGK1 transonic profile of 25.4 cm (10 in.) chord. The static pressure variation along the walls was measured by a 2.54 cm (1 in.) diameter pressure pipe mounted along the centreline of the walls. The turbulent boundary layers at the walls were measured by pitot rakes. For the upper wall, the rakes were located at the stations x/e = -1.5, -0.025 and 1.65 with respect to the origin designated at 0.4 chord length from the leading edge of tbe model. For the lower wall, only one station at x/e = -0.025 was measured. The experiments were performed at Maeh numbers of 0.5 to 0.8, angles of attack of -3.5 to 11.8 degrees and Reynolds number of 21.5×10^6 per chord.

Some typical static pressure distrihutions at both the upper and lower walls for Mach number 0.7 and a range of angles of attack are shown in Figure 1. With positive lift, the pressure coefficient at the lower wall is always possitive, while at the upper wall it starts with a slight positive dip and then becomes negative downstream. The high positive pressure coefficient along the lower wall results a strong outflow through the wall. For C_L greater than 0.6, the boundary-layer measurement shown a very small velocity defect and indicates that the boundary layer is bled nearly completely from the lower wall. Thus the boundary-layer effect is small and can be neglected at moderate and high lift conditions.

The upper wall, on the other hand, has a much more complicate boundary-layer development than the lower wall and the experimental results are shown in Figure 2 for the cases of Mach number 0.7. The boundary layer grows slowly between the first two measuring stations and then rapidly towards the third station. Since the pressure variation along the wall is small, the dominating factor of the boundary-layer development is the crossflow through the wall. However, if the linear wall characteristic is assumed for the inflow variation from the measured wall pressure distribution, the boundary-layer growth so generated does not follow that observed in the experiment. This suggests that the inflow variation is not only related to the pressure distribution but is also modulated by the boundary-layer development.

To deduce the inflow required for such a boundary-layer development, a boundary-layer computation code is employed in auxiliary with the experimental data. A differential method with turbulent kinetic energy equation for the closure of the turbulence terms is chosen[11]. The local inflow through the wall is first assumed as a function of the pressure coefficient and the displacement thickness, and the boundary layer is calculated downstream from the first measuring station, the velocity profile of which is used as the initial condition. The calculated velocity profiles at the second and the third stations are then compared with the measured ones. The wall characteristics model is adjusted until a satisfactory match of the velocity profiles is obtained. The boundary layers calculated in this manner are also shown in Figure 2 for the Mach number 0.7 cases. The inflow variations generating these boundary-layer developments are shown in Figure 3. The variation of the inflow velocity along the wall differs greatly from that of the pressure coefficient as shown in Figure 1.

2.2 Wall Characteristics and Displacement Effects

The nonlinear value of the wall characteristics can be brought out more clearly by plotting the inflow velocity against the pressure coefficient as shown in Figure 4. The general trend of the curves follows closely to those from direct measurements reported in Reference 7. The offsetting of the curves from passing through the origin of the co-ordinates indicates that the inflow has a larger resistance than the outflow. By taking the boundary-layer thickness into account, the wall characteristics can be collapsed to a single correlation curve as shown in Figure 5. For each case, the data follow a common correlation curve to a certain point and then branch off. The value of the normalized displacement thickness δ^*/d at the branch-off point is about 0.25 corresponding to the normalized thickness δ/d about 1 or greater. The correlation curve is approximated by a quadratic as

$$\frac{\rho_w V_w}{\rho_e U_e} = -1.39\,(\xi - \xi_o) - 50.37\,(\xi - \xi_o)^2, \qquad \frac{\delta^*}{d} \leqslant 0.25 \tag{1}$$

where $\xi = C_p\,\delta^*/d$ and $\xi_o = -0.0008$. As the boundary layer becomes thicker, the dependence of the wall characteristics on the boundary-layer thickness is reduced and a linear relation of the inflow velocity and the pressure coefficient holds, Figure 6. The correlation is given as

$$\frac{\rho_w V_w}{\rho_e U_e} = -0.316\left[C_p - \frac{(C_p\,\delta^*/d)_o}{\delta^*/d}\right] + \left[\frac{\rho_w V_w}{\rho_e U_e}\frac{\delta^*}{d}\right]_o \frac{d}{\delta^*}, \qquad \frac{\delta^*}{d} > 0.25 \tag{2}$$

where the subscript o refers to the values at $\delta^*/d = 0.25$, and d is the hole diameter of the perforation.

As shown in Figure 3, the rapidly increase of the inflow velocity along the wall is nearly exponential suggesting that this portion of the boundary layer is close to equilibrium. A similarity correlation can thus be established between the normal velocity at the edge and the mass transfer at the wall as shown in Figure 7. The correlation is well represented by a hyperbola

$$\frac{V_e}{U_e} = 2.125\,\frac{\rho_w V_w}{\rho_e U_e} + \left[1.2656\left(\frac{\rho_w V_w}{\rho_e U_e}\right)^2 + 2.25 \times 10^{-6}\right]^{1/2} \tag{3}$$

The asymptotes are respectively

$$\frac{V_e}{U_e} = 3.25\,\frac{\rho_w V_w}{\rho_e U_e}, \qquad \frac{V_e}{U_e} = \frac{\rho_w V_w}{\rho_e U_e} \simeq \frac{V_w}{U_e} \tag{4}$$

With the wall characteristic correlation and the similarity correlation of the boundary layer known, the boundary-layer development on the wall can readily be calculated once the pressure distribution along the wall is measured. The normal velocity at the edge of the boundary layer includes the displacement effect and the mass transfer at the wall can be written as[12,13]

$$\frac{V_e}{U_e} = \frac{1}{\rho_e U_e}\frac{d}{dx}(\rho_e U_e \delta^*) + \frac{\rho_w V_w}{\rho_e U_e} \tag{5}$$

With V_e/U_e given by Equation (3) and $\rho_w V_w/\rho_e U_e$ by Equations (1) or (2), the variation of the displacement thickness δ^* can be calculated by integrating Equation (5) from a known C_p distribution. The wall characteristics and the displacement effect follow directly from the correlations. By measuring the pressure distribution along the wall, the velocity components U and V at the edge of the boundary layer can now be determined. The boundary condition required for determination of the flow in the tunnel is thus established.

The study has demonstrated the nonlinear wall characteristics caused by the growth of the boundary layer along the wall and a correlation of the pressure-normal velocity relation including explicitly the displacement thickness has been obtained. With the similarity correlation of the boundary layer for the normal velocities at the edge and at the wall, the boundary-layer development along the wall can be determined from the measured pressure distribution and the normal velocity at the edge of the boundary layer evaluated. The boundary condition for the calculation of the flow in the tunnel is now properly defined. The empirical coefficients of the correlations for the wall characteristics depend on the configuration of the wall and those given in the paper are for the NAE tunnel only. The principle of approach, however, is general and could be applied to other tunnels with perforated walls.

3.0 Side-Wall Boundary Layers

In transonic wind-tunnel tests of a two-dimensional airfoil, the growth of the side-wall boundary layer in the vicinity of the model mount is controlled by the pressure field indueed by the airfoil and is therefore three-dimensional. The boundary-layer thickness varies rapidly in the chordwise and the lateral directions of the model and its interaction with the flow over the model distorts the spanwise uniformity of the flow contributing errors to the measurements. This is particularly severe for high transonic flows as the shock strength and its location about the model is sensitive to the perturbation from the adjacent flow field. This effect has been experimentally studied by Bernard-Guelle[14]. Winter and Smith[15] have shown that the interaction effects arise mainly from changes in the displacement thickness of the side-wall boundary layer. Methods have been derived by Barnwell[16] and Sewell[17] to take into account of the averaged thickness of the boundary layer in the two-dimensional governing equation of the flow in the test section, leading to a Mach number "correction" to the tunnel flow.

To lessen the side-wall boundary-layer effect, a common practice is to control the growth of the boundary layer by applying suction at an area of the wall where the model is mounted. This method is employed in the NAE two-dimensional test facility[10,18]. The effectiveness of the control is demonstrated in this paper by comparing the boundary-layer developments without and with surface suction. The three-dimensionality of the flow is emphasized and examined in some details.

Three-Dimensional Boundary-Layer Development

The side-wall boundary layer in a transonic test section is turbulent and compressible. In the vicinity of the model the boundary layer is three-dimension because of the pressure field induced by the airfoil. However the lateral curvature of the streamline, except very close to the leading edge, is small due to the slenderness of the airfoil shape. Thus a small cross-flow formulation can be adopted if the intrinsic streamline co-ordinates are used. The formulation is briefly outlined in the Appendix. To demonstrate the boundary-layer development on the sidewall around the model, calculations have been performed for a typical test case of a transonic airfoil. The test specifications are as follows.

Airfoil — 16% wide transonic profile
c = 25.4 cm (10 in.)
M_∞ = 0.6
Re_∞ = 47.8×10^6/m (14.5×10^6/ft)
α = 3.9 deg.
C_L = 0.60

At this condition, the flow at the upper surface of the airfoil is supercritical with local Mach number up to 1.2. The case is chosen for illustration because of its relative high C_L and a rapid recovery of pressure at the rear portion of an airfoil, providing a severe test case for the suction device.

The suction area extends from x/c = -1.15 to 1.25 and y/c = 1.05 to -0.75 with the origins of the co-ordinates located at the midchord of the airfoil. The inviscid flowfield about the airfoil is calculated by a transonic small disturbance code. The boundary-layer development over the suction area has been calculated for flows without suction and with suction. The nominal suction velocity v_s/u_∞ is 0.0045.

The variation of the pressure gradient parameter β defined as (see Eq. A6),

$$\beta = \frac{H_e}{h_e}\frac{2\xi}{u_e}u_{e\xi}$$

controlling the boundary-layer growth along the streamline is shown in Figure 9. The rapid expansion around the leading edge gives a sharp rise of β and the recompression near the trailing edge forms a deep depression of negative β. The pressure gradient decays laterally away from the airfoil and is insignificant for a distance of y/c greater than ±0.5. The variation of the suction velocity over the same area considered is shown in Figure 10. Because of the large loss coefficient of the porous material forming the suction surface, the large pressure variation near the airfoil induces only a small ripple on the otherwise uniform distribution of suction velocity.

The boundary-layer development under these conditions are shown in Figure 11 in terms of the displacement thickness δ^*[12],

$$\delta^* = \delta_s^* - \frac{1}{\rho_e u_e e_2}\frac{\partial}{\partial r}\int_0^x \rho_e u_e e_1 \delta_n^* ds \qquad (6)$$

where the displacement thicknesses along the streamline δ_s^* and for the crossflow δ_n^* are defined as

$$\delta_s^* = \int_0^\infty \left(1 - \frac{\rho u}{\rho_e u_e}\right)dy$$

$$\delta_n^* = \int_0^\infty \frac{\rho w}{\rho_e u_e}dy$$

Without suction, the displacement thickness δ^* drops rapidly due to the expansion around the leading edge and the upper surface of the airfoil. Towards the trailing edge, δ^* grows steady to a high peak and then decreases further downstream. At the lower side of the airfoil, δ^* varies less severely. A small lump near the stagnation point of the leading edge can be observed and further downstream, the growth of δ^* follows the same trend as the upper surface. Using the equivalent source concept[12], the normal velocity induced just outside the boundary layer due to the displacement effect can be evaluated as

$$\frac{v_e}{u_e} = \frac{1}{\rho_e\, u_e\, e_1\, e_2}\left[\frac{\partial}{\partial s}\left(\rho_e\, u_e\, e_2\, \delta_s^*\right) - \frac{\partial}{\partial n}\left(\rho_e\, u_e\, e_1\, \delta_n^*\right)\right] + \frac{\rho_w\, v_w}{\rho_e\, u_e} \tag{7}$$

The variation of the normal velocity v_e/u_e is shown in Figure 12. The trend of variation follows that of the displacement thickness with a deep depression at the leading edge and a high peak at the trailing edge superimposing to a nearly uniform suction distribution.

When suction is applied, the variation of the displacement thickness δ^* is much less drastic except near the leading edge, Figure 13. The depression there is now due to the double effects of the expansion of the flow and surface suction. Downstream towards the trailing edge, the suction inhibits the growth of δ^* and a much smaller rise results. The corresponding effective normal velocity is shown in Figure 14. The depression near the leading edge remains, the high peak at the trailing edge is reduced to a low hump and the variation is much more gradual as a whole.

The large variation of the displacement thickness and the effective normal velocity could be better appreciated if comparison is made with the growth of the two-dimensional boundary layer on the model surface. Figure 15 shows the developments of the boundary layer with and without suction along a streamline at a lateral distance $y/c = 0.1$ above the model. The growth of the boundary on the model surface is also shown for comparison. Because of the large initial thickness, the wall boundary layer can be greatly reduced by the leading edge expansion. Downstream toward the trailing edge, both the wall layer without suction and the layer on the model grow rapidly against the adverse pressure gradient. The growth rates of these two layers are nearly identical and are reflected in the effective normal velocity induced by the layers as shown in Figure 16. With suction, the growth is suppressed and the induced normal velocity is small for most part of the airfoil. The relative large outflow near the leading edge is equivalent to a local divergence of the flow which may reduce slightly the pressure over the nose region of the model.

Along the junction of the model and the sidewall, the boundary layer is fully three-dimensional. Three-dimensional separation occurs ahead of the blunt nose of the model and a horse-shoe vortex is formed and engulfs the airfoil-wall interaction. Its effect on the measurement of drag of the model has been studied by Barber[20] and Jacobs[21]. This effect can also be effectively reduced or controlled by applying surface suction. For a three-dimension boundary-layer flow, the cross-flow components are greatly reduced when suction is applied and the limiting streamline follows closely to the external streamline[19]. The extent of the three-dimensional separation is thus reduced.

In summary, the effectiveness of the boundary-layer control to the side-wall boundary-layer development has been demonstrated. Because of the three-dimensionality of the flow and the pressure field induced by the model. The boundary-layer development varies rapidly both in the longitudinal and the lateral directions of the model. Three-dimensional separation and vortex formation also occur at the model-wall junction. For such a complicate flow, surface suction seems to provide the best answer to the problem by controlling the growth near the trealing edge and reduces the three-dimensional separation near the nose of the model. Thus provides a more controllable environment for the two-dimensional tests.

APPENDIX

Streamline Co-Ordinates

If the flow-field around the airfoil is known, the streamline can be calculated from the streamline equation

$$\frac{dx}{dz} = \frac{U}{W} \tag{A1}$$

where x, z are the rectangular co-ordinates fixed on the side wall with the origin located at the centre of the airfoil chord. U, W are the velocity components in the x,z-directions respectively. The streamline co-ordinate s is the curve following the streamline and n is its ortbogonal trajectory (Fig. 8).

This inviscid flow outside the boundary layer can be considered as isentropic up to low supersonic Mach numbers. Therefore, a velocity potential ϕ can be defined and the equipotential line is along the n co-ordinate. We then have the following relations:

$$U = \frac{\partial n}{\partial x} \quad , \quad W = \frac{\partial n}{\partial z}$$

$$\rho U = \rho_o \frac{\partial s}{\partial z} \, , \quad \rho W = \rho_o \frac{\partial s}{\partial x} \tag{A2}$$

The curvilinear streamline co-ordinates are related to the fixed Cartesian co-ordinates as follows:

$$ds = \left(\frac{U^2 + W^2}{U}\right) dx$$

$$dn = - \frac{\rho}{\rho_o} \left(\frac{U^2 + W^2}{V}\right) dx \tag{A3}$$

The metrics e_1 and e_2 for the streamline co-ordinates s, n respectively are given as

$$e_1 = \frac{(n_z^2 + n_x^2)^{1/2}}{J\left(\frac{s,n}{z,x}\right)}$$

$$e_2 = \frac{(s_z^2 + s_x^2)^{1/2}}{J\left(\frac{s,n}{z,y}\right)} \tag{A4}$$

where $J\left(\frac{s,n}{x,z}\right)$ is the Jacobian. With the relations given in Equation (A2) the metrics can be reduced to the forms

$$e_1 = \frac{1}{u}$$

$$e_2 = \frac{\rho_o}{\rho} \frac{1}{u} \tag{A5}$$

where $u = (U^2 + W^2)^{1/2}$ is the velocity component in the s-direction.

Boundary-Layer Equations

When the streamline curvature is small, the three-dimensional boundary-layer equations in the intrinsic streamline co-ordinates can be simplified by the small cross-flow approximation[19]. The resulting equations for the turbulent boundary layer are similar in forms to those given in Reference (19) for laminar boundary layers except additional Reynolds stress terms. The equations are written as follows:

$$\left[C\left(1 + \frac{e_t}{\mu}\right) f_{\eta\eta}\right]_\eta + f f_{\eta\eta} + \frac{H_e}{h_e} \frac{2\xi}{u_e} u_{e\xi} (\sigma - f_\eta^2) = 2\xi (f_\eta f_{\eta\xi} - f_\xi f_{\eta\eta})$$

$$\left[C\left(1 + \frac{e_t}{\mu}\right) g_{\eta\eta}\right]_\eta + f g_{\eta\eta} - \frac{2\xi}{u_e e_2} (u_e e_2)_\xi f_\eta g_\eta - \frac{2\xi}{e_1} e_{1\xi} \frac{H_e}{h_e} (\sigma - f_\eta^2) = 2\xi (f_\eta g_{\xi\eta} - f_\xi g_{\eta\eta})$$

$$\left[C\left\{\frac{1}{Pr}\left(1 + \frac{e_t}{\mu} \frac{Pr}{Pr_t}\right)\sigma_\eta + \frac{u_e^2}{H_e}\left(1 - \frac{1}{Pr}\right) f_\eta f_{\eta\eta}\right\}\right]_\eta + f\sigma_\eta = 2\xi (f_\eta \sigma_\xi - f_\xi \sigma_\eta) \tag{A6}$$

where

$$f_\eta = \frac{u}{u_e}, \quad g_\eta = \frac{v}{u_e}, \quad \sigma = \frac{H}{H_e}$$

$$C = \frac{\rho\mu}{\rho_e\mu_e}, \quad Pr = \frac{c_p\mu}{k}, \quad Pr_t = \frac{c_p \epsilon_t}{k_t}$$

In these equations, the concept of eddy viscosity and eddy conductivity have been introduced as

$$-\rho\overline{u'v'} = \epsilon_t \frac{\partial u}{\partial y}$$

$$-\rho\overline{v'w'} = \epsilon_t \frac{\partial w}{\partial y}$$

$$-\rho\overline{H'v'} = \frac{k_t}{c_p} \frac{\partial H}{\partial y} \qquad \text{(A7)}$$

The co-ordinate transformations are given as follows:

$$\xi = \int \frac{\rho_e\mu_e}{\mu_r^2} e_1 e_2^2 u_e \, ds$$

$$\zeta = \int \frac{\rho_e\mu_e}{\mu_r^2} e_2^3 u_e \, dn$$

$$\eta = \frac{\rho_e u_e e_2}{(2\xi)^{1/2}} \int \frac{\rho}{\rho_e} \, dy \qquad \text{(A8)}$$

The boundary conditions can be similarly transformed as

$$f_\eta(\xi,0) = 0$$

$$f(\xi,0) = 0 \text{ or } -(\rho v)_b = \frac{\rho_e \mu_e u_e e_2}{\mu_r} (f + 2\xi f_\xi)_b$$

$$g_\eta(\xi,0) = 0$$

$$\sigma(\xi,0) = \sigma_b(\xi) \text{ or } \sigma_\eta(\xi,0) = 0 \qquad \text{(A9)}$$

and

$$f_\eta(\xi,\infty), \ \sigma(\xi,\infty) \to 1$$

$$g_\eta(\zeta,\infty) \to 0$$

With the co-ordinate transformations, Equation (A8), the boundary-layer equations for the streamwise flow, (the first and the third equations in Eq. (A6)) are in a similar form as a two-dimensional flow. The method developed for the solution of two-dimensional equations can be applied here[11]. Once the streamwise flow is known, the cross-flow equation, (the second equation in Eq.(A6)) can then be integrated for the velocity component normal to the streamline. A computation code has been developed for the present calculations.

REFERENCES

1. Baldwin, B.S. Jr., Turner, J.B., Knechtel, E.D. — *Wall Interference in Wind Tunnels with Slotted and Porous Boundaries at Subsonic Speeds.* NACA TN 3176, May 1954.

2. Goodman, T.R. — *The Porous Wall Wind Tunnel: Part II, Interference Effect on a Cylindrical Body in a Two-Dimensional Tunnel at Subsonic Speeds.* Cornell Aeronautical Laboratory Rept. AD-594-A-3, November 1950.

3. Maeder, P.F. — *Investigation of the Boundary Condition at a Perforated Wall.* Division of Engineering, Brown University, Providence, R.I., Tech. Rept. WT-9, May 1953.

4. Chew, W.L. — *Cross-Flow Calibration at Transonic Speeds of Fourteen Perforated Plates with Round Holes and Airflow Parallel to the Plates.* AEDC-TR-54-65, July 1955.

5. Chew, W.L. — *Characteristics of Perforated Plates with Conventional and Differential Resistance to Cross-Flow and Airflow Parallel to the Plates.* Proceedings of the Propulsion Wind Tunnel Transonic Seminar: Vol. 1, Discussion of Transonic Testing Problems, AEDC, 1956.

6. Lukasiewicz, J. — *Effect of Boundary Layer and Geometry on Characteristics of Perforated Walls for Transonic Wind Tunnels.* Vol. 20, Aerospace Engineering, April 1961, pp. 22-23, 62-68.

7. Jacocks, J.L. — *An Investigation of the Acrodynamic Characteristics of Ventilated Test Section Walls for Transonic Wind Tunnel.* Ph.D. Dissertation, University of Tennessee, Knoxville, December 1976.

8. Freestone, M.M. Henington, P. — *A Scheme for Incorporating the Viscous Effects of Perforated Wind Tunnel Walls in Two-Dimensional Flow Calculations.* The City University, Department of Aeronautics, Research memo. Aero 78/7, April 1979.

9. Chan, Y.Y. — *Analysis of Boundary Layers on Perforated Walls of Transonic Wind Tunnels.* J. of Aircraft, Vol. 18, No. 6, June 1981, pp. 469-473.

10. Ohman, L.H. — *The NAE High Reynolds Number 15" × 60" Two-Dimensional Test Facility: Part I, General Information.* National Aeronautical Establishment, Lahoratory Tech. Rept. LTR-HA-4, April 1974.

11. Chan, Y.Y. — *Compressible Turbulent Boundary Layer Computations Based on Extended Mixing Length Approach.* Canadian Aeronautical and Space Institute Transactions, Vol. 5, No. 1, Mareh 1972, pp. 21-27.

12. Lighthill, M.J. — *On Displacement Thickness.* Journal of Fluid Mechanics, Vol. 4, 1958, pp. 383-392.

13. Fannelop, T.K. — *Displacement Thickness for Boundary Layers with Surface Mass Transfer.* AIAA Journal, Vol. 4, June 1966, pp. 1142-1144.

14. Bernard-Guelle, R. — *Influence des couches limitées latérales de soufflerie dans les essais transsoniques en courant plan.* 12e, Collegue AAAF, Poitier, 1975.

15. Winter, K.G. Smith, J.H.D. — *A Comment on the Origin of End-Wall Interference in Wind-Tunnel Tests of Aerofoils.* Tech. memo. Aero 1816, Royal Aircraft Establishment, August 1979.

16. Barnwell, R.N. — *Similarity Rule for Sidewall Boundary-Layer Effect in Two-Dimensional Wind Tunnels.* AIAA Journal, Vol. 18, No. 9, September 1980, pp. 1149-1151.

17. Sewell, N.G. — *The Effects of Sidewall Boundary Layers in Two-Dimensional Subsonic and Transonic Wind Tunnels.* AIAA-81-1297, June 1981.

18. Chan, Y.Y. — *Boundary Layer Controls on the Sidewalls on Wind Tunnels for Two-Dimensional Tests.* J. of Aircraft, Vol. 17, No. 5, May 1980, pp. 380-382.

19. Chan, Y.Y. — *Small Cross-Flow in Three-Dimensional Laminar Boundary Layers with Suction or Injection.* Aero Report LR-520, National Aeronautical Establishment, Ottawa, Canada, February 1969.

20. Barber, T.J. — *An Investigation of Strut-Wall Interaction Losses.* J. of Aircraft, Vol. 15, No. 10, October 1978, pp. 676-681.

21. Jacobs, P.P., Jr. — *A Method of Correcting for the Effects of the Sidewall Boundary Layer in Two-Dimensional Airfoil Testing.* Tech Memo. TM 80-44, Applied Research Laboratory, The Pennsylvania State University, March 1981.

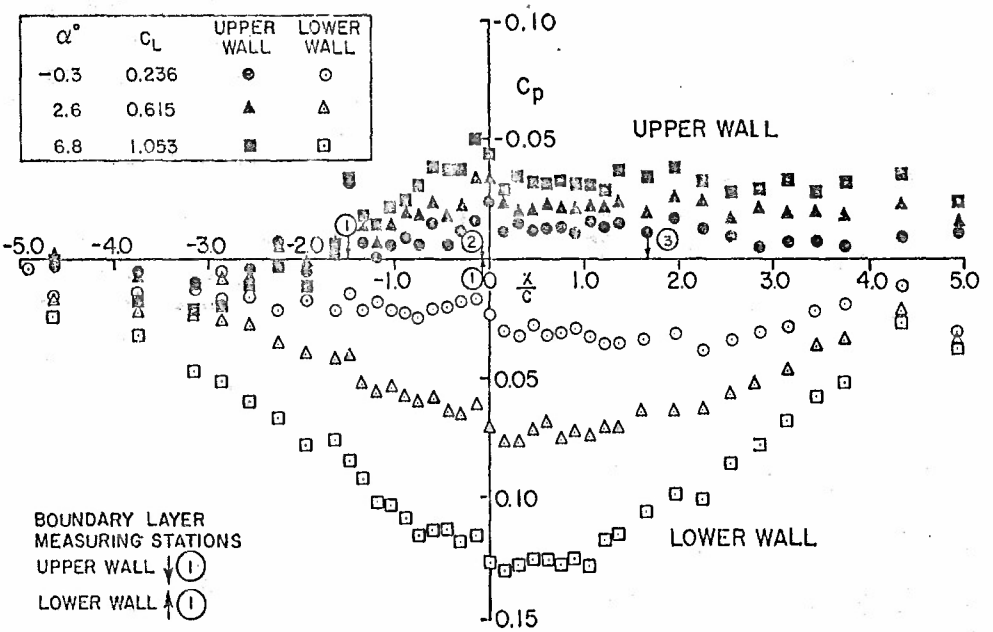


FIG. 1: STATIC PRESSURE DISTRIBUTIONS ALONG UPPER AND LOWER WALLS AT MACH 0.703

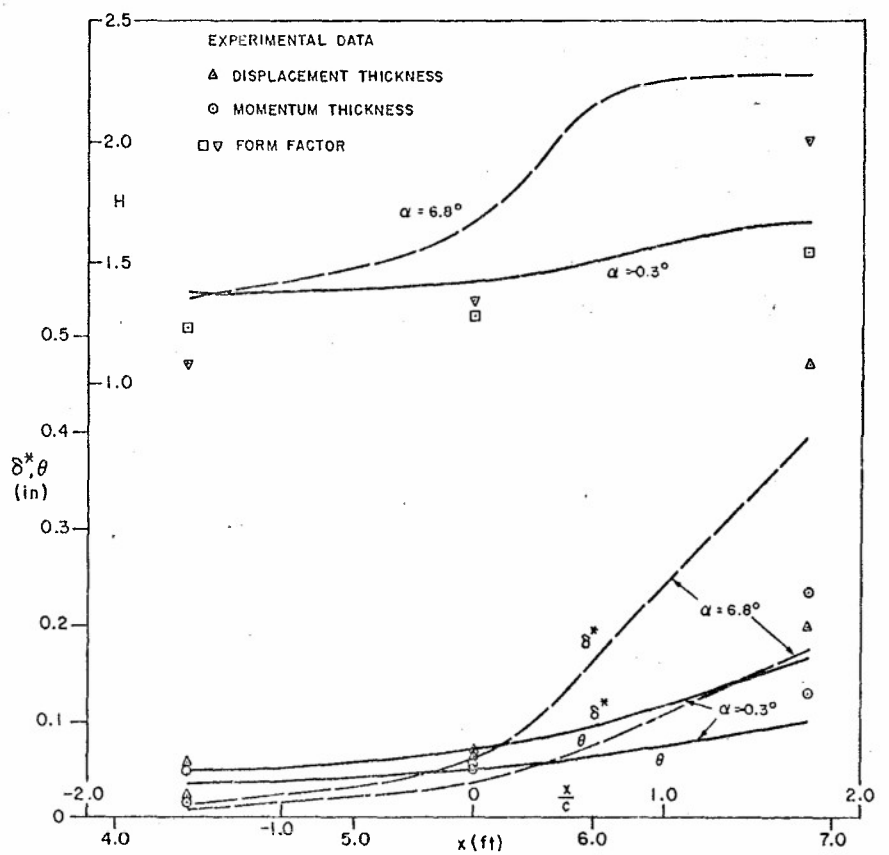


FIG. 2: BOUNDARY-LAYER DEVELOPMENT ALONG THE UPPER WALL, CALCULATED VALUES ARE GIVEN IN LINES

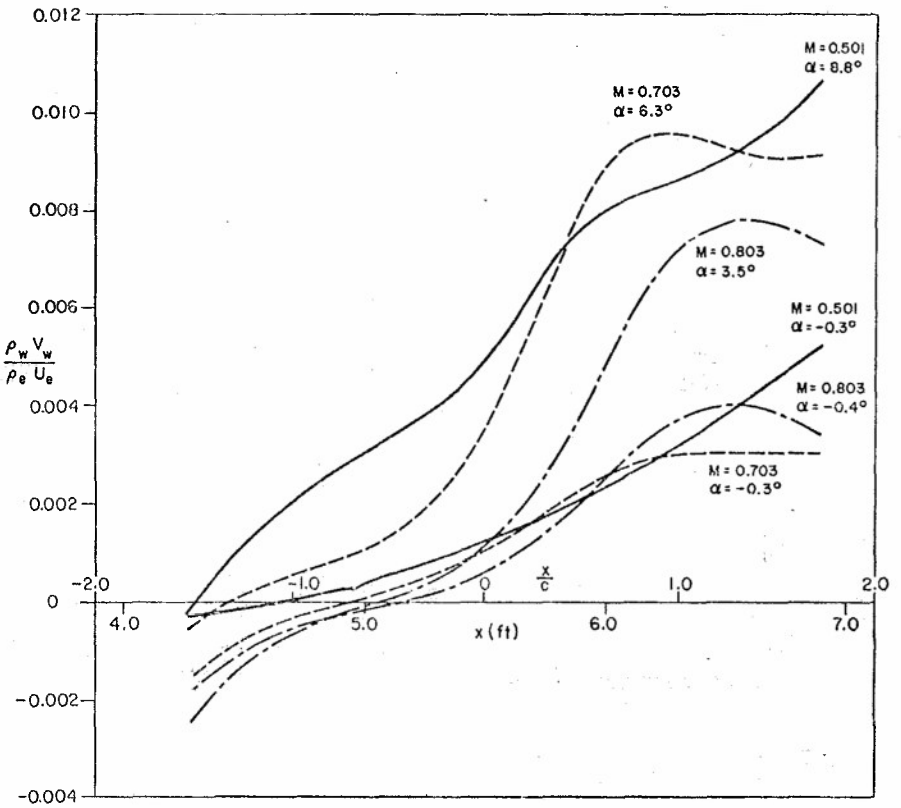


FIG. 3: CALCULATED INFLOW AND OUTFLOW VELOCITY DISTRIBUTIONS AT THE UPPER WALL

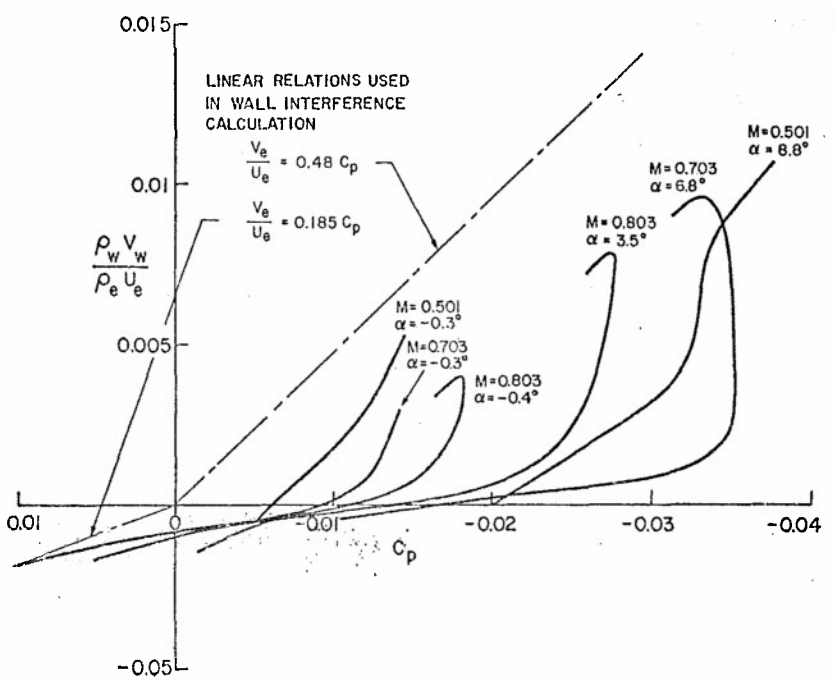


FIG. 4: INFLOW AND OUTFLOW VELOCITIES VERSUS PRESSURE COEFFICIENT AT THE UPPER WALL

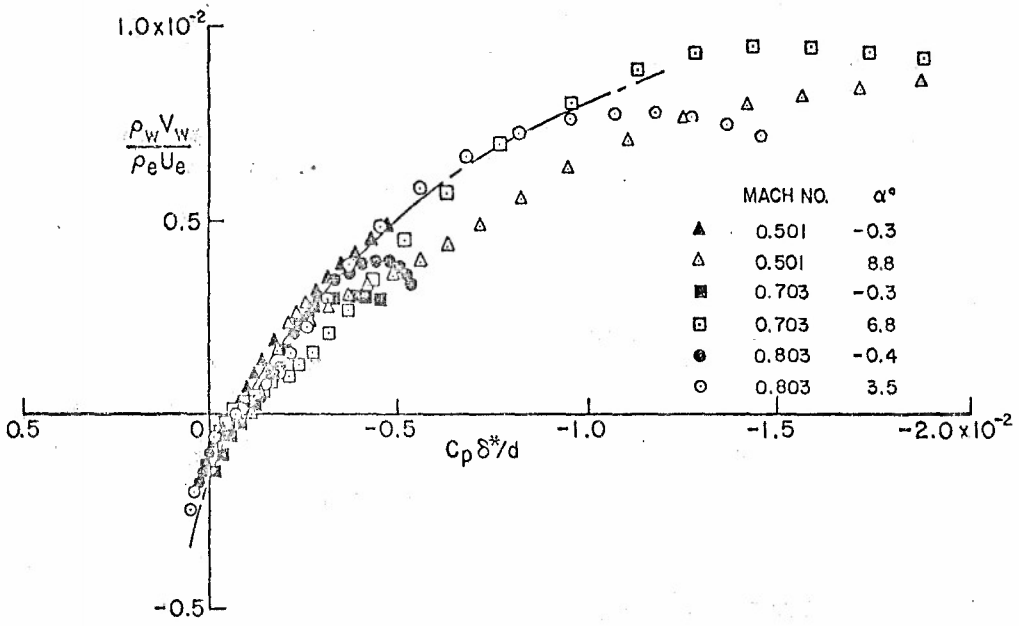


FIG. 5: CORRELATION OF WALL CHARACTERISTICS, $\delta^*/d \leq 0.25$

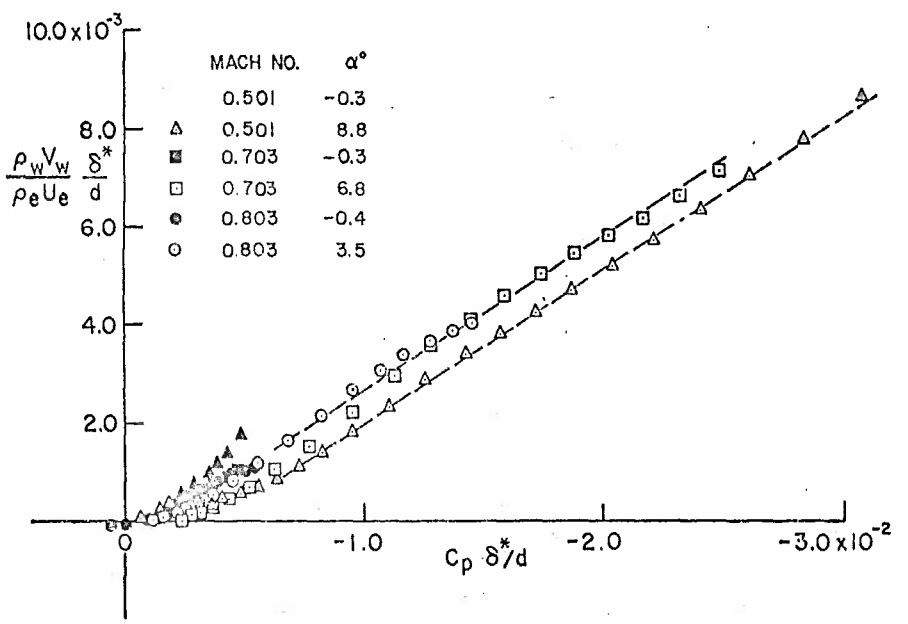


FIG. 6: CORRELATION OF WALL CHARACTERISTICS, $\delta^*/d > 0.25$

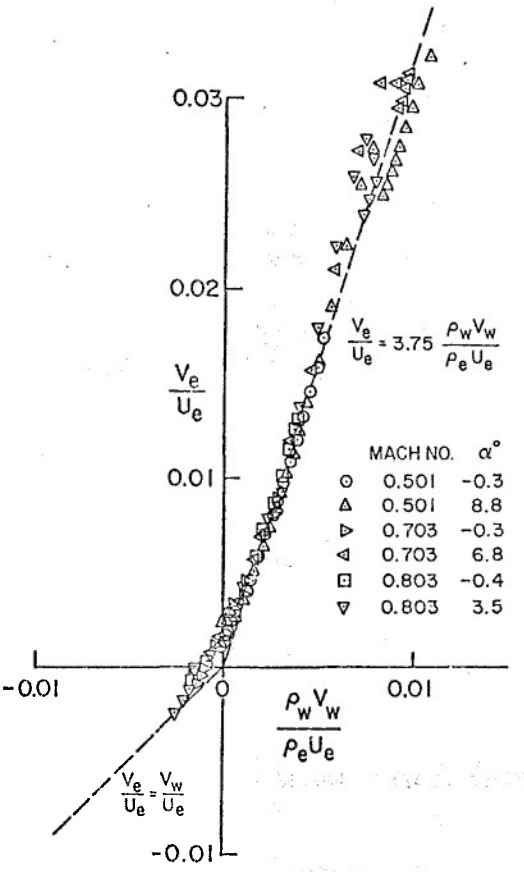


FIG. 7: CORRELATION OF NORMAL VELOCITY AT THE EDGE OF THE BOUNDARY LAYER TO THAT AT THE WALL

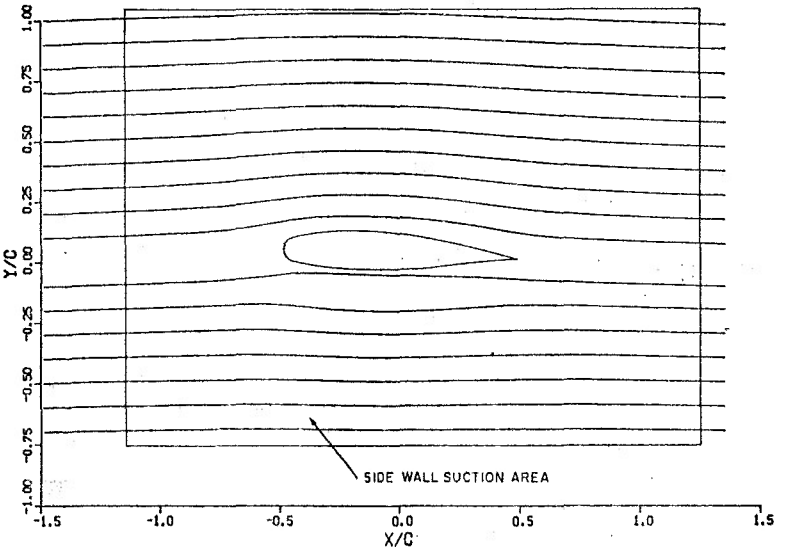


FIG. 8: STREAMLINES ABOUT THE AIRFOIL, ALONG WHICH BOUNDARY-LAYER DEVELOPMENTS ARE CALCULATED

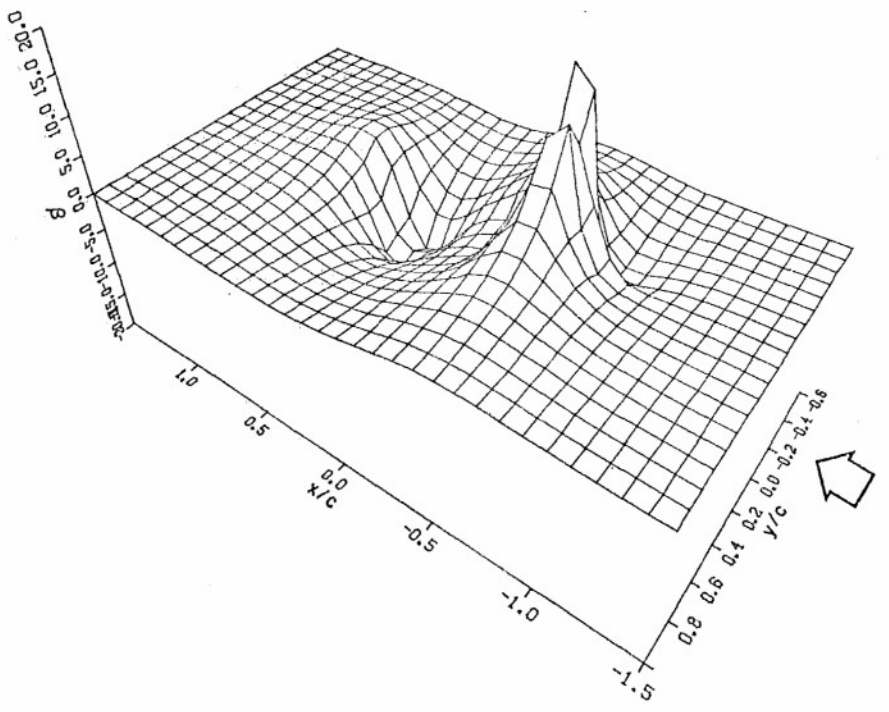


FIG. 9: DISTRIBUTION OF STREAMWISE PRESSURE GRADIENT β

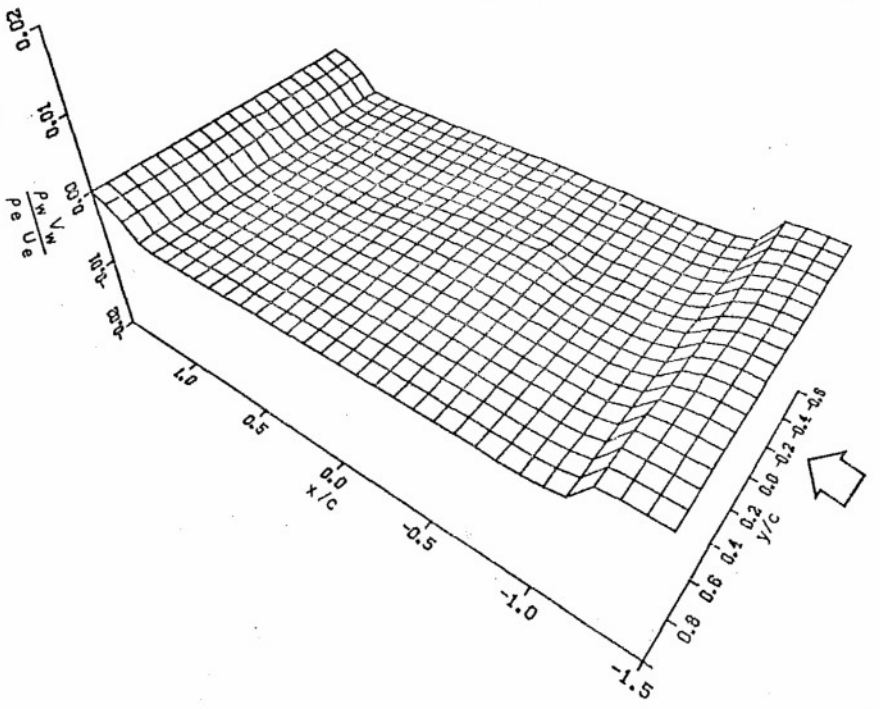


FIG. 10: DISTRIBUTION OF SUCTION VELOCITY AT THE WALL

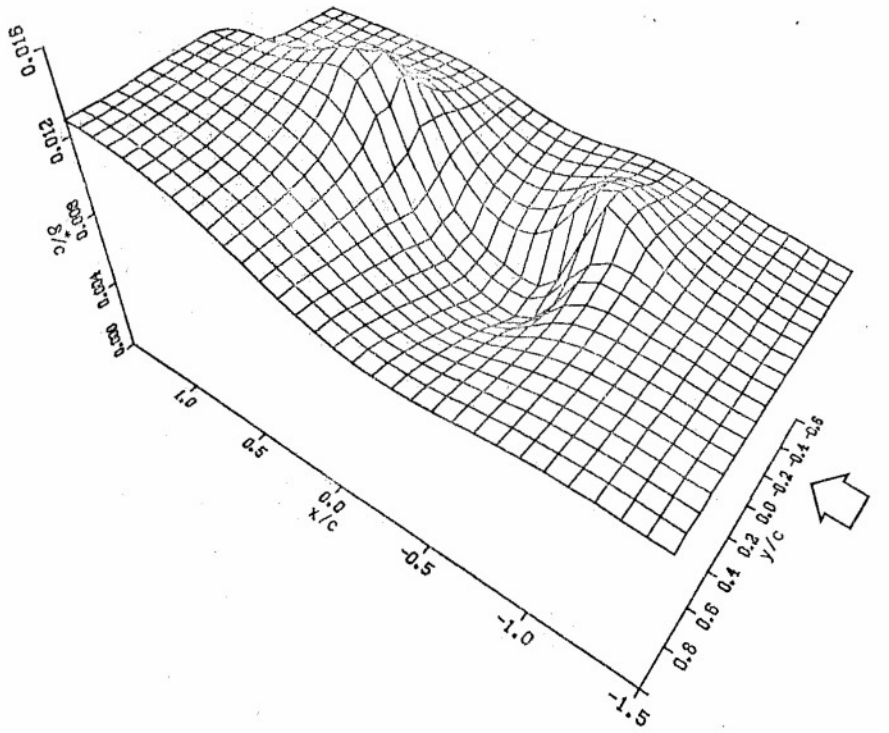


FIG. 11: VARIATION OF DISPLACEMENT THICKNESS, NO SUCTION

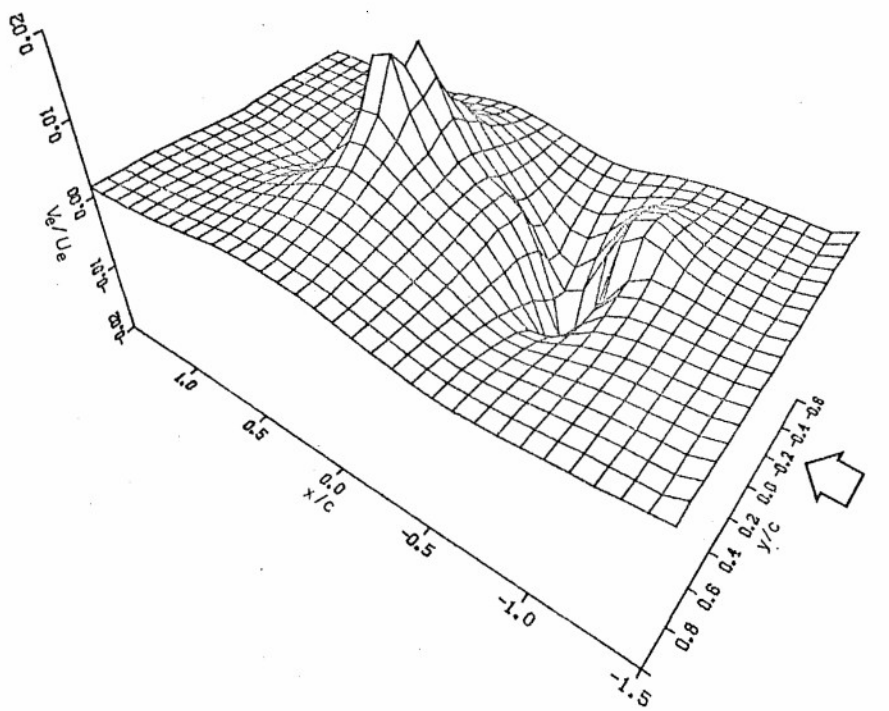


FIG. 12: VARIATION OF EFFECTIVE NORMAL VELOCITY INDUCED BY BOUNDARY LAYER, NO SUCTION

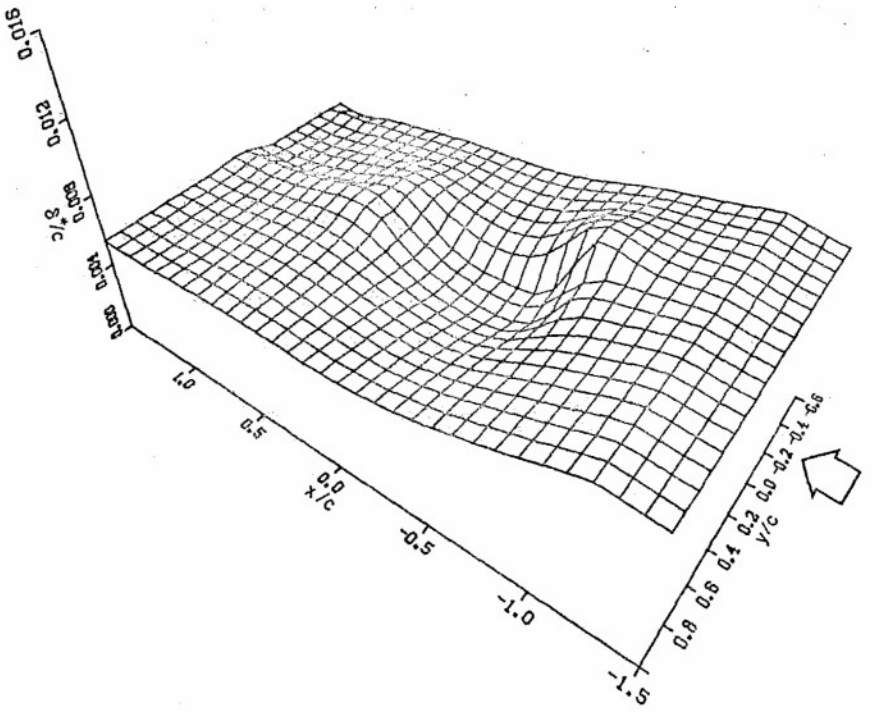


FIG. 13: VARIATION OF DISPLACEMENT THICKNESS, WITH SUCTION

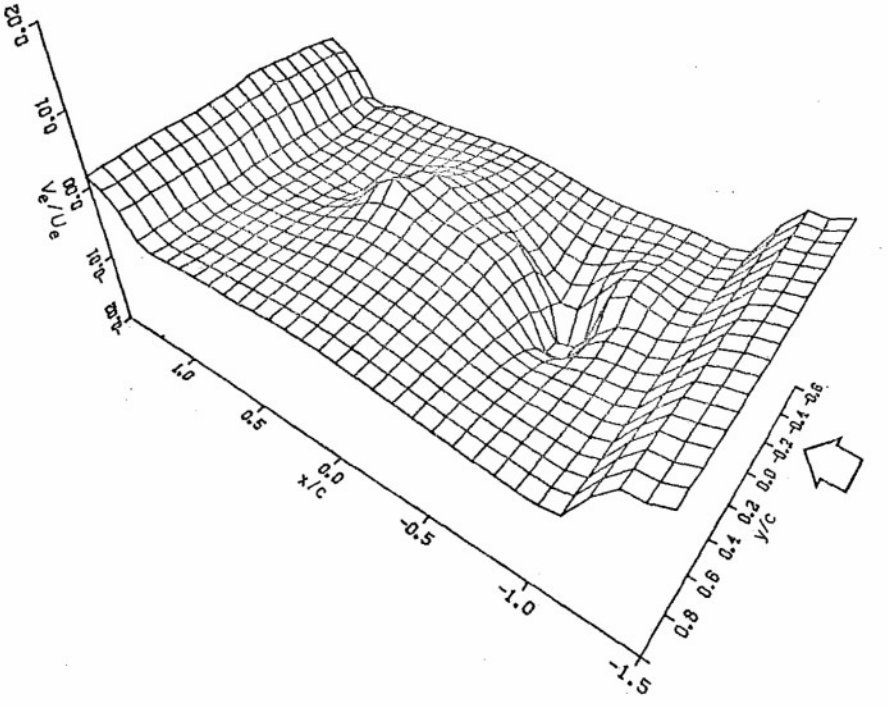


FIG. 14: VARIATION OF EFFECTIVE NORMAL VELOCITY INDUCED BY BOUNDARY LAYER, WITH SUCTION

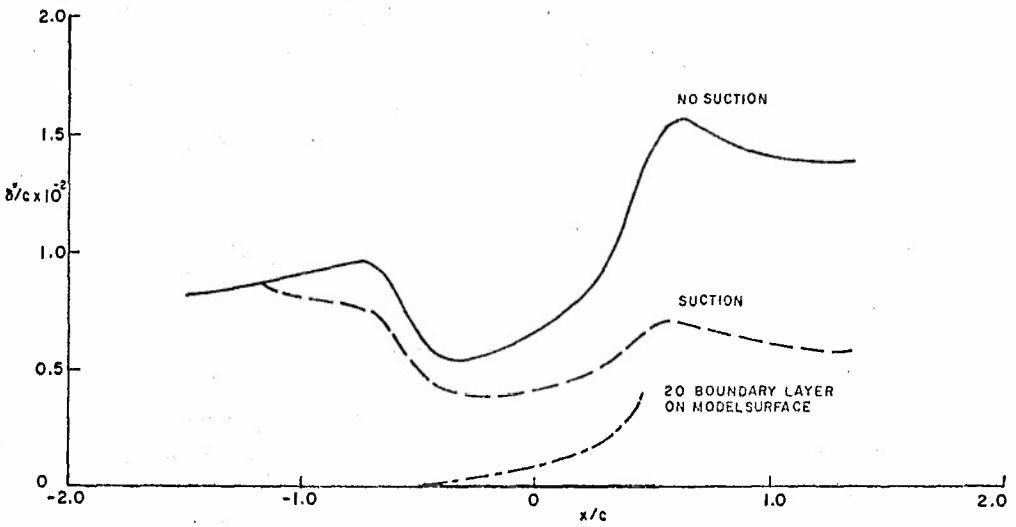


FIG. 15: DISPLACEMENT THICKNESSES WITH AND WITHOUT SUCTION ALONG STREAMLINE y/c = 0.1 AND COMPARISON WITH THAT FROM TWO-DIMENSIONAL BOUNDARY LAYER ON MODEL SURFACE

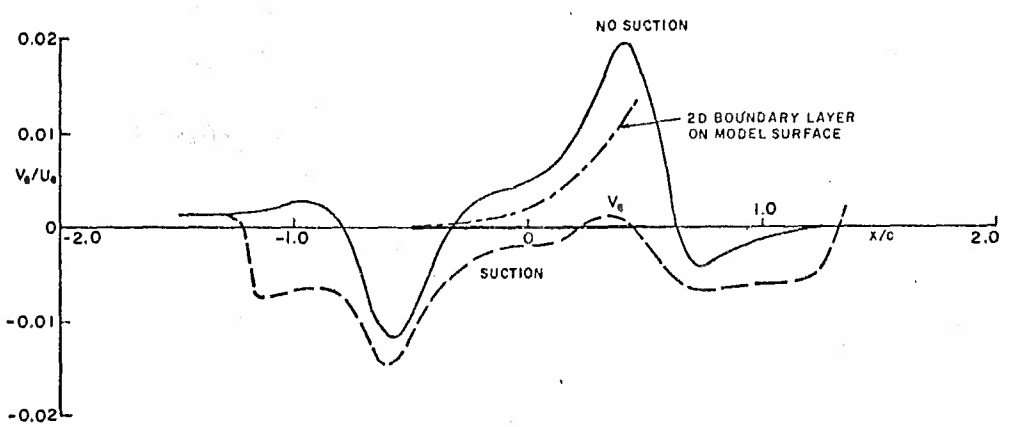


FIG. 16: EFFECTIVE NORMAL VELOCITIES INDUCED BY BOUNDARY LAYER WITH AND WITHOUT SUCTION ALONG STREAMLINE y/c = 0.1 AND COMPARISON WITH THAT FROM TWO-DIMENSIONAL BOUNDARY LAYER ON MODEL SURFACE

THREE DIMENSIONAL WALL CORRECTIONS FOR VENTILATED WIND TUNNELS

by
H. Holst

Deutsche Forschungs- und Versuchsanstalt für Luft- und Raumfahrt e.V.
Aerodynamische Versuchsanstalt Göttingen
Bunsenstrasse 10, D-3400 Göttingen, West-Germany

Summary

Correction factors δ_o and δ_1 (angle of incidence and flow curvature) have been calculated for ventilated wind tunnels by the vortex lattice method. For the cases of open and closed test sections these results agree very good with those calculated using the image technique. For ventilated walls (slotted and/or perforated) results are presented. The vortex lattice method is then used to calculate wall pressures in closed and ventilated test sections. Measurements in a 1.3m closed square test section were made using circular discs for blockage and a rectangular wing as a lift generator. The results (wall pressure distributions and force coefficients) are presented and will be a basis of comparison for wall pressures in a slotted wall test section.

Symbols

a	slot width
β	transonic parameter $\beta = \sqrt{1-M^2}$
B	width of tunnel
b	b = 2s spanwidth
c_X, c_D	drag coefficient
c_L	lift coefficient
c_{Pm}	average pressure coefficient
δ_X	dimensionless longitudinal velocity induced by the tunnel boundaries
δ_o	correction factor for angle of incidence
δ_1	correction factor for streamline curvature
D	diameter of circular disc
f	slot separation
Φ	velocity potential
γ	sweep back angle
H	tunnel height
K	slot geometry parameter
Λ	aspect ratio
M	Mach number
Δ_p	pressure drop through the wall
ρ	density
$\left.\begin{matrix} Q \\ R \end{matrix}\right\}$	porosity factors
s	semispan
s	space coordinate
u	longitudinal velocity induced by the boundaries
σ	σ = b/B relative spanwidth
V_∞	undisturbed flow velocity
x,y,z	coordinates

Indices

n	normal
∞	undisturbed
w	walls
x,y,z	in direction of x,y,z - coordinates
m	average value

1. Introduction

It is known, that the correction factors in closed test sections are positive and in open test sections they are negative. One should therefore achieve a zero correction with an appropriate design of a test section, which walls are partly open and partly closed. This is confirmed by calculations using potential theory and homogeneous boundary conditions, see figure 1. For open and closed test sections the results for interference factors δ_o (angle of incidence correction) follow the prediction of the image technique, and for slotted and/or perforated walls obviously a case of zero correction (at the position of the model) exists. Using partly open and partly closed tunnel walls to minimize the corrections war first proposed in [1], 1941.

2. The vortex lattice method

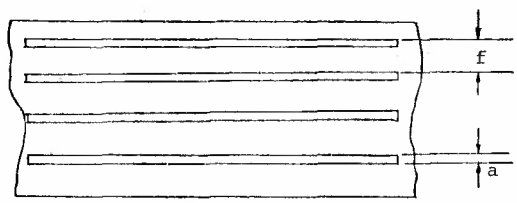
The above mentioned vortex lattice method was used for the calculations of interference factors. The tunnel boundaries are subdivided into panels, the singularities used are vortex squares and the boundary conditions are fulfilled at a set of control points as indicated in figure 2. The model is represented by singularities, i.e. horseshoe vortices for lift, and doublets, sources and sinks for blockage interference. This method was first proposed by Joppa [2] in 1967 and extended to ventilated walls by Borovic [3] in 1972. Figure 3 compares results of the vortex lattice method with other methods and again confirms its validity.

2.1 Homogeneous boundary conditions

The vortex lattice method uses homogeneous boundary conditions, which are fulfilled at a set of control points. For closed test sections, there is no doubt about that the velocity component normal to the wall has to be zero at the walls, and for open test sections there should be no pressure jump across the wind tunnel boundary, i.e. the tangential velocity must be zero (approximately) at the boundaries. For slotted and/or perforated walls it is more difficult to define an appropriate boundary condition according to the wall geometry of the tunnel. Detailed information about slot geometry factor K and porosity factor R is given in [3], [4], [5], [6] and [7], see also the references there.

The slot geometry factor K is defined as

$$K = -\frac{f}{\pi} \ln\left[\sin\frac{\pi a}{2f}\right]$$



where f is the slot separation and a is the slot width as indicated in the sketch above. The porosity factor R is defined (viscous flow through a porous medium) in the following equation:

$$v_n = \frac{R}{\rho V_\infty}\,\Delta_p$$

where v_n is the normal velocity through the wall, ρ is the density, V_∞ the undisturbed flow velocity and Δ_p the pressure drop through the wall.

So an approximate average boundary condition for slotted and/or perforated (ventilated) walls can be written as

$$\frac{\partial\phi}{\partial x} + K\frac{\partial^2\phi}{\partial x\partial n} + \frac{\beta}{R}\frac{\partial\phi}{\partial n} = 0$$

or, using the velocity components

$$u + K\frac{\partial v_n}{\partial x} + \frac{\beta}{R}v_n = 0$$

for the case of slotted walls with viscous effects, β in the transonic parameter and K and R according to the geometry of the walls.

$\frac{\beta}{R}v_n$ represents the pressure jump across the walls related to viscous effects and $K\frac{\partial v_n}{\partial x}$ represents the contribution to the pressure jump due to streamline curvature. Using this boundary condition, calculations have been performed.

2.2 Theoretical results of interference factors for square test sections

Figure 4 shows the influence of the porosity factor Q = R/(1+R) on wall interference. Q = 0 (i.e. R = 0) represents a closed test section, and Q = 1 ($R \to \infty$) represents an open test section. For Q = 0.465 (R = 0.869) we find the case of $\delta_o = 0$ (all four walls perforated), but obviously it is impossible to bring δ_o (angle of incidence correction) and δ_1

(flow curvature) to zero simultaneously. In figure 5 the slot geometry factor K was varied, and again we find δ_0 and δ_1 are not zero for the same value of K. Looking at the spanwise distributions of interference in figure 6, we find that at least the spanwise increase and the level of interference is less compared with interference factors for closed or open test sections (only looking at the absolute values). The experimentator can therefore be more confident applying one correction for the whole model, even for high values of relative spanwidths.

3. Calculation of wall pressures (lift generator)

3.1 Closed walls (Q = 0)

Again using the vortex lattice method, the wall induced longitudinal velocity components at the walls of the main cross section (i.e. $x = x_{model}$) have been calculated for a closed square test section and is shown as influence function f_L in figure 7. It is remarkable, that the curves intersect at $2y/B \approx 0.5$, so that the corresponding wall pressure signal at this spanwise station is nearly independent of the model spanwidth (compare [8]). If one choses this position to pick up wall pressures for interference prediction, one does not need to know the spanwidth of the model. On the other hand one looses accuracy by not taking the minimum/maximum value at the centerline of the top/bottom wall.

3.2 Variation of porosity factor Q

Figure 8 shows the variation of δ_{xw} (dimensionless wall induced velocity component at the wall) with porosity parameter Q. The method of calculation again proves its validity, because for an open test section (no pressure jump through the tunnel boundary) the result is zero - which is not indicated. The level of corresponding wall pressures decreases with increasing porosity parameter Q, so it will be more difficult to get a precise prediction of wall interference - not talking about how to define and to measure wall pressures at perforated or slotted walls.

4. Experiments

Measurements were made to pick up wall pressures and forces simultaneously.These measurements were carried out in a 1.3m closed square test section at DFVLR Braunschweig: Blockage and lift induced wall pressures were investigated separately so far as possible.

4.1 Investigation of blockage effects

Circular discs were used as models and the drag coefficient is plotted vs. the diameter in Figure 9. The blockage of the smallest model was 4.2 per cent, the largest model had 11.6 per cent blockage. The intention was to have significant blockage effects, and looking at the results, you see, that they obviously need to be corrected. Figure 10 shows the wall pressure distribution of the 40cm disc. A correlation with theoretical results has not yet been made.

4.2 Lift generator

The model was a rectangular wing with trailing edge flap and a small fuselage shown in figure 11. The model was mounted on a rear sting. Figure 12 shows c_L vs. c_D. For comparison purposes, the curve for induced drag was drawn. The results presented there have been corrected using $\delta_0 = 0.143$ which results in $\Delta\alpha = 2.6^\circ$ as maximum angle of incidence correction. This should be mentioned, because otherwise no comparison can be made to $c_L^2/\pi\Lambda$. Figure 13 shows the wall pressure distribution. The wall pressure coefficients were averaged over different test series to get a higher accuracy. Naturally, the rectangular wing not only generates lift, but also blockage.

4.3 Separation of lift and blockage effects

It can be seen, that the curves are not antisymmetric to $c_{p_m} = 0$. By adding or subtracting the pressure signals of top and bottom walls from each other, blockage and lift influences can be separated and used for corrections. This is shown in figure 14. For lift there is indicated a theoretical result, which was calculated for not exactly the same relative spanwidth as the model had. Therefore, there are some discrepancies.

5. Further experiments with slotted walls

The Braunschweig wind tunnel used for the measurements presented above is also equipped with a 1.3m square slotted test section, which is approximately 10 per cent geometrically open. It is intended to measure pressures at the solid parts of the walls at the same positions as now with the closed test section. The measurements presented here will be a basis of comparison for the further experiments and the parametric studies of wall interference (porosity factor Q and slot geometry factor K) will be helpful in the interpretation of those results.

6. Concluding remarks

The main problem for ventilated wall test section interference calculations is that a

priori the slot geometry factor K and the porosity factor Q used are unknown talking about effective values. It is, therefore, necessary to carry out measurements in the same tunnel using the same models and try to correlate the results to get further information about ventilated wall interference. The theoretical calculations indicate, that by using ventilated walls, the interference correction situation can be ameliorated, because level and inhomogeneity of δ_0 and δ_1 are reduced significantly. Corrections can then be performed for the whole model with a higher accuracy.

References

[1] Ginzel, J.
Riegels, F.
Vandrey, F.
Korrekturfaktoren fuer Windkanäle mit teilweise offener und teilweise geschlossener Meßstrecke.
Bericht 41/1/6 DFVLR-AVA Göttingen, 1941

[2] Joppa, R.G.
A method of calculating wind tunnel interference factors for tunnels of arbitrary cross sections.
NASA-CR-845, July 1967.

[3] Borovik
Wasserstrom, E.
Rom, J.
Wind tunnel boundary interference corrections.
Theoretical calculations.
Technion-Israel Institute of Technology,
Haifa, Israel, Aeronautical Research Center,
Laboratory Report 0-124, 1972

[4] Baldwin, B.S.
Turner, J.B.
Knechtel, E.D.
Wall interference with slotted and porous boundaries at subsonic speeds.
NACA T.T. 3176, May 1954

[5] Bleekerode, A.L.
Lift interference at low speed in wind tunnels with partly ventilated walls.
Memo WD-75-085, NLR, The Netherlands, 1975

[6] Holst, H.
German activities on wind tunnel corrections.
AGARD-R 692, 1980

[7] Holst, H.
Berechnung von Windkanalinterferenzen nach dem Wirbelgitternetzverfahren.
Bericht IB 157-80 A 01, DFVLR-AVA, 1980

[8] Schulz, G.
Bestimmung von Strahlgrenzenkorrekturen aus Differenzdruckmessungen an den Wänden des Windkanals.
DFVLR Bericht DNW-WAK02

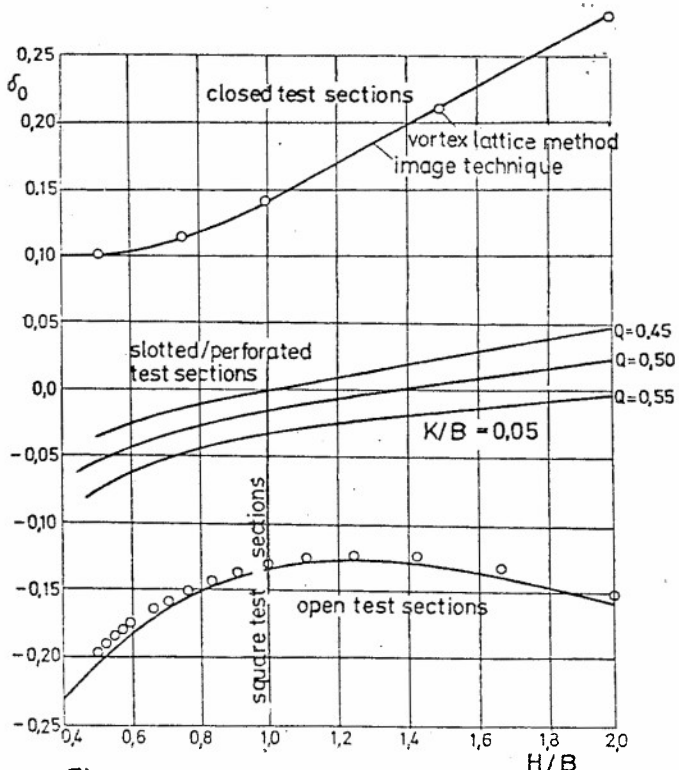


Fig.1 :Minimization of interference factor by "partly open and partly closed" test sections.

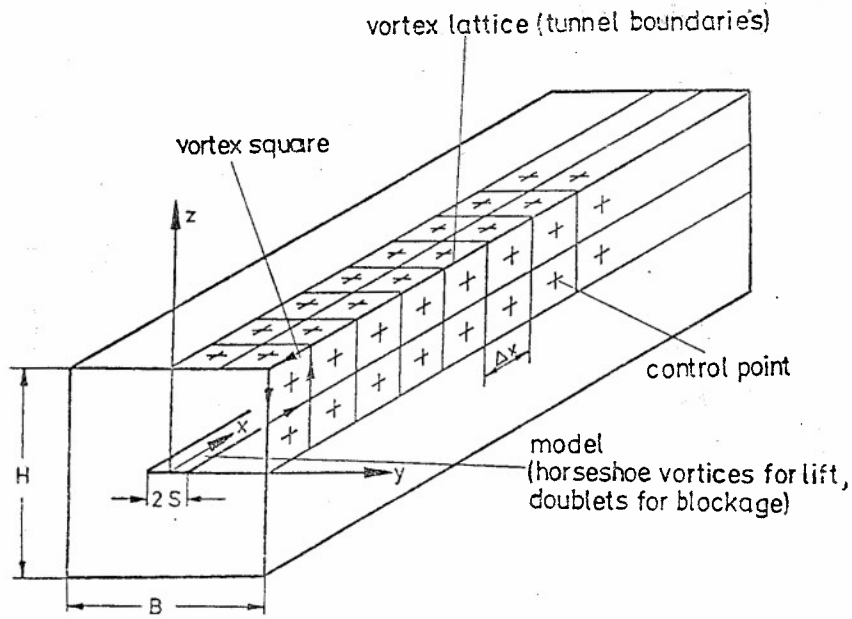


Fig. 2 :Coordinate system and definitions.

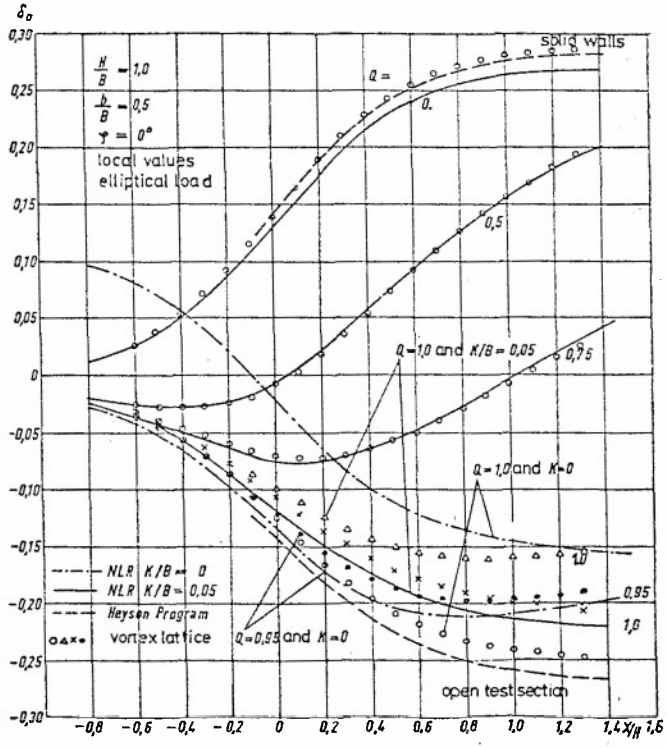


Fig. 3 :Ventilated walls, comparison of different methods.

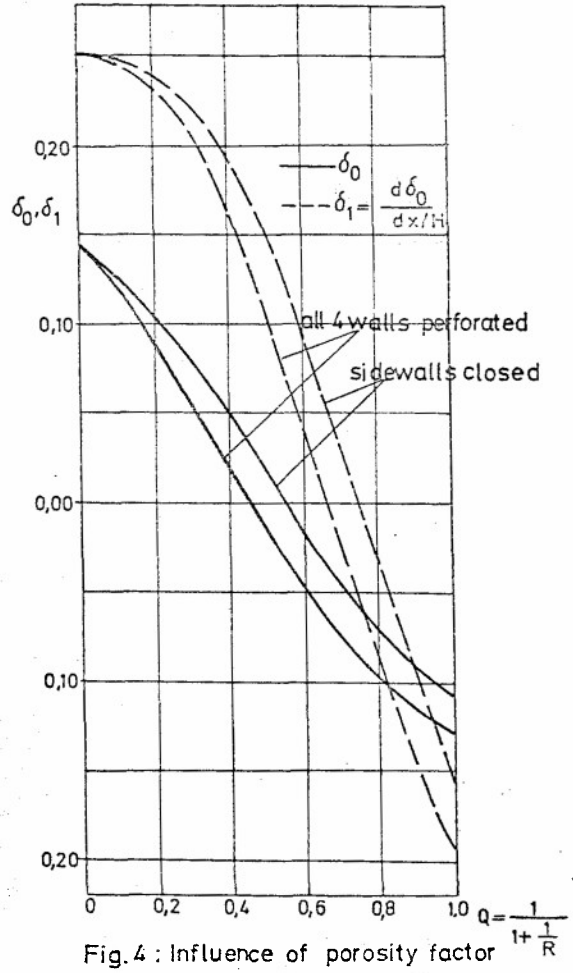


Fig. 4 : Influence of porosity factor R on wall interference.

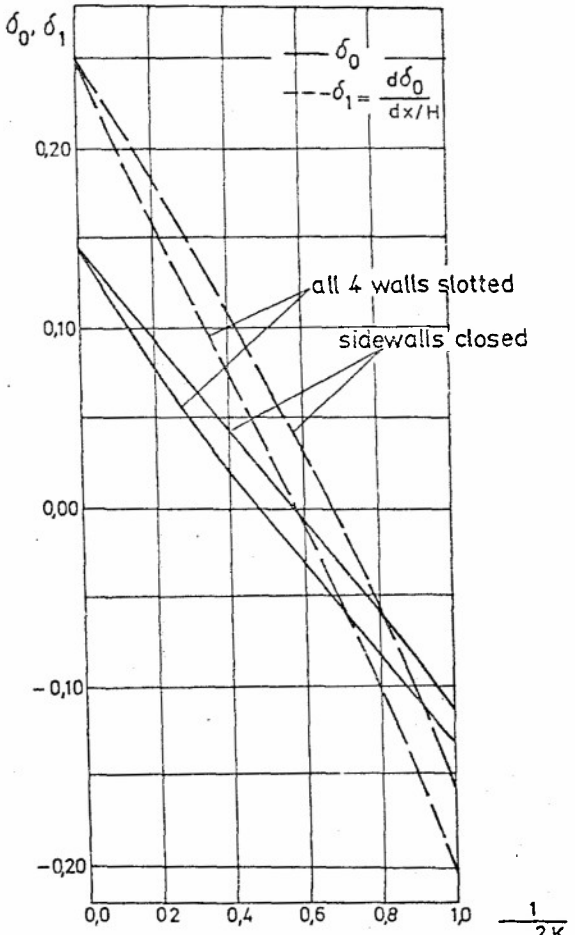


Fig. 5 : Influence of slot geometry factor K on wall interference.

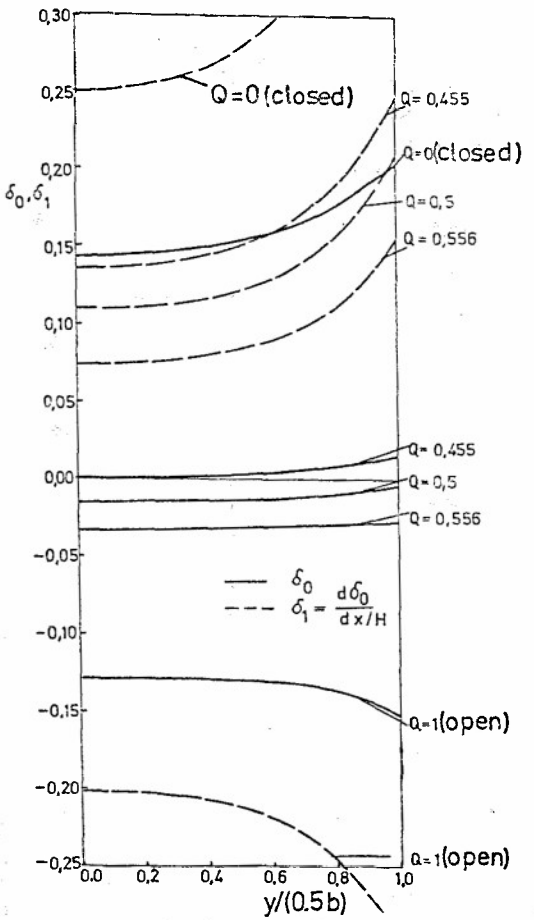


Fig. 6 : Spanwise distributions of interference factors for a square test section.

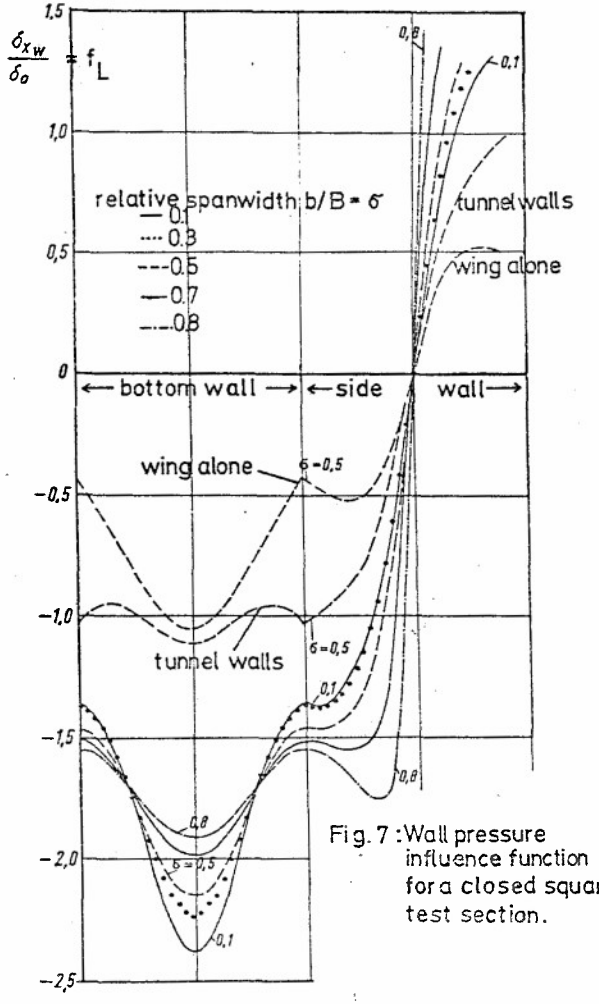


Fig. 7 : Wall pressure influence function f_L for a closed square test section.

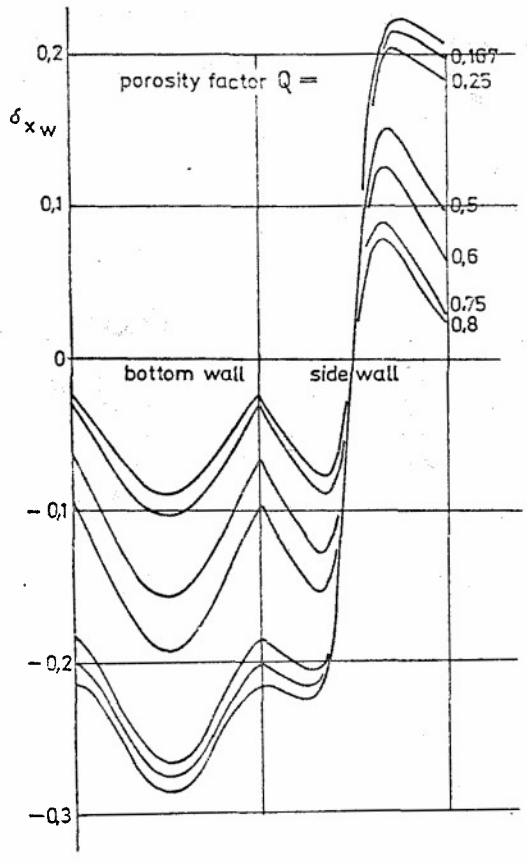


Fig. 8 : Influence of porosity factor on δ_{xw} in the main cross section.

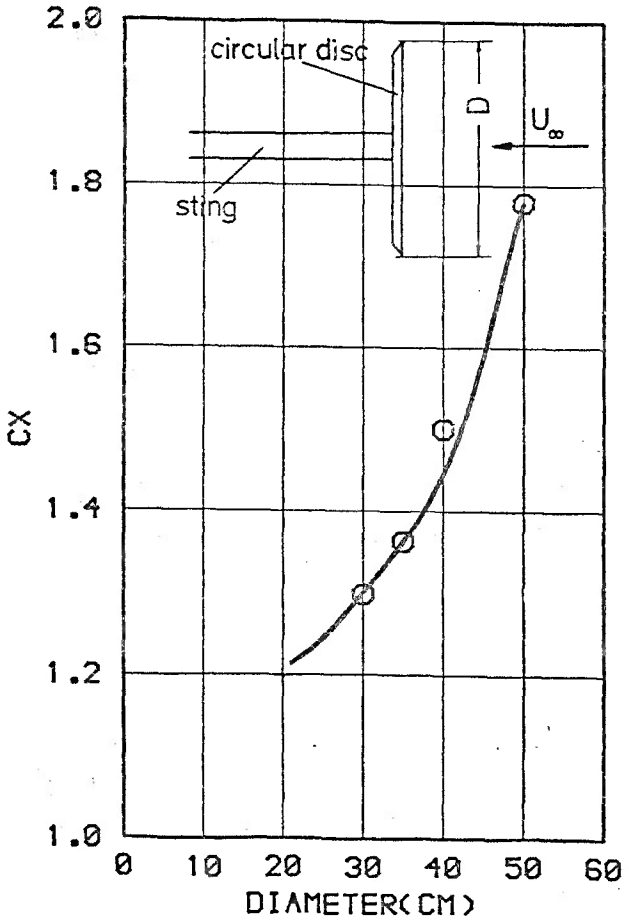


Fig. 9 : Test results for circular discs.

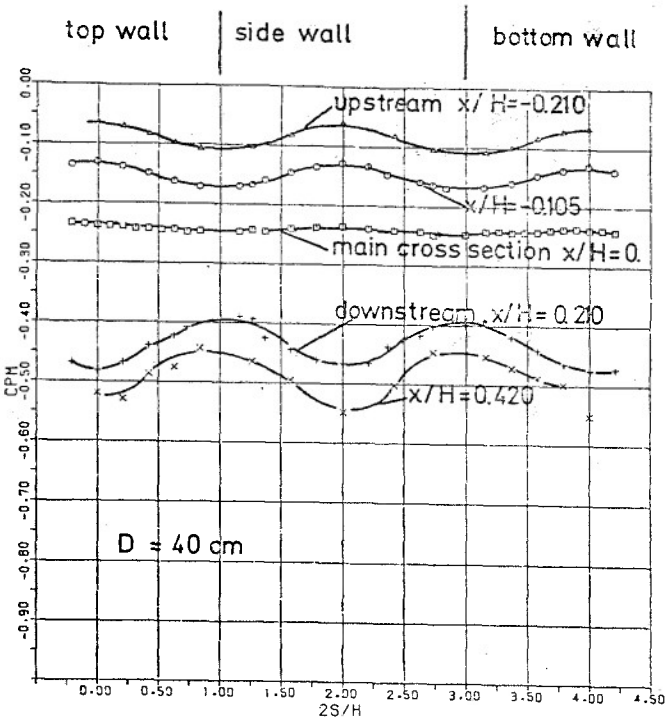


Fig.10 : Circular disc, wall pressure signals
7.436 percent blockage

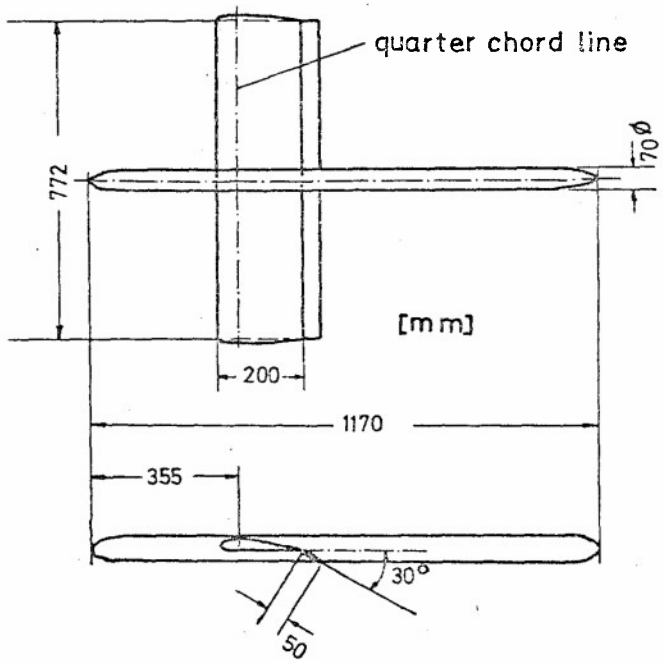


Fig. 11 : Lift generator
Wing profile: CLARK Y
Profile of trailing edge flap: CLARK Y
$S_{wing} = 0.1544\ m^2$
$S_{flap} = 0.039\ m^2$

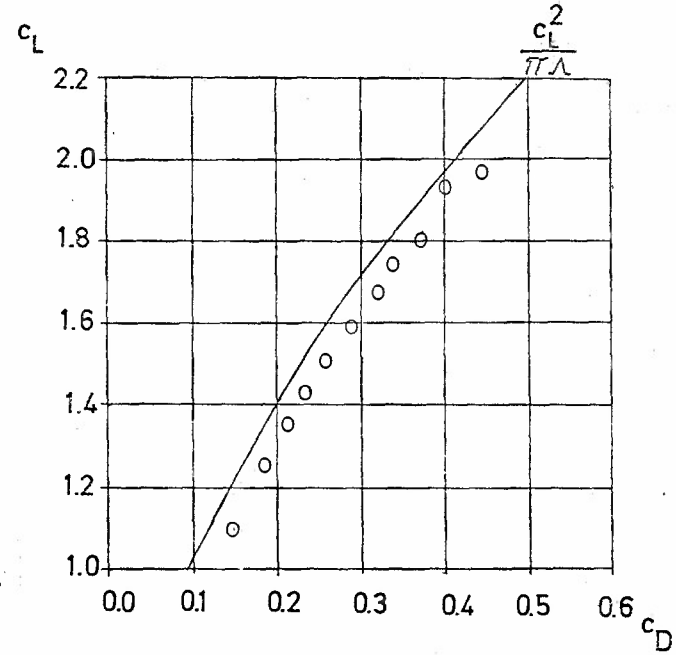


Fig. 12 : Test results for lift generator

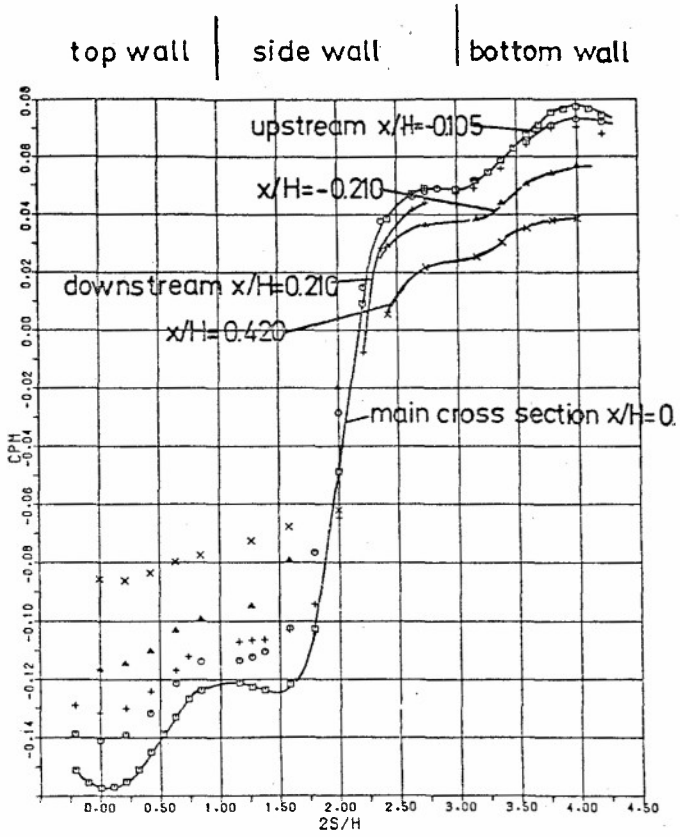
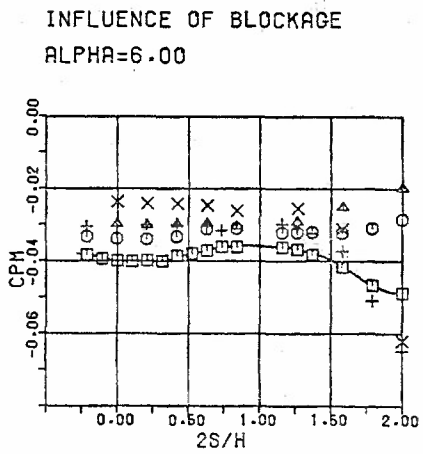


Fig. 13 :Rectangular wing, wall pressure signals



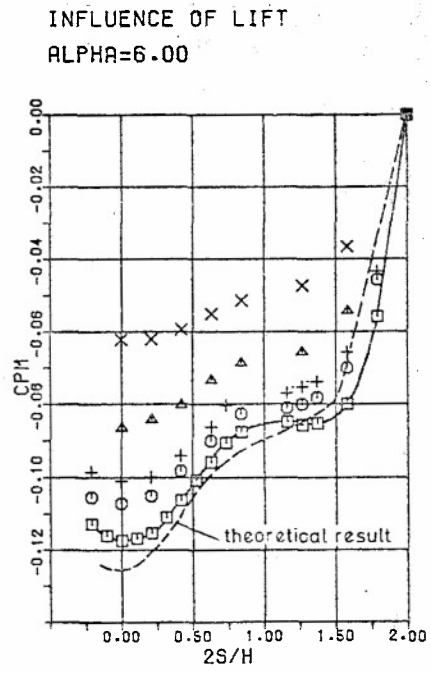


Fig. 14: Rectangular wing, separation of lift and blockage influences.

MEASURED BOUNDARY CONDITIONS METHODS FOR 2D FLOW

by

J. Smith
National Aerospace Laboratory NLR
Anthony Fokkerweg 2
1059 CM Amsterdam
The Netherlands

SUMMARY

Modern developments in wind tunnel wall correction methods are for a major part directed towards the use of in-situ measured boundary conditions in order to eliminate the need to describe the complicated aerodynamic characteristics of test section walls. This paper presents a short general review of the principles of such methods for 2D flow. The major practical problems associated with the application of the methods are discussed and some typical results are shown.

LIST OF SYMBOLS

A_n	=	complex strength of pole of order n
B	=	test section width
c	=	aerofoil chord length
c_{d_w}	=	wake drag coefficient
cl	=	lift coefficient
c_p	=	pressure coefficient
$\bar{c}_p$	=	symmetrical part of wall-c_p: $\bar{c}_p = \frac{1}{2}\{c_p(\text{roof}) + c_p(\text{floor})\}$
$\bar{\Delta}c_p$	=	antisymmetrical part of wall-c_p: $\bar{\Delta}c_p = \frac{1}{2}\{c_p(\text{roof}) - c_p(\text{floor})\}$
H	=	test section height
i	=	imaginary unit : $\sqrt{-1}$
M	=	Mach number
ΔM	=	Mach number correction : $M_c = M_t + \Delta M$
p	=	static pressure
p_t	=	stagnation pressure
q	=	complex conjugate velocity : $q = u - iv$
u	=	axial perturbation velocity component, non-dimensionalised with reference velocity
v	=	vertical perturbation velocity component, non-dimensionalised with reference velocity
x	=	distance along test section axis
X_F, X_R	=	positions of, respectively, front and rear face of control volume, non-dimensionalised with test section height, defined in figure 1
z	=	complex co-ordinate = x + iy
z_o	=	position of poles of model representation
α	=	incidence
$\Delta\alpha$	=	incidence correction : $\alpha_c = \alpha_t + \Delta\alpha$

Subscripts

c	=	corrected for wall interference
i	=	associated with the interference flow field
m	=	associated with the hypothetical model-induced flow field
t	=	not corrected for wall interference

1. INTRODUCTION

Modern developments in wind tunnel wall correction methods are mainly directed towards the use of in situ measured boundary conditions, which should replace the well-known Baldwin type of boundary condition and consist of velocity distributions measured at or near the test section walls.

The methods do not require any explicit information about the aerodynamic characteristics of the test section walls. Consequently, the methods are, in principle, applicable to any type of wall, either ventilated or solid, plane or curved. Besides, they can be applied to each separate data point taken, without the necessity to refer to calibration models.

This paper presents a short general review of the fundamentals of methods using measured boundary conditions, for 2D flow, in an attempt to show their mutual connections. The various methods will not be discussed in detail and are sometimes merely mentioned, but appropriate references will be given. Subsequently, a number of practical problems will be discussed, which are considered to be of general interest, even if only to a specific type of method. Finally, some applications of the two methods available at NLR will be demonstrated.

2. FUNDAMENTALS OF 2D WALL CORRECTION METHODS USING MEASURED BOUNDARY CONDITIONS

Most present-day methods for 2D flow still assume the flow inside the test section to be a superposition of a model-induced flow field, a wall-induced flow field and, of course, the oncoming main flow. Consequently, these methods are basically subsonic and their interpretation of the wall interference phenomenon is strictly identical to that of classical wall interference theory. Some aspects may have been modified but actually the basic difference is only the formulation of the boundary conditions. Within this framework, two types of method can be distinguished. A third type of method does not appeal to the superposition principle.

For the first types of method, consider the complex conjugate velocity $q = u - iv$. It is assumed that q is a superposition of the model-induced velocity q_m and the wall-induced or interference velocity q_i, generated by the walls in response to q_m. The model-induced velocity field q_m is the hypothetical velocity field that would exist if the model were in unbounded flow with nominally the same surface Mach number distribution and the same attitude relative to the test section walls. Besides, it is assumed that q_i is analytic (i.e. satisfies the Cauchy-Riemann equations) throughout the test section and that q_m may be expressed in terms of the principal part of a Laurent series. That is :

assume : a. $q(z) = q_m(z) + q_i(z)$ (2.1)

b. $q_i(z)$ analytic throughout the test section (2.2)

c. $q_m(z) = \sum_{n=1}^{\infty} A_n (z - z_o)^{-n}$ (2.3)

where A_n is the complex singularity strength of order n and z_o is the location of the poles. The point z_o must lie inside the model contour and all velocities are non-dimensionalised with the oncoming reference velocity. For convenience, expression 2.3 will be called the "model representation" throughout this paper.

Since q_i is analytic throughout the test section, it is completely determined (apart from a constant of integration) inside a closed contour C by the distribution of either u_i or v_i on C. This boundary value problem may be solved by means of an appropriate form of "Schwarz's formula" (e.g. Ref.1) so, for convenience, methods based on this principle will here be called "Schwarz type" of methods. They require the measurement of only one velocity component on C, e.g. the axial component u. In that case u_m on C must be calculated from a model representation (Eq. 2.3) in order to determine $u_i = u - u_m$ on C. An additional condition has to be imposed to determine the (in this example imaginary) constant of integration. Methods of this type have been published in reference 2-4 and 10.

A second type of method requires the measurement of both velocity components on C but no model representation at all. Again, consider the assumptions 2.1 - 2.3. Then, by a straightforward application of the "residue theorem", for any point inside C :

$$\frac{1}{2\pi i}\oint_C \frac{q(\zeta)}{\zeta - z}\,d\zeta = \frac{1}{2\pi i}\oint_C \frac{q_i(\zeta)}{\zeta - z}\,d\zeta + \frac{1}{2\pi i}\oint_C \sum_{n=1}^{\infty} \frac{A_n}{(\zeta - z)(\zeta - z_o)^n}\,d\zeta =$$

$$= q_i(z) + \sum_{n=1}^{\infty}\left\{\frac{A_n}{(z - z_o)^n} + (-1)^{n-1}\frac{A_n}{(z_o - z)^n}\right\}$$

Obviously, the summation yields zero, hence :

$$q_i(z) = \frac{1}{2\pi i}\oint_C \frac{q(\zeta)}{\zeta - z}\,d\zeta \qquad (2.4)$$

Consequently, if the distribution of the velocity vector $q = u - iv$ is known on C, $q_i(z)$ can be calculated without any explicit information about the model: the model representation has been eliminated. Note the similarity between equation 2.4 and Cauchy's formula :

$$q_i(z) = \frac{1}{2\pi i}\oint_C \frac{q_i(\zeta)}{\zeta - z}\,d\zeta \qquad (2.5)$$

The latter, however, would require q_i instead of q to be known on C and, therefore, is much less convenient. For convenience, methods based on equation 2.4 or 2.5 will here be referred to as "Cauchy type" of methods. A method of this type has been published in reference 5.

A third type of method does not need the assumptions 2.1 - 2.3 and requires measured pressure distributions near the walls and on the model. From these, an "effective" model shape (i.e. "corrected" for viscous effects) is computed by solving the so-called "inverse" problem. This effective shape is subsequently used to compute its pressure distribution in unbounded flow, iterating on Mach number and angle of attack until a model pressure distribution is obtained which, within a specified overall error, matches with the originally measured one. If this goal can be achieved, the α-M-condition producing the best match (i.e. the least overall error) is the corrected free-stream condition. If the attainable least overall error remains larger than the specified one, the case is judged "incorrigible". Methods of this type might be called "Matching type" of methods and are described in references 6 and 7.

Since the Matching type of method does not appeal to the superposition principle, it can be made applicable to any range of Mach number. Besides, it creates the possibility to compare the corresponding measured and, almost fully, corrected model pressure distributions directly. Therefore, it seems more accessible for an interpretation of the corrigibility of a data point. In Cauchy and Schwarz types of method, the corrigibility criterion is "hidden" in the variations of u_i and v_i along the model. Strictly, a data point is only corrigible if $\partial u_i/\partial x = \partial v_i/\partial x = 0$ in a neighbourhood of the model. In practice, however, the judgement of corrigibility will depend on both some limiting value of the interference velocity gradients and the model's sensitivity to them.

A Cauchy type of method requires extremely little computational effort and is applicable to almost any kind of model. The other two types require a model representation, either in the form of equation 2,3 or through an inverse computation, which seems hardly attractive or even feasible for models more complicated than a simple "clean" aerofoil. Though technically quite a difficult task, solving the problem of measuring the complete velocity vector along the boundary contour (in an economical way) should be more rewarding than designing a wide variety of complicated model representations. In the meantime, Cauchy type of methods are very convenient for use in solid-wall wind tunnels, because it seems plausible that the measurement of the v-component can be omitted in that case by assuming v = 0 at the walls.

A Schwarz type of method is much less elaborate than the Matching type and, for a "clean" aerofoil, requires only little more computational effort than the Cauchy type. Like the Cauchy type, it is basically restricted to subsonic flows but might still be sufficiently accurate in the low-transonic regime. It is a very convenient type for aerofoils in ventilated test sections but can be used for any type of test section. Besides, comparisons between measured and hypothetical model-induced velocities (e.g. Fig. 3) might be useful as a diagnostic tool in a process of wall geometry optimization by, for instance, a variation of slot width in axial direction. (The differences, i.e. the u_j-distributions, are expected to be indicative of local "sources" of blockage and upwash).

For completeness, a summary of principal characteristics of recent (1981) European wall correction methods is presented in table 1. The four methods considered are of either the Cauchy or Schwarz type. The remainder of this paper will mainly bear upon these two types of method.

3. PRACTICAL PROBLEMS

Although the methods are theoretically quite straightforward, their application gives rise to a number of, mainly experimental, problems. Those of general interest are, obviously, related to the measurement of the boundary conditions. A problem of more specific interest to Schwarz type of methods is associated with the model representation. These topics are discussed in this section.

3.1 Measurement of wall data

The horizontal velocity component is generally derived from measured pressure coefficients. Unfortunately, a generally accepted means for measuring distributions of the vertical component v as a routine does not yet exist.

In conventional and compliant solid-wall test sections, pressures are measured by means of orifices in the test section floor and ceiling. Flow direction is derived from the measured actual wall shape, possibly corrected for wall boundary layer displacement thickness. For example, see table 1: RAE, ONERA and NLR II methods ("present instrumentation").

In ventilated-wall wind tunnels, the flow very near the walls is essentially three-dimensional, contrary to the two-dimensional character of the flow in the central region. In principle, the "wall" data should be gathered inside this 2D core flow, for instance by means of "pressure rails" (e.g. table 1 : method NLR I). Unfortunately, there is no proven criterion with respect to a required minimum distance between the adopted boundary contour and the adjacent test section wall, for instance in terms of wall geometry. Consequently, there is no uniformity on this point. An investigation of the importance of this aspect will be discussed in section 4.3.

Because of local disturbances, the theoretical possibility to deduce the test section calibration from empty-test-section wall data does not seem feasible. These local disturbances may be caused by pressure hole imperfections as well as by a lack of flow uniformity due to the test section design and to interference by the instrumentation and possible supports.

Nevertheless, measurements of wall data in the "empty"-test section (i.e. the actual test set-up, so with possibly the wake rake, supports, probes, etc. but without the aerofoil model) are essential. Subtracting these data from those obtained with the model (thus redefining the zero-level of the wall data distributions) eliminates the effects of the aforementioned local disturbances to a major extent. This precaution can even be of vital importance if the measured wall data are to be extrapolated. Of course, in this procedure the usual test section calibration (e.g. obtained with a long static-pressure pipe along the test section centre line) must separately be applied.

3.2 Range of measured wall data

In principle, boundary values should be measured on a contour enclosing the model, e.g. such as depicted in figure 1, but generally they are measured only at or near the walls and over a finite length. Depending on the formulations of the problem (infinite strip or rectangular domain) the measured data must be extrapolated to up- and downstream infinity (Fig. 2a and e.g. Table 1: RAE method) or interpolated across front and rear face (Fig. 2b and e.g. Table 1: NLR II method as well as Ref. 4). If the range of measured wall data is sufficiently large, the contributions of front and rear face are negligible so the wall data may be truncated (e.g. Table 1: ONERA method). In an alternative approach, it is assumed that, near the walls, v becomes zero at some distance beyond the ventilated part of the test section (Fig. 2c and Table 1: NLR I method). In this option the extrapolation is limited to a finite length (The NLR I method uses the geometry of figure 2c for both ventilated and solid walls).

The required accuracy of the extrapolations and interpolations depends on the available range of measured wall data, the type of test section and the formulation of the boundary conditions. Solid-wall wall pressures tend to their asymptotic values much faster than those in a ventilated test section, especially in downstream direction (e.g. Fig. 3), therefore the interpolation or extrapolation problem is probably smaller for a solid-wall test section. The example shown in figure 4 illustrates the effects of the formulation of the boundary conditions. In this example the assumed error in the extrapolated wall pressures hardly affects the results at the hypothetical model position: $x = 0$ in case A (corresponding with the boundary conditions of figure 2a), but has a serious effect in case B (corresponding with figure 2c). Note, however, that if the assumed error distributions were centred about $x/H = -1.0$, the result of case A (at $x = 0$) would also be seriously affected (the curve would simply be translated).

An other example is shown in figure 5. The data were obtained in the NLR PT in its solid-wall configuration. The u_j-distributions are according to the RAE method (Table 1). One extrapolation (of the symmetrical part of the wall pressure distribution) is based on the level of the last measured point and the slope according to the last two points. The other one accounts for the level at $x \rightarrow \infty$ associated with wake drag. The resulting differences in u_j ("blockage") are appreciable in the extrapolation area, but not too bad at the model position (about 5% of the correction or 0.001 in the Mach number correction).

Finally, an example of a linear interpolation across front and rear face is shown in figure 6. This example concerns data from the RAE 8 x 8ft solid-wall wind tunnel and interference velocities calculated by means of the NLR II method (Table 1). The figure suggests that such a linear interpolation becomes sufficiently accurate if $X_R \approx / X_F / \approx 1.0$. However, it also turned out that in that case the contributions of front and rear face to u_j and v_j at $x = 0$ have become almost negligible. Consequently, a truncation at these positions would work as well. Apparently, a linear interpolation is not very effective and should be replaced by a more refined one if a smaller range of measured wall data is available.

From these examples it may be concluded that, if necessary, interpolations or extrapolations should be selected and evaluated carefully.

3.3 Model representation

In classical wall interference theory, the aerofoil model is generally represented by a vortex, a source and a "volume" doublet. Because of the assumed infinite test section length, their exact position seemed of minor importance. The strengths of the poles are estimated from lift, wake drag and model volume, respectively. A consequence is that the doublet strength does not vary with incidence, although it should, as demonstrated both theoretically and experimentally in figure 7. The magnitudes of the calculated interference velocities are proportional to the strengths of the poles.

For Schwarz type wall correction methods, errors in the strengths of the model poles do not propagate proportionally into the resulting wall corrections, because $u_j = u - u_m$ and u has a fixed measured magnitude. Besides, the distribution of u is also fixed spatially. Therefore, the location of the model poles in the test section requires special attention.

An improved model representation has been published by Mokry (Ref. 8). This "higher-order" model representation accounts for poles up to any order desired. Accordingly, the influence of pole location on u_m can be eliminated by increasing the order until convergence is obtained. Besides, it turns out that, in incompressible flow, the increase of the displacement effects with increasing incidence is properly accounted for if the strengths are calculated directly from the line integrals of the velocity distribution on the model (Fig. 8) instead of applying the linearizations also suggested in reference 8. For compressible flow, a modified Goethert rule, as recommended in reference 2, is necessary to estimate the displacement effects accurately (Fig. 8). In this model representation, the equivalent incompressible singularity strengths are written as :

$$A_n = -i \oint_\sigma \left(\frac{x}{\beta} + iy\right)^{n-1} \cdot \left(\beta - \frac{1}{2} M_\infty^2 \sin 2\theta\right) (\vec{V}_t . \vec{ds}) \quad (3.1)$$

where σ is the aerofoil contour, x and y are the model co-ordinates, θ is the model's surface slope, V_t is the total surface velocity and ds is the increment following the model contour. Note that A_n is the complex strength in the equivalent incompressible plane, but that the right-hand-side contains only quantities that belong to the physical plane (For more details, see reference 2).

The model representation of equation 3.1 is incorporated in the method NLR I (Table 1). Some examples of its effects on the calculated interference velocity distributions are shown in figure 9. The chord-to-height ratio is moderate ($c/H = 0.27$) and all model poles are located at the model's quarter-chord position. Note that not only the magnitudes but also the shape of the interference velocity distributions may be affected by the order of the model representation. Most remarkable is the contribution of the "pitching-moment" doublet to upwash: it adds about 0.15° to upwash at mid-chord. No doubt, the higher-order poles grow more important with increasing chord-to-height ratio.

4. SELECTION OF RESULTS

The results to be discussed in this section are selected to illustrate some more specific aspects of modern wall correction methods. For obvious reasons, the majority of examples will involve the methods available at NLR, but it has been shown before that there are many similarities between the various methods.

4.1 Comparison of various methods

A comparison of various wall correction methods has been published by Mokry (Ref. 9). The results, completed with those from the NLR I method and the NAL results for ΔM received from Sawada (private communication), are reproduced in table 2. The NLR I first-order incidence correction should be compared with those by NAE and ONERA because they did not account for the pitching-moment doublet. Again, note its substantial contribution to $\Delta\alpha$ (by comparing the first- and second-order NLR I results) in spite of the small chord-to-height ratio $c/H = 0.17$. Still higher-order poles have negligible effect in this case.

4.2 Comparison of solid- and slotted-wall data

The effectiveness of a measured boundary conditions method is demonstrated in figure 10. The examples concern a symmetrical aerofoil with $c/H = 0.27$ in the NLR Pilot Tunnel. It is shown that the two sets of corrected data (according to the NLR I method) agree quite well, which is a necessary but unfortunately not sufficient condition with respect to the correctness of the method. It has been found that too simple a model representation may also lead to coinciding corrected data, but that in that case the corrected $dC_l/d\alpha$ may vary with the chosen location of the model poles.

It turned out that the blockage correction in the solid-wall test section configuration increases more strongly with increasing reference Mach number than predicted by classical wall interference theory, even at zero-lift. This might be caused by the side-wall boundary layers, but there is no conclusive evidence available.

4.3 Rail versus slat measurements

Since the flow near a ventilated wall (with discrete vents) is 3D, boundary velocities should be measured at sufficient distance from the walls, inside the 2D region of the flow. This can, for instance, be done by means of "pressure rails" (Fig. 11). The Baldwin type of boundary condition suggests that, for slotted-walls, the "homogeneous" flow is reached at about one slot spacing distance from the wall. Unfortunately, there is only little experimental evidence in this respect. Besides, it is generally less expensive and more convenient to equip the walls with static-pressure orifices than to build rails or the likes.

The question concerning rail or wall measurements has been explored in the NLR Pilot Tunnel (PT) by doing both. The distributions of pressure orifices on slats and rails were identical (Fig. 11). The model was a CAST-7 aerofoil with a chord-to-height ratio c/H = 0.33 (Ref. 11).

Some typical examples of calculated $\Delta\alpha$- and ΔM-distributions along the test section axis are shown in figures 13 and 14. Corresponding $c_l - \alpha$ curves are depicted in figure 15. Relative to the rail results, the slat pressures yield values of ΔM which are up to about 0.002 too low; the corresponding incidence corrections may differ as much as approximately 0.15 degrees. These differences exceed those encountered in the repeatability measurements presented in table 3. However, it must be noted that these repeatability results are somewhat flattered, because they were obtained within a run (i.e. the period between wind-on and subsequent wind-off). From figure 10, for instance, it may be argued that the accuracy of $\Delta\alpha$ is probably not better than, say, $\pm$ 0.05 degrees (for the NLR PT with wall data at $-1.45 \leq x/H \leq 0.55$). Nevertheless, it appears that the application of slat pressures instead of rail pressures (at about one slot spacing distance from the wall) causes some loss of accuracy. This loss may be expected to increase with increasing slot-spacing-to-height ratio (which is 0.10 in the PT).

4.4 A peculiar case

A remarkable phenomenon was observed in the NLR Pilot Tunnel during the CAST-7 test program (Ref. 11). The majority of data points was taken with the standard, sting-mounted, wake rake (Rake 1; Fig. 12). Additional data points were taken with a slat-mounted wake rake (Rake 2), with the objective to measure spanwise variation of wake drag. It was observed that merely replacing rake 1 by rake 2, i.e. without altering the incidence and Mach number settings, caused an appreciable change in model pressure distribution (fig. 16).

The model pressure distribution turned out to be affected by the presence of rake 2 but to be independent of its spanwise position, even though this position varied from 2y/B = 0 to 2y/B = 0.375 relative to the test section centre line. Besides, with rake 2 at 2y/b = 0.375, the addition of rake 1 had no effect either. Consequently, the phenomenon could not be attributed to rake/model interference.

It turned out that the phenomenon could be explained in terms of wall interference. Apparently, the presence of rake 2 and its "plumbing" (see figure 12) disturbed the plenum chamber flow, thus changing the wall interference. Comparing model pressure distributions obtained with either rake 1 or rake 2 at approximately equal corrected free-stream conditions indeed shows very good agreement (Fig. 16).

This case illustrates that even seemingly minor changes inside the, admittedly very shallow, plenum chamber of the NLR PT may have an appreciable effect on wall interference. It also illustrates the power of methods using measured boundary conditions. The diagnosis of the phenomenon would hardly be feasible by means of a Baldwin type of method.

5. CONCLUSIONS AND RECOMMENDATIONS

The application of wall correction methods using measured boundary conditions is becoming common practice for 2D-testing. Globally, three types of method can be distinguished :

1. "Cauchy" type: requires the measurement of wall velocity vector distributions but no model representation. The methods are, in principle, restricted to linearized subsonic flows.
2. "Schwarz" type: requires the measurement of distributions of one wall velocity component as well as an accurate model representation. The methods are also, in principle, restricted to linearized subsonic flows.
3. "Matching" type: requires the measurement of distributions of one wall velocity component and both a "direct" and an "inverse" method for calculating flows about aerofoils. The methods are, in principle, not restricted to a certain velocity regime.

No doubt, all these methods are more reliable and more versatile than Baldwin type of methods. For subsonic and, possibly, low transonic flows the Cauchy type is the most versatile since it does not require an explicit model representation and, thus, will be applicable to a variety of models (e.g. aerofoils with or without high-lift devices; separated flows).

The main problem facing the application of Cauchy type of methods to ventilated test sections is the choice and/or development of instrumentation with the capability to measure the required velocity distributions (both u and v !) sufficiently fast (and, of course, sufficiently accurate) in order to be economical for production type of tests. The evolution of the present 2D methods to 3D will closely be related to the solution of this instrumentation problem. In the meantime, Cauchy type of methods are very valuable (and convenient) for 2D tests in solid-wall wind tunnels.

In the absence of reliable means to measure both u and v near ventilated walls, the Schwarz type of method can be applied succesfully for "clean" aerofoils. In that case the model representation of reference 2 is recommendend.

It is convenient, for all methods, to measure the boundary velocities near the walls only. This, however, requires relatively long test sections. Although it is still somewhat premature to define a minimum length, it is expected that the minimum will be of the order of one test section height upstream of the model and one height (solid walls) or more (ventilated walls) in downstream direction. If the test section is relatively short, velocities should also be measured on the front and rear face of the control volume, which requires the development of accurate, non-intrusive, fast-response instrumentation. Obviously, applications of reliable interpolation or extrapolation procedures are attractive alternatives, but they should be selected and evaluated carefully. (In this respect, the upstream part generally presents the minor problem).

For all types of method it is recommended to measure the boundary velocities inside the, nominally, 2D part of the test section flow. However, it has been shown that pressure measurements on ventilated walls may in some cases also be satisfactory.

It is strongly recommended to apply "empty"-test-section corrections to the measured boundary velocities, where "empty" means that the test section should contain everything it contains during the actual tests, apart from the model itself.

7. REFERENCES

1	G. Moretti	Functions of a complex variable, Chapter 11. Prentice- Hall
2	J. Smith	A method for determining 2D wall interference on an aerofoil from measured pressure distributions near the walls and on the model NLR TR 81016 U, 1981
3	C. Capelier J.P. Chevallier F. Bouniol	Nouvelle méthode de correction des effets de parois en courant plan La Recherche Aérospatiale, no. 1978-1, pp. 1-11
4	M. Mokry	Application of the Fast Fourier Transform to two-dimensional wind tunnel wall interference. Journal of Aircraft, Vol. 17, no. 6, pp. 402-408, 1980
5	P.R. Ashill D.J. Weeks	An experimental investigation of the drag of thick supercritical aerofoils - A progress report. RAE TM (Aero) 1765, 1978
6	E.M. Murman	A correction method for transonic wind tunnel wall interference AIAA 12th Fluid and Plasma Dyn. Conf., 1979
7	W.B. Kemp	Transonic assessment of two-dimensional wind tunnel wall interference using measured wall pressures NASA CP-2054, Part 2, 1979
8	M. Mokry	Higher-order theory of two-dimensional subsonic wall interference in a perforated wall wind tunnel NRC Aeron.Rep. LR-553, 1971
9	M. Mokry	Evaluation of transonic wall interference corrections from measured wall pressures in the NAE 15" x 60" perforated wall test section Paper presented at meeting of AGARD WG on transonic test sections, NASA Langley, March 1980
10	H. Sawada	A general correction method of the interference in 2-dimensional wind tunnels with ventilated walls. Transactions of the Japan Society for Aeron. and Space Sciences, Vol. 21, No. 52, 1978
11	J. Smith	Data report on the CAST-7 aerofoil in the NLR Pilot Tunnel NLR TR 81117 L, 1981

ACKNOWLEDGEMENT

The author is indebted to Dr. P.R. Ashill and Mr. D.J. Weeks of RAE for their kind permission to present some of their data and to Mr. Th.E. Labrujère of NLR for developing the NLR II method.

Table 1: Principal characteristics of European wall correction methods (status 1981)

1. ORIGINATOR	RAE	NLR II	ONERA	NLR I
2. TYPE OF METHOD	Cauchy	Cauchy	Schwarz	Schwarz
3. WALL DATA - required data - present instrumentation - inter-/extrapolations - actual boundary conditions	u and v u:wall orifices v=0(solid walls) Quasi-exact extrapolation to $/x/\to\infty$ u and v	u and v u:wall orifices v=0(solid walls) Linear interpolation across front and rear face u and v	u or v u:wall orifices v:wall shape(solid) Truncation outside range of measured data u_i or v_i	u Static-pressure "rails" or wall orifices Approximate extrapolation with T(walls)=T(model) Mixed u_i and v = 0
4. MODEL DATA - required data - model representation	None No	None No	Forces Poles up to second order;classical strengths.Vortex at c/4;source at c/2; volume doublet at maximum thickness position. *)	Pressure distr.+wake drag Poles up to any order,at any position inside model contour;strengths from line integrals of $C_p(x,y)$ and modified compressibility rules;classical source strength
5. METHOD OF SOLUTION	Singularity distributions on boundaries	Analytical expression,integrated numerically	Analytical expression, integrated numerically	Singularity distributions on boundaries
6. ADDITONAL CONDITION(Constant of integration)	Not required	Not required	Implicitly incorporated in analytical expression	Imposed by v = 0 parts of actual boundary conditions
7. OPERATIONAL FOR (1982)	RAE 8 x 8 ft	NLR PT,HST and LST	ONERA T2 and S3 MA	NLR PT,HST and LST
8. REFERENCES	Ref. 5	Unpublished	Ref. 3	Ref. 2

*) Presently extended with pitching-moment doublet at c/4

Table 2

Mokry's test case: Aerofoil BGK-1 in NAE 15" x 60" (c/H = 0.167)
M_t = 0.784; c_{l_t} = 0.764; Re_c = 21 x 10^6;
(Run 20914/4)

	Method	ΔM	Δα°	Notes
NAE Canada	Ref. 4	-.015	-.67	1
ONERA France	Ref. 3	-.015	-.67	
NAL Japan	Ref. 10	-.013	-.58	
NASA Langley	Ref. 7	-.014	-.68	2
		-.015	-.64	3
NLR I The Netherlands	Ref. 2	-.013	-.69	4
		-.015	-.59	5
		-.015	-.59	6

Notes : 1. assuming flow parallel to wind tunnel axis at x/c = -8; y/c = 0
2. match point at 63%c (x/c = 0.38) - shock wave location
3. match point at 44%c (x/c = 0.19)
4. first-order model representation; poles at 25%c
5. second-order model representation; poles at 25%c
6. tenth-order model representation; poles at 25%c

Table 3

Repeatability of correction values (rail pressures; slotted walls)

Test 1101; Aerofoil CAST-7 in NLR Pilot Tunnel (c/H = 0.327)

Data Point	α_t	M_t	C_{l_t}	α_c	M_c	C_{l_c}
113-11-122	1.06	.760	.522	.27	.762	.522
113-11-129	1.06	.761	.520	.28	.762	.521
113-12-141	2.40	.761	.726	1.30	.766	.716
113-12-147	2.40	.760	.727	1.30	.765	.717

N.B.: Repeated points within one run ! (Ref. 11)

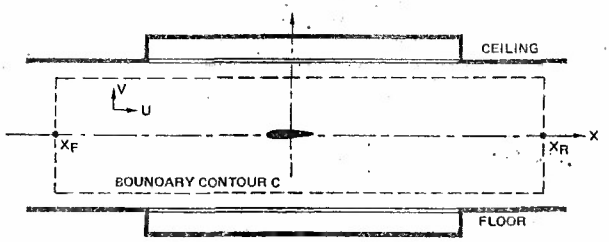


Fig. 1 Co-ordinate system

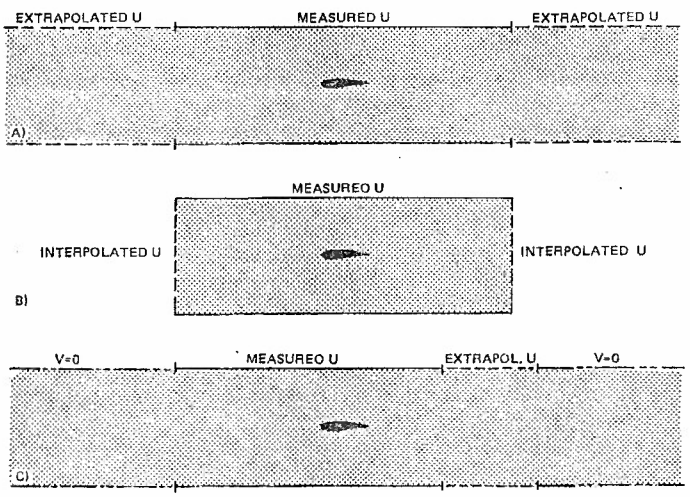


Fig. 2 Determination of boundary conditions :
a) infinite strip (u)
b) rectangle (u)
c) infinite strip (mixed u and v)

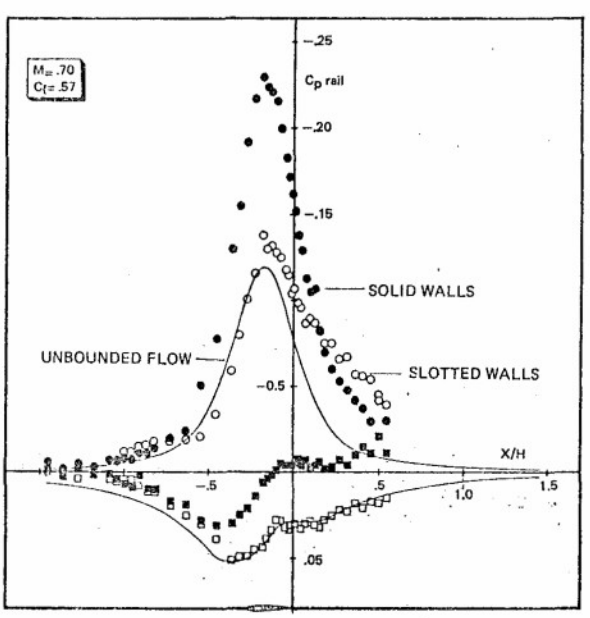


Fig. 3 Pressure rail data
Aerofoil EC-14.5-40 (C/H = .273)

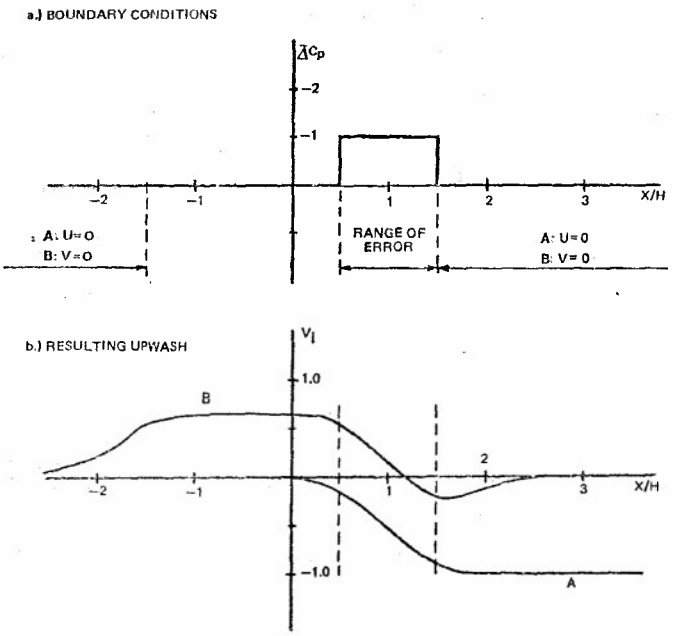


Fig. 4 Sensitivity to schematical extrapolation error, depending on formulation of boundary conditions

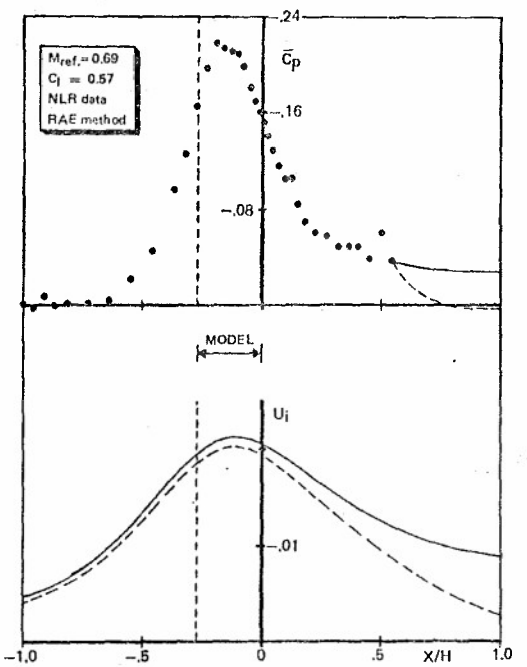


Fig. 5 Example of effect of extrapolation on calculated wall interference (blockage)

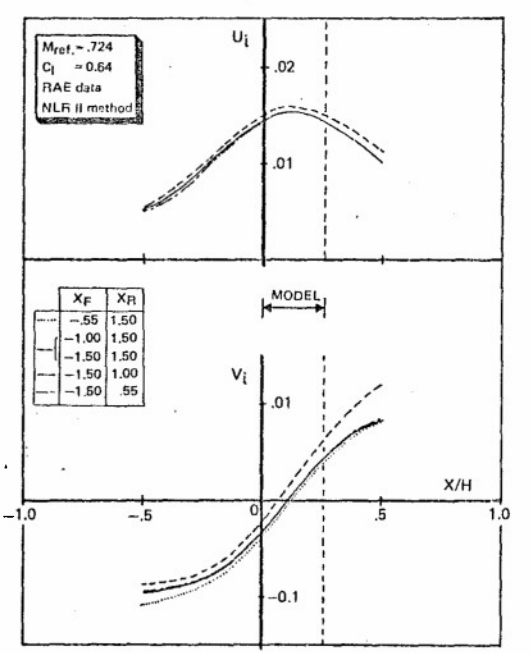
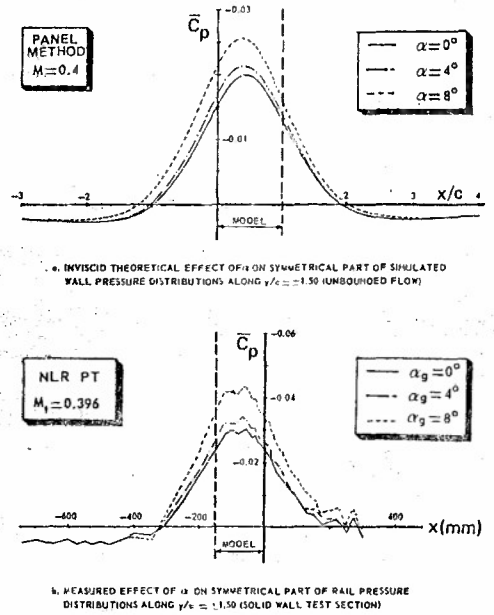


Fig. 6 Example of effect of range of measured wall data for a method with linearly interpolated data on front and rear face (Fig. 2b)



a. INVISCID THEORETICAL EFFECT OF α ON SYMMETRICAL PART OF SIMULATED WALL PRESSURE DISTRIBUTIONS ALONG y/c = ±1.50 (UNBOUNDED FLOW)

b. MEASURED EFFECT OF α ON SYMMETRICAL PART OF RAIL PRESSURE DISTRIBUTIONS ALONG y/c = ±1.50 (SOLID WALL TEST SECTION)

Fig. 7 Comparison of measured and theoretically predicted trend of $\bar{C}_p$-development with increasing incidence

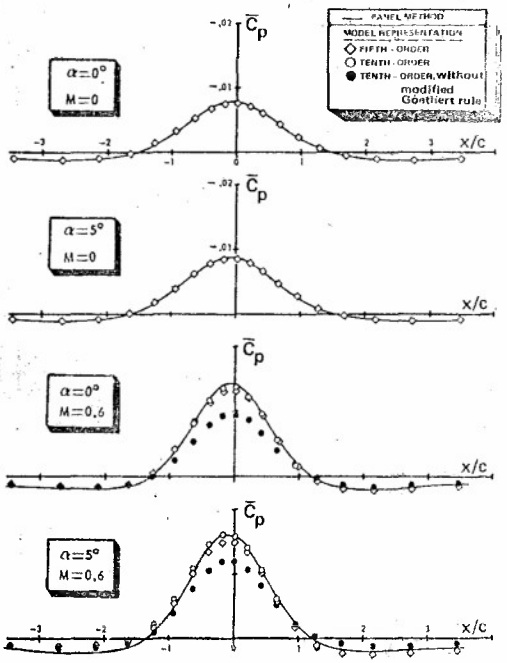


Fig. 8 Symmetrical part of pressure distributions along y/c = ± 1,50 in inviscid unbounded flow (method NLR I)

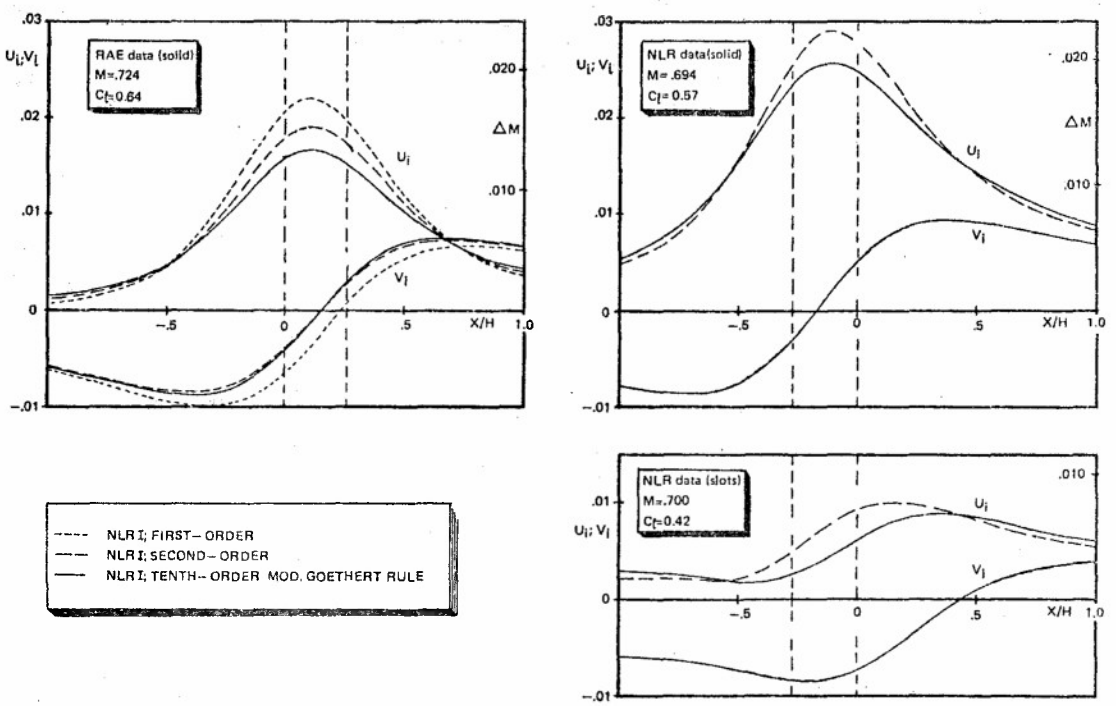
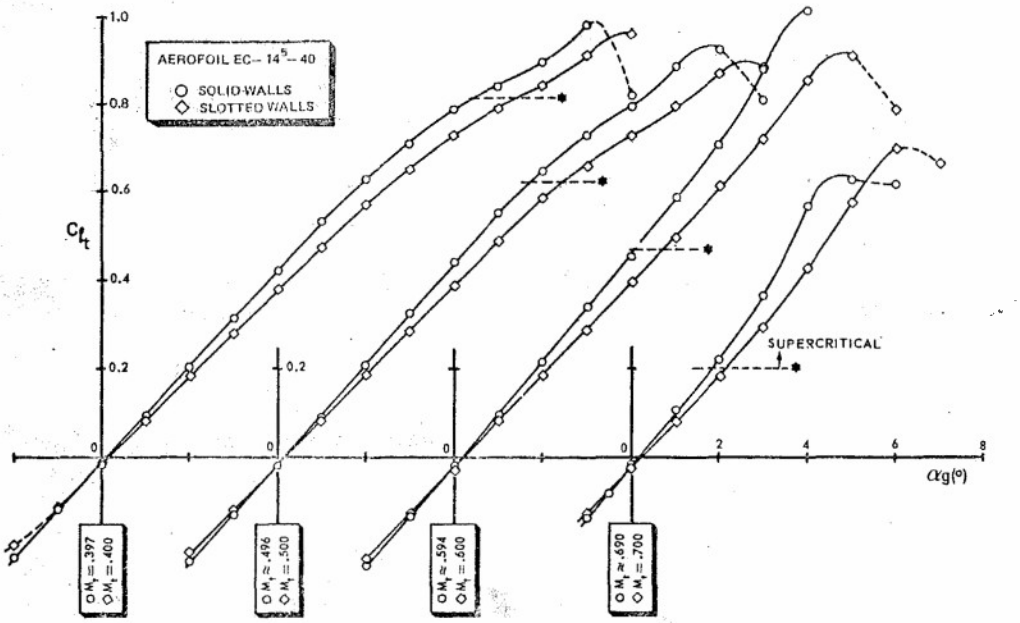


Fig. 9 Effect of model representation on calculated interference velocities (test section centre line)



UNCORRECTED

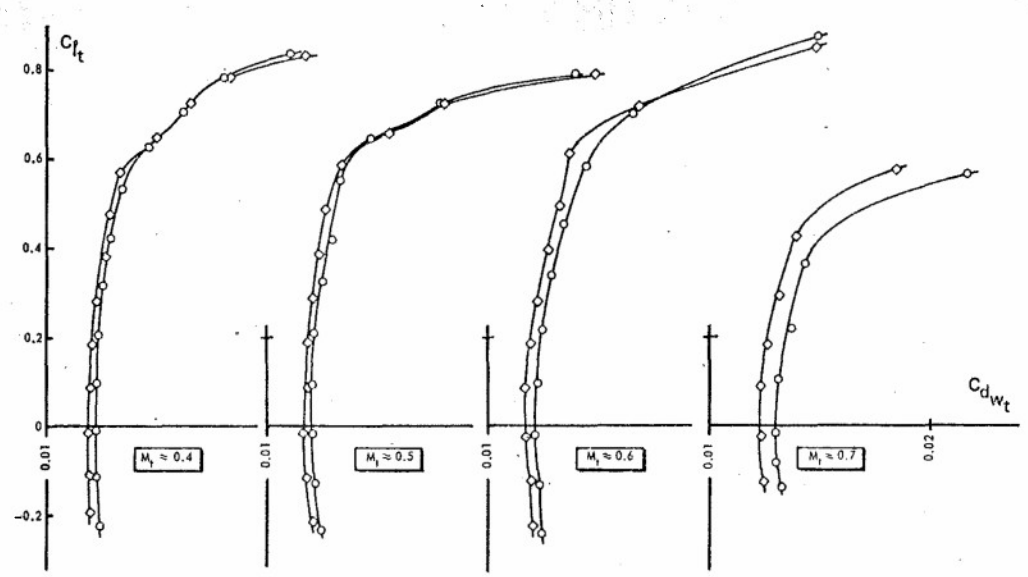
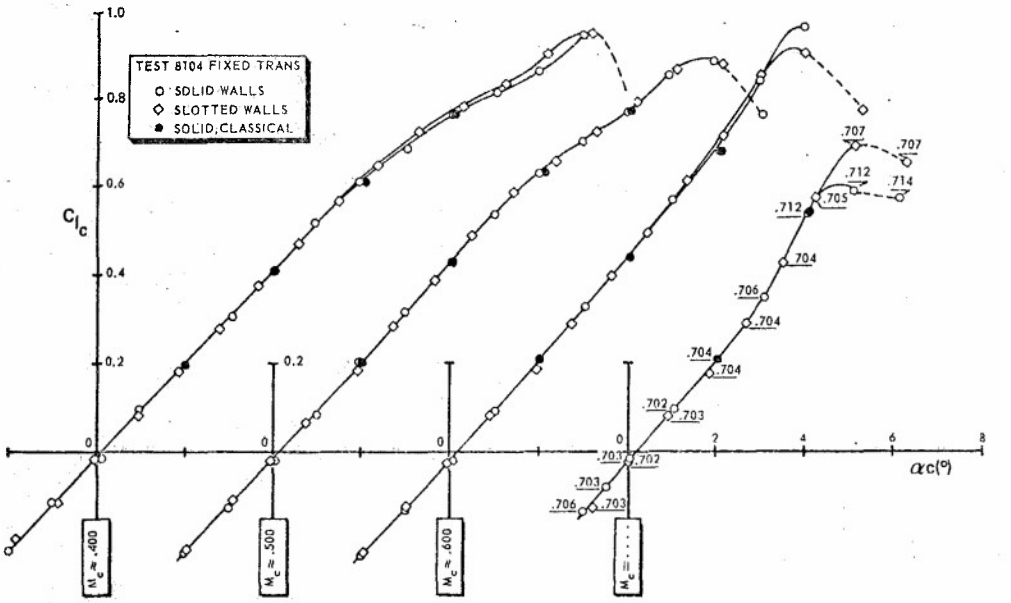


Fig. 10a Comparison of uncorrected solid- and slotted-wall data (NLR PT)



CORRECTED

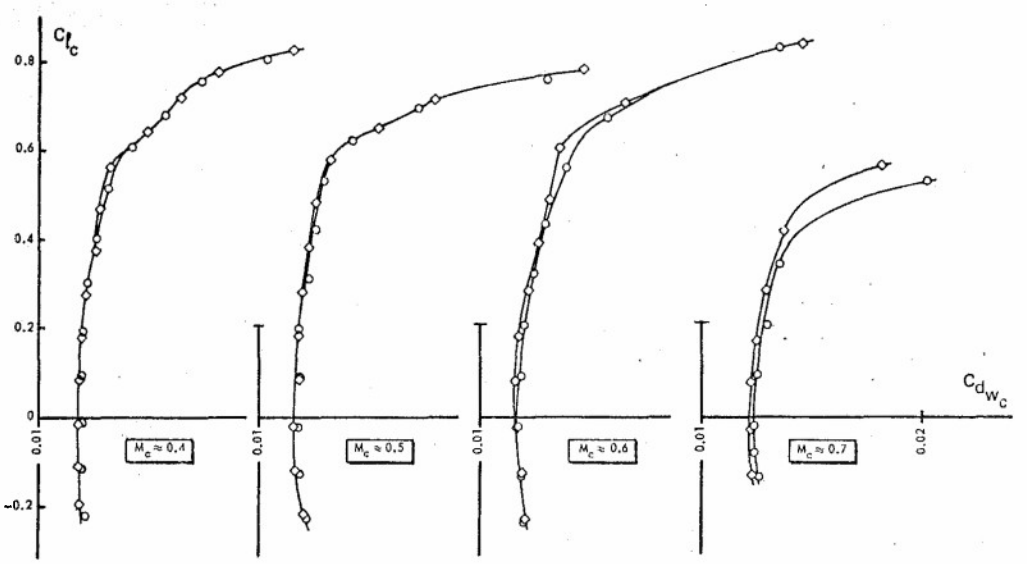
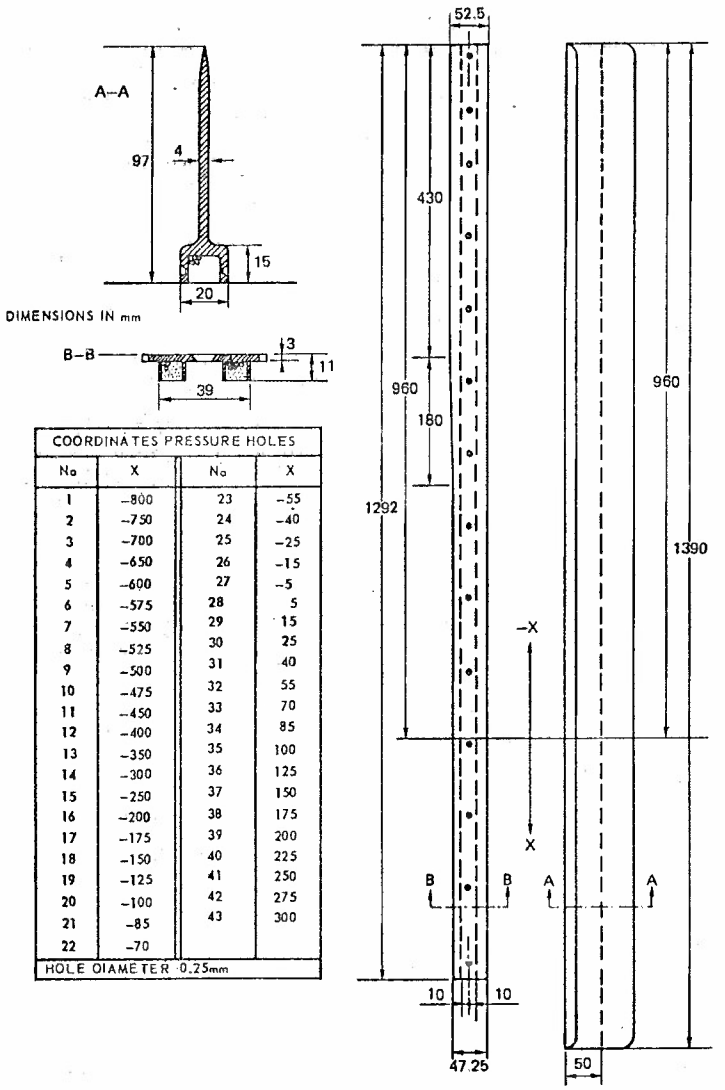


Fig. 10b Comparison of corrected solid- and slotted-wall data(Method NLR 1)



COORDINATES PRESSURE HOLES			
No	X	No	X
1	–800	23	–55
2	–750	24	–40
3	–700	25	–25
4	–650	26	–15
5	–600	27	–5
6	–575	28	5
7	–550	29	15
8	–525	30	25
9	–500	31	40
10	–475	32	55
11	–450	33	70
12	–400	34	85
13	–350	35	100
14	–300	36	125
15	–250	37	150
16	–200	38	175
17	–175	39	200
18	–150	40	225
19	–125	41	250
20	–100	42	275
21	–85	43	300
22	–70		
HOLE DIAMETER 0.25mm			

Fig. 11 Details of pressure rail and slat (NLR PT; H=550 mm)

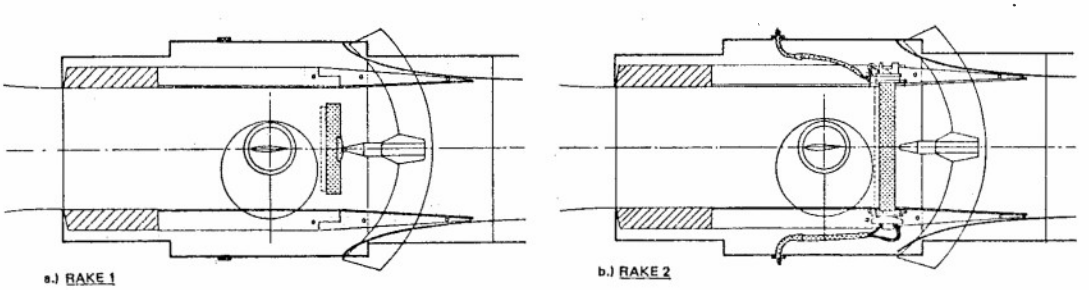
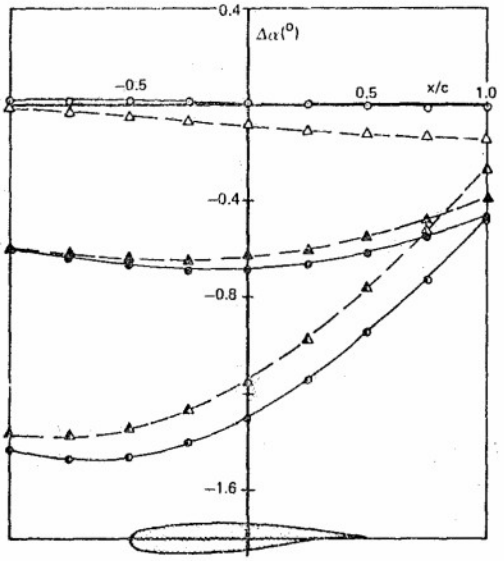


Fig. 12 Sketch of Pilot Tunnel test section with wake rakes



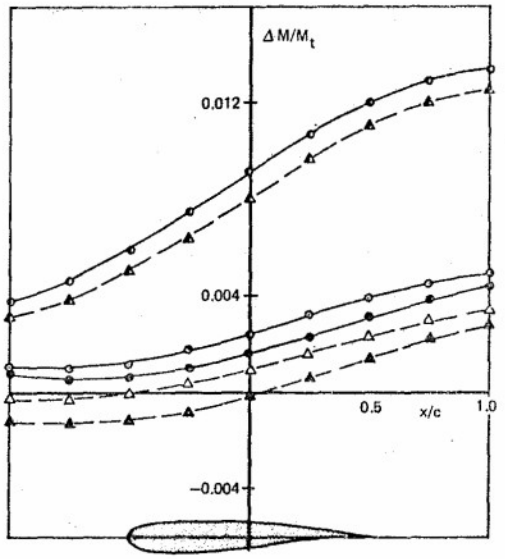
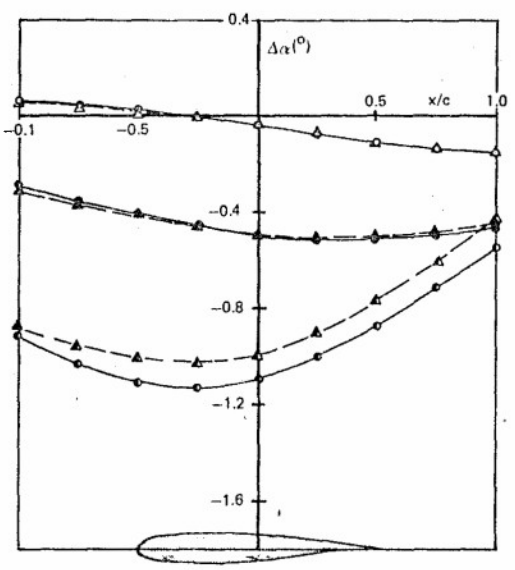


Fig. 13 Distributions of wall interference along the test section centreline at M_t = 0.60, according to rail (113) and slat (23) pressures

	DATAPOINT	M_t	C_{l_t}		DATAPOINT	M_t	C_{l_t}
o	113–8 –72	.600	0.079	Δ	23–15–199	.603	0.075
●	113–9 –91	.602	0.576	▲	23–15–211	.599	0.576
⊙	113–10–117	.601	1.160	◬	23–15–240	.603	1.159



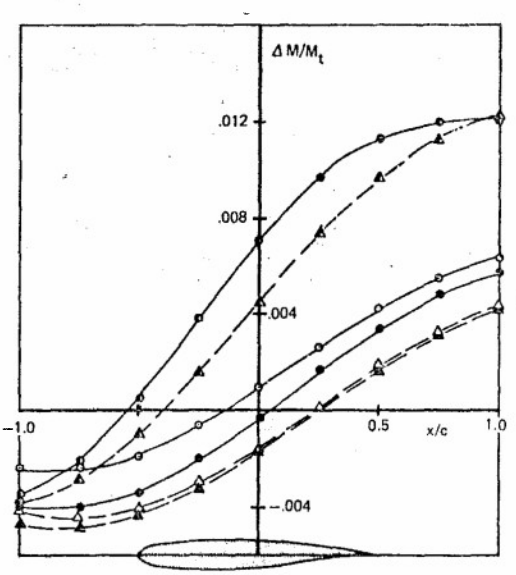


Fig. 14 Distributions of wall interference along the test section centreline at M_t = 0.76, according to rail (113) and slat (23) pressures

	DATAPOINT	M_t	C_{l_t}		DATAPOINT	M_t	C_{l_t}
o	113–8–74	.761	0.057	Δ	23–15–201	.759	0.052
●	113–9–84	.760	0.350	▲	23–15–207	.762	0.350
⊙	113–9–99	.760	0.756	◬	23–15–216	760	0.749

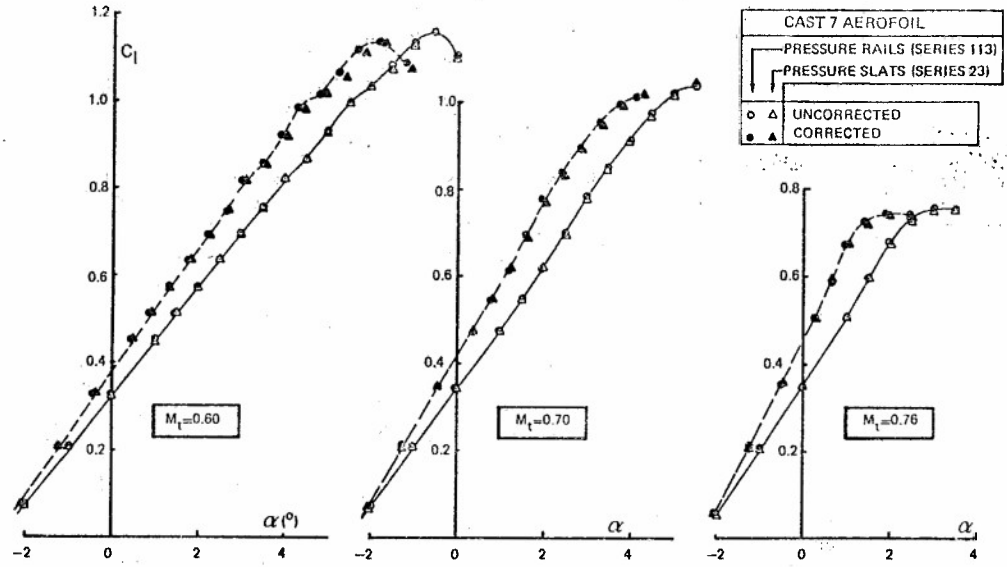


Fig. 15 Lift versus incidence

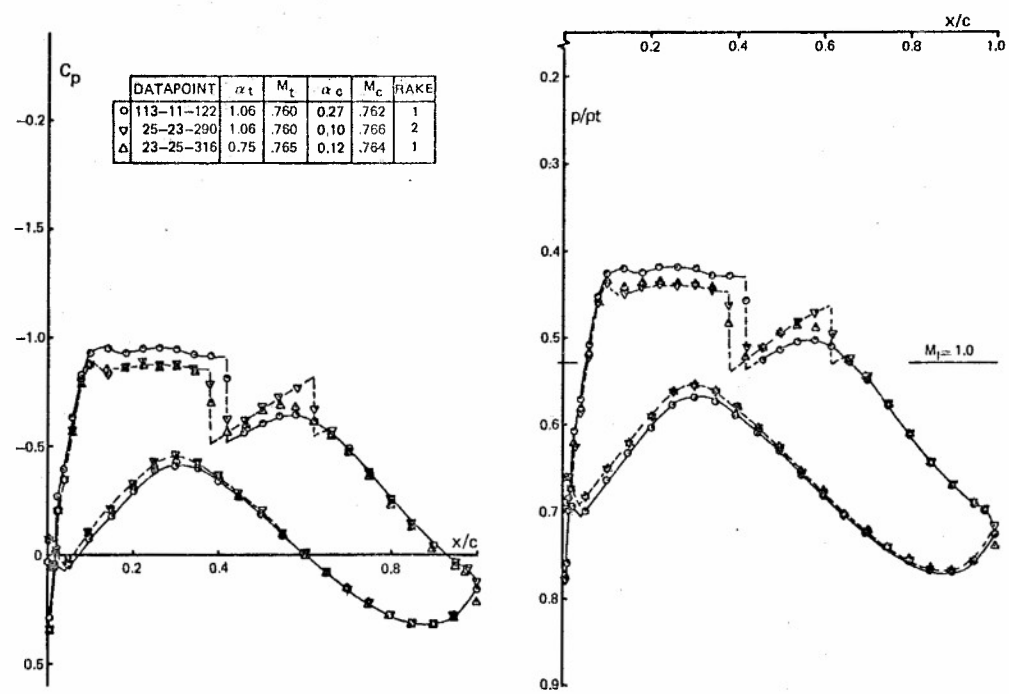


Fig. 16 Comparison of (uncorrected) pressure distributions, showing the wall interference character of the changes in flow conditions associated with changing the wake rake

SUBSONIC WALL INTERFERENCE CORRECTIONS FOR FINITE-LENGTH TEST SECTIONS USING BOUNDARY PRESSURE MEASUREMENTS

M. Mokry
High Speed Aerodynamics Laboratory
National Aeronautical Establishment
National Research Council Canada
Ottawa, Ontario
K1A 0R6

SUMMARY

Subsonic wall interference corrections are evaluated using the Fourier solution for the Dirichlet problem in a circular cylinder, interior to the three-dimensional test section. The required boundary values of the streamwise component of wall interference velocity are obtained from pressure measurements by a few static pressure tubes (pipes) located on the cylinder surface. The coefficients of the resultant Fourier-Bessel series are obtained in closed form and the coefficients of the Fourier sine series are calculated by the fast Fourier transform, so that the method is very efficient and suitable for routine tunnel testing. A practical use of the method is demonstrated on a theoretical example and typical model tests performed in the NAE 5 ft. × 5 ft. wind tunnel.

NOMENCLATURE

a_n, b_n	Fourier components of u
$\hat{a}_n$, $\hat{b}_n$	boundary values of a_n, b_n
$A_{n,k}$, $B_{n,k}$	coefficients of Fourier sine series
C_L	lift coefficient of the model
C_p	pressure coefficient
C_y, C_z	y and z components of C_L
D_n	differential operator
f_n	common notation for a_n and b_n
$\hat{f}_n$	common notation for $\hat{a}_n$ and $\hat{b}_n$
$F_{n,k}$	common notation for $A_{n,k}$ and $B_{n,k}$
I_n	modified Bessel function of the first kind of order n
$j_{n,k}$	kth positive zero of J_n
J_n	Bessel function of the first kind of order n
K_n	modified Bessel function of the second kind of order n
m	integer power of 2, number of equal subdivisions of interval
M_∞	stream Mach number
n	index of the Fourier component
$P_{n,k}$, $Q_{n,k}$	coefficients of the Fourier-Bessel series
q	dummy variable of integration
p_∞	upstream reference pressure
p_{plenum}	plenum pressure
r	radius of the control cylinder
r_m	model radius
r_s	sting radius
s	reduced test section length
S	reference area of the model
u, v, w	reduced components of wall interference velocity

U_∞	stream velocity
V	volume of tbe model
x, y, z	Cartesian co-ordinates
x, ρ, θ	cylindrical co-ordinates
x_1, x_2	x co-ordinates of the upstream and downstream ends of the control cylinder
x_N, x_T	x co-ordinates of the source and sink, representing the model
β	$(1 - M_\infty^2)^{1/2}$
γ	vortex strength
ΔM_∞	Mach number correction
ΔU_∞	velocity correction
$\Delta\alpha_y$, $\Delta\alpha_z$	correction to flow angle in the x, y and x, z planes
θ_o	angle between the lift force and y axis
κ	ratio of specific heats
μ	doublet strength
μ_k, $\nu_{n,k}$	eigenvalues
ξ	reduced x co-ordinate
ρ_∞	upstream density
σ	source strength
σ_μ	strength of the source-sink combination
ϕ	disturbance velocity potential
ϕ_F	"free air" part of ϕ
ϕ_W	"wall interference" part of ϕ

INTRODUCTION

The present paper extends the suhsonic wall correction method of Mokry and Ohman[1] to the three-dimensional case. The theoretical part of the paper has earlier been rcported in Reference 2. Merits of a method that utilizes boundary pressure measurements but does not require knowledge of the cross-flow properties of ventilated test section walls are discussed in References 3 and 4. In essence, the rclationship between the normal velocity and pressure difference across the wall is highly nonlinear, depending upon the boundary layer development on the wall and the pressure field induced by the model. The utilization of tlic measured wall static pressures as the (Dirichlet) boundary condition eliminates the need for a theoretical crossflow model, and thus indirectly ensures that the true nonlinear character of the ventilated wall is properly taken into account. However, since the acquisition of wall static pressures is required for each tunnel test, while the crossflow properties of the wall remain unknown, this approach is suitable as a post-test assessment, but not as prediction.

In contrast to some recent techniques[3-6], relying upon detailed computation of flow past a model both in the wind tunnel and free air, the present paper describes an inexpensive, engineering-type estimation of wall corrections for routine tunnel testing. It is based upon the classical, linear wall interference concept, representing tbc model by singularities, deduced from the model geometry and measured forces[7]. The validity of this approach may be disputed[6], but it should always be possible to compare a sample of the results with those obtained by the more elaborate techniques[3-6], to decide whether in the circumstances the simple correction method is adequate or not. In many instances the corrections turn out to be marginal[5], so that routine use of flow computation techniques is not justified.

The estimation of the far field disturbance due to the model by singularities allows to extract the axial component of wall interference velocity on the test section boundary from tlie measured wall static pressures. The velocity correction at the model position is obtained by solving the Dirichlet problem for the axial velocity in the test section interior. The normal components of interference velocity (incidence and sideslip corrections) are derived from the zero vorticity condition. However, since it is impractical to measure the pressures over the whole wall surfaces, a simpler solution, based on the circular cylinder interior to the test section, is proposed. The pressures are measured only by two or four static pressure tubes (pipes) on the surface of the control cylinder. Using the periodicity condition, the surface distribution of the axial component of the wall interference velocity is approximated hy a Fourier expansion of axisymmetric functions. The values of Fourier components on the upstream and downstream ends of the cylinder are obtained by a "tailored" interpolation that allows a closed-form solution for the coefficients of the resultant Fourier-Bessel series. This type of solution treats the effects of blockage and lift interference separately, providing agreement with the theory of Baldwin et al[9] and Wright[10] of an infinite cylinder test section. The coefficients of the Fourier sine series are, as in the two-dimensional case[1], calculated by the fast Fourier transform, that makes the method very efficient and suitable for routine wind tunnel testing.

This simplified treatment is well justified by the fact that the three-dimensional interference is, due to the nature of propagation of pressure disturbances in space, much less severe than the two-dimensional interference. However, since the static pressure tubes are likely to be attached to the walls or mounted in their vicinity (to be outside wall boundary layers), the circular cylinder modeling restricts the application of the method to circular, octagonal or square cross-sections, as illustrated in Figure 1. The solution for the elliptic cylinder, that would allow a similar treatment of more general eross-sections, has not been worked out yet, although this should not be prohibitively difficult[11]. For half-model tests the reflection principle has to be taken into consideration, so that the test section shapes in Figure 1 are no longer appropriate for the application of the method in its present version. For a possible estimation of the corrections for the general rectangular cross-sections, the reader is referred to References 7 and 8.

GOVERNING EQUATIONS

The model is located at the origin x = y = 0 of the (right-handed) Cartesian system, where x is the co-ordinate along the streamwise oriented wind tunnel axis, Figure 2. The flow is investigated in the region $x_1 < x < x_2$, $0 \leq \rho < r$, using the cylindrical co-ordinates

$$x,\ \rho = (y^2+z^2)^{1/2},\ \theta = \operatorname{atan}\frac{z}{y} \tag{1}$$

It is assumed that the model is small, the incident stream is subsonic and that the disturbanee velocity potential $\phi = \phi\ (x,\rho,\theta)$ satisfies near the cylinder boundary the linearized equation

$$\beta^2 \frac{\partial^2\phi}{\partial x^2} + \frac{1}{\rho}\frac{\partial}{\partial\rho}\left(\rho\frac{\partial\phi}{\partial\rho}\right) + \frac{1}{\rho^2}\frac{\partial^2\phi}{\partial\theta^2} = 0 \tag{2}$$

Aecording to small disturbance theory, the pressure coefficient at $\rho = r$, relates to ϕ as

$$C_p\ (x,r,\theta) = -2\frac{\partial\phi}{\partial x}\ (x,r,\theta) \tag{3}$$

However, since the measuring device — the pressure tube — is in fact a slender body, see Figure 3, the quadratic crossflow velocity components should also be retained in Equation (3). They are omitted here for the sake of linearity and no attempt is made to analyze the error.

In the linearized flow region, that is in the region of validity of Equation (2), we can use the decomposition

$$\phi\ (x,\rho,\theta) = \phi_F\ (x,\rho,\theta) + \phi_W\ (x,\rho,\theta) \tag{4}$$

The potential ϕ_F satisfies Equation (2) in the linearized flow region and in the exterior of the control cylinder and obeys, except in the vicinity of the vortex wake, the farfield condition

$$\phi_F \to 0 \text{ as } x^2 + (\beta\rho)^2 \to \infty$$

Near the cylinder boundary, ϕ_F can be approximated as

$$\phi_F\ (x,\rho,\theta) = \frac{\gamma}{4\pi}\frac{\cos(\theta-\theta_o)}{\rho}\left\{1 + \frac{x}{[x^2+(\beta\rho)^2]^{1/2}}\right\}$$
$$- \frac{\sigma}{4\pi}\frac{x}{[x^2+(\beta\rho)^2]^{1/2}} + \frac{\mu}{4\pi}\frac{x}{[x^2+(\beta\rho)^2]^{3/2}} \tag{5}$$

where θ_o is the angle between the lift force* and the y axis.

The first term of Equation (5), the horseshoe vortex, represents the lift effect of the model. Its strength is

$$\gamma = \frac{1}{2}SC_L \tag{6}$$

The second term, the source, represents the displacement effect of the sting. Assuming that the downstream portion of the sting is a cylinder of radius r_s, the source strength is

$$\sigma = \pi r_s^2 \tag{7}$$

The last term of Equation (5), the doublet, represents the displacement effect of the test model. As shown by Baranoff[12], the strength of a three-dimensional doublet is not affected by compressibility, so that directly

$$\mu = V \tag{8}$$

For improved representation of the far field of an elongated body (missile ete.), we ean replace the doublet term by the source-sink combination

---

*Model force normal to the x axis

$$-\frac{\sigma_\mu}{4\pi}\left\{\frac{1}{[(x-x_N)^2+(\beta\rho)^2]^{1/2}}-\frac{1}{[(x-x_T)^2+(\beta\rho)^2]^{1/2}}\right\}$$

where $x_N < 0$ is the location of the nose source and $x_T > 0$ that of the tail sink, as illustrated in Figure 4. An approximate value of the strength σ_μ is

$$\sigma_\mu = \frac{\mu}{x_T - x_N}$$

In the limit $x_N, x_T \to 0$ we recover the original doublet term and for a long cylindrical body of radius r_m we obtain

$$\sigma_\mu = \pi r_m^2$$

which is also the expected limit for the source (or sink) strength, cf. Equation (7).

As shown by Hackett et al[13], a large variety of axisymmetric bodies can be generated by the source-sink plus source combinations, so that more refined body representations for wall interference purposes seem unnecessary. However, further work is needed to find suitable far field representations for slender bodies at high angles of attack.

The potential ϕ_W satifies Equation (2) inside the cylinder $x_1 < x < x_2$, $0 \leq \rho < r$. The derivatives of ϕ_W with respect to x, y and z determine the wall interference corrections to the components of unit wind tunnel velocity. Their evaluation at the position of the model, $x = \rho = 0$, is the subject of the next sections.

FOURIER SOLUTION OF THE WALL INTERFERENCE PROBLEM

Using the transformation

$$\xi = \frac{1}{\beta}(x - x_1) \tag{9}$$

tbe left-hand side of Equation (2) reduces to the Laplacian in cylindrical co-ordinates. The axial velocity function

$$u(\xi,\rho,\theta) = \frac{\partial\phi_W}{\partial\xi}(x,\rho,\theta) = \beta\frac{\partial\phi_W}{\partial x}(x,\rho,\theta) \tag{10}$$

then satisfies the equation

$$\frac{\partial^2 u}{\partial\xi^2} + \frac{1}{\rho}\frac{\partial}{\partial\rho}\left(\rho\frac{\partial u}{\partial\rho}\right) + \frac{1}{\rho^2}\frac{\partial^2 u}{\partial\theta^2} = 0 \tag{11}$$

in the region $0 < \xi < s$, $0 \leq \rho < r$, where

$$s = \frac{1}{\beta}(x_2 - x_1) \tag{12}$$

From Equations (3), (4), (9) and (10) the values of the axial component of wall interference velocity on the boundary is obtained as

$$u(\xi,r,\theta) = -\beta\left[\frac{1}{2}C_p(x,r,\theta) + \frac{\partial\phi_F}{\partial x}(x,r,\theta)\right] \tag{13}$$

Utilizing the periodicity of u and $\partial u/\partial\theta$ with respect to θ, we represent u in terms of the Fourier series

$$u(\xi,\rho,\theta) = a_0(\xi,\rho) + \sum_{n=1}^{\infty}\left[a_n(\xi,\rho)\cos n\theta + b_n(\xi,\rho)\sin n\theta\right] \tag{14}$$

where, by Equation (11)

$$D_n a_n(\xi,\rho) = 0, \quad n = 0,1,2,\ldots$$

$$D_n b_n(\xi,\rho) = 0, \quad n = 1,2,\ldots \tag{15}$$

and

$$D_n = \frac{\partial^2}{\partial\xi^2} + \frac{\partial^2}{\partial\rho^2} + \frac{1}{\rho}\frac{\partial}{\partial\rho} - \frac{n^2}{\rho^2} \tag{16}$$

The actual number of Fourier components we are able to exploit is given by the number of static pressure tubes. Thus for two tubes located at $\theta = \frac{\pi}{2}$ and $\frac{3}{2}\pi$ we have

$$u(\xi,\rho,\theta) = a_0(\xi,\rho) + b_1(\xi,\rho)\sin\theta \tag{17a}$$

and for four tubes at $\theta = 0, \frac{\pi}{2}, \pi, \frac{3}{2}\pi$, see Figure 2,

$$u(\xi,\rho,\theta) = a_0(\xi,\rho) + a_1(\xi,\rho)\cos\theta + b_1(\xi,\rho)\sin\theta + a_2(\xi,\rho)\cos 2\theta \tag{17b}$$

In order to solve for the Fourier components inside the cylinder, we introduce the boundary values

$$\hat{a}_n(\xi) = a_n(\xi,r)$$

$$\hat{b}_n(\xi) = b_n(\xi,r) \tag{18}$$

and express them in terms of the known values $u(\xi,r,\theta)$, Equation (13). For the two-tube arrangement it follows from Equation (17a)

$$\hat{a}_0(\xi) = \frac{1}{2}[u(\xi,r,\frac{\pi}{2}) + u(\xi,r,\frac{3}{2}\pi)]$$

$$\hat{b}_1(\xi) = \frac{1}{2}[u(\xi,r,\frac{\pi}{2}) - u(\xi,r,\frac{3}{2}\pi)] \tag{19a}$$

and for the four-tube arrangement from Equation (17b)

$$\hat{a}_0(\xi) = \frac{1}{4}[u(\xi,r,0) + u(\xi,r,\frac{\pi}{2}) + u(\xi,r,\pi) + u(\xi,r,\frac{3}{2}\pi)]$$

$$\hat{a}_1(\xi) = \frac{1}{2}[u(\xi,r,0) - u(\xi,r,\pi)]$$

$$\hat{b}_1(\xi) = \frac{1}{2}[u(\xi,r,\frac{\pi}{2}) - u(\xi,r,\frac{3}{2}\pi)]$$

$$\hat{a}_2(\xi) = \frac{1}{4}[u(\xi,r,0) - u(\xi,r,\frac{\pi}{2}) + u(\xi,r,\pi) - u(\xi,r,\frac{3}{2}\pi)] \tag{19b}$$

Using Equations (15), we now can set up the following boundary value problem

$$D_n f_n(\xi,\rho) = 0 \quad , \quad 0<\xi<s, \quad 0\leqslant\rho<r$$

$$f_n(\xi,r) = \hat{f}_n(\xi) \quad , \quad 0<\xi<s$$

$$f_n(0,\rho) = \hat{f}_n(0)(\frac{\rho}{r})^n \quad , \quad 0\leqslant\rho<r$$

$$f_n(s,\rho) = \hat{f}_n(s)(\frac{\rho}{r})^n \quad , \quad 0\leqslant\rho<r \tag{20}$$

where f_n is used as a common notation for both a_n and b_n.

Applying the method of separation of variables, see Reference 2, the solution is obtained in terms of a Fourier series in ξ and Fourier-Bessel series in ρ:

$$f_n(\xi,\rho) = \sum_{k=1}^{\infty} F_{n,k}\frac{I_n(\mu_k\rho)}{I_n(\mu_k r)}\sin\mu_k\xi + \sum_{k=1}^{\infty}\left[P_{n,k}\frac{\sinh\nu_{n,k}(s-\xi)}{\sinh\nu_{n,k}s} + Q_{n,k}\frac{\sinh\nu_{n,k}\xi}{\sinh\nu_{n,k}s}\right]J_n(\nu_{n,k}\rho) \tag{21}$$

where

$$\mu_k = \frac{k\pi}{s}$$

$$\nu_{n,k} = \frac{j_{n,k}}{r} \tag{22}$$

and $j_{n,k}$ denotes the kth positive root of the equation $J_n(\rho) = 0$. Since

$$J_n'(\rho) = \frac{n}{\rho}J_n(\rho) - J_{n+1}(\rho)$$

the roots are easily generated by Newton's method. The first 15 values of $j_{0,k}$ and $j_{1,k}$, needed for the theoretical example below, are listed in Table 1.

The boundary values are incorporated in the coefficients

$$F_{n,k} = \frac{2}{s} \int_0^s \hat{f}_n(\xi) \sin \mu_k \xi \, d\xi$$

$$P_{n,k} = \frac{2}{r^2 J_{n+1}^2(\nu_{n,k} r)} \int_0^r \hat{f}_n(0) \left(\frac{\rho}{r}\right)^n J_n(\nu_{n,k}\rho)\rho \, d\rho$$

$$= \frac{2}{\nu_{n,k} r \, J_{n+1}(\nu_{n,k} r)} \hat{f}_n(0)$$

$$Q_{n,k} = \frac{2}{\nu_{n,k} r \, J_{n+1}(\nu_{n,k} r)} \hat{f}_n(s) \tag{23}$$

It may be noted that the closed form integration of the Fourier-Bessel coefficients in the above formulas is due to employing the factor $(\rho/r)^n$ in the interpolation of the boundary values on cylinder ends, Equations (20). The coefficients of the Fourier sine series can be evaluated, as has been done in the two-dimensional case[1], by the fast Fourier transform:

$$F_{n,k} = \frac{2}{m} \sum_{j=0}^{m-1} \hat{f}_n(s \frac{2j+1}{m}) \sin \frac{2\pi jk}{m}, \qquad k = 1, 2, \ldots, m/2-1 \tag{24}$$

where m is an integer power of 2 and the discrete values of $\hat{f}_n$ are obtained using the odd extension of the boundary function $\hat{f}_n(\xi)$ on the interval $0 < \xi < 2s$. Accordingly, the Fourier sine series of Equation (21) is truncated to the first m/2-1 terms. For consistency, the same number of terms is also used for the truncated Fourier-Bessel series.

WALL INTERFERENCE CORRECTIONS

Having constructed the velocity function (14), we can proceed to evaluate the velocity and Mach number corrections. The correction to stream velocity U_∞ applicable at the model position, is

$$\Delta U_\infty = U_\infty \frac{\partial \phi_W}{\partial x}(0,0,\theta) \tag{25}$$

where from Equations (9) and (10)

$$\frac{\partial \phi_W}{\partial x}(0,0,\theta) = \frac{1}{\beta} u(-\frac{x_1}{\beta},0,\theta) \tag{26}$$

Using Equations (14), (21) and (23), the required axial value

$$u(\xi,0,\theta) = \sum_{k=1}^{m/2-1} A_{0,k} \frac{\sin \mu_k \xi}{I_0(\mu_k r)}$$

$$+ \sum_{k=1}^{m/2-1} \left[\hat{a}_0(0) \frac{\sinh \nu_{0,k}(s-\xi)}{\sinh \nu_{0,k} s} + \hat{a}_0(s) \frac{\sinh \nu_{0,k} \xi}{\sinh \nu_{0,k} s} \right] \frac{2}{\nu_{0,k} r \, J_1(\nu_{0,k} r)} \tag{27}$$

where, according to Equation (24)

$$A_{0,k} = \frac{2}{m} \sum_{j=0}^{m-1} \hat{a}_0(s \frac{2j+1}{m}) \sin \frac{2\pi jk}{m} \tag{28}$$

As expected from the properties of a harmonic function u, the axial correction (25) proves to be independent of angle θ. Accordingly, only the zeroth term of the Fourier expansion (14) contributes in Equation (27).

The Mach number correction is obtained from the differentiated relation between Mach number and velocity as

$$\Delta M_\infty = (1 + \frac{\kappa-1}{2} M_\infty^2) M_\infty \frac{\partial \phi_W}{\partial x}(0,0,\theta) \tag{29}$$

where the x derivative of the interference potential is given by Equation (26).

The corrections to the components of the flow angle (in radians) at the position of the model are

$$\Delta\alpha_y = \frac{\partial\phi_w}{\partial y}(0,0,\theta)$$

$$\Delta\alpha_z = \frac{\partial\phi_w}{\partial z}(0,0,\theta) \qquad (30)$$

where, again, the value of θ is immaterial. As in the two-dimensional case[1], the flow angle correction can be expressed in terms of the velocity function u to within arbitrary constant terms. Integrating the total differentials of $\partial\phi_w/\partial y$ and $\partial\phi_w/\partial z$ along a path between the reference point $x = x_1$, $\rho = 0$ and the model position $x = \rho = 0$, we obtain

$$\frac{\partial\phi_w}{\partial y}(0,0,\theta) - \frac{\partial\phi_w}{\partial y}(x_1,0,\theta) = v(-\frac{x_1}{\beta},0,\theta) - v(0,0,\theta)$$

$$\frac{\partial\phi_w}{\partial z}(0,0,\theta) - \frac{\partial\phi_w}{\partial z}(x_1,0,\theta) = w(-\frac{x_1}{\beta},0,\theta) - w(0,0,\theta)$$

where

$$v(\xi,0,\theta) = \int \frac{\partial u}{\partial y}(\xi,0,\theta)d\xi$$

$$w(\xi,0,\theta) = \int \frac{\partial u}{\partial z}(\xi,0,\theta)d\xi$$

are the conjugate velocity functions. For the application in the above differences, the selection of the integration constant is obviously irrelevant. Using Equations (1), (21) and (23)

$$\begin{Bmatrix} v(\xi,0,\theta) \\ w(\xi,0,\theta) \end{Bmatrix} = \sum_{k=1}^{m/2-1} \begin{Bmatrix} A_{1,k} \\ B_{1,k} \end{Bmatrix} \frac{\cos\mu_k\xi}{2I_1(\mu_k r)} + \sum_{k=1}^{m/2-1} \left[- \begin{Bmatrix} \hat{a}_1(0) \\ \hat{b}_1(0) \end{Bmatrix} \frac{\cosh\nu_{1,k}(s-\xi)}{\sinh\nu_{1,k}s} + \begin{Bmatrix} \hat{a}_1(s) \\ \hat{b}_1(s) \end{Bmatrix} \frac{\cosh\nu_{1,k}\xi}{\sinh\nu_{1,k}s} \right] \frac{1}{\nu_{1,k} r J_2(\nu_{1,k} r)} \qquad (31)$$

where, according to Equation (24)

$$A_{1,k} = \frac{2}{m} \sum_{j=0}^{m-1} \hat{a}_1(s\frac{2j+1}{m}) \sin\frac{2\pi jk}{m}$$

$$B_{1,k} = \frac{2}{m} \sum_{j=0}^{m-1} \hat{b}_1(s\frac{2j+1}{m}) \sin\frac{2\pi jk}{m} \qquad (32)$$

Using Equations (4) and (5) we finally obtain

$$\Delta\alpha_y = v(-\frac{x_1}{\beta},0,\theta) - v(0,0,\theta) + \frac{\partial\phi}{\partial y}(x_1,0,\theta) - \frac{\gamma}{8\pi}\frac{\beta^2}{x_1^2}\cos\theta_0$$

$$\Delta\alpha_z = w(-\frac{x_1}{\beta},0,\theta) - w(0,0,\theta) + \frac{\partial\phi}{\partial z}(x_1,0,\theta) - \frac{\gamma}{8\pi}\frac{\beta^2}{x_1^2}\sin\theta_0 \qquad (33)$$

The flow angles $\partial\phi/\partial y$ and $\partial\phi/\partial z$ at $x = x_1$, $\rho = 0$ can either be measured or, if the test section is sufficiently long, set equal to the upstream flow angles, known from empty tunnel calibration.

The second derivatives $\partial^2\phi_w/\partial x^2$, $\partial^2\phi_w/\partial x\partial y$ and $\partial^2\phi_w/\partial x\partial z$, representing the pressure gradient and streamline curvature effects, are readily obtained by differentiating the series (27) and (31) with respect to ξ. For the tunnel test to be correctable by a simple adjustment in stream Mach number and flow inclination, the second (and higher) derivatives are supposed to be small.

AUTOCORRECTION PROPERTIES OF THE METHOD

As pointed out by Capelier, Chevallier and Bouniol in connection with a similar method[7], the velocity correction compensates automatically for small errors of the reference velocity level. This is of particular importance to three-dimensional ventilated test sections, since very often as reference pressure is taken that measured in the surrounding plenum chamber. Denoting by a tilde the quantities based on the plenum pressure, p_{plenum}, we write for the boundary pressure coefficient

$$\tilde{C}_p(x,r,\theta) = C_p(x,r,\theta) - C_{p_{plenum}}$$

where

$$C_{p_{plenum}} = \frac{p_{plenum} - p_\infty}{\frac{1}{2}\rho_\infty U_\infty^2}$$

According to Equation (13), the boundary value of the axial velocity function is

$$\tilde{u}(\xi,r,\theta) = -\beta\left[\frac{1}{2}\tilde{C}_p(x,r,\theta) + \frac{\partial\phi_F}{\partial x}(x,r,\theta)\right] = u(\xi,r,\theta) + \frac{\beta}{2}C_{p_{plenum}}$$

By linear superposition, the solution on the tunnel axis is obtained as

$$\tilde{u}(\xi,0,\theta) = u(\xi,0,\theta) + \frac{\beta}{2}C_{p_{plenum}}$$

where $u(\xi,0,\theta)$ is given by Equation (27). From small disturbance theory it also follows that the (fictitious) stream velocity corresponding to p_{plenum} is

$$\tilde{U}_\infty = U_\infty\left(1 - \frac{1}{2}C_{p_{plenum}}\right)$$

Consequently, the corrected stream velocity at the model position is

$$U_\infty + \Delta U_\infty = U_\infty\left[1 + \frac{1}{\beta}u\left(-\frac{x_1}{\beta},0,\theta\right)\right] = \tilde{U}_\infty\left[1 + \frac{1}{\beta}\tilde{u}\left(-\frac{x_1}{\beta},0,\theta\right)\right] = \tilde{U}_\infty + \Delta\tilde{U}_\infty$$

if the products of small terms are neglected. Similarly

$$M_\infty + \Delta M_\infty = \tilde{M}_\infty + \Delta\tilde{M}_\infty$$

This simple result has far reaching implications. It shows that, as long as the reference pressure does not differ from the upstream static pressure greatly, we always arrive at the same value of the corrected stream Mach number. The present method thus provides the much needed correspondence between the plenum pressure and the stream Mach number at the position of the model. As a matter of fact, each tunnel run that incorporates the wall pressure measurement qualifies as a calibration run. This also implies that the empty tunnel calibration (plenum pressure versus test section Mach number) should not be applied towards the Mach number corrected according to the present method.

THEORETICAL EXAMPLE

To show the feasibility and accuracy of the present method, a test example is first worked out for a theoretical case of an infinitely long cylindrical test section. For the solid wall boundary condition

$$\frac{\partial\phi}{\partial\rho}(x,r,\theta) = 0, \quad -\infty < x < \infty, \quad 0 \leqslant \theta < 2\pi$$

and ϕ_F described by Equation (5), the exact solution satisfying the upstream condition

$$\lim_{x\to-\infty}\frac{\partial\phi_W}{\partial x}(x,\rho,\theta) = 0$$

is[9,10]

$$\phi_W = \frac{\gamma}{4\pi}\frac{\cos(\theta-\theta_o)}{r}\left[\frac{\rho}{r} - \frac{2}{\pi}\int_0^\infty \frac{K_1(q) + qK_0(q)}{I_1(q) - qI_0(q)} I_1\left(\frac{q\rho}{r}\right)\sin\left(\frac{qx}{\beta r}\right)dq\right]$$

$$+ \frac{\sigma}{2\pi\beta r}\left[\frac{x}{\beta r} - \frac{1}{\pi}\int_0^\infty \frac{K_1(q)}{I_1(q)} I_0\left(\frac{q\rho}{r}\right)\cos\left(\frac{qx}{\beta r}\right)dq\right]$$

$$+ \frac{\mu}{2\pi^2(\beta r)^2}\int_0^\infty \frac{K_1(q)}{I_1(q)} I_0\left(\frac{q\rho}{r}\right) q\sin\left(\frac{qx}{\beta r}\right)dq \qquad (34)$$

Selecting the values r = 1 (arbitrary length units, L), $M_\infty = 0.7$, $C_L = 1.0$, $\theta_0 = 105°$, $r_s = 0.05$ (L), V = 0.02 (L^3), S = 0.1 (L^2) and using Equations (3)-(5), the pressure coefficients are generated at $\theta = 0, \frac{\pi}{2}, \pi, \frac{3}{2}\pi$ and 16 equidistant points on the interval $-1.6 < x < 1.6$ (L), see Table 2. The comparison of the exact correction values, calculated from Equations (29), (30) and (34), with those obtained by the present method from the generated pressures is given in Table 3. It is seen that already such a small pressure sample as that given in Table 2 yields technically acceptable accuracy of the corrections. As shown in Reference 2, further improvement can be obtained by increasing the number of pressure points and extending the interval of x farther upstream and downstream. In practice, there are of course limits imposed by the actual physical length of the test section and the number of pressure orifices that can be scanned.

CORRECTIONS FOR AN AIRCRAFT MODEL

Figures 5a - b show pressure distributions measured by static pressure pipes above ($\theta = 90°$) and below ($\theta = 270°$) a transport aircraft model in the NAE 5 ft. × 5 ft. blowdown wind tunnel. The 1 in. diameter pipes, sketched in Figure 3, are directly attached to the 20% perforated walls. Since the side force is essentially zero, two tubes are sufficient for the determination of the flow angle correction, but for a more accurate evaluation of the Mach number correction four tubes would be preferable, cf. Equations (19a) and (19b). The span of the (straight) wing is 47 in. (78% of the section span), the model volume is V = 1100 $in.^3$ and the reference area, on which the force coefficients are based, is S = 220 $in.^2$. The point where the corrections are evaluated (x/h = 0) is selected to be the intersection of wing quarter-chord lines. It is seen that with respect to the pressure pipes, extending over the perforated test section length, the model is located too far downstream. In the higher incidence case, Figure 5b the upstream pressure coefficients (based on the plenum pressure) converge to zero, but in the lower incidence case, Figure 5a they tend to a slightly negative limit. This is simply an indication that the pressure established during the tunnel run in the plenum chamber is higher than that in the upstream portion of the test section. This affects the Mach number correction, but presumably not the resultant, corrected Mach number (see the autocorrection properties of the method). In both cases, Figures 5a and b, the Mach number correction is found small and the angle of attack correction negligible.

CORRECTIONS FOR A SLENDER MODEL

Figures 6a - c show pressure distributions measured by four static pressure tubes during a test of a rocket launcher model, again in the NAE 5 ft. × 5 ft. wind tunnel. The body has diameter 6.5 in. and length 48 in.; with respect to the rails it is again positioned too far back. The forces are normalized by the circular cross-section of the body. The differences between the upstream pressures on the side tubes ($\theta = 0°$ and 180°) and the top and bottom tubes ($\theta = 90°$ and 270°) are puzzling, particularly since they already exist near zero incidence, see Figure 6a. Admittedly, the axial symmetry is somewhat disturbed by attachment lugs on top of the model and by the downstream influence of a vertical strut[14] (neither is shown in the figures), but we are not sure if this can fully account for the effect. In Figure 6c the proximity of the model nose to the wall has a noticeable influence on the upper wall pressure and the representation of the model far field by the axial source-sink combination is questionable for such a high incidence. In any case, the evaluated Mach number correction is small at all three incidences, Figures 6a - c. The angle of attack correction is small except for the low incidence case, Figure 6a which is not impossible, but contrary to our expectations.

CONCLUSIONS

A practical method has been presented for the assessment of three-dimensional wall interference corrections from boundary pressures, measured by static pressure tubes at the test section walls, and the aerodynamic forces, acting on the model. The method is autocorrective with respect to errors of the reference pressure and provides a link between the plenum pressure and the test section Mach number. The accuracy is demonstrated on a theoretical example of the cylindrical closed wall test section. An application to actual tunnel data from a perforated wall test section shows that the corrections are rather small and that a more elaborate computation of three-dimensional wall interference effects at subcritical flow conditions at the walls seems unwarranted.

ACKNOWLEDGEMENT

The author wishes to thank J.R. Digney and F.C. Tang of the High Speed Aerodynamics Laboratory, National Research Council Canada, for providing their unpublished experimental data and helpful discussions.

REFERENCES

1. Mokry, M.
Ohman, L.H.
Application of the Fast Fourier Transform to Two-Dimensional Wind Tunnel Wall Interference.
Journal of Aircraft, Vol. 17, June 1980, pp. 402-408.

2. Mokry, M.
Evaluation of Three-Dimensional Wall Interference Corrections from Boundary Pressure Measurements.
LTR-HA-51, National Aeronautical Establishment, National Research Council Canada, November 1980.

3. Stahara, S.
Spreiter, J.R.
Transonic Wind Tunnel Interference Assessment — Axisymmetric Flows.
AIAA Journal, Vol. 18, 1980, pp. 63-71.

4. Hinson, B.L.
Burdges, K.P.
Acquisition and Application of Transonic Wing and Far-Field Test Data for Three-Dimensional Computational Method Evaluation.
AFOSR-TR-80-0421, Lockheed-Georgia Co., March 1980.

5. Mercer, J.E.
Geller, E.W.
Johnson, M.L.
Jameson, A.
Transonic Flow Calculations for a Wing in a Wind Tunnel.
Journal of Aircraft, Vol. 18, 1981, pp. 707-711.

6. Rizk, M.H.
Hafez, M.
Murman, E.M.
Lovell, D.
Transonic Wind Tunnel Wall Interfcrence Corrections for Three-Dimensional Models.
AIAA Paper 82-0588, March 1982.

7. Capelier, C.
Chevallier, J.-P.
Bouniol, F.
Nouvelle mèthode de correction des effets de parois en courant plan.
La Recherche Aérospatiale, January-February 1978, pp. 1-11.

8. Sawada, H.
Wind Tunnel Interference in a Test Section with Ventilated Walls.
ICAS-80-23.5, October 1980.

9. Baldwin, B.S.
Turner, J.B.
Knechtel, E.D.
Wall Interference in Wind Tunnels with Slotted and Porous Boundaries at Subsonic Speeds.
NACA TN 3176, May 1954.

10. Wright, R.H.
The Effectiveness of the Transonic Wind Tunnel as a Device for Minimizing Tunnel-Boundary Interference for Model Tests at Transonic Speeds.
AGARD Rept. 294, March 1959.

11. Lotz, I.
Correction of Downwash in Wind Tunnels of Circular and Elliptic Sections.
NACA TM 801, July 1936.

12. v.Baranoff, A.
Tunnel Corrections for Compressible Subsonic Flow.
NACA TM 1162, July 1947.

13. Hackett, J.E.
Wilsden, D.J.
Lilley, D.E.
Estimation of Tunnel Blockage from Wall Pressure Signatures; A Review and Data Correlation.
NASA CR-15,224, March 1979.

14. Brown, D.
Information for Users of the National Research Council's 5-ft. x 5-ft. Blowdown Wind Tunnel at the National Aeronautical Establishment, Third Ed.
LTR-HA-6, National Aeronautical Establishment, National Research Council Canada, September 1977.

TABLE 1

ZEROS OF BESSEL FUNCTIONS J_0 AND J_1

k	$j_{0,k}$	$j_{1,k}$
1	2.40483	3.83171
2	5.52008	7.01559
3	8.65373	10.17347
4	11.79153	13.32369
5	14.93092	16.47063
6	18.07106	19.61586
7	21.21164	22.76008
8	24.35247	25.90367
9	27.49348	29.04683
10	30.63461	32.18968
11	33.77582	35.33231
12	36.91710	38.47477
13	40.05843	41.61709
14	43.19979	44.75932
15	46.34119	47.90146

TABLE 2

PRESSURE COEFFICIENTS ON THE CONTROL CYLINDER
(THEORETICAL EXAMPLE)

x	C_p			
	$\theta = 0$	$\theta = \pi/2$	$\theta = \pi$	$\theta = 3/2\pi$
-1.5	0.00024	-0.00115	-0.00035	0.00104
-1.3	0.00033	-0.00200	-0.00066	0.00167
-1.1	0.00034	-0.00354	-0.00130	0.00258
-0.9	-0.00001	-0.00645	-0.00273	0.00371
-0.7	-0.00154	-0.01207	-0.00599	0.00454
-0.5	-0.00607	-0.02268	-0.01309	0.00351
-0.3	-0.01553	-0.03967	-0.02573	-0.00159
-0.1	-0.02661	-0.05670	-0.03933	-0.00924
0.1	-0.02900	-0.05909	-0.04172	-0.01163
0.3	-0.02176	-0.04590	-0.03196	-0.00782
0.5	-0.01442	-0.03103	-0.02144	-0.00484
0.7	-0.01081	-0.02134	-0.01526	-0.00473
0.9	-0.00962	-0.01606	-0.01234	-0.00590
1.1	-0.00940	-0.01328	-0.01104	-0.00716
1.3	-0.00946	-0.01178	-0.01044	-0.00811
1.5	-0.00956	-0.01095	-0.01015	-0.00876

TABLE 3

WALL INTERFERENCE CORRECTIONS (THEORETICAL EXAMPLE)

	Exact	Present Method $-1.6<x<1.6$ $m = 32$
ΔM_∞	0.00724	0.00715
$\Delta\alpha_y$ (deg)	-0.05900	-0.05420
$\Delta\alpha_z$ (deg)	0.22020	0.20228
$\partial\Delta M_\infty/\partial x$ (1/L)	0.00210	0.00207
$\partial\Delta\alpha_y/\partial x$ (deg/L)	-0.08254	-0.08123
$\partial\Delta\alpha_z/\partial x$ (deg/L)	0.30803	0.30315

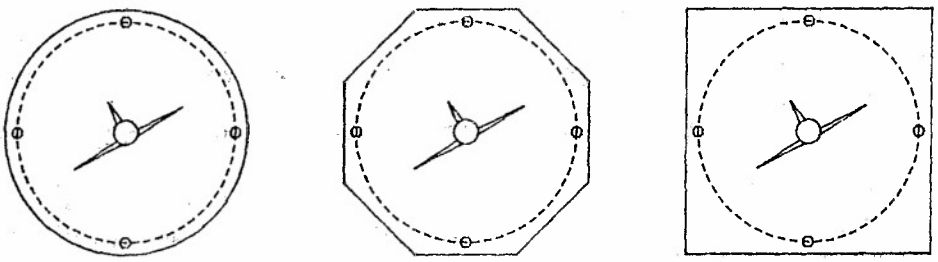


FIG. 1: POSITIONING OF STATIC PRESSURE TUBES

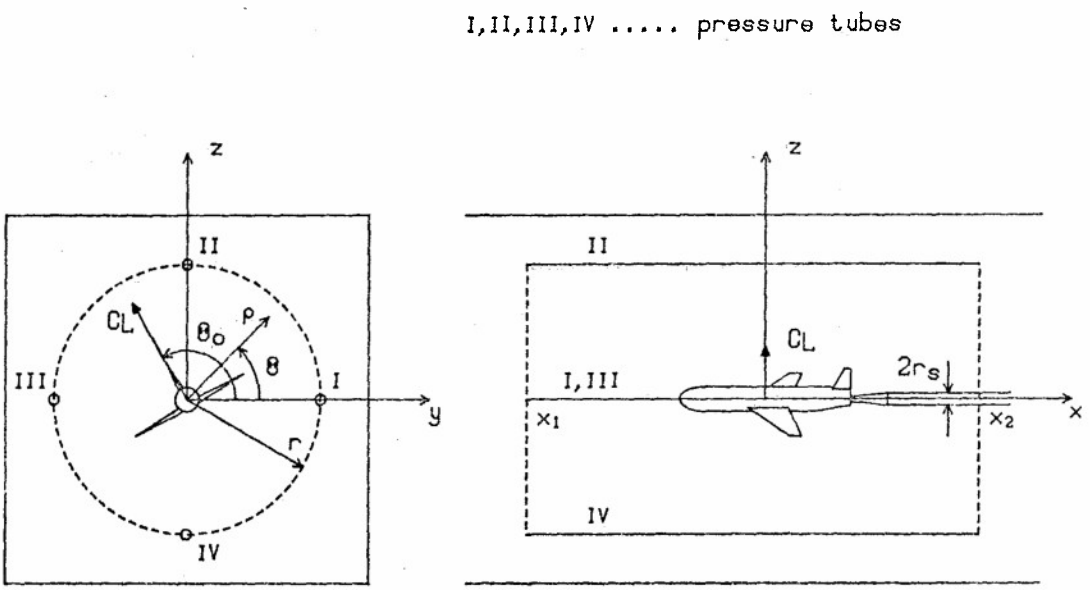


FIG. 2: CO-ORDINATE SYSTEM

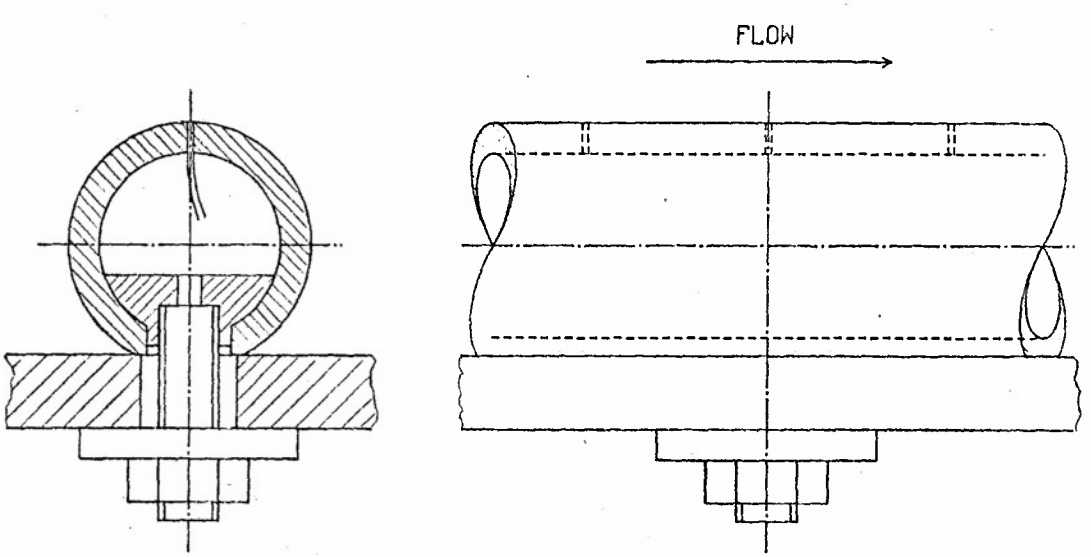


FIG. 3: DETAIL OF THE STATIC PRESSURE TUBE

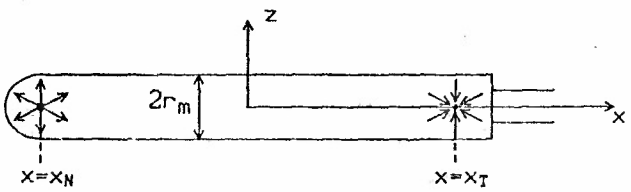


FIG. 4: SOURCE-SINK REPRESENTATION FOR AN ELONGATED BODY

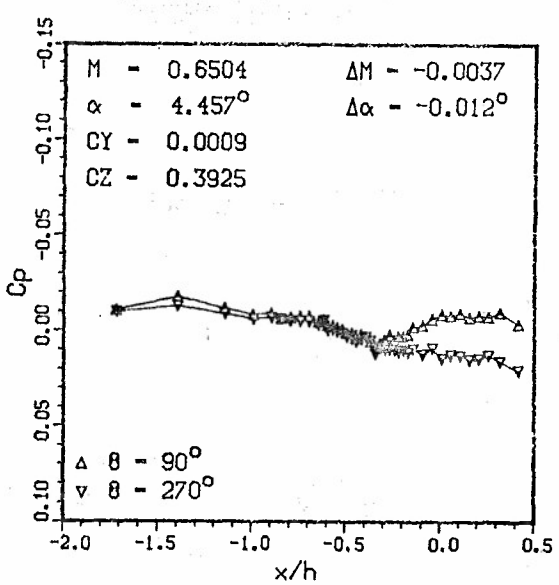
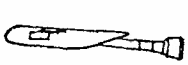


FIG. 5a: WALL PRESSURES FOR AN AIRCRAFT MODEL



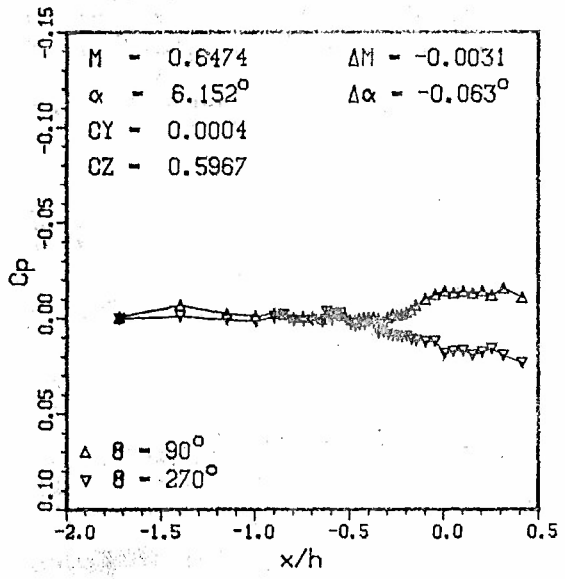
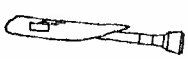


FIG. 5b: WALL PRESSURES FOR AN AIRCRAFT MODEL



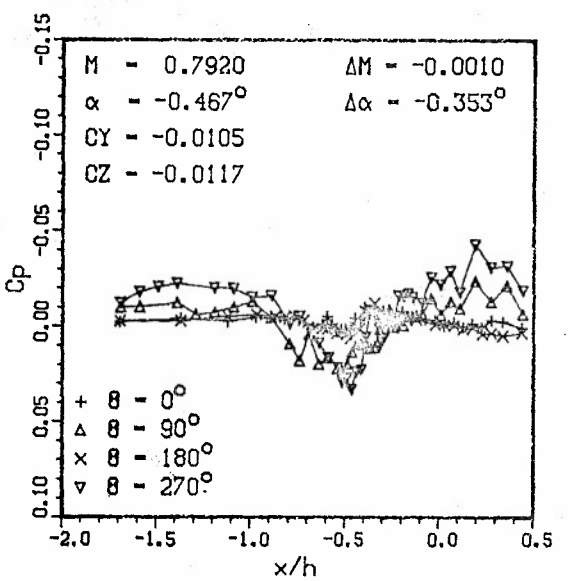
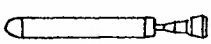


FIG. 6a: WALL PRESSURES FOR A SLENDER MODEL



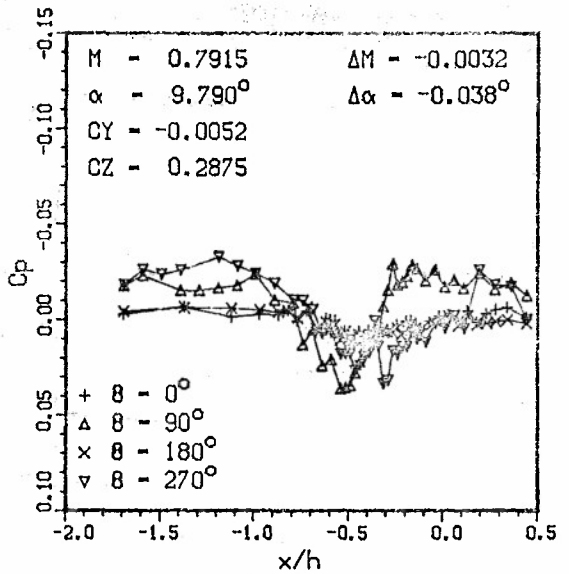


FIG. 6b: WALL PRESSURES FOR A SLENDER MODEL

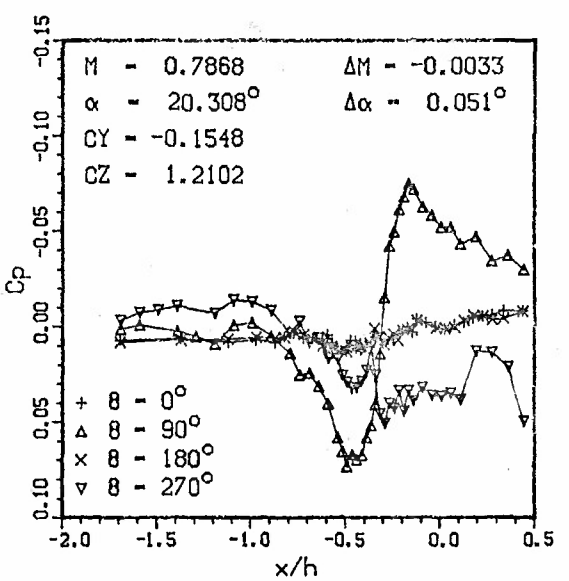


FIG. 6c: WALL PRESSURES FOR A SLENDER MODEL

AMELIORATIONS DES CALCULS DES EFFETS DE PAROIS DANS LES SOUFFLERIES INDUSTRIELLES DE L'ONERA

par Xavier VAUCHERET

Office National d'Etudes et de Recherches Aérospatiales (ONERA)
92320 Châtillon (France)

RESUME

Des améliorations ont été apportées récemment aux calculs des effets de parois dans les souffleries industrielles de l'ONERA. Les descriptions mathématiques des maquettes et de leurs dards supports sont plus élaborées : le nombre de singularités est accru jusqu'à coïncidence des signatures, mesurées et calculées, des ensembles maquette-dard sur les parois des veines guidées d'essais. L'excentrement des singularités est considéré dans le cas des incidences élevées.

Les cartographies de porosité des parois perméables déduites des signatures mesurées en parois perforées permettent de s'affranchir des essais de référence, exécutés antérieurement en veine guidée ou dans des veines de plus grandes dimensions. Les porosités obtenues à partir des termes de blocage (signatures à portance nulle) et de portance (effet de portance sur les signatures) sont en hon accord .

Les corrections des effets de parois sont calculées maintenant pour chaque cas de veine, parois, maquette, dard et pour une grille de Mach, CX, CZ et traduites sous forme polynomiale pour les calculs afferant à chaque point d'un programme d'essai industriel.

ABSTRACT

The methods used to compute wall interference corrections for the ONERA large wind tunnels have received improvements over the years. The mathematical description of the model and its sting support is more and more sophisticated ; an increasing number of singularities is used until an agreement between theoretical and experimental signatures of the model and sting on the walls of the closed test section is obtained. The effect of the singularity displacement from the central position is calculated when the model reaches large angles of attack.

The porosity factor cartography on the perforated walls deduced from the measured signatures avoids to carry out reference tests in larger tunnel as previously. The porosity factors obtained from the blockage terms (signatures at zero lift) and from the lift terms are in good agreement.

In each case (model + sting + test section) wall corrections are now determined, before the tests, as a function of the fundamental parameters M, CD, CL. During the wind tunnel tests, the corrections are quickly computed from these functions.

INTRODUCTION

La discussion finale clôturant le symposium AGARD/FDP de Valloire en 1975 (1) confirmait la nécessité d'appliquer les corrections des effets de parois aux essais réalisés dans les souffleries existantes en écoulement transsonique. De telles corrections ne visent pas à donner des résultats identiques à ceux du vol, par suite des différences de nombres de Reynolds, mais à rétablir les vitesses modifiées par la présence des parois, en grandeur comme en direction. De cette manière, les résultats obtenus à même Reynolds dans diverses souffleries et à différentes échelles de maquettes seraient alors homogènes. Les comparaisons de ce type constituent un guide précieux pour contrôler les calculs d'effets de parois. De nombreux programmes de comparaisons ont ainsi été élaborés : tel fut le cas des essais de maquettes étalons ONERA (2) ou des essais en cours sur la maquette F4 dans le cadre du groupe GARTEUR en ce qui concerne divers organismes. Tel est le souci permanent à l'ONERA en multipliant les comparaisons d'essais réalisés dans les diverses souffleries industrielles S1 - S2 - S3MA et F1 en tridimensionnel (3) .

L'étude des effets de parois a suscité depuis 1919 une abondante littérature. Une étude (4) de ces effets, en parois perforées, donnait en 1977, une liste, certes incomplète, de 77 références publiées. Au moins autant de travaux ont été publiés sur les parois à fentes. Ce nombre important de publications laisserait à penser que le problème est résolu. Il semble qu'il n'en soit rien, en consultant la liste des congrès tenus sur ce sujet, lors des dix dernières années. Les congrès AGARD/FDP tenus à Londres en 1975 (5) , Rhode Ste Genèse en 1976 (6) et Munich en 1980 (7) comportent 27 communications sur les effets de parois. La dernière conférence AIAA tenue cette année à Williamsburg comportait une session entière sur les effets de parois (8) . Il y a lieu, bien entendu de citer le présent congrès, relatif uniquement aux effets de parois, pour lequel 17 exposés sont prévus.

1 - AMELIORATIONS RECENTES DES CALCULS D'EFFETS DE PAROIS A L'ONERA

Les travaux sur les études des parois adaptables actuellement menés en bidimensionnel à l'ONERA ne seront pas considérés ici. Cet exposé concernera seulement le cas des maquettes tridimensionnelles en veines conventionnelles cylindriques utilisées en essais industriels. Les raisons des travaux entrepris pour améliorer les calculs des effets de parois dans de tels cas peuvent être classés en cinq groupes :

- l'accroissement des précisions requises pour les projets d'avions modernes, singulièrement pour les avions de transport civil transsoniques
- l'accroissement des domaines d'incidence pour les chasseurs modernes
- l'augmentation des puissances des ordinateurs disponibles pour les calculs
- les mesures des signatures des ensembles maquette -dard sur les parois des veines d'essais
- l'augmentation des tailles des maquettes, par rapport aux veines d'essais, en vue d'une meilleure représentation de certains détails et d'une élévation du nombre de Reynolds des essais.

Les améliorations récentes des calculs des effets ds parois, exposées dans cette publication, réalisées à l'ONERA, seront décrites selon trois axes d'efforts.

A) Amélioration des descriptions mathématiques des maquettes tant en nombre de singularités qu'en emplacement de celles-ci, spécialement dans le cas des incidences élevées : en effet, par suite de l'implantation en veine de mécanismes permettant des angles plus élevés des maquettes, celles-ci sont amenées à être excentrées. En outre les descriptions incluent les supports de maquettes alors qu'antérieurement les maquettes étaient idéalement considérées comme isolées.

B) Utilisation des mesures des signatures des ensembles maquette-dard sur les parois des veines d'essais pour, d'une part, contrôler en veine guidée la validité de la description mathématique des maquettes-dards, d'autre part, en parois ventilées, en déduire les cartographies de porosités des parois. Cette nouvelle manière de procéder permet donc de s'affranchir des essais de référence antérieurement utilisés (9) tels qu'essais en veine guidée ou dans des souffleries de plus grandes dimensions.

C) Remaniement des méthodes de calculs des corrections d'effets de parois : les tables de coefficients de corrections calculées antérieurement pour une veine donnée, en fonction de nombreux paramètres tels que porosité des parois, envergure relative de maquette, flèche de voilure, répartition de portance en envergure ... seront abandonnées. Les calculs de corrections sont effectués pour chaque cas veine - maquette - dard pour une grille de Mach, Cz, Cx et les corrections déduites sous forme de polynômes en fonction de ces 3 paramètres. Cette manière de procéder permet un calcul rapide des corrections pour chaque point d'essai.

2 - DESCRIPTION MATHEMATIQUE DES MAQUETTES ET DARDS

2.1 - Représentation des volumes

Initialement [4] le volume de la maquette était représenté par un seul doublet situé au centre de la maquette placé conventionnellement au quart de la corde moyenne aérodynamique. Des coefficients empiriques étaient ajoutés pour tenir compte de l'élancement du fuselage et des dimensions relatives de la maquette en veine. Ceci permettrait de calculer le nombre de Mach pris conventionnellement au centre maquette. Par contre on conçoit que le gradient de blocage de volume était erroné avec une seule singularité impropre à rendre compte de la loi des aires. En outre les signatures de la maquette sur les parois de la veine étaient trop concentrées, contribuant à l'estimation d'un blocage prématuré en veine guidée. Après équipement des parois des veines en prise de pressions, il s'avérsit que les signatures calculées différaient notablement des signatures mesurées.

Pour ces diverses raisons, une représentation du fuselage des maquettes par un ensemble de doublets s été utilisée : la longueur fuselage est découpée en N intervalles égaux pour lesquels les volumes élémentaires sont calculés à partir de la loi des aires ainsi que leur centre de gravité respectif . Chaque volume élémentaire est représenté par un doublet situé au centre de gravité du volume ; l'intensité du doublet, proportionnelle au volume élémentaire, est affectée d'un terme de compressibilité déduit du nombre de Mach corrigé calculé en son emplacement après plusieurs itérations.Le nombre de doublets N retenu est celui au-delà duquel les signatures et les répartitions de Mach corrigé sur l'axe fuselage ne sont pas modifiées.

La figure 1 montre les signatures d'un ellipsoïde d'élancement 6, en veine guidée, obtenues avec une description par 1, 2, 3 et 12 doublets. La signature devient asymptotique à partir de 12 doublets. Au-dessous de ce nombre et spécialement avec un seul doublet, les signatures sont trop concentrées et ne font pas étst de l'étalement obtenu avec un nombre suffisant de doublets.

Un règle simple, déduite de calculs pour divers élancements d'ellipsoïdes, consiste à prendre un nombre de doublets égal ou double de l'élancement du fuselage.

La figure 2 fournit la comparaison, obtenue dans une veine guidée de la soufflerie SIMA de 8 mètres de diamètre, des signatures calculées et mesurées d'un missile à échelle grandeur de 5,3 mètres de long. Dans ce cas, l'accord satisfaisant entre ces signatures est obtenu avec 30 doublets. Les signatures calculées "personnalisent" bien la configuration de la maquette ainsi que l'attestaient les mesures données dans le cas du fuselage seul ou du missile complet comportant nacelles et empennages. Les signatures reflètent en quelque sorte la forme de la loi des aires. Les signatures calculées avec un seul doublet, données à titre de référence, en trait interrompu, seraient tout à fait incorrectes car trop concentrées et de Mach maximal trop élevé.

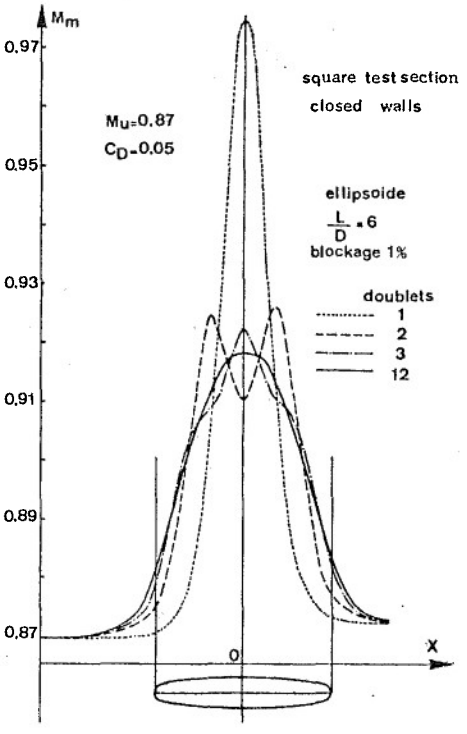


Fig. 1 - Influence du nombre de doublets sur la signsture d'un ellipsoïde en veine guidée.

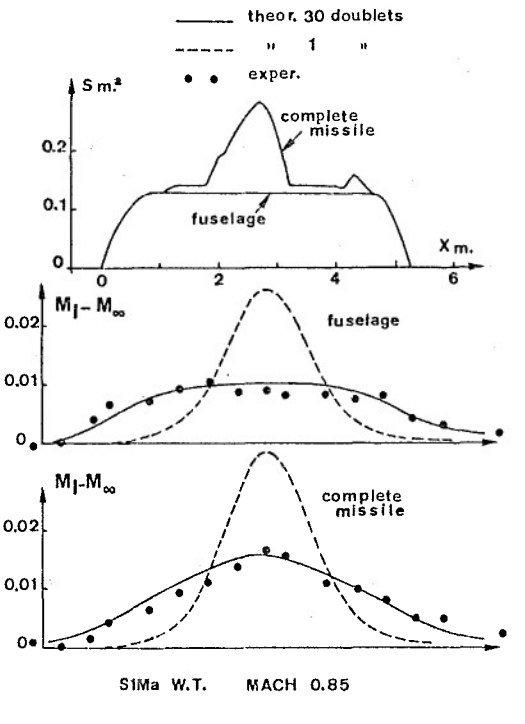


Fig. 2 - Signatures théoriques et expérimentsles d'un missile en veine guidée.

De ce fait, les limites de blocage de la maquette en veine étaient obtenues prématurément par le calcul (figure 3) alors qu'avec un nombre suffisant de doublets, le blocage est prédit à un Mach supérieur de 0,02 environ. Les essais attestent bien que le blocage n'apparait qu'au-delà de Mach 0,9 pour le missile complet.

La répartition du nombre de Mach corrigé le long de l'axe maquette est directement proportionnelle aux coefficients locaux Ω_s[4] pour un seul doublet ou à des coefficients analogues Ω_{sx} pour N doublets. La figure 4 donne, pour différents facteurs de porosité réduite, Q, [4] des parois perforées, les répartitions longitudinales des coefficients Ω_s et Ω_{sx} pour 1 et 20 doublets représentant l'ellipsoïde d'élancement 6 de 1 % d'obstruction. Avec 20 doublets les courbes sont toujours plus atténuées. Sur cette même figure, les corrections de Mach (Mc - Mu), au centre de l'ellipsoïde, sont également réduites par l'emploi d'un nombre correct de doublets.

Il s'ensuit que les corrections de "poussée d'Archimède", dues aux blocages de volume, elles mêmes directement liées aux gradients longitudinaux des coefficients Ω soit Ω'_s et Ω'_{sx} pour 1 et N doublets, sont modifiées (figure 5). Ces corrections ΔC_{x_s} sont alors réduites, en valeur absolue (figure 5).

Si dans le cas d'un ellipsoïde, il était intuitif de situer le doublet unique, pris anciennement, au centre de ce volume, pour un fuselage, une inconnue subsistait lors de l'emploi d'un seul doublet : son emplacement. Selon cette position, la correction ΔC_{x_s} évoluait (figure 6) alors qu'avec un ensemble de doublets suffisant, cette correction est unique.

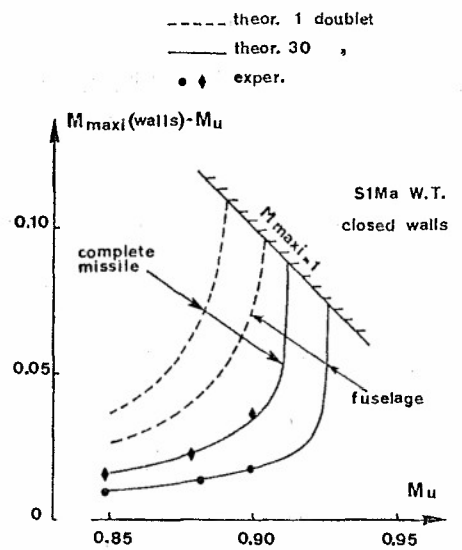


Fig.3 - Prédiction du nombre de Mach de blocage en veine guidée.

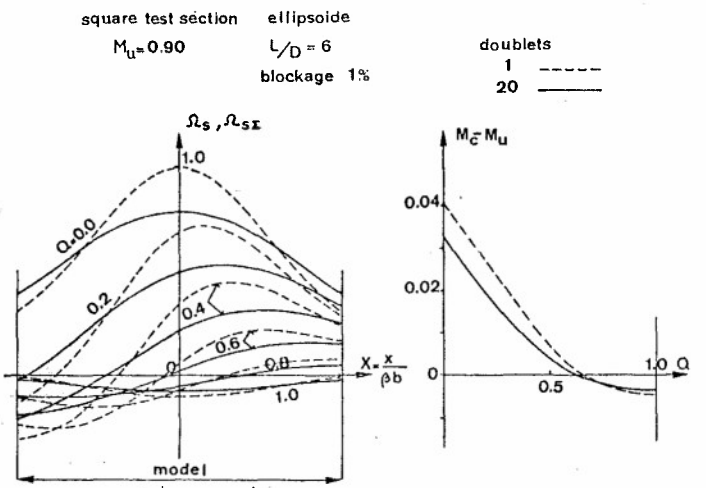


Fig. 4 - Influence de la modélisation d'un ellipsoïde sur la correction de Mach en parois ventilées.

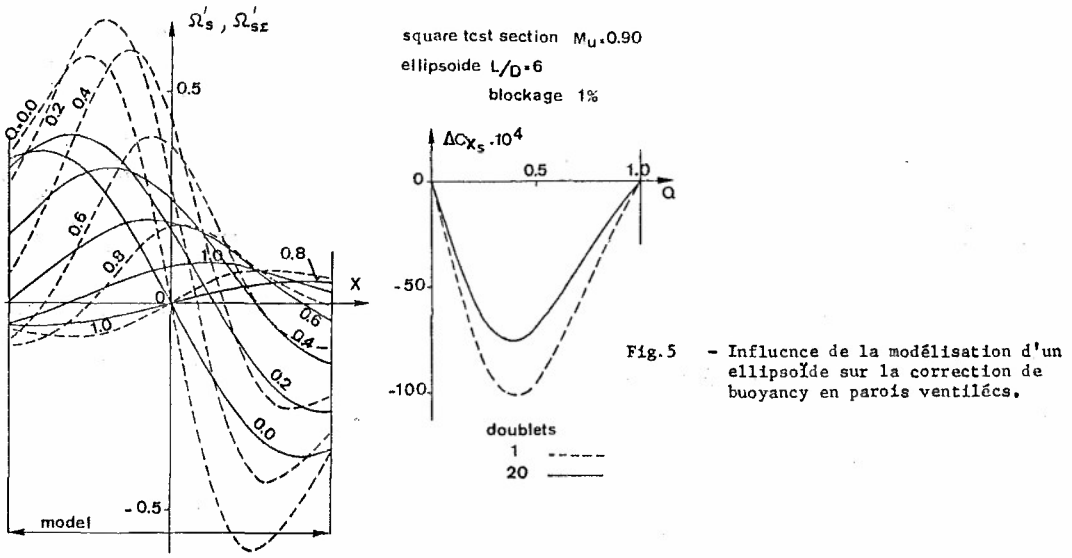


Fig.5 - Influence de la modélisation d'un ellipsoïde sur la correction de buoyancy en parois ventilées.

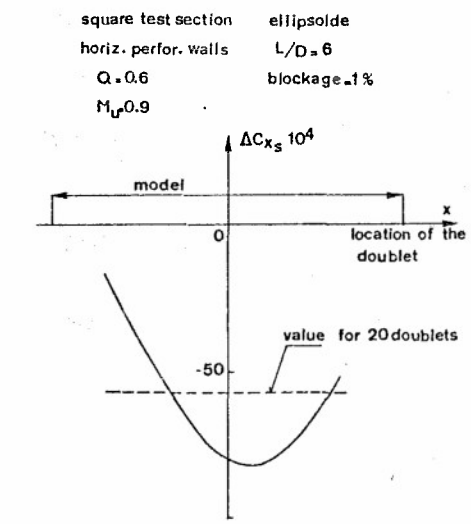


Fig.6 - Influence de la position du doublet sur la correction de buoyancy.

2.2 - Représentation du sillage et des décollements

Dans le cas d'un fuselage, le blocage de sillage était calculé en utilisant une source située au centre maquette, d'intensité proportionnelle au coefficient de traînée mesuré. Dans les calculs récents, la source peut être placée en un endroit quelconque. L'effet du recul de la source du centre maquette au culot est donné figure 7 : il réduit les corrections de Mach tout le long de l'axe fuselage ainsi que le niveau des signatures sur les parois de la veine. Il importe donc de préciser l'emplacement du sillage.

Dans le cas d'une maquette d'avion, le problème de l'emplacement et des singularités utilisées pour représenter le sillage et les décollements à grande incidence est nettement plus complexe. Les meillcures modélisations actuelles sont proposées par HACKETT [9, 10] .

Il y a lieu de noter, ainsi que mentionné au paragraphe 2.1, que les singularités utilisées pour représenter les volumes et les sillages ont des intensités pondérées par le terme de compressibilité déduit du nombre de Mach corrigé à l'emplacement de chaque singularité. Ceci implique un calcul itératif : le nombre d'itérations croit bien entendu avec le nombre de Mach. La figure 7 illustre l'effet des itérations dans le cas du missile précédent à SIMA à Mach 0,90. L'importance de ces itérations est évidente sur le calcul du blocage en veine guidée.

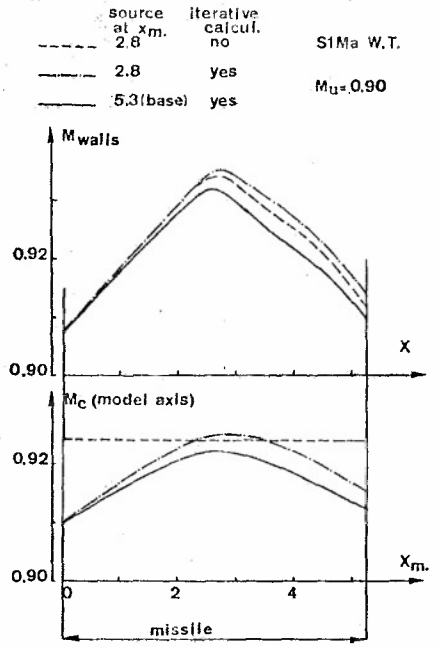


Fig.7 - Influence de la position de la source et des itérations de calcul sur les signatures.

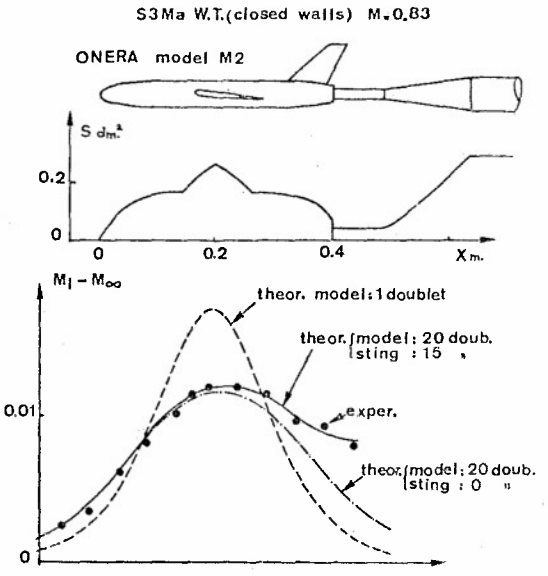


Fig.8 - Signatures de maquette et dard en veine guidée.

2.3 - Prise en considération du dard support

Jusqu'ici la maquette est décrite mathématiquement, en l'absence de son dard support. La figure 8 montre que, dans le cas d'une maquette étalon ONERA M2 [2] montée en dard droit dans la veine transsonique en configuration guidée de la soufflerie S3MA, à Mach 0,83, les signatures mesurées à portance nulle, diffèrent des signatures calculées avec 20 doublets représentant la maquette seule ; la différence est de plus en plus importante vers l'aval.

La modélisation du support à l'aide de 15 doublets, ajoutée à celle de la maquette permet d'obtenir des signatures calculées et mesurées en excellent accord, même en dehors de la zone occupée par la maquette. Il importe donc de tenir compte de la loi des aires des dards supports, d'autant plus que les aires des dards dépassent souvent l'aire du maître couple de la maquette.

Les répartitions de Mach corrigé, le long de l'axe de la maquette, proportionnelles aux coefficients $\mathcal{Q}_{s\Sigma}$, sont données figure 9. Il s'agit ici des effets comparatifs des termes d'interactions de blocage dus aux effets de parois (et non de l'ensemble des potentiels dus à la maquette en atmosphère illimitée φ_m et dus aux interactions φ_i). L'influence du blocage dû au dard, en aval de la maquette, se répercute ici dans toute la zone occupée par la maquette. Cette influence se manifeste d'autant plus que le Mach est réduit.

La dérivée $\mathcal{Q}'_{s\Sigma}$ de la fonction précédente $\mathcal{Q}_{s\Sigma}(x)$ conduit à la correction de poussée d'Archimède ΔC_{xs} induite par les termes de blocage. La figure 9 montre l'altération des courbes $\mathcal{Q}'_{s\Sigma}(x)$. Pour la maquette seule, cette courbe est impaire, ce qui conduit à une correction ΔC_{xs} pratiquement nulle. Par contre, la présence du dard donne des $\mathcal{Q}'_{s\Sigma}$ presque toujours positifs, sauf sur la partie arrière. De ce fait la correction ΔC_{xs} est négative. L'erreur entraînée, en ne considérant pas le dard support est d'environ 10.10^{-4} en traînée donc importante. A cette correction il y a lieu d'ajouter bien entendu, l'influence du dard support sur la maquette en atmosphère illimitée (potentiel φ_m).

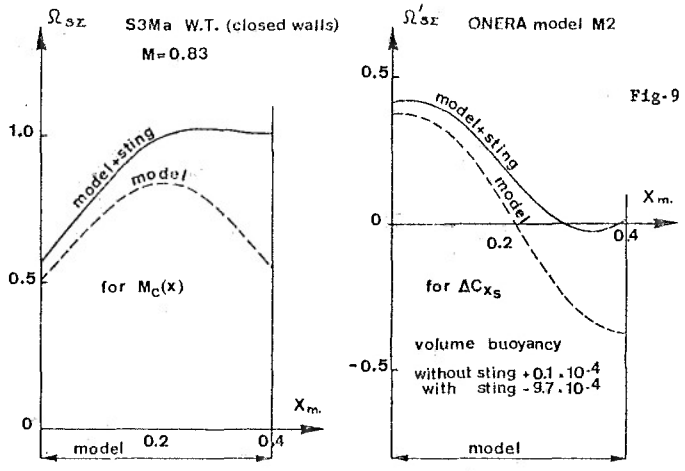


Fig.9 - Influence du dard sur les corrections de blocage.

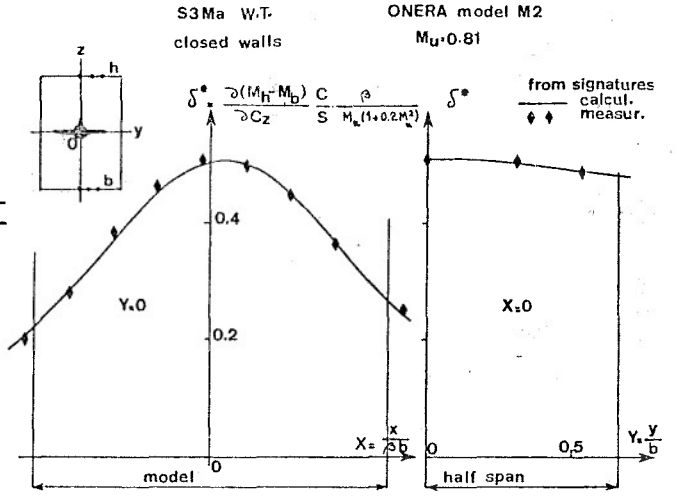


Fig.10 - Comparaison des effets des termes de portance sur les signatures en veine guidée.

2.4 - Représentation de la portance

La représentation de la portance par une nappe tourbillonnaire, non inclinée, tenant compte de l'envergure relative de la voilure, de sa flèche et de la répartition de portance en envergure si elle est connue, est utilisée [4] . Une telle représentation convient pour les incidences modérées mais requiert quelques précautions à forte incidence [3] .

Le contrôle de cette modélisation est obtenu par différence des signatures aux parois haute et basse de la veine. En fait une comparaison des pentes, en un point X, Y de la veine, des courbes des différences entre Mach locaux mesurés sur les 2 parois M_H M_B , en fonction de Cz est obtenue à l'aide d'un coefficient δ^* analogue au coefficient δ [4] de correction d'incidence.

La comparaison, donnée figure 10, en veine guidée de la soufflerie S3MA, toujours pour la maquette étalon ONERA M2, des coefficients δ^* mesurés et calculés, donne une bonne concordance pour la cartographie des signatures sur les 2 parois (courbes à Y = 0 dans le plan de symétrie vertical et à X = 0 dans le plan transversal).Ceci valide donc la modélisation des termes de portance.

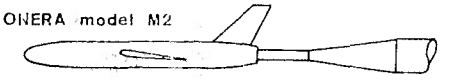
3 - DETERMINATION DES POROSITES DES PAROIS

3.1 - Signatures à portance nulle

Dès lors que les représentations mathématiques des maquettes et dards sont suffisamment sophistiquées pour obtenir des signatures correctes en veine guidée, le problème des conditions limites en parois perforées peut être abordé.

Actuellement, la méthode directe qui consisterait à déduire directement les corrections des effets de parois à partir des signatures mesurées n'est pas utilisée en tridimensionnel. Une méthode indirecte, passant par l'intermédiaire de la cartographie de porosité des parois, est pour l'instant préférée car un objectif fondamental recherché est de démontrer si le concept de la porosité uniforme a lieu ou non d'être abandonné.

Le calcul des signatures est effectué en fonction d'une porosité constante des parois. Sur une telle grille de signatures en fonction de X et Q, les signatures mesurées sont reportées. La figure 11 donne ainsi la signature mesurée, à portance nulle, toujours sur la même maquette étalon ONERA M2, montée en dard droit, en veine guidée et avec des parois horizontales perforées. On voit que cette dernière signature coïncide assez remarquablement avec la signature calculée pour $Q = 0,2$ ce qui, dans ce cas, valide le concept de porosité uniforme. S'agissant d'une maquette centrée, les signatures utilisées ici, à portance nulle, ne dépendent que des termes de blocage.



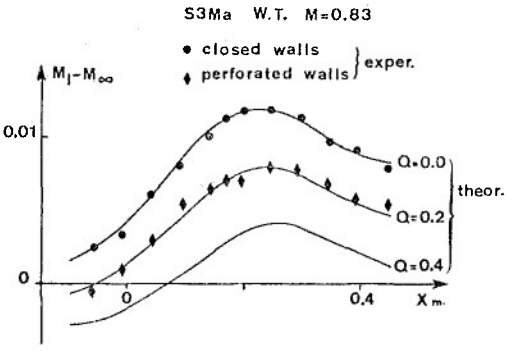
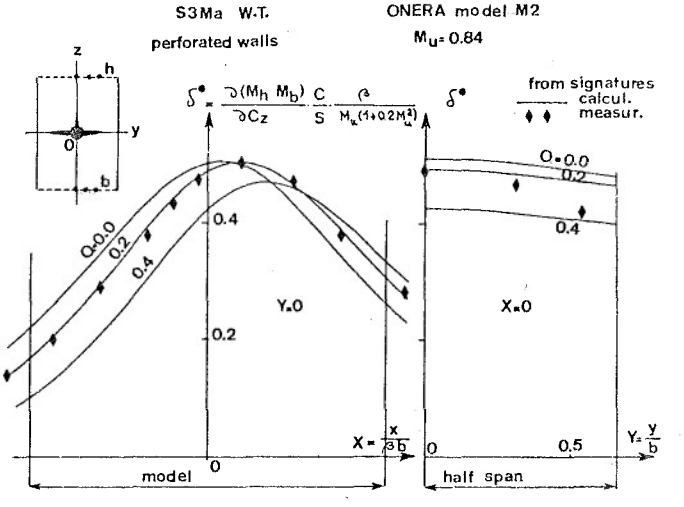


Fig-11 - Détermination des porosités à partir des signatures en parois perforées (termes de blocage).

Fig-12 - Détermination des porosités à partir des signatures en parois perforées (termes de portance).



3.2 - Signatures à portance non nulle

Ainsi qu'indiqué au paragraphe 2.4 la différence des signatures sur les 2 parois haute et basse peut servir à contrôler la validité des modélisations de portance. Une fois celle-ci confirmée en veine guidée, on peut à l'inverse, l'utiliser en parois poreuses, pour obtenir la cartographie de la porosité des parois. La figure 12 illustre cette méthode dans le cas de la maquette étalon ONERA M2 à S3MA en configuration de parois perforées.

Par rapport à la grille $\delta^*(x,y)$ calculée en fonction du paramètre de porosité Q, on déduit que dans le plan de symétrie vertical on obtient la valeur constante de Q de 0,2, en accord avec la valeur trouvée à portance nulle (figure 11). On remarquera donc l'identité des porosités issues des termes de blocage (Cz nul) et de portance. En envergure, on note un accroissement léger de Q de 0,2 à 0,35.

Il apparait donc qu'actuellement, les cartographies de porosité peuvent être déduites des signatures sur parois et que la détermination des porosités en référence d'essais effectuées en veine guidée ou dans une soufflerie de plus grande dimension puisse être abandonnée. Cette nouvelle méthode possède donc deux incontestables avantages, d'une part éviter des essais supplémentaires de référence, d'autre part définir les lois de porosité pour toute gamme de Mach et Reynolds parfois non réalisables lors des essais de référence. Par contre cette méthode nécessite le relevé des signatures donc allonge les durées d'essais, qui peuvent toutefois être limitées en nombre de points de Mach et incidence.

3.3 - Méthode de détermination rapide du Mach corrigé

A partir des formulations des signatures théoriques de la maquette sur les parois [4], une méthode intéressante de détermination du nombre de Mach corrigé a pu être dégagée. Cette méthode consiste à déduire le Mach corrigé Mc du Mach Mm mesuré sur la paroi pleine au droit du maître couple de la maquette (dans le prolongement de l'aile) alors que l'habitude est de calculer Mc à partir du Mach mesuré le plus loin possible en amont de la maquette pour échapper à son influence. Ici au contraire on effectue le calcul de Mc à partir du point le plus interactionné par la maquette.

L'avantage incontestable, ainsi que le démontre la figure 13 est de se passer de la connaissance de la porosité des parois, la correspondance entre Mc et Mm étant pratiquement indépendante de la porosité, en ce point particulier.

Seule la connaissance du volume de la maquette est requise. Cette méthode rapide ne nécessite qu'une durée très courte de calcul et permet de conduire un essai à Mc constant. Toutefois elle nécessite une bonne modélisation des volumes maquettes par prise en compte de la loi des aires. La figure 13 montre ainsi la nécessité d'une modélisation de la maquette par une vingtaine de doublets. Cette figure illustre la très faible variation de la correction Mc - Mm en fonction de la porosité pour une maquette ONERA M5 dans la soufflerie S2MA.

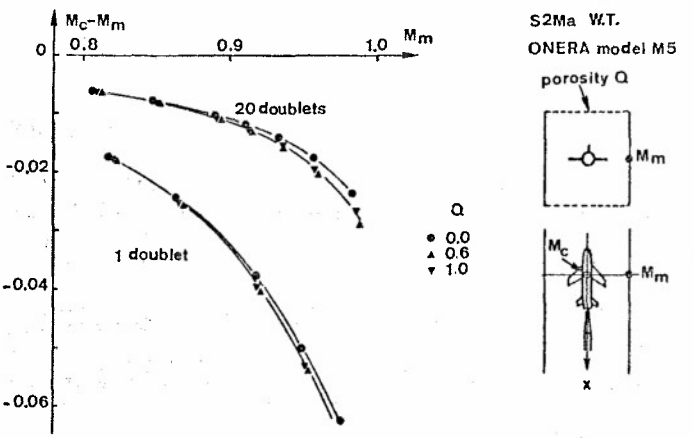


Fig. 13 - Méthode rapide de calcul du nombre de Mach corrigé.

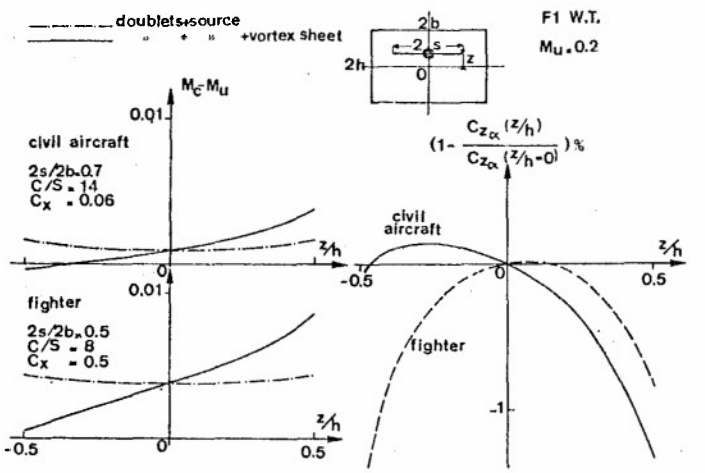


Fig. 14 - Influence de l'excentrement d'une maquette sur les corrections en veine guidée.

4 - INFLUENCE DE L'EXCENTREMENT DES MAQUETTES

Dans les représentations mathématiques exposées au paragraphe 2, toutes les singularités utilisées sont situées dans le plan horizontal médian de la veine d'essais. De telles modélisations s'appliquent convenablement au cas de maquettes centrées en veine et pour des incidences modérées. Dans ce cas, les termes de blocage résultent des singularités de volume et de sillage, et les corrections angulaires d'écoulement découlent des singularités de portance.

Si maintenant des maquettes excentrées sont considérées, ou même des maquettes centrées à forte incidence, il y a lieu de prendre en compte un ensemble de singularités de position quelconque

en veine, en particulier hors du plan horizontal médian de veine. Le calcul des effets de parois se complique singulièrement par des interactions quadratiques : ainsi des corrections angulaires sont induites par les singularités de volume et de sillage et des corrections de blocage résultent des singularités de portance. L'importance de ces termes augmente avec l'excentrement des singularités ; leurs effets ne sont pas négligeables ainsi qu'on peut le constater sur deux exemples donnés ici.

Le premier exemple concerne la nouvelle soufflerie F1 de l'ONERA possédant une veine guidée dans le domaine des faibles vitesses (figure 14). Deux cas types de maquettes d'avion civil et de chasseur, de taille usitée à F1 sont considérés. Les corrections de Mach $M_c - M_u$ sont données en fonction de l'excentrement relatif z/h des maquettes en tenant compte d'une part des singularités de volume et sillage d'autre part en y ajoutant les singularités de portance, l'importance de ces derniers termes est évidente. La figure 14 donne les modifications de gradient de portance apportées par un excentrement maquette. L'éventail des courbes de portance avant correction dépend du type de maquette : l'ordre des courbes en gradient croissant serait alors : excentrement négatif, nul est positif pour l'avion civil, excentrement nul, négatif puis positif pour le chasseur.

Le deuxième exemple correspond à une maquette d'avion civil dans la soufflerie transsonique S2MA à parois horizontales perforées de porosité réduite Q voisine de 0,7. La figure 15 donne les corrections de Mach en fonction de l'excentrement à divers Mach d'essais en considérant les singularités de blocage et de sillage seulement puis en incluant celles de portance : la dissymétrisation des courbes est d'autant plus accusée que le Mach croît. Il en va de même pour les altérations des corrections de gradients de portance.

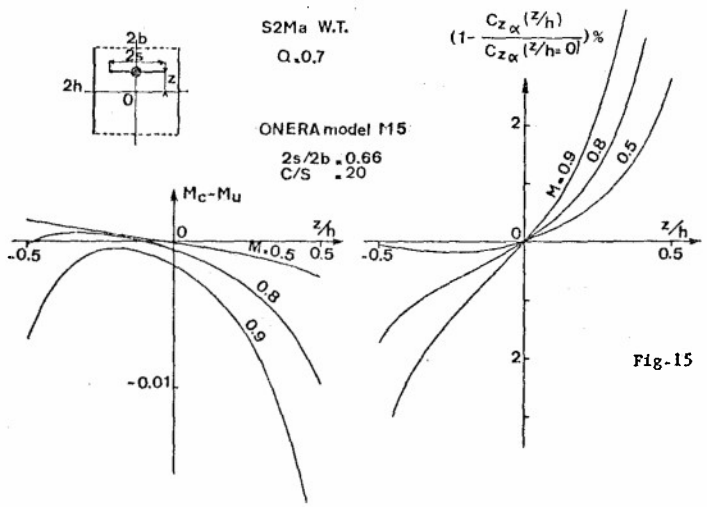


Fig-15 - Influence de l'excentrement d'une maquette sur les corrections en parois perforées.

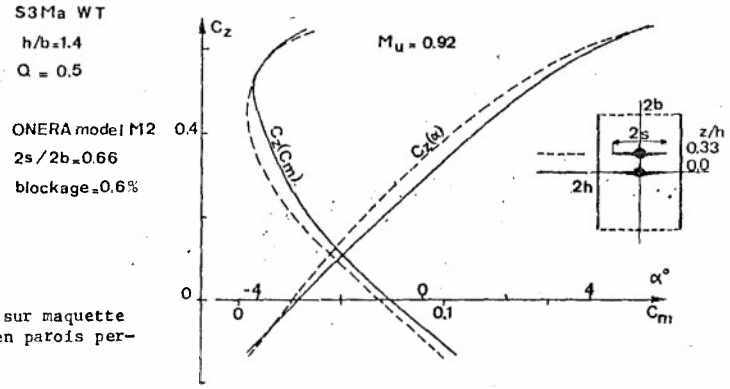


Fig-16 - Résultats d'essais sur maquette à 2 excentrements en parois perforées.

Un résultat d'essais obtenu sur maquette étalon ONERA M2 dans la soufflerie S3MA en parois perforées (figure 16), pour 2 positions de maquette centrée et excentrée positivement, montre que, outre des variations des gradients de portance et des stabilités, l'excentrement modifie l'incidence et le moment de tangage à portance nulle. Pour des maquettes centrées, les calculs classiques de corrections ne peuvent expliquer de tels écarts. Par contre le calcul avec des singularités excentrées permet de les prédire : en effet une correction d'incidence à Cz nul provient des singularités excentrées de volume et de sillage : la figure 17 montre qu'une telle correction croît rapidement avec l'excentrement et le Mach. Le programme de calcul des corrections avec des singularités excentrées en nombre suffisant est en cours d'élaboration.

5 - CALCULS DE CORRECTIONS DES EFFETS DE PAROIS

Compte tenu de la complexité croissante des calculs de corrections d'effets de parois introduite par une représentation plus élaborée des maquettes-dards, surtout dans les cas excentrés, il n'est plus possible de constituer des tables de coefficients de corrections ainsi qu'antérieurement effectué.

Les calculs de corrections sont effectués pour chaque cas de veine, maquette, support dard, avant un essai : ils requièrent des programmes de calcul de plus en plus élaborés. Les corrections sont définies pour une grille de M, CX, CZ couvrant le programme des essais et restituées sous forme de polynômes en fonction de ces 3 paramètres. Lors de l'exécution des essais, les calculs de corrections, effectués pour chaque point d'essai à partir des polynômes précédents, sont alors nettement allégés et applicables à des programmes d'essais industriels.

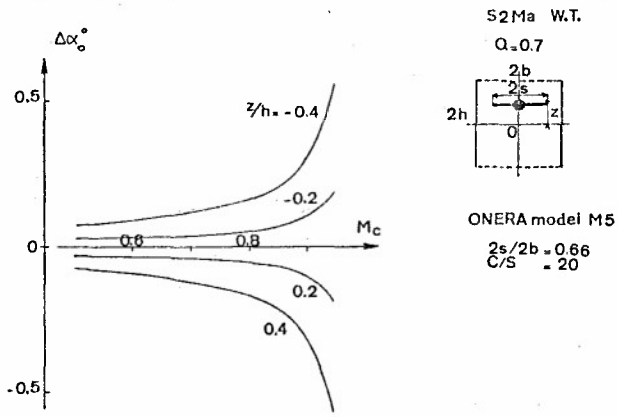


Fig-17 - Influence de l'excentrement d'une maquette sur l'incidence de portance nulle.

	SOLVED	TO SOLVE
2D	direct method : sign.$_u$ → corrections	sign.$_u$ troncature : α_o sign.$_w$
3D	MATH. DESCRIPTION checking by sign.$_u$ (closed walls) fuselage | doublets (x) sting | out of center (z) high α	wing volume doublets (y) vortex sheet inclin. source for separ. region singularities for | apex vortex active jet strut
	CORRECTIONS indirect method : sign.$_u$ → Q(x,y,M) → correct special method → M_c , VQ	direct method : sign.$_u$ → correct. mini number of pressure points sign.$_w$
	CONTROL reference tests	self adaptative walls large wind-tunnels

Fig-18 - Conclusions : résultats acquis, travaux futurs.

CONCLUSIONS : PERSPECTIVES FUTURES

La figure 18 résume les améliorations apportées actuellement et celles qui seront abordées dans le futur. En ce qui concerne les représentations mathématiques des ensembles maquette-dard passés en veine, il reste encore à développer transversalement les lois des aires pour éviter de concentrer par exemple les volumes voilure sur l'axe maquette. Des modélisations des tourbillons d'apex, des jets de nacelles et des mâts restent à définir, ainsi que des moyens pour défléchir les nappes tourbillonnaires. Il y a lieu de bien préciser que, du fait que seuls les champs lointains sont considérés, des modélisations rudimentaires mais suffisantes sont seulement à envisager.

La méthode indirecte de calcul des corrections, avec déterminstion de cartographie de porosités, sera abandonnée au profit d'une méthode de calcul direct à partir des signatures, telle que celle déjà utilisée industriellement en écoulement bidimensionnel [11] . Cette méthode nécessitant la mesure le pressions sur les parois des veines, le nombre minimal de pressions à relever sera en premier lieu recherché pour chaque type de correction afin de réduire au maximum l'équipement des parois donc le volume des données à traiter et de ce fait la durée et le coût des essais.

Le souci permanent des responsables de soufflerie consistera à multiplier les contrôles des corrections à l'aide de toute comparaison possible des résultats, dans une même veine en diverses configurations de parois ou entre diverses souffleries.

REFERENCES

(1) Flight/Ground testing facilities correlation
ACARD CP 187 (Valloire - 1975)

(2) POISSON-QUINTON Ph. - VAUCHERET X.
Prévision des caractéristiques aérodynamiques d'un avion à partir de la comparaison des résultats sur une maquette étalon dans diverses grandes souffleries transsoniques
AGARD CP 242 (Paris - 1977)

(3) VAUCHERET X.
Améliorations envisagées pour résoudre les problèmes rencontrés su cours d'essais à grande incidence de maquettes en soufflerie
AGARD Report n° 692 (Münich - 1980)

(4) VAUCHERET X.
Corrections de parois en soufflerie transsonique - Porosité équivalente
Publication ONERA n° 1977-3

(5) Wind tunnel Design and testing techniques
AGARD CP 174 (Londres 1975)

(6) Numérical methods and wind tunnel testing
AGARD CP 210 (Rhode - Ste Genese - 1976)

(7) Wind tunnel corrections for high angle of attack models
AGARD report n° 692 (Münich - 1980)

(8) AIAA 12th Aerodynamic testing conference
(Williamsburg - 1982)

(9) HACKETT J.E - WILSDEN D.J.
Estimation of wind tunnel blockage from wall pressure signatures : a review of recent work at Lockeed - Georgia
AIAA paper n° 78-828 (1978)

(10) HACKETT J.E.
Living with solid walled wind tunnels
AIAA 12th Aerodynamic testing conference
AIAA 82-0583 (1982)

(11) CAPELIER C. - CHEVALLIER J.P - BOUNIOL F.
Nouvelle méthode de correction des effets de parois en courant plan
La Recherche Aérospatiale n° 1978-1.

ON THE USE OF ADAPTIVE WALLS FOR TRANSONIC WIND TUNNEL TESTING[X)]

by

U.Ganzer
Institut für Luft-und Raumfahrt
Technische Universität Berlin
Marchstr. 14, Sekr. F2, D-1000 Berlin 10
West Germany

SUMMARY

A wind tunnel test section with two adaptive walls for aerofoil testing and another one with eight flexible walls for 3-D model tests have been developed at the TU Berlin. They are described with respect to their constructional features, the calculation procedure for determining the adapted wall configuration and the computer-based automatic control system. Test results obtained for the supercritical aerofoil CAST 7 are presented to demonstrate the potentiality of the adaptive wall concept in 2-D model tests. First test result with the 3-D test section using an ONERA C 5 body of revolution are shown to verify the feasability of the adaptive-wall technique for three-dimensional model tests. An alternative 3-D test section design as developed by DFVLR is discussed in some detail.

1. INTRODUCTION

Over the past ten years a new approach to the problem of wind tunnel wall interference has been evolving. The method is known as the adaptive-wall technique. It is based on the premise that if streamlines near the wind tunnel wall may be allowed to take its interference free shape, then the intire flow in the working section is free of wall interference and the forces and pressures on the model would represent free-air data. The main problem was the development of a practical scheme for adjusting the wall boundary condition.

The basic ideas leading to such scheme were first published in 1973 by Ferri and Baronti (1) and by Sears (2). Ferri and Baronti suggested a method for wall interference correction based on the measurement of two independent flow quantities near the wall, such as static pressure and flow direction. The method included computation for an unbounded far field and comparison of the results with measured data.

The work of Sears aimed at a 'self correcting wind tunnel' where in an iterative procedure the wall boundary conditions are adjusted until they correspond to an interference-free flow. The adjustment is based on the comparison of data measured and calculated along a control surface near the test section wall. This did provide the basic principle for the adaptive-wall technique.

2. THE ADAPTIVE-WALL PRINCIPLE

The wall boundary condition in a wind tunnel working section can be adjusted either by using porous walls with variable suction (3,4,5) or flexible walls (6,7,8). For explaining the principle of the adaptive-wall technique reference will be made to the flexible wall solution.

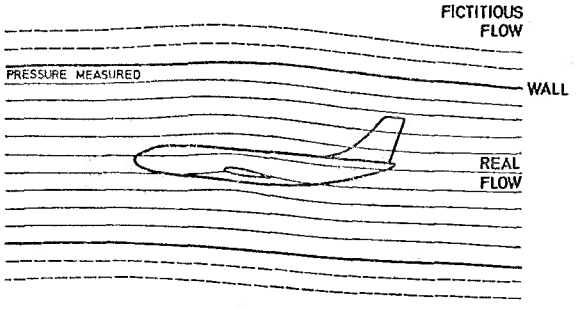


Figure 1:
The principle of adaptive walls

In a test section with adapted walls the streamlines correspond to those of an unrestricted flow field, Figure 1. Neglecting wall boundary layer in a first approach, the wall must have a streamline-shape and can be seen as just one stream-surface in an unconfined flow field. Two flow quantities can easily be measured along the wall, i.e. pressure and flow curvature. On the other hand, one flow property can be calculated from another one by using small disturbance theory and the assumption of laterally unconfined flow. For this calculation the concept of a fictitious external flow field is used. One then calculates the pressure for the fictitious flow over the known wall shape. This calculated pressure is compared with the measured pressure distribution. Only if both pressures - the calculated and the measured one - are the same, can the wall shape be considered adapted.

Otherwise some mean value between the two pressure distributions is taken and a new wall shape is calculated which would produce this pressure distribution in the fictitious flow. The wall is then deformed according to the calculated new shape and again the pressure distribution is measured and compared with the one just prescribed for the calculation. The procedure is repeated until the differences in the model measurements for two successive iterations are within a prescribed margin.

x) This research is supported by the German Ministry of Science and Technology (BMFT) and the German Research Association (DFG)

3. THE CALCULATION PROCEDURE FOR THE FICTITIOUS EXTERNAL FLOW

The calculation procedure for the 2-D as well as for the 3-D case is based on small disturbance theory. In the 2-D case the solution is straight forward: As the pressure is directly related to the u-component of the disturbance velocity and the v-component yields the wall shape, the well known integral equation relating u and v can be used.

In the 3-D case the calculation of the wall shape producing some prescribed pressure distribution in the fictitious external flow is carried out by the panel method. The wall of the test section is divided into panels of equal size, 24 in length direction, 8 in circumferential direction. Because of the symmetry condition for model flow without yaw, the number of panels used for calculation was only 5 x 24 = 120. Sources and sinks of constant strength were used for each panel and the disturbance potential as produced by all singularities was calculated for control points 1/4 of panel length upstream of the panel centre. Thus the integral equation of the first kind describing the external flow is solved by the discretisation as inherent in the panel method. This results into a system of linear equations for the singularity strength $\vec{\sigma}$, which reads like $A\vec{\sigma} = \vec{u}_t$. Here A is a matrix resulting from the geometrical shape of the panelized control surface and depends also on the Mach number. However, for a given Mach number the matrix can be calculated before the test. The values u_t are the tangential disturbance velocity components which are given by the prescribed pressure distribution.

The calculated singularity strength's then will have to be used for calculating the normal component of the disturbance velocity $u_n$which leads to the desired new wall shape. This results into a simple relation, which reads like $B\vec{\sigma} = \vec{u}_n$, where B is again a matrix depending only on the test section geometry and Mach number. It is obvious that the two equations may be combined to yield $BA^{-1}\vec{u}_t = \vec{u}_n$, so u_n may be calculated by simple multiplication. The great advantage of this procedure is that the required storage is reduced substantially, which is essential for an on-line adaption.

4. CONTROL OF THE ADAPTIVE WALLS

The control circuit for the position of the adaptive walls is in the first place made up by the displacement transducers, a multiplexer, a microprocessor, the motor drive unit and the DC motors, Figure 2.

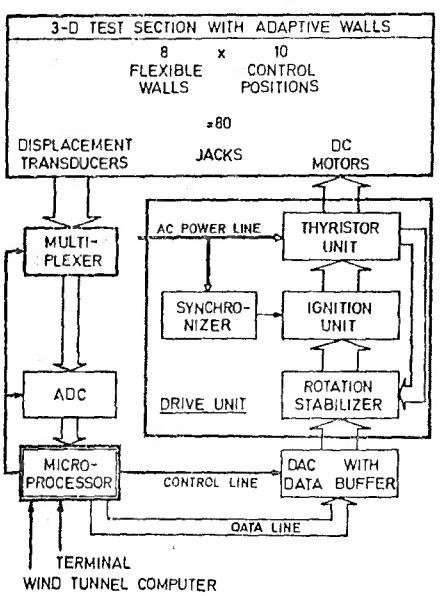


Figure 2:
Flow diagram of control system for adaptive-wall wind tunnels

The potentiometric displacement transducers provide analog values of the actual wall position. A multiplexer is scanning the displacement transducers and feeds the readings into the microprocessor via an analog/digital converter (ADC).

The microprocessor is the key element in the control circuit. Every 100 ms it comperes the actual wall position as indicated by the displacement transducers with the nominal position either as calculated by the wind tunnel computer or as prescribed by the wind tunnel user via the terminal. Depending on the amount of difference between nominal and actual position, the microprocessor initiates either an action of the precontroler or the endcontroler.

Precontroler and endcontroler are just software routines of the microprocessor. The endcontroler determines power values for each DC motor direct proportional to the required displacement of the jacks. With the large amplification factor (V_R = 200) assigned to the endcontroler, in general the power values will be much beyond those allowed for the DC motors. Thus, as long as larger displacements are required, the precontroler is acting. It provides maximum power (24V) to that motor, which on one wall has to produce the largest displacement. All other motors on that wall will receive individually reduced power. The reduction is given by the ratio of their individual displacement work to the maximum value. In this way all motors start driving the jacks at the same time and also stop at the same time, so that the loads on the flexible walls are minimized.

The endcontroler is of quasi-steady PD (proportional, differential) time-responds type. It becomes active only when the required wall displacement is very small (in the order of 1/3 mm or less). It takes over, when the power value it determines is equal to the one the precontroler had assigned to the individual motor.

All the power values as determined by the microprocessor (precontroler or endcontroler) are stored in the data buffer for one control period. On the other hand, they are given to the drive unit via a digital/analog converter (DAC). Their amplitude is used to produce an equivalent phase shift for the ignition pulses against the zero passage of the line voltage which provides the power for the thyristors. In this way, a gating control is generated in the power the DC motors receive from the thyristor.

Comparison of motor voltage and current provides information about motor rotation. This is used in the rotation stabilizer to account for changes in rotation due to high loads.

The advantage of this control system is that by using the microprocessor as a main control device, hardware requirements are reduced substantially. In addition to that, power requirements of the drive unit are kept small, which also has the adventage that cooling problems are avoided.

5. CONSTRUCTIONAL FEATURES OF THE 2-D AND 3-D TEST SECTION

A sketch of the 2-D test section for two-dimensional model tests is shown in Figure 3. It has a square working section of 15 x 15 cm. The test section length is 69 cm. The two flexible walls on top and bottom are made of fibreglass, 1 mm thick. Each wall can be adjusted by means of 8 jacks. The jacks are driven by DC electro-motors. Maximum displacement of ± 25 mm is possible. A displacement feeler from a potentiometer touches a piece of metal, glued on the flexible wall. With this arrangement the reading of wall position is within an accuracy of 0.07 mm. A double-hinge system of the jacks allows local inclination of the wall as well as some displacement, Figure 4.

A rubber band seals the flexible walls against the sidewalls. The aerofoil is mounted in the glass windows which are put in an excentric position in a disk. This disk is turned for changing angle of attack, so that the aerofoil at incidence gets nearer to the top or bottom wall respectively. In this way the central streamline can become the stagnation line almost at any incidence.

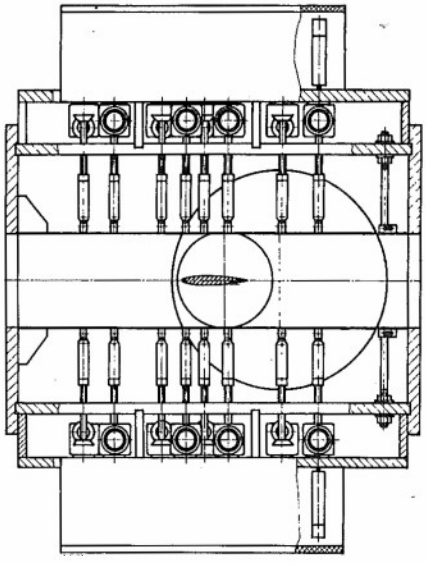


Figure 3: Sketch of 2-D test section

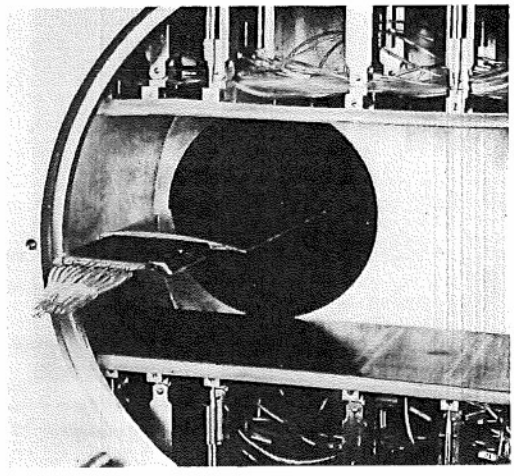


Figure 4: 2-D test section with CAST 7 aerofoil. One window removed

The 3-D test section is sketched in Figure 5. It has eight flexible walls which are subject to a two-dimensional deformation very similar to that arranged in the 2-D test section. The eight walls form an octagon-shaped cross section of 18 x 15 cm in main dimensions.

It is believed that this design is a reasonable compromise with respect to the desired three-dimensional wall configuration and a restricted mechanical complexity. One of the main problems in this design was the sealing of the corners between the individual walls. Spring-steel lamellas have found to be an adequate solution, Figure 6. Four of the walls have 146 lamellas spot-welded on each side. These are sliding on the adjacent walls. The great advantage of this solution is, that circumfersntial forces are being avoided, which could result into undesired waviness of the walls. On the other hand, such a solution is thought to be applicable at cryogenic flow condition.

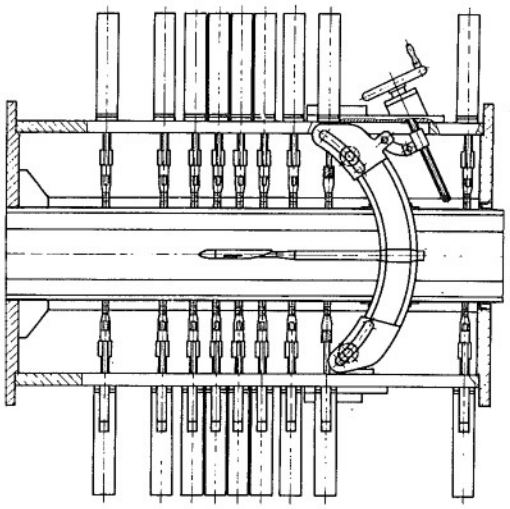


Figure 5: Sketch of the 3-D test section

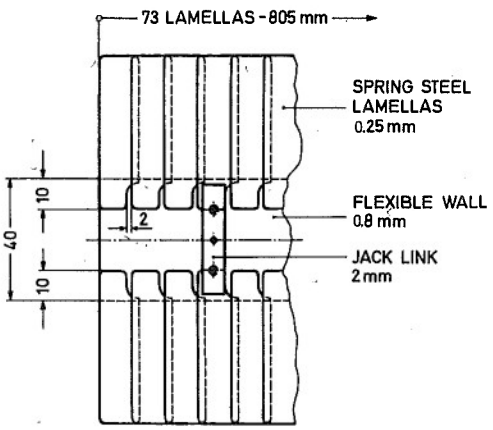


Figure 6: Spring-steel lamellas on wall

In Figure 7 the octagon-shaped working section is shown with eight flexible walls sealed against each other by spring-steel lamellas.

The complete test section is presented in Figure 8. The DC motors fixed on the outside dominate the picture. The impression of a considerable increase in mechanical complexity as compared with conventional transonic test section is somewhat misleading, as the working section itself is extremly small. For larger working sections the size of the motors and the jacks will not have to be increased in the same proportion.

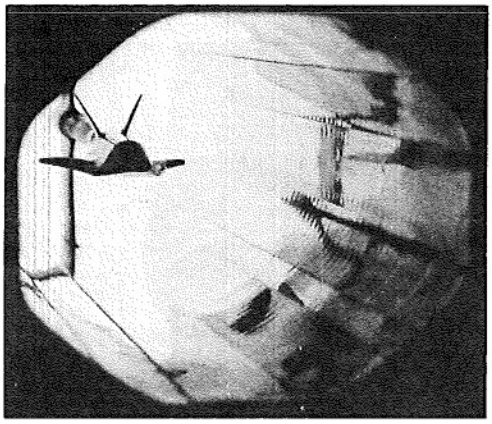


Figure 7: The octagon-shaped working section

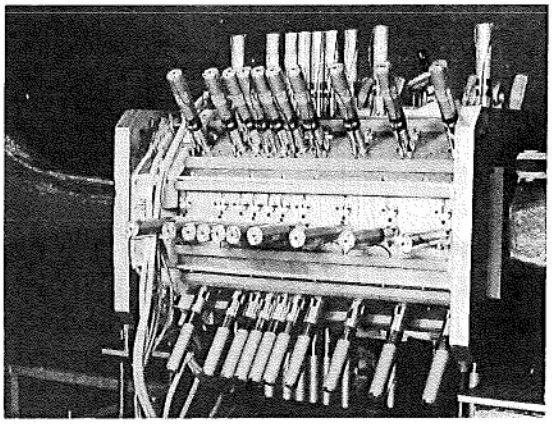


Figure 8: The 3-D test section

6. EXPERIMENTAL RESULTS

6.1 Results for CAST 7 Aerofoil

Experiments in the 2-D test section had started with a conventional NACA 0012 aerofoil and later were concentrated on the supercritical CAST 7. This aerofoil is a Dornier design with the official designation CAST 7/Do A1. Its main features are a moderate rear loading and moderate adverse pressure gradient, so that the aerofoil is relatively insensitive to Reynolds number effects. On the other hand, the aerofoil exhibits high sensitivity to changes in Mach number and angle of attack near design condition, i.e. $M_\infty = 0.76$ $\alpha = 0.57°$.

A comprehensive test program was carried out for the CAST 7 aerofoil as agreed to by the GARTEur Action Group 02. It included angle of attack sweeps at main stream Mach numbers $M_\infty = 0.60$, 0.70 and 0.76, as well as Mach number sweeps at angles of attack providing lift coefficients of $c_L = 0.52$ and 0.73 at $M_\infty = 0.76$. Transition was fixed at 7 % chord in all tests using 107 μ Ballotini roughness.

Only two sets of test results are shown here which may be taken as representative, Figure 9 and Figure 10.

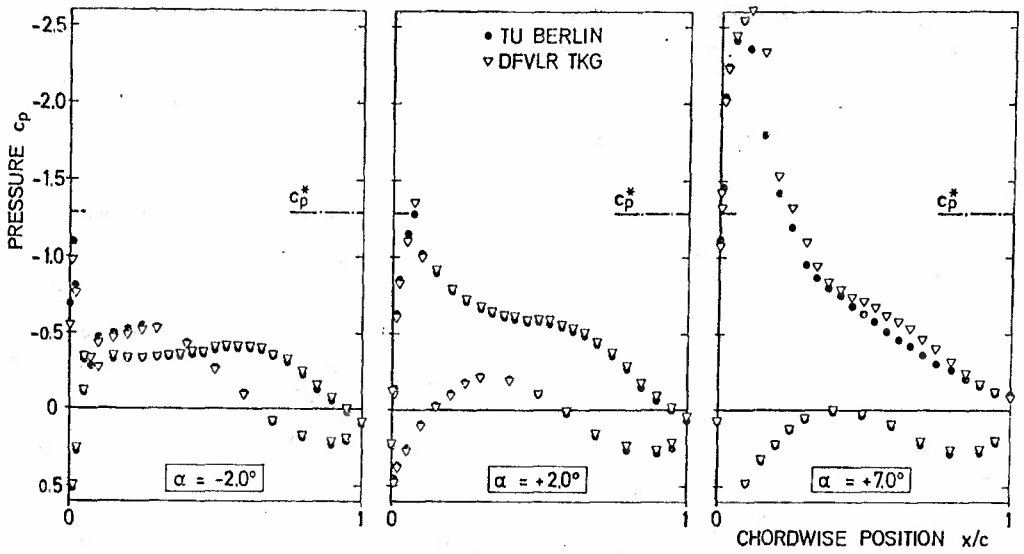


Figure 9: Pressure distribution CAST 7 M_∞ = 0.60 Re = 1.2×10^6

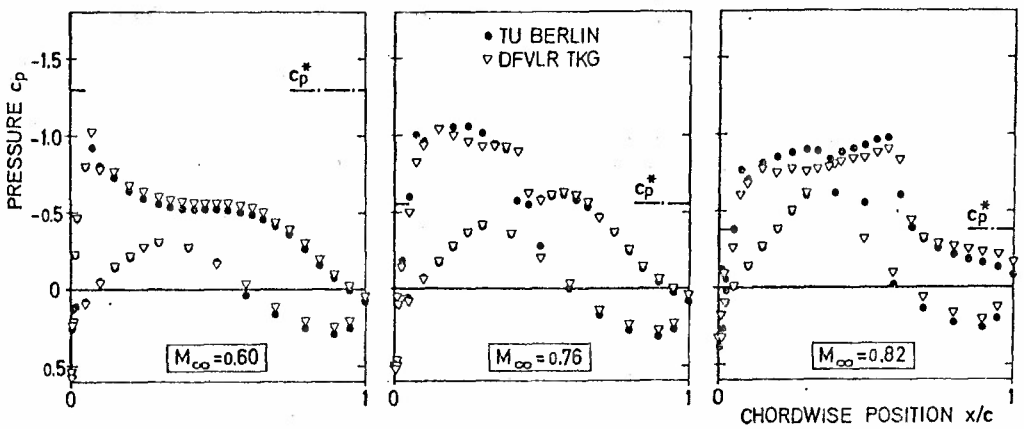


Figure 10: Pressure distribution CAST 7 α = 0.8° Re = $1.2 \div 1.4 \times 10^6$

The full points refer to the results obtained in the test section with adaptive walls in Berlin. Tunnel height to aerofoil chord ratio in this case was 1.5. Comparison is made with test results obtained in the DFVLR Göttingen 1 x 1 m transonic tunnel with a height to chord ratio of 10 by using the same model.

The discrepancies between the results obtained in the two tunnels may be due to several factors. It is believed that deficiencies in the adaptation procedure for the TU Berlin tunnel play only a minor role. Against that in the Göttingen tunnel there exists a Mach number gradient caused by the boundary layer growth along the parallel side walls, which were used as endplates to the aerofoil model. In addition to that the sidewalls were of limited extension (0.5 m upstream and downstream the model) and so did only approximately reproduce the flow condition, which exist in the TU Berlin tunnel. It is believed that these two factors did have a major impact on the test results.

Figure 11 gives some information about the influence of side wall flow condition on the test results. In the right hand part of the figure the pressure variation across the span is plotted as measured with a laser-2-focus-velocimeter. The traversing was made at 3 different chordwise positions slightly above the aerofoil surface and in addition two traverses were made just downstream of the trailing edge, slightly above and below the wake. They show substantial variation of pressure across the span. Obviously, the aerofoil shock causes a separation of the sidewall boundary layer which at its upstream end produces compression waves, running toward the centre line. As the pressure taps of the aerofoil model were not placed along the centre line, but somewhat lateral of it - the arrows indicate the spanwise tap position for the three chordwise values - the surface pressure distribution as shown in the left hand diagram deteriorates from that one would measure along mid-span.

These result for the sidewall influence indicate that careful reproduction of sidewall flow condition is necessary, when comparison of test results from different tunnels is intended. On the other hand, it broaches the question of flow control along the side wall, perhaps in some way deduced from the adaptive wall concept, if large aspect ratios are to be avoided.

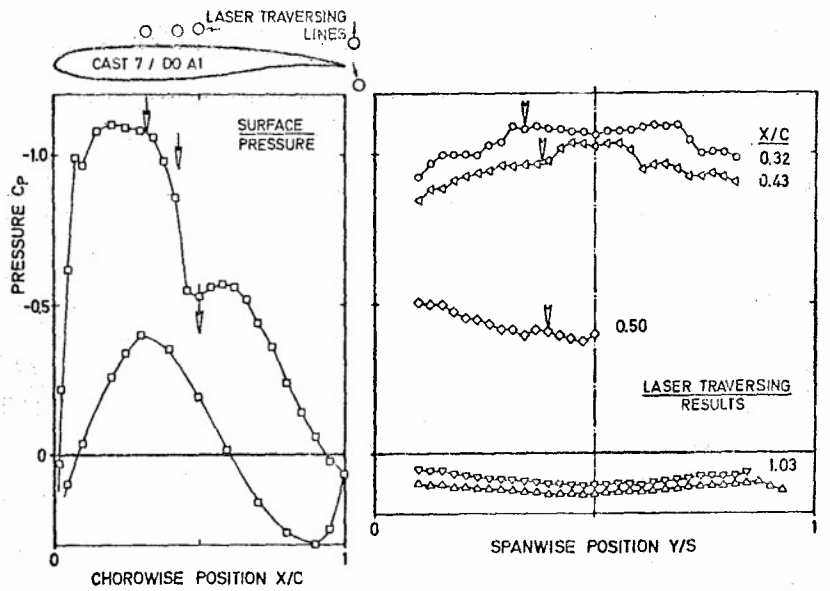


Figure 11: Spanwise variation of pressure in the flow field as measured with laser-velocimeter, compared with surface pressure measurements
CAST 7 M_∞ = 0.76 α = 1 Re = $1.4 \cdot 10^6$

6.2 Results for C5 Body of Revolution

For the first tests in the 3-D test section with eight flexible walls the C5 body of revolution was used. This is a calibration model designed by ONERA. Pressure distributions at several transonic main stream Mach numbers are available for comparison (9).

Figure 12 shows the Mach number distribution along one of the eight walls for a nominal main stream Mach number of M_∞ = 0.699. It compares the Mach number distribution for the cases with and without model. All walls were essentially plane, only adjusted in the region of the support and slightly divergent, so as to produce a constant Mach number in the test section without model. It can be seen that this aim was not entirely achieved. In particular in the regions where jack spacing was rather wide Mach number variation was considerable. This indicates, that if wall pressure measurements are to be taken for wall adaptation, it will be useful to have empty tunnel data for reference.

Taking the difference between empty tunnel data and data measured with the model, the pressure distribution looks fairly smooth, Figure 13. Such curves are well suited to be used as boundary condition to calculate an improved wall shape. If the wind tunnel walls are then adapted, the measured pressure distribution along the wall changes in the expected manner.

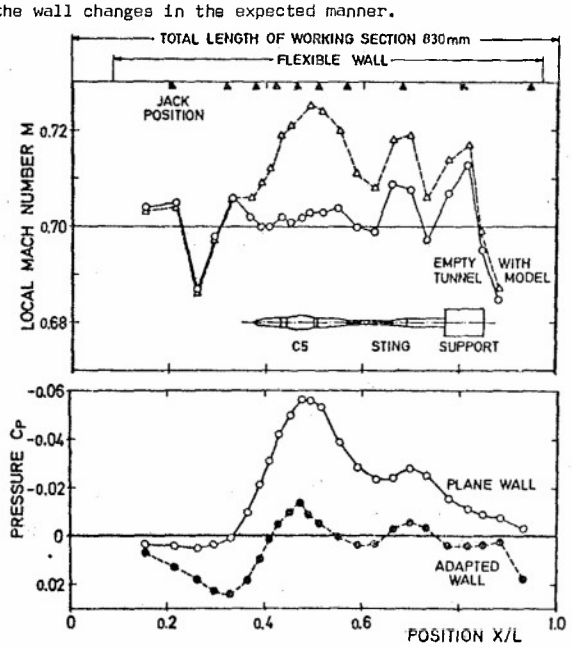


Figure 12: Mach number distribution along wall 2 with and without C5 model, plane walls M_∞ = 0.699

Figure 13: Pressure signature of C5 model on wall 2, plane & adapted (2nd iteration) M_∞ = 0.699

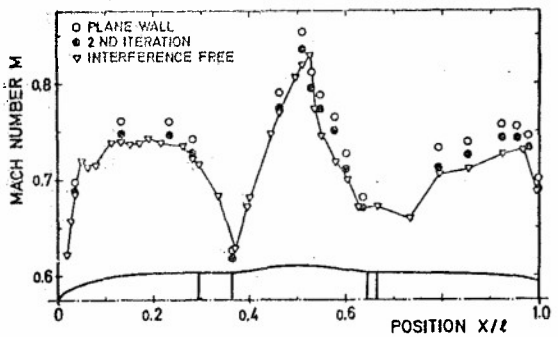


Figure 14: Mach number distribution for ONERA C5 body of revolution M_∞ = 0.699

Finally, Figure 14 shows the resultent pressure distribution for the ONERA C5 body of revolution. The body shape is sketched on the lower axis. The changes in pressure distribution due to the wall adaptation are not as spectacular as in the case of 2-D testing. However the improvements are well noticeable and some of the larger differences to the interference free values might find an explanation in the different Reynolds number (Re = 2·10 in our case against Re = 15·10 in the case of interference free data). Just downstream of the suction peak at 50 % of the body length there might be a separation bubble in our case, also near the end of the body the boundary layer becomes relatively thick at the lower Reynolds number.

Some more tests with this C5 model at higher Mach numbers are just being made. At M_∞ = 0.84 the working section was choked with the walls kept plane. Wall adaptation avoided the blockage and a pressure distribution on the modal was produced showing similar good agreement as in the case of M_∞ = 0.699.

7. THE DFVLR DAM PROJECT - AN ALTERNATIVE TEST SECTION DESIGN

The state of the art of 3-D test sections with adaptive wall does not yet allow a firm conclusion as to the extent to which a precise three-dimensional wall shaping is essential for obtaining reliable test results. The DFVLR DAM project is a test section design which aimes at a very accurate 3-D wall shape, Figure 15.

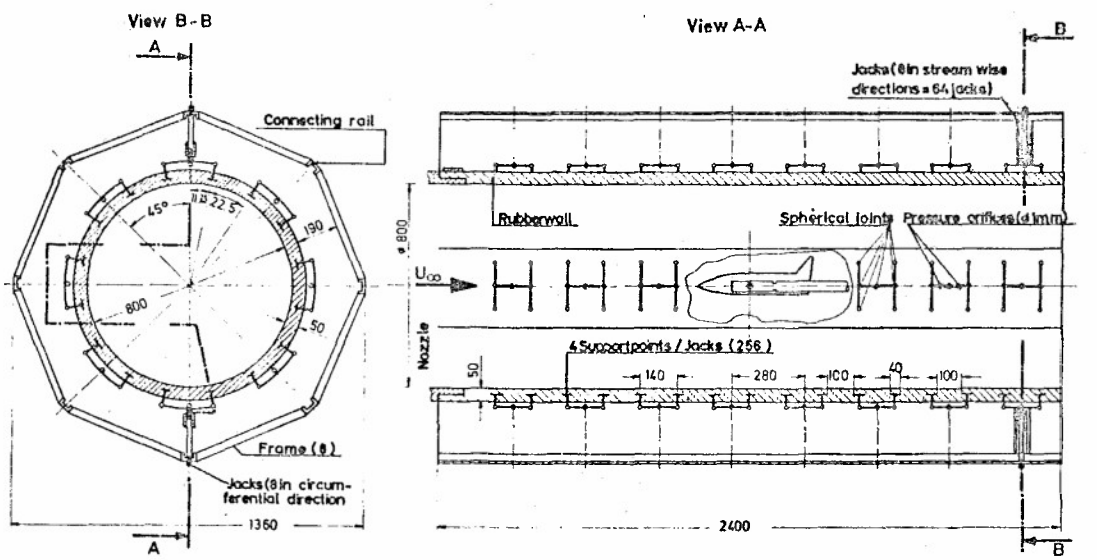


Figure 15: DFVLR 'Dehnbare Adaptive Meßstrecke' (DAM) - a 3-D deformable rubber tube test section

It consists of a cylindrical rubber tube which can be deformed by 64 jacks. Each jack acts via 4 support points on the rubber wall. The hinged connection to the jacks allows for some local inclination and displacement of the support points. The DAM test section has a length of 2.40 m, a diameter of 80 cm and a wall thickness of 6 cm. The large thickness is required for providing stiffness against bending.

The taps for pressure measurement have been located at 1/4 and 3/4 position between the support points. This has been calculated as position of minimum error due to wall waviness effects. The calculation procedure for determing the adapted wall configuration is a one-step method. It assumes that the pressure disturbances produced by the model and those resulting from the wall deformation can be superimposed. Setting equal the velocity components determined for the internal flow and the fictitious external flow, results in a system of linear equations providing the wanted wall shape. The rubber-tube with integrated support joints is already manufactured. It is supposed to be installed into the 0.75 x 0.75 m high-speed tunnel by the end of 1982.

8. CONCLUSION

Test results obtained for the supercritical aerofoil CAST 7 in a wind tunnel with two adaptive walls give proof of the feasability of this technique for transonic aerofoil testing. The adaptation procedure, which includes the calculation of the wall configuration and its control by a computer-based automatic control system, has been proved reliable and sufficiently fast to be used for on-line adaptation. So, in general, it might be concluded here, that the flexible wall technique provides an adequate solution to the problem of wall interferences resulting from upper and lower wall. It can now be considered as well established and generally applicable to transonic aerofoil testing. Further improvement of aerofoil test technique will first of all require a treatment of the side-wall effects.

The first test results with a body of revolution in a test section with eight flexible walls show, that also for three-dimensional model tests substantial reduction in wall-interference can be achieved and transonic blockage can be avoided when using adaptive walls. The test results confirm the applicability of panel method for calculating improved wall configurations. Conclusions as to the extent of the proper three-dimensional wall shaping essential to improve the reliability of test results beyond the present state of the art in conventional tunnels, can not yet be drawn.

9. REFERENCES

(1) A. Ferri, P. Baronti — "A method for transonic wind tunnel corrections" AIAA Journal, Vol. 11, Jan. 1973

(2) W.R. Sears — "Self correcting wind tunnels" The Sixteenth Lanchester Memorial Lecture Calspan Rep. RK-5070-A-2, July 1973

(3) R.J. Vidal, J.C. Erickson and P.A. Catlin — "Experiments with a self-correcting wind tunnel" AGARD CP 174, Oct. 1975

(4) B. Satyanarayana, E. Schairer, S. Davis — "Adaptive-wall wind tunnel development for transonic testing" J. of Aircraft, Vol. 18, No. 4, April 1981

(5) R.L. Parker Jr., W.L. Sickles — "Application of adaptive wall techniques in a three-dimensional wind tunnel with variable porosity" AIAA Paper No. 80-0157, Jan. 1980

(6) J.-P. Chevallier — "Soufflerie transsonique a perois auto-adaptable" ONERA T.P. n° 1975-119, 1975

(7) M.J. Goodyer, S.W.D. Wolf — "The development of a self-streamlining flexible walled transonic test section" AIAA Paper No. 80-0440, March 1980

(8) U. Ganzer — "Adaptable wind tunnel walls for 2-D and 3-D model tests" ICAS Paper 80-23.3, Oct. 1980

(9) J. Barche (Ed.) — "Experimental data base for computer program assessment" AGARD - AR - 138, May 1979

UTILISATION DE PAROIS ADAPTABLES POUR LES ESSAIS EN COURANT PLAN

par

J.P. ARCHAMBAUD:: et J.P. CHEVALLIER::::

Office National d'Etudes et de Recherches Aérospatiales (ONERA)

R E S U M E

Une méthode nouvelle de calcul des effets de parois donne une réponse précise aux questions de principe posées par l'utilisation de parois adaptables : longueur, raccordements, effet de défauts résiduels, conditions de référence. L'optimisation de la convergence du processus d'adaptation et le développement d'une technologie efficace permettent à la soufflerie du CERT d'obtenir, en une seule rafale, les conditions d'essais requises pour fournir des résultats significatifs. Des exemples (sur le profil CAST 7) démontrent l'efficacité globale d'une méthode dont l'extension aux écoulements tridimensionnels est considérée.

USE OF ADAPTIVE WALLS IN 2D TESTS

S U M M A R Y

A new method for computing the wall effects give precise answers to some questions arising in adaptive wall concept applications : length of adapted regions, fairings with up-and downstream regions, residual misadjustments effects, reference conditions. The acceleration of the iterative process convergence and the development of an efficient technology used in CERT T2 wind tunnel give in a single run the required test conditions. Sample taken from CAST 7 tests demonstrates the efficiency of the whole process to obtain significant results with consideration of 3D case extension.

NOTATIONS -

C	constante d'intégration
$f(\xi), g(\xi)$	fonctions auxiliaires définies par (5) et (12)
C_{x_p}	coefficient de traînée de pression
C_{x_f}	coefficient de traînée de frottement
C_{x_t}	coefficient de traînée totale (sillage)
M	nombre de Mach
p	pression
p_i	pression génératrice
T_i	température génératrice
h	hauteur de veine
u, v	composantes du champ de perturbation sur la surface de contrôle proche des parois u_p, v_p, mesurées $u = \frac{\partial \varphi}{\partial x}$ $v = \frac{\partial \varphi}{\partial y}$
x, y	coordonnées longitudinale et verticale dans la veine en courant plan
β	facteur de compressibilité $\beta = \sqrt{1-M_\infty^2}$
φ	potentiel de perturbation de l'écoulement confiné
φ_m	potentiel de perturbation dû au modèle en écoulement illimité
φ_i	potentiel d'interaction dû aux parois
ξ	variable d'intégration suivant x
ω, ω^*	facteur de relaxation, valeur optimale

Indices :

B, H	parois basse, haute
c	calculé par résolution de l'écoulement virtuel externe
d, i	méthode directe (forme donnée), inverse (vitesse donnée)
p	paroi
P, I	parties paires et impaires
o	écoulement infini amont
réf.	de référence

:: Ingénieur de Recherches - ONERA-CERT - 31055 TOULOUSE CEDEX - FRANCE

:::: Chef de la Division d'Aérodynamique Expérimentale - ONERA _ 92320 CHATILLON - FRANCE

INTRODUCTION -

Minimiaer les effets des parois de soufflerie en donnant aux lignes de courant qui bornent la veine d'essai une forme identique à celle qu'elles prendraient à la même distance du modèle dans un écoulement illimité est une idée qui remonte au moins aux années 40 [1].

Elle connaît depuis une dizaine d'années un très fort regain d'intérêt grâce à la considération d'un domaine virtuel externe prolongeant jusqu'à l'infini celui de la soufflerie [2, 3, 4] et dans lequel le calcul permet de s'assurer que les composantes de perturbation mesurées au voisinage des parois en présence du modèle correspondent bien à cet écoulement. Publié au moment où le développement des moyens et méthodes de calcul le rendait applicable [5, 6, 7], ce concept a donné lieu à des choix divers du mode d'action sur la composante transversale de l'écoulement, choix souvent dictés par le souci de conserver en partie les installations existantes [8, 9].Cependant, si des problèmes propres à chaque type de paroi se posent (parois déformables [6, 7], perforées [7, 9] ou à fentes [8]), les mêmes questions générales doivent être abordées pour toutes les solutions :

a) Quelle longueur donner à la portion de veine adaptée pour que, par rapport au modèle, les raccords avec le collecteur et le diffuseur n'apportent que des perturbations négligeables ?

b) Comment, dans une veine dont les déformations interdisent le recours aux classiques étalonnages veine vide, trouver les conditions précises de référence de vitesse, en module et direction ?

c) Quels sont les effets de parois résiduels liés aux inévitables défauts d'adaptation ?

d) Comment accélérer la convergence du processus d'adaptation pour réduire à des niveaux tolérables les corrections résiduelles sans grever le coût des essais par un trop grand nombre d'itérations.

Telles sont les questions auxquelles les travaux poursuivis à l'ONERA après les premiers essais sur une installation pilote [6] devaient permettre de répondre pour donner toute son efficacité à une soufflerie nouvelle installée au CERT [10].

Leur aboutissement était aussi souhaité dans le cadre de deux groupes de travail : le GARTeur AG02 concerné par les "Méthodes d'essais bidimensionnels transsoniques" dont l'activité fait l'objet d'une communication particulière [37] et le groupe AGARD "Transonic Test Section" [12].

Le développement d'une méthode de calcul des effets de parois [11] utilisant effectivement les composantes de perturbation mesurées sur une surface de contrôle proche des limites de veine et applicable de ce fait quelles que soient les conditions aux limites apporte aux trois premières questions une réponse claire. Elle sera donc tout d'abord rappelée. La description classique des corrections en terme de vitesse, d'incidence et de leurs gradients aussi bien que des considérations de symétrie conduisent à distinguer dans le modelage des lignes de courant quatre termes. La séparation de ces termes facilite l'optimisation des facteurs de relaxation pour accélérer la convergence du processus d'adaptation.

L'application des principes ainai développéa ne peut ae faire sana une technologie appropriée qui sera donc décrite avant de montrer par quelques exemples l'efficience globale du système. Compte tenu de ces exemples et des ordres de grandeurs attendua, on propose aussi une extension possible du procédé aux écoulements tridimensionnels.

1 - METHODES NOUVELLES DE CALCUL DES EFFETS DE PAROIS -

1.1 - Généralités -

Le calcul de corrections résiduelles dans une veine approximativement adaptée pour éviter le blocage de l'écoulement peut permettre suivant une idée de M. Carrière d'économiser le temps d'essai supplémentaire requis pour parfaire son adaptation et les dispositifs compliqués et coûteux pour modeler parfaitement toutes les parois. Le développement de méthodes nouvelles était d'autre part encouragé par les recommandations du groupe de travail constitué à l'initiative de l'AGARD [12]. Elles mettaient en doute la validité des conditions aux limites communément admises pour les parois ventilées et invitaient à utiliser les distributions de pression mesurées aux paroia dans le calcul des corrections. Suivant des voies différentes, plusieurs auteurs ont développé presque simultanément de telles méthodes. Mokry , Peake et Bowker [13] ont introduit des coefficients de porosité effectifs basés aur les mesures de pression pariétales. Des méthodes de singularités ont été développées par Kemp [14], Smith [16], Hackett et Wilsden [19] et Blackwell [20]. C.F. Lo [17] d'une part et Mokry et Ohman [18] d'autre part ont fait appel aux transformées de Fourier. Sawada [21] a développé un potentiel de perturbation satisfaisant l'équation des petites perturbations transsoniques, en série de fonctions des composantes de perturbation mesurées sur une surface de contrôle. Moyennant l'abandon, d'ailleurs peu justifié, d'un terme intégral et en conservant l'hypothèse classique d'un champ propre du modèle identique à ce qu'il serait en écoulement illimité, il a exprimé la correction du module de la vitesse en fonction des déflexions de l'écoulement et la correction d'incidence en fonction des distributions de vitesse. Ces expressions intégrales ne mettent pas en évidence la décroissance des effets en fonction de la distance au modèle, c'est pourquoi, dans le but recherché ici, la méthode de Capelier et al [11] semble préférable. Elle explicite, comme Sawada l'a fait ultérieurement [22, 23], les fonctions d'influence utiles.

1.2 - Rappel de la formulation de la méthode des signatures -

Les principales hypothèses sont, comme dans les méthodes classiquea, les suivantes :

- écoulement subsonique compressible, assimilé par la règle de Glauert à un écoulement incompressible dont les vitesses de perturbation dérivent d'un potentiel φ ;

- décomposition du potentiel en deux termes φ_m et φ_i correspondant respectivement au modèle et aux effets de parois

$$\varphi_i = \varphi - \varphi_m \qquad (1)$$

Le potentiel φ_m correspond à l'écoulement illimité autour d'un modèle présentant les mêmes singularités représentatives que le modèle soumis au champ perturbé φ_i. En conséquence le potentiel d'interaction des parois φ_i ne présente aucune singularité entre les limites de veine. La détermination du potentiel φ_i est effectuée grâce aux conditions suivantes :

- φ_i satisfait à l'équation du potentiel : $\beta^2 \frac{\partial^2 \varphi}{\partial x^2} + \frac{\partial^2 \varphi}{\partial y^2} = 0$ (2)

- φ_i est continu à l'intérieur d'une surface de contrôle constituée de deux plans parallèles voisins des parois ;

- $\frac{\partial \varphi_i}{\partial x} = \frac{\partial \varphi}{\partial x} - \frac{\partial \varphi_m}{\partial x}$ et $\frac{\partial \varphi_i}{\partial y} = \frac{\partial \varphi}{\partial y} - \frac{\partial \varphi_m}{\partial y}$ (3) (4)

sont connues sur chacun de ces plans puisque les $\frac{\partial \varphi_m}{\partial x}$ et $\frac{\partial \varphi_m}{\partial y}$ sont données par les mesures effectuées sur le modèle et les $\frac{\partial \varphi}{\partial x}$ et $\frac{\partial \varphi}{\partial y}$ par les mesures effectuées sur la surface de contrôle.

La solution du problème, par transformation conforme est donnée en annexe de la référence [11] dans le cas où seul $\partial \varphi / \partial x$ est connu sur la surface de contrôle. Les corrections de vitesse et d'incidence correspondent au potentiel d'interaction φ_i. En posant :

$$f(\xi) = \frac{\partial \varphi}{\partial x}(\xi) - \frac{\partial \varphi_m}{\partial x}(\xi) \qquad (5)$$

sur les aurfaces de contrôle avec f_B pour la paroi basse et f_H pour la paroi haute, on trouve, sur l'axe de la veine :

$$\frac{\partial \varphi_i}{\partial x}(x) = \frac{1}{\beta h} \int_{-\infty}^{\infty} \frac{f_B(\xi) + f_H(\xi)}{2 \operatorname{Ch} \frac{\pi(\xi - x)}{\beta h}} d\xi \qquad (6)$$

$$\frac{\partial \varphi_i}{\partial y}(x) = \frac{1}{h} \int_{-\infty}^{\infty} \frac{f_H(\xi) - f_B(\xi)}{e^{2\pi \frac{(\xi - x)}{\beta h}} + 1} d\xi + C \qquad (7)$$

et pour les corrections de gradient et de courbure :

$$\frac{\partial^2 \varphi_i}{\partial x^2}(x) = \frac{\pi}{\beta^2 h^2} \int_{-\infty}^{\infty} \frac{f_B(\xi) + f_H(\xi)}{2 \operatorname{Ch}^2 \pi(\xi - x)/\beta h} d\xi \qquad (8)$$

$$\frac{\partial^2 \varphi_i}{\partial y^2}(x) = \frac{2\pi}{\beta h^2} \int_{-\infty}^{\infty} \frac{f_H(\xi) - f_B(\xi)}{\left[e^{\frac{2\pi(\xi - x)}{\beta h}} + 1 \right]^2} d\xi \qquad (9)$$

L'utilisation de ces formules soulève deux difficultés :

a) f_B et f_H s'expriment en fonction de $\partial \varphi / \partial x$, potentiel de perturbation, ce qui suppose déjà connue la vitesse de l'écoulement non perturbé qui, en fait, ne le sera qu'après application de la correction.

b) lea bornes infinies des intégrales nécessitent une extrapolation des fonctions f_B et f_H qui peut être d'autant plus incertaine qu'elle dépend de la valeur choisie pour l'écoulement non perturbé.

En ce qui concerne l'effet d'une erreur initiale systématique δV_o sur la valeur brute de la vitesse attribuée à l'écoulement non perturbé, on trouve que les vitesses locales de perturbation sont faussées de $-\delta V_o$. Introduites dans les fonctions f_B et f_H elles donnent un terme correctif supplémentaire :

$$\delta\left(\frac{\partial \varphi_i}{\partial x}\right) = \frac{1}{\beta h} \int_{-\infty}^{\infty} \frac{-2\delta V_o}{2 \operatorname{Ch} \frac{\pi \xi}{\beta h}} d\xi \qquad (10)$$

soit en posant $\lambda = \frac{\pi \xi}{\beta h}$ $\quad d\xi = \frac{\beta h}{\pi} d\lambda$

$$\delta\left(\frac{\partial \varphi_i}{\partial x}\right) = \frac{-\delta V_o}{\pi} \int_{-\infty}^{\infty} \frac{d\lambda}{\operatorname{Ch} \lambda} = -\delta V_o \qquad (11)$$

Ce terme correctif supplémentaire compense exactement l'erreur initiale δV_o.

La seconde difficulté concernant l'extrapolation des fonctions f_B et f_H peut être évitée moyennant la troncature des intégrales ramenant par exemple les bornes à la longueur effective de la veine d'esaai.

L'erreur ainsi introduite est totalement négligeable du fait que dans les formules (1) et (3) les fonctions f_B et f_H sont bornées (et tendent même vers zéro pour $\xi \to \infty$) et que figure au dénominateur la fonction $\operatorname{Ch} \pi(\xi - x)/\beta h$, très rapidement croissante avec ξ et qui ôte toute importance aux régions éloignées du modèle. Cette remarque valide la précédente pour une veine de longueur finie. La représentation (fig. 1) de la fonction d'influence concernant les vitesses montre d'ailleurs que la région sur laquelle il est nécessaire de connaître f_B et f_H diminue lorsque le nombre de Mach augmente.

Dans le cadre de l'approximation linéaire, la zone d'influence prépondérante tend même verz zéro lorsque le nombre de Mach tend vers l'unité ; cette limite n'a pas de sens physique puisqu'il conviendrait au moins d'étendre à la corde du profil la moyenne des nombres de Mach corrigés sur l'axe. Mais on peut à coup sûr conclure que les mesures de vitesse pariétale effectuées sur trois demi-hauteurs de veine de part et d'autre du modèle suffisent à déterminer sans erreur appréciable les vitesses de référence supérieures à M=0,3

La formule (2) qui donne la correction d'incidence ne présente pas les mêmes avantages : la fonction d'influence tend vers l'unité pour la région amont, ainsi privilégiée en tant que référence et il faut que la veine soit suffisamment longue pour que $p_B - p_H$ tende effectivement vers zéro. Ceci n'évite pas du point de vue pratique une certaine incertitude que l'on peut évaluer à partir de la formule (2). Pour une veine vide, la différence des vitesses entre plancher et plafond, supposée constante et intégrée sur une longueur égale à la hauteur de veine donne l'ordre de grandeur $\Delta\alpha \simeq u_H - u_B$. Pour connaître l'incidence à quelques centièmes de degré près, il faudrait connaître u_H et u_B à 1/2000 près.

Pour échapper à ces difficultés, reprenant la démonstration des formules (1) à (4) donnée en [11], on suppose connue non plus la partie réelle du potentiel complexe mais sa partie imaginaire. En posant :

$$g(\xi) = \frac{\partial \varphi}{\partial y} - \frac{\partial \varphi_m}{\partial y} \qquad (12)$$

Paquet [15] aboutit à une formulation conjuguée qui donne en particulier sur l'axe :

$$\frac{\partial \varphi_i}{\partial y}(x) = \frac{1}{\beta R} \int_{-\infty}^{\infty} \frac{g_H(\xi) + g_B(\xi)}{2\,\mathrm{Ch}\,\pi(\xi - x)/\beta R}\, d\xi \qquad (13)$$

la constante d'intégration apparaît dès lors dans l'expression de $\partial \varphi_i / \partial x$ et l'expression (13) présente pour la détermination de l'incidenee, les mêmes avantages que (6) pour le calcul de la vitesse. Elle démontre que la direction du vent à l'emplacement du modèle est, déduction faite du terme maquette, une moyenne des pentes de l'écoulement sur la surface de contrôle pondérée d'une fonction, très rapidement décroissante, de la distance au modèle (fig. 1). Elle peut donc s'appliquer sans dommage avec troncature des limites d'intégration. Une erreur initiale sur la référence à partir de laquelle sont mesurées les pentes de l'écoulement se trouve aussi corrigée automatiquement.

La précision requise sur les mesures de pente n'est pas supérieure à celle que l'on recherche pour la direction du vent et l'on peut, si les mesures angulaires sont effectuées sur un grand nombre de points de la surface de contrôle bénéficier de l'effet statistique de nombreuses mesures indépendantes.

Les formules (6) et (13) présentent donc des avantages de prineipe décisifs pour la détermination du nombre de Mach et de la direction de référence de l'écoulement. Leur application se heurte cependant aux pratiques usuelles et aux difficultés suivantes :

a) comme dans les méthodes classiques une représentation du modèle par singularités est nécessaire et elle devient difficile dans le domaine transsonique où la limite d'application n'est pas évidente.

b) les mesures précises de la direction de l'écoulement sont en dépit des travaux de Wittliff ou de Bodapati et al [24] plus délicates eneore que des mesures de vitesse au voisinage de parois perméables.

Nous verrons plus loin que ces difficultés peuvent être tournées et ne retiendrons, pour les veines adaptables, qu'une conclusion dont la validité dépasse le cadre des hypothèses utilisées pour expliciter la fonction d'influence de (6) et (13). Les vitesse et direction de référence de l'écoulement à l'emplacement du modèle ne dépendent respectivement que des vitesses et directions mesurées sur une surface de contrôle proche des limites de veine avec une influenee rapidement décroissante vers l'amont et vers l'aval.

2 - *PROCESSUS D'ADAPTATION DES PAROIS* -

Avant de décrire en détail la technologie employée pour mettre en forme les parois pleines et souples utilisées à T2, retenons pour exposer le principe de leur adaptation que nous disposons de nombreuses prises de pression pariétales et mesures de déplacement donnant des distributions $v_{p_i}(x)$ et $y_p(x)$ et qu'un rapide calcul de couche limite, basé sur les pressions mesurées, permet de corriger les $y_p(x)$ des épaisseurs de déplacement pour connaître la forme des lignes de coursnt limitant l'écoulement de fluide parfait

Le principe de l'adaptation, maintes fois exposé [2, 3, 4, 5, 6, 7, 8, 9, 13, 24 ...], fait appel à la résolution, dans le domaine virtuel illimité sans singularités, d'un problème comportant comme données sur la surface de contrôle plane proche de la paroi, soit les vitesses longitudinales de perturbation mesurées u_p déduites des pressions, soit les vitesses transversales de perturbation v_p correspondant aux pentes $\partial y_p / \partial x(x)$.

Les solutions (par fonction de Green, ou méthodes numériques) fournissent respectivement v_c ou u_c et l'adaptation sera obtenue lorsque simultanément

$$u_p(x) = u_c(x) \qquad \forall x.$$
$$v_c(x) = v_p(x) \qquad (14)$$

Si l'on a pris comme données du champ virtuel u_p , le calcul donne v_c et la comparaison portera sur l'égalité $v_c = v_p$? puisque la condition $u_c = u_p$ est réalisée au départ. Si $v_c \neq v_p$ on tentera d'améliorer l'adaptation par un processus de relaxation dans lequel une forme linéaire de v_c et v_p doit fournir une valeur améliorée :

$$v_a(x) = \overline{\omega_i}\, v_c(x) + (1 - \overline{\omega_i})\, v_p(x) \qquad (15)$$

Ce processus est-il convergent ? Comment choisir le facteur de relaxation pour obtenir une convergence rapide ? La convergence assure-t-elle la validité de la solution obtenue ? Nous n'aborderons pas cette dernière question , la démonstration d'existence et d'unicité étant donnée par Ciavaldini [30].

La réponse à la première question n'est pas évidente : Sears trouve que l'étude la plus convaincante réside dans une simulation numérique de l'ensemble du processus [25] car les études purement analytiques se limitent à des elasses plutôt simples de modèles et de souffleries [26, 27] ; il étudie néanmoins les effets d'imperfections dans le contrôle [28] qui n'empêchent pas la convergence vers une solution imparfaite mais meilleure qu'avant itération.

Notre propre expérience [6] avec un coefficient de relaxation de 0,5, c'est-à-dire voisin des valeurs optimales proposées ultérieurement [26, 27], a montré qu'une divergence pouvait apparaître lorsque les sensibilités des écoulements externe et interne à une variation de v sont très différentes. Cette

possibilité a également été signalée par Judd et al [29].

La sensibilité de l'écoulement interne aux variations de ω est, du fait de la loi des aires en subsonique élevé, beaucoup plus importante que celle de l'écoulement externe. Il est évident que si dans ce cas une divergence est à craindre avec un coefficient de relaxation de 0,5, on peut aussi le choisir de façon à assurer la stabilité mais au prix d'un nombre d'itérations plus élevé. En fait une valeur bien choisie du coefficient de relaxation amènerait en une seule étape à l'adaptation [27] mais cette valeur peut dépendre étroitement de l'écoulement sur le modèle : en régime d'interaction forte entre couche limite et onde de choc, un faible gradient longitudinal du nombre de Mach modifie position de choc, décollement, C_x et épaisseur de sillage. Pour optimiser le choix du mode de relaxation, il est apparu intéressant d'analyser les formes de veine en les décrivant non par les données immédiates $y_H(x)$ et $y_B(x)$ mais en terme de hauteur de veine $h(x) = y_H - y_B$ et de ligne médiane $m(x) = (y_H + y_B)/2$ et de considérer pour chacune de ces fonctions une décomposition en parties paires et impaires :

$$h_p(\pm x) = (h(x) + h(-x))/2 \qquad h_i(x) = -h_i(-x) = (h(x) - h(-x))/2$$
$$m_p(\pm x) = (m(x) + m(-x))/2 \qquad m_i(x) = -m_i(-x) = (m(x) - m(-x))/2 \qquad (16)$$

Pour des veines de formes simples ces fonctions correspondent respectivement à l'évasement de la veine, à sa divergence, à la cambrure de sa ligne moyenne et au calage de celle-ci par rapport à l'horizontale. On peut associer ces termes aux effets induits par le volume de la maquette, son sillage, sa portance et la référence d'incidence. La sensibilité des écoulements interne et externe aux variations de cambrure de la ligne moyenne est très voisine et l'analyse de Lo et Kraft peut lui être appliquée [27]. Pour le calage, à l'inverse de la divergence, la sensibilité de l'écoulement externe est évidemment supérieure à celle de l'écoulement interne. On verra dans les applications qu'il n'est pas nécessaire de déterminer les facteurs partiels avec une grande précision pour obtenir une convergence tout à fait satisfaisante.

3 - REMARQUES -

3.1 - Les considérations qui précèdent sur l'apport de la méthode nouvelle de calcul des effets de parois dans l'utilisation d'une veine munie d'un dispositif actif de contrôle actif de l'écoulement transversal sont d'une application générale quel que soit le type de paroi. On a cependant mis en évidence la nécessité, pour déterminer avec précision la direction de référence de l'écoulement, de recourir à des mesures de même nature, sur toute la surface de contrôle pour obtenir une moyenne pondérée significative. Bien que ce motif n'ait pas été à l'origine du choix de la solution retenue (parois pleines mobiles) pour la soufflerie T2, il semble "a posteriori" que ce soit la seule qui puisse apporter avec la précision requise, sans dispositifs supplémentaires (sondes, laser ...) et dans le minimum de temps, la connaissance de la direction de l'écoulement.

3.2 - Pour simplifier l'acquisition de conditions de référence dans une veine qui, sans être parfaitement adaptée, se rapproche néanmoins de cette condition, on a proposé [31] en ce qui concerne le module de la vitesse de calculer l'écoulement virtuel externe pour la forme donnée de la nappe de courant en fonction de la vitesse à l'infini et de choisir celle-ci pour minimiser les écarts pondérés entre vitesses locales calculées et mesurées. La fonction de pondération initialement proposée était l'inverse des carrés de distance au centre veine. Compte tenu de l'analyse des corrections résiduelles, il est cohérent d'adopter pour la pondération la fonction $1/(\mathrm{Ch}\,\pi(\xi - x)/\beta h)$ qui figure dans la formule (6) pour la correction de vitesse.

Explicitons celle-ci pour faire apparaître les termes provenant des mesures à la paroi et du champ du modèle :

$$\frac{\partial \varphi_i(x)}{\partial x} = \frac{1}{\beta h} \int_{-\infty}^{\infty} \frac{\left[\left(\frac{\partial \varphi}{\partial x}(\xi)\right)_H + \left(\frac{\partial \varphi}{\partial x}(\xi)\right)_B\right]_m - \left[\left(\frac{\partial \varphi}{\partial x}(\xi)\right)_H + \left(\frac{\partial \varphi}{\partial x}(\xi)\right)_B\right]_c}{2\,\mathrm{Ch}\,\pi\frac{\xi - x}{\beta h}} d\xi \qquad (17)$$

le second crochet, indicé m, représente en écoulement illimité les survitesses dues au modèle sur la surface de contrôle. Celles-ci sont par définition identiques à celles que l'on obtiendrait en présence d'une parfaite adaptation de la veine confinée. Si nous admettons l'existence d'un facteur de relaxation optimal ω^* définissant cette distribution à partir des éléments mesurés (indicés f) et calculés (indice c) à l'étape précédente ; on a :

$$\left[\frac{\partial \varphi}{\partial x}(\xi)\right]_m = \omega^* \left(\frac{\partial \varphi}{\partial x}\right)_c + (1 - \omega^*)\left(\frac{\partial \varphi}{\partial x}\right)_f \qquad (18)$$

qui porté dans la formule précédente donne :

$$\frac{\partial \varphi_i(x)}{\partial x} = \frac{\omega^*}{2\beta h} \int_{-\infty}^{\infty} \frac{\left[\left(\frac{\partial \varphi}{\partial x}(\xi)\right)_H + \left(\frac{\partial \varphi}{\partial x}(\xi)\right)_B\right]_f - \left[\left(\frac{\partial \varphi}{\partial x}(\xi)\right)_H + \left(\frac{\partial \varphi}{\partial x}(\xi)\right)_B\right]_c}{\mathrm{Ch}\left(\pi(\xi - x)/\beta h\right)} d\xi \qquad 19$$

Si nous choisissons la vitesse de référence pour que les moyennes pondérées des distributions de $\frac{\partial \varphi}{\partial x}(\xi)$ calculées et mesurées soient égales, la correction de vitesse est nulle. Nous avons donc, avant que l'adaptation ne soit parfaite, une définition de la vitesse de référence cohérente avec la méthode de calcul des effets de parois et qui ne nécessite pas de recourir à une représentation du modèle ni à la connaissance de ω^*.

La même démonstration s'applique à la détermination de la direction de référence en substituant les grandeurs de même nature. Etablie à partir des hypothèses permettant la linéarisation, elle conserve néanmoins un sens physique lorsque M tend vers 1 à condition d'abandonner la fonction de pondération devenue trop "pointue". Un autre motif d'élargir la zone d'influence prépondérante de la paroi vient de l'extension du modèle pour lequel ce n'est pas seulement la vitesse au centre veine qui importe mais une certaine moyenne le long de

la corde. Pratiquement l'abandon du facteur de compressibilité β peut constituer une solution acceptable.

Il faut souligner que la connaissance de la vitesse de référence en module et direction définie au mieux dans une veine en voie d'adaptation laisse subsister d'éventuels défauts de courbure et de divergence.

3.3 - *Extension aux écoulements tridimensionnels* -

La méthode nouvelle de calcul des effets de parois [11] a été dès l'origine étendue à l'écoulement tridimensionnel périodique correspondant à l'essai d'un modèle dans une veine rectangulaire dont les parois latérales demeurent planes et dont les parois hautes et basses peuvent être plus ou moins adaptées [15].

Aux formules établies à partir des distributions de pression s'ajoutent, grâce à l'introduction de la direction mesurée de l'écoulement, des formules conjuguées qui, comme pour l'écoulement bidimensionnel, prennent la même forme auto-correctrice, et autorisent par la présence de fonctions Ch aux dénominateurs les mêmes troncatures d'intégrales.

On remarque en outre que dans les séries exprimant des corrections en fonction de la décomposition harmonique des fonctions f ou $g(x,y)$ dans le sens de l'envergure les fonctions d'influence décroissent très vite aussi bien en fonction de x que de leur rang. On peut en induire, compte tenu de l'ordre de grandeur des corrections, que l'on doit pouvoir proposer, en une bonne première approximation, d'opérer de la façon suivante :

La soufflerie étant équipée pour assurer les déformations des parois en courant plan, utiliser la moyenne transversale des mesures de vitesse pariétale pour assurer au mieux l'adaptation qui définit nombre de Mach et incidence et annuler globalement gradient longitudinal et défaut de courbure. Calculer suivant la méthode nouvelle les corrections résiduelles dues aux maquettes images par rapport aux parois latérales et à la non uniformité transversale de l'écoulement.

Le résultat justifiera probablement de se limiter, si une adaptation plus étroite se révélait nécessaire, à des solutions relativement simples comme celles de Ganzer [32, 33] (veine octogonale), ou de Whitfield et al [34] (6 lames indépendantes par paroi).

3.4 - Les conclusions obtenues sur la faible influence des régions lointaines de la maquette à l'amont et à l'aval ne doivent pas prêter à confusion. L'écoulement qui aborde la région adaptée doit être aussi pur que possible : les filtres amont, le dessin du convergent et des raccords avec la zone adaptée, les angles de parois, les supports et les couches limites latérales, doivent être traités pour éviter l'introduction d'écoulements secondaires parasites auxquels ne remédierait nullement l'adaptation des parois.

4 - *DESCRIPTION DES MOYENS MIS EN OEUVRE* -

4.1 - *Soufflerie T2* -

La soufflerie T2 est une maquette à l'échelle 1/10e du projet proposé par l'ONERA pour la construction d'une grande soufflerie transsonique européenne. Elle fonctionne depuis 1975 [35].

Il s'agit d'une soufflerie à induction, constituée par un circuit fermé d'environ 25 m de long. Elle fonctionne depuis peu en cryogénie et l'utilisation de parois déformables dans ce domaine est envisagée en 1983. Le circuit est pressurisable jusqu'à 5 bars ; le nombre de Mach est compris entre 0,3 et 1,1. L'intensité de turbulence dans la veine d'essai est de l'ordre de 0,002. T2 fonctionne par rafales de 30 à 60 s. Au démarrage, circuit prégonflé, l'écoulement stationnaire s'établit en 10 s environ.

Le coude n° 1 (fig. 2) est muni d'aubages dont le bord de fuite laisse échapper des jets d'air sous pression (p_j = 7 b ; M_j = 1,6). Ces jets entraînent le fluide contenu dans le circuit, à travers une partie retour basse vitesse, la chambre de tranquillisation (1,8 x 1,8 m^2), le collecteur (rapport de contraction 20), la veine, un col et enfin un tronçon à paroi poreuse où a lieu une évacuation partielle. Le col stabilise l'écoulement dans la veine et empêche toute remontée de perturbations issues des zones d'évacuation et d'injection.

4.2 - *Veine d'essai* -

La veine est l'élément important de la soufflerie dans ce genre d'expérimentation. Pour les essais bidimensionnels présents, sa conception a fait l'objet de soins particuliers afin de connaître le plus exactement possible les conditions aux frontières du domaine (définition géométrique et mesures de pression) et d'agir avec précision sur les parois.

Cette veine a pour dimensions L = 1,32 m - l = 0,39 m, h = 0,37 m. Elle est formée par deux parois verticales fixes et parallèles et par deux parois haute et basse flexibles, en tôle d'acier de 1,5 mm d'épaisseur. A l'amont, ces parois déformables sont vissées sur la fin du collecteur pour réaliser une continuité de pente ; sur leurs bords longitudinaux, des joints en téflon assurent l'étanchéité et le glissement. A l'aval, l'ouverture verticale de la veine, variable selon les configurations d'essais, est prolongée par deux volets mobiles liés au col (fig. 3) pour éviter de brusques changements de section.

Chaque paroi flexible est déformée par 16 vérins hydrauliques pas à pas (pas élémentaire 0,2 mm ; course maximale 25 mm) commandés par des moteurs électriques à impulsion. Ces vérins sont plus rapprochés dans la zone d'influence de la maquette. Chaque vérin, par l'intermédiaire d'un système de biellettes à faible jeu (inférieur à 1/10 mm), déplace identiquement deux points d'un raidisseur transversal soudé à la paroi (fig. 4). La liaison biellette-raidisseur est constituée d'une rotule afin d'éviter l'apparition de moments de flexion locaux. Nous avons constaté une bonne planéité transversale des parois.

Les cotes des frontières déformables sont repérées par des comparateurs potentiométriques placés au droit des vérins (précision 5/100 mm). Les origines de mesure de ces potentiomètres correspondant à une paroi plane et horizontale ; dans cette position, un relevé manuel de cotes met en évidence quelques défauts, négligeables dans la zone de la maquette mais plus accentués entre les vérins les plus espacés, aux extrémités de la veine ; ces bombements de la paroi, inférieurs à 3/10 mm se répercutent néanmoins de façon visible sur les relevés de pression (fig. 5).

Chaque paroi flexible est équipée de 91 prises de pression ($\emptyset$ = 0,4 mm), plus resserrées dans la région de la maquette et disposées sur 3 génératrices longitudinales.

4.3 - Maquette -

Les résultats présentés sont relatifs à un profil CAST 7. C'est un profil supercritique d'épaisseur relative 12 %, choisi par le groupe CARTeur dans le but de comparer différentes souffleries.

Nous avons utilisé 2 maquettes de 120 et 200 mm de corde, équipées respectivement de 102 et 103 prises de pression de diamètre $\emptyset$ = 0,4 mm ; chaque maquette peut être placée à une position quelconque entre l'axe veine et 80 mm en dessous (20 % de la hauteur veine).

L'incidence de la maquette est ajustée manuellement à $\pm$ 1' par rapport à l'horizontale.

La transition est déclenchée artificiellement à 7 % de corde sur les deux faces par des grains de carborundum collés sur une bande de largeur 1 mm. Le choix des grains a été défini à partir d'un critère de déclenchement de la transition correspondant sensiblement à l'épaisseur de déplacement de la couche limite laminaire devant la rugosité.

4.4 - Mesures et acquisition -

L'instrumentation de la soufflerie, outre les voies analogiques (capteurs, amplificateurs), comprend un ordinateur HP 1000 et ses périphériques. Les diverses séquences sont programmées par ce calculateur qui assure l'acquisition des données à la cadence de 1000 points/s (pressions, cotes) et commande le déplacement des vérins ; parallèlement, il enregistre les résultats acquis sur un fichier disque.

Toutes les prises de pression sont regroupées sur 7 têtes de scanivalves "classiques" comprenant chacune 48 prises explorées à la cadence de 10 prises /s ; on mesure en fait $p - p_{réf}$ par des capteurs différentiels pour avoir une meilleure précision.

Le sillage est sondé à une corde en aval du bord de fuite de la maquette par deux prises de pression statique et d'arrêt solidaires d'un dard d'exploration.

Les données analogiques de pression et de position sont converties en valeurs numériques traitées par le calcul.

5 - DEROULEMENT D'UN ESSAI -

Un essai complet pour une configuration donnée nécessite 2 rafales, la première est consacrée à l'auto-adaptation des parois par le processus itératif, la deuxième est réservée au sondage du sillage.

5.1 - Adaptation des parois -

On présente ici l'enchaînement des opérations nécesaaires à l'adaptation des parois ; chaque phase sera détaillée dans les paragraphes suivants.

De manière à minimiser le nombre d'itérations, on positionne initialement les parois sur une forme dite initiale se rapprochant autant que possible du résultat cherché. Dans ces conditions, l'adaptation est réalisée en temps réel, en 3 à 5 itérations qui se succèdent dans la même rafale. Le calculateur gère seul les différentes opérations à exécuter.

Chaque itération peut se décomposer comme suit :

- positionnement des parois durée : 1 s
- mesure des pressions sur les parois et le profil 5 s
- calcul des nouvelles formes de parois 4 s

} 10 s.

A la fin de la rafale, il est possible de tracer les nombres de Mach locaux et les formes de parois pour chacune des itérations, les nombres de Mach locaux et coefficients de pression sur le profil ; on peut également intégrer les pressions sur le profil pour obtenir les C_x, C_z, C_m à chaque étape de l'adaptation.

Ces résultats sont très utiles pour définir la qualité de la convergence ; en effet, on fixe le nombre d'itérations avant l'essai ; aucun critère de convergence n'intervient pendant la rafale. L'adaptation de la veine est jugée bonne lorsque la répartition du nombre de Mach n'évolue plus d'une itération à la suivante ; il peut tout de même subsiter une oscillation locale entre 2 positions voisines de vérin (0,2 mm).

5.2 - Formes initiales -

On utilise deux modes de recherche des formes initiales. Premièrement, on positionne simplement les parois sur une géométrie adaptée, résultat d'un essai précédent relatif à une configuration peu différente : même nombre de Mach infini, incidences voisines ; même incidence, nombres de Mach infini voisins.

La deuxième solution est donnée par un calcul d'écoulement autour de singularités ponctuelles en atmosphère infinie, les singularités (source, doublet, tourbillon) dont les intensités sont estimées à partir des C_{x_i} section profil et C_y approximatifs, sont placées au centre de la maquette. On en déduit la forme d'un conduit limité par les lignes de courant issues de l'entrée veine, que l'on élargit après un calcul des couches limites pariétales.

Le positionnement des parois sur ces formes initiales est effectué avant le début de la rafale. On ajuste ensuite l'ouverture des volets mobiles, à l'entrée du col, sur la section aval de la veine pour éviter les discontinuités de surface. Ce réglage n'est pas retouché pendant l'essai, mais la faible variation des extrémitéa des parois flexibles au cours des itérations justifie cette démarche.

5.3 - *Positionnement des parois* -

Au début de chaque itération, on s'assure que la géométrie à réaliser est mécaniquement admissible (test sur le rayon de courbure local). Si elle l'est, on fait un relevé de cotes avant déformation, puis le positionnement s'effectue par étapes sur des formes intermédiairea affinées ; enfin, un deuxième relevé de cotes enregistre la forme réellement atteinte. A tout moment, un refus de déplacement d'un vérin interrompt l'essai.

5.4 - *Calcul des formes nouvelles* -

- Les nouvelles formes sont définies par une méthode inverse linéaire : on suppose $u_c(x) = u_f(x) = -u_\infty \frac{K_p}{x}$

La vitesse verticale $v_c(x)$ dans le champ virtuel externe est calculée par une méthode de Green appliquée sur un plan horizontal :

$$v_c(x) = \int_{-\infty}^{\infty} \frac{u_c(\xi)}{\xi - x} d\xi$$

Enfin, la nouvelle ligne de courant est connue par intégration à partir de l'entrée veine :

$$y(x) = y_{\text{entrée veine}} + \int_{x_{\text{entrée veine}}}^{x} \frac{v(\xi)}{V_\infty + u(\xi)} d\xi$$

La différence entre l'ancienne et la nouvelle ligne de courant donne le déplacement à imposer à la paroi.

- La compensation de l'effet d'obstruction des 4 couches limites pariétales est reportée sur chacune des parois flexibles. Chacune d'elles compense sa propre couche limite (calculée à partir des pressions mesurées) et celle qui existe sur une des deux portes verticales (considérées comme plaque plane à V_∞). Les calculs sont effectués par une méthode intégrale [36] qui utilise au départ les grandeurs de la couche limite turbulente sondée en fin de collecteur.

- Pour une meilleure relaxation du processus, les pressions et cotes mesurées sont décomposées en parties paire et impaire de 2 fonctions liées à la hauteur de veine et à la ligne médiane (voir fin chapitre 2). Il est donc nécessaire de créer un maillage calcul symétrique en x . Dans le cas présent, on allonge fictivement la veine vers l'aval en rajoutant des points virtuels. Dans ce maillage calcul, chaque point est une moyenne de plusieurs prises de pression. La décomposition du calcul en 4 morceaux indépendamment relaxés sépare en fait les effets de volume (V), de source (S), de portance (P) et de calage de la déformée moyenne (VDM). Des essais veine vide à partir de formes initiales correspondant à chaque effet nous ont permis d'optimiser grossièrement les coefficients de relaxation ; ils dépendent peu du nombre de Mach. Pour nos essais nous avons retenu les valeurs suivantes :

	L'incidence	$-2° \grave{a} -1°$	$0° \grave{a} +5°$
ω_i	V	0.3	0.2
	S	0.2	0.2
	P	0.6	0.4
	VDM	0.6	0.6

Dans le calcul du champ virtuel externe par la méthode de Green, l'intégration de u sur la surface de contrôle horizontale et infinie est décomposée en trois parties :

$$v_c(x) = \int_{-\infty}^{\infty} \frac{u(\xi)}{\xi - x} d\xi = \int_{-\infty}^{\text{entrée veine}} + \int_{\text{entrée}}^{\text{sortie}} + \int_{\text{sortie veine}}^{+\infty}$$

Le terme central correspond à la veine allongée et fait intervenir les mesures de pression. Les termes extrêmes sont estimés pour les effets volume, source et portance, par intégration analytique de l'expression $u(\xi)/(\xi - x)$ relative aux singularités respectives ; il est en effet permis d'utiliser cette modélisation pour l'évaluation du champ maquette dans des termes du second ordre alors que la méthode d'adaptation revendique, comme avantage principal de pouvoir se passer de cette représentation.

6 - *RESULTATS TYPIQUES* -

6.1 - *Cas d'une adaptation classique* -

L'exemple correspond à la maquette de 120 mm de corde, placée sur l'axe veine, à 1° d'incidence, à Mo = 0,70. Au départ, la divergence des parois compense seulement les couche limites (fig. 5) ; les lignes de courant limitant le domaine de fluide parfait sont donc approximativement parallèles. Dans ce canal à parois pleines et pour ce cas portant, la vitesse atteint des valeurs élevées sur la paroi haute (M = 0,8). Dès la deuxième itération, ce maximum décroît et l'allure générale des répartitions de vitesse est atteinte. La troisième itération améliore l'adaptation et la quatrième confirme le résultat à un pas de veine près (0,2 mm).

On peut remarquer la convergence de type oscillatoire du processus liée aux coefficients de relaxation choisis et la rapidité de celle-ci en dépit d'une géométrie initiale de parois éloignée de la forme adaptée.

Sur la maquette, l'adaptation, en débloquant l'écoulement, fait avsncer le choc de plus de 10 % de corde et fait baisser le niveau général sur les 2 faces (fig. 6).

6.2 - *Influence de la position de la maquette dans la veine* -

Théoriquement, un déplacement vertical de la maquette dans le référentiel de la veine doit entraîner une adaptation différente des parois sans modifier le champ des pressions sur le profil. Ceci constitue un teat intrinsèque du processus complet dont les approximations ne sont pas nécessairement totalement justifiées.

Ce test a été réalisé à T2, dans la configuration Mo = 0,76, α= 1°, profil de 120 mm de corde. La maquette a été placée sur l'axe veine puis 80 mm (20 % de la hauteur d'entrée veine) en dessous (fig. 7).

On peut conatater que l'abaissement de la maquette, dans ce cas portant, s élargie le demi-canal supérieur en diminuant les survitesses de la paroi haute. Ce résultat est appréciable lorsqu'on se rapproche des limites de validité des hypothèaes de calcul, en particulier de la formulstion linéaire pour des nombres de Mach locaux voisins de 1.

Sur le profil et dans le aillage, on distingue de faibles différences (fig. 8).

6.3 - *Angle d'incidence* -

Le problème de l'angle d'incidence de la maquette dans un écoulement de longueur finie a été développé dans les parties précédentes.

Expérimentalement, noua avons déplacé des parois adaptées (Mo = 0,70 ; α= 1°) par simple rotation autour de l'entrée veine d'un angle $\Delta\alpha = \pm 0{,}18°$. Dans les deux cas, les parois sont approximativement adaptées.

On peut voir figure 9 que les valeurs de α correspondant à ces essais sont en bon accord avec la courbe générale $C_z(\alpha)$ obtenue en faisant tourner le profil. Ce résultat permet de conclure que :

. le changement du raccordement collecteur-veine a une influence négligeable au niveau de la maquette ;

. la direction de référence de l'écoulement non perturbé est bien définie par la pente des parois au voisinage du modèle.

6.4 - *Gradient longitudinal de vitesse* -

Pour tester la possibilité d'appliquer une correction de gradient longitudinal de vitesse, une variation systématique de la divergence de veine a été réalisée en faisant, comme précédemment, pivoter les formes adaptées (fig. 10a). Le coefficient de traînée de pression est porté figure 10b en fonction de cette divergence à laquelle correspond un grsdient longitudinal de pression statique. La correction classique de poussée d'Archimède donne dans ce cas (M = 0,70, profil de 120 mm de corde) une pente nettement plus faible que l'évolution constatée pour un écoulement ralenti par la divergence de veine.

6.5 - *Possibilités effectives de l'installation* -

La figure 11 regroupe les différentes formes de parois flexibles obtenues après adaptation autour de la maquette de 200 mm de corde placée en position basse ; le nombre de Mach infini vaut 0,70 ; l'incidence varie entre - 2° et + 4° ; on remarque une évolution régulière des formes entre - 2° et + 2°, puis un ralentissement de cette évolution (α= 3°) à l'approche de la valeur maximale de C_z suivi d'un important élargissement aval de la veine (α= 4°) correspondant à l'augmentation brutale de la traînée.

CONCLUSIONS -

Par rapport aux questions soulevées dans l'introduction, l'utilisation pratique de parois adaptables dans la soufflerie T2 pour les essais de profil permet de donner les réponses suivantes :

a) compte tenu de la décroissance rapide, avec la distance au modèle, de la fonction d'influence des défauts d'adaptation, la longueur de parois adaptables choisie pour T2 apparaît suffisante et dans ces conditions les raccords au collecteur et col aval sont sans importance.

b) bien que, dans un souci de gain de temps, les conditions précises à l'infini n'aient pas été recherchées dans les essais présentés par référence à l'ensemble des mesures pariétales, quelques contrôles [38] ont montré que les différences étaient de l'ordre des erreurs de mesure.

c) il appsraît par contre que le pas choisi (0,2 mm) pour le déplacement des parois peut laisser subsister même pour un profil d'assez grande corde un défaut de cambrure (0,2°) non négligeable par rapport à la préciaion requise dans la définition du profil.

d) la séparation en quatre termes suivant les symétries permet, par un choix convenable de coefficienta de relaxation constants , d'accélérer suffisamment la convergence du processus d'adaptation pour qu'une seule rafale suffise à atteindre le seuil de réglage. L'sccroissement du coût d'essai correspond donc à un doublement du temps puisqu'une autre rafale est actuellement nécessaire à l'acquisition des mesures (sillage et pression) sur le profil.

Outre ces réponses aux questions initiales, les possibilités offertes d'effectuer des essais hors adaptation ont permis de tester des méthodes de calcul de corrections et aussi d'éprouver en ce qui concerne le gradient longitudinal de vitesse, la validité de la correction de trsînée.

Il demeure aux nombres de Mach élevés des incertitudes sur la possibilité d'appliquer, en présence d'effets non linéairea, des corrections liées aux perturbations non uniformes (cambrure et gradient de vitesse), ce

qui nous conduit à conclure que le prix à payer pour une adaptation suffisante des conditions aux limites et une connaissance précise des références doit être accepté dès que des résultats précis sont recherchés.

REFERENCES

1 C.N.H. LOCK - J.A. BEAVAN
Tunnel interference at compressibility speeds using the flexible walls of the rectangular high-speed tunnel
ARC R et M 2005, 1944

2 A. FERRI, P. BARONTI
A method for transonic wind tunnel corrections.
AIAA Journal, vol 11 n° 1, janvier 1973, pp. 63-66.

3 W.R. SEARS
Self correcting wind tunnels.
Aer. Journ. Vol 78 n° 758-759, fev. mars 1974

4 R. LECENDRE
Souffleries transsoniques auto-correctrices.
Ommagio a Carlo Ferrari Lib. Leurotto et Bella Turin 1974, pp. 457-
et T.P. ONERA 1975-33

5 R.J. VIDAL, J.C. ERICKSON, P.A. CATLIN
Experiments with a selfcorrecting wind tunnel.
AGARD CP 174, paper n° 11, Octobre 1975.

6 J.P. CHEVALLIER
Soufflerie transsonique à parois auto-adaptables.
AGARD CP 174, Paper n° 12, Octobre 1975.

7 H.J. GOODYER
A low speed self streamlining wind tunnel
AGARD C.P. 174, paper n° 13, Octobre 1975.

8 T.M. WEEKS
Reduction of transonic slotted wall interference by means of slat contouring.
AFFDL TR 74-139, 1976.

9 E.M. KRAFT, R.L. PARKER
Experiments for the reduction of wind tunnel interference by adaptive wall technology.
AEDC T.R. 79-51, Oct.1979

10 C. QUEMARD, A. MIGNOSI
Définition d'une soufflerie à induction de haute qualité à la soufflerie transsonique pressurisée.
T2 de l'ONERA-CERT.
18e Conf. Israelienne Haïfa 19.5.1976.

11 C. CAPELIER, J.P. CHEVALLIER, F. BOUNIOL
Nouvelle méthode de correction des effets de parois en courant plan.
14e Colloque d'Aérodynamique Mémoire 21, TOulouse, Novembre 77 et R.A. n° 1/1978, pp. 1-11.

12 M. PINDZOLA, J.W. BINION, J.P. CHEVALLIER
Comments on wall interference control and corrections.
AGARD CP 187, Avril 1976.

13 J.M. MOKRY, D.J. PEAKE, A.J. BOWKER.
Wall interference on two dimensional supercritical airfoils using wall pressure measurements to determine the porosity factors for tunnel floor and ceiling.
NAE NRCC Ottawa, Aer. Rep. 4-R-574, fev. 1974.

14 W.B. KEMP
Toward the correctable interference transonic wind tunnel.
9th AIAA Aer. Testing Conf. 6/1976

15 J.B. PAQUET
Perturbations induites par les parois d'une aoufflerie.
Thèse Ing. Doc. Lille, 26 Juin 1979

16 J. SMITH
Preliminary evaluation of a method for determining 2 dim. wall interfcrence
NLR Memo AC 77-008, Mars 1977.

17 C.F. LO
Tunnel interference assessment by boundary measurements.
AIAA Journ. Vol 16 n° 4, avril 1978, pp. 4-413.

18 M. MOKRY, L.H. OHMAR
Application of the fast Fourier transform to this dimensional tunnel wall interference.
J. of Aircraft Vol 17, nb 6, Juin 1980, pp.

19 J.E. HACKETT, D.J. WILSDEN
Estimation of wind tunnel blockage from wall pressure signatures : a review of recent work at Lockheed Georgia.
AIAA Rep. 78-828

20 J.A. BLACKWELL
Wind tunnel blockage correction for two-dimensional transonic flow.
J. Aircraft vol 16 n° 4, Avril 1979, pp. 256-2 , AIAA Pap. 78-805.

21 H.SAWADA
A general correction method of the interference in 2-dimensional wind tunnels with ventilated walls.

22 H. SAWADA et alii.
An experiment of lift interference on 2 dimensional wings in a wind tunnel with perforated walls.
N.A.L. T.R. 563, Mars 1979

23 H. SAWADA
Experimental study about 2-dimensional blockage effect.
N.A.L. T.R. 591, Novembre 1979.

24 S. BODAPATI, E. SCHAIRER, P. DAVIS
Adaptive wall wind tunnel development for transsonic testing.
AIAA Pap. 80.0441.

25 W.R. SEARS, R.J. VIDAL, J.E. ERICKSON, A. RITTER
Interference free wind tunnel flows by adaptive wall technology.
J. of Aircraft vol 14 n° 11, Nov. 1977 pp. 1042-1050

26 W.R. SEARS
A note on adaptive wall wind tunnels.
ZAMP vol 28, 1977, pp. 915-927.

27 C.F. LO, E.M. KRAFT
Convergence of the adaptive wall wind tunnel.
AIAA J. vol 16, Jan. 1978, pp. 67-72.

28 W.R. SEARS
Adaptive wind tunnels with imperfect control.
J. Aircraft vol 16 n° 5, pp. 344-3-8, art. 79-4072 Juin 1978

29 M. JUDD, M.J. COODYER, J.W. WOLF
Application of the computer for on site definition and control of wind tunnel shape for minimum boundary interference.
ACARE CP 210, Juin 1976, Pap. N° 6.

30 J.C. CIAVALDINI
Analyse numérique des écoulements compressibles autour d'un profil placé en atmosphère infinie.
Thèse Doctorat Rennes 17 Oct. 1980.

31 J.M. CELY
Auto-adaptation et corrections de parois de soufflerie transsonique.
Thèse Ing. Doc. Toulouse, 27 Septembre 1979.

32 U. CANZER
Wind tunnels with adapted walls for reducing wall interference.
A. Flugwiss Weltraumforsch Vol. 3, Mars-Avril 1979, pp. 129-133.

33 U. CANZER
Adaptable wind tunnel walls for 2D and 3D model tests.
ICAS Conf. Pap. 23.3, Munich 1980

34 J.D. WHITFIELD, J.L. JACOCKS, W.E. DIETZ, S.R. PATE
Demonstration of the adaptive wall concept applied to an automotive wind tunnel.
AIAA 12th Aer. Test. Conf., Mars 1982.

35 A. MICNOSI, C. QUEMARD
Performances et qualités d'écoulement de la soufflerie à induction T2.
La Recherche Aérospatiale n° 1976-4.

36 MICHEL R., C. QUEMARD, J. COUSTEIX
Méthode pratique de prévision des couches limites turbulentes bi et tridimensionnelles.
Colloque d'Aérodynamique Appliquée, AAAF, Saint-Louis, Novembre 1971.

37 A. ELSENAAR, E. STANEWSKY
A report of a GARTEUR Action Group on "Two-dimensional Transonic Testing Methods".
AGARD Specialist Meeting, Londres 1982

38 P.R. ASHILL, D.J. WEEKS
A method for determining wall interference corrections in solid wall tunnels from measurements of static pressure at the walls.
AGARD Specialist Meeting, Londres 1982.

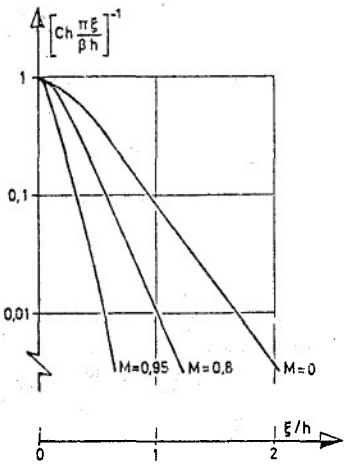


Fig. 1 - Fonction d'influence pondérant les effets de parois en fonction de la distance au modèle suivant la direction de l'écoulement.

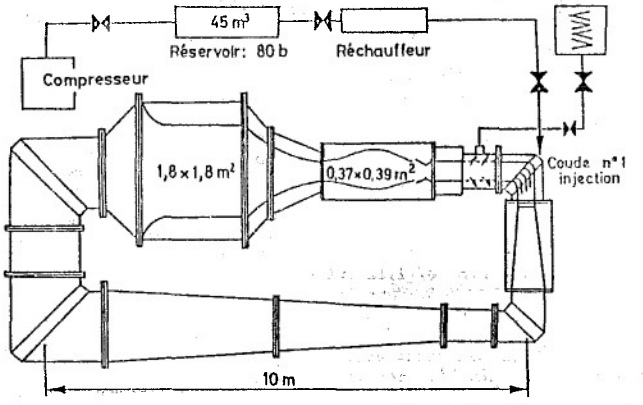


Fig. 2 - Schéma de la soufflerie T2 du CERT

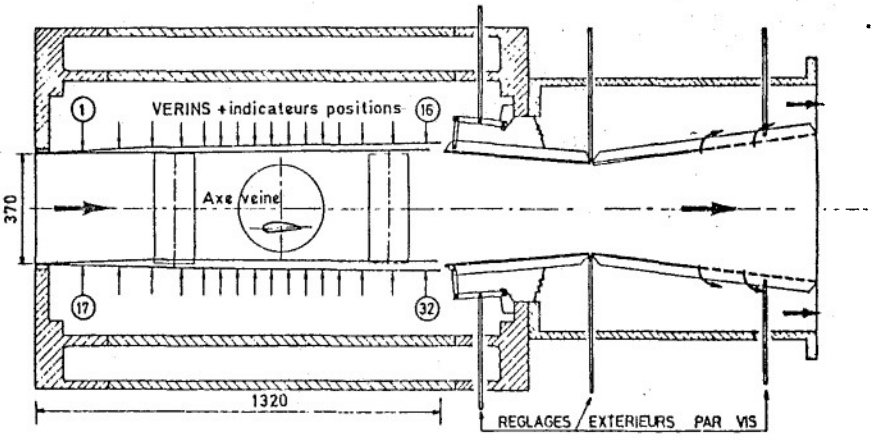


Fig. 3 - Veine à parois déformables

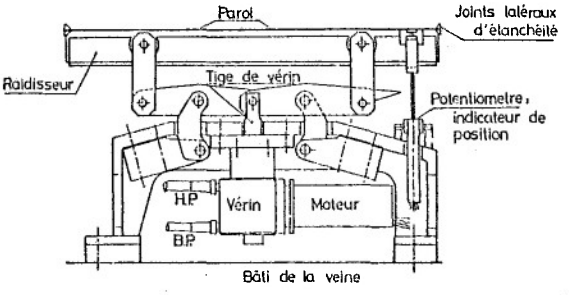
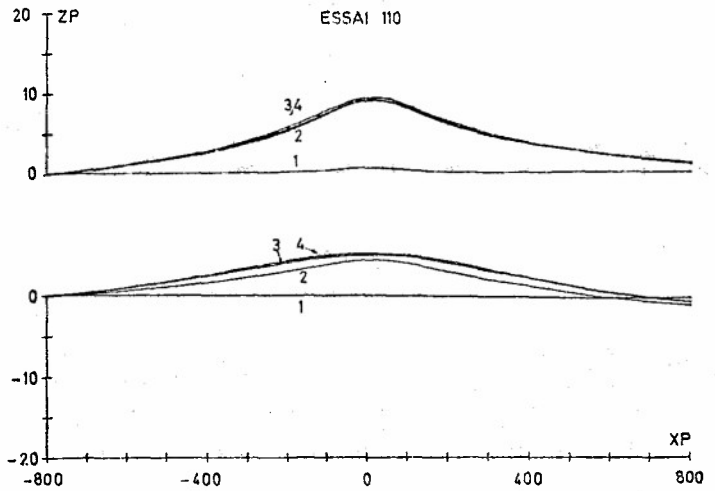


Fig. 4 - Cinématique de liaison vérin-paroi



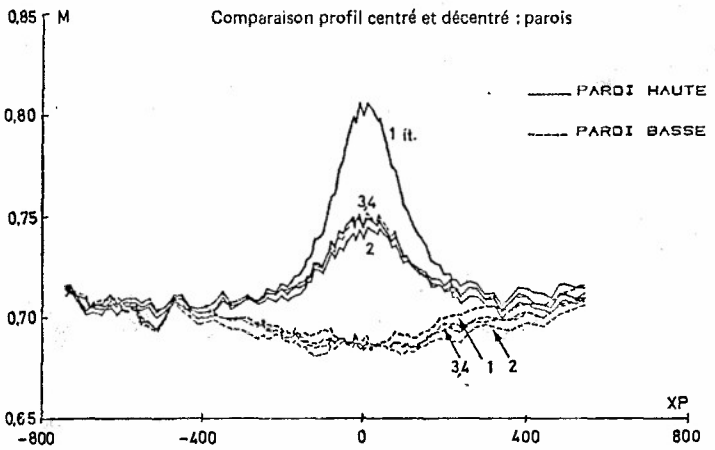
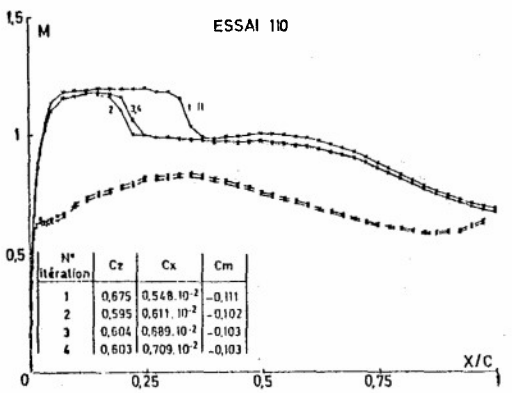
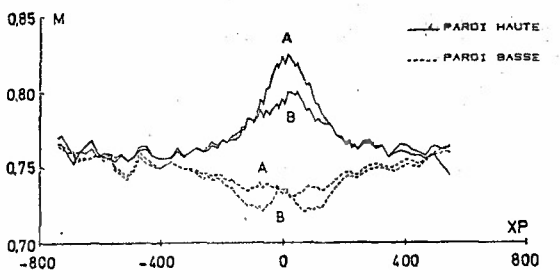


Fig. 5 - Evolution des distributions des nombres de Mach locaux et des formes de parois au cours du processus itératif.



N° itération	Cz	Cx	Cm
1	0,675	0,548.10⁻²	-0,111
2	0,595	0,611.10⁻²	-0,102
3	0,604	0,689.10⁻²	-0,103
4	0,603	0,709.10⁻²	-0,103

Fig. 6 - Evolution des nombres de Mach locaux sur le profil au cours du processus itératif et coefficients globaux.



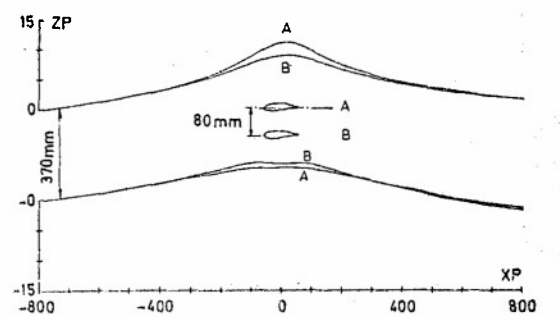


Fig. 7 - Comparaison des nombres de Mach et formes de parois pour profil centré et décentré

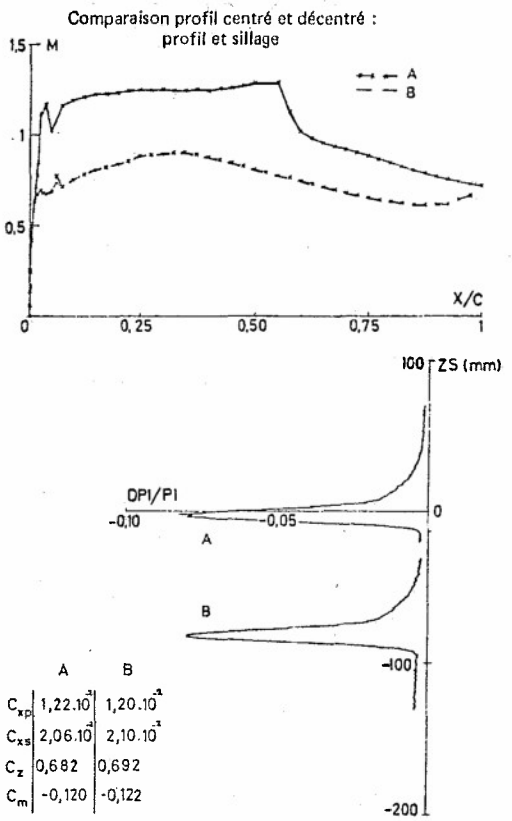


Fig. 8 - Nombre de Mach locaux sur le profil sillages et coefficients globaux pour le profil CAST 7 en position centrée et décentrée.

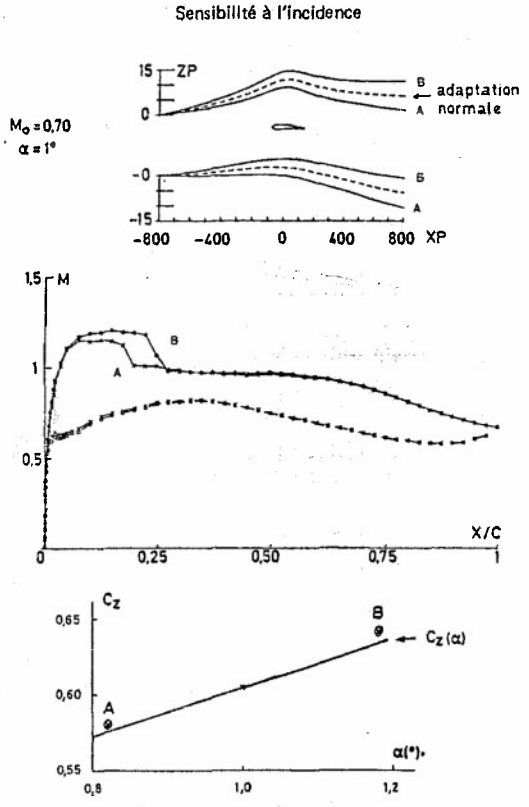


Fig. 9 - Effet d'une rotation des parois.

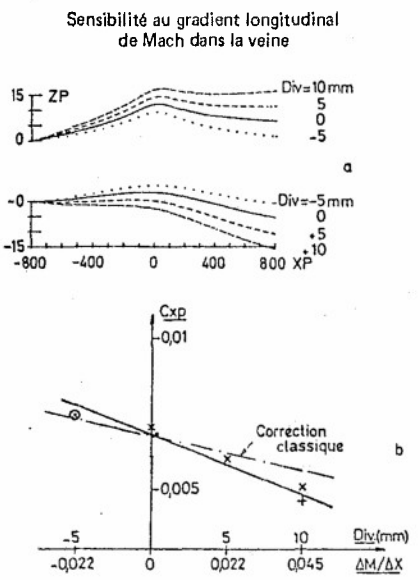


Fig. 10 - Effet d'une divergence des parois.

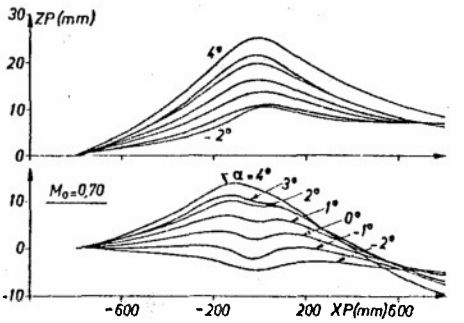


Fig. 11 - Formes de parois pour diverses incidences du modèle

THE STATUS OF TWO- AND THREE-DIMENSIONAL TESTING IN THE UNIVERSITY OF SOUTHAMPTON TRANSONIC SELF-STREAMLINING WIND TUNNEL

BY
S.W.D. WOLF, I.D. COOK AND M.J. GOODYER
Department of Aeronautics and Astronautics
University of Southampton, Southampton SO9 5NH
Hampshire, England

Summary

An automated test section has been used to validate and develop a flexible walled testing technique which eliminates some sources of uncertainty in boundary interference effects which exist in conventional transonic test sections. The flexible floor and ceiling of the test section have been adjusted to contours which produce a constant Mach number distribution along each wall with no model present. These 'aerodynamically straight' contours form the basis for all streamlining. With a model in the test section, the 'wall data' is shown to contain information on the models performance, including quite good information on lift. Two-dimensional validation testing has continued with a cambered NPL 9510 section, larger and of more challenging design than a NACA 0012-64 section previously tested. Lift data up to Mach 0.87 is compared with reference data. Drag information on a NACA 0012-64 section is presented to indicate the powerful effects of streamlining. Preliminary three-dimensional testing in the two dimensional test section has demonstrated that model and support blockage can be relieved by wall contouring. Further three-dimensional testing awaits the development of a suitable algorithm for calculating boundary interference effects and predicting the wall movements required to minimise these effects.

SYMBOLS

C_D	Drag coefficient
$C_{M_{l.e.}}$	Pitching moment coefficient about leading edge
C_N	Normal force coefficient
C_p	Pressure coefficient
C_p^*	Sonic pressure coefficient
M	Local Mach number
M_∞	Freestream Mach number
R_c	Chord Reynolds number
α	Angle of attack
δ_w^*	Wake displacement thickness
σ	Standard deviation

1. Introduction

The Transonic Self-Streamlining Wind Tunnel (TSWT)[1] has been operating in an automatic mode for some time now, allowing concentration during the past year or two on improving and widening experimental technique and experience.*

In the two dimensional area the recent research effort has included the testing of an NPL 9510 section. Besides being cambered and of more modern section than aerofoils so far utilised in our flexible walled tunnels, the ratio of chord to test section height is also larger. Comparisons are made between data obtained at subsonic and transonic speeds with this aerofoil in the flexible walled tunnel, and reference data. The scope of two-dimensional testing has also been extended to include the measurement of drag with a wake traversing mechanism. The technique has been developed using a NACA 0012-64 section.

Information on the behaviour of the model is available from wall data.[1] Effort has so far been devoted to deriving lift, pitching moment and wake thickness data for an aerofoil. While it will be seen that the data is of variable quality, in some circumstances its availability could prove a useful supplement to the usual sources.

Preparations for three-dimensional testing have been underway for some time, but only recently has serious testing begun in the flexible walled test section. At the present time we are on the early part of the learning curve, but some preliminary experimental information is presented. One important

*This work is funded by NASA under Grant NSG-7172 monitored through Langley Research Center, and by the British Science and Engineering Research Council.

outcome from this early work has been the evident need for more precision in wall measurements than has been the case in two-dimensional testing: the model-induced wall perturbations are rather small.

Related partly to this need for greater precision has been a move to more closely define what constitute straight walls for the test section. Straight walls are intended to give constant Mach number along the test section when empty. Errors in the definition of such wall contours will be reflected in errors in streamlining which could prove unacceptable in three-dimensional testing, and at the higher transonic speeds in two-dimensional testing. Because of its underlying importance in all of the aerodynamic work undertaken in this tunnel, this paper begins with a report on the "straight wall" work, before proceeding to the other topics introduced above.

2. Straight Walls

Contouring of the TSWT flexible walls towards streamlines depends on the magnitudes of the flow disturbances caused by a model within the test section, and also on computations of imaginary flowfields extending from the flexible walls to infinity. Both quantities depend upon the displacements of the walls from straight and therefore raise the issue of what constitutes a 'straight' set of walls.

The TSWT test section is a nominal 15.24cm. (six inches) square in cross section and has flexible top and bottom walls 1.12 metres (44 inches) long, each fitted with 20 motorised screw-jacks as shown in Figure 1. The sidewalls are rigid and non-porous. Static pressures are measured along their lengths, allowing the local Mach number to be calculated and adjusted by means of jack movement. The positions of the walls are monitored with transducers. The tunnel is closed circuit with an induced drive using dried compressed air. The flow has atmospheric stagnation conditions in the test section. The tunnel reference Mach number is derived from the settling chamber stagnation pressure and the centre-sidewall reference static orifice positioned level with the beginning of the flexible walls as indicated on Figure 1. A photograph of the test section is shown on Figure 2. Rows of jack drive motors are visible above and below the test section. An aerofoil model is mounted in the schlieren window blanks.

The aim in determining straight walls was in fact to slightly diverge the two flexible walls from the geometrically straight, by roughly equal amounts which were necessary to absorb the growth of the displacement thickness of the boundary layers on all four walls. The divergence, which if carried out correctly will result in constant Mach number along the test section equal to the reference value M_∞, is presumably a function of the Reynolds number and Mach number. In this tunnel the two vary together because of the nominally fixed stagnation conditions and therefore it is necessary only to vary and control one, Mach number for convenience. Wall contours derived in this way are described as "aerodynamically straight". In the streamlining of the walls around a model at a particular reference Mach number, wall displacements should be referenced to the aerodynamically straight contours for that Mach number.

Sets of such contours have been derived from time to time in the past on an ad-hoc basis satisfying immediate needs, but it was felt that improvements were possible. For example, a pair set for Mach 0.7 showed a standard deviation (σ) of the local Mach number from M_∞ of 0.004 for the first 18 jacks, a value which it was judged could and should be reduced.

The method used in refining the straight walls was the old streamlining method which simply uses the rule that, in subsonic flow, the Mach number at a point on a wall will be reduced by moving the wall locally away from the test section centreline, and vice-versa. The relationship between the wall movement δy and desired change of local Mach number δM which worked satisfactorily with this test section was simply $\frac{\delta y}{\delta M} \approx 0.4$ to 0.5 inches. As examples of improvement, values of σ are now

M_∞	σ
0.7	0.0022
0.8	0.0025
0.9	0.0034

While the aerodynamically straight contours can be determined experimentally over a range of Mach number and the contours appropriate for a model test be determined by interpolation, it has been found that the variations of wall contours are rather a weak function of Mach number. To date it has proved adequate to determine only a few such aerodynamically straight contours and to designate each as the aerodynamically straight contour for a band of reference Mach numbers.

Three sets of aerodynamically straight contours have been derived for current use with this wind tunnel. They cover the Mach bands 0.3 to 0.725, 0.725 to 0.825, and 0.825 to 0.9, (A, B and C respectively) and are held on file for use during the initial stages of streamlining, and for use during the computations associated with streamlining. Figure 3 shows the Mach number distributions along both walls when set to the C contours and run (empty) at various Mach numbers. It is seen that σ is not significantly affected by M_∞ in this range. Satisfactory results have been obtained to date by assuming that the imaginary flowfields over such contours are undisturbed. However, one further stage of refinement might yet be taken, aside from the obvious one of reducing further the Mach number deviations which can still consistently be seen to be present. That is to recognise instead that the walls are in fact not straight, and then to determine their distortions from the true straight by using the observed Mach number distributions. It is likely that this and other procedures will be explored in the near future.

3. Two-Dimensional Model Wake Data

Previously reported two-dimensional validation data from TSWT[1] has considered only model lift. A wake traverse technique[2] has now been developed for use in a transonic flexible walled test section to determine model drag. The technique adopted uses control hardware and software compatible with TSWT.

The wake probe is a combination of a disc-static type and a pitot type as shown on Figure 4. Since the probe would be traversed in a region of test section flow influenced by the model induced downwash, the probe design was chosen for its insensitivity to flow angle in one plane, in this case the vertical.

The probe was calibrated in the empty test section of TSWT with the walls set "aerodynamically straight" (see Section 2) over a range of M_∞ up to 0.856, and also in another low speed wind tunnel having the same size of test section. The probe was positioned on the tunnel centreline and a C_p correction was determined, based on the tunnel reference static pressure and reference Mach number. Compressibility effects are visible in the probe calibration curve, shown on Figure 4, at the higher Mach numbers.

In view of the low blockage of the probe and its mounting tubes and of the fact that they do not form a two- dimensional shape, it was decided to perform the wake traverses with the flexible walls fixed at streamline contours. These contours were determined during routine streamlining with only the two-dimensional aerofoil model installed in the test section.

For the preliminary wake traverses discussed here, a NACA 0012-64 schlieren model of 10.16cm (4 inch) chord was used. The ratio of test section height to model chord was 1.5. The traverses were performed on the tunnel centreline, 2¼ chords downstream of the trailing edge and over sufficient vertical distance to locate both edges of the wake, that is where the local Mach number became near constant with probe movement.

Under computer control, the probe was moved vertically from its current location to any predetermined position within the available 10.16cm (4 inch) measurement range. Probe movement was sufficiently slow to allow continual sampling of the probe pressures and position during a steady sweep.

Each data set was reduced off-line using a reported numerical technique[3] to determine the drag coefficient C_D. The static pressure indicated by the probe was corrected for probe interferences using the calibration curve. An approximate correction for the displacement effect of the probe was also included. The value of the drag coefficient was found to depend strongly on properly identifying the edge of the wake.

Traverses were performed at reference Mach numbers of 0.3, 0.5, 0.6, and 0.7 for angles of attack of 0^o, 2^o and 4^o, with the walls streamlined. The resultant drag data is summarised on Figure 5 as a plot of C_D-v-M_∞ over the range of angle of attack. The onset of wave drag is evident above Mach 0.6, particularly at the higher angle of attack. Also included on Figure 5 are reported drag coefficients at $M_\infty = 0.17$ which show reasonable agreement with the TSWT data trends at the lower speeds. The low Reynolds number of the TSWT tests ($R_c = 0.67 - 1.3 \times 10^6$) has limited the amount of relevant reference drag data.

To supplement the above streamlined-walls data, a wake traverse was performed with the walls set aerodynamically straight for the case $M_\infty = 0.7$; $\alpha = 4^o$. A large difference between wakes with straight and streamlined walls had already been observed from the spark schlieren pictures shown on Figure 6. The wake traverses confirmed this finding as can be seen by the wake profiles also shown on Figure 6. This case serves to illustrate the severe interference which can be generated by a shallow straight walled test section at high subsonic Mach numbers. The act of wall streamlining correctly positioned the model shock[1] and is shown here to produce a reasonable value for drag, while simultaneously relieving wake blockage.

4. Model Performance Derived from Wall Data

It is proving possible to infer a limited amount of model aerodynamic data from the measurements which are routinely made at the walls during the streamlining process. This may be done at any stage in the streamlining, but the data presented here applies only to calculations made for cases where the walls are streamlined around the model, which is a pressure plotted two-dimensional section, NACA 0012-64 of 4 inch (10.16cm) chord.

Several comparisons between model-derived and wall-derived lift coefficients are shown on Figure 7. Lift is derived from the walls by integrating the top and bottom wall static pressure distributions, and adding an estimate of the change of vertical component of momentum between the incoming air at jack 1 and the outgoing air at jack 19. The flow in the region of jack 1 on both walls is noticeably perturbed, by an almost equal amount on each wall, only by the circulations due to lift and due to the wall loadings[4] at the test section ends. Therefore at this streamwise station the streamline slopes are almost equal, the absolute velocity is only slightly disturbed from the free-stream value, and therefore the vertical component of momentum is little in doubt. At the test section outlet (taken here as level with jack 19) the same arguments apply to the inclination and one-dimensionality of the flow. However, the velocity at outlet is disturbed from the free-stream value. In the absence of aerofoil shock waves, and after wall streamlining, the disturbance is confined to the wake. A wake survey would provide the outlet momentum, but in the cases presented here the wake survey data was not available. Therefore it was simply assumed that the outlet momentum flux was the same as at inlet, but with the flow at a slope determined by the walls at the outlet.

The resultant lift coefficient comparisons are seen on Figure 7 to be good, despite the sources of approximation just noted.

Pitching moment coefficient $C_{M_{\ell.e}}$ derived in much the same way, is shown on Figure 8. The high level of scatter coupled with a general over-estimate of magnitude, leads to the conclusion that at the present state of development, this method can only be used as a rough guide.

The third type of aerofoil model data which has been extracted from wall data is simply the wake displacement thickness. This is taken as being the average movement apart of jacks 18 and 19. The mean position is 4¼ chords downstream of the trailing edge where the flow is nearly one-dimensional. The data is also shown on Figure 8. One check-point was available from a wake traverse (see Section 3) further upstream, giving some confirmation of the correct order of thickness. Methods are available and will be incorporated in due course, for improving on the precision of these estimates.

5. Further Two Dimensional Validation Tests

Validation tests in TSWT have been continued using a NPL 9510 section[5]. This is an 11% thick cambered model having a chord of 15.24cm (6 inches) equal to the test section width and nominal height.

In order to reduce the number of unknowns when evaluating the data from the TSWT tests, data was obtained on this model in the NASA Langley Research Center (LRC) ¼ Metre Transonic Cryogenic Wind Tunnel. A slotted two-dimensional test section with a height/chord ratio just greater than two was used. The tests were performed at above ambient stagnation pressure and below ambient temperature giving chord Reynolds numbers about 66% higher than in TSWT. A transition band was fitted to the model around the nose and extending to 3% chord for all the LRC tests.

Data from the original NPL tests[5] was also used for comparison. This data was obtained from a 25.4cm (10 inch) chord model in an NPL transonic tunnel fitted with a slotted walled test section, 76.2cm (30 inches) in height, equal to 3 chords. The tests were performed at ambient stagnation conditions giving chord Reynolds numbers also 66% greater than for TSWT. A transition band was fitted to the lower surface of the model from 6-8% chord for all NPL tests, and for the majority of the tests from 4-6% chord on the upper surface.

In TSWT a total of fifty-one streamlining cycles* were completed during the tests, thirty with a transition band the same as in the LRC tests and twenty-one with no transition band. The test Mach number ranged from 0.5 to 0.87, with angle of attack varying from zero to 6°.

When comparing TSWT data with that from LRC and NPL it should be noted that i) the latter two data sets have not been corrected for boundary interferences, ii) there are differences in the chord Reynolds numbers. However, the reference data constitutes the best available at low Reynolds numbers and it can be used as an indication of model performance.

5.1 Comparison of Validation Data with Reference Data

Favourable comparisons between TSWT and LRC** data can be made. There is a tendency for the TSWT data (transition unfixed) to give slightly better agreement with LRC data at low Mach numbers and low angles of attack than TSWT data (transition fixed). While this may be a Reynolds number effect, it could also be caused by other differences in test conditions. At high Mach numbers, the model shock positions are very sensitive to the boundary layer condition and there is a correspondingly large difference in model performance for the cases of transition fixed and unfixed. This is shown to good effect on Figure 9, a plot of the normal force coefficient versus angle of attack for $M_\infty = 0.8$. The TSWT data (transition fixed) shows fair agreement with LRC data.

LRC data was unavailable above Mach 0.81, but runs were carried out in TSWT at higher Mach numbers to test the ability of the tunnel to converge on streamlines with a large model present. In particular, it was important to locate the test conditions at which the wall setting strategy began to break down in the manner previously reported.[1] The highest Mach number at which wall streamlining was achieved was 0.87 with $\alpha = 2^\circ$. It is interesting to observe the variation of C_N over the Mach number band 0.5 to 0.87 at this angle of attack as shown on Figure 10. A shock stall is evident at about Mach 0.85. Again there is reasonable agreement with the LRC data.

The data set from NPL does not seem to compare at all well with either TSWT or LRC. On Figure 9 there is a disparity equivalent to an angle of attack of over half a degree at this Mach number. There is a pronounced reduction of lift curve slope in the NPL data beyond about $\alpha = 2^\circ$, not evident in the TSWT data. Evidence of an angle of attack error is also shown on Figure 10, where the NPL results are above the remainder up to the shock stall. The shift of the onset of shock stall from Mach 0.85 in TSWT to Mach 0.79 in the NPL tests is also indicative of a difference in angle of attack.

We believe that TSWT wall streamlining removed any significant interference due to the floor and ceiling of the test section. Other interferences associated with all wind tunnel tests may still be present. The data presented here has been recorded with the walls streamlined. The qualities of streamlining are quantified, and defined as levels of residual flexible wall interference which are judged to be acceptable based on our past operational experience[1]. All routine TSWT streamlining reported here at freestream Mach numbers up to 0.8 was terminated with the following maximum errors induced by the flexible walls:

*A streamlining cycle is a series of iterations bringing the walls to streamlines.

**Unpublished work.

α: 0.017°
Camber: 0.07°
C_p: 0.01

The raw NPL data is known to contain boundary interferences affecting particularly the angle of attack and serves to illustrate, again, the variation of data from different wind tunnels with different conditions including test section geometries and Reynolds numbers.

5.2 TSWT Performance with a Larger Model

For all the NPL 9510 validation tests, wall streamlining was routinely carried out at speeds up to and including Mach 0.8, with typically one or two iterations being required per streamlining cycle. The number of iterations was dependent on the change in test conditions between successive streamlining cycles. On all but three tests the streamlining cycle was initiated with the walls contoured to "known shapes", (which were usually the streamline contours from the previous test) rather than from straight. A known shape is a wall contour, the coordinates of which and the imaginary velocity over which are known. Angle of attack was varied in convenient 1° steps, both up and down, at constant Mach numbers between 0.5 and 0.8.

Above Mach 0.8 the number of iterations for streamlining tended to increase. Finally at Mach 0.87, $\alpha = 2^{\circ}$, the walls could not be adjusted so that the measures of streamlining quality were as good as usual, despite numerous iterations. The peak wall Mach number was 1.0869 on the top wall, indicating that the models supercritical patch was of sufficient strength at the wall[1] to invalidate the wall setting strategy. No allowance for shock/wall boundary layer interaction[1] was introduced during any of the tests reported here.

A family of wall contours is shown on Figure 11 covering a range of angle of attack at a freestream Mach number of 0.7. These are streamlined wall contours, showing the strong effect of a large model and its attitude on test section shape. The change of upwash with lift is apparent ahead of the model, with the opposite effect downstream. It should perhaps be re-emphasised that the walls take up these shapes quite automatically, in response to measurements made only at the walls.

The variation of streamline wall contours with Mach number is shown on Figure 12 over the Mach number range 0.5 to 0.87 for $\alpha = 2^{\circ}$. An effect of compressibility is visible in the walls moving apart in the region of the model, progressively more rapidly as Mach number is increased above 0.7.

For tests at Mach 0.8 and below, the only limitation on model angle of attack was the available wall movement. This limit is reached with the existing hardware at the following test conditions: $M_{\infty} = 0.5$, $\alpha = 6^{\circ}$; $M_{\infty} = 0.7$, $\alpha = 5^{\circ}$; $M_{\infty} = 0.75$, $\alpha = 4^{\circ}$. The severity of the wall movement required for streamlining is clearly shown on Figure 2 for the case $M_{\infty} = 0.87$, $\alpha = 2^{\circ}$. More wall movement than the current restrictions allow (limited by transducer stroke at present) is available should it be required.

The NPL 9510 tests have provided further useful experience with the on-line TSWT control system.[1] Streamlining cycles were performed rapidly under computer control with wall setting times of order minutes, one iteration typically taking thirty seconds. In fact, thirty streamlining cycles were completed in less than the time it took to perform the first ever streamlining cycle at Southampton in 1973 - two working weeks!

6. Three-Dimensional Testing

Although designed for two-dimensional testing, it has long been assumed that TSWT could also be used to reduce the interference effects experienced by three-dimensional models at high speeds. The reduction in interference would arise from differential movement of the walls, relieving blockage, and collective movement, adjusting centreline curvature.

In order to first establish an interference-free data base, two identical wing-body models, one a force model and the other a pressure model, have been tested at Mach numbers up to 0.85 in the 7 x 10 High Speed Tunnel at NASA Langley Research Center. These models are now at Southampton and tests have started on the force model. The model is sting mounted on a 6-component strain-gauge balance, the sting being supported by a cylindrical strut attached to the tunnel side-wall. Angle of attack changes are made by rotating the strut and then adjusting it vertically so that the model remains in the centre of the test section. Figure 13 shows the model and its support system set for 6° angle of attack.

One of the most urgent tasks was to demonstrate that TSWT could relieve the blockage introduced by the model and its support system, to allow testing at high subsonic Mach numbers. With the walls straight, approximate calculations led us to expect choking at the model at $M_{\infty} = 0.83$ and at the support strut at $M_{\infty} = 0.61$. It is clear that in this case it is the support strut that first limits the reference Mach number and since it is of a two-dimensional nature, the two-dimensional wall setting strategy was applied in order to relieve the blockage. Evidence of the blockage caused by the strut and its subsequent elimination by contouring of the walls is shown on Figure 14. The streamlining of the walls was carried out at the initial choking Mach number of approximately 0.61 with the model at 6° angle of attack. The powerful effect of the streamlining process on blockage is apparent from the much reduced Mach peaks inline with the strut after streamlining. This allows testing at higher speeds: an example of the Mach number distributions at $M_{\infty} = 0.7$ is also shown on Figure 14, together with the wall contours in use. The test section is still unchoked. The asymmetry in the various curves arises from the influence of model lift, and from the off-centre position of its support strut which was close to the bottom wall in these tests as shown on Figure 13. The trend in peak Mach number on the lower wall suggests that the tunnel would choke again in this region at a reference Mach number somewhat above 0.8.

In fact this will not be the case. There is ample movement available in the walls to allow testing at higher speeds: we have already demonstrated Mach 0.94 with this model, which is above the speed for which we have reference data.

In contrast to the two-dimensional tests and despite the tunnel walls being close to the model it can be seen from Figure 14 that the centreline Mach number perturbations in the region of the model are very small. Figure 15 shows disturbances in the region of the model in more detail and it can be seen that the maximum Mach number perturbation is less than 4%. It is disappointing at this stage to see such small perturbations since they are proportional to the wall loadings, from which predictions are made of necessary wall movements for the reduction of interference. This was confirmed by other tests where wall movements based on our standard two-dimensional wall setting strategy showed no apparent effect upon the model forces and moments. These results and our previous experiences have led us to the conclusion that we need more comprehensive and more precise static pressure information from the walls in the region of the model. Off-centreline data on the top and bottom walls has been collected and analysed and a typical example is shown also in Figure 15. As expected the off-centreline Mach number perturbations follow closely those on the centreline, but they are smaller in magnitude. Although the flexible walls cannot be contoured in a spanwise direction the off-centreline data is being used in evaluating wall induced interferences and in developing a strategy for minimising wall interference. This work is in too early a stage to be reported.

The magnitudes of the wall interferences on lift are indicated on Figure 16, where our interference-free reference data is compared with uncorrected TSWT straight wall data and the same data after conventional closed wall wind tunnel corrections have been applied.[6] The corrected TSWT data lies close enough to the Langley data to suggest that the observed discrepancies in the uncorrected data are due solely to the effects of wall interference.

While we are confident that the mechanical movement available in the walls can bring about changes more than sufficient to correct lift, at the present time we have no working algorithm to bring about the required changes.

7. Conclusions

i) The choice of "straight walls" forms an important basis for streamlining. While suitable walls have been derived showing good Mach number distributions up to Mach 0.9, refinement may still be necessary particularly for three-dimensional work.

ii) Preliminary data from the wake traverse mechanism suggests that the technique is satisfactory. Streamlining the walls has a strong effect on the wake, as well as on lift as has already been shown.

iii) Model lift data derived from the walls is reasonable, but other data so far derived is proving to be unreliable.

iv) The streamlining technique developed with the aid of a relatively small aerofoil model has proved adequate for streamlining around a large model of more challenging section. The streamlining strategy again began to break down once the walls became supercritical.

v) The two-dimensional streamlining strategy adequately eliminates the blockage of the three-dimensional model support, but is unsuitable for controlling the wall interferences experienced by the model at low Mach numbers. A modified approach is required.

8. References

1. Goodyer, M.J., Wolf, S.W.D., "The Development of a Self-Streamlining Flexible Walled Transonic Test Section", AIAA Paper 80-0440R, May 1981.

2. Wolf, S.W.D., "A Wake Traverse Technique for use in a Two-Dimensional Transonic Flexible Walled Test Section", Progress Report to NASA on Grant NSG-7172, April 1982.

3. Lock, C.N.H., Hilton, W.F., Goldstein, S., "Determination of Profile Drag at High Speeds by a Pitot Traverse Method", ARC R&M No.1981, September 1940.

4. Judd, M., Wolf, S.W.D., Goodyer, M.J., "Analytical Work in Support of the Design and Operation of Two-Dimensional Self-Streamlining Test Sections", NASA CR-145019. July 1976.

5. Hall, D.J., Quincey, V.G., Lock, R.C., "Some Results of Wind Tunnel Tests on an Aerofoil Section (NPL 9510) combining a 'Peaky' Upper Surface Pressure Distribution with Rear Loading", ARC CP-1292, July 1969.

6. Garner, H.C. et al, "Subsonic Wind Tunnel Wall Corrections", AGARDograph 109, 1966.

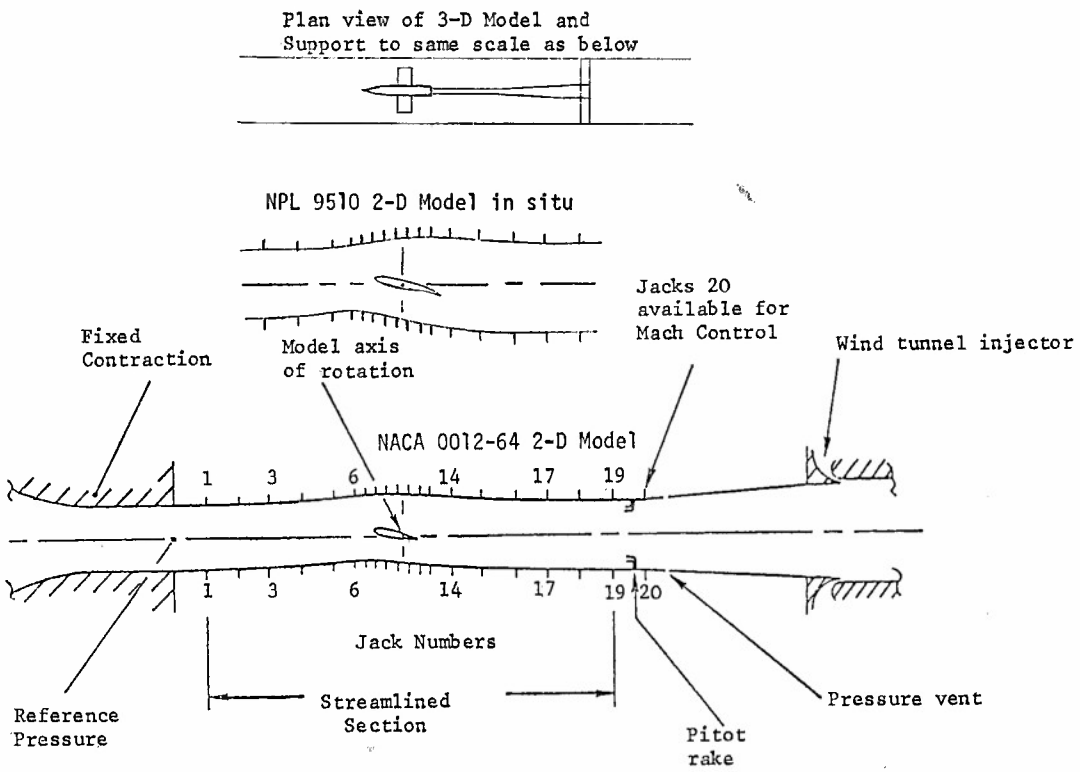


FIG. 1 Transonic flexible walled test section layout

Walls streamlined for the test condition $M_\infty \simeq 0.87$; $\alpha = 2^\circ$

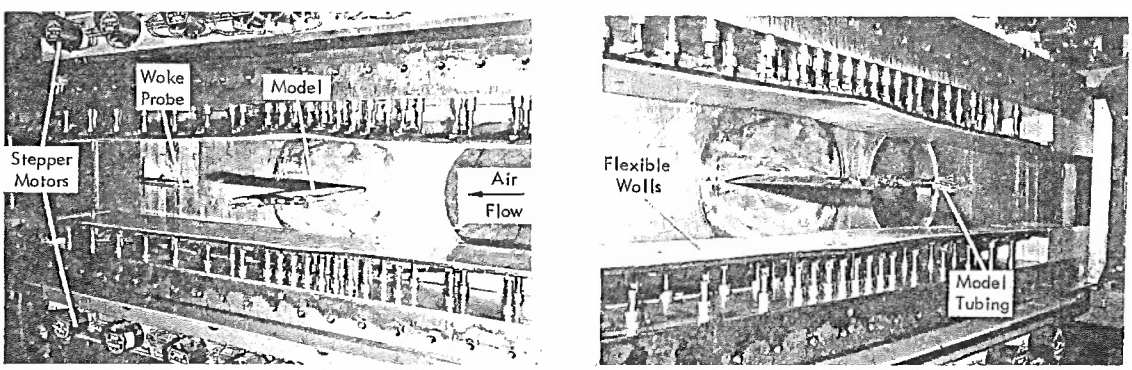


FIG. 2 NPL 9510 MODEL AND WAKE PROBE MOUNTED IN TSWT

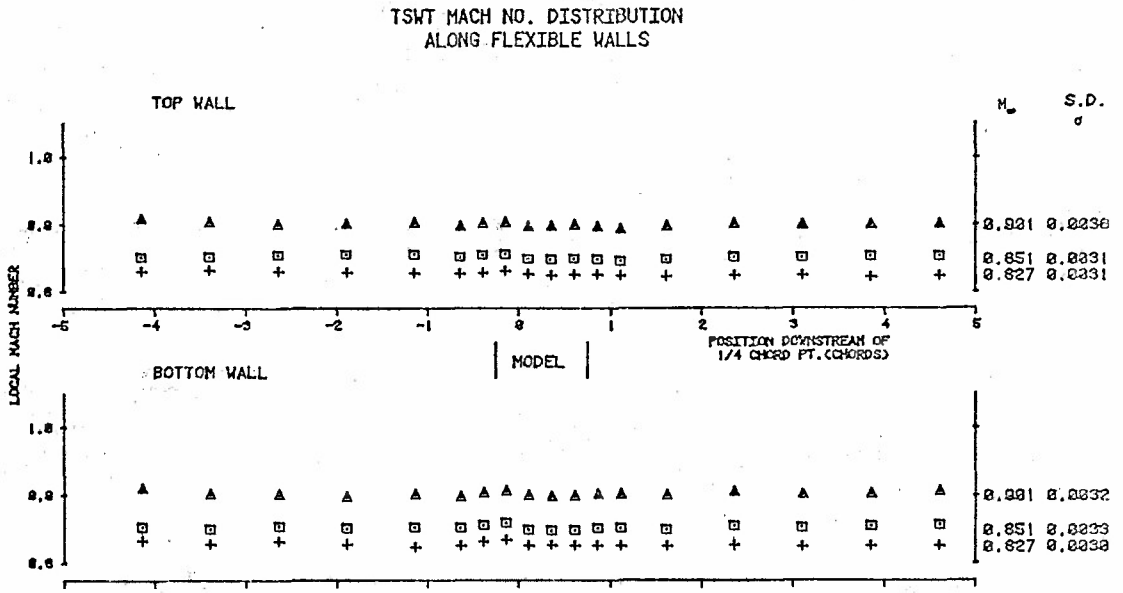
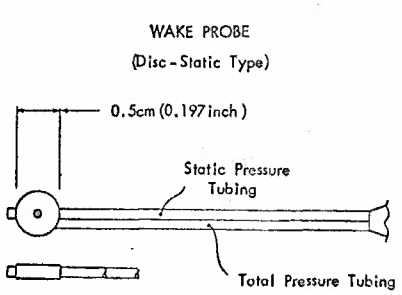


FIG. 3 MACH NUMBER DISTRIBUTIONS ALONG FLEXIBLE WALLS SET TO C CONTOUR



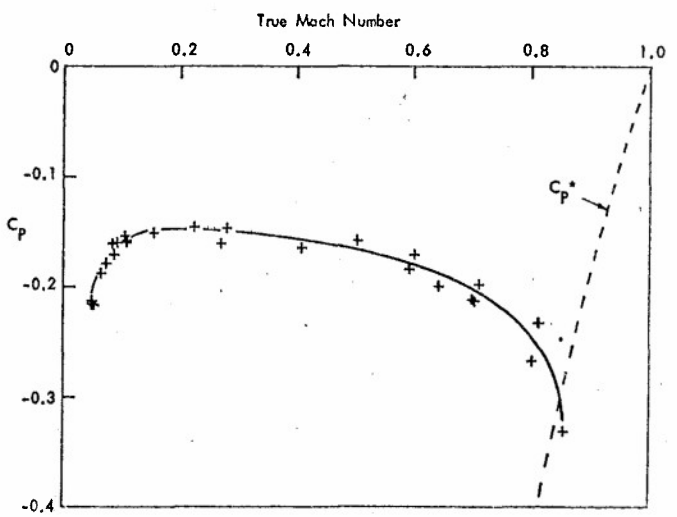


FIG. 4 WAKE PROBE CALIBRATION

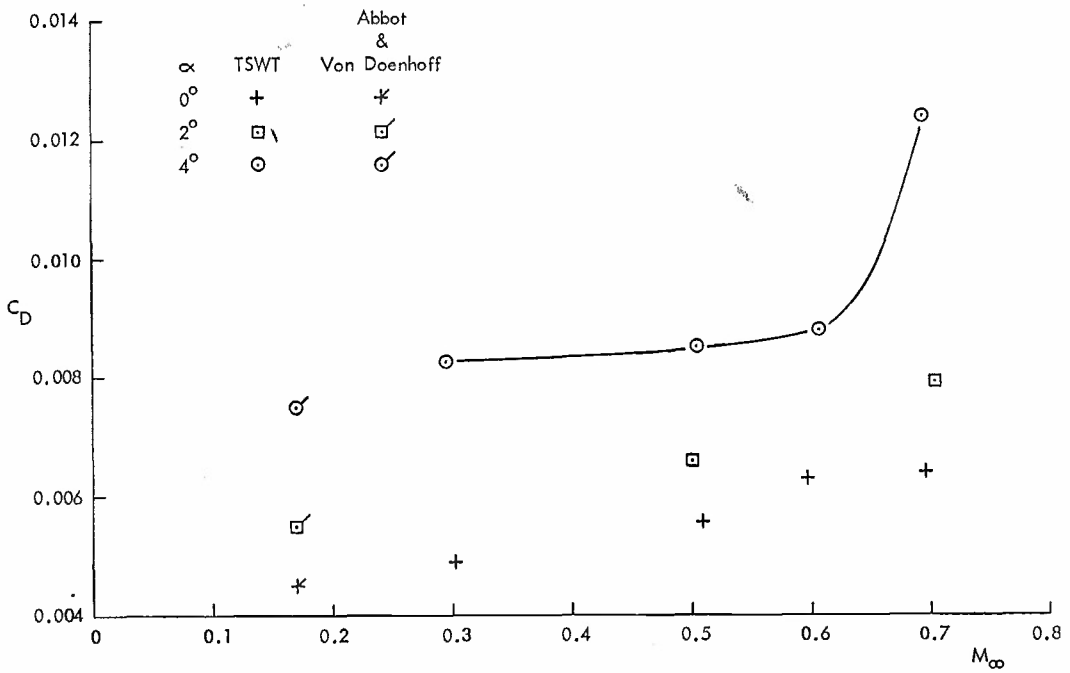


FIG. 5 NACA 0012-64 WAKE TRAVERSE DATA. WALLS STREAMLINED

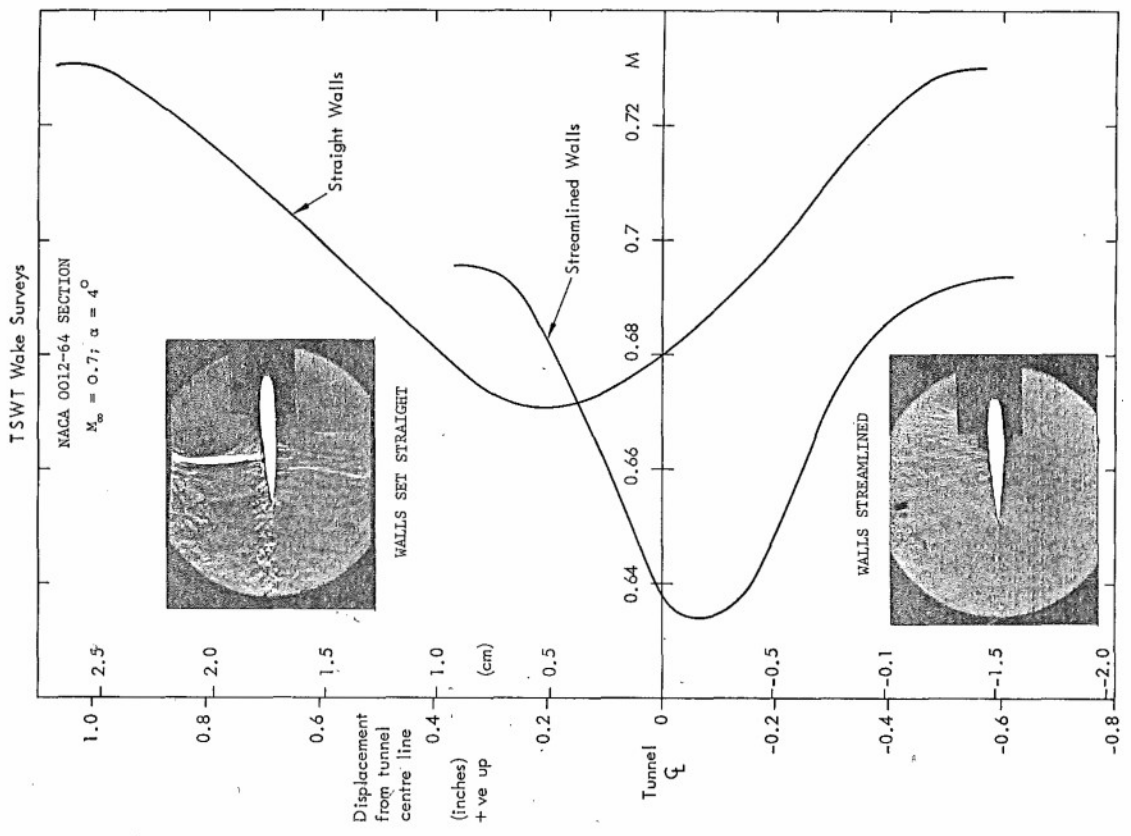
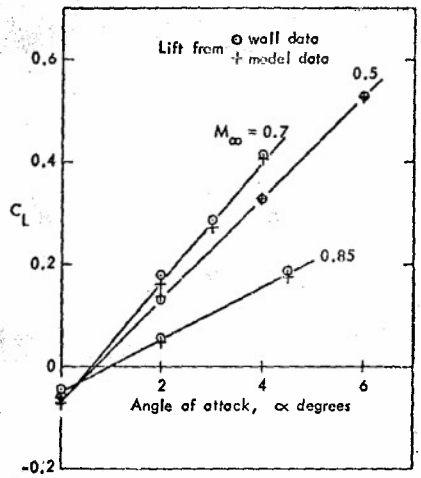


FIG. 6 COMPARISON OF NACA 0012-64 SECTION WAKES WITH THE TEST SECTION WALLS SET STRAIGHT AND STREAMLINED :



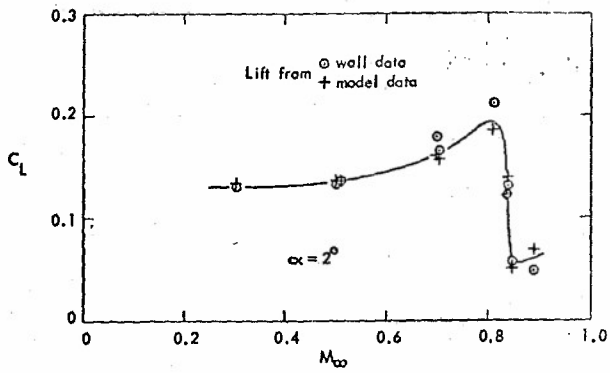
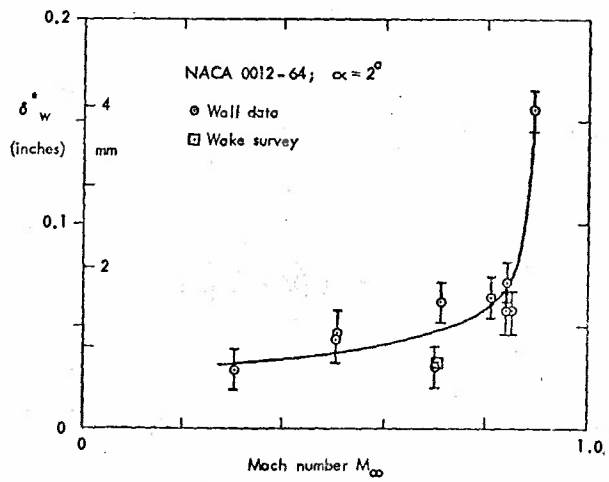


FIG. 7 TWO-DIMENSIONAL TESTING OF NACA 0012-64 : COMPARISONS OF LIFT COEFFICIENTS DETERMINED FROM WALL AND MODEL DATA.



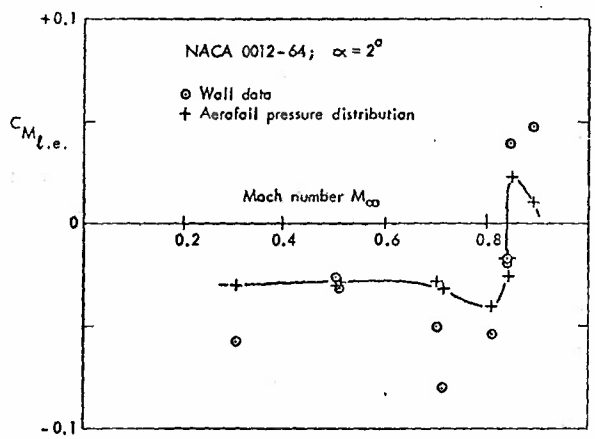


FIG. 8 AEROFOIL WAKE THICKNESS AND PITCHING MOMENT

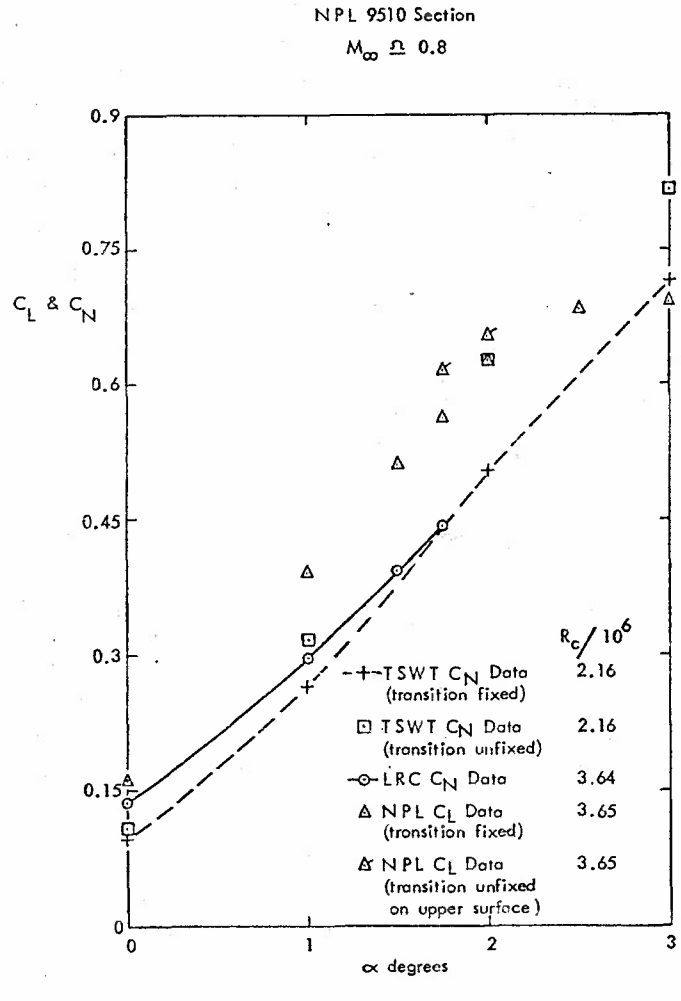


FIG. 9 VARIATION OF NORMAL FORCE COEFFICIENT WITH ANGLE OF ATTACK: M_∞ = 0.8

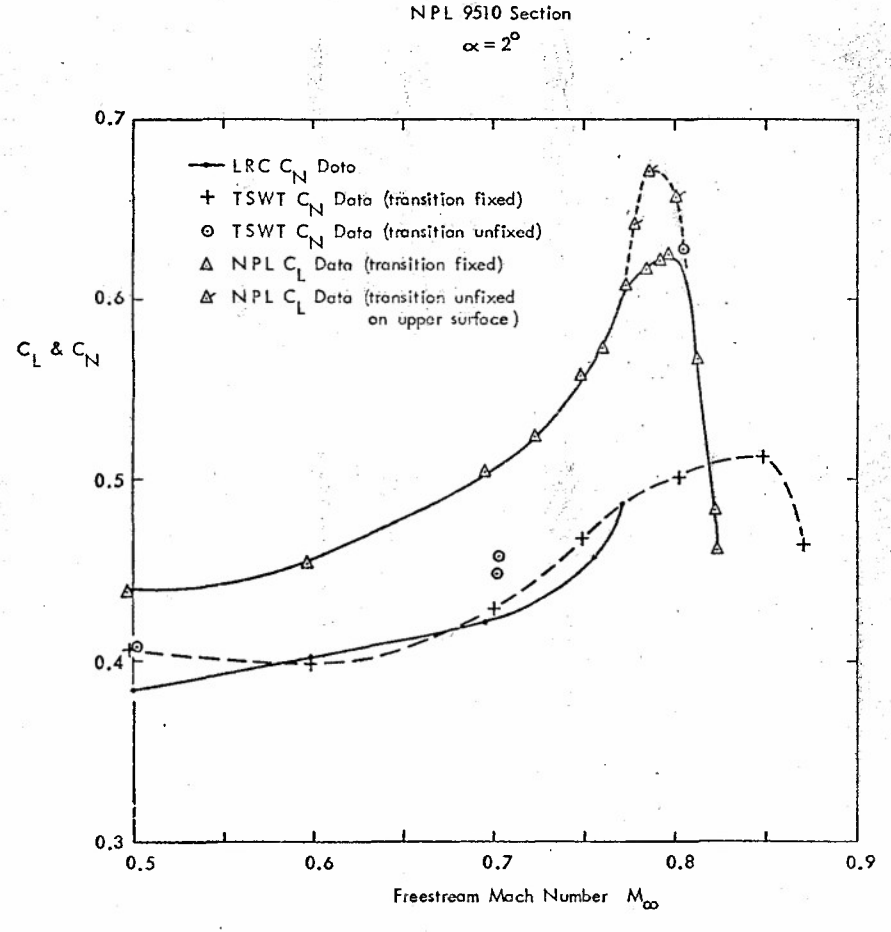


FIG. 10 VARIATION OF NORMAL FORCE WITH MACH NUMBER; $\alpha = 2^\circ$

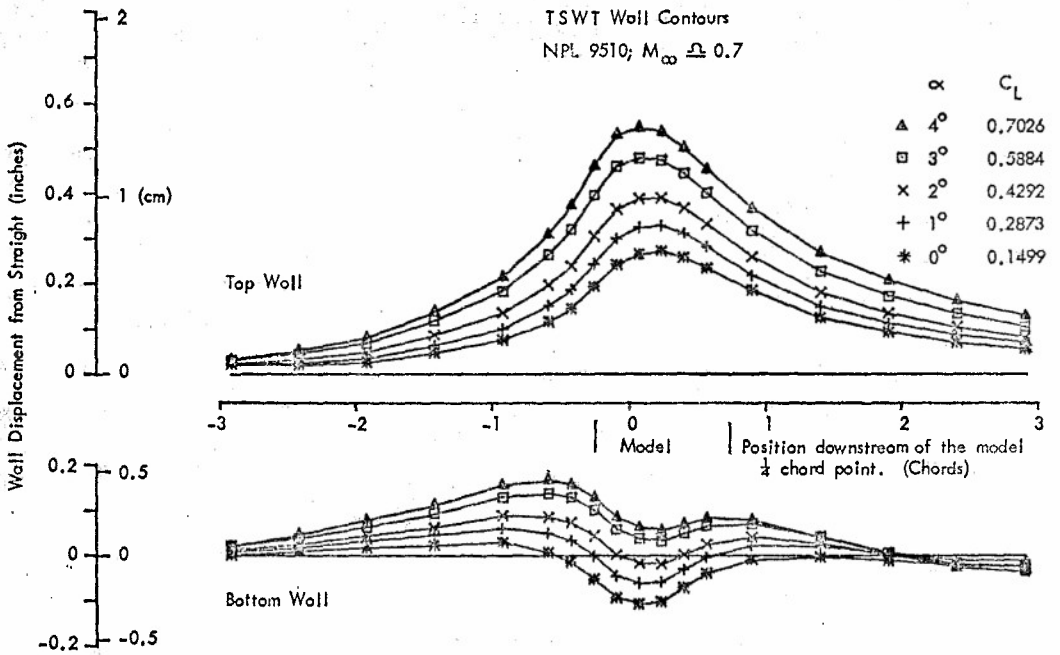


FIG. 11 WALL CONTOURS FOR VARYING ANGLE OF ATTACK AT $M_\infty \triangleq 0.7$

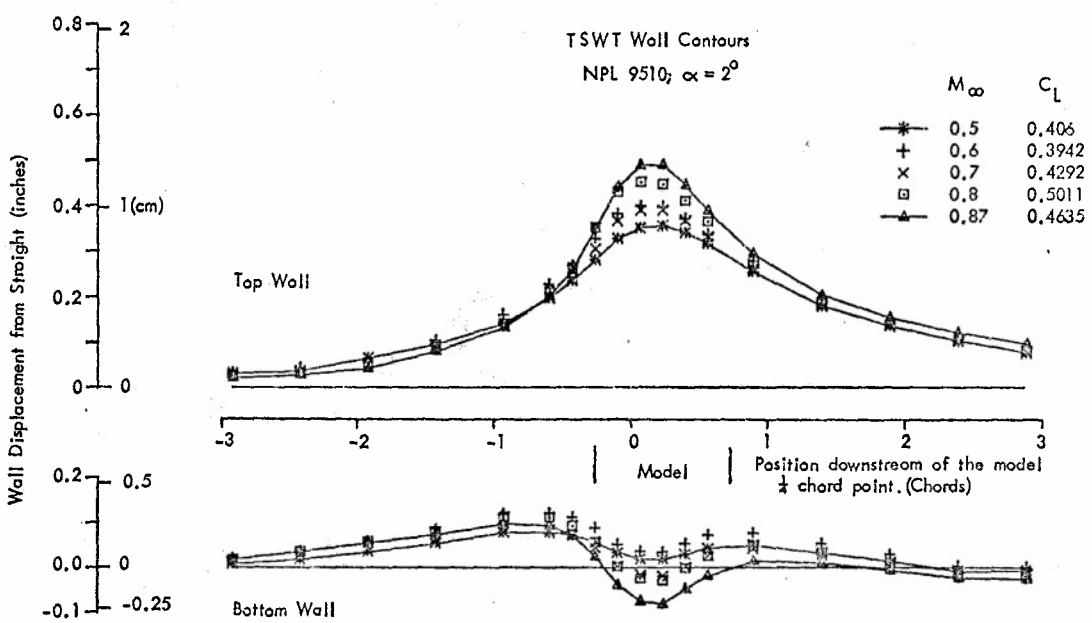


FIG. 12 WALL CONTOUR VARIATIONS WITH MACH NUMBER, $\alpha = 2°$

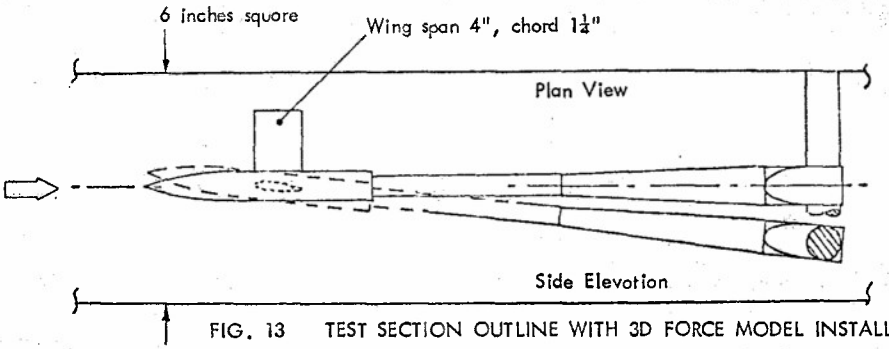


FIG. 13 TEST SECTION OUTLINE WITH 3D FORCE MODEL INSTALLED. MODEL SHOWN AT 6° o-o-a.

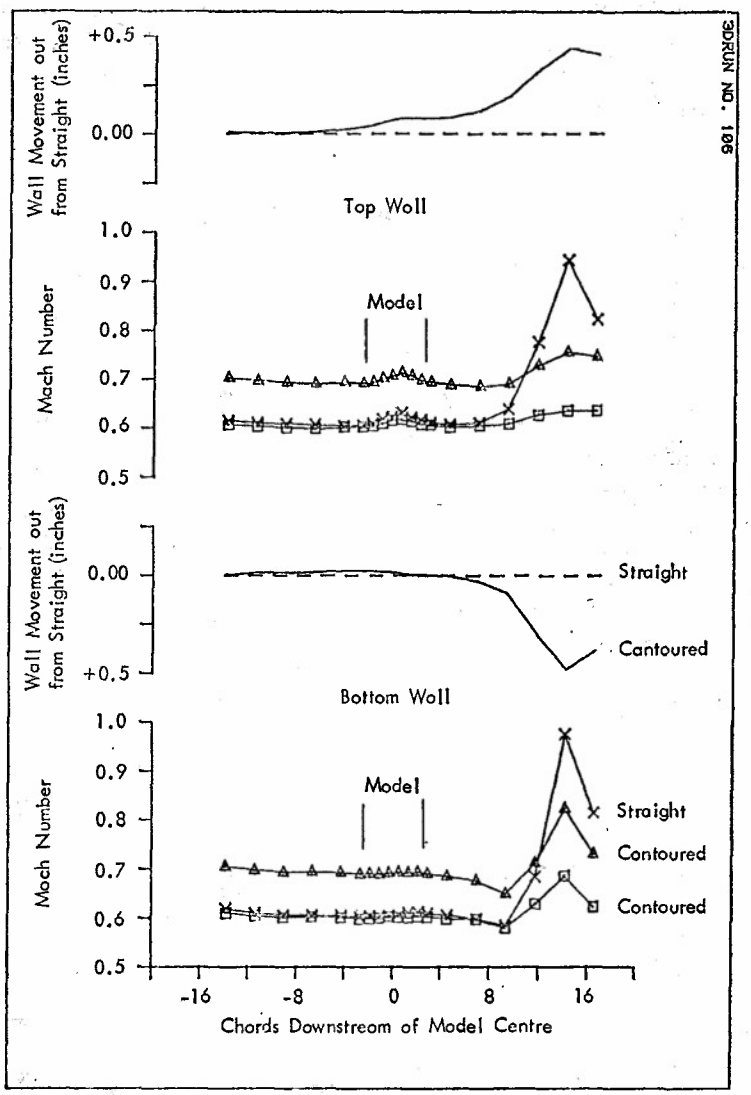


FIG. 14 WALL MOVEMENTS AND MACH NUMBER DISTRIBUTIONS ON TOP AND BOTTOM WALLS SHOWING RELIEF OF BLOCKAGE AT THE MODEL SUPPORT STRUT. WALLS AERODYNAMICALLY STRAIGHT AND CONTOURED.

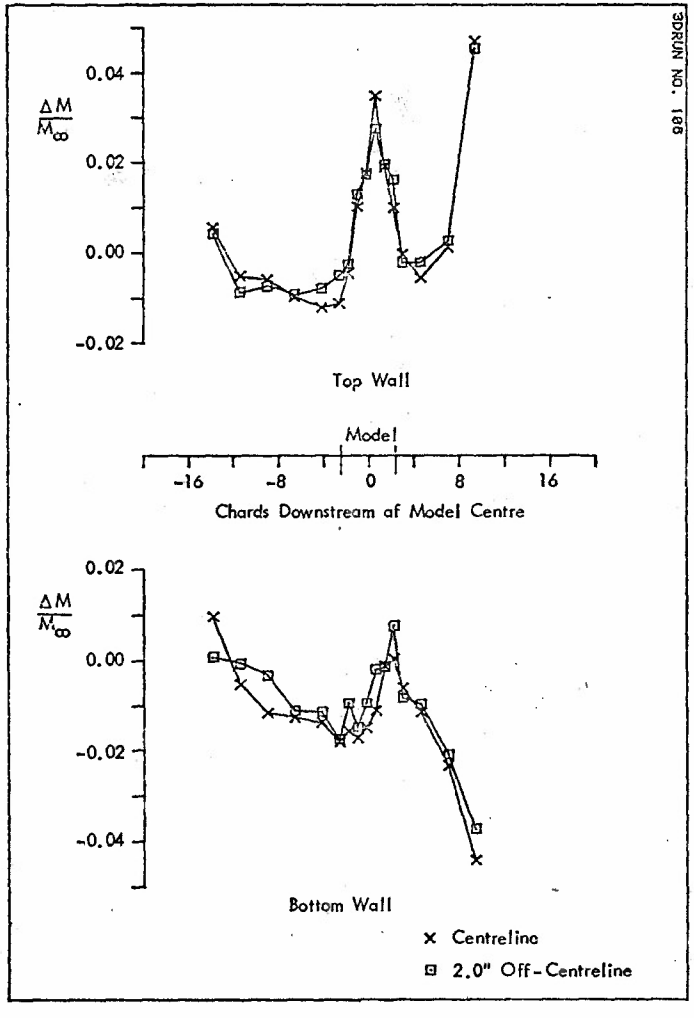


FIG. 15 COMPARISON OF TOP AND BOTTOM WALL CENTRELINE AND OFF-CENTRELINE MACH NUMBER VARIATIONS. WALLS ARE AERODYNAMICALLY STRAIGHT.

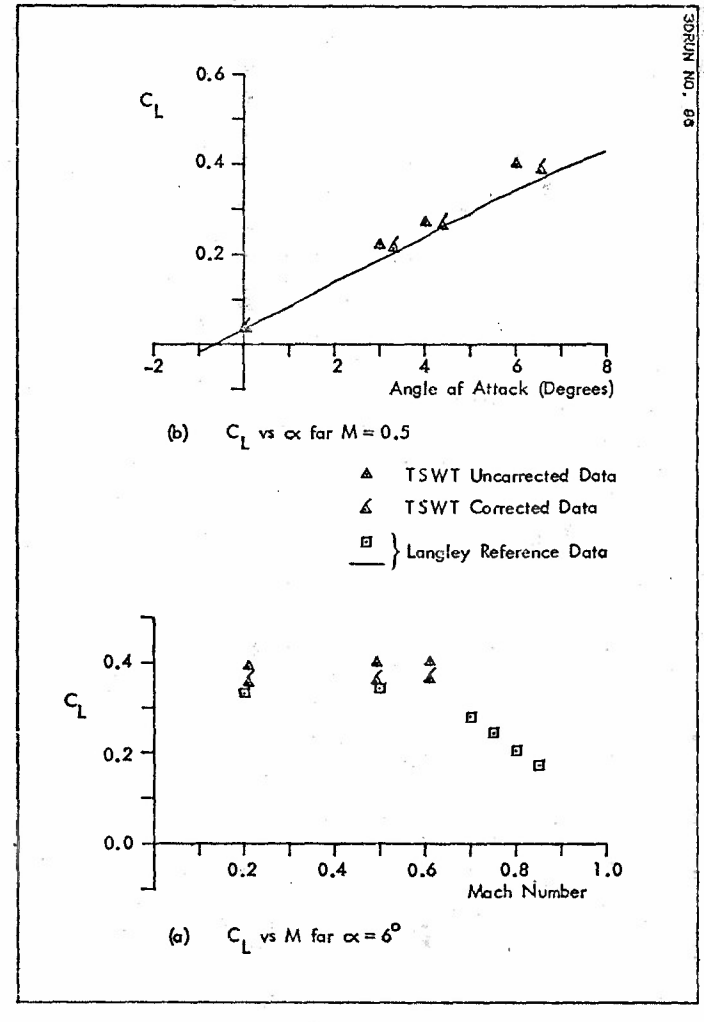


FIG. 16 VARIATION OF C_L WITH MACH NUMBER AND ANGLE OF ATTACK FOR 3D FORCE MODEL.

ADAPTIVE-WALL WIND-TUNNEL RESEARCH AT AMES RESEARCH CENTER

Edward T. Schairer and Joel P. Mendoza
Ames Research Center, Moffett Field, California 94035, U.S.A.

SUMMARY

Adaptive-wall wind-tunnel research conducted at Ames Research Center, NASA, is summarized. This research includes small-scale two-and three-dimensional wind-tunnel experiments and numerical experiments with a three-dimensional adaptive-wall simulator. In the two-dimensional experiment, an NACA 0012 airfoil was tested in a 25- by 13-cm slotted-wall test section. Airflow through the test-section walls was controlled by adjusting the pressures in segmented plenums. Interference-free conditions were successfully attained in subsonic and transonic flows. Based on the design of this small-scale test section, an adaptive-wall test section is being constructed for the 2- by 2-Foot Transonic Wind Tunnel at Ames. For the three-dimensional experiment, the 25- by 13-cm wind tunnel was modified to permit cross-stream wall adjustments. The test model was a semispan wing mounted to one sidewall. Wall interference was substantially reduced at several angles of attack at Mach 0.60. A wing-on-wall configuration was also modeled in the numerical experiments. These flow simulations showed that free-air conditions can be approximated by adjusting boundary conditions at only the floor and ceiling of the test section. No sidewall control was necessary. Typical results from these experiments are discussed.

SYMBOLS

b	wing semispan, cm
c	wing chord, cm
$\bar{c}$	wing mean aerodynamic chord, cm
C_L	lift coefficient
Cp	pressure coefficient
M	Mach number
R	Reynolds number
U_∞	longitudinal free-stream velocity, m/sec
w	vertical velocity, m/sec
x	longitudinal direction, positive downstream, measured from airfoil leading edge in two-dimensional experiments, and from wing quarter chord in three-dimensional experiments, cm
y	spanwise direction, positive outboard of wing root, cm
z	vertical direction, positive above wing, cm
α	angle of attack, deg

INTRODUCTION

Wind tunnels with walls that can be adjusted to eliminate wall interference were demonstrated in England during World War II (Refs. 1-3). These wartime experiments were motivated by the need to reduce blockage interference and eliminate choking in transonic wind tunnels. This was accomplished by bending the tunnel floor and ceiling to conform to free-air streamlines. Although the British experiments were successful, calculations of the streamline shapes were laborious, and a separate computation was required for each combination of model, model attitude, and free-stream condition. After the War, the emphasis of British wind-tunnel research was switched to the development of ventilated-wall test sections.

Recent papers by Ferri and Baronti (Ref. 4) and Sears (Ref. 5) have stimulated new interest in developing adjustable-wall wind tunnels. Ferri and Sears showed that wall interference can be estimated based on measured flow conditions alone, without any knowledge of the model. This insight has greatly simplified the problem of determining the wall adjustments needed to produce interference-free flow. Furthermore, the calculation of free-air conditions can be performed on-line with small contemporary computers. Thus, the prospects for developing practical adaptive-wall wind tunnels are much better today than they were 40 years ago.

Interest in adaptive-wall wind tunnels has also been renewed because flight conditions of modern aircraft are becoming increasingly difficult to simulate in conventional wind tunnels without significant wall interference. In complicated flow problems, analytically "correcting" wind-tunnel data for wall interference is, at best, very difficult. Avoiding excessive wall interference by testing small models in relatively large test sections comes at the expense of Reynolds number simulation. In addition, this approach makes inefficient use of the airstream and may become prohibitively costly as wind tunnels become more expensive to operate.

An adaptive-wall wind tunnel alleviates wall interference by utilizing capabilities of both the tunnel and a computer. The wind tunnel represents the flow near the model which, because of its complexity, cannot be adequately simulated numerically. The computer economically predicts the unconfined far-field flow, which is relatively simple. Tunnel-wall conditions are adjusted until conditions at the interface between the near-field flow (wind tunnel) and far-field flow (computer) are compatible.

The objective of adaptive-wall wind-tunnel research at Ames Research Center is to develop test sections in which unconfined two- and three-dimensional transonic flows can be simulated. To be practical, the procedures for eliminating wall interference must be fast, accurate, reliable, and automatic. The research program consists of parallel experimental and theoretical studies. The experimental program began with small-scale two- and three-dimensional tests. These tests have been completed, and a summary of these results is presented in this paper. The next major step in the experimental program will be a demonstration of a two-dimensional adaptive-wall test section in the Ames 2- by 2-Foot (0.61- by 0.61-m) Transonic Wind Tunnel. The test section is under construction and operation is scheduled for the Spring of 1983.

The operation of adaptive-wall wind tunnels was simulated using numerical models. Among the configurations studied was the small-scale three-dimensional adaptive-wall wind tunnel as described in this paper. Typical results are presented here.

Adaptive-wall research at Ames has focused on slotted-wall test sections in which airflow through the walls is controlled by adjusting the pressures in plenum compartments. This approach was selected primarily because of the wide use of slotted-wall test

sections at Ames. In addition, a subdivided plenum allows for simultaneous adjustment of wall conditions in both streamwise and cross-stream directions, as is required in a three-dimensional adaptive-wall test section. Finally, slotted walls, as opposed to perforated walls, provide space between the slots, permitting the use of nonintrusive, optical measurement techniques.

ADAPTIVE-WALL PROCEDURE

The adaptive-wall procedure used in the Ames studies was conceived by Davis (Ref. 6) and is a modification of Sears' approach (Ref. 5). Whereas Sears predicts free-air conditions by measuring two different flow quantities on one surface surrounding the model, Davis's method requires that only one flow quantity be measured on two surfaces. This can significantly simplify the experimental problem.

Figure 1 illustrates schematically Davis's adaptive-wall procedure applied to the special case of two-dimensional, symmetric flow. In this case, the two surfaces surrounding the model can be reduced to two parallel lines extending infinitely far upstream and downstream. Flow past the model is divided into two regions: a near-field region between the model and the outer line (field level), and a far-field region extending from the inner line (source level) to infinity. In the wind-tunnel experiment, the near-field region is represented by the flow past the model in the wind tunnel; in computer simulations, this flow is represented numerically. In both the wind-tunnel tests and the simulations, the far-field region is represented by a theoretical model of unconfined flow.

The first step in the adaptive-wall procedure (Fig. 1) is to determine the distribution of some flow quantity along the source and field lines in the near-field region. In the present studies, vertical velocity (upwash) was the chosen flow quantity because it is a perturbation quantity which can be easily measured with a laser veloeimeter. The measured upwash at the source level is used as one boundary condition in the theoretical representation of the outer-flow region. At the other (far-field) boundaries, free-air conditions are imposed (perturbations vanish at infinity). The corresponding free-air distribution of vertical velocity at the field level is then computed ("outer-flow solution") and compared with the actual distribution determined experimentally (in the wind tunnel) or numerically (in the computer simulation). Differences between the actual and free-air velocity distributions at the field level are due to wall interference and are used as a basis for adjusting the flow conditions at the wind-tunnel walls. In the wind-tunnel experiments, wall conditions were changed by adjusting the airflow through the slotted walls. In the numerical simulation, wall adjustments were made by imposing normal velocity boundary conditions at panels simulating the test-section walls. Since wall adjustments change the conditions at the source level, the adaptive-wall procedure is repeated until the actual and free-air vertical velocity distributions at the field level converge.

SMALL-SCALE EXPERIMENTS

Small-scale two- and three-dimensional adaptive-wall experiments were performed in the Ames 25- by 13-cm Indraft Wind Tunnel (Fig. 2). The model for the two-dimensional experiment was a NACA 0012 airfoil; in the three-dimensional experiment, the model was a semispan wing mounted on one of the sidewalls of the test section. For both experiments, the test section had slotted upper and lower walls and solid plexiglas sidewalls. Separate top and bottom plenums were divided into compartments, and the pressure in each compartment was independently adjustable. In the two-dimensional experiment, the compartments were arranged longitudinally with each compartment spanning the width of the test section (Fig. 3). The compartments nearest the model were smaller than upstream and downstream compartments because velocity gradients near the model were expected to be large. The three-dimensional test section had the same longitudinal arrangement of compartments, but each of the six upper and lower compartments closest to the model was subdivided into three cross-stream compartments.

Laser velocimetry (LV) was used to measure vertical velocities at control points on the source and field surfaces (Fig. 4). The velocimeter could traverse in the streamwise and vertical directions, and measurements were made at the midspan station for the two-dimensional tests. For the three-dimensional experiment, the velocimeter could, in addition, traverse in the spanwise direction. Motion of the velocimeter, data acquisition, and data reduction were automatically controlled on-line, using a dedicated minicomputer.

Interference-free velocities at the field-level control points were predicted using linear compressible flow theory. The two-dimensional problem was solved analytically (Ref. 6); however, an approximate, finite-difference solution was necessary for the three-dimensional problem. In both cases, the solutions were computed on-line and displayed graphically. The solution required several seconds of computation time for the two-dimensional problem and about 30 sec for the three-dimensional case. The computer speed was about 0.5 million floating point operations per second (MFLOPS).

Pressure adjustments in the plenum compartments were computed from influence coefficients which had been empirically determined in the empty test section before the experiments. Each influence coefficient represented the change in vertical velocity at a control point on the field surface produced by a unit change in pressure in one plenum compartment. The influence-coefficient matrix was inverted and multiplied by desired velocity changes at the field level to determine required plenum pressure changes.

Each plenum compartment was connected to high- and low-pressure air reservoirs by means of flexible plastic hose, PVC pipe, and two ball valves (Fig. 2). Twenty such channels of air were required for the two-dimensional experiment, and 36 for the three-dimensional test. A pressure change in a particular plenum compartment was produced by manually adjusting the appropriate ball valve.

Two-Dimensional Experiments

The NACA 0012 airfoil in the adaptive-wall test section is illustrated in Fig. 3. The height-to-chord ratio of the model in the test section was 1.66, and static pressure orifices were located its upper and lower surfaces. The experiments were conducted at Mach numbers between 0.6 and 0.8 and at angles of attack of 0° and 2°.

Figure 3 also illustrates the points at which upwash was measured at the source and field levels. The source levels were located just beyond optical obstructions produced by the model supports. The field levels were located far enough away from the tunnel walls to avoid the boundary layer and three-dimensional perturbations produced by individual slots.

The adaptive-wall procedure converged to free-air conditions when the supersonic zone on the upper surface of the airfoil remained below the source level. This conclusion is based on a comparison of the measured velocities at the field-level control points with the

free-air velocities predicted by the outer-flow solver. The conclusion was corroborated by comparing the pressure distribution measured aeross the chord of the airfoil with interference-free pressure data (Ref. 7).

Figure 5 illustrates a sample case (Mach 0.78, $\alpha = 0°$) in which free-air conditions were successfully approximated. The figure shows field-level velocities and model pressure distributions before and after plenum pressures were adjusted. Because the flow was symmetric at an angle of attack of 0°, velocity measurements were only made at the source and field levels above the airfoil. The top and bottom walls were adjusted symmetrically. Before the walls were adjusted, there were significant differences between the measured velocity distribution at the field level and the free-air distribution predicted by the outer flow solver. The shock wave position, evident from the pressure data, was downstream of its free-air location (Ref. 7). After three cycles of wall adjustments, both the velocity and pressure distributions were in much better agreement with the free-air data.

When the supersonic zone extended beyond the source level (for example, Mach 0.8, $\alpha = 2°$), the adaptive-wall procedure did not converge on unconfined flow. This was partly because linear theory was used to predict free-air velocities at the field level. In addition, the 25- by 13-cm Wind Tunnel could not produce steady free-stream flow at this condition. Nonlinear solutions to the outer flow problem are being developed and will be available when the 2- by 2-foot adaptive-wall test section becomes operational. Further details of the two-dimensional experiment are given in Ref. 8.

Three-Dimensional Experiments

The test section for the three-dimensional adaptive-wall experiment is illustrated schematically in Fig. 6. The model was an unswept, untwisted, tapered wing semispan. The airfoil (NACA 65A006) was constant from root to tip. The wing is a replica of a model tested at Langley in 1951 as part of a program to investigate the interference characteristics of ventilated-wall test sections (Ref. 9). This model was selected for the adaptive-wall experiment because free-air data were available from Ref. 9. The ratio of the test-section height to the wing mean aerodynamic chord ($\bar{c}$) was 1.5, and the ratio of the test-section width to the wing semispan was 1.47. The model was constructed of solid stainless steel and was supported by a balance that provided force and moment data.

Figure 7 is a cross-sectional view of the test section showing the source and field surfaces and the locations at which LV measurements were made. Vertical velocities were measured at seven such cross sections, beginning 1.15 $\bar{c}$ upstream and ending 1.15 $\bar{c}$ downstream of the wing quarter chord. Acquisition and reduction of the LV data required 20 min.

The adaptive-wall experiments were performed at Mach 0.60 and at angles of attack between 0° and 6°. In all of the experiments, wall interference was substantially reduced after the wall boundary conditions had been adjusted according to the adaptive-wall procedure. This finding is supported by several comparisons of data from the experiment with free-air data. First, the vertical velocities measured at the field surface were compared with the free-air velocities predicted by the outer flow solver. In addition, the measured vertical velocities were compared with velocities predicted by numerical simulation of the model in unconfined flow. Finally, the change in lift coefficient produced by the wall adjustments indicates a reduction in wall interference.

Figure 8 illustrates vertical velocity data along two longitudinal lines at the field surface at Mach 0.6, $\alpha = 5.3°$. (The insets illustrate the positions of the lines where measurements were made relative to the model.) Data labeled "passive wall" were measured before the wall boundary conditions were adjusted. The "adapted wall" data were measured after two cycles of wall adjustments. The "outer-flow solution" is the estimate of free-air conditions made after the second cycle of wall adjustments. The figure shows that differences between the measured data and the outer-flow solution were smaller after the walls were adjusted, indicating a reduetion in wall interference. Similar reductions occurred at other locations on the field surface. The corresponding change in the lift coefficient of the model is illustrated in Fig. 9. The figure also includes interference-free data from the Langley experiments (Ref. 9).

Vertical velocities for another flow condition (Mach 0.6, $\alpha = 2°$) are illustrated in Fig. 10. The top half of the figure compares the passive wall upwash with (1) the free-air upwash predicted by the outer flow solution and (2) the upwash determined by numerical simulation of the wing in unconfined flow. The bottom half of the figure shows the effects of three cycles of wall adjustments. Differences between the measured upwash, the outer-flow solution, and the unconfined-flow solution were substantially smaller after the walls were adjusted.

It is evident in Figs. 8-10 that wall interference was not eliminated after the last cycle of wall adjustments. One reason was that the outer-flow solver underpredicted the velocity changes required to match free-air conditions. Another factor was that the required velocity changes at the field surface could not be accurately produced. This was due to the complex flow through the slotted walls and to the over-simplified influence coefficient method used to represent it. Also contributing to the residual errors was the inability to control the velocity distribution on the vertical face of the field surface outboard of the wing tip. Interference errors on this face, however, were small compared with the initial errors on the other faces. Finally, the maximum available suction in several plenum compartments was not sufficient to produce the required pressure changes. Further details of the three-dimensional experiment will be published in the near future.

2- BY 2-FOOT ADAPTIVE-WALL TEST SECTION

An adaptive-wall test section for the 2- by 2-Foot Transonic Wind Tunnel is under construction. This test section is designed to demonstrate the practical application of adaptive-wall technology to two-dimensional transonic testing. The design of the test section (Fig. 11) is similar to that of the test section used in the small-scale experiments; however, it includes several important improvements. Flow through the slotted walls will be controlled by 64 slide valves, each driven by a stepping motor and controlled by a small computer. Ultimately, wall adjustments will be made automatically without intervention by the tunnel operator. As in the small-scale experiment, laser velocimetry will be used to measure vertical velocities in the test section. A very fast, computer-controlled traverse system is being developed which will substantially reduce LV data acquisition times. A nonlinear outer-flow solver is being developed to estimate free-air conditions when there are supersonic zones in the outer region. The solution will be computed by a minicomputer coupled to an array processor.

NUMERICAL SIMULATION

The operation of three-dimensional adaptive-wall wind tunnels was simulated numerically, using both a linear-panel flow code (Ref. 10) and a transonic potential-flow code (FLO29) (Ref. 11). The primary objective of the numerical simulations was to demonstrate convergence of the adaptive-wall procedures to free-air conditions or to demonstrate alternative methods for establishing interference-free conditions in the test section or both. An additional objective was to study the placement of plenum compartments and to establish the number of compartments required to eliminate wall interference.

One of the configurations modeled using the linear code was the semispan wing in the 25- by 13-cm adaptive-wall test section (Fig. 12). The floor and ceiling panels near the wing corresponded to the locations of plenum compartments. Far upstream and downstream of the wing, the floor and ceiling were solid. The inboard sidewall, being a plane of symmetry, was assumed to be solid. Simulations were performed assuming both a solid and an adjustable outboard sidewall. Adjustments to the outboard sidewall were simulated by imposing normal (cross-flow) boundary conditions at the wall panels near the wing.

Conditions for the numerical simulations were Mach 0.60 and $\alpha = 2°$. The simulations began with solid-wall boundary conditions. Figure 13a compares the solid-wall upwash along one line at the field surface with the free-air velocities predicted by the outer-flow solver and with the true free-air upwash. The outer-flow solution under-estimated the velocity changes needed to match free-air conditions; however, the directions of the changes were correct.

The effects of one cycle of wall adjustments are illustrated in Fig. 13b. Boundary conditions at the walls, including the outboard sidewall, were adjusted so that velocities at the field surface approximately matched the outer-flow solution. These adjustments reduced the differences between the actual (adapted wall) and free-air upwashes and decreased the lift coefficient to a value closer to the free-air value. A new outer-flow solution called for additional velocity changes which would have further improved the agreement with the free-air data. Without systematic overcorrection of the walls, however, the rate of reduction of wall interference would be quite slow. Additional cycles of the adaptive-wall procedures were not attempted.

The numerical flow simulation studies were also used to demonstrate that if the actual free-air vertical velocity distributions at the field surface were known in advance, then the boundary conditions at the panels of the floor and ceiling of the wind tunnel could be adjusted so that velocities at the field surface would match the free-air velocities. Free-air velocities, rather than being successively approximated by the outer-flow solver, were calculated directly using the linear code. At the floor and ceiling panels, boundary conditions were adjusted so that velocities at field-surface control points matched the free-air velocity distributions at the field surface. The agreement between the free-air and adapted-wall velocity data is quite good. The adapted-wall lift coefficient also agrees well with the free-air value.

The numerical simulations demonstrated that for a wing-on-wall configuration, free-air conditions can be approximated by adjusting only floor and ceiling panels and not the sidewalls. These results provided the basis for the arrangement of plenum compartments in the 25- by 13-cm wind tunnel. The same result was obtained for a different wing-on-wall configuration simulated using the FL029 code.

The numerical simulations also demonstrated the advantage of directly computing free-air conditions. Wall adjustments can be made in one step, instead of many steps, as required if the iterative adaptive-wall procedure is used. The direct method may be applicable to configurations where the model and flow near the model are amenable to numerical simulation. However, for complex models or flows, numerical simulation may not be possible. These complex flows are of paramount interest precisely because they cannot be modeled numerically. Details of the numerical studies will be published in the near future.

CONCLUDING REMARKS

A program of combined numerical and wind-tunnel experiments has shown that two- and three-dimensional unconfined flows can be simulated in adaptive-wall test sections. At the same time, a number of issues have been identified that will be the subjects of future research.

The small-scale two-dimensional experiments showed that a slotted-wall wind tunnel with a subdivided plenum can be used to produce interference-free flow in those cases in which the supersonic bubble is not too large. Where stronger shock waves with extensive regions of supercritical flow exist, the basic technique must be augmented with a nonlinear outer-flow solver. This capability will be included in the new 2- by 2-Foot Adaptive Wall Wind Tunnel now under construction. The small-scale three-dimensional experiments were compromised because velocity changes required to eliminate wall interference could not be accurately produced. Further small experiments are planned to examine plenum pumping requirements and the relation between plenum pressures and test-section velocities.

Numerical simulation of the wing-on-wall experiment showed that one cycle of the adaptive-wall procedure reduced wall interference. Although convergence of the procedure to free-air conditions was not demonstrated, the rate of reduction of wall interference appeared to be slow. Convergence will be investigated in the future. An alternative procedure, involving direct computation of free-air flow past the model, was successfully demonstrated. This is reminiscent of the approach used in the British wartime experiments. The direct approach may now be practical for simple configurations (for example, attached flow past an airfoil) because of progress in computational aerodynamics. For more complex flow problems, the direct approach could provide a good first approximation of wall adjustments needed to produce free-air flow. The adaptive-wall procedure could then be applied to eliminate residual interference.

REFERENCES

1. Preston, J.; and Sweeting, N.: The Experimental Determination of the Interference on a Large Chord Symmetrical Joukowski Aerofoil Spanning a Closed Tunnel, Aeronautical Research Committee, R&M No. 1997, Dec. 1942.

2. Preston, J.; Sweeting, N.; and Cox, D.: The Experimental Determination of the Two-Dimensional Interference on a Large Chord Piercy 12/40 Aerofoil in a Closed Tunnel Fitted with a Flexible Roof and Floor, Aeronautical Research Committee, R&M No. 2007, Sept. 1944.

3. Lock, C.; and Beavan, J.: Tunnel Interference at Compressible Speeds Using Flexible Walls of a Rectangular High Speed Tunnel, Aeronautical Research Committee, R&M No. 2005, 1944.

4. Ferri, A.; and Baronti, P.: A Method for Transonic Wind Tunnel Corrections, AIAA J., vol. 11, Jan. 1973, pp. 63-66.

5. Sears, W. R.: Self-Correcting Wind Tunnels, Calspan Report No. RK-5070-A-2, July 1973; also Aeronaut. J., vol. 78, Feb.-Mar. 1974, pp. 80-89.

6. Davis, S.: A Compatibility Assessment Method for Adaptive-Wall Wind Tunnels, AIAA J., vol. 19, Sept. 1981, pp. 1169-1173.

7. Vidal, R. K.; Catlin, P. A.; and Chudyk, D. W.: Two-Dimensional Subsonic Experiments with a NACA 0012 Airfoil, Calspan Report RK-5070-A-3, Dec. 1973.

8. Satyanarayana, B; Schairer, E.; and Davis, S.: Adaptive-Wall Wind Tunnel Development for Transonic Testing, J. Aircraft, vol. 18, no. 4, Apr. 1981.

9 Sleeman, W.; Klevatt, P.; and Linsley, E.: Comparison of Transonic Characteristics of Lifting Wings from Experiments in a Small Slotted Tunnel and the Langley High-Speed 7- by 10-Foot Tunnel, NACA RM L51F14, Nov., 1951.

10. Hess, J. L.: Calculation of Potential Flows about Arbitrary Three-Dimensional Lifting Bodies, Douglas Aircraft Co., Inc., Report MDC-J5679-01, Oct. 1972.

11. Mercer, J.; Geller, E.; Johnson, M.; and Jameson, A.: A Computer Code to Model Swept Wings in an Adaptive Wall Transonic Wind Tunnel, AIAA Paper 80-0156, Pasadena, Calif., Jan. 14-16, 1980.

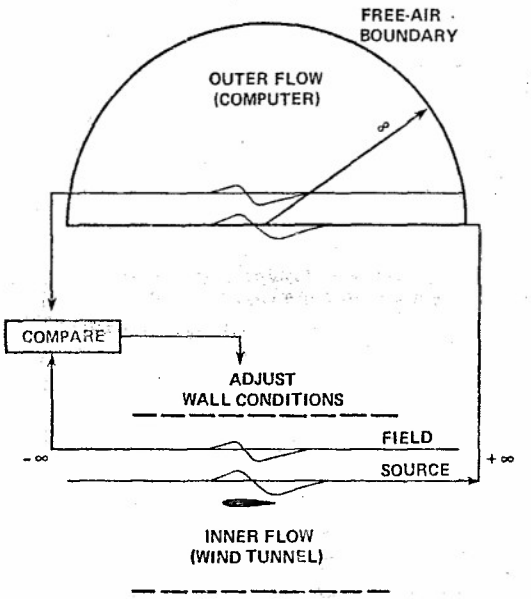


Fig. 1. Adaptive-Wall Procedure

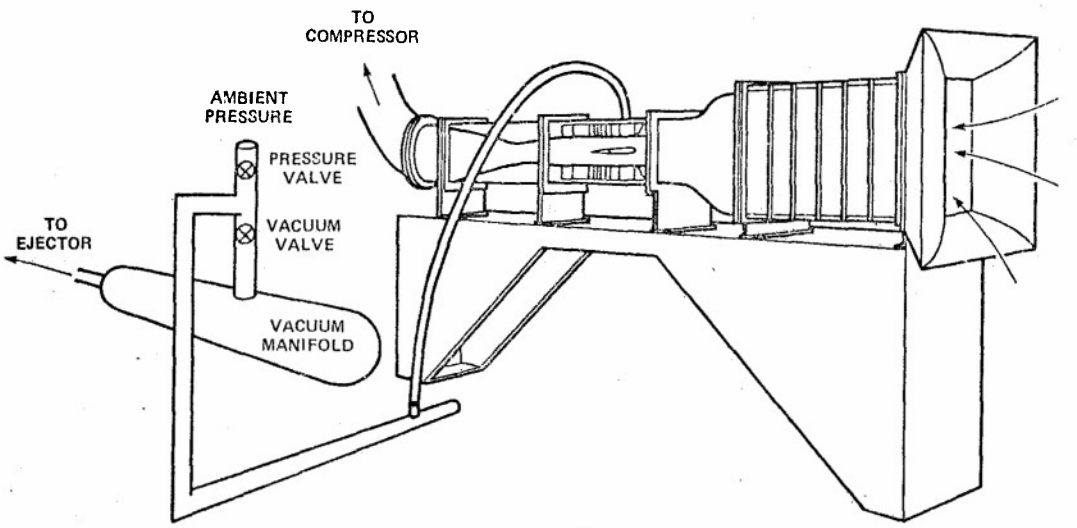


Fig. 2. 25- by 13-cm Adaptive-Wall Wind Tunnel

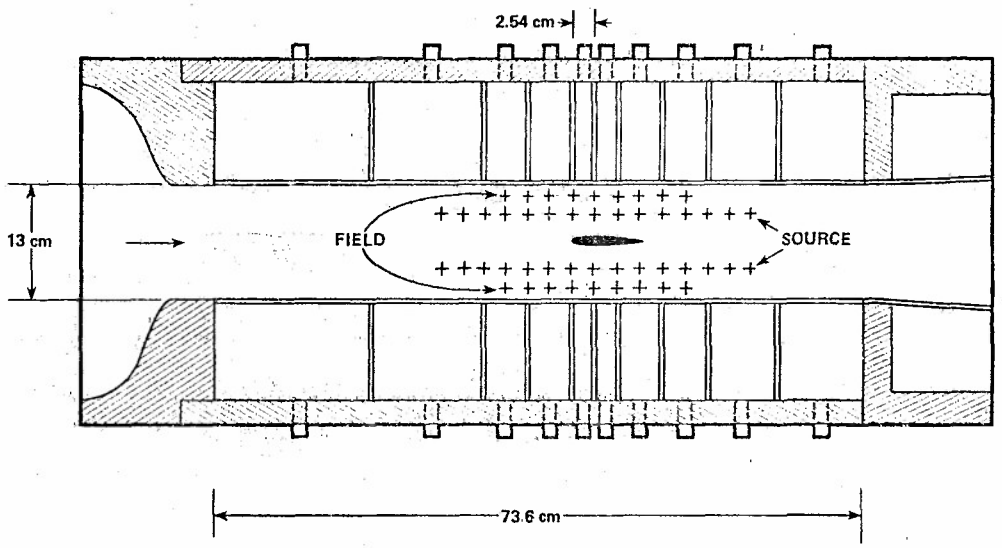


Fig. 3. Two-Dimensional Adaptive-Wall Test Section

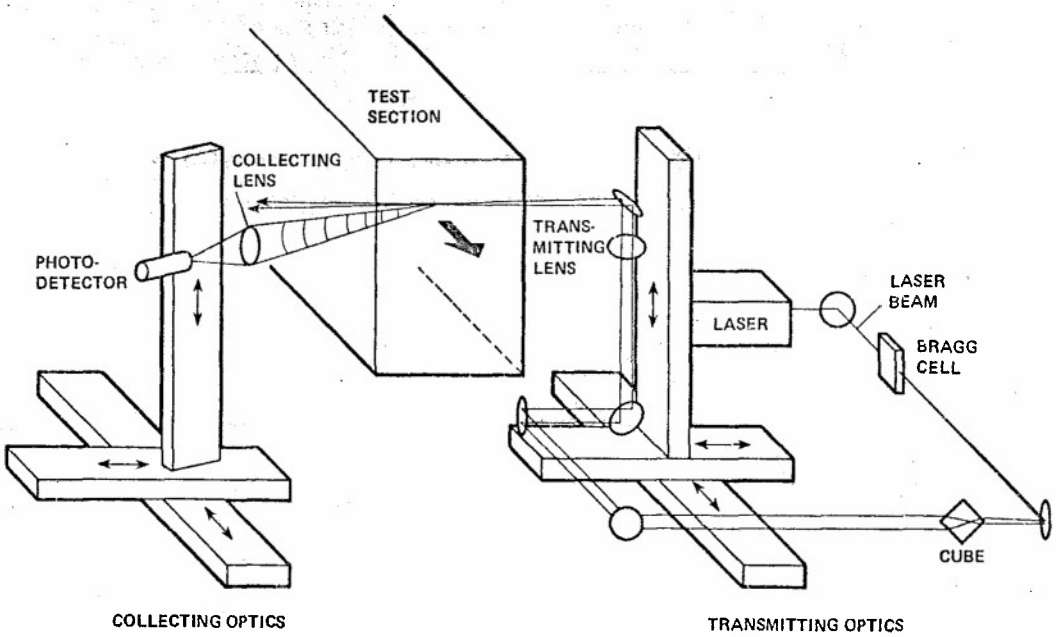


Fig. 4. Laser Velocimeter

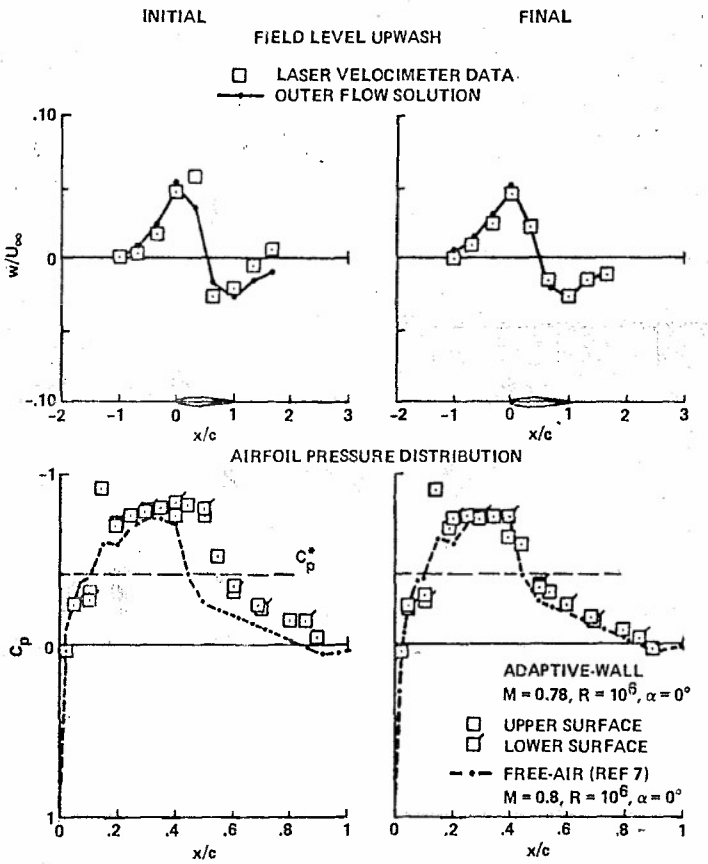


Fig. 5. Two-Dimensional Adaptive-Wall Data

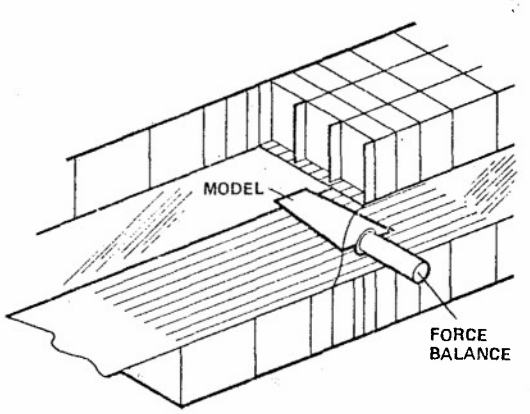


Fig. 6. Three-Dimensional Adaptive-Wall Test Section

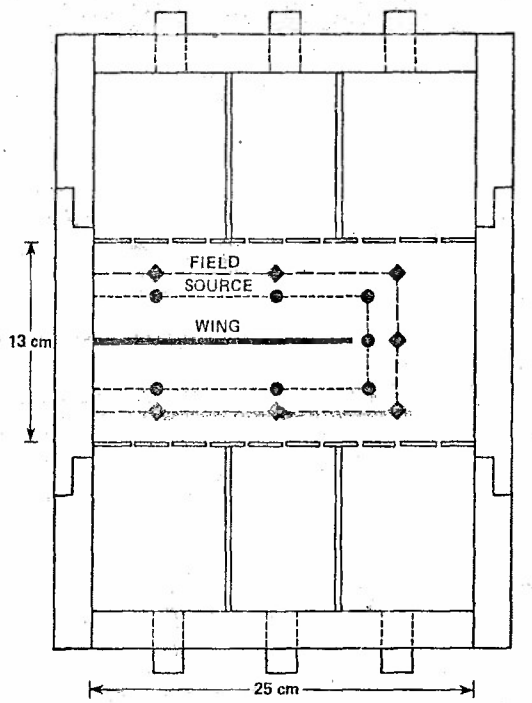


Fig. 7. Laser Velocimeter Measurement Locations

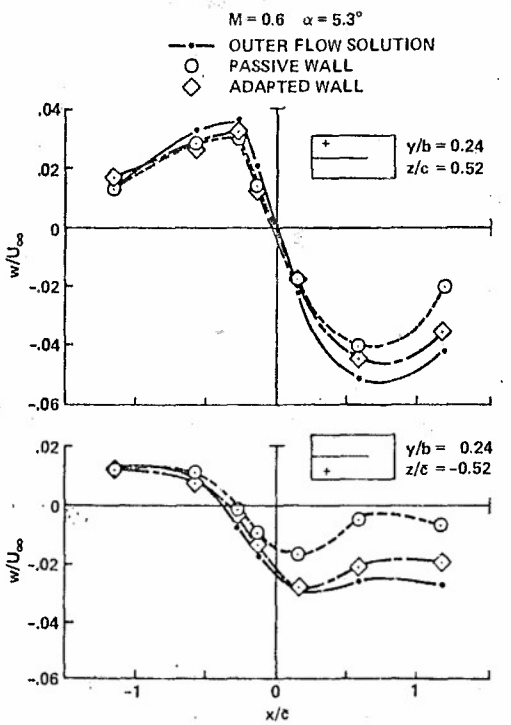


Fig. 8. Effect of Adaptive-Wall Procedure on Upwash Distribution

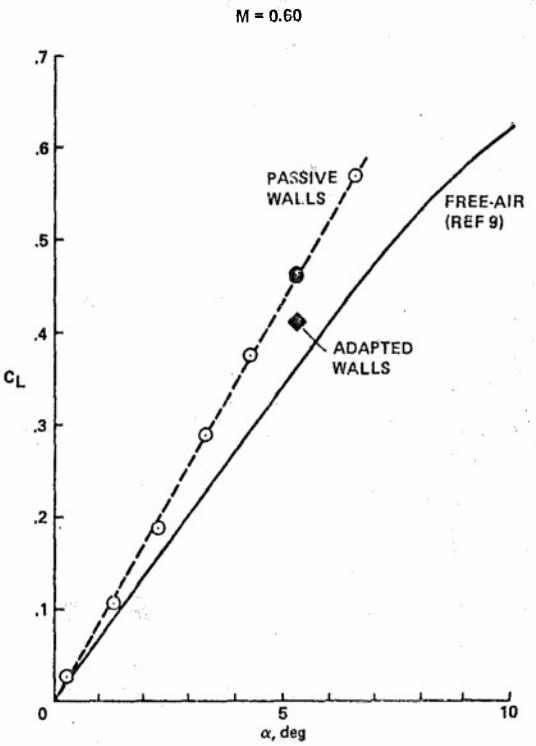


Fig. 9. Effect of Adaptive-Wall Procedure on Lift Coefficient

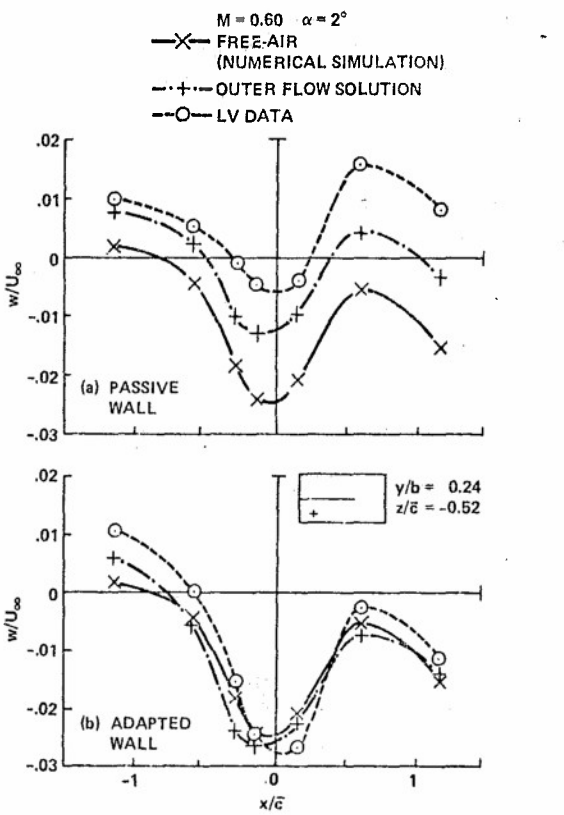


Fig. 10. Comparison of Measured Upwash with Outer Flow Solution and Numerical Simulation

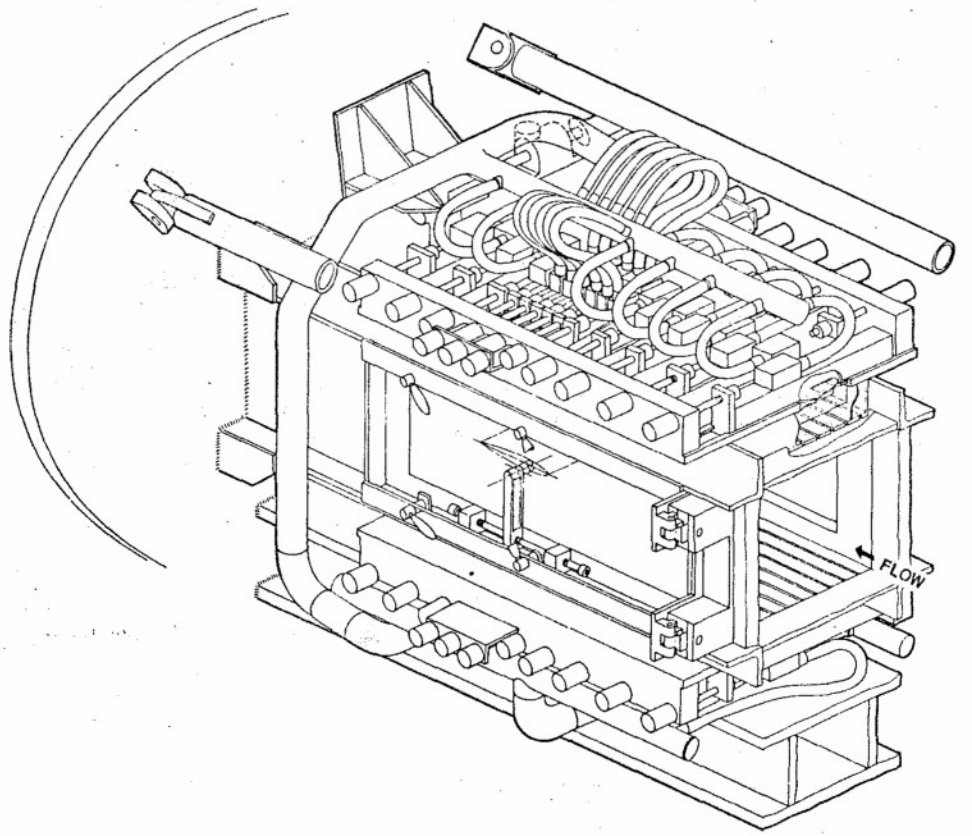


Fig. 11. Two-by-Two Foot Transonic Wind Tunnel Adaptive-Wall Test Section

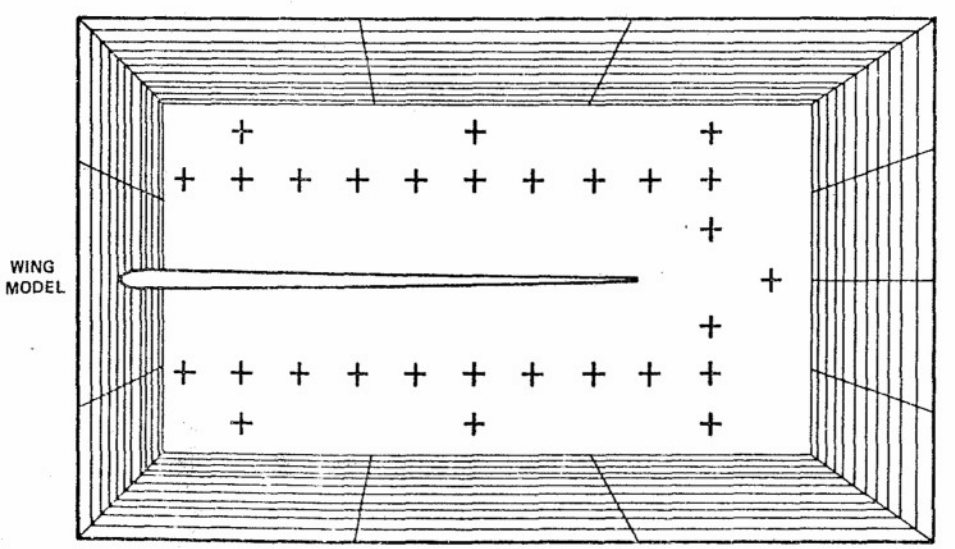


Fig. 12. Numerical Simulation of 25- by 13-cm Adaptive-Wall Wind Tunnel

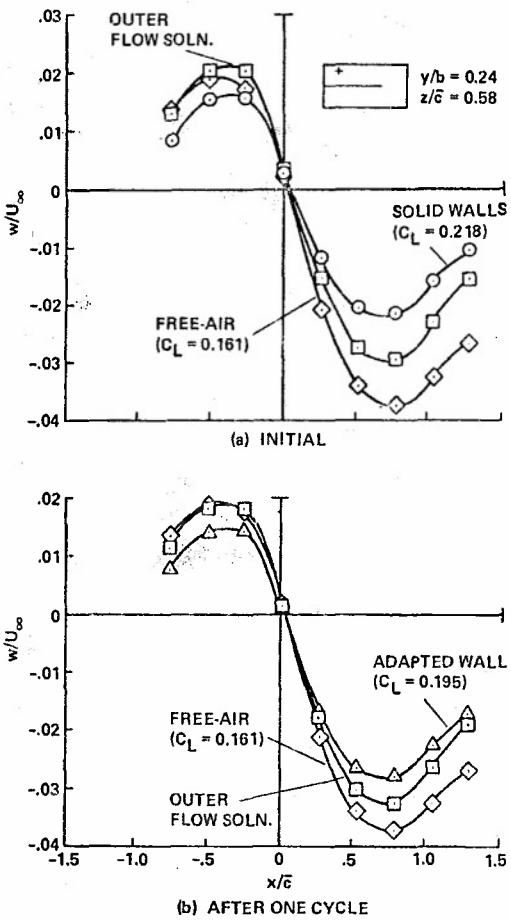


Fig. 13. Numerical Simulation: Effect of one Cycle of Adaptive-Wall Procedures

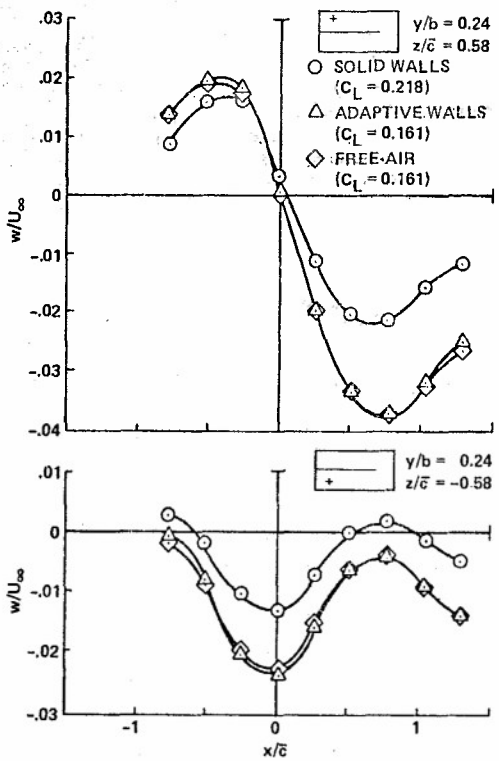


Fig. 14. Numerical Simulation: Effect of Adjusting Top and Bottom Wall Boundary Conditions to Match Free-Air Upwash

DEVELOPMENT OF A THREE-DIMENSIONAL ADAPTIVE WALL TEST SECTION WITH PERFORATED WALLS*

R. L. Parker, Jr. and J. C. Erickson, Jr.
Calspan Field Services, Inc., AEDC Division
Arnold Air Force Station, Tennessee 37389

SUMMARY

A brief description of two-dimensional, porous adaptive wall development at the Calspan Advanced Technology Center and the Arnold Engineering Development Center (AEDC) is given. Three-dimensional exploratory experiments at AEDC employing adaptive techniques to adjust variable porosity walls individually to minimize the interference on a generalized transonic model are summarized. Recent work at AEDC has concentrated on the embodiment of the adaptive wall concept for three-dimensional applications. A fully automated, computer controlled, closed loop three-dimensional adaptive wall system has been designed, fabricated and assembled in the AEDC Aerodynamic Wind Tunnel (1T). Development of the subsystems has included the interface measurement instrumentation, the exterior-flow computation method, the actively controllable wall configuration, microprocessor-controlled hardware for the walls and instrumentation and the overall minicomputer based adaptive wall control algorithm. Specifically, a two-velocity-component static pipe system has been selected for the interface measurement system. Transonic small disturbance theory is being used to compute the exterior flow region and a segmented, variable porosity configuration has been selected for the test section walls. Experiments with the three-dimensional test section are scheduled to begin in May 1982.

NOMENCLATURE

C_p	Pressure coefficient, $(p - p_\infty)/q_\infty$
c	Two-dimensional airfoil chord length
g	Error function at constraint point along the interface, $C_{p_M} - C_{p_D}$
L	Length of porous wall
ℓ	Length of porous wall segment
M	Local Mach number
p	Local static pressure
q	Local dynamic pressure
R	Radius of interface
V_n	Velocity component normal to the interface
x,r,θ	Cylindrical coordinate system
x,y,z	Rectangular coordinate system
α	Model angle of incidence
γ	Specific heat ratio
ϕ	Disturbance velocity potential
ψ	Optimization code merit function

SUBSCRIPTS

D	Desired quantity, as determined from exterior-flow computation
M	Measured quantity
x,r,θ	Differentiation with respect to x,r,θ, respectively
∞	Free-stream conditions

I. INTRODUCTION

Adaptive wall technology offers the promise of achieving high quality wind tunnel data in the transonic flow regime. The reduction of interference in an adaptive-wall wind tunnel is achieved by controlling the flow field in the vicinity of the tunnel walls. Measurement is made of two components of the disturbance velocity at discrete points along control surfaces, or interfaces, in the flow field within the tunnel. A theoretical representation for the flow field external to the control surfaces, including the boundary condition for unconfined flow, i.e., that all disturbances vanish at infinity, is used to determine if those measured velocity components satisfy functional relationships which are consistent with interference-free flow. If they do not, an iteration procedure provides a new approximation for the flow field at the interfaces, and the flow control in the vicinity of the walls is readjusted successively until the measured quantities are consistent with the boundary condition for unconfined flow. In this way, theory and experiment are combined to minimize wall interference.

Development of adaptive wall test sections has been underway both in the United States and in Europe for about ten years. The development programs have differed in the type of boundary control mechanism used for the test section walls. European researchers have concentrated on the flexible impermeable wall concept, whereas efforts in the United States have dealt predominantly with ventilated walls, both slotted and perforated. In addition to the distinction in the respective boundary control mechanisms, ventilated

---

*The research reported herein was performed by the Arnold Engineering Development Center (AEDC), Air Force Systems Command (AFSC). Work and analysis for this research were done by personnel of Calspan Field Services, Inc., AEDC Division, operating contractor for aerospace flight dynamics testing at AEDC. Further reproduction is authorized to satisfy needs of the U. S. Government.

tunnels have measurement requirements that differ significantly from those for tunnels with impermeable walls. This paper describes specifically the development of adaptive wall systems with perforated walls.

Transonic adaptive wall development using porous test section walls has been conducted at the Calspan Advanced Technology Center (ATC) and at Arnold Engineering Development Center (AEDC). The development work began at Calspan ATC with a two-dimensional test section with perforated walls and segmented plenum chambers and is summarized in Section II.A. Two-dimensional development was also conducted at AEDC using locally variable porosity walls and globally variable porosity walls both with and without limited segmented plenum chamber control. These experiments are described in Section II.B.

Adaptive wall experiments also were conducted for three-dimensional flow at AEDC in the AEDC Aerodynamic Wind Tunnel (4T). In these exploratory experiments, discussed in Section II.C, adaptive wall techniques were employed to adjust the uniformly variable porosity walls individually to minimize the interference on a generalized transonic model.

The adaptive wall development at Calspan ATC and AEDC served to verify the validity of the concept and provided a foundation for extending development to three-dimensional flow fields. Since the ultimate adaptive wall application at AEDC is in three-dimensional test sections, the effort has been concentrated in this area over the past two years. The major portion of this paper, Section III, concentrates on this effort.

Each of the individual components and systems of a fully automated three-dimensional adaptive wall test section for the AEDC Aerodynamic Wind Tunnel (1T) is described in Section III. These include the wind tunnel model and its interference-free tests in Tunnel 4T, the exterior flow calculation procedure, and the hardware and software of the automated control system. Those systems which required the greatest attention, based upon prior experience with porous adaptive wall test sections, were the interface instrumentation, the actively controllable wall configuration, and an automated procedure for adjusting the walls. The background investigations that led to specific choices for these key systems are summarized. The test section has been assembled in Tunnel 1T and experiments will commence in May 1982.

II. EARLY PERFORATED WALL TEST SECTION DEVELOPMENT

A. CALSPAN (ATC) 2-D DEVELOPMENT

Development of adaptive porous wall test sections was started at the Calspan ATC in 1971, Refs. 1 through 5. A two-dimensional test section was implemented in the 0.305-Meter (1-Foot) Tunnel, a closed-circuit, continuous-flow facility that operates at Mach numbers from about 0.5 to 0.95 at a unit Reynolds number of 6.56×10^6 per meter (2.0×10^6 per foot). The adaptive wall test section (Refs. 1 and 2) is 0.305m (12 inches) high, 0.254m (10 inches) wide and is adjustable over a 1.422m (56 inches) length. The top and bottom walls are perforated with normal holes with a 22.5 percent open-area ratio. The plenum chambers behind the perforated walls have been divided into eighteen (18) segments, ten (10) on the top and eight (8) on the bottom, and each is connected to a pressure and a suction source through individual control valves. The pressure source is the tunnel stilling chamber, and the suction source is an auxiliary compressor discharging into the tunnel circuit in the diffuser. Six plenum chambers in the immediate vicinity of the model have provisions for varying the porosity linearly in the streamwise direction although this capability was not used in the development experiments.

Two models were employed during the experiments at Calspan ATC. Each was a two-dimensional wing model with an NACA-0012 airfoil section. One model has a 0.152m (6-inch) chord and the other has a 0.102m (4-inch) chord. The models represent a 6 percent and 4 percent blockage respectively in the 0.305m (1-foot) tunnel. The 0.152m (6-inch) chord model has force instrumentation, and both models have pressure instrumentation. The 0.152m (6-inch) chord model was tested (Refs. 1 and 3) in the Calspan ATC 2.439M (8-Foot) Transonic Wind Tunnel for reference data.

The static pressure and the normal flow angle were measured at the interface surface. The distribution of static pressure along the interface was obtained with a static pipe. The flow angle was obtained by a number of wall-mounted flow angularity probes in the early experiments and by two-velocity-component static pipes in the latter experiments. The two-velocity-component static pipe is described in Section III.C and in Refs. 6 and 7. The static pressure and flow angle were converted to the perturbation velocities parallel and normal to the interface respectively for use in the exterior region computation code. Transonic, small disturbance theory was employed to compute the exterior flow region with the distribution of the normal velocity component as the boundary condition at the interface.

Adaptive wall experiments in the Calspan ATC test section were performed with iterative manual control, and in general successful results were obtained. Iterations that had essentially converged were found, initially at Mach numbers up to 0.725 and model incidence up to 2 degrees with the 6-percent blockage model (Refs. 1 and 2), and later with supercritical flow at the walls for a free-stream Mach number of 0.9 and up to 4 degrees angle of incidence with the 4-percent blockage model (Ref. 8).

B. AEDC 2-D DEVELOPMENT

Two-dimensional adaptive wall development occurred at the AEDC during the period from 1976 to 1979 (Refs. 9 and 10). The experiments were conducted in the Aerodynamic Wind Tunnel (1T) which is a continuous-flow, nonreturn wind tunnel equipped with a two-dimensional, flexible nozzle and an auxiliary plenum evacuation system. Tunnel 1T has a test section which is 0.305m (1-foot) square in cross section and 0.953m (3.125 feet) long and has removable walls. For the two-dimensional experiments, the test section sidewalls were solid. The tunnel is operated at a total pressure of approximately 1.365×10^5 Pa (2850 psf).

Several wall configurations were investigated during these 2-D experiments. Experiments were conducted with a uniformly variable porosity wall similar to the design of the AEDC Aerodynamic Wind Tunnel (4T) walls. Another wall configuration had the capability of locally varying the angle of perforations. Holes were drilled in spheres that were sandwiched between two matched drilled plates. The hole angle could be varied 360 deg by means of rotating rods to which the spheres were attached. Finally, a wall configuration was investigated that coupled the uniformly variable porosity wall with two localized subplena on each of the top and bottom walls to provide local control over the velocity through the wall.

All of the AEDC 2-D adaptive wall experiments employed a two-dimensional model with an NACA-0012 airfoil section. The model has a 0.152m (6-inch) chord and represented a 6 percent solid blockage in the 0.305m (1-foot) square test section. The model was mounted to the solid sidewalls on the test section vertical centerline.

Static pressure and flow angle were measured at the interface in the AEDC experiments similar to those at Calspan ATC. The static pressure distribution was obtained with a static pipe. The flow angle was obtained with individual miniature aerodynamic probes mounted from the wall in the early experiments and, in the latter experiments, with aerodynamic probes that were traversed longitudinally along the upper and lower interface surfaces.

The flow angle and pressure were converted to the perturbation velocities normal and parallel to the interface for use in the exterior region computational program. The exterior flow region was computed by using transonic small disturbance theory with the normal velocity as a boundary condition.

Adaptive wall experiments with manual iteration were conducted for cases of free-stream Mach number through 0.8 and 4 degrees model incidence and a free-stream Mach number of 0.9 and 0 degrees incidence with the 6-percent blockage model. Essentially converged solutions were obtained in these experiments.

C. 3-D EXPLORATORY EXPERIMENTS

The early 2-D experiments at AEDC with global wall control, or uniformly variable porosity walls, demonstrated that significant improvement toward unconfined flow in the test section with large blockage models could be achieved. Specifically, it was observed that a dominant criterion for setting the walls to reduce wall interference on the model was to match the measured minimum pressure at the interface with that as computed for unconfined flow. Variable porosity walls, similar to those of the AEDC Tunnel 4T, in conjunction with plenum pressure control were effective for adjusting the pressure at the interface in a global sense. Therefore, preliminary 3-D experiments were conducted in Tunnel 4T to evaluate the effectiveness of the globally variable porosity capability for 3-D adaptive wall control and to identify problem areas for 3-D development. The results of these experiments are reported in Ref. 11.

Tunnel 4T is a closed-loop, continuous flow, variable density tunnel with a test section that is 1.219m (4-foot) square in cross section and 3.810m (12.5 foot) long. The 60-degree inclined hole variable porosity walls can be individually adjusted from 0 to 10-percent open area.

The model employed for these experiments was a swept wing/tail and body configuration that represented a 1.33-percent solid blockage in Tunnel 4T. The ratio of the wing span to the tunnel width was 0.72, and the wing chord-to-tunnel half-height ratio was 0.393. The model has NACA-0012 lifting surfaces swept at an angle of 30 degrees and an internal 6-component balance as well as extensive pressure instrumentation.

The interface flow angle and pressure distribution were measured with a 40-degree included angle, conical head flow angularity probe. The probe was traversed along the interface by means of the Tunnel 4T captive trajectory system (CTS) which is normally used for store separation testing.

The exterior flow region was calculated from the transonic small disturbance equation wherein the flow angle along the interface was employed as the near field boundary condition for the exterior region calculations. The numerical method that was used for solving the exterior flow region for the exploratory 3-D experiments is essentially the same as that described in Section III.D.

Adaptive wall experiments were conducted at Mach numbers 0.7, 0.9, and 0.95 and a model incidence of 4 degrees. Asymmetric wall porosity settings were determined using the adaptive technique and the wall interference on the model wing pressure distribution

and model lift and drag was reduced significantly. However, the interference on the tail pressure distribution and model pitching moment could not be reduced simultaneously. It was concluded, therefore, that a distributed porosity along the wall is required for the three-dimensional test section application. This conclusion motivated the wall development program that is discussed in Section III.E.

III. 3-D DEVELOPMENT

The two-dimensional adaptive wall development programs at Calspan ATC and AEDC served to verify the validity of the concept and demonstrated the viability of perforated walls in an adaptable test section. The three-dimensional exploratory experiments at AEDC showed that the technology was ready to be extended to three-dimensional applications, which is to be the ultimate application of the adaptive wall concept at AEDC. Therefore, in 1980, the technology program at AEDC was directed toward the development of a three-dimensional test section and its associated components. A totally automated, computer controlled demonstration test section was to be developed, assembled and evaluated. The following sections describe the individual component development of this three-dimensional test section.

A. FACILITY

The adaptive wall test section is being installed in the Aerodynamic Wind Tunnel (1T), shown in Figure 1. The standard Tunnel 1T fixed geometry test section has been removed and the new automated 0.305 x 0.305 m (1 x 1 ft) adaptive wall test section inserted, while the Tunnel 1T compressor, stilling chamber, nozzle, and diffuser remain unchanged.

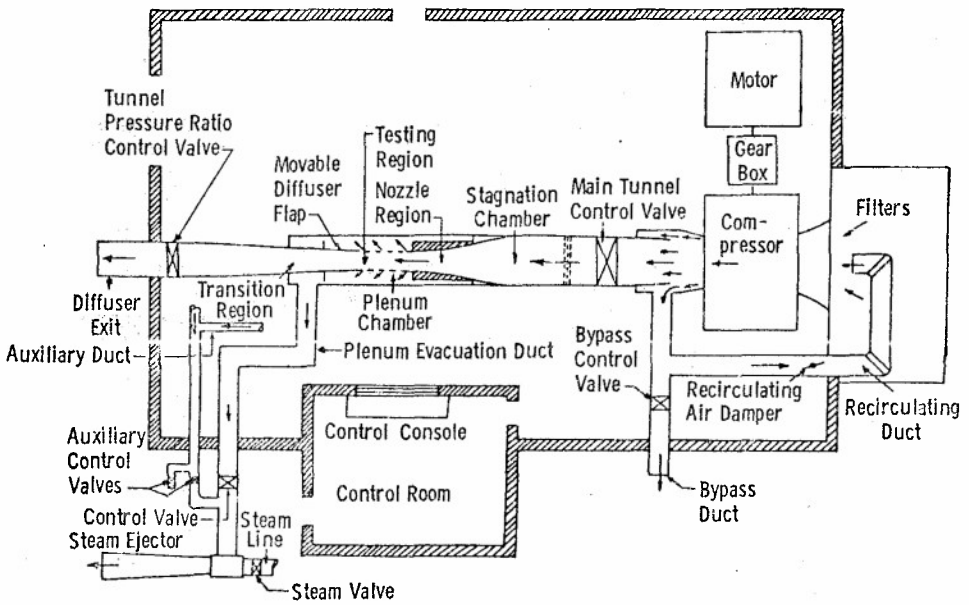


Figure 1. Tunnel 1T

An automated tunnel flow control system maintains the pressure ratio across the test section and the plenum evacuation system by means of motor driven valves controlled by the Mach number control microprocessor. Desired values of the pressure ratio and plenum pressure are determined within the control algorithm (Section IV.G) and communicated to the Mach number control microprocessor.

The model support system is comprised of a sting support boom that is rigidly attached to the sector support. The model is sting mounted to the sting support boom. Model attitude is automatically established and maintained by the automated model attitude positioning system (AMAPS) which continuously accounts for sting deflections due to aerodynamic forces on the model.

B. MODEL

A test model was specially designed and fabricated for the initial 3-D adaptive wall experiments. It was desired to have a model that would generate a flow field similar to a typical transonic flight vehicle. Therefore, a wing/tail/body configuration with swept lifting surfaces was chosen. The lifting surfaces have NACA-0012 airfoil sections with constant chord to facilitate mathematical description for flow field computations. The NACA-0012 profile was also selected because its flow behavior is well documented.

Model size was given much consideration. The wing span of the model is obviously limited by the tunnel width. For the model design, a wing span-to-tunnel width ratio of

0.7 was chosen as representative for adaptive wall applications. With the wing span-to-tunnel width ratio of 0.7 as the limiting factor, solid blockage ratios were computed for models in a square cross section test section considering typical modern flight vehicles. It was revealed that the typical model size to be tested in a 3-D adaptive wall test section would range from solid blockage ratios of 1.5 to 3. A model-to-tunnel solid blockage ratio of 2.5 was chosen for the initial 3-D experiments. The model planform and critical dimensions are given in Figure 2.

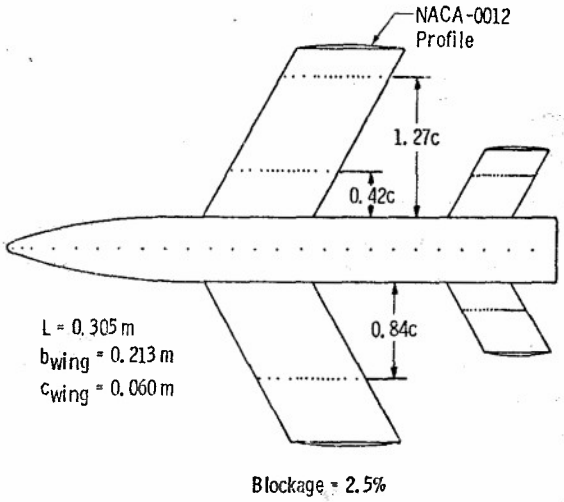


Figure 2. Three-Dimensional Experimental Model

The model has both force and pressure instrumentation. There are 134 pressure orifices on the model. The nose of the model is designed as a hemispherical head, 5-orifice flow angularity meter. There are chordwise rays of pressure orifices on the upper and lower surfaces of the wing at the 40-, 60-, and 85-percent span location. There is a chordwise ray of pressure orifices on the upper and lower surfaces of the tail at the 70-percent span location. There is a ray of pressure orifices along the top centerline of the body. The sting support is integral to the model and is gaged and calibrated to measure normal force, pitching moment and sting deflection.

Reference data for the model were obtained in Tunnel 4T. The data are assumed to be free from interference since the model-to-tunnel solid blockage ratio is 0.156 percent. Data were obtained over the Mach number range from 0.6 to 1.2. The model attitude was varied from -8 to +12 degrees, and data were obtained with the model in both the upright and inverted positions to compensate for tunnel flow angularity. The data were obtained at the nominal operating unit Reynolds number of Tunnel 1T throughout the Mach number range and at additional Reynolds numbers depending on the Mach number. The Mach numbers and Reynolds numbers at which reference data were obtained are shown in Table I.

Table I. Model Reference Data Matrix

Mach Number	Reynolds Number x 10^{-6} (Based on Wing Chord)			
0.6			0.79	
0.65	0.69		0.83	
0.7	0.69		0.87	0.99
0.75	0.69	0.83	0.91	0.99
0.8	0.69	0.83	0.94	
0.9	0.69	0.83	0.99	
0.925	0.69	0.83	1.00	0.95
0.95	0.69	0.83	1.01	
0.975	0.69	0.83	1.01	
1.0			1.02	
1.05			1.03	
1.1			1.04	
1.2			1.04	

Angle of Incidence - 0, 0.5, 1, 1.5, ±2, 2.5, ±3, ±4, 4.5, ±6, 7.5, ±8, 8.5, 10, 12 degrees

Angle of Roll - 0, 180 degrees

C. INTERFACE INSTRUMENTATION

Application of adaptive wall techniques in a ventilated wall test section requires the measurement of two independent flow variables at an interface surface near the test section wall, but outside the wall boundary layer. It has been accepted in adaptive wall investigations to date that the most convenient flow variables to deal with are the perturbation velocities normal and parallel to the interface surface. These variables are obtained through measurement of the flow angle and static pressure, respectively.

Selection of a method of obtaining the measurements of the static pressure and flow angle for the 3-D test section was a considerable task in itself. The method must be capable of making rapid, accurate measurements at a sufficient number of locations to define adequately the distribution of both variables along the 3-D interface. Various techniques were examined for the present application including laser velocimetry, stationary and translating multiple probe arrangements, and two-velocity-component static pipes. Laser velocimetry was eliminated because measurements cannot be made rapidly enough and because of difficulties in providing optical access. Multiple probes were eliminated because of the numbers required, their blockage effects, calibration requirements and the danger of their being misaligned inadvertently. Therefore, a system employing the static pipes was selected.

The normal velocity component can be obtained from the two-velocity-component static pipes as follows. Pressure orifices are located on a circular cross-section pipe diametrically opposed along the direction of the normal to the interface. The static pressure is measured at both orifice locations so that, locally, the average static pressure and the pressure difference across the pipe diameter can be evaluated. In effect, this can be regarded as measuring the local static pressure and its gradient. The streamwise derivative of the normal velocity, dv/dx, midway between the two surfaces can be inferred by assuming irrotationality. The advantage of this measurement technique is that static pressure is relatively easy to measure with good precision and spatial resolution, and many measurements can be made over short time periods. The detailed analysis of this technique is discussed in Refs. 6 and 7.

The interface instrumentation system is comprised of two static pipes. The pipes can be rotated along a circular surface 0.254m (10 inches) in diameter about the centerline of the test section. The pipes are mounted 180-degrees opposed on this surface. Each pipe has two rows of orifices, diametrically opposed, along the entire length of the test section. The pipes are rotated such that the pressure differential is measured and thus the velocity determined in the radial direction. Therefore, a cylindrical interface can be described by this system that is 0.254m (10 inches) in diameter and spans the entire length of the test sections. The interface measurement system is shown in Figure 3. The pipes are supported by circular track drive systems in the stilling chamber and the diffuser. Rotation of the pipes is accomplished through the control system described in Section III.F.

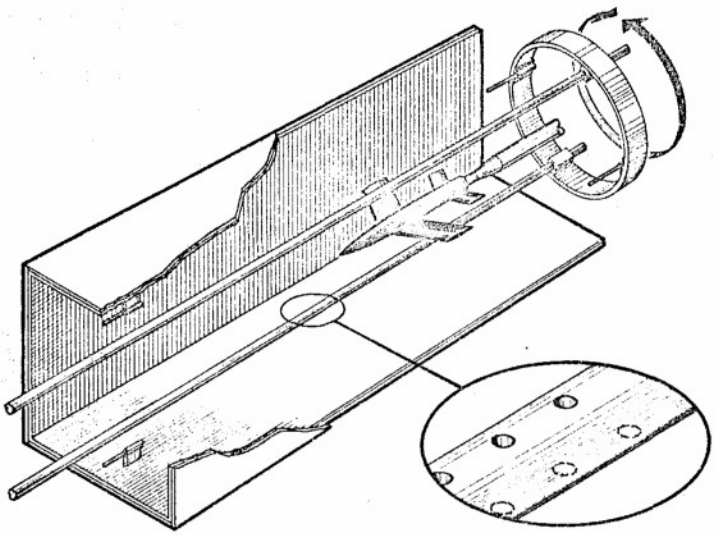


Figure 3. Interface Flow Variable Measurement System

As discussed above, only the derivative of the flow angle in the longitudinal direction can be determined by the two-velocity-component static pipes. The absolute values of the radial velocity at the test section entrance and exit are determined by hemispherical head flow angularity probes. A probe is mounted on each of the top and bottom walls at the test section entrance. These probes serve to verify that the flow enters the test section parallel to the walls. Two probes are mounted on the rotating track system at the test section exit. These probes, which are mounted 90 degrees from the pipes, will rotate with the pipes and will allow for description of the absolute flow angle over the entire downstream circular surface.

The description of the flow angle and pressure distribution along the cylindrical interface will be employed by the exterior flow computational code and the wall control algorithm as described in Sections III.D and III.G, respectively.

D. EXTERIOR-FLOW COMPUTATION

The principal theoretical aspect of the adaptive wall method is the evaluation of the functional relationships that satisfy the conditions for unconfined flow in the region exterior to the interface. This requires the solution of the 3-D flow field exterior to the interface with the distribution of one of the measured flow variables prescribed there as the boundary condition.

Operating experience in the two-dimensional adaptive wall test sections at AEDC and Calspan ATC demonstrated that control of perforated-wall tunnels can be applied most effectively by setting the desired streamwise disturbances, say the distribution of pressure coefficient, C_{P_D}, over the entire interface. That is, the normal velocity component, V_n, is used as the boundary condition in order to obtain, after relaxation, the desired C_{P_D}. Setting C_{P_D} was found to be necessary, especially for flows that are supercritical at the walls. Attempts to set V_n, instead, were invariably unsuccessful (Ref. 6).

The exterior region contains no immersed bodies (and, hence, no boundary layers), and the interface is sufficiently removed from the experimental model so that the disturbances from the model have attenuated. Consequently, inviscid, small-disturbance theory is applicable to the exterior region.

For the AEDC 3-D experiments, the transonic small disturbance equation (TSDE) will be used to compute the exterior flow solution. As described in Section III.C, the control surface will have a circular cross section and, therefore, the TSDE will be applied in divergence-free form, using cylindrical coordinates, as

$$\left[\left(1 - M_\infty^2\right)\phi_x - \frac{\gamma + 1}{2} M_\infty^2 \phi_x^2\right]_x + \frac{1}{r}\left[r\,\phi_r\right]_r + \frac{1}{r}\left[\frac{1}{r}\,\phi_\theta\right]_\theta = 0.$$

A numerical solution to the TSDE is obtained by using the Murman finite difference method in Ref. 12. The difference equations are constructed using central difference operators in the subsonic region, upwind difference operators in the supersonic region, and a special shock operator to preserve the conservative property of the numerical method. A line relaxation algorithm is used to solve the finite difference equations implicitly along radial lines while sweeping in the azimuthal direction and marching in the streamwise direction.

A cross sectional plane of the boundary value problem for the exterior region is shown in Figure 4. The boundary condition along the interface, which is at radius R, is specified as the distribution of the velocity normal to the cylindrical surface. An unconfined flow boundary condition, $\phi = 0$, is specified at a distance equal to 4R. Since the flowfields of the model to be tested are symmetrical laterally, a symmetry boundary condition, $\phi_\theta = 0$, is used at $\theta = 0$ degrees, and 180 degrees. The boundary condition at the upstream and downstream planes is specified as $C_p = 0$.

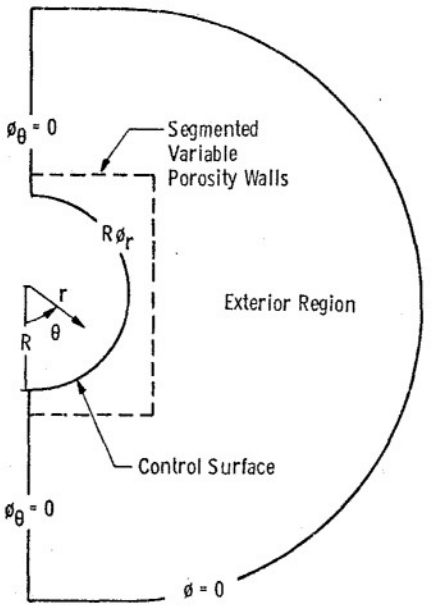


Figure 4. Boundary Value Problem for Exterior Computational Region

E. WALL CONFIGURATION DEVELOPMENT

The philosophy employed throughout the AEDC adaptive wall program was to develop an adaptive wall configuration that could be applied to existing transonic test facilities with minimum modification. This philosophy has directed the wall control development toward ventilated wall configurations with concentration on perforated walls. Considerations for attenuating pressure waves that reach the wall in transonic flows have also dictated ventilated wall configurations. Each of the known methods for controlling the transpiration velocity through ventilated walls was considered in the selection of a configuration for the 3-D test section.

There are two general methods for varying the transpiration velocity through ventilated walls. One method controls the pressure on the plenum side of the wall, thus providing suction or blowing from the plenum. The other method changes the actual crossflow characteristics of the wall itself. Spatial variation of wall control for these methods can be obtained in a number of ways. Plenum pressure control can be achieved by segmenting the plenum chamber, as described in Section II for porous walls at Calspan ATC and AEDC, and as investigated for slotted walls at NASA Ames Research Center (Ref. 13). Changing the actual wall crossflow characteristics can be done in several ways, as shown at AEDC for porous walls. Segmenting the walls to have porosity which can vary from segment to segment is one attractive way of achieving this in three dimensions. The crossflow characteristics of slotted walls can be controlled by inserting baffles in the slots (Ref. 14). Spatial variation of wall control in this case can be gained by varying the baffle angle.

An evaluation program was conducted as to the relative effectiveness of three of these wall configurations. The evaluation was conducted in Tunnel 1T. Prototypes of a variable porosity configuration with segmented porosity control, a slotted configuration with variable angle baffles in the slots and a 5-percent, 60-degree inclined hole porous configuration with segmented plenum chambers were installed, one at a time, as the top test section wall. A solid contoured wall was designed for the bottom test section wall to simulate the flow field over the top surfaces of a 30-degree swept wing/tail combination. The sidewalls were solid. A static pipe was placed 0.0254m (1 inch) below the top wall, the typical location for the control surface in an adaptive wall test section. The pipe could be traversed laterally across the entire test section. The walls were evaluated by systematically varying the individual control elements of each configuration (porosity, plenum suction, or baffle angle) and measuring the effect on the pressure distributions at the static pipe location. The evaluation was conducted through the Mach number range from 0.5 to 1.2 and is summarized qualitatively as follows.

The segmented plenum configuration offered the maximum control throughout the Mach number range, as would be expected. The magnitude of control is limited only by the air-moving machinery associated with the configuration and choking of the flow through the perforations. The variable baffle angle, slotted wall configuration offered slightly more control than the segmented, variable porosity configuration at Mach number 0.7 and below. Above Mach number 0.7, the segmented, variable porosity configuration offered more control than the slotted configuration, and its superiority increased as Mach number increased above 0.7. In fact, at Mach numbers above 0.8, the segmented, variable porosity wall offered nearly as much boundary control as the segmented plenum chamber configuration as tested.

The complexity of implementing the various configurations into an adaptive wall test section was examined. The slotted wall configuration is easily implemented into a test section and it offers the advantage of permitting optical access into the test section. The variable porosity wall is also easily implemented into the test section although it eliminates optical access. The segmented plenum configuration is the most complex to implement because of the associated machinery and plumbing. Considering the effectiveness of control in the upper transonic Mach number regime and the relative complexity of implementation, the segmented, variable porosity configuration was chosen as the best candidate for the 3-D test section walls.

The top and bottom segmented, variable porosity wall configurations for the 3-D test section each have twenty-four individually adjustable segments. The segments are arranged in four lateral rows, each with six streamwise segments (see Figure 5). Each segment is 0.076m (0.25 ft) wide and the lengths of the segments (ℓ/L), beginning upstream, are 0.251, 0.143, 0.143, 0.143, and 0.177, respectively, where L is 0.953m (3.125 feet). The sidewalls each have eight individually adjustable segments. These are arranged in two vertical rows, each with four streamwise segments (see Figure 5). Each sidewall segment is 0.152m (0.5 foot) high and the lengths (ℓ/L) are 0.520, 0.106, 0.106, and 0.269, respectively.

The above arrangement of segments for the variable porosity walls was chosen as follows. Free air solutions were obtained for representative transonic vehicles and, specifically, the flow angle and pressure distributions were investigated in the field at the location where the test section walls would be. The arrangement of the individual segments was selected to fit the general gradient distribution of the flow angle at the wall.

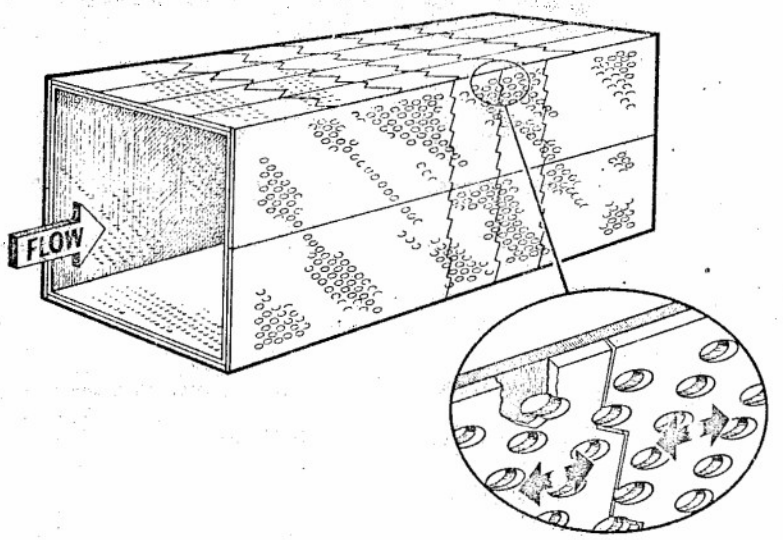


Figure 5. Segmented, Variable Porosity Wall Test Section

F. WALL AND STATIC-PIPE CONTROL HARDWARE

The control system for positioning the wall segments and static pipes is a sixty-five channel microprocessor based system. Commands to the microprocessor for effecting wall or pipe position changes are provided by the host PDP 11/34 minicomputer, which contains the overall adaptive wall control system algorithm to be described in Section III.G.

Stepping motors drive each of the sixty-four wall segments through a rack and pinion mechanism. Linear potentiometers are utilized as the wall segment position sensing devices. The static pipes are rotated by one control channel commanding two stepping motors. One motor is located in the stilling chamber and the other in the diffuser. The position of each end of the static pipes is sensed by rotary potentiometers. As the static pipes are driven, the output of each potentiometer, upstream and downstream, is continuously monitored by the microprocessor to ensure that the ends are tracking evenly. The potentiometers on both the wall segments and the pipes also provide an output proportional to position as affirmation that a commanded movement was successfully accomplished.

The control system, shown in Figure 6, contains, in addition to the microprocessor and stepping motors, 65 power switching units, 8 28v power supplies, 65 processor interfaces, and 65 translator modules. The power switching units transmit power from the

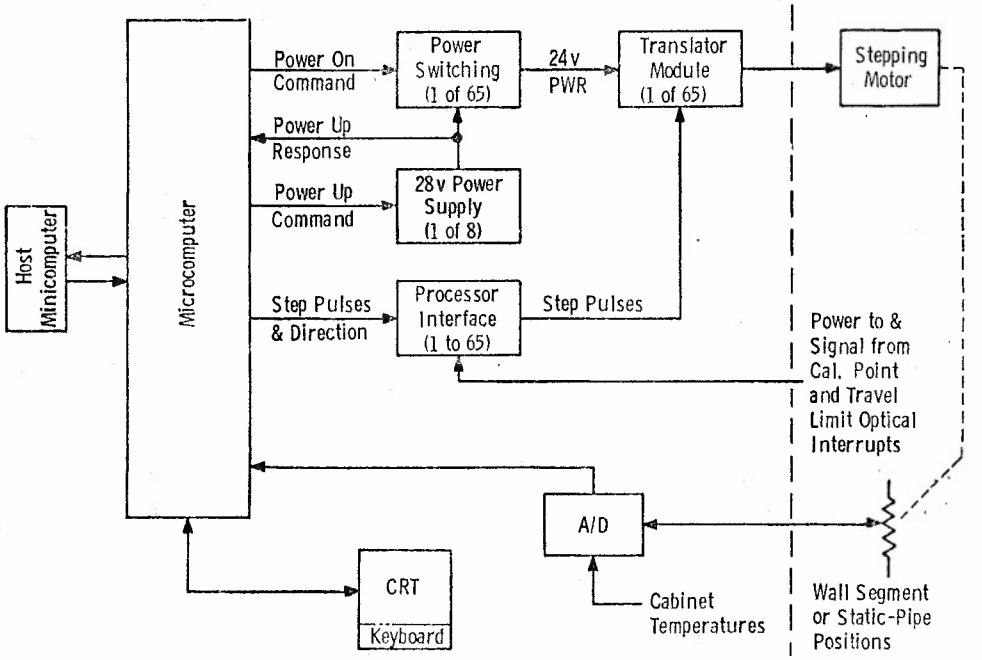


Figure 6. 1T Adaptive Wall Control System Block Diagram

power supplies to selected translator modules. The processor interface elements control the drive pulses to the translator modules. The translator modules convert each step pulse into a 4-phase, 6-step sequence of pulses and provide power for the stepping motors.

This system allows for system energy conservation in that it is designed so that the stepping motors have power applied only when a particular wall segment is moved. The optimal sequence of moving the individual wall segments to effect a particular distribution of porosity is determined by the microprocessor logic software. When a wall segment movement is commanded, the microprocessor checks the operational status of the associated power supply and instructs the power switching unit to supply power to the translator module, which in turn transmits power to the motor and moves the segment.

Each wall segment and static-pipe positioning mechanism is equipped with calibration point and travel limit optical interrupters. The calibration point optical interrupters are used on a daily basis for mechanical system health monitoring. They are used in conjunction with the potentiometers to verify that the readout system and mechanical drive mechanism are functioning properly. The travel limit detectors prohibit collisions between any two adjacent wall segments.

Operator intervention with the microprocessor is possible through a keyboard located in the test unit control room. Output from the microprocessor can be displayed on a CRT and/or a printer also within the test unit control room.

G. ADAPTIVE WALL CONTROL SYSTEM ALGORITHM

The relationship between an adjustment to an individual wall-control variable, e.g., a variable-porosity segment, and the resulting change in C_p on the interface is not confined to the immediate locality of that control. Numerical simulations (Ref. 15) of the actual flow near the boundaries of perforated wall tunnels, as well as extensive experimental experience, have shown this. Indeed, if free-stream conditions are held fixed at the entrance to the test section, the change in the C_p response to a change in an individual control variable occurs not only in the immediate neighborhood of the control, but everywhere downstream of it into the diffuser. Therefore, unlike impermeable, flexible-walled tunnels, the relationship between the adjustment of a wall-control variable and the response of the flow variable that is to be set is not a direct one. This was manifested in the two-dimensional experiments at AEDC and ATC in that excessive trial and error manual adjustments were required of the tunnel operator.

Consequently, an important aspect of the three-dimensional adaptive wall tunnel system has been the necessity to develop an automated technique to set C_{P_D} both accurately and rapidly without a tunnel operator in the loop. The procedure discussed below will accomplish the required wall-control adjustments through total computer control.

The procedure developed is based upon extensive experience that has been gained at AEDC in computer-oriented testing techniques during the last several years. This effort began with tests of the remotely-controllable, variable-camber Self-Optimizing Flexible Technology (SOFT) wing model (Refs. 16 and 17). In this concept, the wing shape can be adapted conformally in a manner to maximize or minimize various merit functions, while simultaneously satisfying specified constraints. A cornerstone of the SOFT wing concept is the use of a constrained optimization code first written by Levinsky, et al. (Ref. 18). This code was subsequently modified at AEDC to accommodate more general wind tunnel testing applications (Ref. 19). It is this constrained optimization code that is being employed for determining the wall segment adjustments required to obtain a best fit of the measured interface pressure distribution compared to the desired C_{P_D}. The code is based upon the gradient projection method originated by Rosen (Refs. 20 and 21), and summarized by others, e.g., Fox (Ref. 22).

In the present application, the optimization code, as modified further for this task, controls the entire adaptive wall iteration process as outlined schematically in Figure 7. The code is implemented on the host PDP 11/34 minicomputer located in the test unit control room and dedicated to these experiments.

Initial conditions for a given test configuration are selected, including the desired tunnel pressure ratio and plenum pressure. These are based on actual measurements of upstream conditions and are communicated to the Mach number control microprocessor by the optimization code. The initial approximations to the wall segment settings are passed to the microprocessor controlling the walls, thus beginning the Baseline Mode. The code also passes static-pipe positioning commands to the microprocessor and calls for measurements of the static-pipe and probe pressures, from which C_{P_M} and V_{n_M} can be evaluated using the static-pipe theory. The model data are also acquired at this time. The V_{n_M} are then used as the boundary conditions for the exterior flow calculation procedure (Section III.D), which is a subprogram of the optimization code. After the iterative relaxation of the calculated and measured C_p distributions, the exterior-flow subprogram returns the desired interface pressure distribution C_{P_D}. The optimization code then continues and evaluates a merit function, ψ, that is defined as an appropriately weighted integration of the rms difference between C_{P_D} and C_{P_M}. Constraints are also defined, if desired, by requiring the equality of C_{P_D} and C_{P_M} at specific points on the interface. The differences between these values are the constraint error functions g.

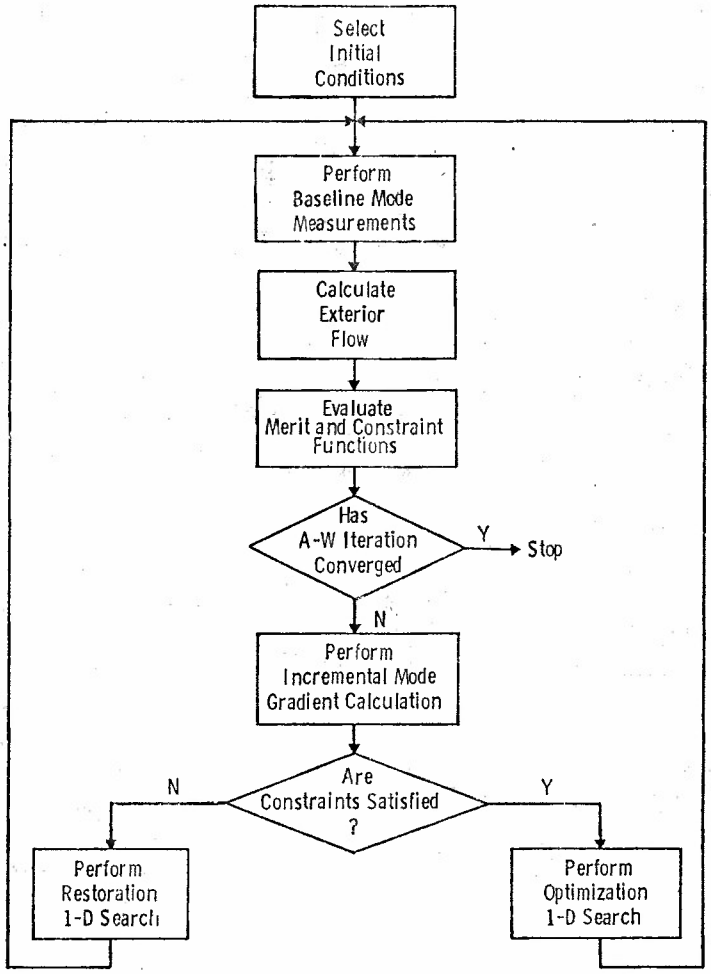


Figure 7. Automated Adaptive Wall Iterative Procedure

At this point the agreement between C_{P_M} and C_{P_D} is assessed by checking if ψ is less than some specified value and if the constraints are satisfied to within some specified tolerance. If they are, the case has converged and the test is complete. If they are not, the tasks continue to make a complete pass through the procedure in Figure 7.

The next step, if convergence has not been achieved, is to perform the Incremental Mode to determine gradients of ψ and the g functions with respect to the wall-control variables. The gradients are found from additional sets of measurements of C_{P_M} at wall settings obtained by perturbing each control variable, in turn, about its Baseline Mode setting. Next, it is checked again whether all the constraints are satisfied to within the tolerance. If any one or more of them is not satisfied, a restoration process ensues to bring the g to within tolerance. This is accomplished by minimizing the sum of the squares of the individual g functions. If all of the constraints are satisfied, a minimization of the Lagrangian function, which is the sum of ψ and the product of the g functions and Lagrange multipliers, follows.

Both the restoration and minimization processes are termed One-Dimensional Searches because they proceed with different step sizes in a single direction. This search direction is defined in terms of specific relationships among the wall-control variables that have been found from appropriate operations on the experimentally-defined gradient information. A One-Dimensional Search is continued for successively increasing step sizes until the restoration function or Lagrangian function has passed through a minimum. The resultant optimum state is considered to provide the best fit to C_{P_D} and is selected as the next Baseline. As shown in Figure 7, the procedure is repeated until C_{P_M} and the newly calculated Baseline C_{P_D} agree.

Numerical simulations of the flow within a two-dimensional segmented-porosity tunnel were carried out and will be discussed briefly here. The process of Figure 7 was not simulated in its entirety, but rather that part of it that provides the best experimental fit to a given C_{P_D} distribution.

The modeling of the aerodynamic effects of the AEDC segmented, variable-porosity wall-control configuration was carried out using generalizations of techniques developed for the segmented-plenum Calspan ATC walls (Ref. 15). In the ATC investigation, empirical characteristics for the transpiration velocity through the walls, as a function of the pressure difference across the walls, were combined with a transpired turbulent boundary-layer integral prediction method to investigate the effect of the wall control on the flow about the model, which was calculated in an inviscid-flow approximation. These simulations demonstrated that at low subsonic speeds, at least, an adaptive wall tunnel with a finite number of plenum chambers for wall control nevertheless can achieve what is, for practical purposes, unconfined flow about the model.

The empirical wall characteristics were retained in the present simulations of the segmented, variable-porosity walls. However, a generalized correlation of the results of representative boundary-layer calculations was used to provide the displacement effect of the growth of the transpired boundary layer. In the initial simulations, the inviscid flow calculations were made with a finite-difference solution technique for the transonic small-disturbance equations.

A configuration with two wall-control variables was selected to examine the basic elements of the unconstrained optimization procedure. The airfoil model is a 6-percent solid blockage nonlifting ($\alpha = 0$) NACA-0012 airfoil at $M_\infty = 0.6$. Plenum pressure and global wall porosity are the two control variables. For each pair of values of the control variables, a complete transonic-flow calculation was made. The results of the unconstrained optimum fit to the calculated unconfined-flow pressure distribution, C_{P_D}, is shown schematically in Figure 8. Even with this relatively crude wall-control configuration, a satisfactory representation of unconfined-flow conditions could be achieved.

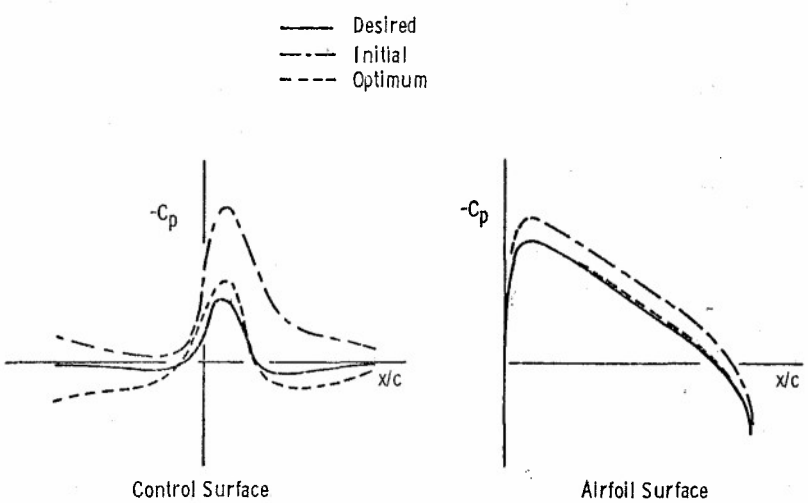


Figure 8. Wall Control Algorithm Results

The complete constrained optimization code could be simulated efficiently only with the use of a further generalization of the ATC simulation model. That is, tunnel-empty theory derived in Ref. 15 for the velocity induction in the test section was used to compute perturbations from a one-time calculation of the flow over the model in free air using the transonic finite-difference code. Use of this generalization enabled rapid, automatic simulations of the entire optimization process.

Results comparable to those of Figure 8 were obtained using the complete code with the more efficient velocity induction calculation model. Then the number of control variables was increased to as many as 20, and up to 18 constraints were added. Nonlifting configurations ($\alpha = 0$) were treated at $M_\infty = 0.6$ and 0.8 as well as a lifting case at $M_\infty = 0.6$ and $\alpha = 4$ degrees.

Among the results of this series of simulations are the following observations. There was more than one local optimum in several cases, depending upon the initial wall-control settings that were chosen. Each of these had a merit function of comparable magnitude, but different in detail, in the fit to C_{P_D}. Such a phenomenon is not unusual in nonlinear optimization problems (Ref. 22) because the existence of a global optimum cannot be proved theoretically. Any of the local optima obtained would have been a satisfactory choice for the new Baseline in Figure 7. It should be emphasized that manual adjustments of the wall control, as described in Section II, for example, generally led to fits to C_{P_D} that incurred errors that were never quantified; i.e., the fit was far from a perfect one.

No clear-cut conclusion could be drawn from the simulations regarding the effectiveness of specifying constraints in addition to minimizing the merit function. For example, if the initial wall settings are such that the flow is far from an optimum fit to C_{P_D}, application of constraints may be the quickest way of achieving a reasonable fit. However,

when closer to an optimum fit, an unconstrained optimization usually obtains a good overall fit more rapidly. A final choice of constraint strategy will be made as the experiments proceed in Tunnel 1T.

IV. CONCLUDING REMARKS

Adaptive wall wind tunnels with two-dimensional test sections have been developed at the Calspan ATC and the AEDC. The Calspan ATC program, which started in 1971, employed a 22.5-percent normal hole porous wall and segmented plenum chambers for active boundary control. The AEDC program, which started in 1976 employed several porous wall configurations which used variable porosity or both variable porosity and limited segmented plenum chambers for active boundary control. An exploratory program for three-dimensional flow was also conducted at the AEDC in which adaptive techniques were employed to adjust the variable porosity walls of Tunnel 4T to minimize the interference on a generalized transonic model. All of these programs demonstrated the basic viability of the adaptive wall concept. They also clarified those aspects of the entire adaptive wall system that required greater attention, particularly interface instrumentation, the actively controllable wall configuration, and an automated procedure for adjusting the walls.

In 1980, the adaptive wall program at AEDC was directed toward the development of a three-dimensional test section. Over the past two years, each of the individual components and systems of a fully automated three-dimensional adaptive wall test section has been developed. These have been designed, fabricated, and installed in the AEDC Aerodynamic Wind Tunnel (1T). A generalized model was designed for the initial three-dimensional experiments. It is a wing/horizontal tail/body configuration and represents 2.5-percent solid blockage in the 0.305 meter (1 foot) square cross section test section. The lifting surfaces have NACA-0012 profiles and are swept at an angle of 30 degrees. The model has force and pressure instrumentation. Reference data, free from wall interference, have been obtained with the model in Tunnel 4T.

Considerable development effort went into the individual components of the system. The system for measuring the interface flow variables (perturbation velocities normal and parallel to the interface surface) consists of a pair of two-velocity-component static pipes. These pipes can be positioned anywhere along the circumference of the circular cross section interface by a rotating pipe positioning system. The exterior flow region is computed from transonic small disturbance theory. An extensive development program took place to select a suitable wall configuration. The walls chosen are segmented, variable porosity 60-degree inclined hole configurations. The top and bottom walls each have twenty-four individually adjustable segments and the sidewalls each have eight.

A sixty-five channel, microprocessor based control system has been developed to adjust automatically the sixty-four wall segments and to position the static pipe system. Test section Mach number and model attitude also are controlled automatically. An overall control algorithm is resident in a host minicomputer system that is responsible for the automated systems control. The control algorithm contains an optimization code based on the gradient projection method that determines the wall segment adjustments required to obtain the best fit of the measured interface pressure distribution compared to that computed from the exterior, unconfined flow region.

Assembly of the test section in Tunnel 1T was completed in April 1982 and the experimental program commenced in May 1982. The experiments have been designed, first, to evaluate the flow generation properties of the test section, second, to verify the communication between the various systems and to integrate the automated controls and, third, to perform adaptive wall experiments with a generalized transonic model present in the test section. The test section will be operating in its fully automated form in October 1982.

REFERENCES

1. Vidal, R. J., Erickson, J. C., Jr., and Catlin, P. A., Calspan Corporation, "Experiments with a Self-Correcting Wind Tunnel," October 1975, AGARD-CP-174; also Calspan Report No. RK-5070-A-4, October 1975.

2. Sears, W. R., Vidal, R. J., Erickson, J. C., Jr., and Ritter, A., Calspan Corporation, "Interference-Free Wind-Tunnel Flows by Adaptive-Wall Technology," 3-8 October 1976, ICAS Paper No. 76-02, 10th Congress of the International Council of the Aeronautical Sciences, Ottawa, Canada; also Journal of Aircraft, Vol. 14, No. 11, November 1977, pp. 1042-1050.

3. Vidal, R. J., Catlin, P. A., and Chudyk, D. W., Calspan Corporation, "Two-Dimensional Subsonic Experiments with an NACA-0012 Airfoil," December 1973, Calspan Report No. RK-5070-A-3.

4. Vidal, R. J. and Erickson, J. C., Jr., Calspan Corporation, "Experiments on Supercritical Flows in a Self-Correcting Wind Tunnel," 19-21 April 1978, AIAA Paper No. 78-788, AIAA 10th Aerodynamic Testing Conference, San Diego, California.

5. Vidal, R. J. and Erickson, J. C., Jr., Calspan Corporation, "Research on Adaptive-Wall Wind Tunnels," November 1978, AEDC-TR-78-36 (AD-A062110).

6. Erickson, J. C., Jr., Wittliff, C. E., and Daughtry, D. C., Calspan Advanced Technology Center, "Further Investigations of Adaptive-Wall Wind Tunnels," October 1980, AEDC-TR-80-34 (AD-A091774).

7. Nenni, J. P., Erickson, J. C., Jr., and Wittliff, C. E., Calspan Advanced Technology Center, "Measurement of Small Normal Velocity Components in Subsonic Flows by Use of a Static Pipe," to be published in 1982, AIAA Journal.

8. Erickson, J. C., Jr., Wittliff, C. E., Padova, C., and Homicz, G. F., Calspan Advanced Technology Center, "Adaptive-Wall Wind-Tunnel Investigation," February 1981, Calspan Report No. RK-6040-A-2.

9. Kraft, E. M. and Parker, R. L., Jr., ARO, Inc., "Experiments for the Reduction of Wind Tunnel Wall Interference by Adaptive-Wall Technology," October 1979, AEDC-TR-79-51 (AD-A076555).

10. Parker, R. L., Jr. and Sickles, W. L., ARO, Inc., "Two-Dimensional Adaptive-Wall Experiments," February 1981, AEDC-TR-80-63 (AD-A095199).

11. Parker, R. L., Jr. and Sickles, W. L., Calspan Field Services, Inc./AEDC Division, "Application of the Adaptive Wall Concept in Three-Dimensions," Journal of Aircraft, Vol. 18, No. 3, March 1981, pp. 176-183.

12. Murman, E. M., Bailey, F. R., and Johnson, M. L., "TSFOIL - A Computer Code for Two-Dimensional Transonic Calculations, Including Wind-Tunnel Wall Effects and Wave Drag Evaluation," March 1975, NASA SP-347.

13. Bodapati, S., Schairer, E., and Davis, S., "Adaptive-Wall Wind-Tunnel Development for Transonic Testing," March 18-20, 1980, AIAA Paper No. 80-0441, AIAA 11th Aerodynamic Testing Conference.

14. Jacocks, J. L., Sinclair, D. W., and Parker, R. L., Jr., ARO, Inc., "Evaluation of the Acoustic and Aerodynamic Characteristics of Several Slot-Baffle Configurations for Transonic Wind Tunnel Walls," January 1981, AEDC-TR-79-59 (AD-A093957).

15. Erickson, J. C., Jr. and Homicz, G. F., "Numerical Simulation of a Segmented-Plenum, Perforated, Adaptive-Wall Wind Tunnel." AIAA Journal, Vol. 20, No. 5, May 1982, pp. 612-623.

16. Levinsky, E. S., McClain, A. A., and Schappelle, R. H., General Dynamics Corp., and Palko, R. L., Clay, T. H., and Lohr, A. D., ARO, Inc., "Semispan Wind Tunnel Test Evaluation of a Computer-Controlled Variable Geometry Wing (Self-Optimizing Flexible Technology Wing Program)," January 1979, AEDC-TR-78-51 (AD-B033600L).

17. Levinsky, E. S., McClain, A. A., Schappelle, R. H., General Dynamics Corp., and Palko, R. L., Clay, T. H., and Crawford, M. A., ARO, Inc., "Wind Tunnel Test of an Improved Computer-Controlled Variable-Geometry Wing (Self-Optimizing Flexible Technology Wing Program)," January 1981, AEDC-TR-80-42 (AD-B054795).

18. Levinsky, E. S., McClain, A. A., and Schappelle, R. H., General Dynamics Corp., "Self Optimizing Flexible Technology Wing Program, Semispan Wind Tunnel Test of a Generalized Variable Geometry Wing Panel Model Design and Aerodynamic Analysis," February 14, 1977, Report ONR-CR212-224-3.

19. Palko, R. L. and Crawford, M. A., Calspan Field Services, Inc./AEDC Division, "Experimental Verification of an Aerodynamic Parameter Optimization Program for Wind Tunnel Testing," November 1981, AEDC-TR-81-23, (AD-A107727).

20. Rosen, J. B., Shell Development Co., "The Gradient Projection Method for Nonlinear Programming. Part I - Linear Constraints," Journal of the Society for Industrial and Applied Mathematics, Vol. 8, No. 1, March 1960, pp. 181-217.

21. Rosen, J. B., Shell Development Co., "The Gradient Projection Method for Nonlinear Programming - Part II, Nonlinear Constraints," Journal of the Society for Industrial and Applied Mathematics, Vol. 9, No. 4, December 1961, pp. 514-532.

22. Fox, R. L., Optimization Methods for Engineering Design, Reading, Massachusetts, Addison-Wesley Publishing Company, 1971.

ACKNOWLEDGMENT

This paper is based, in part, on research carried out at Calspan ATC sponsored by the Office of Naval Research, the Air Force Office of Scientific Research, the Arnold Engineering Development Center, and the National Aeronautics and Space Administration.

ROUND TABLE DISCUSSION
ON
"WALL INTERFERENCE IN WIND TUNNELS"

Dr. Laster

It has been a long day, and we will not keep you much beyond the time that you see in your schedule, but at thia time we will go into a short discussion. To explain the procedure, we are going to have each of our panel chairmen here to make summary comments about their respective seasion and the contents of the papers presented there-in. Then following that, we will open up the floor for comments and questions. Let us start, and I will ask Prof. Young if he would comment on Session 1.

Prof. Young

I am going to begin with a basic question: what is the underlying assumption of any generalized proceas of determining wind tunnel interference? I suppose that it is that the flow around the model in the wind tunnel can be identified with the flow around the model in free air, but at a different incidence hopefully differing little from the one in the tunnel and at a different Mach number, also differing little from the one in the tunnel. What is implied is that the corrections are essentially small and that they can be readily determined as due to overall changes of incidence and speed. However, it is evident, even from the earliest attempts at determining wind tunnel interference, that there is associated with the wind tunnel wall constraints an effective change of shape of the model and we have at some stage to take account of that change of shape. Thus, the simplest of classical approaches for two-dimensional aerofoil measurements showed that there is a change of camber and we therefore sought to introduce a camber correction which hopefully would account for the shape change.

The classical or standard methods of correctiou, which were developed as long ago as about 1930 by Prandtl, Glauert and others, tried to deal with the problem by introducing a system of images of the model in the tunnel walls and treating those images as relatively aimple combinations of sources, line vortices or horseshoe vortices. For a long time, that served our needs very well. As long as we were dealing with relatively low lift coefficients and sub-critical Mach numbers and modela that were not too large in relation to the size of the tunnel, those methods worked. However, in recent years the deaign pressures have been such as to extend our investigations to higher lift coefficienta, Mach numbers in the transonic range and beyond, and with models of complex geometry and about as large as we think the tunnel can accommodate. These pressures have brought to the fore the need to improve our methods of calculating wind tunnel corrections.

There were two papers during the session for which I was chairman which exemplified two kinds of approach that are being adopted to improve on the old standard methods for fixed walls, essentially by improving the processes of determining the effects of the walls or the equivalent images. In the case of the paper by Dr. Ashill and Dr. Weeks, we saw that they were able to produce a perturbation potential flow method relating the corrections to measured velocities or pressures at the walls. However, their paper demonstrated that you could readily run into situations where simple overall correction factors to incidence and Mach number were not adequate. Further, they showed that the shape change effect was by no means negligible but when a simple camber correctiou was introduced it was not very successful . So, one must give further consideration to the change of shape and ask the question how far we can correct for it by any of the standard processes. In the case of the paper by Holt and Hunt, the approach was to use panel methods, i.e. methods of distributed singularities, etc., over the model and tunnel walls and that also showed a fair degree of success in improving on the accuracy of the old approach and in tackling problems of complex wind tunnel installations. But again, one was faced with the question as to how far one can go, what are the limits in incidence, lift, blockage, or Mach number beyond which such methods cease to be reliable? I would like to return to that point again in a moment. Another point that I think is worth drawing your attention to in the paper by Holt and Hunt, waa the need to show in any representation of a complete model in a tunnel of representing the relaxed wakes with both longitudinal and lateral curvature.

We also had papers which drew attention to other sources of error which hitherto had not been given as much thought to as they should be. We had the paper by Barnwall and Sewell which showed that the sidewall boundary layer was an important factor, and one was gratified to aee that they were able to reduce the data they had available by means of a similarity framework to something that looked promising. Perhaps, with an improvement in the assumptions about the velocity distribution in the boundary layer and if account were taken of the effect of the model on the sidewall boundary layers, the accuracy of their correlation could be improved. Also, we had an interesting paper by Aulehla and Eberle which argued that the kind of scale effects that we have all worried about over the years may well be essentially related to what is happening to the wall boundary layera with change of Reynolds number. It was clear from the discussion that some members of the audience were not completely convinced that the effects of the changes of the wall boundary layer as compared with those on the model itself were really as dominant as was suggested by the authors, but I think they convincingly demonstrated that there may well be a significant scale effect arising from changes in the wall boundary layer. I was not convinced that the changes on the model could always be discounted because it aeemed to me that although the boundary layer on the model might be much smaller than that on the tunnel, the changes in the boundary layer with scale effect really reflect themselves as effective changes of shape of the model. These changes need not be very large under certain conditions to produce quite large effects, particularly in transonic flow where you may get aignificant changes of shock position or under high lift conditions where you may get significant changes in separation position. Finally, we had a paper by Elsenaar who compared the results obtained to date from a number of different tunnels on the same model aerofoil. Unfortunately, his results are not yet in print because his presentation was essentially interim. However, he did show a heartening degree of agreement between the various seta of reaults. There were some differences, but most of them could with a little hindsight be explained.

I would like to come back to this general questions of change of shape which I have stressed. It seems to me that you can correct for it along classical lines as long as you can expect the effects of change of shape to be small and linear. However, with increase of incidence, Mach number or model size, the changes of shape must eventually be such that you cannot treat them as small and their aerodynamic effects as simply additive to the basic case equivalent to small changes of incidence, Mach number and camber. At this stage, the changes may be associated with important shock movements or important separation point movements. When that occurs, then I for one am forced to agree from all that I have heard that the adaptive wall approach is the only right one, because then you are developing a wind tunnel for which the corrections are necessarily small, if not zero. Therefore, it may well be that the future will lie with the use of adaptive wind tunnels, not too complicated one hopes, but perhaps in which on can permit small residual corrections for which the methods that we have heard described for fixed walls could still be used. That is something to be settled in the near future. My colleagues here will no doubt have something more to say about that.

Dr. Ohman

Ventilated walls come in many forms and shapes as you've seen; slotted, perforated, or even louvered, if you remember the last paper of the session. We looked in fair detail on the slotted wall characteristics, in fact, I think from Berndt's presentation that we could draw the conclusion that he feels confident we can now design a slot configuration for interference free flow, mind you, at the moment restricted to the non-lifting case. Perhaps we here have a serious contender for the adaptive wall. We learned also about the wall boundary layer development along perforated walls as well as on the side walls in the 2-D facilities, where Chan demonstrated significsnt deformation on the displacement surface due to the pressure field generated by the model. Sidewall suction clearly moderates the deformation of the sidewall boundary layer. Ultimately, I presume, he would like to use a 3-D transonic code, if it ever became available to us, where you could include the sidewall boundary layer displacement surface in the geometric description of the model. This would then give you means for calculating the degree of interference due to the deformation of the boundary layer. We are no doubt struck by the contrast and success already touched upon by Prof. Young of the Barnwell global approach, which ignores these local effects. How do we consolidste these two rather different views? There is definite concensus that wall boundary measurements must be carried out in order to effect reliable wall corrections. The methods for obtaining the corrections may differ, as exemplified in the papers by Smith and Holst, but the net results are close to one another anyhow. A very remarkable result, that I think is worth emphasizing, is the so-called autocorrective properties of the Mokry method, also inherent in the Capelier, Chevallier, Bouniol method from ONERA. The fact that small errors in the reference free stream Mach number are compensated for in the correction procedures is a rather comforting thought. I mention this because there seems to be some concern in some places on how to separate model Reynolds number effects from tunnel wall Reynolds number effects, again Prof. Young did touch upon this. If, as I am led to believe, some of these problems are due to lack of proper tunnel calibration, then I say, "shame on you", go back and do it or otherwise try the Mokry approsch. In the case of the ONERA wind tunnels, we no doubt get the impression from Vaucheret's presentation that the state of the art there is so well developed that pretest corrections can now be worked out, based on the knowledge of the model-sting-test section geometry. That is no doubt one step ahead of the rest of us, a situation that we cannot leave unchallenged. Finally, I would like to pose a question to the audience. If you were to design and build a transonic test section today for a production facility, what wall configuration would you choose?

Dr. Laster

That is an interesting challenge.

Prof. Sears

Going back to the area of the adaptable wall tunnel, I must say that I think that the papers of this afternoons session were very encouraging. I thoroughly agree with the previous speakers that the exact role to be played by the adaptive wall tunnel in the future remains to be determined by experience. I visualize a map where the abscissa is the freestream Mach number and the ordinate is either the blockage or the total lift or some combination thereof. In the upper right-hand part of the diagrsm, we are convinced, for accuracy you have to adapt the walls. Down in the lower left-hand corner of that diagram, or if you are making qualitative measurements - you have the experience of the wall setting of last week, or your last model, or your competitor's model. You don't care, anyway. In between them there will be an area where the wall might be adapted in a simplified fashion. For example, if you run through a range of some parameter or other, you might not have to change the adaptation at all. The operator could make checks as he goes along. Remember that the measurement of these redundant aerodynamic data on the interface, for any wind tunnel (provided the instrumentation is there), is always a precise method of determining whether you have wind tunnel wall interference. You can always turn that on, or you can imagine that the instrumentation is always on line and a red light comes on when it says there is excessive wall interference.

This hardware and software that Mr. Parker described in connection with the AEDC tunnel seems to give us a good view of how the adaptive wall tunnel of the future will be operated and what it will be surrounded by. There will be all those computers that he showed, and software and links and feedback that can all be turned off when they are not needed and can be turned on when they are needed. You can have coarse setting and fine setting and change these as you go along. Maybe the only configuration that will really be fully adapted to the limits of the equipment will be the final cruise configuration. For tests that are purely for development of the flaps and slots of a landing configuration, it wouldn't seem necessary to have all that accuracy.

When I say that, I am aware that the history of the aeronautical world shows that everybody wants everything turned on whenever their test is being run. But maybe the cost of wind tunnel time and power will drive us, and we won't turn on all the goodies until we really have to.

One more word: I think that the development is coming along very well. I think that the hardware/software, that kind of operating equipment, looks good and the exterior flow calculation problem is no problem, the codes are developed and they can be on line and the exterior flow outside the interface can be continually updated with just a delay of seconds. Some questions are still open, of course: whether the tunnel should have deformable solid walls or have variable ventilated walls and what the instrumentation should be; those things we have yet to find out. That is what the development is all about.

Let me just close by telling you what my basic assumption is. My basic assumption is that the important cases that we ought to be worrying about are just exactly the cases where Prof. Young's assumption will not be valid. That is not a disagreement between us; he said essentially the same thing, that the wind tunnel will remain an invaluable and necessary adjunct to the airplane design process, but it will become more and more, as time goes on, an adjunct to numerical simulations of airplane and missile configurations. The operators will, or perhaps they should, use a great deal of sense and wisdom in picking out those configurations that actually are going to be tested in the wind tunnel, or at least are going to be tested with all the fine tuning turned on. Those are exactly those cases because they are three-dimensional, blended wing body configurations. Frankly, I think that they have almost nothing to do with two-dimensional airfoil tests. They are viscous, they have got boundary layers and shock waves. Even if they don't have any shock waves in the cruise configuration, they will have to be tested off-design, so there will be shock waves and they will operate with powered nacelles, obviously. In any such cases, I think it is much too much to hope that anything called a wind tunnel wall correction can be valid.

If this is the correct picture, then, as I say, the customer will not run over great ranges of angle of attack and great ranges of Mach number and great ranges of all the control settings. I think that that is already out of date. They are already in the mode of running selected flight trajectory points. It will be that kind of operation, so that the cost of the time of adapting the wind tunnel won't be as frightening as it may seem today. This super wind tunnel whose accuracy will be demanded by the age of the computational fluid dynamics will be directed towards specific soft points in the computation, in the computer simulations, and then it will be directed along flight trajectory combinations of the parameters.

Dr. Laster

We will spend just a few moments taking comments, although we are a little past our time. I am aware that there are a couple of comments that might be posed from the audience.

Dr. Hackett

I would like to take this opportunity to thank the panel and the authors for some really stimulating papers. It seems that there has been an explosive development since the AGARD meeting in 1975. At that meeting and then again in 1980, we gave papers which told of Lockheed's work on the use of wall pressure signatures for interference estimation. I would like to spend a moment or two giving the latest position on this work. This will be a very brief capsule of a paper which I gave at the AIAA aerodynamic testing meeting in March (Ref. 1). Fig. 'A' is an illustration of the fact that we use wall pressures to size singularities, located about the centerline of the tunnel. The left side shows sources used to solve the blockage problem, the right side shows horseshoe vortices, used to determine tunnel-induced upwash. Some comments were made earlier in this meeting about the difficulty of having to guess where these were and with regard to their geometry. We can find strengths with little difficulty. I would like to make the comment that, in quite extensive investigations, we have found the system to be quite forgiving with regard to geometric assumptions. We used as our baseline the 1975 work on blockage which employed three sources (or sinks) at variable locations. The reason for going to the more recent fixed configuration with more units was purely one of speed. If we make a comparison in the case of blockage between, say, a twelve unit system and the movable three unit system, we find that the agreement is very good indeed, despite the fact that more elements are used in the former case, and they cover a more extended streamwise extent. The sensitivity to element arrangement is not great in the case of blockage.

In the case of the horseshoes, we have looked into the question of sweep and angle of attack, both singly and combined. We find that, in most cases, simple horseshoes suffice. The choice of span is not sensitive; the circulation values tend to restore lift if the span is estimated slightly wrongly. I think that this answer is a comment in an earlier paper about the "pressure signature" method. Of course, what you get in return for having to make geometric assumptions is a method in which there is no need to measure two components of velocity in the tunnel. This contributes significantly to both convenience and speed in use.

Prof. Young earlier asked a question about how far can we go in terms of model loading in a given tunnel. Slide 'B' shows some pressure distributions which help to illustrate the nature of the limitations. The middle rectangle is a side wall, and there is a half roof at the top and a half floor in the lower part of the figure. The situation is one with a jet flapped three-dimensional wing at a C_L of about somewhere between 7 and 8. The outline of the wing is shown in the upper and lower views. What has been done is to match the centerline pressures using the method just described for both blockage and lift. After matching the pressures on the centerline of the wall, the centerline of the roof and the centerline of the floor, the remainder of that field is calculated from the singularities which result.

Quite high suctions may be seen on the roof and quite high pressures on the floor. I want to draw your attention particularly to the right hand side of the middle rectangle (i.e., the aft part of the sidewall) where there is a low pressure region opposite to the vortices. This is caused by the upwash which has become very large at this C_L and represents the only coupling between the lift and the blockage solutions. The time that the method starts to break down, which is somewhere between the 7 or 8 C_L of this particular case, is when the vortex's image in the wall starts to move it vertically in the tunnel and the coupling term gets messed up. In fact, at very high C_L's (i.e., up to about 16) we had to "turn off" the interactive term between the blockage and the angle of attack solutions. So that is one of the places where things start to break down.

Another limitation occurs at low speed when tunnel flow breakdown occurs if suitable floor BLC is not applied. At somewhat greater C_L's than for Figure 2, the jet hit the ground, spread forward, and caused the large floor vortex which characterizes tunnel flow breakdown. We were able to blow hard along the floor tangentially and get rid of the floor vortex. and we were again able to correct our data successfully. All of this is mentioned in Reference 1: I would be glad to arrange for copies to be sent to those interested in further detail. Reference 1: J.E. Hackett, "Living With Solid-Walled Wind Tunnels.", AIAA Paper No. 82-0583, March 1982. (See Figures - Young)

Dr. Laster

Let me mention that if you comment or ask a question, please mention your name and your organization.

Mr. Aulehla

Since Prof. Young referred to the critical comment made by the Canadian fellow yesterday in the discussion of my presentation I realize that there is still some basic misunderstanding. Evidently my presentation was not very clear and I apologize for my Bavarian English.

To-day during lunch time I had a short discussion with the Canadians about the main issue of my presentation. As a result, I think, they would now agree with me. I would like to ask the Canadian speaker whether this is in fact the case.

Dr. Elfstrom

Yes.

Mr. Aulehla

All right, may I then ask those who are interested in this topic to read our paper very carefully. The point I was going to make is as follows: If any variable density wind tunnel of the conventional type has been calibrated only at one total pressure and not over the whole Reynolds number range of the test, then in sensitive measurements spurious Reynolds number trends will inevitably be obtained.

Post script

Note that some conventional variable density tunnels received a high precision calibration over the full Reynolds number range rather late in their operational phase while another group of tunnels still do not have or do not use such a calibration.

Mr. Bucciantini

I have a certain experience in the industrial design of airfoils utilizing various wind tunnel facilities. On the adaptive walls, my thought is that the present procedure of correcting the results in wind tunnel for free flight fail or are poor generally in extreme flow conditions (large separated flows, strong shock waves, at the stall, etc.) Now, these methods with adaptive walls, which aim at improving the present standard of reliability of tunnel data are based on models which are not valid in the conditions where the current procedures fail.

Therefore, I think that much care must be taken into applying in practice this adaptive wall concept. From what I have seen, all the corrections remain to be applied, even if reduced. I think that a lot of work in terms of validation is to be done before transfering this concept in industrial practice. That is my personal consideration on this very fascinating area which is opening. The idea is very clever, but probably in terms of actual possibility, a lot of things must be done before saying that this is a resl step ahead.

Dr. Laster

I believe we just have time for a couple more comments.

Mr. Vayssaire
(Reports on extract from a memoire CNAM Paris 1982) by Fiat - Model Support System Interference in Wind Tunnel by J.-J. Fiat, Avions Manel Dassault - Breguet Aviation, 92210 Saint Cherd France

The panel method is developed to calculate the actual wall interferences in wind tunnels. That method is used to analyze the testing environment and to take into account the various arrangements of model support systems and their effect on the results of wind tunnel tests. Researching sting length to maintain interference levels at reduced values is possible. An example is shown in Fig. 1. A vertical incidence strut is mounted in a circular, solid walls, working-section (soufflerie S5 - C.E.A.T. Toulouse) with arrangements of housing sting support (Fig. 2. Sting angle of attack: $\alpha = 0^o$ and 15^o).

Perturbation velocity components: u, v, w are obtained by the calculation everywhere within the working section (where V_o is the velocity of undisturbed stream). They are used to correct test results.

Some examples are given by Fig. 3 and Fig. 4 - it appears: i) an axial buoyancy force correction on the model due to longitudinal pressure gradient associated to blocksge of rear support bodies, ii) a flow angularity correction due to effective local upwash interference and streamline curvsture.

With a ating length of 0.8 meter, the interference is negligable.

Dr. Laster

I think that we might take one more question.

Dr. McCroskey

An interesting issue brought to light in this Specislists' Meeting is that of REYNOLDS NUMBER EFFECTS ON THE TEST MODEL versus REYNOLDS NUMBER EFFECTS OF THE FACILITY. Our present quandary in this regard csn be illustrated by the seemingly simple question, "What is the lift-curve slope, C_{L_α}, of a conventional two-dimensionsl, symmetrical airfoil at various Reynolds Numbers in subsonic flow?" The question is posed for Mach numbers and angles of attack low enough to preclude both separation and shock waves.

The figure shows test data for the NACA 0012 airfoil assembled from approximately 20 sources. Most of these sources are considered highly respectable and are widely quoted; e.g., the older NACA airfoil tests at low speeds (symbols 2-4), modern NASA results (5, 6), a well-known industrisl facility (10-12), careful NPL and RAE studies (13-15), the AGARD Working Group 04 Data Base (17), etc. The solid squsres represent the ONERA measurements that Mr. Barnwell referred to in Paper No. 3, with and without side-wall boundary layer control. These would seem to represent the extremes of FACILITY REYNOLDS NUMBER EFFECTS that can be attributed to tunnel side-wall boundary layers. The solid dismond represents the Southhampton TSWT results quoted in Paper No. 15 for $M = 0.5$. Clearly the scatter and the data preclude defining the REYNOLDS NUMBER EFFECTS ON THE MODEL to an acceptable level of precision. Could we say that this experimental information would satisfy either

(1) a customer for airfoil data,
(2) a researcher seeking fundamental information, or
(3) a validation of numerical methods?

This rather pessimistic picture is counterbalanced by the new developments, corrections, and techniques that we have seen st this meeting, which when put into practice should increase our confidence in wind tunnel results. Therefore, I would like to challenge the "wall correctors" and the "wall adapters" to define precisely the correct behavior of C_{L_α} vs Re .

Dr. Iaster

Thank you, I think thst is a worthy challenge. We have used much more of our time here than we had allocated to us, so let us declsre the technical portion of this session at an end and we will turn our attention back to our panel chairman, M. Monnerie.

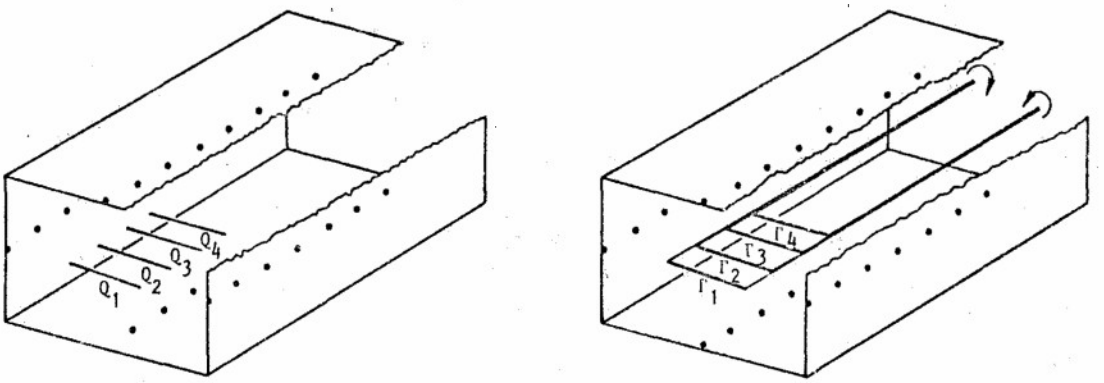
M. Monnerie

(Translated from the French)

Ladies and Gentlemen, these two intensive working daya are now finished and, tsking into account the number of participants and number of comments and questions, we can claim that this meeting was s great success. It is obvious that the quality and the interest of the pspers wss great, and, in that connection also, it has been a great success. This is due to the contributions of lots of people snd I would like to thank sll who took part in the work of this meeting:
- First of all the British ACARD Delegstes who welcomed us here in this very big and impressive Church House building;
- Secondly, as far as the technical part of the business is concerned, the program committee of this meeting, its chairman Dr. Laster, the chairmen and the authors whose joint action has enabled us to define as clearly as possible where we stand with regard to correction or elimination of wall effects;
- Then the Royal Aircrsft Establishment which opened the doors to its highly performing wind tunnel, and organized its visit so that each one could focus his attention on what was of greatest interest for him;
- Also everyone who helped us, Group Captain Hillary, the local coordinator, and his secretary Mrs. Scott, the interpretors, the projectionist, and the engineers who looked after the sound system;
- Finally Mr. Rollins and his secretary Melle Rivault, who did everything to organize this meeting since September 1980 and who deserve our special thanks.

Before ending, I would like to tell you about the program which has been prepared by the FDP: From the 20th to the 22nd of September in Trondheim, Norway, a Symposium on Missile Aerodynsmics. From the 21st to the 25th of March 1983, at the Von Karmen Institute, a special course on the Aerodynamics of Controls. From the 25th of April, a Symposium on Vortex Aerodynamics in the Netherlands. In May 1983, s special course on Subsonic/Transonic Interaction at the VKI and st WPAFB. Finally, during the week of the 26th of September 1983, a Symposium in Turkey on Wind Tunnels and Testing Techniques.

That is all, goodbye, have a good trip home, and I hope to see you at one of the sbove-mentioned activities. The meeting is adjourned.

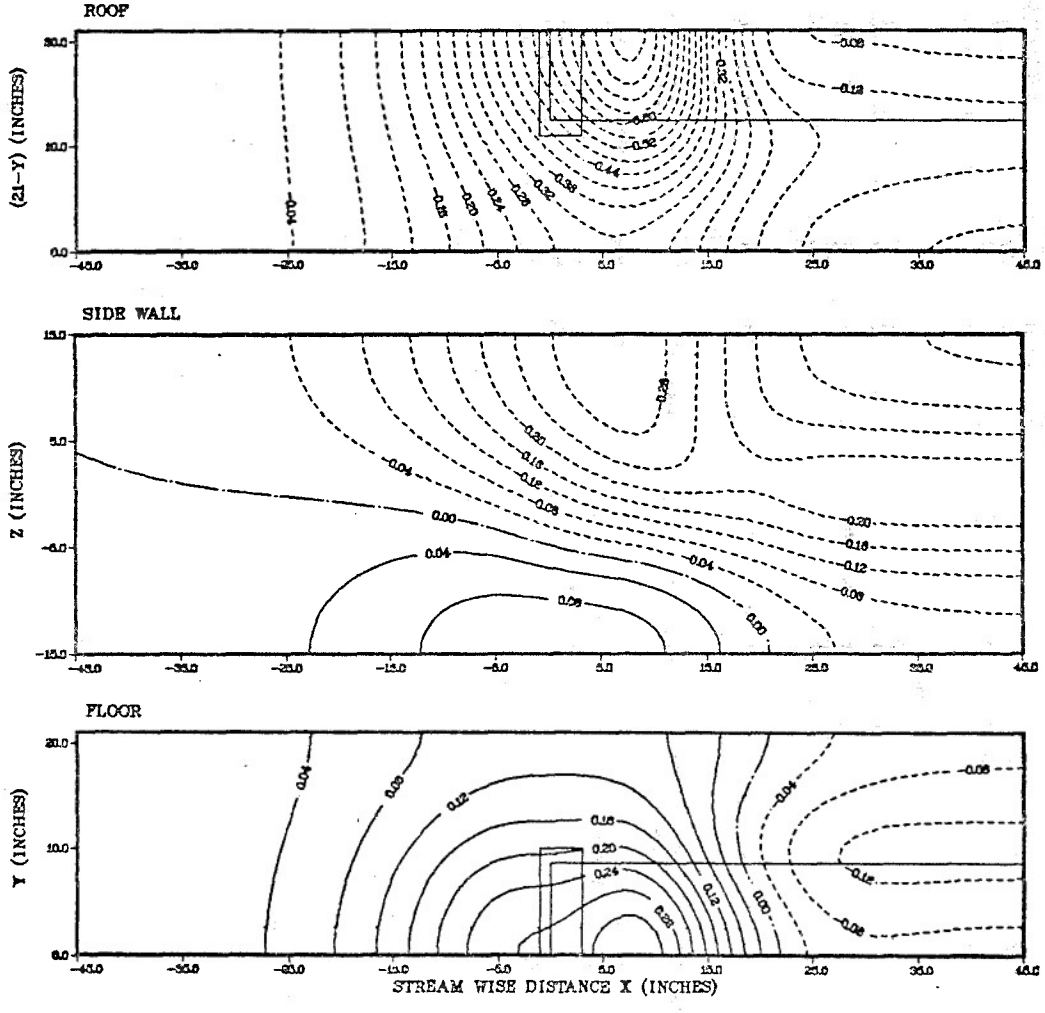


(a) LINE SOURCE ARRANGEMENT

(b) HORSE-SHOE VORTEX ARRANGEMENT

NOTE: SWEEP AND PITCH OF LINE SINGULARITIES MAY BE EMPLOYED

FIGURE A ARRANGEMENT OF SINGULARITIES FOR THE 'WALL PRESSURE SIGNATURE' METHOD *(HACKETT)*



$S/C = 0.0618$

$C_\mu = 2.0$

$C_L = 7.6$

$C_D \approx 2.0$

FIGURE B PRESSURE CONTOURS ON TUNNEL SURFACES UNDER NEAR-BREAKDOWN CONDITIONS *(HACKETT)*

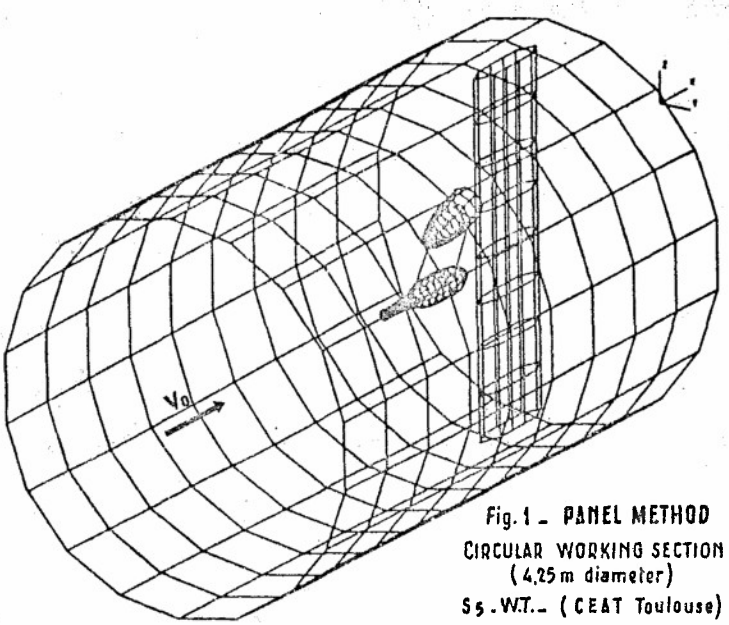


Fig. 1 – PANEL METHOD
CIRCULAR WORKING SECTION
(4,25 m diameter)
S5 . W.T. – (CEAT Toulouse)
with vertical strut + sting
(VAYSSAIRE)

Fig 2 *(VAYSSAIRE)*

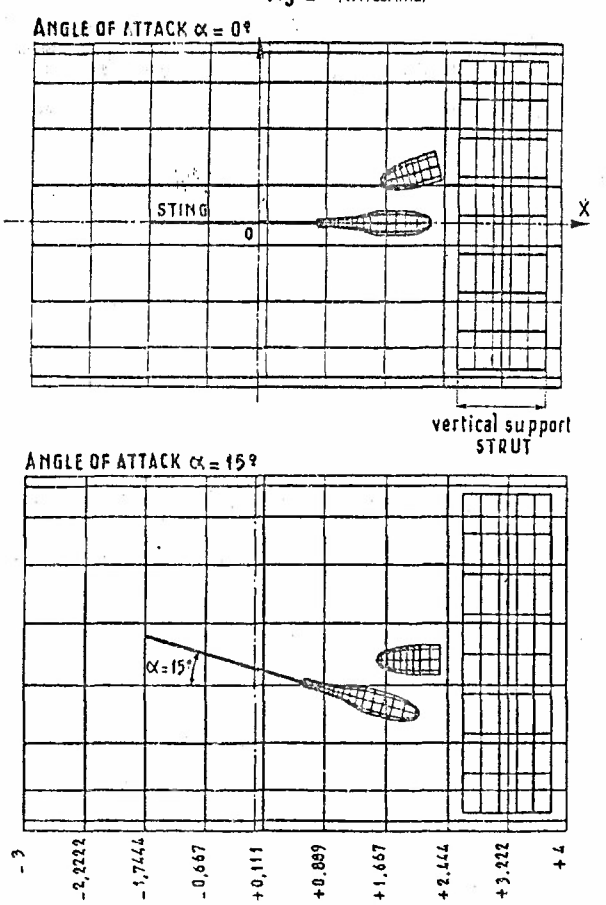


Fig 3 - AXIAL PERTURBATION STREAM VELOCITY INTERFERENCE IN THE AXIAL DIRECTION (along the axis of the W.S.) *(VAYSSAIRE)*

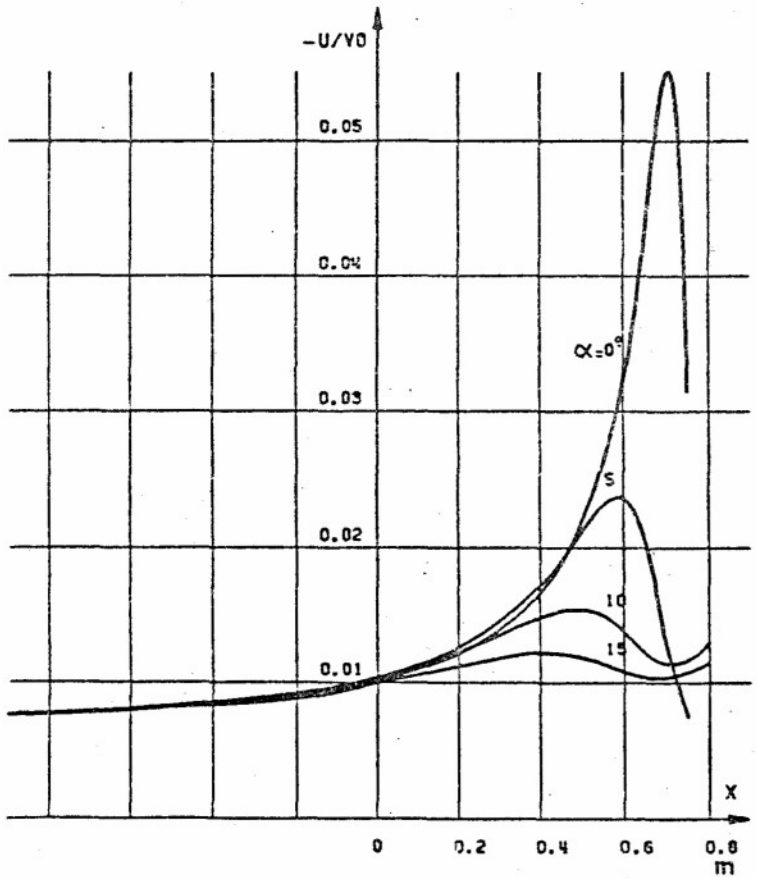
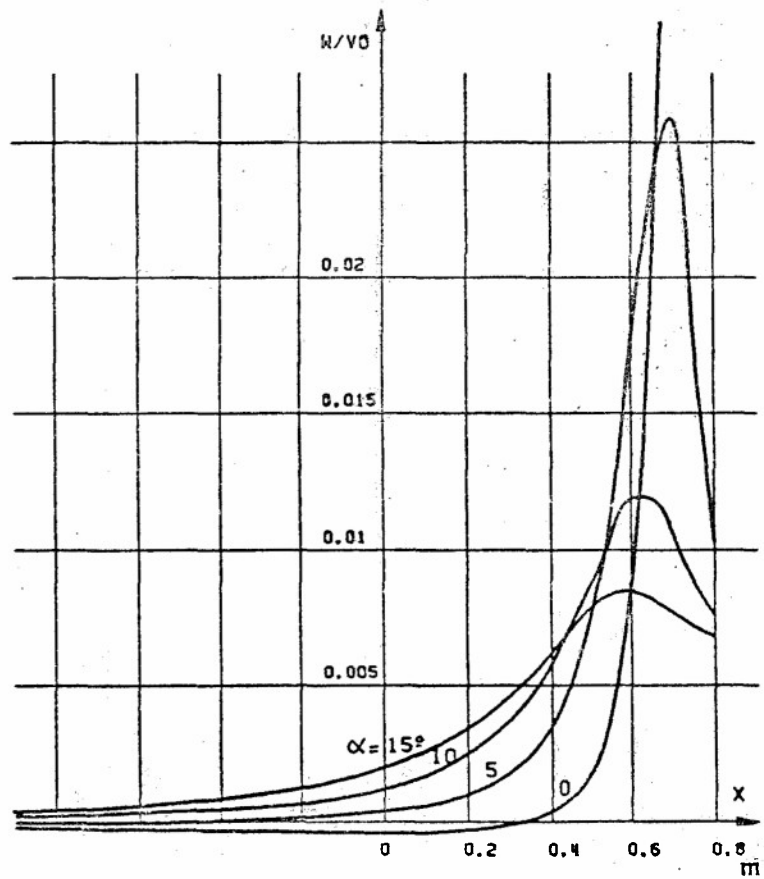
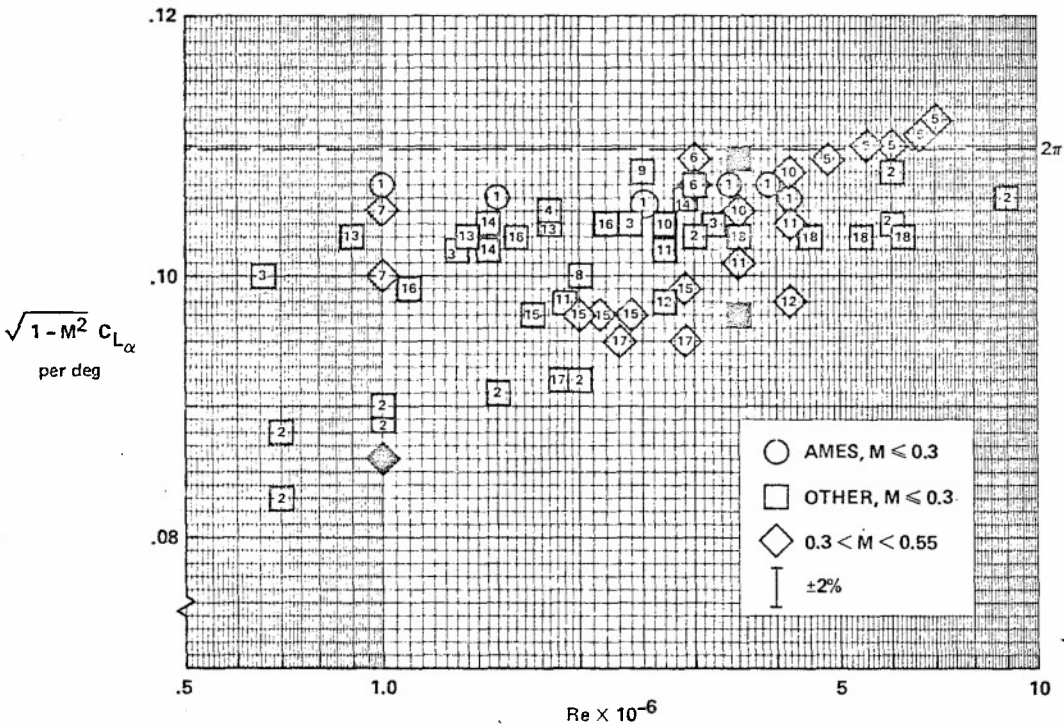


Fig 4 - AXIAL DISTRIBUTION OF THE UPWASH INTERFERENCE (streamline curvature) *(VAYSSAIRE)*



REYNOLDS NO. EFFECTS — MODEL OR FACILITY? *(McCROSKEY)*

LIFT CURVE SLOPE — NACA 0012



Sym.	Source
1	NASA TM 84245
2	NACA TN 1945
3	NACA Report 586
4	NACA TN 3361
5	NASA TMX 73990
6	NASA TM 81927
7	CALSPAN RK-5070-A-3
8	AIAA J. Dec 1974 p 1771
9	NASA TP 1100
10-12	UTRC 8-ft; var. sources
13	RAE TR 68303
14	NPL Aero Rep. 1308
15	ARC CP-1261
16	ONERA Doc. 76 /1157.AN
17	AGARD AR-138
18	NACA TM 1240

REPORT DOCUMENTATION PAGE

1. Recipient's Reference	2. Originator's Reference	3. Further Reference	4. Security Classification of Document
	AGARD-CP-335	ISBN 92-835-0321-X	UNCLASSIFIED

5. Originator Advisory Group for Aerospace Research and Development
North Atlantic Treaty Organization
7 rue Ancelle, 92200 Neuilly sur Seine, France

6. Title
WALL INTERFERENCE IN WIND TUNNELS

7. Presented at
the Fluid Dynamics Panel Specialists' Meeting held at Church House, London SW1, United Kingdom, 19–20 May 1982.

8. Author(s)/Editor(s)	9. Date
Various	September 1982
10. Author's/Editor's Address	**11. Pages**
Various	228

12. Distribution Statement This document is distributed in accordance with AGARD policies and regulations, which are outlined on the Outside Back Covers of all AGARD publications.

13. Keywords/Descriptors

Wind tunnels
Walls
Aerodynamic interference
Aerodynamics
Correction
Subsonic flow
Transonic flow
Reynolds number
Aeroelasticity

14. Abstract

The purpose of the Specialists' Meeting was to bring experimental aerodynamicists together to review and discuss current usage and basic developments for wind tunnel wall corrections. The meeting concentrated upon subsonic and transonic flow wall corrections and included consideration of Reynold's number corrections, wall and support interference, flow quality, and aeroelasticity among others. The meeting was organized into sessions of solid wall, ventilated wall, and adaptive wall wind tunnels and a summarizing Round Table Discussion.

The Specialists' Meeting was sponsored by the Fluid Dynamics Panel of AGARD.

AGARD Conference Proceedings No.335 Advisory Group for Aerospace Research and Development, NATO WALL INTERFERENCE IN WIND TUNNELS Published September 1982 228 pages The purpose of the Specialists' Meeting was to bring experimental aerodynamicists together to review and discuss current usage and basic developments for wind tunnel wall corrections. The meeting concentrated upon subsonic and transonic flow wall corrections and included consideration of Reynold's number corrections, wall and support interference, flow quality, and aeroelasticity among others. The meeting was organized P.T.O.	AGARD-CP-335 Wind tunnels Walls Aerodynamic interference Aerodynamics Correction Subsonic flow Transonic flow Reynolds number Aeroelasticity	AGARD Conference Proceedings No.335 Advisory Group for Aerospace Research and Development, NATO WALL INTERFERENCE IN WIND TUNNELS Published September 1982 228 pages The purpose of the Specialists' Meeting was to bring experimental aerodynamicists together to review and discuss current usage and basic developments for wind tunnel wall corrections. The meeting concentrated upon subsonic and transonic flow wall corrections and included consideration of Reynold's number corrections, wall and support interference, flow quality, and aeroelasticity among others. The meeting was organized P.T.O.	AGARD-CP-335 Wind tunnels Walls Aerodynamic interference Aerodynamics Correction Subsonic flow Transonic flow Reynolds number Aeroelasticity
AGARD Conference Proceedings No.335 Advisory Group for Aerospace Research and Development, NATO WALL INTERFERENCE IN WIND TUNNELS Published September 1982 228 pages The purpose of the Specialists' Meeting was to bring experimental aerodynamicists together to review and discuss current usage and basic developments for wind tunnel wall corrections. The meeting concentrated upon subsonic and transonic flow wall corrections and included consideration of Reynold's number corrections, wall and support interference, flow quality, and aeroelasticity among others. The meeting was organized P.T.O.	AGARD-CP-335 Wind tunnels Walls Aerodynamic interference Aerodynamics Correction Subsonic flow Transonic flow Reynolds number Aeroelasticity	AGARD Conference Proceedings No.335 Advisory Group for Aerospace Research and Development, NATO WALL INTERFERENCE IN WIND TUNNELS Published September 1982 228 pages The purpose of the Specialists' Meeting was to bring experimental aerodynamicists together to review and discuss current usage and basic developments for wind tunnel wall corrections. The meeting concentrated upon subsonic and transonic flow wall corrections and included consideration of Reynold's number corrections, wall and support interference, flow quality, and aeroelasticity among others. The meeting was organized P.T.O.	AGARD-CP-335 Wind tunnels Walls Aerodynamic interference Aerodynamics Correction Subsonic flow Transonic flow Reynolds number Aeroelasticity

into sessions of solid wall, ventilated wall, and adaptive wall wind tunnels and a summarizing Round Table Discussion.

The Specialists' Meeting was sponsored by the Fluid Dynamics Panel of AGARD and was held at Church House, London SW1, United Kingdom, 19–20 May 1982.

ISBN 92-835-0321-X

into sessions of solid wall, ventilated wall, and adaptive wall wind tunnels and a summarizing Round Table Discussion.

The Specialists' Meeting was sponsored by the Fluid Dynamics Panel of AGARD and was held at Church House, London SW1, United Kingdom, 19–20 May 1982.

ISBN 92-835-0321-X

into sessions of solid wall, ventilated wall, and adaptive wall wind tunnels and a summarizing Round Table Discussion.

The Specialists' Meeting was sponsored by the Fluid Dynamics Panel of AGARD and was held at Church House, London SW1, United Kingdom, 19–20 May 1982.

ISBN 92-835-0321-X

into sessions of solid wall, ventilated wall, and adaptive wall wind tunnels and a summarizing Round Table Discussion.

The Specialists' Meeting was sponsored by the Fluid Dynamics Panel of AGARD and was held at Church House, London SW1, United Kingdom, 19–20 May 1982.

ISBN 92-835-0321-X